Physico-chimie d'intérêt astrophysique & Formation et évolution de la matière organique cométaire.

Nicolas Fray

DIPLOME D'HABILITATION A DIRIGER DES RECHERCHES

Physico-Chimie d'intérêt astrophysique
&
Formation et évolution de la matière organique cométaire.

Nicolas FRAY

Soutenue le 5 novembre 2013.

Devant le jury composé de :

○ Jean-Claude Guillemin	Président
○ Thierry Chiavassa	Rapporteur
○ Eric Quirico	Rapporteur
○ Dominique Bockelée-Morvan	Rapportrice
○ Anny-Chantal Levasseur-Regourd	Examinatrice
○ Robert Georges	Examinateur
○ Yves Bénilan	Examinateur

UPEC UNIVERSITÉ PARIS-EST CRÉTEIL | FACULTÉ DES SCIENCES ET TECHNOLOGIE

lisa | Laboratoire Inter-universitaire des Systèmes Atmosphériques

Melencolia I, gravure sur cuivre exécutée par Albrecht Dürer en 1514[1].

[1] Le phénomène à l'intérieur de l'arc-en-ciel serait la grande comète de l'hiver 1513-1514 ou la chute de la météorite d'Ensisheim en 1492, selon les interprétations.

TABLE DES MATIÈRES

Avant-propos.

Ce document a pour objectif de présenter les travaux de recherche que j'ai réalisés depuis la fin de ma thèse soutenue en Octobre 2004. Il regroupe les travaux effectués durant mon stage post-doctoral au LPG[2] (Laboratoire de Planétologie de Grenoble) ainsi que ceux réalisés depuis mon intégration en septembre 2006 au sein du groupe de Physico-Chimie Organique Spatiale du LISA (Laboratoire Interuniversitaire des Systèmes Atmosphériques) en tant que maître de conférences.

J'ai choisi de présenter une sélection des projets auxquels j'ai participé très activement plutôt que l'ensemble des articles auxquels je suis associé. L'introduction présente de manière générale le contexte de mes recherches en physico-chimie d'intérêt astrophysique. J'expose par la suite les trois principaux projets auxquels j'ai participé : i.) la spectroscopie dans l'ultraviolet du vide, ii.) les équilibres solide-gaz à basses températures et iii.) la caractérisation de la matière organique réfractaire contenue dans les comètes. J'introduirai chacun de ces trois thèmes en présentant le contexte astrophysique et les motivations de ces projets. Je développe de manière plus étendue la caractérisation de la matière organique cométaire puisque le développement du projet « OREGOC » (ORigine et Evolution des Glaces et des composés Organiques Cométaires) constitue mon investissement le plus important depuis ma nomination en tant que maître de conférences. Je conclurai part un chapitre de perspectives.

Un curriculum vitae détaillé, incluant les listes exhaustives des publications auxquelles je suis associé, des contrats de recherche que j'ai gérés et des encadrements de stage de recherche, est fourni en annexe. Les articles référencés dans le texte sont rassemblés en fin de document afin d'en faciliter la lecture.

[2] Depuis la création de l'IPAG (Institut de Planétologie et d'Astrophysique de Grenoble) en janvier 2011, le LPG n'existe plus en tant que tel.

1. Introduction.

1.1. Astrochimie et Origines.

De nos jours, l'un des questionnements scientifiques intéressants fortement le grand public est celui qui touche aux origines. Ces origines sont multiples et commencent par l'origine de l'Univers, il y a environ 13,6 milliards d'années. Il ne sera ici question que de l'origine des objets du système solaire externe et de l'origine de la matière organique présente dans certains objets du système solaire et en particulier des comètes.

Les comètes sont vraisemblablement les objets les plus riches du système solaire du point de vue chimique. La molécule la plus abondante dans l'environnement cométaire est l'eau, mais au total de 25 molécules gazeuses ont été détectées dans l'environnement cométaire avec des abondances très diverses (Bockelée-Morvan et al., 2004). Cette diversité en phase gazeuse constitue déjà à elle seule une très grande richesse chimique. De plus, un matériau carboné en phase solide a été mis en évidence grâce aux mesures par spectrométrie de masse in situ réalisées en 1986 dans la coma de 1P/Halley dans les grains cométaires (Kissel et al., 1986b). Certains auteurs estiment que la masse de ce matériau carboné représente de 30 à 50 % de la masse des grains présents dans la coma (Fomenkova, 1999). Les comètes auraient pu apporter sur la Terre primitive une partie de l'eau contenue dans les océans ainsi que des composés organiques qui auraient pu favoriser l'apparition de la vie. La fraction de l'eau terrestre ayant pu être apportée par des comètes a été revue à la hausse récemment. En effet, un rapport D/H dans l'eau cométaire égal à celui de l'eau terrestre a été mesuré dans une comète de la famille de Jupiter (103P/Hartley 2) (Hartogh et al., 2011). De plus, une valeur relativement faible, comparée aux précédentes mesures, du rapport D/H a aussi été mesurée dans une comète de Oort (C/2009 P1 Garradd) (Bockelée-Morvan et al., 2012). Ces nouvelles mesures laisse penser que les comètes auraient pu apporter plus de 10 % de l'eau terrestre qui était la valeur faisant consensus il y a encore quelques années (Hartogh et al., 2011). La nature physico-chimique du matériau carboné présent dans les comètes est encore très mal connue. Sa caractérisation chimique permettrait de mieux connaître les apports exogènes de matière organique qui ont pu avoir lieu sur la Terre primitive et qui aurait pu favoriser l'éclosion de la vie sur Terre.

La chimie atmosphérique en phase gazeuse aurait pu être quant à elle une source endogène de matière organique prébiotique. De nos jours, l'atmosphère de Titan possède toujours une chimie atmosphérique intense conduisant à la formation d'aérosols organiques. L'étude des processus chimiques se déroulant dans l'atmosphère de Titan est donc aussi un sujet d'intérêt pour l'astrochimie.

D'autre part, les noyaux cométaires sont vraisemblablement les objets du système solaire qui ont le moins évolué depuis leur formation. En particulier, les comètes contiennent des espèces hyper-volatiles comme le monoxyde de carbone (CO) et le méthane (CH_4) ce qui montre qu'elles n'ont pas subit de chauffage important depuis leur formation. De plus, quels que soient les mécanismes d'évolution envisagés, ceux-ci n'ont pas d'effet au-delà de quelques dizaines de mètres sous la surface (Stern, 2003) alors même que les noyaux ont des dimensions de l'ordre du kilomètre ou de la dizaine de kilomètres. Les comètes sont donc les objets les plus primitifs du système solaire et c'est pourquoi elles sont considérées comme les « pierres de Rosette » du système solaire. L'étude des comètes nous apporte donc des contraintes sur les conditions qui ont régné dans la nébuleuse primitive et sur la formation du système solaire dans son ensemble.

1.2. Des processus physico-chimiques cométaires à mes travaux de recherche.

Bien que le nombre de noyaux cométaires survolés par des sondes spatiales devienne relativement élevé[3], la majorité des informations chimiques que nous possédons sur les comètes provient de l'étude de l'environnement cométaire. Ces observations sont menées à la fois par des missions spatiales et des télescopes au sol ou en orbite autour de la Terre. Si les missions spatiales permettent de révéler certaines composantes difficilement observables depuis la Terre, comme la phase carbonée réfractaire, certains ions en phase gazeuse ou simplement la surface des noyaux, les observations depuis la Terre permettent l'étude d'un plus grand nombre de comètes et donc la comparaison d'un grand nombre d'objets. Afin de remonter à la nature physico-chimique des noyaux cométaires à partir de notre connaissance de leur environnement, des modèles numériques prenant en compte les différents processus physico-chimiques se déroulant à la surface et dans la coma doivent être développés. La paramétrisation de ces modèles repose en grande partie sur des mesures en laboratoire des grandeurs physico-chimiques pertinentes. La majorité de mon travail traite de ces mesures en laboratoire.

La figure 1 montre de manière simplifiée quelques processus physico-chimiques ayant lieu à la surface et dans l'environnement des noyaux cométaires[4]. Ce schéma a été publié dans l'article suivant :

> Cottin H., and **Fray N.** (2008) Distributed sources in comets. *Space Science Reviews,* 138(1-4), 179-197.

[3] Les 6 noyaux cométaires qui ont été survolés par des missions spatiales sont : 1P/Halley, 26P/Grigg-Skjellerup, 19P/Borelly, 81P/Wild 2, 9P/Tempel 1 et 103P/Hartley 2.

[4] Un schéma plus complet et quasi-exhaustif peut être trouvé dans Rodgers et al. (2004).

Il nous avait permis de définir de manière précise le phénomène de source distribuée. L'intérêt de ce schéma dans ce document est qu'il permet de synthétiser l'ensemble des travaux de recherche que je vais développer dans les pages suivantes.

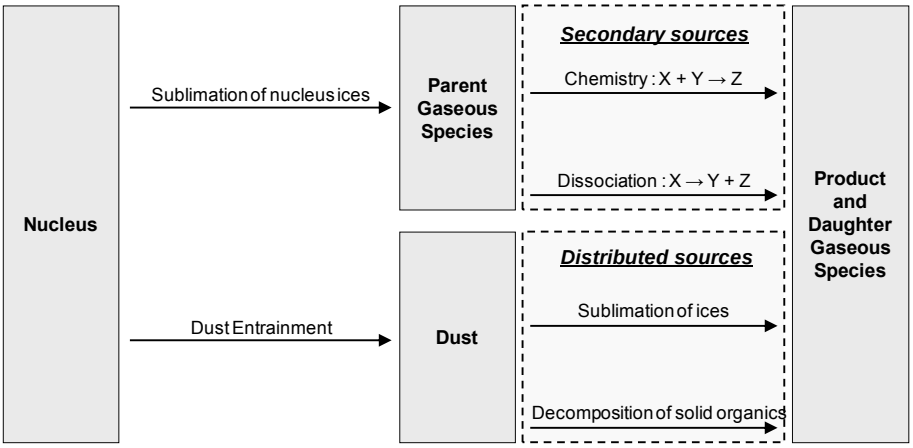

Figure 1 : Schéma simplifié montrant quelques-uns des processus physico-chimiques ayant lieu à la surface ou dans l'environnement des noyaux cométaires. Ce schéma a été publié dans Cottin & Fray (2008) et nous a servi a donner une définition précise du phénomène de source distribuée.

En effet dans ce document, j'ai choisi de présenter 3 thématiques différentes :

- La mesure quantitative de spectres d'absorption dans le domaine de l'ultraviolet moyen et du vide. Ces données spectrales sont nécessaires aux calculs des taux de photodissociation et donc à la modélisation des processus photochimiques ayant lieu en phase gazeuse dans les environnements cométaires.
- Les équilibres solide-gaz des glaces pures et des clathrates d'hydrates. Ce travail s'applique évidemment à la sublimation des glaces se produisant à la surface et à la sous-surface des noyaux cométaires mais aussi à la sublimation des glaces contenues dans les grains éjectés et qui se déroule vraisemblablement dans la coma interne.
- La caractérisation de la matière organique de haut poids moléculaire contenue dans les comètes. Les développements actuels, liés à la fois à des expérimentations de laboratoire et à la préparation des observations de l'instrument spatial COSIMA[5], nous permettront de mieux contraindre la nature physico-chimique de la phase carbonée réfractaire contenue dans les comètes ainsi que sa contribution à la phase gazeuse.

Bien que les travaux que je vais présenter puissent tous avoir une application cométaire, j'ai choisi de les présenter de manière indépendante dans trois chapitres séparés traitant des trois thématiques énoncées précédemment. Chaque chapitre débutera par une description du contexte astrophysique et des motivations des travaux que j'ai effectués. Cette démarche me permet de présenter certains travaux dans un cadre plus large que la seule étude des comètes. En effet, les spectres dans le domaine de l'ultraviolet ou les équilibres solide-gaz sont des données intrinsèques à chaque molécule qui peuvent être appliquées à de très nombreux environnements astrophysiques. Il est en effet notable que

[5] COSIMA (COmetary Secondary Ion Mass Analyzer) est une spectromètre de masse dédié à l'étude des grains cométaires situé sur l'orbiteur de la mission Rosetta.

les objectifs initiaux de mes travaux concernant la spectroscopie UV et les équilibres solide-gaz à basses températures étaient, respectivement, l'étude de l'atmosphère de Titan et des processus se déroulant lors du refroidissement de la nébuleuse solaire.

2. La spectroscopie VUV de molécules gazeuses.

2.1. Contexte et motivations du projet.

L'équipe de Physico-Chimie Organique Spatiale du LISA possède depuis de très nombreuses années un monochromateur fonctionnant dans l'ultraviolet moyen (180-300 nm) couplé à une cellule thermostatée pouvant être refroidie. Ce dispositif a permis de mesurer la variation avec la température des sections efficaces d'absorption de nombreux composés présents, ou suspectés d'être présents, dans l'atmosphère de Titan. Yves Bénilan avait depuis de nombreuses années le projet d'effectuer ce type de mesure à des longueurs d'onde inférieures à 180 nm. L'oxygène moléculaire présent dans l'atmosphère terrestre absorbant à ces longueurs d'onde, de telles mesures nécessitent l'emploi de système sous vide. En 2006, lors de la publication du premier article (Shemansky et al., 2005) présentant les résultats de UVIS (UltraViolet Imaging Spectrograph, spectromètre UV à bord de la sonde Cassini couvrant une gamme de 56 nm à 190 nm) concernant l'atmosphère de Titan, il est devenu évident que les sections efficaces d'absorption de certains composés présents ou suspectés dans l'atmosphère de Titan devaient être mesurées avec une résolution spectrale égale ou meilleure à celle du spectromètre UVIS, en s'affranchissant des effets de saturation et à des températures les plus représentatives possibles de celles rencontrées dans la haute atmosphère de Titan. En effet, certaines structures dans les spectres observés ne pouvaient pas être reproduites (voir la figure 2 de Shemansky et al., 2005) et, dans les « Supporting Online Materials », on pouvait lire « In particular, resonance features in the observed data obviously attributable to species such as C_2H_2, C_4H_2, and HCN show much deeper absorption in the UVIS data than can be produced in the synthesis using the experimental cross sections. This is an indicator that the laboratory experimental measurements contained inadequate spectral resolution in these regions resulting in cross sections determined from saturated data» (Shemansky et al., 2005).

Outre le besoin de nouvelles mesures expérimentales pour l'interprétation des observations, la mesure des sections efficaces dans le domaine de l'ultraviolet du vide présente aussi un intérêt notable pour la photochimie. En effet, ces sections efficaces

d'absorption permettent le calcul du taux de photodissociation et du transfert radiatif dans les atmosphères. Les sections efficaces utilisées pour le calcul des taux de photodissociation dans les modèles photochimiques en phase gazeuse de l'atmosphère de Titan peuvent être trouvées dans Hébrard et al. (2006), concernant les atmosphères cométaires, on pourra se référer à Huebner et al. (1992) et à Crovisier (1994).

2.2 Conception et méthodologie du projet.

Ne disposant pas au laboratoire d'un monochromateur sous vide pouvant atteindre une résolution de l'ordre de 0.05 nm, les mesures ont été réalisées grâce à des monochromateurs installés sur des synchrotrons. La plupart des mesures ont été réalisées à BESSY[6] (synchrotron localisé aux environs de Berlin) sur deux lignes de lumière différentes : la première (U125/2) est équipée d'un monochromateur de 10 m de focale et d'un dispositif interne de calibration en longueur d'onde tandis que la seconde est constituée d'un monochromateur de 3 m (DIP 12-1B). Une campagne de mesure a aussi été réalisée sur la ligne DESIRS[7] du synchrotron SOLEIL[8] (synchrotron localisé sur le plateau de Saclay, au sud-ouest de Paris).

Les premiers tests effectués grâce à la cellule d'absorption disponible au LISA et ayant un parcours optique de 1 m ont montré que cette cellule n'était pas adaptée aux mesures des sections efficaces élevées. En effet, si on considère une section efficace de 5×10^{-16} cm^2 et un parcours optique de 1 m, une transmission de 10 % est atteinte pour une pression d'environ 2 µbars (densité d'environ 5×10^{13} molécules.cm^{-3} à température ambiante). Afin de se placer dans des gammes de pression facilement mesurables avec précision, une nouvelle cellule présentant un parcours optique de 12 cm a été développée. La température de celle-ci est contrôlée grâce à un flux d'azote gazeux provenant d'un tanker d'azote liquide et dont le débit est contrôlée par une vanne cryogénique pilotée par une boucle de rétroaction de type PID.

De nombreuses sections efficaces, ainsi que leur dépendance en température, ont été mesurées récemment par d'autres groupes. Néanmoins, ces mesures récentes ne concernent que des molécules disponibles dans le commerce, comme le dioxyde de carbone - CO_2 (Yoshino et al., 1996), le méthane - CH_4 (Chen and Wu, 2004), l'acétylène - C_2H_2 (Wu et al., 2001), l'éthylène - C_2H_4 (Wu et al., 2004) ou l'éthane - C_2H_6 (Chen and Wu, 2004). Ayant des compétences en synthèse chimique[9] et en purification d'échantillons, nous nous sommes concentrer sur les molécules non disponibles dans le commerce.

Afin de vérifier l'absence de saturation dans nos mesures, nous avons acquis de nombreux spectres à des pressions différentes afin de bien vérifier la linéarité de l'absorption avec la pression.

---

[6] BESSY : Berliner Elektronenspeicherring-Gesellschaft für Synchrotronstrahlung.

[7] DESIRS : Dichroïsme Et Spectroscopie par Interaction avec le Rayonnement Synchrotron

[8] SOLEIL : Source Optimisée de Lumière d'Énergie Intermédiaire du LURE.

[9] La plupart des synthèses ont été effectuées au LISA, d'autres, en particulier celles de C_4N_2 et de HC_5N, ont été effectuées par Jean-Claude Guillemin.

Mon implication dans ce projet est importante puisque j'ai participé à la quasi-intégralité des campagnes de mesures sur synchrotron (plus d'une dizaine) et j'ai activement participé à la réduction des données, c'est-à-dire le calcul d'un spectre unique à partir de l'ensemble des données expérimentales.

2.3. Résultats obtenus.

Nous avons rapidement obtenus des résultats concernant le diacétylène (C_4H_2) et le cyanoacétylène (HC_3N) couvrant une très large gamme de longueurs d'onde (de 80 à 220 nm) et une gamme de température la plus large possible (Figure 2). Ces mesures ont notamment montré que la structure d'absorption observée à 144.5 nm, mais qui n'était pas correctement simulée dans l'article original de Shemansky et al. (2005), était due à C_4H_2.

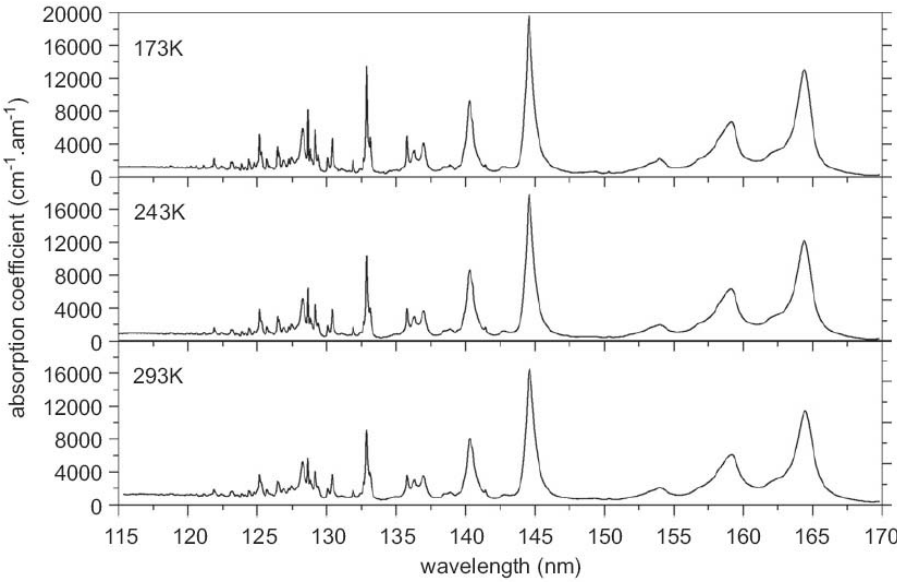

Figure 2 : Coefficient d'absorption du diacétylène (C_4H_2) de 115 à 170 nm en fonction de la longueur d'onde et à trois températures différentes : 173, 243 et 293 K (Ferradaz et al., 2009).

Nous nous sommes aussi intéressés à la spectroscopie VUV du cyanodiacétylène (HC_5N). En effet, la présence de ce composé dans l'atmosphère Titan est suspectée (Coll et al., 1995; De Vanssay et al., 1995) et son spectre VUV était totalement inconnu. Ces mesures nous ont en particulier permis de déterminer une limite supérieure d'abondance dans la haute atmosphère de Titan (Fray et al., 2010).

L'ensemble des données concernant C_4H_2, HC_3N et HC_5N ont été publiées dans les deux articles suivants :

> Ferradaz T., Bénilan Y., **Fray N.**, Jolly A., Schwell M., Gazeau M.-C., Jochims H.-W. and Guillemin J.-C. (2009) Temperature dependant photoabsorption cross sections of cyanoacetylene and diacetylene in the mid- and vacuum-UV: Application to Titan's Atmosphere. Planetary and Space Science, 57(1), 10-22.

et

Fray N., Bénilan Y., Gazeau M.-C., Jolly A., Schwell M., Arzoumanian E., Ferradaz T., Es-Sebbar E. And Guillemin J.-C. (2010) Temperature-dependant photoabsorption cros-section of cyanoacetylene in the vacuum UV. Journal of Geophysical Research (Planets), 115, E06010

D'autre part, nous avons aussi mesuré les sections efficaces d'absorption de l'acide cyanhydrique (HCN), du cyanogène (C_2N_2) et dicyanoacétylène (C_4N_2) pour plusieurs températures. Ces données devraient être publiées prochainement. Concernant HCN, nous avons constaté que les sections efficaces mesurées par Nuth & Glicker (1982), et qui sont couramment utilisées pour calculer le taux de photodissociation de HCN, sont plus élevées que nos mesures (Figure 3). En particulier, la section efficace à 121.6 nm (longueur d'onde de la raie Lyman α de l'hydrogène atomique) est surestimée d'au moins 20 %. Cette observation constitue un cas particulier puisque dans le cas des autres molécules nous avons au contraire montré que certaines données étaient saturées et que les sections efficaces d'absorption étaient donc trop faibles.

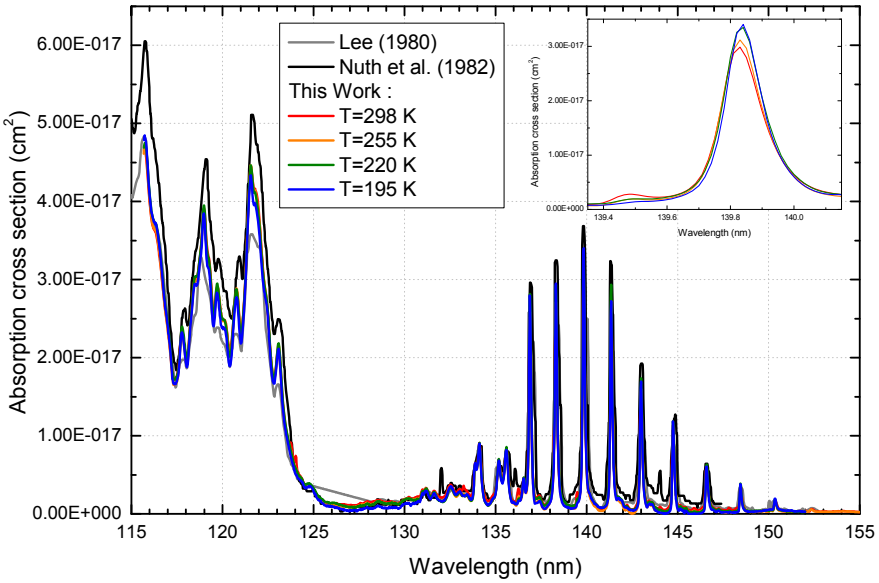

Figure 3 : Sections efficaces d'absorption de HCN en fonction de la longueur d'onde pour différentes températures : 195, 220, 250 et 298 K. Nos mesures sont superposées à celles réalisées par Lee (1980) et Nuth & Glicker (1982).

Il faut noter que les sections efficaces d'absorption de C_4H_2, HC_3N et HCN que nous avons mesurées à basses températures ont été utilisées pour traiter les observations effectuées par UVIS et ont donc permis in-fine de déterminer les densités volumiques de ces trois espèces dans l'atmosphère de Titan pour des altitudes comprises entre 500 et 1000 km (Koskinen et al., 2011).

2.4 De l'atmosphère froide de Titan vers les atmosphères des Jupiters chauds.

La connaissance des sections efficaces dans le domaine de l'ultraviolet du vide est nécessaire aux modèles photochimiques des atmosphères. Aussi, nous avons été contactés dès 2009, par Franck Selsis et Michel Dobrijevic du LAB (Laboratoire d'Astrophysique de Bordeaux) afin de mesurer des sections efficaces dans le domaine VUV à des températures

élevées et représentatives de celles rencontrées dans les atmosphères des Jupiters chauds. En effet, les sections efficaces actuellement utilisées dans les modèles photochimiques sont souvent celles mesurées à température ambiante. Nous avons donc développé un nouveau dispositif construit autour d'un four permettant d'atteindre une température de 1300°C. Je me suis en particulier impliqué dans la conception d'une cellule d'absorption capable de supporter des températures supérieures à 1000°C sans déformation mécanique. La soudure de brides ultra-vide sur un tube en Kanthal (alliage fer-chrome-aluminium développé spécifiquement pour des applications à très hautes températures) s'est révélée être un véritable challenge.

Nous avons donc mesuré les sections efficaces du dioxyde de carbone (CO_2) pour des températures variant de la température ambiante jusqu'à 800 K. Nous avons utilisé à la fois un rayonnement synchrotron pour les mesures aux longueurs d'onde inférieures à 200 nm et le spectromètre disponible au LISA les mesures aux plus grandes longueurs d'onde. Nous avons montré que les sections efficaces pour des longueurs d'onde supérieures à 190 nm augmentent de plus de deux ordres de grandeur lorsque la température augmente de 300 à 800 K. La photodissociation du CO_2 est donc plus rapide aux hautes températures qu'à la température ambiante. D'autre part, le transfert radiatif dans les hautes couches des atmosphères étant différent lorsque les sections efficaces à chauds sont prises en compte, ceci à un impact sur la photochimie d'autres molécules telles l'ammoniac (NH_3) et le monoxyde de carbone (CO). Ces résultats ont été publiés très récemment dans l'article suivant :

> Venot O., **Fray N.**, Bénilan Y., Gazeau M.-C., Hébrard E., Larcher G., Schwell M., Dobrijevic M. and Selsis F. (2013) High-temperature measurements of VUV absorption cross sections of CO2 and application to exoplanets. Astronomy & Astrophysics, 551, A131

2.5. Perspectives.

Les mesures de spectroscopie dans le domaine de l'ultraviolet seront poursuivies. Nous envisageons en particulier de mesurer les sections efficaces de l'ammoniac (NH_3) à hautes températures afin d'améliorer la représentativité des modèles photochimiques des atmosphères des Jupiters chauds. D'autre part, nous avons été récemment sollicités pour mesurer les sections efficaces du dioxyde de carbone (CO_2) à très basses températures. Ces mesures auront, entres autres, pour objectif d'améliorer le traitement de données acquises par SPICAM (spectromètre UV à bord de Mars-Express) et concernant la haute atmosphère de Mars. En effet, les données à plus basses températures concernant le CO_2 ont été effectuées à 195 K (Yoshino et al., 1996) alors que la température dans les hautes atmosphères de Mars est plus basse. D'autre part, une étude préliminaire sur le taux de photodissociation de HCN et son impact sur la chimie dans l'environnement cométaire a été initiée.

3. Les équilibres thermodynamiques des glaces pures et des clathrates d'hydrates à basses températures.

3.1. Contexte et motivations du projet.

Les clathrates d'hydrates sont des solides cristallins majoritairement constitués de molécules d'eau liées entre elles par des liaisons hydrogènes et formant des cavités. Des molécules, comme le méthane, peuvent être piégées dans ces cavités. La présence des clathrates d'hydrates dans les différents objets du système solaire a été proposée depuis de nombreuses années (Miller, 1961)[10]. D'autre part, il a été montré que la formation de clathrates d'hydrates est possible, d'un point de vue thermodynamique, dans les grains glacés durant le refroidissement de la nébuleuse solaire (Lunine and Stevenson, 1985). Ces auteurs avaient prédit que la formation de clathrates d'hydrates dans la nébuleuse devait entraîner un enrichissement en gaz rares dans l'atmosphère de Jupiter par rapport aux abondances observées dans le Soleil. Cet enrichissement a été mis en évidence, une dizaine d'années plus tard, grâce au spectromètre de masse de la sonde atmosphérique de la mission Galileo (Mahaffy et al., 2000). Suite à cette mesure, de nombreux modèles cherchant à expliquer de manière quantitative ces enrichissements ont été développés (Gautier et al., 2001). Néanmoins, les mesures expérimentales concernant l'équilibre thermodynamique entre les clathrates d'hydrates, la glace d'eau et le gaz[11] ont été effectuées pour des températures et des pressions beaucoup plus élevées que celles auxquelles les clathrates d'hydrates pourraient se former dans la nébuleuse solaire (Iro et al., 2003 ; Hersant et al., 2004). Les modèles astrophysiques reposent donc sur des extrapolations à très basses températures.

[10] Il s'agit bien de Stanley Miller, beaucoup plus connu pour ses travaux de chimie prébiotique que pour son intérêt aux clathrates d'hydrates.

[11] Cet équilibre est communément appelé l'équilibre « H-I-V » pour Hydrates – Ice – Vapor.

La plupart des données expérimentales concernant l'équilibre des clathrates d'hydrates avec la glace d'eau et un gaz ont été compilées dans les articles suivants : Lunine & Stevenson (1985), Yoon et al. (2002 & 2004) et Sloan & Koh (2007). De plus, de nombreuses données sont aussi accessibles sous forme tabulées sur un site du NIST : http://gashydrates.nist.gov/HydrateViewer/

Afin de valider les lois utilisées dans les modèles, de nouvelles mesures expérimentales s'imposaient. J'ai débuté ce travail lors de mon post-doctorat au LPG. J'ai tout d'abord conçu, avec l'aide de Bernard Schmitt et Olivier Brissaud, le dispositif expérimental permettant ce type de mesure. J'ai ensuite mis au point, après de nombreux tests, le protocole expérimental permettant la mesure de la pression d'équilibre des clathrates d'hydrates à une température donnée. Suite à ma nomination en tant que maître de conférences au LISA en Octobre 2006, j'ai quitté le LPG au bout de seulement 1 an de post-doctorat sans avoir pu finaliser le travail commencé. Je suis donc retourné au LPG deux fois sur des missions de longue durée afin de finaliser mon travail puis de former à l'utilisation du dispositif expérimental Ulysse Marboeuf qui m'a succédé en tant que post-doctorant sur cette thématique.

3.2. L'équilibre de sublimation-condensation des glaces pures.

En parallèle du développement du système expérimental, j'ai débuté un travail bibliographique sur l'équilibre de sublimation-condensation des glaces pures. L'objectif initial était de définir les conditions expérimentales dans lesquelles les gaz pourraient former des clathrates d'hydrates sans se condenser sous forme de glaces. Rapidement, je me suis aperçu que certaines lois utilisées dans les modèles astrophysiques étaient imprécises voir fausses. L'objectif de ce travail a donc évolué pour finalement aboutir à une large compilation de données expérimentales permettant de proposer à l'ensemble de la communauté astrophysique les lois de sublimation qui nous semblent les plus précises possibles. Ce travail a été publié dans l'article suivant :

> **Fray N.** and Schmitt B. (2009) Sublimation of molecules of astrophysical interest. A bibliographic review. Planetary and Space Science, 57(14-15), 2053-2080.

Le cas le plus problématique est celui du monoxyde de carbone (CO) pour lequel la loi de sublimation utilisée dans de nombreux modèles cométaires est en fait une extrapolation à basses températures de l'équilibre vaporisation-liquéfaction (Figure 4).

J'ai surtout montré que la prise en compte de la variation avec la température de l'enthalpie de sublimation, qui peut être calculée grâce à la connaissance des capacités calorifiques des phases solide et gazeuses, permet d'effectuer des extrapolations très précises à basses températures. En particulier dans le cas du dioxyde de carbone (CO_2), j'ai montré qu'il est possible d'extrapoler les mesures de Giauque & Egan (1937) réalisées pour des pressions supérieures à 10^{-2} bar, jusqu'à une pression de 10^{-13} bar, c'est à dire sur 11 ordres de grandeur, sans erreur systématique et avec une précision uniquement limitée par la dispersion des mesures expérimentales aux plus basses pressions (voir la Figure 1 de Fray & Schmitt, 2009).

En résumé, j'ai recherché les données thermodynamiques en relation avec l'équilibre de sublimation-condensation pour 53 molécules. J'ai réussi à compilé 1842 mesures

expérimentales de pression de sublimation pour 30 molécules différentes et pour 27 d'entres elles, j'ai proposé des lois polynomiales qui me semblent les plus précises possibles. Celles-ci ont vocation d'être utilisées dans les modèles astrophysiques prenant en compte les processus de sublimation ou de condensation. D'autre part, en conclusion, j'ai aussi donné la liste des molécules dont lesquelles la gamme de mesure des pressions de sublimation pourraient être étendue. La figure 5 présente une synthèse de ce travail.

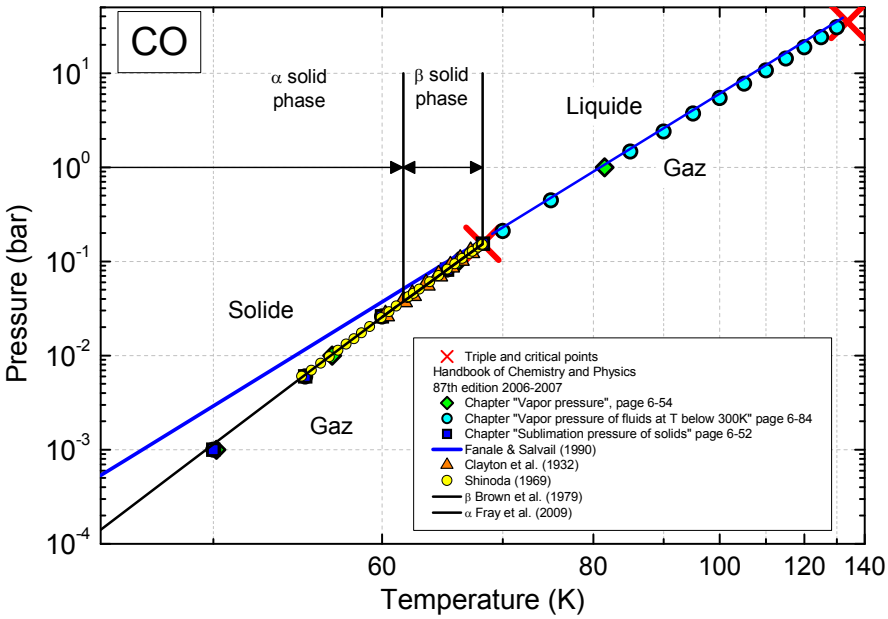

Figure 4 : Diagramme de phase du monoxyde de carbone (CO). Les deux croix rouges représentent les points triple et critique. Les points verts, bleus clairs et bleus foncés représentent les données extraites du « Hanbook of Chemistry and Physics » (Lide, 2007) alors que les points jaunes et oranges représentent les données expérimentales de Shinoda (1969) et Clayton & Giauque (1932). La droite bleue est la loi de « sublimation » proposée par Fanale & Salvail (1990), utilisée dans de nombreux modéles traitant de l'évolution des noyaux cométaires et dont l'usage est recommandé par Prialnik et al. (2004). Il est évident que cette loi est une extrapolation à basses températures de l'équilibre de liquéfaction-vaporisation.

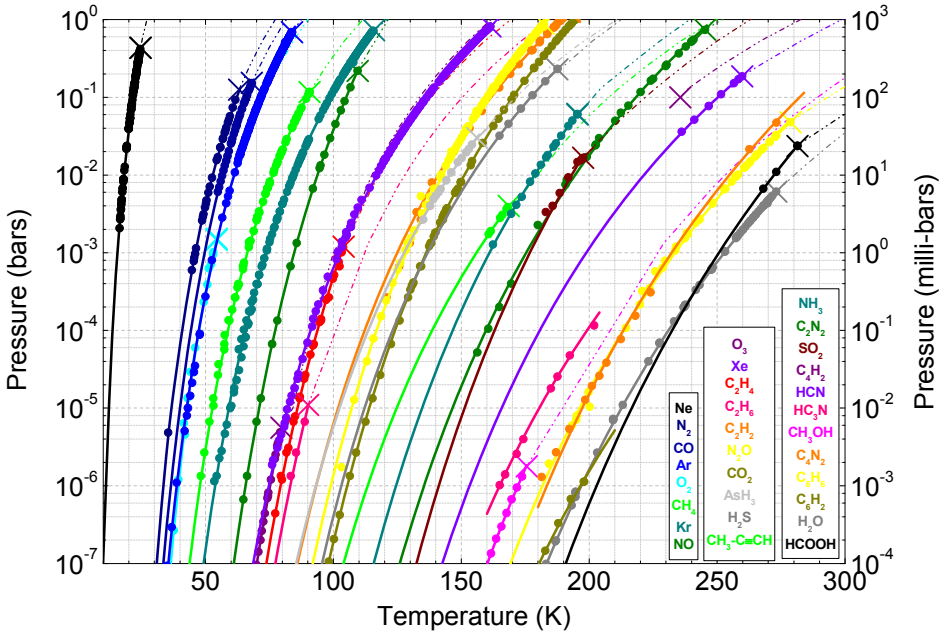

Figure 5 : Synthèse présentant les lois de sublimation pour 30 molécules.

3.3. L'équilibre thermodynamique des clathrates d'hydrates.

L'équilibre des clathrates d'hydrates de CO_2 était déjà bien connu avant le début de notre étude, mais surtout les pressions d'équilibres mesurées par différents auteurs présentaient un bon accord (voir la figure 5 de Fray et al. (2010)). L'objectif principal de nos mesures concernant les clathrates d'hydrates de CO_2 était donc la qualification du dispositif expérimental et du protocole de mesure. L'accord avec les mesures précédentes s'étant révélé satisfaisant (±2% d'erreurs relatives), nous avons poursuivi des mesures concernant les clathrates d'hydrates de Xénon (Xe), de méthane (CH_4), d'acétylène (C_2H_2), d'éthane (C_2H_6) et de krypton (Kr).

L'ensemble des données thermodynamiques sur les clathrates d'hydrates que nous avons mesurées ont été synthétisées sur la figure 6. La figure 7 permet de comparer les lois précédemment utilisées dans les modèles astrophysiques avec celles que nous avons proposées. Ces données ont été publiées dans les deux articles suivants :

> **Fray N.**, Marboeuf U., Brissaud O. And Schmitt B. (2010) Equilibrium data of methane, carbon dioxide and xenon clathrate hydrates below the freezing point of water. Applications to astrophysical environments. *Journal of Chemical and Engineering Data*, 55(11), 5101-5108.

et

> Marboeuf U., **Fray N.**, Brissaud O., Schmitt B., Bockelée-Morvan D. and Gautier D. (2012) Equilibrium pressure of ethane, acetylene and krypton clathrate hydrates below the freezing point of water. *Journal of Chemical and Engineering Data*, 57(12), 3408-3415

Les mesures ont permis d'étendre les gammes de température et de pression sur lesquelles des mesures expérimentales ont été réalisées. C'est en particulier le cas pour l'acétylène (C_2H_2), l'éthane (C_2H_6) et le xénon (Xe). Cette extension de la gamme de mesure permet de proposer des lois d'extrapolations à basses températures qui nous semblent plus fiables. Néanmoins, l'implication principale de nos travaux est la remise en cause des lois utilisées pour l'équilibre des clathrates d'hydrates des gaz rares (Figure 7) qui étaient basées sur une unique publication (Barrer and Edge, 1967). En effet, les mesures de Barrer & Edge (1967) concernant le xénon (Xe) et le krypton (Kr) présentent systématiquement une déviation importante lorsqu'elles sont comparées à nos propres mesures. Dans le cas du krypton, la pente de nos mesures est en très bon accord avec celle mesurée récemment par Jin et al. (2011) ce qui tend à confirmer nos mesures. D'après les lois que nous venons de proposer, à une pression donnée, les clathrates d'hydrates de xénon et de krypton doivent se former à plus haute température que ce qui était prévu précédemment. Aussi ces clathrates d'hydrates de xénon et de krypton devraient se former plus tôt durant le refroidissement de la nébuleuse ce qui peut renforcer le rôle des clathrates d'hydrates pour enrichir l'atmosphère de Jupiter en gaz rares.

En plus des mesures des pressions d'équilibres, nous avons calculé l'enthalpie de dissociation des clathrates d'hydrates. En effet, cette grandeur est nécessaire au calcul des échanges thermiques. C'est en particulier le cas des modèles simulant la production de gaz par les noyaux cométaires. Comme dans le cas de la sublimation des glaces pures, j'ai calculé les variations avec la température de l'enthalpie de dissociation des clathrates d'hydrates à partir des capacités calorifiques des différentes phases en présence. Ces calculs permettent de réconcilier les différentes données expérimentales acquises à différentes températures

(Marboeuf et al., 2012). Ces calculs prenant en compte toutes les variations en température ont été appliqués à un modèle de production de gaz à partir des noyaux cométaires publiés dans l'article suivant :

> Marboeuf U., Schmitt B., Petit J.-M., Mousis O. and **Fray N.** (2012) A cometary nucleus model taking into account all phase changes of water ice: amorphous, crystalline, and clathrate. *Astronomy and Astrophysics,* 542, A82

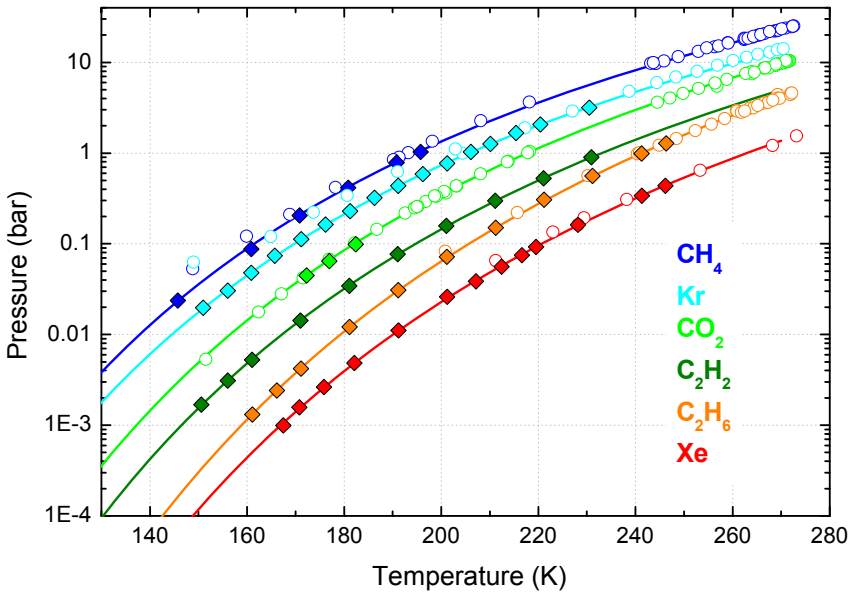

Figure 6 : Synthèse des mesures concernant l'équilibre entre les clathrates d'hydrates, la glace d'eau et le gaz pour 6 espèces différentes : CH_4, Kr, CO_2, C_2H_2, C_2H_6, Xe. Les nouvelles mesures sont représentées par des carrées pleins alors que les données issues de la littérature sont représentées par des cercles vides. Les courbes sont les lois d'équilibre que nous avons proposées.

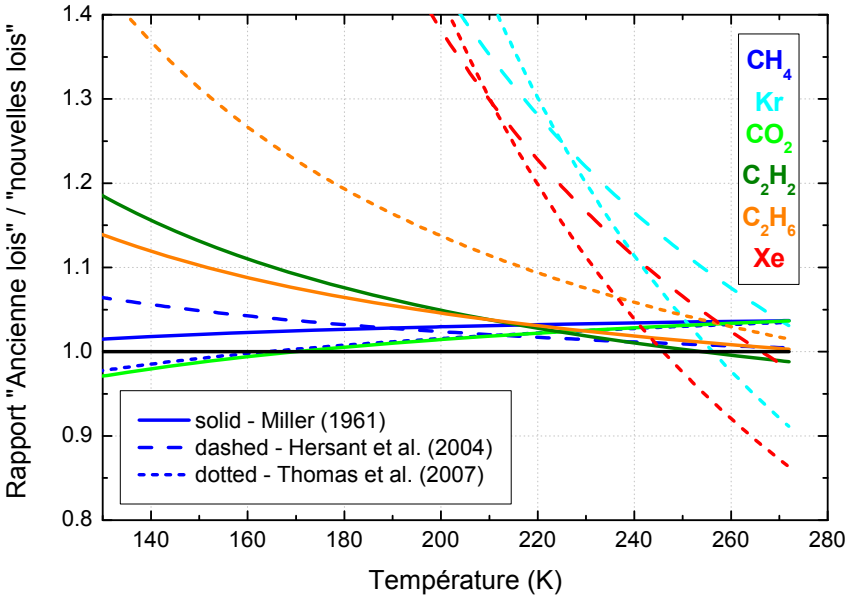

Figure 7 : Rapport entre les lois utilisées dans les modèles astrophysiques et les « nouvelles » loi que nous avons proposées (Fray et al., 2010 et Marboeuf et al., 2012). Les couleurs codent les différentes molécules considérées. Concernant les modèles astrophysiques, j'ai considéré trois articles dans lesquels les lois utilisées sont explicitées : Miller (1961) en trait plein, Hersant et al. (2004) en pointillés longs et Thomas et al. (2007) en pointillés courts.

4. La matière organique de haut poids moléculaire contenue dans les comètes.

4.1. Les connaissances actuelles sur la matière organique réfractaire cométaire.

De nombreuses molécules organiques ont été détectées en phase gazeuse dans l'environnement cométaire comme le méthane (CH_4), l'éthane (C_2H_6) ou le méthanol (CH_3OH). A ce jour, la molécule gazeuse la plus complexe identifiée dans les comètes est l'éthylène glycol ($HOCH_2CH_2OH$) et son abondance de 0.25 % par rapport à l'eau en fait une des molécules organiques les plus abondante dans l'environnement cométaire (Crovisier et al., 2004). Même si la phase gazeuse des comètes est très riche d'un point de vue chimique nous nous concentrerons ici sur la partie la moins connue ; c'est-à-dire la matière organique solide présente dans les grains cométaires.

La mise en évidence de matière organique en phase solide dans les grains cométaires a été effectuée grâce aux mesures par spectrométrie de masse in-situ réalisées en 1986 dans l'environnement de la comète 1P/Halley. Les deux spectromètres de masses « PUMA » dédiés à l'étude des poussières à bord des deux sondes Véga (Kissel et al., 1986b) ainsi l'instrument « PIA » à bord de Giotto (Kissel et al., 1986a) ont donné des résultats similaires montrant la présence d'une phase riche en carbone dans les grains cométaires. Ces résultats ont ensuite été confirmés par le spectromètre « CIDA » à bord de la sonde Stardust à la fois lors du survol de 81P/Wild 2 (Kissel et al., 2004) et mais aussi lors du survol de 9P/Tempel 1 (Veverka et al., 2013). Certains grains semblent être composés majoritairement de composés organiques. Si l'abondance élémentaire du carbone par rapport aux éléments minéraux (Fe, Si, Mg, Ca,…) est supérieure à 10 alors ces grains ont été dénommés « CHON » grains. Ils représentent 22 % des grains des grains analysés (Fomenkova et al., 1994). D'après Fomenkova (1999), le rapport massique entre les minéraux et les organiques solides est compris entre 1 et 2. Il faut aussi garder en mémoire que la masse estimée des grains

analysés varie entre 5×10^{-17} g et 5×10^{-12} g[12] et que la masse totale de l'ensemble des grains analysés ne représentent que quelques nanogrammes (Fomenkova, 1999).

La présence de diverses molécules organiques a été proposée sur la base des observations réalisées par l'instrument PUMA 1 (Kissel and Krueger, 1987). Néanmoins, ces identifications restent très controversées. Fomenkova (1999) a écrit à ce sujet « The majority of grains […] contain heteropolymers and/or variable mixtures of carbon phases and complex organic compounds - various compounds which are consistent with structures of alcohols, aldehydes, ketones, acids and amino acids, and their salts. *Exact make-up of these mixtures cannot be unambiguously identified from the available data*. ».

Si l'identification moléculaire reste discutée, il semble néanmoins que la coma interne de 1P/Halley contienne plus de grains « CHON » que la coma externe (Fomenkova et al., 1994) ce qui laisse penser que la matière organique peut subir une sublimation ou une décomposition directement dans la coma. De plus, les rapports élémentaires N/C, O/C et H/C ont pu être mesurés. Les valeurs moyennes pour la matière organique sur l'ensemble des grains analysés sont d'environ 0.04, 0.25 et 1, respectivement (Kissel and Krueger, 1987; Jessberger et al., 1988; Krueger et al., 1991)[13]. Ces valeurs sont légèrement plus élevées que celles trouvées dans la matière organique insoluble des chondrites carbonées de type CR qui est considéré comme la matière organique météoritique la plus primitive par Alexander et al. (2007). De plus, la valeur des rapports élémentaires peut varier de manière significative d'un grain à l'autre, ce qui montre une très grande diversité chimique (Jessberger et al., 1988; Fomenkova et al., 1994). L'observation d'une telle diversité dans un même environnement laisse penser que la comète 1P/Halley a hérité de matériaux provenant d'origines différentes ou d'un matériau ayant subit différentes évolutions (Fomenkova et al., 1994).

Il faut ici mentionner la mission Stardust qui a collecté des grains dans l'environnement cométaire. Ceux-ci ont ensuite été ramenés sur Terre pour une analyse en laboratoire (Brownlee et al., 2006). Malheureusement, les résultats concernant la phase carbonée sont extrêmement controversés tant du fait du très fort échauffement subit lors de la collecte que de la contamination de l'aérogel dans lequel ces grains ont été collectés (Sandford et al., 2010). Cette contamination, initialement présente sous la forme de groupements $-CH_3$, a pu être convertie en d'autres phases carbonées lors de l'impact des particules cométaires ce qui peut remettre notamment en cause l'origine de certains des HAPs[14] détectés dans les échantillons Stardust (Sandford et al., 2010).

La présence d'un matériau carboné réfractaire dans les grains cométaires est avérée mais sa nature reste encore largement méconnue. Cette méconnaissance provient de la difficulté d'observer cette phase organique grâce aux télescopes situés au sol ou en orbite. En effet, très peu de signatures spectrales peuvent être attribuées à un matériau organique en phase solide. L'origine de la bande située entre 3.2 et 3.6 µm (2750 - 3150 cm^{-1}) est très

[12] Si on considère une densité de 1 $g.cm^{-3}$, ces masses correspondent à des diamètres compris entre 40 nm et 2 µm environ.

[13] D'après Fomenkova (1999), les mesures d'abondances de C et N sont robustes, alors que les mesures concernant O et H ont pu être influencées par des phénomènes mal compris se déroulant lors de l'impact des grains à très grande vitesse sur les cibles.

[14] HAPs : Hydrocarbures Aromatiques Polycycliques, aussi appelés PAHs en anglais.

discutée, il est possible que cette bande provienne de la fluorescence du méthanol en phase gazeuse même si une contribution de la phase solide n'est pas à exclure (Bockelée-Morvan et al., 1995). Une bande située vers 7.25 µm (1380 cm^{-1}) a été observée grâce au télescope Spitzer dans plusieurs comètes et à plusieurs distances héliocentriques (Woodward et al., 2007; Bockelée-Morvan et al., 2009). Cette bande n'ayant pu être attribuée à aucune molécule gazeuse, elle est pourrait être due à une phase solide. A ma connaissance ces deux bandes infrarouges sont les seules signatures spectrales observées dans les comètes depuis la Terre dont l'origine pourrait être liée à la présence d'une matière organique solide. Ces rares signatures spectrales montrent la difficulté pour caractériser la matière organique solide contenue dans les comètes grâce à des observations depuis le sol ou l'orbite terrestre.

Néanmoins, la nature de la phase réfractaire carbonée contenue dans les comètes peut être contrainte grâce à l'étude d'échantillons extraterrestres disponibles en laboratoires et qui sont vraisemblablement d'origine cométaire. C'est en particulier le cas des IDPs (Interplanetary Dust Particles) qui sont collectées dans la haute stratosphère. Des analyses ont montré la présence de HAPs (Clemett et al., 1993), de chaînes aliphatiques (Flynn et al., 2003) et d'anomalies isotopiques en H et N (Floss et al., 2006). D'autres part, les UCAMMs (Ultra-Carbonaceous Antartic Micro-Meteorites) présentent des teneurs massique en matière carbonée qui peuvent dépasser 50% ainsi que des rapports élevées en deutérium sur des surfaces relativement importantes (Duprat et al., 2010). D'autre part, comme dans les comètes, les silicates contenus dans ces échantillons sont majoritairement cristallins. Les matériaux contenus dans ces micro-météorites ne proviennent donc pas uniquement du milieu interstellaire (Duprat et al., 2010).

En conclusion, la présence d'un matériau carboné réfractaire dans les grains et les noyaux cométaires est avérée. Malheureusement, les études par spectrométrie de masse in-situ n'ont pas encore permis de révéler la nature physico-chimique de celui-ci même si les rapports élémentaires ont pu être mesurés. Les télescopes au sol ou en orbite ne semblent pas être en mesure de caractériser cette matière organique réfractaire. Finalement, c'est les échantillons extraterrestres, dont l'origine est vraisemblablement cométaire, qui ont apportés les informations les plus précises. Afin de progresser dans notre connaissance de la matière organique réfractaire contenue dans les comètes, j'ai suivi deux voies : i.) l'expérimentation en laboratoire qui permet de reproduire la synthèse et l'évolution d'analogues à la matière organique cométaire ainsi que ii.) la préparation à l'interprétation des données qui seront acquises par COSIMA (spectromètre de masse à bord de l'orbiteur de la mission Rosetta et qui est dédié à l'étude de la poussière).

4.2. Les travaux en laboratoire : le projet « OREGOC ».

4.2.1. Motivations et objectifs du projet OREGOC.

Au sein du groupe de Physico-chimie organique spatiale du LISA, les travaux réalisés avant le développement de ce nouveau projet, ont permis de caractériser quantitativement les décompositions photolytique et thermique du polyoxyméthylène (POM)[15] (Cottin et al., 1999; Cottin et al., 2000 ; Fray et al., 2004). L'inclusions de ces données quantitatives dans un modèle de l'environnement cométaire prenant en compte la décomposition du POM

[15] Le PolyOxyMéthylène, aussi appelé POM, est un polymère du formaldéhyde (H_2CO).

solide en formaldéhyde (H_2CO) gazeux a permis de reproduire plusieurs observations astrophysiques qui n'étaient alors que partiellement interprétées. C'est en particulier le cas de la distribution spatiale du formaldéhyde (H_2CO) gazeux dans la coma de la comète de 1P/Halley (Cottin et al., 2004 ; Fray et al., 2004) mais aussi l'évolution héliocentrique des taux de production de formaldéhyde (H_2CO) gazeux dans la comète C/1995 O1 (Hale-Bopp) (Fray et al., 2006). Ces travaux montrent que la présence de POM, ou de composés similaires, dans les noyaux et les grains cométaires est très fortement probable. Ils montrent aussi les possibilités d'évolution et de décomposition du matériau organique solide présent dans les grains cométaires ainsi que l'importance des mécanismes thermiques. Néanmoins, les dispositifs expérimentaux alors utilisés possédaient des gammes de températures restreintes et ces travaux étaient limités par l'usage de composés chimiques commerciaux.

L'idée initiale du projet OREGOC (ORigine et Evolution des Glaces et des composés Organiques Cométaires), qui était le cœur du projet de recherche que j'avais présenté lorsque j'ai postulé sur le poste de maître de conférence que j'occupe désormais, était la poursuite des travaux réalisés au LISA tout en développant un nouveau dispositif expérimental ambitieux permettant de s'affranchir des limites des précédents dispositifs expérimentaux. Ce nouveau dispositif devait donc permettre l'étude i.) de l'évolution thermique, jusqu'à au moins 600 K, d'analogues à la matière organique cométaire préalablement synthétisés dans les conditions les plus représentatives possibles des nuages moléculaires denses ou des zones externes des disques protoplanétaires et ii.) des processus de production de gaz (sublimation et décomposition) à partir d'échantillons solides. Ces processus sont synthétisés sur la figure 8 et les objectifs scientifiques accessibles sont les suivants :

- Synthèse d'analogues à la matière organique cométaire par photolyse et réchauffement de mélanges de glaces.

- Caractérisation chimique de la phase solide sur toute la gamme de température accessible.

- Mesure de données quantitatives concernant les processus de production d'espèces gazeuses afin d'interpréter les observations de la phase gazeuse des comètes et en particulier celles concernant les sources distribuées.

- Production d'analogues à la matière organique cométaire pour la calibration d'instruments spatiaux et en particulier de COSIMA.

- Comparaison avec les cosmomatériaux disponibles en laboratoires, comme les IDPs ou les micrométéorites.

Ces objectifs sont synthétisés sur la figure 8 et tous convergent vers l'objectif principal du projet OREGOC qui est de contraindre la nature physico-chimique de la matière carbonée réfractaire contenue dans les noyaux et les grains cométaires.

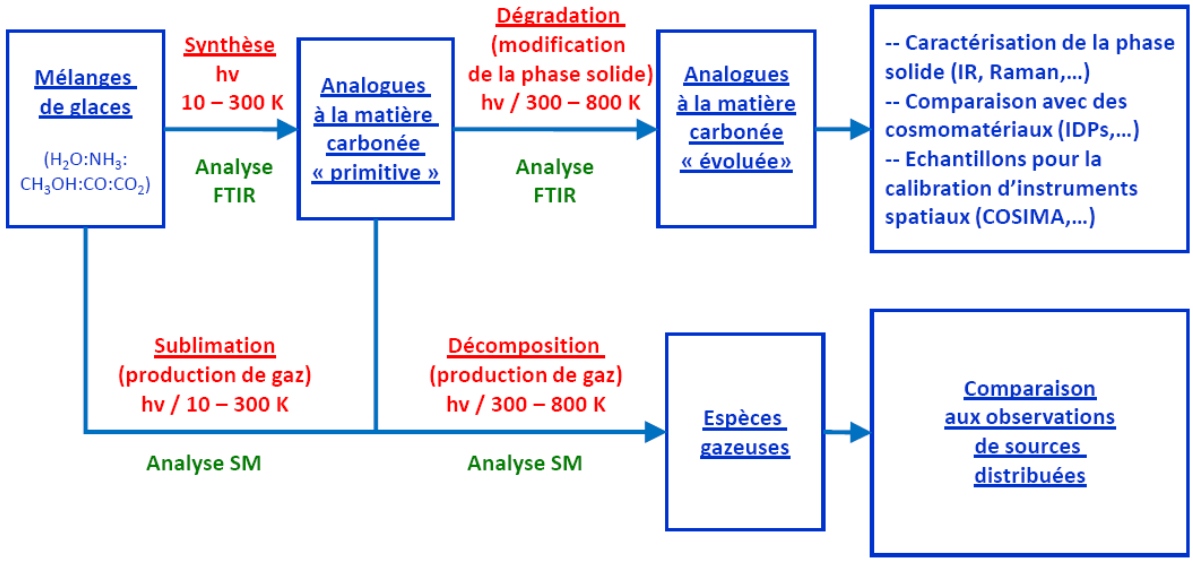

Figure 8 : Schéma synthétique présentant les processus physico-chimiques pouvant être étudiés par le dispositif expérimental développé dans le cadre du projet OREGOC ainsi que leurs applications à des questionnements astrophysiques. Le mélange initial de glaces est donné à titre indicatif, d'autres molécules peuvent être rajoutées. La température de 300 K est elle aussi donnée à titre indicatif. Cette température correspond à la température à laquelle la majorité des analyses « ex-situ » des analogues produits ont été réalisées, néanmoins il faut considérer la synthèse de nouvelles espèces et l'évolution thermique des analogues comme des processus continus depuis les plus basses températures jusqu'au plus élevées.

4.2.2. Développement du projet OREGOC.

Le développement du dispositif expérimental lié au projet OREGOC, depuis la recherche de financements jusqu'à sa maintenance et son entretien en passant évidemment par son développement technique, est de manière évidente l'investissement le plus important que j'ai réalisé depuis ma nomination en tant que maître de conférences. Mon implication dans toutes les étapes nécessaires jusqu'au fonctionnement complet du dispositif est très importante. Néanmoins, le développement de ce projet n'aurait pu se faire sans les conseils et l'aide de certains collègues : Yves Bénilan, Hervé Cottin et Marie-Claire Gazeau en particulier.

Je ne détaillerai pas ici toutes les étapes du développement de ce projet et du dispositif expérimental associé. Une chronologie synthétique (Figure 9) présente les principales étapes du développement du projet et la liste des contrats de recherche que j'ai gérés est jointe en annexe. La figure 10 présente une photographie du dispositif.

D'un point de vue analytique, le spectromètre infrarouge à transformée de Fourier est dédié à l'étude la phase solide alors que le spectromètre de masse permet l'analyse de la phase gazeuse produite lors du chauffage de l'échantillon solide. Un système interférentiel peut venir remplacer le spectromètre de masse afin de mesurer l'épaisseur des films solides et compléter la spectroscopie infrarouge pour certaines mesures quantitatives sur la phase solide. Grâce à une interface que j'ai développée[16], ces différentes mesures, ainsi que celle de la température de l'échantillon, sont synchronisées et en enregistrées en fonction du temps afin de pouvoir être corrélées et d'étudier toutes les variations temporelles.

[16] Cette interface a été développée en Labview.

Septembre 2006	Nomination au LISA en tant que maître de conférences.
Octobre 2006	**1ére demande de financement liée au projet OREGOC.**
Décembre 2007	Livraison du cryostat.
Mars 2008	Livraison du contrôleur de température.
Juin 2008	Livraison du spectromètre infrarouge.
Mai 2009	Livraison de l'enceinte et de la table optique associée.
De Mai à décembre 2009	Montage du dispositif, alignement du faisceau infrarouge externe et couplage à la rampe d'injection des gaz.
Décembre 2009	**1er spectre infrarouge d'un film de glace.**
De Janvier à Octobre 2010	**Etude de la décomposition thermique du POM** synthétisé par réchauffement d'un mélange H_2CO :NH_3 et analyses des échantillons produits par un spectromètre de masse analogue à COSIMA (*Thèse de Léna Le Roy*).
Septembre 2010	Livraison du spectromètre de masse.
D'octobre à décembre 2010	Montage d'une lampe VUV et du spectromètre de masse sur le dispositif expérimental.
Février 2011	**1ére production d'un analogue** potentiel à la matière organique cométaire suite **à une photolyse** d'un mélange H_2O :CH_3OH :NH_3 suivie d'un réchauffement. (*Post-doctorat de Giacomo Briani*). **1^{ére} étude expérimentale de l'évolution thermique jusqu'à 600 K.**
Juin 2011	Séminaire invité au PIIM (Laboratoire de Physique des Interactions Ioniques et Moléculaires à Marseille) qui initiera une collaboration puis la publication d'un article commun en Janvier 2013.
Juin 2011	1ére analyse d'un analogue potentiel à la matière organique grâce à un modèle-sol de COSIMA (*Thèse de Léna Le Roy & Post-doctorat de Giacomo Briani*)
De septembre à décembre 2011	Conception d'une nouvelle lampe VUV.
Janvier 2012	**Acceptation de la 1^{ére} publication.**
De Février à Juin 2012	Optimisation du spectre d'émission de la lampe VUV et mesure du flux de la lampe VUV après la mise au point de nouvelles méthodes d'actinométrie (*Stage de M2R de Michaëlle Bouilloud*)
A partir de septembre 2012	Mesures des sections efficaces intégrées des glaces pures de H_2O, CH_3OH, CO, CO_2, NH_3, CH_4, H_2CO et HCOOH. Calibration de la vitesse de formation des films de glace (Thèse *de Michaëlle Bouilloud*)

Figure 9 : Chronologie synthétique du développement du dispositif expérimental « OREGOC ».

On peut tout de même noter que le développement s'est fait pas à pas en prenant le temps de faire les calibrations nécessaires. Par exemple, avant d'effectuer la première étude concernant le polyoxyméthylène (POM), nous avons calibré les vitesses de formation des films de glaces afin de bien contrôler le rapport de mélange entre le formaldéhyde (H_2CO) et l'ammoniac (NH_3) qui sont injectés de manière indépendante afin d'éviter toute réaction chimique avant la formation des glaces. Dans le cas, de l'étude de l'hexaméthylènetétramine (HMT), nous avons réalisé des mesures du flux de photons incident de la lampe afin de contrôler au mieux l'étape initiale de photolyse.

Autant que possible, nous souhaitons réaliser des expérimentations que nous qualifions de « globales ». Les protocoles de celles-ci sont contraints par nos connaissances astrophysiques actuelles plus que par la volonté d'étudier une molécule ou un processus en

particulier. Aussi la nature des réactifs présents dans les mélanges initiaux de glaces ainsi que leurs rapports d'abondance sont contraints par l'observation des glaces dans les nuages moléculaires denses ou les environnements des étoiles naissantes. Durant l'étape de photolyse, nous tentons de simuler aux mieux les spectres VUV présents dans les milieux astrophysiques et lors du chauffage nous utilisons les rampes de températures les plus lentes possibles afin de laisser le système chimique évoluer le plus librement possible. L'objectif est d'assurer la meilleure représentativité astrophysique possible des expérimentations.

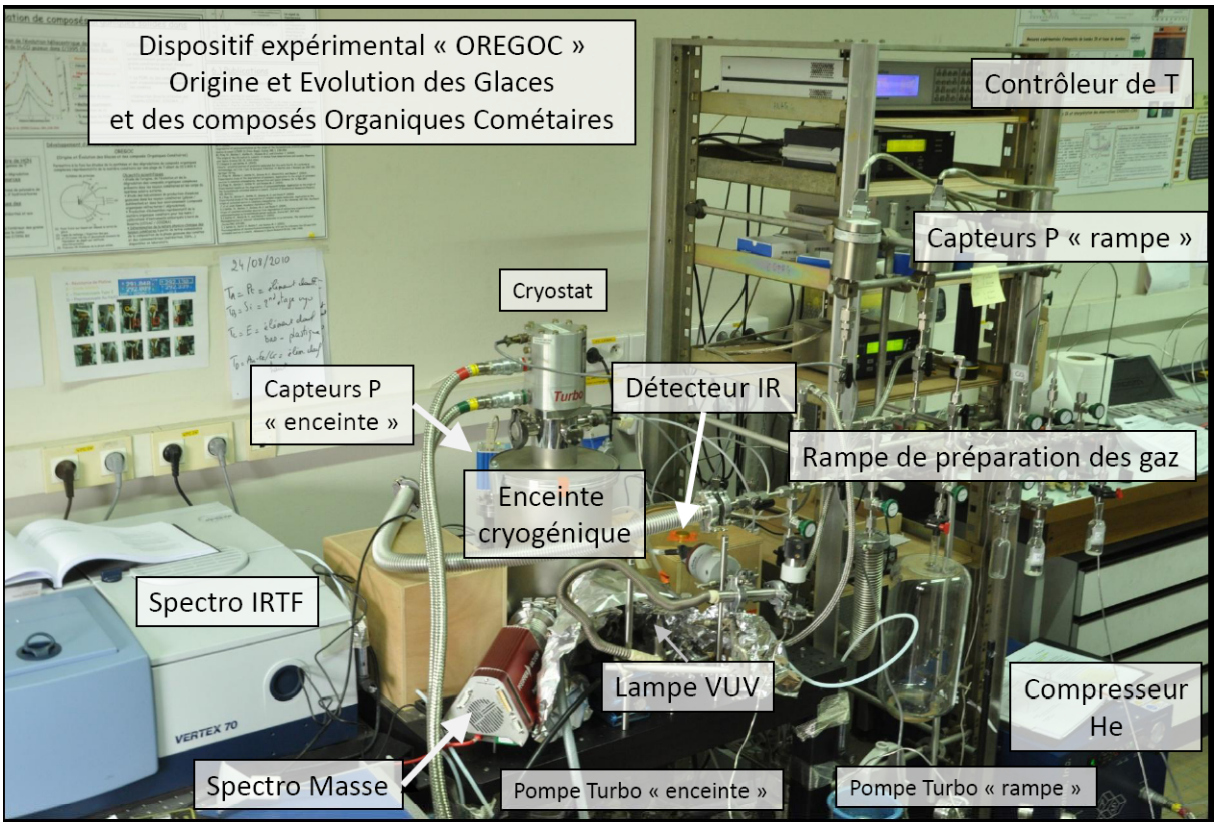

Figure 10 : Photographie du dispositif expérimental « OREGOC ». La lampe VUV installée correspond au 1er modèle utilisé, une nouvelle lampe a été développée depuis. Le spectromètre de masse peut être retiré afin d'installer un système interférentiel permettent la mesure de l'épaisseur du film solide.

4.3. Vers l'observation in-situ : l'instrument COSIMA.

COSIMA (COmetary Secondary Ion Mass Analyzer) est le spectromètre de masse à bord de l'orbiteur de la mission Rosetta dédié à l'étude des grains cométaires. Depuis octobre 2012, j'ai rejoint de manière officielle l'équipe COSIMA en tant que « Associated Scientist ». Ceci me permettra d'avoir accès aux données prétraitées grâce aux logiciels mis en place par l'équipe « COSIMA », mais aussi d'avoir accès aux données pendant les 6 premiers mois durant lesquels les données brutes ne seront pas publiques. Ayant participé à l'encadrement de la thèse de Léna Le Roy depuis sont début, j'ai suivi les travaux de calibration de cet instrument depuis 2008.

COSIMA est un spectromètre d'ions secondaires à temps de vol (TOF-SIMS) (Kissel et al., 2007). Le principe de cet instrument est d'exposer à la coma de 67P/Churyumov-Gerasimenko des cibles métalliques sur lesquelles vont venir s'impacter les grains

cométaires. Après la collecte, les cibles seront déplacées devant un microscope optique afin de localiser les grains puis face au faisceau d'ions primaires (In^+) qui générera les ions secondaires provenant des grains cométaires. Ceux-ci seront alors séparés en fonction de leur rapport masse/charge avant d'être détectés. La figure 11 présente un schéma simplifié de l'instrument qui contient aussi une station chimique permettant de chauffer les cibles jusqu'à 140°C ainsi qu'une zone de stockage contenant 72 cibles chacune mesurant 1 cm x 1 cm.

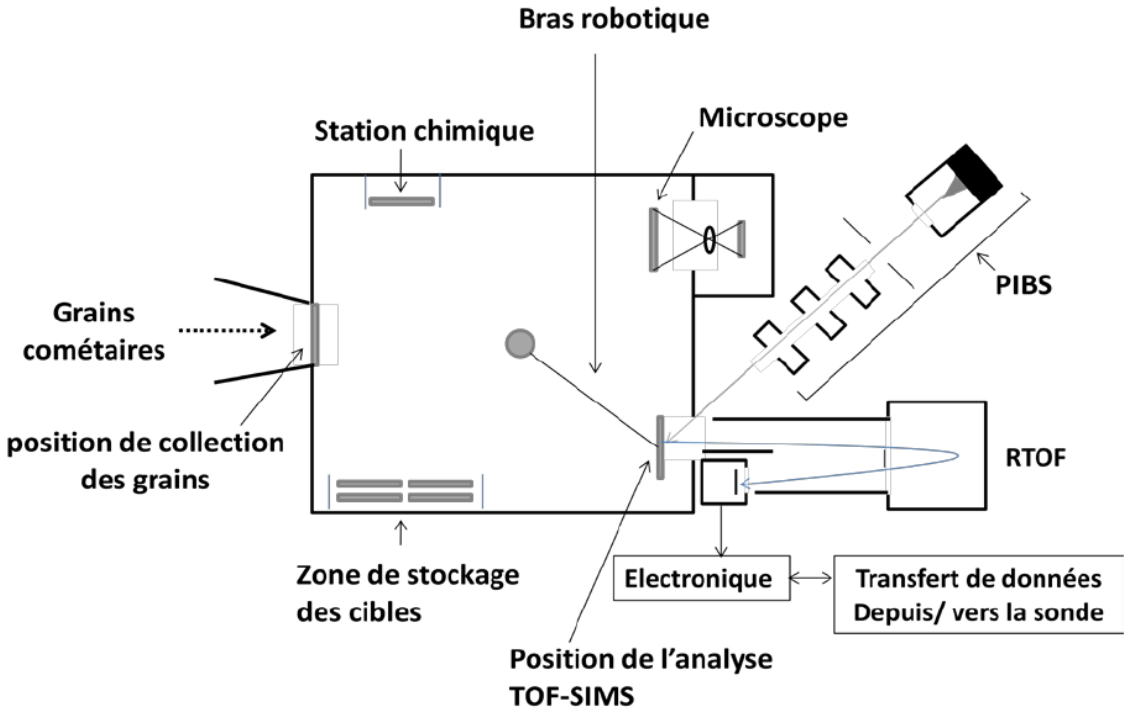

Figure 11 : Schéma de principe de l'instrument COSIMA. Cette illustration est adaptée de Kissel et al. (2007).

Les principales caractéristiques de cet instrument sont sa très large gamme mesure (de 1 à 3500 amu) et sa très bonne résolution (R=m/δm) de l'ordre de 2000 à m/z=100 pour un instrument spatial. D'autre part, le microscope optique a une résolution de 13.7 µm/pixel et la taille du faisceau d'ions primaires à une taille de l'ordre de 20 µm à la surface des cibles. COSIMA devrait donc analyser prioritairement de grains ayant des dimensions de l'ordre de quelques dizaines de microns. D'autre part, COSIMA peut fonctionner dans deux modes différents permettant de collecter soit les ions négatifs soit les ions positifs.

Les principaux objectifs de COSIMA sont l'analyse moléculaire et minérale des grains cométaires ainsi que la mesure des rapports élémentaires et isotopiques. Ces mesures seront effectuées non seulement dans le cadre de la chimie du disque protoplanétaire dans lequel les noyaux cométaires se sont formés afin de déterminer l'origine (ou les origines ou les évolutions) des matériaux contenus dans les comètes mais aussi dans le cadre de la chimie prébiotique afin de déterminer si les apports cométaires sur la Terre primitive ont pu jouer un rôle dans l'apparition de la vie sur Terre.

4.4. Quelques résultats.

Pour l'instant, nous avons en particulier étudié la production de polyoxyméthylène (POM, polymère du formaldéhyde) ainsi que les analogues produits par photolyse puis réchauffement d'un mélange initial H_2O :CH_3OH :NH_3. Dans ce dernier cas, nous avons en particulier identifié, à différentes températures, l'ensemble des intermédiaires réactionnels conduisant à la formation d'hexaméthylènetétramine (HMT, $C_6H_{12}N_4$) qui est une des molécules présentes dans les analogues à la matière organique cométaire. D'autre part, certains de ces analogues ont été analysés par les modèles sol de COSIMA afin de calibrer l'instrument spatial et de préparer l'interprétation des futures données cométaires. A partir de l'ensemble des spectres de références acquis sur les instruments sol de COSIMA, j'ai aussi recherché des méthodes permettant la mesure des rapports élémentaires.

4.4.1. Le polyoxyméthylène (POM).

Les travaux réalisés avant le début du projet « OREGOC » ont montré que la présence de polyoxyméthylène (POM) dans les noyaux et les grains cométaires est fortement probable. Néanmoins, ces travaux ne constituent pas une preuve de la présence de POM dans les noyaux cométaires. Désormais le meilleur moyen de démontrer la présence de POM dans les comètes semble être une détection directe par spectrométrie de masse in-situ grâce à l'instrument COSIMA. Nous avons donc cherché à caractériser la signature spectrale du POM avec COSIMA et à contraindre les opérations de vol à effectuer afin de maximiser les chances de détecter ce composé.

Cette étude a été effectuée par Léna Le Roy dans le cadre de sa thèse, que j'ai co-encadrée, et a été publiée dans l'article suivant :

> Le Roy L., Briani G., Briois C., Cottin H., **Fray N.**, Thirkell L., Poulet, G. and Hilchenbach, M. (2012). On the prospective detection of polyoxymethylene in comet 67P/Churyumov-Gerasimenko with the COSIMA instrument onboard Rosetta. Planetary and Space Science, 65(1), 83-92.

L'objectif de cette étude est de comparer certaines propriétés d'échantillons de POM commerciaux et d'échantillons de POM synthétiques. Afin de synthétiser le POM, nous nous sommes placés dans les conditions permettant de maximiser la conversion de formaldéhyde (H_2CO) en POM ; le but étant d'obtenir des échantillons de taille suffisante pour pouvoir réaliser des études cinétiques et des analyses par spectrométrie de masse. Les rendements de conversion de H_2CO en POM ont été étudiés de manière quasi-exhaustive par Schutte et al. (1993). Nous avons donc synthétisé du POM par un réchauffement lent d'un mélange H_2CO :NH_3 dans une proportion 1 :2.

Les échantillons de POM commerciaux et synthétiques ont été analysés grâce au spectromètre de masse d'ions secondaires à temps de vol (TOF-SIMS) disponible au LPC2E[17]. Cet instrument possède des caractéristiques instrumentales quasi-identiques à COSIMA. Les spectres de masse des échantillons commerciaux et synthétiques sont très similaires (voir Le Roy et al., 2012). Les spectres d'ions positifs présentent une très grande régularité jusqu'à des masses élevées de l'ordre de 600 amu. En effet, les motifs présents dans le spectre de

[17] LPC2E : Laboratoire de Physique et Chimie de l'Environnement et de l'Espace. Ce laboratoire est situé à Orléans.

masse se répètent avec une période de 30.011 amu qui correspond à la masse molaire du formaldéhyde (figure 12). Au contraire, les spectres d'ions négatifs ne présentent aucune signature spécifique au POM. Aussi afin de détecter le POM dans les spectres de masse cométaires, il faudra donc rechercher prioritairement une période de 30.011 amu dans les spectres d'ions positifs.

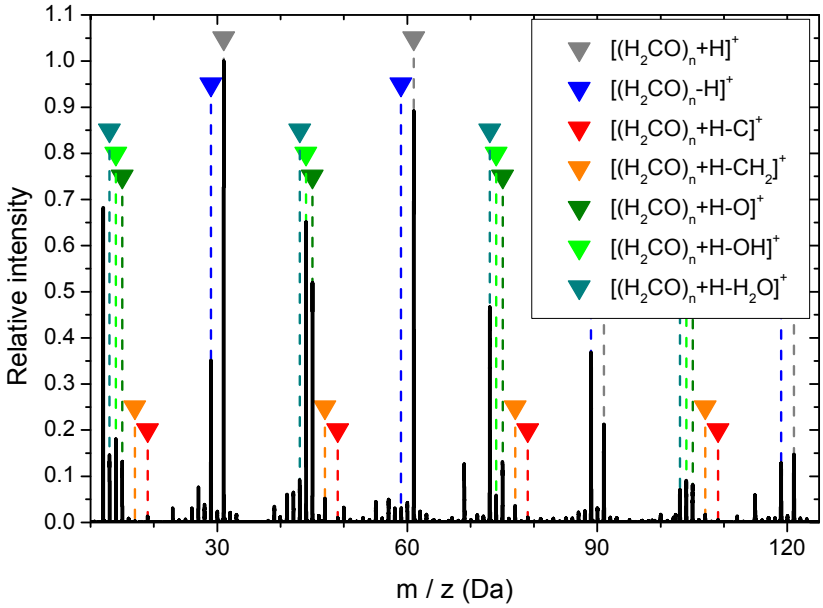

Figure 12 : Spectre de masse en ions positifs d'un échantillon de POM synthétisé par chauffage d'un mélange H_2CO :NH_3. Les triangles de couleur permettent d'attribuer les principaux fragments du POM mais aussi de montrer la période de 30.011 amu présente dans ce spectre.

L'objectif des études cinétiques est de contraindre les opérations de vol afin de maximiser les chances de détection du POM. En effet après leur collecte et avant leur analyse, les grains cométaires peuvent être stockés à l'intérieur de l'instrument, dans lequel règne une température pouvant atteindre 303 K (Kissel et al., 2007). Cette étude cinétique a montré que la décomposition du POM ne suivait pas une cinétique d'ordre 1 comme attendu, mais une cinétique plus complexe. La mise en évidence de cette cinétique complexe a été possible grâce au suivi de la décomposition du POM sur des temps très longs (plusieurs jours) ce qui est faisable grâce à la stabilité du dispositif OREGOC. Néanmoins, les temps caractéristiques de décomposition du POM synthétiques sont similaires à ceux déjà mesurés sur des échantillons commerciaux (voir la figure 11 de Le Roy et al., 2012). La décomposition du POM à l'intérieur de l'instrument COSIMA est probable, mais le temps caractéristiques de décomposition étant relativement long à 303 K (plus de 10 jours) la détection du POM reste faisable si les analyses sont effectuées rapidement après la collecte des grains. De plus, des analyses successives d'un même grain devraient pouvoir mettre en évidence la diminution de la quantité de POM en fonction du temps ce qui permettrait de confirmer non seulement les attributions spectrales mais aussi le processus de décomposition. D'autre part, COSIMA possédant la capacité de chauffer jusqu'à 400 K les cibles sur lesquelles les grains auront été collectés, il est possible d'accélérer volontairement la décomposition du POM à l'intérieur de l'instrument.

D'autre part, comme Schutte et al. (1993) l'avait déjà observé, nous avons constaté que la polymérisation du H_2CO en POM peut se dérouler à de très basses températures de l'ordre 40 K.

Cette étude a donc permis non seulement de mettre en évidence la signature du POM qui devra être recherchée afin d'identifier ce composé dans les grains cométaires mais aussi de contraindre les opérations spatiales à réaliser afin de maximiser les chances de détection.

Nous pouvons remarquer que cette étude est une étape intermédiaire dans le développement du projet « OREGOC ». Le dispositif expérimental utilisé n'incluait ni lampe photochimique ni spectromètre de masse pour étudier la phase gazeuse émise lors du chauffage de la phase solide[18]. Par contre, nous avons testé à cette occasion les protocoles permettant de contrôler les rapports de mélange du film initial de glace ainsi que la stabilité du dispositif sur des temps relativement longs ce qui permet de mesurer rigoureusement des cinétiques lentes sur des échantillons préalablement synthétisés à très basses températures.

4.4.2 L'hexaméthylènetétramine (HMT).

Après cette étude sur le polyoxyméthylène (POM), nous souhaitions rentrer dans le cœur du projet « OREGOC », c'est-à-dire l'étude de l'évolution thermique d'un analogue de matière organique cométaire ainsi que l'étude simultanée des phases solides et gazeuses afin de caractériser les mécanismes de production de gaz. Nous avons choisi de mener cette 1^{ére} étude complète sur des analogues dont la nature avait déjà été caractérisée par le passé par d'autres équipes. Nous avons donc choisi de travailler à partir de mélange initiaux H_2O :CH_3OH :NH_3 et H_2O :CH_3OH :NH_3 :CO_2 comme l'avait fait Bernstein et al. (1995) et Munoz-Caro & Schutte (2003).

D'autre part, des discussions avec l'équipe SDM (Spectrométries et Dynamique Moléculaire) du PIIM (Laboratoire de Physique et des Interactions Ioniques et Moléculaires) ont permis de se rendre compte que les expérimentations que nous menions étaient très complémentaires. Ceci nous a permis de proposer conjointement un mécanisme chimique de formation du HMT par la photolyse puis le réchauffement d'un mélange initial H_2O :CH_3OH :NH_3 pour lequel nous avons détecté la plupart des intermédiaires réactionnels.

L'ensemble des expérimentations présentées ici ont été réalisées par Giacomo Briani qui a profité d'un financement post-doctoral de 1 an que j'ai obtenu auprès de l'université Paris-Est Créteil (UPEC).

Les études concernant le mécanisme réactionnel conduisant à la formation de l'hexaméthylènetétramine (HMT, $C_6H_{12}N_4$) ont été publiées dans l'article suivant :

> Vinogradoff V., **Fray N.**, Duvernay F., Briani G., Danger G., Cottin H., Theulé P. and Chiavassa T. (2013). Importance of the thermal reactivity for hexamethylenetetramine (HMT) formation from simulated interstellar ices. Astronomy and Astrophysics, 551, A128

Le HMT est une molécule qui a été détectée par des nombreux auteurs dans les analogues produits par photolyse et réchauffement d'un mélange de glaces contenant du méthanol (CH_3OH) et de l'ammoniac (NH_3) fortement dilué dans l'eau (Bernstein et al., 1995; Munoz-Caro and Schutte, 2003). Néanmoins, le mécanisme de formation du HMT n'était connu qu'en solution aqueuse et aucun des intermédiaires de formation n'avait été détecté

[18] Au moment de cette étude, nous possédions d'ores et déjà une lampe photochimique. Par contre, le spectromètre de masse n'avait pas encore pu être financé.

dans une phase solide. Comme Bernstein et al. (1995) et Munoz-Caro & Schutte (2003), nous avons aussi fait le choix de travailler avec des réactifs dilués dans la glace d'eau avec des proportions de 10 % afin de se rapprocher des abondances observées dans les grains glacés autour d'étoiles venant de naître (Gibb et al., 2004; Dartois, 2005; Oberg et al., 2011).

Les expériences qui ont été menées au LISA grâce au dispositif expérimental « OREGOC » débutait donc avec un mélange de glaces H_2O :CH_3OH :NH_3 en proportion 10 :1 :1 (EXP1 sur les figures 13 et 14). Afin d'augmenter la quantité de matière produite après le réchauffement à 300 K, la photolyse a été réalisée simultanément au dépôt des glaces[19]. Les expériences réalisées au PIIM se sont concentrées sur la chimie induite par le seul réchauffement de mélanges initiaux composés de H_2CO :NH_3 :HCOOH (EXP 2) et CH_2NH :HCOOH (EXP3). Bien que ces deux dernières expériences n'utilisent pas de photons comme source d'énergie initiale et que les mélanges de réactifs initiaux soient différents, la complémentarité de celles-ci apparait de manière évidente sur le figure 13. Cette figure 13 représente la différence des spectres infrarouges acquis à 300 K (EXP1) ou à 330 K (EXP2 et EXP3) et ceux acquis à 260 K. Cette figure montre la formation de l'hexaméthylènetétramine (HMT) à partir de l'ion protoné de la triméthylènetriamine ($TMTH^+$) ainsi que la diminution de l'ion formate ($HCOO^-$) qui est très vraisemblablement le contre-ion négatif à la $TMTH^+$.

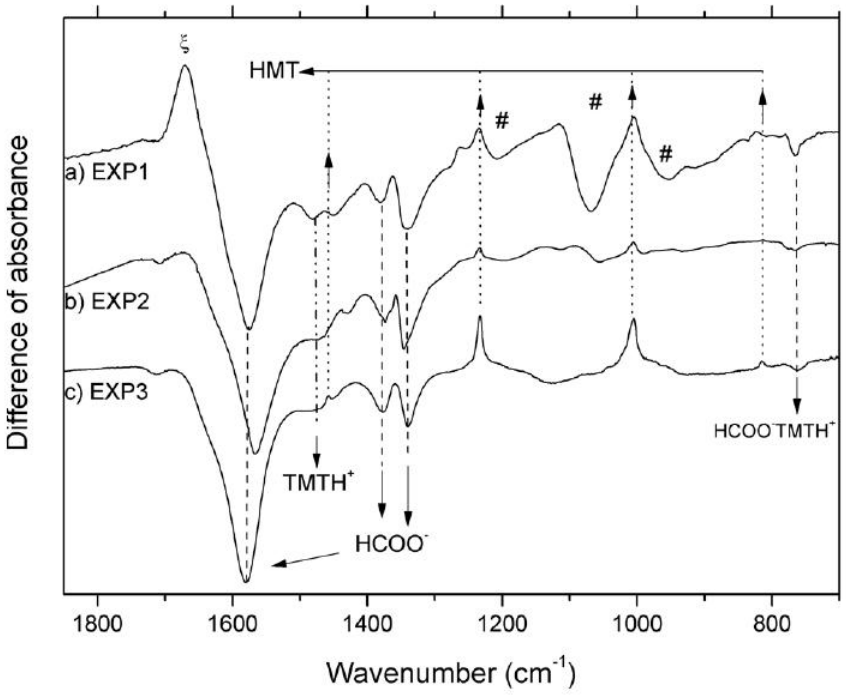

Figure 13 : Différences des spectres infrarouges acquis à 300 K (EXP1) ou à 330 K (EXP2 et EXP3) et de ceux acquis à 260 K durant les trois expériences considérées. La formation de HMT ainsi que la disparition du $TMTH^+$ sont indiqués par des marques verticales. Les symboles # et ζ indiquent la position de bandes non attribuées dans l'expérience 1.

La figure 14 présente de manière schématique le mécanisme de formation du HMT en phase solide. La plupart des intermédiaires réactionnels, le formaldéhyde (H_2CO), l'aminométhanol (NH_2CH_2OH) et l'ion protoné de la triméthylènetriamine ($TMTH^+$), ont été

[19] La profondeur de pénétration des photons VUV dans une glace majoritairement constituée d'eau est de l'ordre de 100 nm. L'augmentation de la quantité d'analogues produits après photolyse et chauffage ne peut donc être obtenue que grâce à une photolyse simultanée au dépôt des glaces ou à des photolyses successives de plusieurs dépôts de l'ordre de 100 nm d'épaisseur.

détectés à différentes températures dans les spectres infrarouges de la première expérience (Vinogradoff et al., 2013).

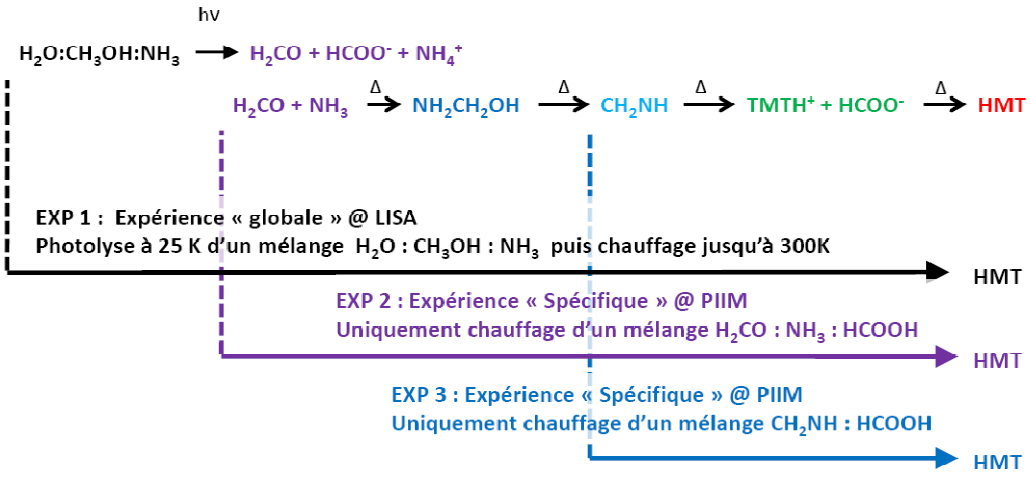

Figure 14 : Mécanisme simplifié de la formation du HMT en phase solide à partir de la photolyse d'un mélange H_2O :CH_3OH :NH_3. Cette figure montre aussi la complémentarité des différences expériences qui ont été menées.

Ce mécanisme montre l'importance des réactions chimiques activées par le chauffage dans la synthèse de la matière carbonée solide restante à 300 K. En effet, le HMT n'est pas un produit provenant de la seule photolyse, sa synthèse n'est possible qu'en présence d'un chauffage. Ceci est confirmé par les études théorique menées au PIIM et qui ont permis de calculer les énergies d'activation des différentes étapes chimiques conduisant à la synthèse du HMT (Vinogradoff et al., 2012). Néanmoins, il faut garder à l'esprit que, le seul chauffage sans photolyse, d'un mélange H_2O :CH_3OH :NH_3 ne conduit pas à la formation de molécules solides à 300 K. L'étape initiale de photolyse est nécessaire à la formation de H_2CO qui réagit ensuite sous l'effet du chauffage pour conduire au final à la production de HMT. Néanmoins, contrairement au POM, la formation du HMT n'est observée, en laboratoire, qu'à partir de température relativement élevée de l'ordre de 270-280 K. Ces résultats montrent aussi que tous les intermédiaires, l'aminométhanol (NH_2CH_2OH), la méthanimine (CH_2NH) et la triméthylènetriamine (TMT) en particulier, peuvent être recherchés dans des milieux astrophysiques.

Cette étude a aussi montré la complémentarité des approches menées au LISA et au PIIM. En effet, les expériences cherchant à décrire spécifiquement certaines réactions chimiques, en utilisant un mélange initial simplifié, sont nécessaires à l'interprétation des expériences simulant une plus grande complexité. Cette collaboration sera donc poursuivie en particulier pour l'identification des espèces produites lors de l'ajout de CO et CO_2 dans le mélange initial.

D'autre part, certains processus physico-chimiques se déroulant lors du chauffage d'un mélange H_2O :CH_3OH :NH_3 préalablement photolysé n'ont pas encore pu être identifiés. La figure 13 montre quelques bandes infrarouges non attribuées, mais surtout la composante gazeuse émise durant le chauffage entre 180 et 300 K semble très riche. Cette composante gazeuse a été analysée de manière continue par spectrométrie de masse. Les spectres de masse enregistrés sont relativement complexes et l'identification des molécules gazeuses ainsi que les corrélations avec l'évolution de la phase solide restent à faire. Des expérimentations spécifiques partant de mélanges initiaux simplifiés (H_2O :CH_3OH ou

H_2O :NH_3 ou CH_3OH :NH_3) seront sûrement nécessaires pour pouvoir interpréter correctement ces spectres de masse.

La plupart des expériences menées à partir de mélange contenant du méthanol (CH_3OH) et de l'ammoniac (NH_3) ont inclus un chauffage jusqu'à 600 K. Pour l'instant, nous nous sommes concentrés sur l'évolution thermique du HMT dans les analogues de matière organique cométaire. Les résultats des ces études seront prochainement publiés dans l'article suivant :

> Briani G., **Fray N.**, Cottin H., Benilan Y., Gazeau M.-C. and Perrier S. HMT production and sublimation during thermal process of cometary organic analogs. Implications for its detection with the ROSETTA instruments. Icarus, minor revisions.

Outre l'évolution thermique à hautes températures, nous avons testé différents mélanges initiaux; en l'occurrence : H_2O :CH_3OH :NH_3 et H_2O :CH_3OH :NH_3 :CO_2. L'objectif de l'ajout de CO_2 est de contraindre au mieux le mélange à partir des observations astrophysiques. En effet, l'abondance de CO_2 dans les glaces entourant les étoiles jeunes est supérieure à 10 %. La matière organique restante solide à 300 K et qui est produites à partir de ces deux mélanges, est relativement similaire (voir figure 4 de Briani et al., minor revisions). La principale différence concerne la composante oxygénée, néanmoins dans les deux cas les signatures spectrales les plus évidentes sont celles du HMT.

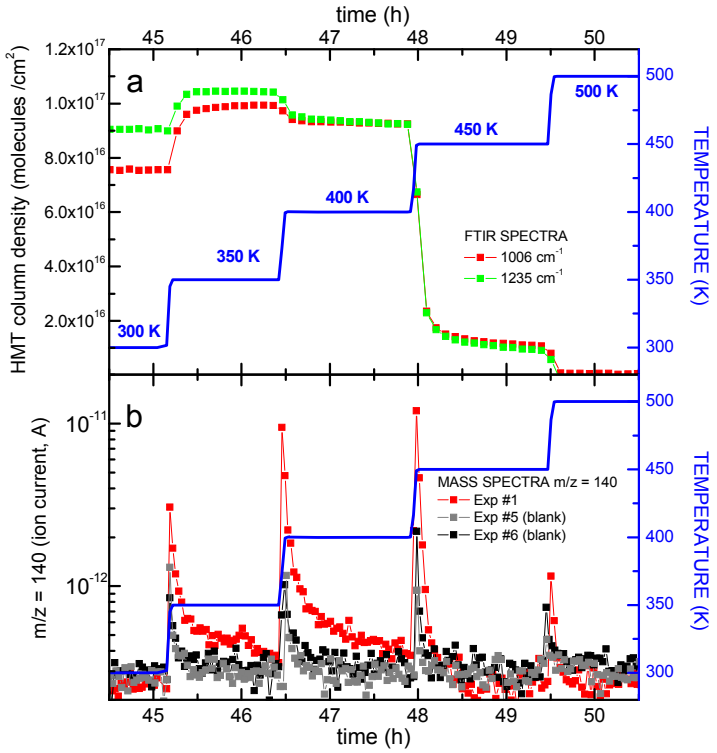

Figure 15 : Suivi temporel du HMT en phase solide par spectrométrie infrarouge (en haut) et en phase gazeuse par spectrométrie de masse (en bas). La courbe bleue représente l'évolution de la température.

Lors de l'évolution thermique, nous avons observé une production du HMT pour des températures supérieures à 300 K alors même que le dernier intermédiaire stable du HMT, le $TMTH^+$, n'est pas détecté directement dans les spectres infrarouges à 300 K. Néanmoins, la signature du $TMTH^+$ est observée dans la différence de spectres acquis à différentes températures (voir figure 10 de Briani et al., submitted). Surtout, nous avons détecté une signature claire du HMT en phase gazeuse grâce à la spectrométrie de masse. Cette

observation montre que lors du chauffage d'un analogue, le HMT sublime ; sa décomposition en molécules plus petites semble inexistante ou très faible. Le suivi simultané des phases solide (en spectroscopie infrarouge) et gazeuse (en spectrométrie de masse) montre que la sublimation est simultanée à la production. Une quantification du HMT présent à la fois en phase solide et en phase gazeuse a révélé que la sublimation représente environ 70 % de la production entre 300 et 350 K. De plus grâce aux données thermodynamiques présentes dans la littérature, j'ai calculé la courbe de sublimation du HMT pur. Il s'avère que la sublimation du HMT pour des températures supérieures à 300 K est plus facile à expliquer que sa présence en phase solide à 300 K dans un milieu soumis à une pression totale de l'ordre de quelques 10^{-8} mbar. La présence de HMT gazeux dans des environnements astrophysiques, en particulier dans l'environnement cométaire, doit donc être considérée[20]. Dans le cadre de la mission Rosetta, le HMT pourrait être détecté à la fois en phase solide et gazeuse, respectivement par les instruments COSIMA et ROSINA[21].

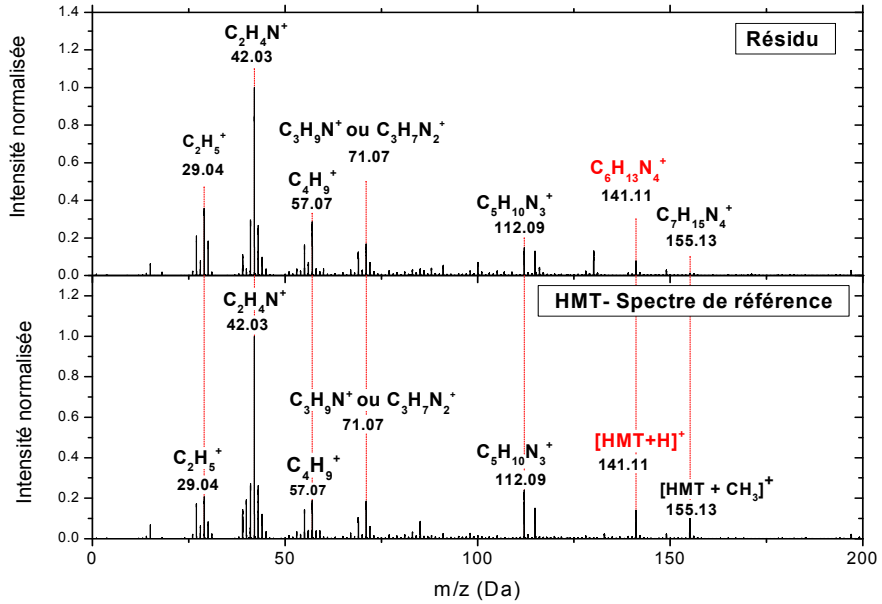

Figure 16 : Comparaison des spectres de masses obtenus avec un spectromètre de masse analogue à COSIMA du HMT pur (en bas) et d'un analogue produit grâce à OREGOC (en haut).

Outre les études de processus réalisés directement avec « OREGOC », nous avons aussi synthétisé des analogues à partir de la photolyse et du réchauffement de mélanges H_2O :CH_3OH :NH_3 qui ont été analysés avec le spectromètre de masse disponible au LPC2E (Orléans). Ces spectres révèlent encore une fois de manière claire la présence de HMT (figure 16). Bien que l'analyse par spectroscopie infrarouge révèle la présence d'amides et d'acides carboxyliques (Briani et al., minor revision), la présence de composés oxygénés n'est pas évidente dans ces spectres de masses. Ceci pourrait être du à des différences dans les rendements de ionisation des différentes molécules. En effet, l'acquisition de spectres de référence avait montré que les acides carboxyliques s'ionisent difficilement, à l'inverse du

[20] Le HMT faisant partie du groupe de symétrie Td, il ne possède ni moment dipolaire ni transition rotationnelle. Sa détection en phase gazeuse ne peut donc pas être effectuée dans le domaine sub-millimétrique.

[21] ROSINA (The ROsetta Spectrometer for Ion and Neutral Analysis) est un ensemble de deux spectromètres de masse dédié à l'étude de la phase gazeuse de l'environnement cométaire. Cet instrument est à bord de l'orbiteur de la mission Rosetta.

HMT qui s'ionise très facilement. Néanmoins, les spectres de masses des analogues présentent des pics qui ne sont pas liés au HMT et qui ne sont pas attribués de manière univoque (m/z = 100.08 amu et 130.16 amu notamment). L'analyse détaillée de ces spectres est toujours en cours.

4.4.3. La mesure in-situ des rapports élémentaires avec COSIMA.

Depuis le début du travail concernant la calibration de COSIMA et la préparation au traitement des futures observations spatiales, un grand nombre de spectres de référence de molécules organiques a été acquis, la plupart par Léna Le Roy durant sa thèse et d'autres par Christelle Briois. Depuis mon intégration dans l'équipe COSIMA, je me suis attaché à considérer l'ensemble de ces spectres de manière globale afin de trouver une méthode permettant la mesure quantitative des rapports élémentaires et en particulier du rapport N/C. La technique d'ionisation par bombardement d'ions primaires induisant une fragmentation des molécules étudiées, tous les spectres présentent des pics aux faibles rapports masse/charge. J'ai donc sélectionné quelques pics aux faibles m/z qui ne sont spécifiques d'aucune molécule particulière. Mon attention s'est portée plus spécifiquement sur les pics aux masses entières 27, 28 et 29 dans le cas des spectres d'ions positifs. En effet, quelque soit la molécule étudiée les pics aux masses 27 et 29 sont dus aux ions moléculaires $C_2H_3^+$ et $C_2H_5^+$, respectivement. Le pic à la masse 28 est généralement du à l'ion radicalaire $C_2H_4^+$ dans le cas des molécules non azotées et à l'ion moléculaire CH_2N^+ dans le cas des molécules azotées. Ces attributions ont été vérifiées en comparant la masse exacte des ions et la position précise des pics. Les ions moléculaires étant plus probables que les ions radicalaires en TOF-SIMS les rapports d'intensité étudiés (I_{28}/I_{27} et I_{28}/I_{29}) sont faibles pour les molécules non azotées et élevés pour les molécules azotées (Figure 17). Il est donc possible de détecter la présence d'azote dans certains spectres. Néanmoins, dans le cas des polymères de HCN, l'azote n'est pas détecté alors qu'il est présent. Les observations très similaires ont été faites en étudiant les pics aux masses entières 39, 40 et 41 qui correspondent à l'addition d'un atome de carbone par rapport au cas précédent.

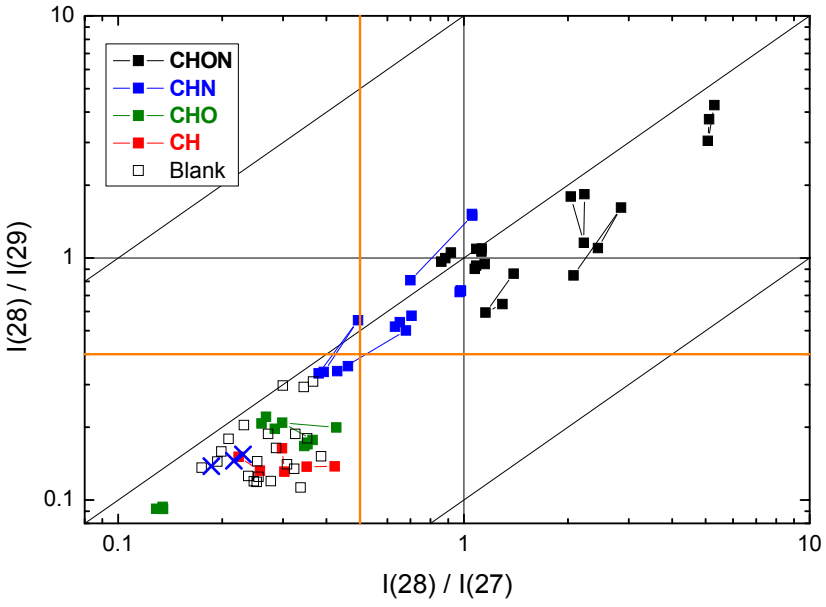

Figure 17 : Rapport d'intensité des pics aux masses 28 et 29 en fonction de celui aux masses 28 et 27. La couleur des points code la composition élémentaire des molécules étudiées. Les carrés blancs correspondent aux spectres acquis sur des cibles ne contenant pas d'échantillon (contamination). Pour

tous les spectres se situant dans le quart supérieur droit de cette figure, la présence d'azote est mise en évidence.

Dans le cas des spectres de référence, la nature des molécules étudiées est connue ; le rapport d'intensité des pics étudiés peut donc être tracé en fonction du rapport élémentaire N/C. Nous constatons sur la figure 18 que si la corrélation entre ces deux paramètres existe alors elle est très faible. La seule étude de l'intensité des pics 28 et 29 ne semble pas permettre la mesure du rapport N/C avec des barres d'erreurs suffisamment faibles pour pouvoir exploiter ces mesures dans un cadre planétologique. Les autres rapports d'intensité étudiés, pour les spectres d'ions positifs et négatifs, donnent des résultats similaires. Afin de mesurer le rapport élémentaire N/C de manière plus précise, j'envisage de considérer l'ensemble des rapports d'intensités déjà étudiés de manière plus globale ainsi que l'étude de nouveaux pics.

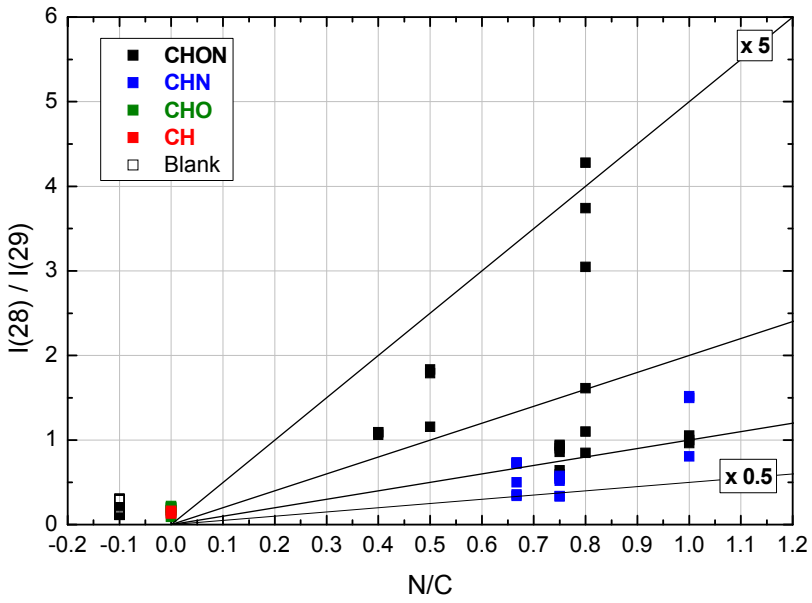

Figure 18 : Rapport d'intensité des pics aux masses entières 28 et 29 en fonction du rapport élémentaire N/C dans les spectres de référence de molécules pures.

5. Perspectives.

La principale perspective à moyen terme est de manière évidente l'analyse des observations in-situ qui seront réalisées par COSIMA à partir de l'automne 2014[22]. En effet, l'étude in-situ des poussières cométaires par spectrométrie de masse semble être le meilleur moyen pour accéder à la nature physico-chimique de la matière organique solide sur des grains dont l'origine cométaire est avérée. La comète 67P/Churyumov-Gerasimenko (67P) sera seulement la 4^{éme} comète dont les grains seront analysés par spectrométrie de masse in-situ, ces données sont donc rares et précieuses.

Jusqu'à l'arrivée de Rosetta dans l'environnement de 67P/Churyumov-Gerasimenko, je continuerai le travail commencé afin de trouver la méthode la plus précise possible pour quantifier le rapport élémentaire N/C tout en l'étendant aux rapports O/C et H/C. Une fois les premières observations réalisées, je pense me concentrer sur quelques points en particulier :

- La recherche de la présence du polyoxyméthylène (POM) en phase solide. Une détection du POM viendrait confirmer une partie des travaux que j'ai réalisés au cours de ma thèse. Des calculs préliminaires montrent, que lorsque 67P sera au périhélie, le POM se sera vraisemblablement décomposé de manière significative avant la collecte des grains. Cette recherche devra donc être effectuée très rapidement lorsque la comète se situera encore à environ 3 UA.
- La comparaison des spectres de masse provenant de différents grains collectés sur une même cible afin de rechercher une possible hétérogénéité de composition entre les grains. Etant donné que COSIMA analysera prioritairement des grains de quelques dizaines de microns, il n'est pas certain qu'une hétérogénéité chimique sera présente à cette échelle. Si une hétérogénéité est mise en évidence, elle pourra être interprétée par des origines différentes ou des évolutions différentes du(des) matériau(x) constitutif(s) des grains.

[22] Les premiers spectres de masses ne seront vraisemblablement acquis qu'après l'atterrissage du lander sur le noyau.

- Pour un même grain, il sera intéressant de suivre l'évolution temporelle des spectres afin de mettre éventuellement en évidence un changement de nature chimique pouvant résulter du chauffage (environ 300 K) à l'intérieur de l'instrument.
- La comparaison des grains collectés sur différentes cibles, c'est-à-dire à différentes distances héliocentriques, pourrait aussi permettre de mettre en évidence des processus de dégradation se déroulant directement dans la coma et qui pourraient être dus à l'augmentation de température des grains lorsque la comète se rapprochera du Soleil.

En parallèle, je continuerai les travaux d'expérimentation en laboratoire permettant de synthétiser des analogues à la matière organique cométaire et d'en étudier l'évolution thermique. Je décris ci-dessous quelques points spécifiques concernant les futurs travaux qui pourront être menés grâce au dispositif « OREGOC ».

Nous avons déjà commencé un travail concernant l'optimisation du spectre d'émission de nos lampes VUV[23] afin de le rendre le plus représentatif possible de celui présent dans différents milieux astrophysiques. En effet, si on compare les spectres d'émission des lampes VUV utilisées pour la photolyses des glaces (Hagen et al., 1979; Cottin et al., 2003) avec les spectres présents dans les nuages moléculaires denses (Gredel et al., 1987) ou les spectres du Soleil (Thuillier et al., 2004), il devient évident que ces lampes ne simulent que très partiellement les spectres astrophysiques. Pour l'instant, dans le cadre du stage de M2R de Michaëlle Bouilloud, nous avons réussi à augmenter l'émission de l'hydrogène atomique (Lyman α à 121.6 nm) par rapport à celle l'hydrogène moléculaire (environ 160 nm) (spectre (a) de figure 19). Ce spectre est semblable à celui présent dans les nuages moléculaires denses (Gredel et al., 1987). Néanmoins, l'objectif principal est de pouvoir obtenir de manière reproductible un spectre quasi-monochromatique à Lyman α (spectre (b)[24] de la figure 19) afin de simuler les spectres stellaires. Je tiens à finaliser cette étude afin de renforcer la représentativité astrophysique des expérimentations que nous menons. De plus, une expérience préliminaire semble montrer que la chimie induite par la photolyse d'un mélange de glaces pourrait dépendre du spectre d'émission de la lampe, ce dernier point doit être vérifié.

Le méthane a été détecté en phase solide dans les grains glacés autour des étoiles naissantes (Gibb et al., 2004; Dartois, 2005; Oberg et al., 2011). Son abondance est de quelques pourcents, ce qui est relativement faible. Peu d'expérimentations ont été effectuées en incluant du méthane dans un mélange contenant de l'eau, du méthanol et de l'ammoniac. Je souhaite étudier l'impact d'un ajout d'une faible quantité de méthane sur la chimie conduisant à la formation d'analogues ainsi si cet ajout conduit à la formation d'analogues différents ou non.

[23] Ce travail a été rendu possible grâce à l'acquisition d'un spectromètre VUV permettant de mesurer les spectres d'émission entre 115 et 200 nm avec une résolution de l'ordre de 0.5 nm.

[24] Ce spectre (b) est celui d'une de nos lampes photochimiques. La reproduction de ce spectre nous pose quelques soucis, mais nous avons bon espoir d'y arriver très prochainement.

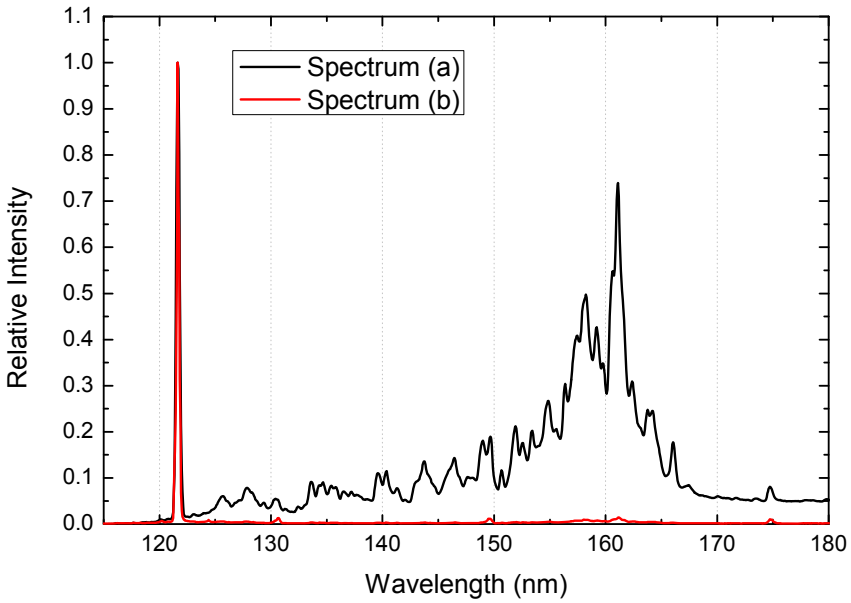

Figure 19 : Spectres d'émission VUV de lampe (plasma de H_2 entretenu par une décharge micro-onde) que nous utilisons pour photolyser des mélanges de glaces.

A ce jour, une seule mesure des rapports élémentaires N/C et O/C a été réalisée par spectroscopie XANES[25] sur des analogues à la matière organique cométaire (Nuevo et al., 2011). Les méthodes classiques, par pyrolyse, de mesure des rapports élémentaires nécessitent des échantillons de quelques milligrammes. A ce jour, nous sommes capables de synthétiser des analogues de l'ordre de 100 à 200 microgrammes pour des durées de photolyse d'environ 15 heures. L'augmentation de la quantité de matière produite passera vraisemblablement par des expérimentations beaucoup plus longues ou par l'augmentation des flux de photons de nos lampes. Etant donné que les rapports élémentaires ont déjà été mesurés dans les comètes (Jessberger et al., 1988; Fomenkova et al., 1994), les IDPs, les micrométéorites (Matrajt et al., 2003) et les météorites carbonées (Alexander et al., 2007), ces analyses permettront une comparaison directe des analogues produits avec les observations astrophysiques. D'autre part, une augmentation de la quantité d'analogue permettra aussi de pouvoir caractériser la fraction restante après un fort chauffage jusqu'à 600 K ce qui n'a pas pu être effectué à l'heure actuelle et éventuellement de mesurer la variation des rapports élémentaires durant l'évolution thermique.

Il a été montré que l'analyse couplée par spectroscopie infrarouge et Raman des échantillons d'origine extraterrestre permettre d'obtenir des informations complémentaires (Brunetto et al., 2011; Dartois et al., 2013). Aussi, des analyses par spectroscopie Raman sur les analogues à la matière carbonée cométaire sont envisagées comme cela a déjà pu être fait sur des tholins[26] et des polymères de HCN (Quirico et al., 2008).

Les perspectives décrites ci-dessus ont toutes pour objectif soit une meilleure représentativité des expérimentations soit une comparaison directe avec les cosmomatériaux disponibles au laboratoire dont l'origine cométaire est probable (IDPs et micrométéorites notamment). Afin que la comparaison entre les analogues de laboratoire et

[25] XANES : X-ray Absorption Near Edge Structure

[26] Tholins : Analogues synthétiques aux aérosols présents dans l'atmosphère de Titan.

les cosmomatériaux soit la plus pertinente possible, elle doit prendre en compte l'ensemble de la matière organique présente dans les objets astrophysiques. L'un des objectifs des expériences de laboratoire est donc la production d'un matériau macromoléculaire insoluble présentant de faibles rapports élémentaires N/C et O/C. L'objectif final reste inchangé : caractériser au mieux la matière organique contenue dans les comètes ainsi que son origine et son évolution.

Concernant les travaux sur les équilibres solide – gaz à basses températures, la collaboration avec Bernard Schmitt sera poursuivie, en particulier par l'inclusion de l'ensemble des données acquises dans la base de données GhoSST (Grenoble Astrophysics and Planetology Solid Spectroscopy and Thermodynamics). Concernant la spectroscopie VUV, nos travaux seront poursuivis tant pour améliorer les modèles photochimiques des Jupiters chauds que pour fournir des données les plus représentatives possibles en terme de température et de résolution spectrale pour l'exploitation des observations des hautes atmosphères par occultations stellaires et solaires. D'autre part, les spectres VUV déjà acquis pourront être utilisés afin de fournir les taux de photodissociation les plus précis possible pour la photochimie des atmosphères cométaires.

Références citées dans le texte.

Alexander, C. M. O. D., et al., 2007. The origin and evolution of chondrites recorded in the elemental and isotopic compositions of their macromolecular organic matter. Geochimica Et Cosmochimica Acta. 71**,** 4380-4403.

Barrer, R. M., Edge, A. V. J., 1967. Gas hydrates containing argon, krypton and xenon - Kinetics and energetics of formation and equilibria. Proceedings of the Royal Society of London Series a-Mathematical and Physical Sciences. 300**,** 1-&.

Bernstein, M. P., et al., 1995. Organic Compounds Produced by Photolysis of Realistic Interstellar and Cometary Ice Analogs Containing Methanol. The Astrophysical Journal. 454**,** 327.

Bockelee-Morvan, D., et al., 1995. On the origin of the 3.2 to 3.6-micron emission features in comets. Icarus. 116**,** 18-39.

Bockelee-Morvan, D., et al., 2009. Water in comets 71P/Clark and C/2004B1 (LINEARà with Spitzer. Astrophysical Journal. 696**,** 1075-1083.

Bockelée-Morvan, D., et al., The composition of cometary volatiles. In: G. W. Kronk, (Ed.), Comets II, 2004, pp. 391-423.

Bockelée-Morvan, D., et al., 2012. Herschel measurements of the D/H and 16O/18O ratios in water in the Oort-cloud comet C/2009 P1 (Garradd). Astronomy and Astrophysics. 544**,** L15.

Briani, G., et al., minor revision. HMT production and sublimation during thermal process of cometary organic analogs. Implications for its detection with the ROSETTA instruments. Icarus.

Brownlee, D., et al., 2006. Comet 81P/Wild 2 Under a Microscope. Science. 314**,** 1711-.

Brunetto, R., et al., 2011. Mid-IR, Far-IR, Raman micro-spectroscopy, and FESEM-EDX study of IDP L2021C5: Clues to its origin. Icarus. 212**,** 896-910.

Chen, F. Z., Wu, C. Y. R., 2004. Temperature-dependent photoabsorption cross sections in the VUV-UV region. I. Methane and ethane. Journal of Quantitative Spectroscopy & Radiative Transfer. 85**,** 195-209.

Clayton, J. O., Giauque, W. F., 1932. The heat capacity and entropy of carbon monoxide. Heat of vaporization. Vapor pressures of solid and liquid. Free energy to 5000 degrees K. from spectroscopic data. Journal of the American Chemical Society. 54, 2610-2626.

Clemett, S. J., et al., 1993. Identification of Complex Aromatic Molecules in Individual Interplanetary Dust Particles. Science. 262, 721-725.

Coll, P., et al., Organic-chemistry in Titan's astmosphere - New data from laboratory simulations at low temperature. In: A. C. LevasseurRegourd, F. Raulin, Eds.), Prebiotic Chemistry in Space, 1995, pp. 93-103.

Cottin, H., et al., 1999. SEMAPh.Or.E COMETAIRE, a tool for the study of the photochemical decomposition of probable large organic molecules in comets. First application: Polyoxymethylene. Physics and Chemistry of the Earth Part C-Solar-Terrestial and Planetary Science. 24, 597-602.

Cottin, H., et al., 2000. An experimental study of the photodegradation of polyoxymethylene at 122, 147 and 193 nm. Journal of Photochemistry and Photobiology a-Chemistry. 135, 53-64.

Cottin, H., et al., 2003. Photodestruction of relevant interstellar molecules in ice mixtures. Astrophysical Journal. 590, 874-881.

Cottin, H., et al., 2004. Origin of cometary extended sources from degradation of refractory organics on grains: polyoxymethylene as formaldehyde parent molecule. Icarus. 167, 397-416.

Cottin, H., Fray, N., 2008. Distributed sources in comets. Space Science Reviews. 138, 179-197.

Crovisier, J., 1994. Photodestruction rates for cometary parent molecules. Journal of Geophysical Research. 99, 3777-3781.

Crovisier, J., et al., 2004. Ethylene glycol in comet C/1995 O1 (Hale-Bopp). Astronomy and Astrophysics. 418, L35-L38.

Dartois, E., 2005. The ice survey opportunity of ISO. Space Science Reviews. 119, 293-310.

Dartois, E., et al., 2013. UltraCarbonaceous Antarctic micrometeorites, probing the Solar System beyond the nitrogen snow-line. Icarus. 224, 243-252.

De Vanssay, E., et al., 1995. Experimental simulation of Titan's organic chemistry at low temperature. Planetary and Space Science. 43, 25-31.

Duprat, J., et al., 2010. Extreme Deuterium Excesses in Ultracarbonaceous Micrometeorites from Central Antarctic Snow. Science. 328, 742-745.

Fanale, F. P., Salvail, J. R., 1990. The Influence of CO ice on the activity and near-surface differentiation of comet nuclei. Icarus. 84, 403-413.

Ferradaz, T., et al., 2009. Temperature-dependent photoabsorption cross-sections of cyanoacetylene and diacetylene in the mid- and vacuum-UV: Application to Titan's atmosphere. Planetary and Space Science. 57, 10-22.

Floss, C., et al., 2006. Identification of isotopically primitive interplanetary dust particles: A NanoSIMS isotopic imaging study. Geochimica Et Cosmochimica Acta. 70, 2371-2399.

Flynn, G. J., et al., 2003. The origin of organic matter in the solar system: evidence from the interplanetary dust particles. Geochimica Et Cosmochimica Acta. 67, 4791-4806.

Fomenkova, M. N., et al., 1994. Carbonaceous components in the comet Halley Dust. Geochimica and Cosmochimica Acta. 58, 4503-4512.

Fomenkova, M. N., 1999. On the organic refractory component of cometary dust. Space Science Reviews. 90, 109-114.

Fray, N., et al., 2004. New experimental results on the degradation of polyoxymethylene: Application to the origin of the formaldehyde extended source in comets. Journal of Geophysical Research-Planets. 109.

Fray, N., et al., 2006. Heliocentric evolution of the degradation of polyoxymethylene: Application to the origin of the formaldehyde (H2CO) extended source in Comet C/1995 O1 (Hale-Bopp). Icarus. 184, 239-254.

Fray, N., Schmitt, B., 2009. Sublimation of ices of astrophysical interest: A bibliographic review. Planetary and Space Science. 57, 2053-2080.

Fray, N., et al., 2010. Equilibrium Data of Methane, Carbon Dioxide, and Xenon Clathrate Hydrates below the Freezing Point of Water. Applications to Astrophysical Environments. Journal of Chemical and Engineering Data. 55, 5101-5108.

Gautier, D., et al., 2001. Enrichments in volatiles in Jupiter: A new interpretation of the Galileo measurements. Astrophysical Journal. 550, L227-L230.

Giauque, W. F., Egan, C. J., 1937. Carbon dioxide. The heat capacity and vapor pressure of the solid. The heat of sublimation. Thermodynamic and spectroscopic values of the entropy. Journal of Chemical Physics. 5, 45-54.

Gibb, E. L., et al., 2004. Interstellar ice: The Infrared Space Observatory legacy. Astrophysical Journal Supplement Series. 151, 35-73.

Gredel, R., et al., 1987. The C/CO ratio in dense interstellar clouds. The Astrophysical Journal Letters. 323, L137-L139.

Hagen, W., et al., 1979. Interstellar molecules formation in grain mantles - Laboratory analog experiments, results and implications. Astrophysics and Space Science. 65, 215-240.

Hartogh, P., et al., 2011. Ocean-like water in the Jupiter-family comet 103P/Hartley 2. Nature. 478, 218-220.

Hébrard, E., et al., 2006. Photochemical kinetics uncertainties in modeling Titan's atmosphere: A review. Journal of Photochemistry and Photobiology C-Photochemistry Reviews. 7, 211-230.

Hersant, F., et al., 2004. Enrichment in volatiles in the giant planets of the Solar System. Planetary and Space Science. 52, 623-641.

Huebner, W. F., et al., 1992. Solar photo rates for planetary atmospheres and atmospheric pollutants. Astrophysics and Space Science. 195, 1-289.

Iro, N., et al., 2003. An interpretation of the nitrogen deficiency in comets. Icarus. 161, 511-532.

Jessberger, E. K., et al., 1988. Aspects of the major element composition of Halley dust. Nature. 332**,** 691-695.

Jin, Y., et al., 2011. Phase Equilibrium Conditions for Krypton Clathrate Hydrate below the Freezing Point of Water. Journal of Chemical and Engineering Data. 56**,** 58-61.

Kissel, J., et al., 1986a. Composition of comet Halley dust particles from Giotto Observations. Nature. 321**,** 336-337.

Kissel, J., et al., 1986b. Composition of comet Halley dust particles from Vega observations. Nature. 321**,** 280-282.

Kissel, J., Krueger, F. R., 1987. The organic component in dust from comet Halley as measured by the mass spectrometer on board Vega-1. Nature. 326**,** 755-760.

Kissel, J., et al., 2004. The Cometary and Interstellar Dust Analyzer at Comet 81P/Wild 2. Science. 304**,** 1774-1776.

Kissel, J., et al., 2007. COSIMA - High resolution time-of-flight secondary ion mass spectrometer for the analysis of cometary dust particles onboard Rosetta. Space Science Reviews. 128**,** 823-867.

Koskinen, T. T., et al., 2011. The mesosphere and thermosphere of Titan revealed by Cassini/UVIS stellar occultations. Icarus. 216**,** 507-534.

Krueger, F. R., et al., 1991. The organic matter of Comet Halley as inferred by joint gas phase and solid phase analyses. Space Science Reviews. 56**,** 167-175.

Le Roy, L., et al., 2012. On the prospective detection of polyoxymethylene in comet 67P/Churyumov-Gerasimenko with the COSIMA instrument onboard Rosetta. Planetary and Space Science. 65**,** 83-92.

Lee, L. C., 1980. CN (A2PII->X2S+) and CN (B2S+-> X2S+) yiels from HCN photodissociation. Journal of Chemical Physics. 72**,** 6414-6421.

Lide, D. R. (Ed.) 2007. CRC Handbook of Chemistry and Physics, 87th ed., Boca Raton, FL.

Lunine, J. I., Stevenson, D. J., 1985. Thermodynamics of clathrate hydrate at low and high-pressures with application to the outer solar-system. Astrophysical Journal Supplement Series. 58**,** 493-531.

Mahaffy, P. R., et al., 2000. Noble gas abundance and isotope ratios in the atmosphere of Jupiter from the Galileo Probe Mass Spectrometer. Journal of Geophysical Research. 105**,** 15061-15072.

Marboeuf, U., et al., 2012. Equilibrium Pressure of Ethane, Acetylene, and Krypton Clathrate Hydrates below the Freezing Point of Water. Journal of Chemical and Engineering Data. 57**,** 3408-3415.

Matrajt, G., et al., 2003. A nuclear microprobe study of the distribution and concentration of carbon and nitrogen in Murchison and Tagish Lake meteorites, Antarctic micrometeorites, and IDPs: Implications for astrobiology. Meteoritics & Planetary Science. 38**,** 1585-1600.

Miller, S. L., 1961. The occurence of gas hydrates in the solar system. Proceedings of the National Academy of Sciences of the United States of America. 47**,** 1798-1808.

Munoz-Caro, G. M., Schutte, W. A., 2003. UV-photoprocessing of interstellar ice analogs: New infrared spectroscopic results. Astronomy & Astrophysics. 412**,** 121-132.

Nuevo, M., et al., 2011. XANES analysis of organic residues produced from the UV irradiation of astrophysical ice analogs. Advances in Space Research. 48**,** 1126-1135.

Nuth, J. A., Glicker, S., 1982. The vacuum ultraviolet spectra of HCN, C2N2 and CH3CN. Journal of Quantitative Spectroscopy & Radiative Transfer. 28**,** 223-231.

Oberg, K. I., et al., 2011. The Spitzer ice legacy: Ice evolution from cores to protostars. Astrophysical Journal. 740.

Prialnik, D., et al., Modeling the structure and activity of comet nuclei. In: G. W. Kronk, (Ed.), Comets II, 2004, pp. 359-387.

Quirico, E., et al., 2008. New experimental constraints on the composition and structure of tholins. Icarus. 198**,** 218-231.

Rodgers, S. D., et al., Physical processes and chemical reactions in cometary comae. In: G. W. Kronk, (Ed.), Comets II, 2004, pp. 505-522.

Sandford, S. A., et al., 2010. Assessment and control of organic and other contaminants associated with the Stardust sample return from comet 81P/Wild 2. Meteoritics and Planetary Science. 45**,** 406-433.

Schutte, W. A., et al., 1993. An experimental study of the organic molecules produced in cometary and interstellar ice analogs by thermal formaldehyde reactions. Icarus. 104**,** 118-137.

Shemansky, D. E., et al., 2005. The Cassini UVIS Stellar Probe of the Titan Atmosphere. Science. 308**,** 978-982.

Shinoda, T., 1969. Vapor pressure of carbon monoxide in condensed phases. Bulletin of the Chemical Society of Japan. 42**,** 2815-&.

Sloan, D., Koh, C., 2007. Clathrate Hydrates of Natural Gases, Third editon. Marcel Dekker Incorporated.

Stern, S. A., 2003. The evolution of comets in the Oort cloud and Kuiper belt. Nature. 424**,** 639-642.

Thomas, C., et al., 2007. Clathrate hydrates as a sink of noble gases in Titan's atmosphere. Astronomy & Astrophysics. 474**,** L17-L20.

Venot, O., et al., 2013. High-temperature measurements of VUV-absorption cross sections of CO2 and their application to exoplanets. Astronomy and Astrophysics. 551**,** 131.

Veverka, J., et al., 2013. Return to Comet Tempel 1: Overview of Stardust-NExT results. Icarus. 222**,** 424-435.

Vinogradoff, V., et al., 2012. The mechanism of hexamethylenetetramine (HMT) formation in the solid state at low temperature. Physical Chemistry Chemical Physics. 14**,** 12309-12320.

Vinogradoff, V., et al., 2013. Importance of thermal reactivity for hexamethylenetetramine formation from simulated interstellar ices. Astronomy & Astrophysics. 551.

Woodward, C. E., et al., 2007. Water in comet C/2003 K4 (linear) with spitzer. Astrophysical Journal. 671**,** 1065-1074.

Wu, C. Y. R., et al., 2001. Measurements of temperature-dependent absorption cross sections of C2H2 in the VUV-UV region. Journal of Geophysical Research-Planets. 106**,** 7629-7636.

Wu, C. Y. R., et al., 2004. Temperature-dependent photoabsorption cross sections in the VUV-UV region: Ethylene. Journal of Geophysical Research-Planets. 109.

Yoon, J. H., et al., 2002. Generalized model for predicting phase behavior of clathrate hydrate. Aiche Journal. 48**,** 1317-1330.

Yoon, J. H., et al., 2004. PSRK method for gas hydrate equilibria: I. Simple and mixed hydrates. Aiche Journal. 50**,** 203-214.

Yoshino, K., et al., 1996. Absorption cross section measurements of carbon dioxide in the wavelength region 118.7-175.5 nm and the temperature dependence. Journal of Quantitative Spectroscopy & Radiative Transfer. 55**,** 53-60.

Annexes.

- Curriculum Vitae
- Liste des publications
- Encadrements et formation par la recherche
- Activités d'enseignement
- Contrats de recherche
- Sélection d'articles

Curriculum Vitae

FRAY Nicolas
Né le 13 Avril 1977
Tél : 01 45 17 15 43
Fax : 01 45 17 15 64
nicolas.fray@lisa.u-pec.fr

Laboratoire Interuniversitaire des Systèmes Atmosphériques (LISA)
UMR 7583 du CNRS
Université Paris-Est Créteil (UPEC) et Université Paris Diderot (UPD)

Maître de conférences – Section 34
LISA – Groupe de Physico-Chimie Organique Spatiale

PROJETS PROFESSIONNELS

● Processus solide – gas : Stabilité thermodynamique des glaces pures et des clathrates d'hydrates. Expérimentation en laboratoire et applications aux objets du système solaire et en particulier des comètes.

● Spectroscopie dans le domaine UV : Expérimentation en laboratoire et sur synchrotron. Applications à l'observation des atmosphères planétaires par occultations stellaires ou solaires.

● Composition et origine des comètes :

○ Synthèse d'analogues à la matière organique cométaire par photolyse et réchauffement de mélange de glaces.

○ Caractérisation physico-chimique et évolution thermique de ces analogues.

○ Préparation à l'interprétation des observations de COSIMA (spectromètre de masse à bord de Rosetta).

SITUATIONS ANTERIEURES

2006 Post-doctorat au laboratoire de Planétologie de Grenoble (LPG) – Financement CNES.
2005 ATER de Physique à l'université Paris 12.

FORMATION

2004 Doctorat de l'université Paris 12. « Etude expérimentale et théorique de la contribution de la composante organique réfractaire à la phase gazeuse dans l'environnement cométaire ».
Directeur (trice) : Yves Bénilan et Marie-Claire Gazeau
Mention très honorable avec félicitations du jury.

2001 DEA : « Méthode instrumentale en astrophysique et applications spatiales » à l'IAP (ED « Astronomie et Astrophysique en Ile de France »). *Mention Très-Bien*

2000 Agrégation de sciences physiques, option physique (52ème sur 150)

1999 Licence et Maîtrise de « Physique fondamentale » à l'université Paris VI. *Mention Assez-Bien*

1997 Classes Préparatoires Physique-Chimie.

1995 Baccalauréat série S. *Mention Bien*

RESPONSABILITES

● Responsable du plateau technique de physique de la Faculté des Sciences et Technologie de l'Université Paris-Est Créteil depuis Juillet 2012.

Le plateau technique regroupe l'ensemble des enseignements de travaux pratiques de physique quelque soit la filière à laquelle appartiennent les étudiants (MIPC, SVT, CB,..).

Gestion et mise en place des plannings pédagogiques de toutes les filières pour les 3 années de licence (516 séances de TP de 3 heures chacune sur l'année universitaire 2012-2013)

Réponses aux appels d'offre de crédits pédagogiques et gestion des crédits pour le renouvellement et la maintenance des matériels.

● Associated Scientist de l'équipe COSIMA (Spectromètre de masse à bord de la sonde spatiale Rosetta) depuis Octobre 2012.

● Participation au comité de sélection du poste MCF 0118 en 2011 (Section 34/63, UVSQ, LATMOS)

● Représentant du LISA depuis 2011 à la commission de la Faculté des Sciences et Technologie de l'UPEC chargée du recrutement des ATERs physique.

DIVERS

● Participation à des jurys de doctorat :

[1] Participation, en tant qu'invité, au jury de doctorat de Jean-Yves Bonnet.
Directeur de thèse : Eric Quirico.
Université Joseph Fourier de Grenoble - Institut de Planétologie et d'Astrophysique de Grenoble (IPAG) - Le 30 Janvier 2012

[2] Participation, en tant qu'examinateur, au jury de doctorat de Prasad JOSHI
Directeur de thèse : Lahouari KRIM
Université Pierre & Marie Curie - Laboratoire de Dynamique, Interactions et Réactivité (LADIR) - Le 29 Mars 2012

● Délégations au CNRS

Année universitaire 2011-2012 : Délégation à 100 %
Année universitaire 2012-2013 : Délégation à 50 %

● Reviewer pour Icarus, Chemical Physics, ApJ et PSS.

● Séminaires invités :

Le 31 Aout 2010 au LPG (Laboratoire de Planétologie de Grenoble, désormais IPAG)
Le 6 Juin 2011 au PIIM à Marseille (Laboratoire *de Physique des Interactions Ioniques et Moléculaires).*
Le 1er Mai 2013 Physics Institute, Space Research and Planetary Sciences, Bern (Suisse)

Liste des publications

PUBLICATIONS DANS DES REVUES INTERNATIONALES A COMITE DE LECTURE

[P22] Briani G., **Fray N.**, Cottin H., Benilan Y., Gazeau M.-C. and Perrier S.
HMT production and sublimation during thermal process of cometary organic analogs. Implications for its detection with the ROSETTA instruments.
Icarus, minor revisions.

[P21] Venot O., **Fray N.**, Bénilan Y., Gazeau M.-C., Hébrard E., Larcher G., Schwell M., Dobrijevic M. and Selsis F. (2013)
High-temperature measurements of VUV absorption cross sections of CO2 and application to exoplanets.
Astronomy & Astrophysics, 551, A131
http://dx.doi.org/10.1051/0004-6361/201220945

[P20] Vinogradoff V., **Fray N.**, Duvernay F., Briani G., Danger G., Cottin H., Theulé P. and Chiavassa T. (2013)
Importance of the thermal reactivity for hexamethylenetetramine (HMT) formation from simulated interstellar ices.
Astronomy and Astrophysics, 551, A128
http://dx.doi.org/10.1051/0004-6361/201220870

[P19] Marboeuf U., **Fray N.**, Brissaud O., Schmitt B., Bockelée-Morvan D. and Gautier D. (2012)
Equilibrium pressure of ethane, acetylene and krypton clathrate hydrates below the freezing point of water.
Journal of Chemical and Engineering Data, 57(12), 3408-3415
http://dx.doi.org/10.1021/je3004595

[P18] Marboeuf U., Schmitt B., Petit J.-M., Mousis O. and **Fray N.** (2012)
A cometary nucleus model taking into account all phase changes of water ice: amorphous, crystalline, and clathrate.
Astronomy and Astrophysics, 542, A82
http://dx.doi.org/10.1051/0004-6361/201118176

[P17] Schwell M., Benilan Y., **Fray N.**, Gazeau M.-C., Es-Sebbar Et., Gaie-Levrel F., Champion N. and Leach S. (2012)
Ionization photophysics and rydberg spectroscopy of diacetylene.
Molecular Physics, 110(21-22), 2843-2856
http://dx.doi.org/10.1080/00268976.2012.704084

[P16] Le Roy L., Briani G., Briois C., Cottin H., **Fray N.**, Thirkell L., Poulet, G. and Hilchenbach, M. (2012)
On the prospective detection of polyoxymethylene in comet 67P/Churyumov-Gerasimenko with the COSIMA instrument onboard Rosetta.
Planetary and Space Science, 65(1), 83-92.
http://dx.doi.org/10.1016/j.pss.2012.01.011

[P15] Schwell M., Bénilan Y., **Fray N.**, Gazeau M.-C., Es-Sebbar E., Garcia G. A., Nahon L., Champion N. and Leach S. (2012)
VUV photoionization of acetamide studied by electron / ion coincidence spectroscopy in the 8-24 eV photon energy range. *Chemical Physics,* 393(1), 107-116.
http://dx.doi.org/10.1016/j.chemphys.2011.11.032

[P14] **Fray N.,** Marboeuf U., Brissaud O. And Schmitt B. (2010)
Equilibrium data of methane, carbon dioxide and xenon clathrate hydrates below the freezing point of water. Applications to astrophysical environments.
Journal of Chemical and Engineering Data, 55(11), 5101-5108.
http://dx.doi.org/10.1021/je1006604

[P13] Vuitton V., Bonnet J.-Y., Frisari M., Thissen R., Quirico E., Dutuit O., Schmitt B., Le Roy L., **Fray N.**, Cottin H., Sciamma-O'Brien E., Carrasco N. and Szopa C. (2010)
Very high resolution mass spectrometry of HCN polymers and tholins.
Faraday Discussions, 147, 495-508.
http://dx.doi.org/10.1039/c003758c

[P12] Guan Y.Y., **Fray N.**, Coll P., Macari F., Chaput D., Raulin F. and Cottin H. (2010)
UVolution: Compared photochemistry of prebiotic organic compounds in low Earth orbit and in the laboratory.
Planetary and Space Science, 58(10), 1327-1346.
http://dx.doi.org/10.1016/j.pss.2010.05.017

[P11] **Fray N.**, Bénilan Y., Gazeau M.-C., Jolly A., Schwell M., Arzoumanian E., Ferradaz T., Es-Sebbar E. And Guillemin J.-C. (2010)
Temperature-dependant photoabsorption cros-section of cyanoacetylene in the vacuum UV.
Journal of Geophysical Research (Planets), 115, E06010
http://dx.doi.org/10.1029/2009JE003518

[P10] **Fray N.** and Schmitt B. (2009)
Sublimation of molecules of astrophysical interest. A bibliographic review.
Planetary and Space Science, 57(14-15), 2053-2080.
http://dx.doi.org/10.1016/j.pss.2009.09.011

[P09] Ferradaz T., Bénilan Y., **Fray N.**, Jolly A., Schwell M., Gazeau M.-C., Jochims H.-W. and Guillemin J.-C. (2009)
Temperature dependant photoabsorption cross sections of cyanoacetylene and diacetylene in the mid- and vacuum-UV: Application to Titan's Atmosphere.
Planetary and Space Science, 57(1), 10-22.
http://dx.doi.org/10.1016/j.pss.2008.10.005

[P08] Quirico E., Montagnac G., Lees V., McMillan P.F., Szopa C., Cernogora G., Rouzaud J.-N., Simon P., Bernard J.-M., Coll P., **Fray N.**, Minard R.D., Raulin F., Reynard B. and Schmitt D. (2008)
New experimental constraints on the composition and structure of tholins.
Icarus, 198(1), 218-231.
http://dx.doi.org/10.1016/j.icarus.2008.07.012

[P07] Cottin H., and **Fray N.** (2008)
Distributed sources in comets.
Space Science Reviews, 138(1-4), 179-197.
http://dx.doi.org/10.1007/s11214-008-9399-z

[P06] Cottin H., Coll P., Coscia D., **Fray N.**, Guan Y. Y., Macari F., Raulin F., Rivron C., Stalport F., Szopa C., Chaput D., Viso M., Bertrand M., Chabin A., Thirkell L., Westall F. and Brack A. (2008)
Heterogeneous solid/gas chemistry of organic compounds related to comets, meteorites, Titan, and Mars: Laboratory and in lower Earth orbit experiments.
Advances in Space Research, 42(12), 2019-2035.
http://dx.doi.org/10.1016/j.asr.2007.09.017

[P05] Lasue J., Levasseur-Regourd A.-C., **Fray N.**, and Cottin H. (2007)
Inferring the interplanetary dust properties. From remote observations and simulations.
Astronomy and Astrophysics, 473(2), 641-649.
http://dx.doi.org/10.1051/0004-6361:20077623

[P04] **Fray N.**, Bénilan Y., Biver N., Bockelée-Morvan D., Cottin H., Crovisier J., and Gazeau M.-C. (2006)
Heliocentric evolution of the degradation of polyoxyméthylène : Application to the origin of the formaldehyde (H_2CO) extended source in comet C/1995 O1 (Hale-Bopp).
Icarus, 184(1), 239-254.
http://dx.doi.org/10.1016/j.icarus.2006.04.014

[P03] **Fray N.**, Bénilan Y., Cottin H., Gazeau M.-C. and Crovisier J. (2005)
The origin of the CN radical in comets : A review from observations and models.
Planetary and Space Science, 53(12), 1243-1262.
http://dx.doi.org/10.1016/j.pss.2005.06.005

[P02] **Fray N.**, Bénilan Y., Cottin H. and Gazeau M.-C. (2004)
New experimental results on the degradation of polyoxymethylene. Application to the origin of the formaldehyde extended source in comets.
Journal of Geophysical Research (Planets), 109, E07S12.
http://dx.doi.org/10.1029/2003JE002191

[P01] **Fray N.**, Bénilan Y., Cottin H., Gazeau M.-C., Minard R.D. and Raulin F. (2004)
Experimental study of the degradation of polymers. Application to the origin of extended sources in cometary atmospheres.
Meteoritics and Space Science, 39(4), 581-587.
http://dx.doi.org/10.1111/j.1945-5100.2004.tb00920.x

AUTRES PUBLICATIONS A COMITES DE LECTURE

[A03] Schwell M., Gaie-Levrel F., Bénilan Y., Gazeau M.-C., Fray N., Saul G., Champion N., Leach S. and Guillemin J.-C. (2013)
VUV spectroscopy and photochemistry of five interstellar and putative prebiotic molecules
ECLA: European Conference on Laboratory Astrophysics, EAS Publications Series, 58, 301-306
http://dx.doi.org/10.1051/eas/1258050

[A02] Quirico E., Szopa C., Cernogora G., Lees V., Derenne S., McMillan P.F., Montagnac G., Reynard B., Rouzaud J.-N., **Fray N.**, Coll P., Raulin F., Schmitt B. And Minard B. (2008)
Tholins and their relevance for astrophysical issues.
Proceedings of the International Astronomical Union, 4(S251), 409-416
http://dx.doi.org/10.1017/S1743921308022059

[A01] **Fray N.**, Bénilan Y., Cottin H., Gazeau M.-C. and Raulin F. (2004)
Experimental study of the degradation of complex organic molecules. Application to the origin of extended source in cometary atmospheres.
Life in the Universe, 187-190, *Seckbach J. et al. (eds) Kluwer Academic Publishers 374 p.*

Encadrements et formation par la recherche

ENCADREMENTS DE THESES.

[2] **2011 – en cours :**
Thèse de Michaëlle Bouilloud (de 10/2012 – en cours).
Soutenance prévue en Septembre 2015
Directeur de thèse : Yves Bénilan
Co-directeur de thèse : Nicolas Fray
Evolution thermique d'analogues de matériaux organiques réfractaires extraterrestres.

[1] **2008 – 2011 :**
Thèse de Léna LE ROY (10 / 2008 – 12 / 2011).
Soutenue le 19 décembre 2011
Directeur de thèse : Gilles Poulet
Co-directeur de thèse : Hervé COTTIN
Co-encadrant à 33 %
Préparation à la caractérisation in-situ de la matière organique cométaire par spectrométrie de masse : application à l'instrument COSIMA

ENCADREMENTS DE POST-DOCTORAT.

[2] **2011-2012 :**
ATER de Léna LE ROY (01/09/2011 au 30/08/2012).
Encadrant à 66 %
Financement UPEC
Analogues à la matière organique cométaire : Production par photolyse et réchauffement de glaces puis caractérisation les modèles sol de COSIMA.

[1] **2010-2011 :**
Post-doctorat de Giacomo BRIANI (01/10/2010 au 31/09/2011).
Encadrant à 100 %
Financement UPEC
Etude expérimentale de la dégradation et de la décomposition thermique d'analogues à la matière organique réfractaire cométaire.

ENCADREMENTS DE STAGES DE LICENCE ET DE MASTER.

[5] **2012 :**
Michaëlle Bouilloud
Stage de M2R (de 02/2012 à 06/2012)
Encadrant à 100 %
Caractérisation et optimisation d'une lampe adaptée à la photochimie VUV en vue d'améliorer la représentativité et l'efficacité de la synthèse d'analogues à la matière organique cométaire.

[4] **2010**
Céline BLIN et Yuyi Stéphanie LA
Stage de L3 (de 04/2010 à 06/2010)
Co-encadrant à 50% (Direction : Hervé COTTIN à 50%).
Spectre de la Glycine dans le domaine de l'ultraviolet.

[3] **2010**
Narimane ZEGHBIB
Stage de L3 (de 04/2010 à 06/2012)
Direction (75%) (Co-encadrant : Hervé COTTIN à 25%)
Etude de la décomposition thermique de polymères de HCN dans l'environnement cométaire.

[2] **2008 :**
Léna LE ROY
Stage de M2R (de 02/2008 à 06/2008)
Co-direction à 50 % (Direction : Hervé COTTIN à 50%)
Synthèse et étude de la dégradation thermique des polymères des HCN : Application aux sources distribuées de CN dans les comètes.

[1] **2007**
Jérémy FLEUR
Stage de L3 (de 04/2007 à 06/2007)
Direction à 100%
Dégradation de composés organiques complexes. Application à l'environnement cométaire

Activités d'enseignement

● Enseignement en Physique (85%) et Sciences de l'Univers (15%)

● Depuis ma nomination, j'ai effectué tous les ans quelques heures supplémentaires par rapport à mes obligations statutaires (192h équivalent TD). J'ai enseigné principalement au niveau Licence avec une répartition approximative de 15 % de cours, 45 % de travaux dirigés et 40 % de travaux pratiques.

● Au fil des années, j'ai participé à la quasi intégralité des enseignements de physique en Licence (Mécanique du point, Electromagnétisme, Optique Géométrique, Optique Physique, Electrocinétique…).

● Durant mes deux années de délégation CNRS, j'ai poursuivi mes enseignements de vulgarisation en astronomie à destination des étudiants non-scientifiques de l'Université Paris-Est Créteil.

● Dans le cadre du Master 1 « Sciences pour l'ingénieur », j'ai participé à la création de TPs portant sur le logiciel « Labview » (contrôle d'instruments et acquisition de données) que j'utilise fréquemment pour mes recherches.

Contrats de recherche

Je ne mentionne ici que les contrats de recherche dont j'étais le responsable. Tous concernent le développement du projet « OREGOC ». J'ai participé à d'autres contrats de recherche, en particulier ceux liés aux projets de spectroscopie VUV et à l'instrument COSIMA.

Au total, depuis ma nomination en tant que maître de conférences, j'ai géré 214.2 k€ HT. Ce montant a presque intégralement été dépensé pour l'achat du matériel composant le dispositif expérimental « OREGOC ».

[14]	2013	PNP (1)	3.8 k€ HT
[13]	2013	Soutien Recherche de l'UPEC (2)	9.7 k€ HT
[12]	2012	DIM ACAV (Région Ile de France) (3)	16 k€ HT
[11]	2012	Soutien Interne du Laboratoire	14 k€ HT
[10]	2011	PIR EPOV (4)	12 k€ HT
[9]	2010	PIR EPOV (4)	20 k€ HT
[8]	2010	OSU EFFLUVE (5)	1.5 k€ HT
[7]	2009	INSU Mi-Lourd	20 k€ HT
[6]	2008	CG 94 (6)	8.5 k€ HT
[5]	2008	Gdr Exobio	6 k€ HT
[4]	2007	CNES (*)	39 k€ HT
[3]	2007	Soutien Interne Labo	12 k€ HT
[2]	2007	PID OPV (7)	35 k€ HT
[1]	2007	BQR P12 (8)	16.7 k€ HT

(*) Cette somme a été attribuée spécifiquement pour la jouvence d'un spectromètre infrarouge utilisé pour le programme EXPOSE. Nous avons conçu OREGOC pour le rendre compatible avec une utilisation commune de cet instrument pour les deux projets.
(1) PNP : Programme National de Planétologie
(2) UPEC : Université Paris-Est Créteil
(3) DIM ACAV : Domaine d'Intérêt Majeur « Astrophysique et Conditions d'Apparition de la Vie
(4) PIR EPOV : Programme Interdisciplinaire de Recherche « Environnements Planétaires et Origines de la Vie »
(5) OSU EFLUVE : Observatoire de Sciences de l'Univers « *Enveloppes FLUides* : *de la Ville à l'Exobiologie* «
(6) Conseil Général du Val de Marne
(7) PID OPV : Programme InterDisciplinaire « Origines des Planètes et de la Vie »
(8) BQR P12 : Bonus Qualité Recherche de l'Université Paris 12

Sélection d'articles

La liste ci-dessous correspond aux articles cités dans le texte. L'ensemble de ces articles sont compilés dans les pages suivantes.

● *[Article 1]* **Fray N.** and Schmitt B. **(2009)** Sublimation of molecules of astrophysical interest. A bibliographic review. *Planetary and Space Science*, 57(14-15), 2053-2080.

● *[Article 2]* **Fray N.**, Marboeuf U., Brissaud O. And Schmitt B. **(2010)** Equilibrium data of methane, carbon dioxide and xenon clathrate hydrates below the freezing point of water. Applications to astrophysical environments. *Journal of Chemical and Engineering Data*, 55(11), 5101-5108.

● *[Article 3]* Marboeuf U., **Fray N.**, Brissaud O., Schmitt B., Bockelée-Morvan D. and Gautier D. **(2012)** Equilibrium pressure of ethane, acetylene and krypton clathrate hydrates below the freezing point of water. *Journal of Chemical and Engineering Data*, 57(12), 3408-3415

● *[Article 4]* Marboeuf U., Schmitt B., Petit J.-M., Mousis O. and **Fray N. (2012)** A cometary nucleus model taking into account all phase changes of water ice: amorphous, crystalline, and clathrate. *Astronomy and Astrophysics,* 542, A82

● *[Article 5]* Ferradaz T., Bénilan Y., **Fray N.**, Jolly A., Schwell M., Gazeau M.-C., Jochims H.-W. and Guillemin J.-C. **(2009)** Temperature dependant photoabsorption cross sections of cyanoacetylene and diacetylene in the mid- and vacuum-UV: Application to Titan's Atmosphere. *Planetary and Space Science*, 57(1), 10-22.

● *[Article 6]* **Fray N.**, Bénilan Y., Gazeau M.-C., Jolly A., Schwell M., Arzoumanian E., Ferradaz T., Es-Sebbar E. And Guillemin J.-C. **(2010)** Temperature-dependant photoabsorption cros-section of cyanodiacetylene in the vacuum UV. *Journal of Geophysical Research (Planets),* 115, E06010

● *[Article 7]* Venot O., **Fray N.**, Bénilan Y., Gazeau M.-C., Hébrard E., Larcher G., Schwell M., Dobrijevic M. and Selsis F. **(2013)** High-temperature measurements of VUV absorption cross sections of CO2 and application to exoplanets. Astronomy & Astrophysics, 551, A131

● *[Article 8]* Cottin H., and **Fray N. (2008)** Distributed sources in comets. *Space Science Reviews,* 138(1-4), 179-197.

● *[Article 9]* Le Roy L., Briani G., Briois C., Cottin H., **Fray N.**, Thirkell L., Poulet, G. and Hilchenbach, M. **(2012)** On the prospective detection of polyoxymethylene in comet 67P/Churyumov-Gerasimenko with the COSIMA instrument onboard Rosetta. *Planetary and Space Science,* 65(1), 83-92.

● *[Article 10]* Vinogradoff V., **Fray N.**, Duvernay F., Briani G., Danger G., Cottin H., Theulé P. and Chiavassa T. **(2013)** Importance of the thermal reactivity for hexamethylenetetramine (HMT) formation from simulated interstellar ices. *Astronomy and Astrophysics*, 551, A128

● *[Article 11]* Briani G., **Fray N.**, Cottin H., Benilan Y., Gazeau M.-C. and Perrier S. HMT production and sublimation during thermal process of cometary organic analogs. Implications for its detection with the ROSETTA instruments. *Icarus, submitted.*

ARTICLE 1

Fray N. and Schmitt B. (2009)

Sublimation of molecules of astrophysical interest. A bibliographic review.

Planetary and Space Science, 57(14-15), 2053-2080.

Planetary and Space Science 57 (2009) 2053–2080

Contents lists available at ScienceDirect

Planetary and Space Science

journal homepage: www.elsevier.com/locate/pss

Sublimation of ices of astrophysical interest: A bibliographic review

N. Fray [a,b,*], B. Schmitt [b]

[a] LISA, Laboratoire Interuniversitaire des Systèmes Atmosphériques, UMR 7583 du CNRS, Universités Paris 7 et 12, 61 Avenue du Général de Gaulle, 94010 Créteil Cedex, France
[b] Laboratoire de Planétologie de Grenoble, Université Joseph Fourier, CNRS/INSU, Bâtiment D de Physique, BP 53, 38041 Grenoble Cedex 9, France

ARTICLE INFO

Article history:
Received 2 April 2009
Received in revised form
10 September 2009
Accepted 14 September 2009
Available online 20 September 2009

Keywords:
Vapour pressure
Sublimation
Condensation
Volatiles
Ices
Solids

ABSTRACT

The sublimation and condensation of ices play a very important role in the formation of planetary systems, in the evolution of some solar system bodies as well as in the equilibrium and matter exchanges between surface and atmosphere of most planets and satellites. The precise knowledge of vapour pressure of molecular solids at all relevant temperatures is mandatory, but the published sublimation relations are not always accurate enough. All published experimental measurements, and empirical and thermodynamical relations for the vapour pressure of 53 different species in their pure solid phases are reviewed. For several species, we also calculate the vapour pressure with accurate thermodynamic formulae from the triple point down to low temperatures. For 27 species (H_2O, O_2, O_3, CO, CO_2, CH_3OH, HCOOH, CH_4, C_2H_2, C_2H_4, C_2H_6, C_6H_6, HCN, HC_3N, C_2N_2, C_4N_2, N_2, NH_3, NO, N_2O, H_2S, SO_2, AsH_3, Ne, Ar, Kr, and Xe) we are able to propose vapour pressure relations, either empirical or theoretical, valid over a large range of temperatures, representative of astrophysical environments. All these relations are more accurate than those currently used in the astrophysical literature. In particular, most of the relations commonly used in the astrophysical literature are based on the data reported by Lide (2006) in the CRC Handbook of Chemistry and Physics, which are inaccurate for several compounds. The most problematic case is CO ice, for which a sublimation relation extrapolated from the liquid–gas equilibrium (Fanale and Salvail, 1990) is used in most of the models simulating the activity of comet nuclei.

1. Introduction

Ices are ubiquitous in the solar system. They have been detected at the surface of most solar system bodies or in their atmospheres (Schmitt et al., 1998). Some of these bodies, like comet nuclei, KBOs, and icy satellites of the giant planets, contain large amounts of ices. These ices are not necessarily water ice and the most volatile species, such as N_2, CO, and CH_4, are not always trapped in amorphous water ice either. Indeed, pure or nearly pure ices of volatile species can exist at equilibrium on several objects of the outer solar system. For example, N_2, CH_4, H_2O, and CO have been detected at the surface of Pluto and Triton (Cruikshank et al., 1993; Owen et al., 1993; Quirico et al., 1999). On Pluto, some CH_4 and CO are incorporated in the almost pure ($>99\%$) N_2 matrix, but there is also evidence for CH_4 in a pure state (Douté et al., 1999). Thus, the properties of pure ices, even for very volatile species such as CH_4 and N_2, are of astrophysical interest.

At the very beginning of solar system formation most of the molecular species present in the solar nebula, except the most volatile species, such as H_2 and He, condensed during the cooling of the solar nebula (Yamamoto et al., 1983; Lewis, 1972). The subsequent sublimation of these species played, and still do play, a very important role in atmospheric formation. Cometary atmospheres are the most spectacular case since most of the volatiles that are observed today in cometary comae are produced by sublimation from the nuclei (Bockelée-Morvan et al., 2004; Espinasse et al., 1991; Squires and Beard, 1961). On some planets or satellites, ices and gas are involved in seasonal and climatic cycles. In these cases, energy is transported by sublimation and condensation through latent heat, with the bulk of gas flowing from regions receiving sunlight to areas receiving less or no solar energy, leading to cyclic seasonal transports of volatile ices. This is the case on Triton and Pluto, where dominant N_2 ice sublimates from the illuminated hemisphere, flows to and then condenses on the night hemisphere (Spencer et al., 1997; Grundy and Stansberry, 2000). On Mars a similar energy transport causes seasonal sublimation of CO_2 at one hemisphere and condensation at the surface of the opposite hemisphere. CO_2 being the main constituent of the Martian atmosphere, the total pressure of the atmosphere varies by about 30% over the seasonal cycle (Leighton and Murray, 1966; Encrenaz, 2001). On Io, the SO_2 atmosphere is

* Corresponding author at: LISA, Laboratoire Interuniversitaire des Systèmes Atmosphériques, UMR 7583 du CNRS, Universités Paris 7 et 12, 61 Avenue du Général de Gaulle, 94010 Créteil Cedex, France. Tel.: +33 1 45 17 15 56; fax: +33 1 45 17 15 64.
E-mail address: nicolas.fray@lisa.univ-paris12.fr (N. Fray).

0032-0633/$ - see front matter © 2009 Elsevier Ltd. All rights reserved.
doi:10.1016/j.pss.2009.09.011

probably due to sublimation of SO_2 ice patches or to plume sources (Trafton et al., 1998). Thus, the atmospheres of Pluto, Triton, Io, and Mars, despite having very different compositions and temperatures, are primarily supported by the vapour pressure of the dominant and most volatile ices on their surfaces. This is also certainly the case for most of the largest trans-Neptunian objects, where N_2-rich and CH_4 ices are detected (Merlin et al., 2009). In other atmospheres, the condensation of organic compounds and their sedimentation can act as a sink (Samuelson, 1998). This situation occurs in the atmosphere of Titan where numerous hydrocarbons and nitriles that are formed by photochemistry in the upper stratosphere and the ionosphere, condense in the form of aerosols or clouds in the lower stratosphere. The first Titan, condensate that has been clearly identified is C_4N_2 (Samuelson et al., 1997), but several other pure or mixed condensates, such as HCN, HC_3N, C_2H_2, C_2H_6, C_3H_8, and C_2H_5CN, could co-exist (Coustenis et al., 1999). In giant planets, numerous molecular species can also condense in crystalline form (Samuelson, 1998). In Uranus and Neptune atmospheres, some ice clouds of CH_4, H_2S, NH_4SH and H_2O could exist, although there is no direct spectroscopic identification for any of those condensates (de Pater et al., 1991). Even on Earth, H_2O condenses in the form of ice particles in cirrus and polar stratospheric clouds (Peter, 1998). On Mars, distinct CO_2 and H_2O ice clouds have also been identified.

Thus, the sublimation and condensation of ices play a very important role in the formation of planetary systems, in the evolution of some solar system bodies as well as in the equilibrium and matter exchanges between surface and atmosphere of most planets and satellites. Consequently, accurate knowledge of the sublimation–condensation curve of molecular solids at all relevant temperatures is mandatory to determine the various gas–solid equilibriums and to model their exchanges on these objects. Unfortunately, as will be shown, the sublimation relations that are currently used in the astrophysical literature are not always accurate. The purpose of this article is to review the sublimation properties of pure ices of astrophysical interest. First, all the published experimental data concerning the sublimation pressure of compounds of astrophysical interest have been compiled. In a second step, relations to extrapolate to low temperatures are proposed, which could be easily used by the astrophysical community. This study deals with the sublimation–condensation equilibrium. For the liquefaction–vaporization equilibrium, we recommend the use of some other works such as Stull (1947a, 1947b), Boublik et al. (1984), and Lide (2006).

2. Thermodynamic and empirical relations of sublimation

The sublimation–condensation relations that we would like to propose should allow us to calculate, as accurately as possible, the sublimation pressure of studied species at any temperature. Indeed, for most species, experimental data have been measured at temperatures that are generally much too high to be representative of the astrophysical environments where these compounds are, or could be, present in the solid form. In this section, we present different ways to derive the sublimation curves at low temperatures. First, we describe the 'thermodynamic calculation', which is based on exact thermodynamic laws. Secondly, we present empirical relations used to interpolate and extrapolate experimental data and also results of the thermodynamic calculations. One should note that SI units have been used for all calculations presented in this article, but values of pressure are expressed in bar, which is the unit usually used in planetology.

2.1. Thermodynamic calculation

When a pure compound in gas phase is in equilibrium with its solid phase, the chemical potentials of both phases are equal. This equality leads to the Clausius–Clapeyron equation (see Eq. (1)), giving the slope of the equilibrium curve at a given temperature as a function of sublimation enthalpy ($\Delta H_{sub}(T)$ in J mol^{-1}) and molar volume of both phases (v in m^3 mol^{-1}).

$$\left(\frac{dP_{sub}}{dT}\right)_{eq} = \frac{\Delta H_{sub}(T)}{T.(v_{gas} - v_{sol})} \quad (1)$$

Although this equation is generally believed to be unsolvable without preliminary substitution of a simple expression for $\Delta H_{sub}(T)$ and $\Delta v(T) = v_{gas} - v_{sol}$, it has been demonstrated by Mosselman et al. (1982) that it can be transformed to an 'exact differential equation'. The integration of the equation leads to thermodynamic relations, which can be used for calculations of vapour pressure and enthalpy of sublimation as a function of temperature. These relations are given in different forms in Gottschal and Korvezee (1953), Fisher and McMillan (1958), Brown and Ziegler (1979), Mosselman et al. (1982), and Feistel and Wagner (2007). Calculations of the vapour pressure curve make use of (1) a given point of the vapour pressure curve (generally the triple point), (2) heat capacity (C_p) and molar volume of the solid phase as a function of temperature, (3) sublimation enthalpy value at a given pressure and temperature (generally the triple point), (4) enthalpies and temperatures of all solid phases transitions, (5) heat capacity of the gas phase or thermodynamic functions of ideal gas calculated from statistical mechanics, and (6) an equation of state for the gas phase.

This thermodynamic approach allows the calculation of vapour pressure as a function of temperature without any particular hypothesis if all thermodynamic functions are known for the considered compound. This approach has been used by Brown and Ziegler (1979) to calculate the sublimation curves of H_2, O_2, N_2, F_2, CO, CO_2, Ne, Ar, Kr, Xe, CH_4, C_2H_4, and C_2H_6 and by Feistel and Wagner (2007) for H_2O.

Here, we suppose that the gas can be modelled as a 'perfect gas' and that the molar volume of the solid (v_{sol}) can be neglected against that of the gas phase (v_{gas}). Both hypotheses are good approximations since the calculation is performed at temperatures corresponding to low equilibrium pressures.

The Clausius–Clapeyron equation can then be written as

$$\left(\frac{dP_{sub}}{dT}\right)_{eq} = \frac{\Delta H_{sub}(T) P_{sub}}{RT^2} \quad (2)$$

For a perfect gas, we have $dH_{gas}(T) = C_{p,gas}(T).dT$, where $= C_{p,gas}(T)$ is the molar heat capacity of the gas (in J K^{-1} mol^{-1}), and for ice we have $dH_{sol}(T) = C_{p,sol}(T)dT$. The sublimation enthalpy as a function of the temperature can then be expressed as

$$\Delta H_{sub}(T) = \int_{T_0}^{T} \Delta C_P(T)dT + \Delta H_{sub}(T_0) \text{ with } \Delta C_P(T) = C_{P,gas}(T) - C_{P,sol}(T)$$

where T_0 is a reference temperature for which the sublimation enthalpy is known. Finally, the Clausius–Clapeyron equation can be integrated:

$$\ln(P_{sub}) = \int_{T_0}^{T} \frac{\Delta H_{sub}(T)}{RT^2} dT + \ln(P_{sub0}) \quad (3)$$

Knowing the sublimation pressure and enthalpy at a temperature T_0, as well as the temperature dependence of $C_{P,sol}(T)$ and $C_{P,gas}(T)$, the sublimation pressure can be calculated at any temperature. Generally $C_{P,sol}(T)$ has been measured experimentally, but $C_{P,gas}(T)$ cannot be measured due to the low vapour pressure at low temperature. Nevertheless, $C_{P,gas}(T)$ can be

calculated thanks to the relation given by Vidler and Tennyson (2000), which used the internal partition function of the considered species. For some compounds, values of the internal partition function can be found in the HITRAN database (Rothman et al., 2005). This procedure was used by Feistel and Wagner (2007) to compute the sublimation pressure of water ice. The internal partition function in the HITRAN database is given only for temperatures higher than 70 K, so for lower temperatures, we extrapolated these data considering that this function is proportional to T for linear molecules and to $T^{1.5}$ for asymmetric molecules. The validity of this extrapolation has been checked thanks to the data at low temperature given by JPL (http://spec.jpl.nasa.gov/) and CDMS (http://www.astro.uni-koeln.de/site/vorhersagen/) databases.

In practise, we choose a reference temperature T_0 at which some experimental measurements are available. Then, knowing the heat capacities of the gas and the solid, we compute the sublimation pressure at any temperature.

To test this method, we have calculated the sublimation pressure of solid CO_2 considering only the experimental data of Giauque and Egan (1937), which range from 154 to 196 K. To perform this calculation, we use the heat capacity of ice measured by Giauque and Egan (1937), and the heat capacity of gas is calculated, thanks to the relation given by Vidler and Tennyson (2000), from the internal partition function of CO_2 molecules given in the HITRAN database. Temperature T_0 is chosen equal to 170 K. The resulting sublimation pressures are compared to the other available experimental data (Meyers and Van Dusen, 1933; Tickner and Lossing, 1951; Bryson et al., 1974; Fernandez-Fassnacht and Rio, 1984; Eiler et al., 2000) ranging from 70 to 216 K. We also compare this thermodynamic calculation with the usual empirical relation ($\ln(P_{sub}=A+B/T)$) obtained considering only the experimental data of Giauque and Egan (1937). All results, including deviations of the calculations from the measured pressure, are presented in Fig. 1.

In the middle panel of Fig. 1, we can see that the thermodynamic calculation reproduces all experimental measurements with deviations between −50% and +50%, whereas pressure measurements range over 12 orders of magnitude. These deviations may seem quite high, but they mostly reflect the dispersion of measurements at very low temperatures and pressures (below 10^{-7} bar). Moreover, the slope of this thermodynamic calculation seems to be more accurate as deviations from experimental data are equally distributed around zero. This is not the case for the empirical extrapolation, which overestimates all measurements at temperatures lower than 150 K. Thus, this thermodynamic method seems to be accurate. When the heat capacities are available, we extrapolate experimental measurements of sublimation pressure at low temperatures using this thermodynamic method.

2.2. Empirical extrapolations

Sometimes, the heat capacity of ice or gas is unknown, precluding the use of thermodynamic calculations. Then, it is necessary to use an empirical relation to interpolate the existing experimental data and to extrapolate them to low temperatures. In the literature, numerous empirical relations derived from the Clausius–Clapeyron equation can be found assuming that:

(i) the gas is perfect,
(ii) the molar volume of the condensed phase is negligible against that of the gas, and they differ by assuming different variations of the sublimation enthalpy with temperature

- If the sublimation enthalpy is supposed to be independent of temperature; then the sublimation pressure follows the relation $\ln(P_{sub})=A+B/T$, which is the most common and simplest empirical relation.
- If the sublimation enthalpy is supposed to vary linearly with temperature, the sublimation pressure follows the relation $\ln(P_{sub}=A+B/T)+C\ln(T)$ which is generally called the 'Dupré' or the 'Rankine' relation.
- If the sublimation enthalpy is supposed to vary as a second-order function of temperature, the sublimation pressure follows the relation $\ln(P_{sub}=A+B/T)+C\ln(T)+DT$.

A few other empirical expressions are used. In particular the sublimation pressure is sometimes extrapolated using polynomials such as $\ln(P_{sub})=A_0+\sum_{i=1}^{n}A_i/T^i$.

Good interpolations of experimental data are obtained by using these empirical relations but for extrapolation some of them are inadequate, and can even present a slope change at low temperature, which has no physical meaning. All the empirical relations have been applied to the experimental CO_2 measurements of Giauque and Egan (1937) and compared to the measurements of the CO_2 sublimation pressure (Fig. 2). As can be seen in Fig. 2, the extrapolation, which used a polynomial function of the third order, presents a change of slope at about 50 K, which has no physical meaning. All empirical relations, except the first one ($\ln(P_{sub}=A+B/T)$), can present this type of behaviour. As coefficient B is always negative, the last empirical relation ($\ln(P_{sub})=A+B/T$) is the only permanently increasing function with temperature. Thus, when the thermodynamic method cannot be used, we choose to extrapolate the experimental data with this simple empirical relation. In some cases, we also propose a more accurate interpolation of experimental data with higher-order polynomials, but this is only valid in the temperature range of these data.

These high-order polynomials are also used to accurately interpolate the results of the thermodynamic calculations between the triple point and the lowest temperature calculated (typically at 70 K). However, for the same reason as above, the polynomial relations should not be used as an extrapolation relation at lower temperatures.

3. Bibliographic review

3.1. Presentation of the review

We have carried out a survey of experimental measurements of the sublimation pressure of 53 species that are present or could be present in astrophysical environments. We have found data in the literature for 30 species and compiled them. The purpose of this review is to provide analytical relations, allowing easy and accurate calculation of the sublimation pressure at very low temperature. Table 1 lists the 53 species for which we have looked for sublimation pressure measurements together with previous review articles and books (Stull, 1947a, 1947b; Honig and Hook, 1960; Brown and Ziegler, 1979; Lide, 2006) in which sublimation pressure data have already been compiled, as well as articles of planetological interest in which sublimation relations have been provided (Yamamoto et al., 1983; Prialnik et al., 2004; Huebner et al., 2006). Table 1 gives the sub-section number in which some comments on individual species are provided and can be used as an index. Table 2 summarizes, for most of the studied species, the values of the triple point temperature and pressure found in the NIST Chemistry WebBook (National Institute of Standards and Technology, /http://webbook.nist.gov/chemistry/), the database of AirLiquide (http://encyclopedia.airliquide.com/encyclopedia.asp), and the 87th edition of the CRC Handbook of Chemistry and Physics (Lide, 2006). Table 3 gives general information on the

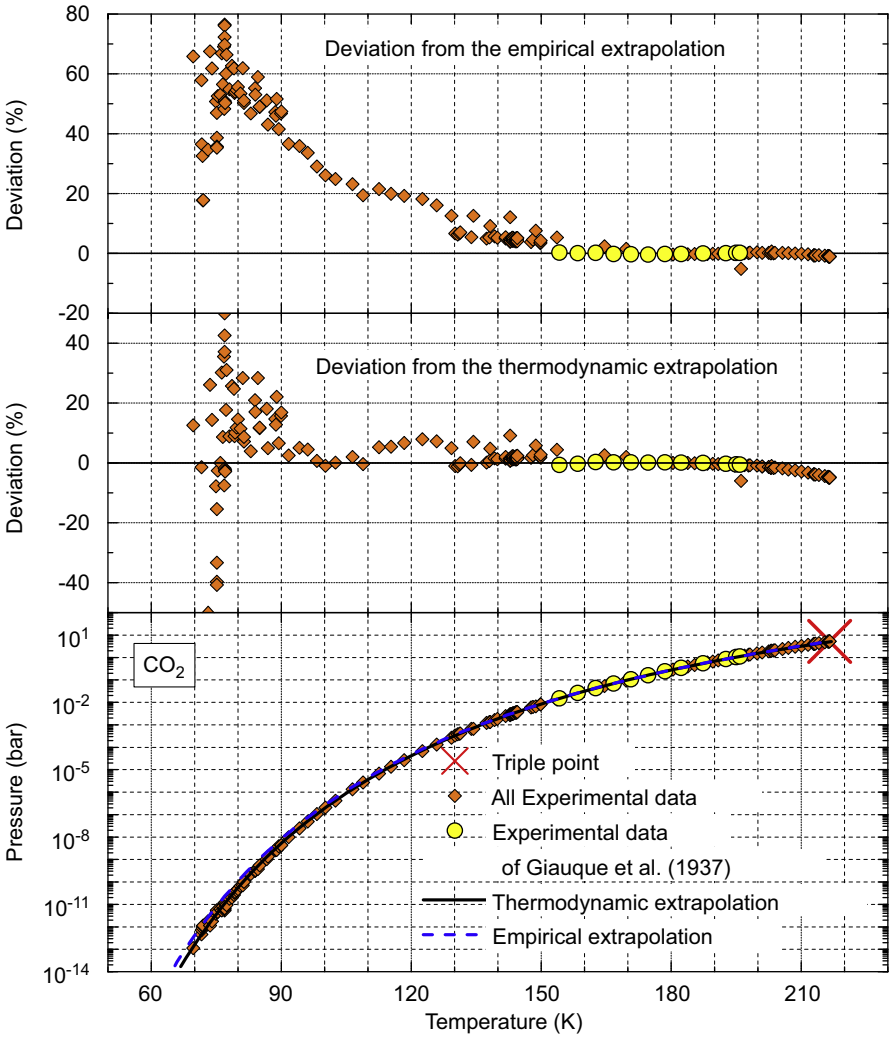

Fig. 1. Lower panel represents the sublimation pressure of CO_2 as a function of temperature. All the experimental data that we have compiled (Meyers and Van Dusen, 1933; Tickner and Lossing, 1951; Bryson et al., 1974; Fernandez-Fassnacht and Rio, 1984; Eiler et al., 2000) are represented as diamonds, except those measured by Giauque and Egan (1937), which are represented as circles. The thermodynamic and empirical extrapolations are represented as solid and dashed lines, respectively. Middle and upper panels represent the deviation of the thermodynamic and empirical extrapolations, respectively, from the experimental data.

experiments (temperature and pressure ranges of measurements, number of experimental points) in all used bibliographic sources.

For each solid crystalline phase of each species, we fit a polynomial expression of the form

$$\ln(P_{sub}) = A_0 + \sum_{i=1}^{n} A_i/T^i \quad (4)$$

to the sublimation pressure data over the temperature range of stability of the phase. Full polynomial relations (noted '*T*', for interpolated thermodynamic relations, in Table 4) have been determined for data computed by the thermodynamic approach described in Section 2.1. When this thermodynamic approach is not possible (see Section 2.2), the simple empirical relation $\ln(P_{sub})=A_0+A_1/T$ (denoted by 'E', for empirical extrapolation, in Table 4) is used to fit experimental measurements. This provides the most reliable extrapolation of data at lower temperature. In two cases (NO and N_2O) we also used an empirical interpolation (denoted by 'I', for interpolation, in Table 4) of experimental measurements with a high-order polynomial. Detailed informations on these fits, especially deviations from the experimental data, are given in Table 4. Table 5 provides the coefficients of the polynomial relations. These coefficients are generally given with 4 digits (15 for H_2O) because some negative and positive terms in the polynomials are almost equal and thus need high precision coefficients to preserve the accuracy of the thermodynamic calculations.

In the next section, we discuss available data for each species and accuracy of the proposed thermodynamic or empirical relations. Note that these new relations are always more accurate than the empirical ones currently used in astrophysical literature.

3.2. Comments on individual species

3.2.1. H_2O (water)

The triple point of H_2O is located at 273.16 K and $(6.11657 \pm 0.0001) \times 10^{-3}$ bar (Wagner and Pruss (2002) and Table 2). We can note that the temperature at the triple point of H_2O corresponds by definition to one of the defined fixed point of the temperature scale ITS-90. We have collected 216 experimental measurements ranging from 130 K (4.78×10^{-13} bar) to 273.15 K (6.11×10^{-3} bar; Douslin and Osborn, 1965; Jancso et al., 1970; Bryson et al., 1974; Marti and Mauersberger, 1993; White et al., 1998; Mauersberger and Krankowsky, 2003; Shilling et al., 2006; Table 3 and Fig. 3). Water ice can have crystalline or amorphous

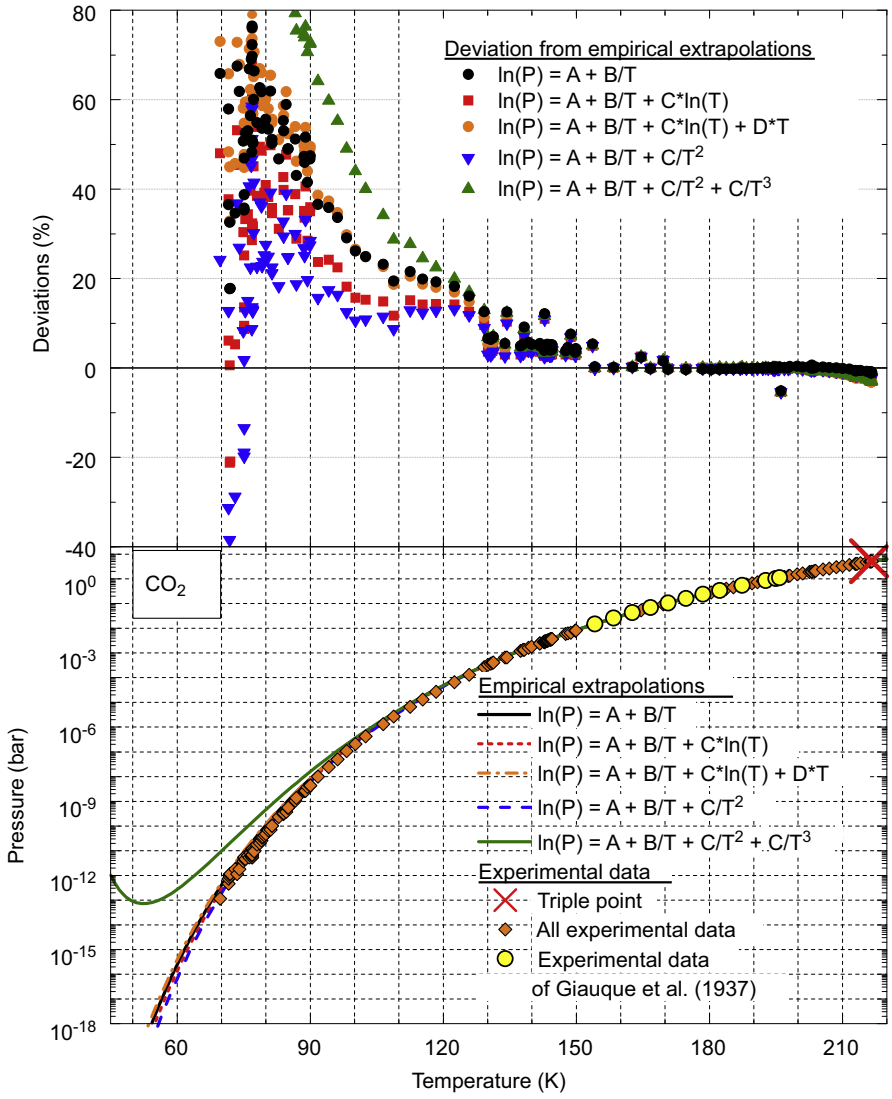

Fig. 2. Lower panel represents the sublimation pressure of CO_2 as a function of temperature. All the experimental data that we have compiled (Meyers and Van Dusen, 1933; Tickner and Lossing, 1951; Bryson et al., 1974; Fernandez-Fassnacht and Rio, 1984; Eiler et al., 2000) are represented as diamonds, except those measured by Giauque and Egan (1937), which are represented as circles. All the empirical relations that we have used to extrapolate the data of Giauque and Egan (1937) are represented by lines of different colours. Upper panel represents the deviation of the different empirical extrapolations from the experimental data. For interpretation of the references to colour in this figure legend, the reader is referred to the web version of this article.

structure. In the studies of Marti and Mauersberger (1993) and Mauersberger and Krankowsky (2003), water ice has been deposited very slowly between 200 and 225 K. Under these conditions, water ice is almost certainly crystalline hexagonal ice (Ih). As Douslin and Osborn (1965) and Jancso et al. (1970) have worked at relatively high temperatures, their ice samples were also probably crystalline. Shilling et al. (2006) have checked the state of their ice samples by X-ray diffraction and performed 3 measurements on crystalline hexagonal ice (Ih). In the other studies (Bryson et al., 1974; White et al., 1998), it is not clear if the ice was amorphous or crystalline. Lide (2006) reports data for the sublimation equilibrium, which are in agreement with the previous experimental measurements (Fig. 3). Numerous relations have been published in the literature to compute the vapour pressure of hexagonal water ice (Washburn, 1924; Jancso et al., 1970; Yamamoto et al., 1983, Wagner et al., 1994; Murphy and Koop, 2005; Prialnik et al., 2004; Huebner et al., 2006; Feistel and Wagner, 2006, 2007). We have compared all these relations to the experimental data. The most complete and precise work has been published by Feistel and Wagner (2007). They have used the most recent data (measurements of vapour pressure and heat capacity of hexagonal ice) to compute the vapour pressure of hexagonal water ice using an accurate thermodynamic approach. If we consider only the measurements of Marti and Mauersberger (1993) and Mauersberger and Krankowsky (2003), which have been obtained on crystalline ice, the deviation, between experimental measurements and this theoretical relation, reaches −27% and +15% (Fig. 3). This mostly reflects experimental dispersion of the measurements of Mauersberger and Krankowsky (2003) although if we consider all compiled experimental data, deviations vary between −40% and +180% (Fig. 3). The high vapour pressure values are possibly due to the presence of amorphous ice in the samples condensed below 140 K by Bryson et al. (1974) and White et al. (1998). Indeed it has already been shown by numerous authors (Kouchi, 1987; Sack and Baragiola, 1993) that vapour pressure of amorphous ice is higher by one or two orders of magnitude than for crystalline ice. All these authors have shown that vapour pressure for amorphous ice strongly depends on condensation temperature and on the rate of condensation. Therefore, no sublimation relation for amorphous water ice can be proposed as it does not depend only on temperature.

Table 1
Data on sublimation or evaporation pressures and extrapolation relations available in review articles and books.

Sub-section[a]	Species	Stull (1947a, 1947b)	Honig and Hook (1960)	Brown and Ziegler (1979)	Lide (2006)	Yamamoto et al. (1983)	Prialnik et al. (2004)	Huebner et al. (2006)
1	H_2O	X	X	–	X	X	X	X
2	H_2O_2	X	–	–	X	–	–	–
3	O_2	X	X	X	X	–	–	–
4	O_3	X	–	–	X	–	–	–
5	CO	X	X	X	X	X	X	X
6	CO_2	X	X	X	X	X	X	X
7	H_2CO	X	–	–	X	–	–	–
8	CH_3OH	X	–	–	X	–	X	–
9	HCOOH	X	–	–	X	–	–	–
10	$HCOOCH_3$	X	–	–	X	–	–	–
11	$HOCH_2CH_2OH$	X	–	–	X	–	–	–
12	CH_4	X	X	X	X	X	X	X
13	C_2H_2	X	–	–	X	X	X	X
14	C_2H_4	X	–	X	X	–	–	–
15	C_2H_6	X	–	X	X	–	X	–
16	C_3H_4 (a)	X	–	–	X	–	X	––
17	C_3H_4 (p)	X	–	–	X	–	X	–
18	C_3H_6	X	–	–	X	–	–	–
19	C_3H_8	X	–	–	X	–	–	–
20	C_4H_2	X	–	–	–	–	–	–
21	C_6H_2	–	–	–	–	–	–	–
22	C_6H_6	X	–	–	X	–	–	–
23	HCN	X	–	–	X	X	X	X
24	HNC	–	–	–	–	–	–	–
25	HC_3N	–	–	–	X	–	–	–
26	CH_3CN	X	–	–	X	–	–	–
27	CH_3CH_2CN	X	–	–	X	–	–	–
28	C_2N_2	X	–	–	X	–	–	X
29	C_4N_2	–	–	–	–	–	–	–
30	N_2	X	X	X	X	X	–	X
31	NH_3	X	X	–	X	X	X	X
32	NO	X	X	–	X	–	–	X
33	NO_2	–	–	–	–	–	–	–
34	N_2O	X	X	–	X	–	–	X
35	HNCO	–	–	–	–	–	–	–
36	NH_2CHO	X	–	–	X	–	–	–
37	H_2S	X	X	–	X	–	X	X
38	SO_2	X	X	–	X	–	–	–
39	CS_2	X	X	–	X	–	–	–
40	OCS	X	X	–	X	–	–	–
41	H_2SO_4	X	–	–	X	–	–	–
42	NH_4SH	X	–	–	–	–	–	–
43	H_2CS	–	–	–	–	–	–	–
44	Cl_2	X	X	–	X	–	–	–
45	ClS_2	–	–	–	–	–	–	–
46	ClO	–	–	–	–	–	–	–
47	PH_3	X	–	–	X	–	–	–
48	AsH_3	X	–	–	–	–	–	–
49	SiH_4	X	–	–	X	–	–	–
50	Ne	X	X	X	X	–	–	X
51	Ar	X	X	X	X	–	–	X
52	Kr	X	X	X	X	–	–	X
53	Xe	X	X	X	X	–	–	X

[a] Numbers quoted in the first column correspond to the subsection of Section 3.2 in which we review in detail the data for each species.

We can also note that under certain conditions, water can form crystalline cubic ice (Ic). Only 3 experimental measurements of vapour pressure of the cubic phase have been performed over the temperature range 180–190 K (Shilling et al., 2006; Fig. 3). The authors have determined that the value is $10.5\% \pm 0.3\%$ higher than the vapour pressure of the hexagonal phase. We can assume that the vapour pressure of Ic ice is 10.5% higher than for Ih ice at all temperatures where this phase is stable but this hypothesis has to be confirmed by experimental measurements at $T < 180$ K and $T > 190$ K. No other vapour pressure relation for Ic ice can be proposed for now.

In astrophysical models, different empirical sublimation relations are used. They have been proposed by Yamamoto et al. (1983), Fanale and Salvail (1984) (which is used by Prialnik et al., 2004), and Huebner et al.(2006). These relations present higher deviations from the experimental data than those computed by Feistel and Wagner (2007). We recommend the use of the thermodynamic relation computed by Feistel and Wagner (2007), which can be expressed by an empirical function (see Eqs. (5) and (6) and parameter values in Table 6). In both equations, T_t and P_t stand for the temperature and pressure at the triple point, respectively. Both values are given in Table 2.

$$\ln\left(\frac{P_{subl}(T)}{P_t}\right) = \frac{3}{2}\ln\left(\frac{T}{T_t}\right) + \left(1 - \frac{T_t}{T}\right)\eta\left(\frac{T}{T_t}\right) \quad (5)$$

$$\eta\left(\frac{T}{T_t}\right) = \sum_{i=0}^{6} e_i \left(\frac{T}{T_t}\right)^i \quad (6)$$

Table 2
Triple point determinations.

Species	NIST Webbook		Air Liquide		CRC Handbook (Lide, 2006)		Others references		Selected	
	T (K)	P (bar)	T (K)	P (bar)	T (K)	P (bar)	T (K)	P (bar)	T (K)	P (bar)
H_2O	273.16	$(0.0061 \pm 0.0001) \times 10^{-3}$	–	–	273.16	6.1166×10^{-3}	273.16[a]	$(6.11657 \pm 0.0001) \times 10^{-3}$[a]	273.16	$(6.11657 \pm 0.0001) \times 10^{-3}$
O_2	54.33 ± 0.06	–	54.35	1.52×10^{-3}	–	–	54.352[b]	1.46×10^{-3}[b]	54.33 ± 0.06	$(1.49 \pm 0.03) \times 10^{-3}$
O_3	–	–	80.6	1.14×10^{-5}	–	–	79.6 ± 0.3[c]	$(5.6 \pm 0.6) \times 10^{-6}$[c]	79.6 ± 0.3	$(5.6 \pm 0.6) \times 10^{-6}$
CO	68.03 ± 0.14	–	68.14	0.1535	68.13	0.154	–	–	68.1 ± 0.1	0.1537 ± 0.0003
CO_2	216.58 ± 0.03	5.185 ± 0.005	216.58	5.185	216.58	5.18	–	–	216.58 ± 0.03	5.185 ± 0.005
H_2CO	155.1 ± 0.3	–	–	–	–	–	–	–	155.1 ± 0.3	$(4 \pm 1) \times 10^{-4}$[d]
CH_3OH	175.5 ± 0.5	–	–	–	–	–	–	–	175.5 ± 0.5	$(1.8 \pm 0.2) \times 10^{-6}$[d]
HCOOH	281.42 ± 0.07	0.0236 ± 0.0001	–	–	–	–	–	–	281.42 ± 0.07	0.0236 ± 0.0001
$HOCH_2CH_2OH$	258.8 ± 2.4	–	–	–	–	–	–	–	258.8 ± 2.4	–
CH_4	90.67 ± 0.03	0.1169 ± 0.0006	90.68	0.117	90.69	0.117	90.6854 ± 0.0003[e]	0.11696 ± 0.00002[e]	90.6854 ± 0.0003	0.11696 ± 0.00002
C_2H_2	192 ± 1	1.2825 ± 0.004	192.60	1.282	192.4	1.26	–	–	192 ± 1	1.275 ± 0.015
C_2H_4	104.0 ± 0.1	0.0012 ± 0.0001	103.97	0.0012	–	–	–	–	104.0 ± 0.1	0.0012 ± 0.0001
C_2H_6	91 ± 6	$(1.1 \pm 0.1) \times 10^{-5}$	89.24	1.1×10^{-5}	–	–	90.34 ± 0.01[f]	$(1.1 \pm 0.1) \times 10^{-5}$[f]	90.34 ± 0.01	$(1.1 \pm 0.1) \times 10^{-5}$
C_3H_4 (a)	136.59 ± 0.20	–	–	–	–	–	–	–	136.59 ± 0.20	$(9.3 \pm 0.4) \times 10^{-5}$[d]
C_3H_4 (p)	168.5 ± 0.3	–	–	–	–	–	–	–	168.5 ± 0.3	$(3.9 \pm 0.2) \times 10^{-3}$[d]
C_3H_6	87.8 ± 0.8	–	–	–	–	–	–	–	87.8 ± 0.8	10^{-7}–10^{-8}[d]
C_3H_8	85 ± 3	$(1.687 \pm 0.003) \times 10^{-9}$	–	–	–	–	85.47 ± 0.05[f]	$(1.685 \pm 0.001) \times 10^{-9}$[f]	85.47 ± 0.05	$(1.685 \pm 0.001) \times 10^{-9}$
C_4H_2	–	–	–	–	–	–	–	–	235.6 ± 3.5[d]	0.1 ± 0.03[d]
C_6H_6	278.5 ± 0.6	–	–	–	–	–	278.68 ± 0.02[g]	$(4.785 \pm 0.005) \times 10^{-2}$[g]	278.68 ± 0.02	$(4.785 \pm 0.005) \times 10^{-2}$
HCN	259.86 ± 0.02	–	259.85	0.187	259.83	0.1862	–	–	259.85 ± 0.03	0.1866 ± 0.0004
CH_3CN	229.32 ± 0.02	–	–	–	–	–	–	–	229.32 ± 0.02	$(2.0 \pm 0.1) \times 10^{-3}$[d]
CH_3CH_2CN	180.37 ± 0.02	–	–	–	–	–	–	–	180.37 ± 0.02	$(3.8 \pm 0.1) \times 10^{-6}$[d]
C_2N_2	245.32 ± 0.02	0.751 ± 0.013	245.32	0.738	–	–	–	–	245.32 ± 0.02	0.744 ± 0.009
N_2	63.14 ± 0.06	0.1255 ± 0.0005	63.148	0.1253	–	–	–	–	63.14 ± 0.06	0.1255 ± 0.0005
NH_3	–	0.06060 ± 0.00005	195.41	0.06077	195.4	0.0612	–	–	195.41 ± 0.01	0.0609 ± 0.0003
NO	–	–	–	–	109.5	0.219	–	–	109.5 ± 0.1	0.219 ± 0.001
N_2O	–	0.8790 ± 0.0001	182.34	0.878	–	–	182.30 ± 0.05[h]	0.879 ± 0.001[h]	182.30 ± 0.05	0.879 ± 0.001
NH_2CHO	275.66 ± 0.8	–	–	–	–	–	–	–	275.66 ± 0.8	–
H_2S	187.65 ± 0.07	0.232 ± 0.005	187.45	0.227	187.6	0.227	–	–	187.57 ± 0.15	0.229 ± 0.008
SO_2	197.64 ± 0.05	0.0167 ± 0.0001	197.63	0.0167	–	–	–	–	197.64 ± 0.05	0.0167 ± 0.0001
CS_2	161.45 ± 0.40	–	–	–	–	–	–	–	161.45 ± 0.40	$(2 \pm 1) \times 10^{-5}$[d]
OCS	134.32 ± 0.20	–	–	–	–	–	–	–	134.32 ± 0.20	$(5 \pm 2) \times 10^{-4}$[d]
Cl_2	172.12 ± 0.15	$(1.390 \pm 0.003) \times 10^{-2}$	172.15	1.4×10^{-2}	–	–	–	–	172.12 ± 0.15	$(1.39 \pm 0.01) \times 10^{-2}$
PH_3	139.41 ± 0.20	–	139.35	3.6×10^{-2}	–	–	–	–	139.41 ± 0.20	$(3.6 \pm 0.1) \times 10^{-2}$
AsH_3	–	–	156.25	0.03	–	–	156.23 ± 0.02[i]	$(2.98 \pm 0.02) \times 10^{-2}$[i]	156.23 ± 0.02	$(2.98 \pm 0.02) \times 10^{-2}$
Ne	24.56 ± 0.05	0.433 ± 0.003	24.55	0.433	–	–	–	–	24.56 ± 0.05	0.433 ± 0.003
Ar	83.79 ± 0.06	0.689 ± 0.001	83.78	0.687	83.81	0.688	83.8058[j]	0.68891 ± 0.00002[j]	83.8058	0.68891 ± 0.00002
Kr	115.9 ± 0.2	0.7315 ± 0.0006	115.95	0.731	115.8	0.731	–	–	115.9 ± 0.2	0.7315 ± 0.0006
Xe	161.4 ± 0.3	0.816 ± 0.001	161.35	0.816	161.4	0.817	–	–	161.4 ± 0.3	0.816 ± 0.001

[a] Triple point of H_2O reviewed by Wagner and Pruss (2002).
[b] Triple point of O_2 measured by Mullins et al. (1963).
[c] Triple point of O_3 measured by Hanson and Mauersberger (1986).
[d] We obtained these triple point values by various extrapolations (see text).
[e] Triple point of CH_4 reviewed by Friend et al. (1989).
[f] Triple points of C_2H_6 and C_3H_8 reviewed by Younglove and Ely (1987).
[g] Triple point of C_6H_6 reviewed by Goodwin (1988).
[h] Triple point of N_2O measured by Yato et al. (1975).
[i] Triple point of AsH_3 measured by Sherman and Giauque (1955).
[j] Triple point of Ar reviewed by Tegeler et al. (1999).

Table 3
Detailed bibliography.

Chemical name	Species	References	Temperature range (K)	Pressure range (bar)	Number of experimental points
Water	H_2O	Douslin and Osborn (1965)	241.72–271.09	3.32×10^{-4}–5.16×10^{-3}	8
		Jancso et al. (1970)	194.64–271.68	8.00×10^{-7}–5.40×10^{-3}	77
		Bryson et al. (1974)	131.80–187.02	8.44×10^{-13}–1.97×10^{-10}	39
		Marti and Mauersberger (1993)	173.15–273.15	1.43×10^{-8}–6.11×10^{-3}	11
		White et al. (1998)	130–167.2	4.78×10^{-13}–3.21×10^{-9}	14
		Mauersberger and Krankowsky (2003)	164.5–169.9	1.64×10^{-9}–7.07×10^{-9}	61
		Shilling et al.(2006)	181.3–191.2	4.2×10^{-8}–2.48×10^{-7}	6
		All data	130–273.15	4.78×10^{-13}–6.11×10^{-3}	216
Oxygen	O_2	Hoge (1950)	51.30–53.09	6.27×10^{-4}–1.01×10^{-3}	3
		Aoyama and Kanda (1934)	37.6–53	2.7×10^{-7}–9.4×10^{-4}	10
		All data	37.6–53.09	2.7×10^{-7}–1.01×10^{-3}	13
Ozone	O_3	Hanson and Mauersberger (1986)	65.2–79.2	8.4×10^{-9}–4.9×10^{-6}	25
Carbon monoxide	CO	Clayton and Giauque (1932)	60.24–67.02	2.664×10^{-2}–0.124	8
		Shinoda (1969)	54.78–68.07	6.050×10^{-3}–0.152	28
		All data	54.78–68.07	6.050×10^{-3}–0.152	36
Carbon dioxide	CO_2	Ambrose (1956)	178.45–197.80	0.237–1.306	16
		Fernandez-Fassnacht and Rio (1984)	194.23–216.56	0.977–5.174	21
		Meyers and Van Dusen (1933)	194.35–216.52	0.990–5.171	28
		Giauque and Egan (1937)	154.20–195.83	1.511×10^{-2}–1.114	12
		Eiler et al. (2000)	130.1–169.6	3.333×10^{-4}–9.354×10^{-2}	56
		Tickner and Lossing (1951)	106.45–153.65	1.333×10^{-6}–1.333×10^{-2}	13
		Bryson et al. (1974)	69.69–102.5	1.15×10^{-13}–4.213×10^{-7}	61
		All data	69.69–216.56	1.148×10^{-13}–5.174	207
Methanol	CH_3OH	Lucas et al. (2005)	133.4–173.7	8.6×10^{-11}–1.3×10^{-6}	20
Formic acid	HCOOH	Coolidge (1930)	268.08–281.40	6.64×10^{-3}–2.39×10^{-2}	3
Methane	CH_4	Karwat (1924)	76.89–87.25	1.163×10^{-2}–7.113×10^{-2}	8
		Tickner and Lossing (1951)	48.15–77.65	1.333×10^{-6}–1.333×10^{-2}	13
		Armstrong et al. (1955)	53.15–90.66	1.073×10^{-5}–0.116	53
		All data	48.15–90.66	1.33×10^{-6}–0.116	74
Acetylene	C_2H_2	McIntosh (1907)	177.85–191.95	0.405–1.263	9
		Tickner and Lossing (1951)	98.55–145.15	1.333×10^{-6}–1.333×10^{-2}	13
		Burrell and Robertson (1915a)	129.9–189.1	1.33×10^{-3}–1.013	17
		All data	98.55–191.95	1.33×10^{-6}–1.263	39
Ethylene	C_2H_4	Tickner and Lossing (1951)	79.45–102.45	1.33×10^{-6}–6.66×10^{-4}	9
		Menaucourt (1982)	77.3–103.78	4.40×10^{-7}–1.17×10^{-3}	16
		All data	77.3–103.78	4.40×10^{-7}–1.17×10^{-3}	25
Ethane	C_2H_6	Tickner and Lossing (1951)	83.35–88.75	1.33×10^{-6}–6.66×10^{-6}	3
Propyne	C_3H_4 (p)	Van Hook (1967)	160.7–168.2	1.73×10^{-3}–3.85×10^{-3}	6
Butadiyne	C_4H_2	Khanna et al. (1990)	127–152	6×10^{-10}–2.5×10^{-8}	4
Hexatriyne	C_6H_2	Shindo et al. (2003)	170.9–198.1	2.1×10^{-8}–1.1×10^{-6}	6
Benzene	C_6H_6	Deitz (1933)	184.3–200.2	1.93×10^{-6}–1.04×10^{-5}	4
		Milazzo (1956)	195.18–273.07	8×10^{-6}–3.26×10^{-2}	10
		Jackowski (1974)	220.79–278.68	3.20×10^{-4}–4.78×10^{-2}	21
		Ha et al. (1976)	228.69–273.16	6.41×10^{-4}–3.23×10^{-2}	14
		All data	184.3–278.68	1.93×10^{-6}–4.78×10^{-2}	49
Hydrogen cyanide	HCN	Lewis and Schutz (1934)	236.2–259.3	3.6×10^{-2}–0.18	7
Propiolonitrile	HC_3N	Benilan et al. (1994)	164.9–201.5	1×10^{-6}–1.2×10^{-4}	9
Cyanogen	C_2N_2	Perry and Bardwell (1925)	179.94–240.79	2.3×10^{-3}–0.550	11
		Ruehrwein and Giauque (1939)	202.42–245.27	2.40×10^{-2}–0.738	10
		Benilan (1995)	156.3–169.5	5.2×10^{-5}–4×10^{-4}	4
		All data	156.3–245.27	5.2×10^{-5}–0.738	25
Butynedinitrile	C_4N_2	Saggiomo (1957)	262.6–273.2	2.15×10^{-2}–4.72×10^{-2}	2
		Khanna et al. (1990)	147–152	3.6×10^{-10}–7.6×10^{-9}	4
		Benilan (1995)	181.4–224	1.3×10^{-6}–3.08×10^{-4}	10
		All data	147–273.2	3.6×10^{-10}–4.72×10^{-2}	16
Nitrogen	N_2	Giauque and Clayton (1933)	54.78–61.70	1.697×10^{-2}–9.277×10^{-2}	8
		Borovik et al. (1960)	21.20–26.40	1.47×10^{-13}–4.27×10^{-10}	9
		Frels et al. (1974)	35.40–59.17	4.840×10^{-6}–5.113×10^{-2}	21
		All data	21.20–60.67	1.467×10^{-13}–7.367×10^{-2}	38
Ammonia	NH_3	Karwat (1924)	162.39–193.45	1.27×10^{-3}–5.01×10^{-2}	8
		Overstreet and Giauque (1937)	176.92–195.36	8.2×10^{-3}–6.08×10^{-2}	7
		All data	162.39–195.36	1.27×10^{-3}–6.08×10^{-2}	15
Nitric oxide	NO	Johnston and Giauque (1929)	94.62–109.49	1.22×10^{-2}–0.219	8
		Ernest (1961)	64.85–94.95	6.66×10^{-7}–1.33×10^{-2}	10

Table 3 (*continued*)

Chemical name	Species	References	Temperature range (K)	Pressure range (bar)	Number of experimental points
		All data	64.85–109.49	6.66×10^{-7}–0.219	18
Nitrous oxide	N_2O	Burrell and Robertson (1915b)	129.05–182.15	1.33×10^{-3}–0.867	14
		Black et al. (1930)	103.15–123.15	1.73×10^{-6}–4.08×10^{-4}	7
		Blue and Giauque (1935)	148.48–182.26	2.43×10^{-2}–0.879	9
		Bryson et al. (1974)	68.1–80.2	1.14×10^{-12}–1.21×10^{-9}	38
		Atake and Chihara (1974)	146.07–182.21	1.77×10^{-2}–0.865	26
		Yato et al. (1975)	143.88–182.29	1.31×10^{-2}–0.880	74
		Terlain (1983)	125.17–147.54	6.09×10^{-4}–2.12×10^{-2}	12
		All data	68.1–182.29	1.14×10^{-12}–0.88	180
Hydrogen sulphide	H_2S	Giauque and Blue (1936)	164.90–182.84	3.21×10^{-2}–0.161	5
Sulphur dioxide	SO_2	Burrell and Robertson (1915b)	178.75–197.15	6.66×10^{-4}–1.6×10^{-2}	4
		Bergstrom (1922)	183.05–196.85	3.3×10^{-3}–1.56×10^{-2}	4
		Schmitt and Rodriguez (2003)	120	1.38×10^{-8}	1
		All data	120–197.15	1.38×10^{-8}–1.6×10^{-2}	9
Arsine	AsH_3	Johnson and Pechukas (1937)	136.15–154.15	2.67×10^{-3}–2.47×10^{-2}	13
Neon	Ne	Henning and Otto (1936)	22.04–23.64	0.131–0.288	11
		Bigeleisen and Roth (1961)	16.42–24.50	2.1×10^{-3}–0.418	91
		Ancsin (1978)	20.29–24.38	4.61×10^{-2}–0.400	34
		White et al. (1998)	5.98–9.13	1.39×10^{-14}–8.27×10^{-9}	12
		Metcalf (2002)	5.50–7.00	4.80×10^{-16}–4.62×10^{-12}	8
		All data	5.50–24.50	4.8×10^{-16}–0.418	156
Argon	Ar	Lee et al. (1970)	68.82–83.75	1.59×10^{-2}–0.683	133
		Leming and Pollack (1970)	35.51–83.73	3.06×10^{-9}–0.685	79
		Chen et al. (1978)	74.65–83.76	0.170–0.685	38
		White et al. (1998)	23.06–28.14	8.97×10^{-14}–1.21×10^{-10}	5
		Metcalf (2002)	20.53–26.13	6.56×10^{-16}–1.03×10^{-11}	13
		All data	20.53–83.76	6.56×10^{-16}–0.685	268
Krypton	Kr	Leming and Pollack (1970)	45.13–114.91	2.800×10^{-7}–0.674	106
		Fisher and McMillan (1958)	63.00–80.00	5.706×10^{-5}–4.230×10^{-3}	18
		Chen et al. (1978)	103.72–115.63	0.192–0.720	37
		All data	45.13–115.63	2.800×10^{-7}–0.720	161
Xenon	Xe	Leming and Pollack (1970)	70.08–158.71	5.066×10^{-7}–0.675	118
		Chen et al. (1978)	142.83–161.33	0.183–0.813	60
		Tessier et al. (1982)	101.21–119.93	8.219×10^{-4}–1.511×10^{-2}	12
		Bryson et al. (1974)	53.70–59.50	$5.973\ 10^{-11}$–$1.373\ 10^{-9}$	7
		All data	53.70–161.33	5.973×10^{-11}–0.813	197

3.2.2. H_2O_2 (hydrogen peroxide)

The location of the triple point of H_2O_2 is unknown. Lide (2006) reports data only for the evaporation–liquefaction equilibrium and no measurements concerning the sublimation pressure have been found. Thus, no vapour pressure relation is proposed.

3.2.3. O_2 (oxygen)

The triple point of O_2 is located at 54.33 ± 0.06 K and $(1.49\pm0.03)\times10^{-3}$ bar (Table 2). We have collected 13 experimental measurements ranging from 37.6 K (2.7×10^{-7} bar) to 53.09 K (1.01×10^{-3} bar; Aoyama and Kanda, 1934; Hoge, 1950; Table 3). Lide (2006) reports data only for the evaporation–liquefaction equilibrium. Solid O_2 has three different crystalline phases, the temperatures of the phase transitions are 23.781 K (α–β transition) and 43.772 K (β–γ transition; Mullins et al., 1963). Brown and Ziegler (1979) have computed three thermodynamic relations (Tables 4 and 5): the first one for $20\text{ K}<T<23.781$ K (α solid phase), the second one for $23.781\text{ K}<T<43.772$ K (β solid phase), and the last one for $43.772\text{ K}<T<54.33$ K (γ solid phase). The first relation cannot be checked as no experimental measurements have been performed for $T<23.781$ K. Nevertheless, the other two relations reproduce the measurements with an accuracy of $\pm40\%$, which reflects the dispersion of the experimental points (Table 4 and Fig. 4). We consider that the thermodynamic relations calculated by Brown and Ziegler (1979) are reliable and recommend their use. No other relations have been proposed in the astrophysical literature.

3.2.4. O_3 (ozone)

The determinations of the O_3 triple point location of the 'Air Liquide' company and of Hanson and Mauersberger (1986) do not agree (Table 2). Nevertheless, the data of Hanson and Mauersberger (1986) seem to be more realistic and we can consider that the triple point of O_3 is located at 79.6 ± 0.3 K and $(5.6\pm0.6)\times10^{-6}$ bar (Table 2). We have collected 25 experimental measurements ranging from 65.2 K (8.4×10^{-9} bar) to 79.2 K (4.9×10^{-6} bar; Hanson and Mauersberger, 1986; Table 3 and Fig. 5). Lide (2006) reports data only for the evaporation–liquefaction equilibrium. No data concerning the heat capacity of the O_3 ice have been found. Thus we are not able to compute any thermodynamic relation. We recommend the use of the empirical relation calculated by Hanson and Mauersberger (1986), which reproduces their own experimental measurements with an accuracy of $\pm3.7\%$ (Tables 4 and 5).

3.2.5. CO (carbon monoxide)

The triple point of CO is located at 68.10 ± 0.1 K and 0.1537 ± 0.0003 bar (Table 2). We have collected 36 experimental measurements ranging from 54.78 K (6.05×10^{-3} bar) to 68.07 K (0.152 bar; Clayton and Giauque, 1932; Shinoda, 1969; Table 3).

Table 4
Informations on the polynomials of extrapolations.

Species	Polynomial designation	Solid phase	Type of extrapolation[a]	Temperature range (K)[b]	Number of data points	Degree of polynomial	Standard deviation (%)	Maximum deviation (%)	Reference
H_2O	H_2O-1	Ih	T	0–273.16 (triple p.)	210	–	22	180	Feistel and Wagner (2007)
O_2	O_2-1	α	T	20–23.78 (phase tr.)	0	3	–	–	Brown and Ziegler (1979)
	O_2-2	β	T	23.78 (phase tr.)–43.77 (phase tr.)	5	3	26	48	Brown and Ziegler (1979)
	O_2-3	γ	T	43.77 (phase tr.)–54.33 (triple p.)	8	3	19	43	Brown and Ziegler (1979)
O_3	O_3-1	–	E	< 79.6 (triple p.)	25	1	2.3	4.1	Hanson and Mauersberger (1986)
CO	CO-1	α	T	14–61.55 (phase tr.)	14	5	1.2	3.2	This work
	CO-2	β	T	61.55 (phase tr.)–68.1 (triple p.)	22	3	0.9	2.0	Brown and Ziegler (1979)
CO_2	CO_2-1	–	T	40–194.7	161	5	14.5	63	Brown and Ziegler (1979)
	CO_2-2	–	I	194.7–216.58 (triple p.)	46	2	0.33	0.72	This work
CH_3OH	CH_3OH-1	α	E	< 157.36 (phase tr.)	12	1	2.8	5.0	Lucas et al. (2005)
	CH_3OH-2	β	E	157.36 (phase tr.)–175.5 (triple pt)	8	1	2.8	5.7	Lucas et al. (2005)
HCOOH	HCOOH-1	–	E	< 281.4 (triple p.)	3	1	0.58	0.94	This work
	HCOOH-2	–	T	15–281.4 (triple p.)	3	4	0.9	1.2	This work
CH_4	CH_4-1	I	T	20.6 (phase tr.)–90.68 (triple p.)	74	4	7.9	36	Brown and Ziegler (1979)
C_2H_2	C_2H_2-1	–	E	< 192.3 (triple p.)	26	1	3.4	8.5	This work
C_2H_4	C_2H_4-1	(II) & I	T	(20)–50–104.0 (triple p.)	25	4	9.3	29	Brown and Ziegler (1979)
C_2H_6	C_2H_6-1	II & I	T	20–90.34 (triple p.)	3	5	16	22	Brown and Ziegler (1979)
C_6H_6	C_6H_6-1	–	E	< 278.68 (triple p.)	49	1	11	41	This Work
HCN	HCN-1	–	T	15–259.85 (triple p.)	7	4	1.9	3.5	This work
HC_3N	HC_3N-1	–	E	< 201.5	9	1	3.9	7.1	This work
C_2N_2	C_2N_2-1	–	E	< 245.32 (triple p.)	25	1	9.4	24	This work
C_4N_2	C_4N_2-1	–	E	< 273.2	16	1	30	89	This work
N_2	N_2-1	α	T	10–35.61 (phase tr.)	10	5	19	28	This work
	N_2-2	β	T	35.61 (phase tr.)–63.14 (triple p.)	28	4	1.5	4.6	This work
NH_3	NH_3-1	–	T	15–195.41 (triple p.)	15	4	1.6	4.2	This work
NO	NO-1	–	E	< 109.50 (triple p.)	18	1	1.5	4.3	This work
	NO-2	–	I	64.85–109.50 (triple p.)	18	5	0.8	1.8	This work
N_2O	N_2O-1	–	E	< 182.30 (triple p.)	180	1	11	50	This work
	N_2O-2	–	I	68.1–182.30 (triple p.)	180	4	10	47	This work
H_2S	H_2S-1	–	E	< 187.57 (triple p.)	5	1	0.27	0.43	This Work
	H_2S-2	I	T	126.2 (phase tr.)–187.57 (triple p.)	5	4	0.03	0.05	This Work
SO_2	SO_2-1	–	T	15–197.63 (triple p.)	8	4	5.0	9.6	This Work
AsH_3	AsH_3-1	–	E	< 156.23 (triple p.)	13	1	2.6	6.0	This Work
Ne	Ne-1	–	T	3.7–12.5	20	3	94	158	Brown and Ziegler (1979)
	Ne-2	–	T	12.5–24.56 (triple p.)	136	4	2.8	8.6	Brown and Ziegler (1979)
Ar	Ar-1	–	T	20–83.79 (triple p.)	262	4	36	207	Brown and Ziegler (1979)
Kr	Kr-1	–	T	20–115.87 (triple p.)	145	6	7.1	35	Brown and Ziegler (1979)
Xe	Xe-1	–	T	20–161.4 (triple p.)	193	5	6.7	46	Brown and Ziegler (1979)

[a] This column provides the type of extrapolation that is used. 'T', 'E' and 'I' stand for thermodynamic, empirical, and interpolation relations, respectively.
[b] In this column, we have specified when the temperature limits correspond to a solid–solid phase transition (phase tr.) or to the triple point (triple p.). When nothing is specified, the temperature limit corresponds only to the limitation of the calculation.

Lide (2006) reports data for the sublimation and evaporation equilibriums, which agree with the previous experimental measurements. CO exists in two different crystalline phases (α and β), the temperature of the phase transition is 61.55 ± 0.05 K (Clayton and Giauque, 1932). Brown and Ziegler (1979) have computed the thermodynamic relations of sublimation for both phases. At temperatures higher than 61.55 K (β phase), the interpolated thermodynamic relation proposed by Brown and Ziegler (1979) reproduces the experimental data very well , with an accuracy of $\pm 2.4\%$ (Table 4). Thus, we did not compute a new thermodynamic relation but we give the interpolation coefficients from Brown and Ziegler (1979) in Table 5. For temperatures below 61.55 K (α phase), the relation proposed by Brown and Ziegler (1979) does not reproduce correctly the experimental measurements of Clayton and Giauque (1932) and Shinoda (1969). Therefore we propose our own thermodynamic

Table 5
Coefficients of the polynomials of extrapolations.

Species	Polynomial designation	A_0	A_1 (K)	A_2 (K^2)	A_3 (K^3)	A_4 (K^4)	A_5 (K^5)	A_6 (K^6)
H_2O	H_2O-1	See text as well as Eqs. (5) and (6) and Table 6						
O_2	O_2-1	$1.541\times10^{+1}$	$-1.148\times10^{+3}$	$3.349\times10^{+2}$	$6.021\times10^{+1}$	0	0	0
	O_2-2	$1.335\times10^{+1}$	$-1.012\times10^{+3}$	$-2.971\times10^{+3}$	$2.926\times10^{+4}$	0	0	0
	O_2-3	$1.018\times10^{+1}$	$-8.035\times10^{+2}$	$-7.080\times10^{+3}$	$7.553\times10^{+4}$	0	0	0
O_3	O_3-1	$1.746\times10^{+1}$	$-2.352\times10^{+3}$	0	0	0	0	0
CO	CO-1	$1.043\times10^{+1}$	$-7.213\times10^{+2}$	$-1.074\times10^{+4}$	$2.341\times10^{+5}$	$-2.392\times10^{+6}$	$9.478\times10^{+6}$	0
	CO-2	$1.025\times10^{+1}$	$-7.482\times10^{+2}$	$-5.843\times10^{+3}$	$3.939\times10^{+4}$	0	0	0
CO_2	CO2-1	$1.476\times10^{+1}$	$-2.571\times10^{+3}$	$-7.781\times10^{+4}$	$4.325\times10^{+6}$	$-1.207\times10^{+8}$	$1.350\times10^{+9}$	0
	CO2-2	$1.861\times10^{+1}$	$-4.154\times10^{+3}$	$1.041\times10^{+5}$	0	0	0	0
CH_3OH	CH_3OH-1	$1.918\times10^{+1}$	$-5.648\times10^{+3}$	0	0	0	0	0
	CH_3OH-2	$1.706\times10^{+1}$	$-5.314\times10^{+3}$	0	0	0	0	0
HCOOH	HCOOH-1	$2.189\times10^{+1}$	$-7.213\times10^{+3}$	0	0	0	0	0
	HCOOH-2	$2.164\times10^{+1}$	$-6.942\times10^{+3}$	$-6.579\times10^{+4}$	$3.316\times10^{+6}$	$-6.004\times10^{+7}$	0	0
CH_4	CH_4-1	$1.051\times10^{+1}$	$-1.110\times10^{+3}$	$-4.341\times10^{+3}$	$1.035\times10^{+5}$	$-7.910\times10^{+5}$	0	0
C_2H_2	C_2H_2-1	$1.340\times10^{+1}$	$-2.536\times10^{+3}$	0	0	0	0	0
C_2H_4	C_2H_4-1	$1.540\times10^{+1}$	$-2.206\ 10^{+3}$	$-1.216\times10^{+4}$	$2.843\ 10^{+5}$	$-2.203\ 10^{+6}$	0	0
C_2H_6	C_2H_6-1	$1.511\times10^{+1}$	$-2.207\times10^{+3}$	$-2.411\times10^{+4}$	$7.744\times10^{+5}$	$-1.161\times10^{+7}$	$6.763\times10^{+7}$	0
C_6H_6	C_6H_6-1	$1.735\times10^{+1}$	$-5.663\times10^{+3}$	0	0	0	0	0
HCN	HCN-1	$1.393\times10^{+1}$	$-3.624\times10^{+3}$	$-1.325\times10^{+5}$	$6.314\times10^{+6}$	$-1.128\times10^{+8}$	0	0
HC_3N	HC_3N-1	$1.301\times10^{+1}$	$-4.426\times10^{+3}$	0	0	0	0	0
C_2N_2	C_2N_2-1	$1.653\times10^{+1}$	$-4.109\times10^{+3}$	0	0	0	0	0
C_4N_2	C_4N_2-1	$1.909\times10^{+1}$	$-6.036\times10^{+3}$	0	0	0	0	0
N_2	N_2-1	$1.240\times10^{+1}$	$-8.074\times10^{+2}$	$-3.926\times10^{+3}$	$6.297\times10^{+4}$	$-4.633\times10^{+5}$	$1.325\times10^{+6}$	0
	N_2-2	8.514	$-4.584\times10^{+2}$	$-1.987\times10^{+4}$	$4.800\times10^{+5}$	$-4.524\times10^{+6}$	0	0
NH_3	NH_3-1	$1.596\times10^{+1}$	$-3.537\times10^{+3}$	$-3.310\times10^{+4}$	$1.742\times10^{+6}$	$-2.995\times10^{+7}$	0	0
NO	NO-1	$1.691\times10^{+1}$	$-2.016\times10^{+3}$	0	0	0	0	0
	NO-2	$1.2352\times10^{+2}$	$-4.7607\times10^{+4}$	$7.7292\times10^{+6}$	$-6.4950\times10^{+8}$	$2.7061\times10^{+10}$	$-4.4739\times10^{+11}$	0
N_2O	N_2O-1	$1.622\times10^{+1}$	$-2.971\times10^{+3}$	0	0	0	0	0
	N_2O-2	6.5664	$1.2711\times10^{+3}$	$-6.6835\times10^{+5}$	$4.4959\times10^{+7}$	$-1.0967\times10^{+9}$	0	0
H_2S	H_2S-1	$1.298\times10^{+1}$	$-2.707\times10^{+3}$	0	0	0	0	0
	H_2S-2	8.933	$-7.260\times10^{+2}$	$-3.504\times10^{+5}$	$2.724\times10^{+7}$	$-8.582\times10^{+8}$	0	0
SO_2	SO_2-1	$1.560\times10^{+1}$	$-3.5.08\times10^{+3}$	$-9.401\times10^{+4}$	$4.152\times10^{+6}$	$-6.946\times10^{+7}$	0	0
AsH_3	AsH_3-1	$1.176\times10^{+1}$	$-2.382\times10^{+3}$	0	0	0	0	0
Ne	Ne-1	9.886	$-2.699\times10^{+2}$	$1.283\times10^{+2}$	$-1.624\times10^{+2}$	0	0	0
	Ne-2	$1.061\times10^{+1}$	$-3.086\times10^{+2}$	$9.860\times10^{+2}$	$-9.069\times10^{+3}$	$3.514\times10^{+4}$	0	0
Ar	Ar-1	$1.069\times10^{+1}$	$-8.932\times10^{+2}$	$-3.567\times10^{+3}$	$6.574\times10^{+4}$	$-4.280\times10^{+5}$	0	0
Kr	Kr-1	$1.077\times10^{+1}$	$-1.223\times10^{+3}$	$-8.903\times10^{+3}$	$2.635\times10^{+5}$	$-4.260\times10^{+6}$	$3.575\times10^{+7}$	$-1.210\times10^{+8}$
Xe	Xe-1	$1.098\times10^{+1}$	$-1.737\times10^{+3}$	$-1.332\times10^{+4}$	$4.349\times10^{+5}$	$-7.027\times10^{+6}$	$4.447\times10^{+7}$	0

The form of the polynomial is given in Eq. 4 and pressure is expressed in bar.

relation (Tables 4 and 5). This thermodynamic relation for the α phase has been calculated using the values of heat capacity of CO ices measured by Clayton and Giauque (1932) from 14 K to the temperature of the solid (α)–solid (β) transition and the constant value of (7/2)*R* for the heat capacity of the gas, which corresponds to the value of a perfect diatomic gas. This relation reproduces the experimental data with an accuracy of ±3.3%, which reflects the dispersion of the experimental measurements. In most of the models of cometary activity (Prialnik et al., 2004), the relation that is used for CO sublimation is the empirical one proposed by Fanale and Salvail (1990). This relation is erroneous as the triple point pressure is overestimated by about 10% and the slope

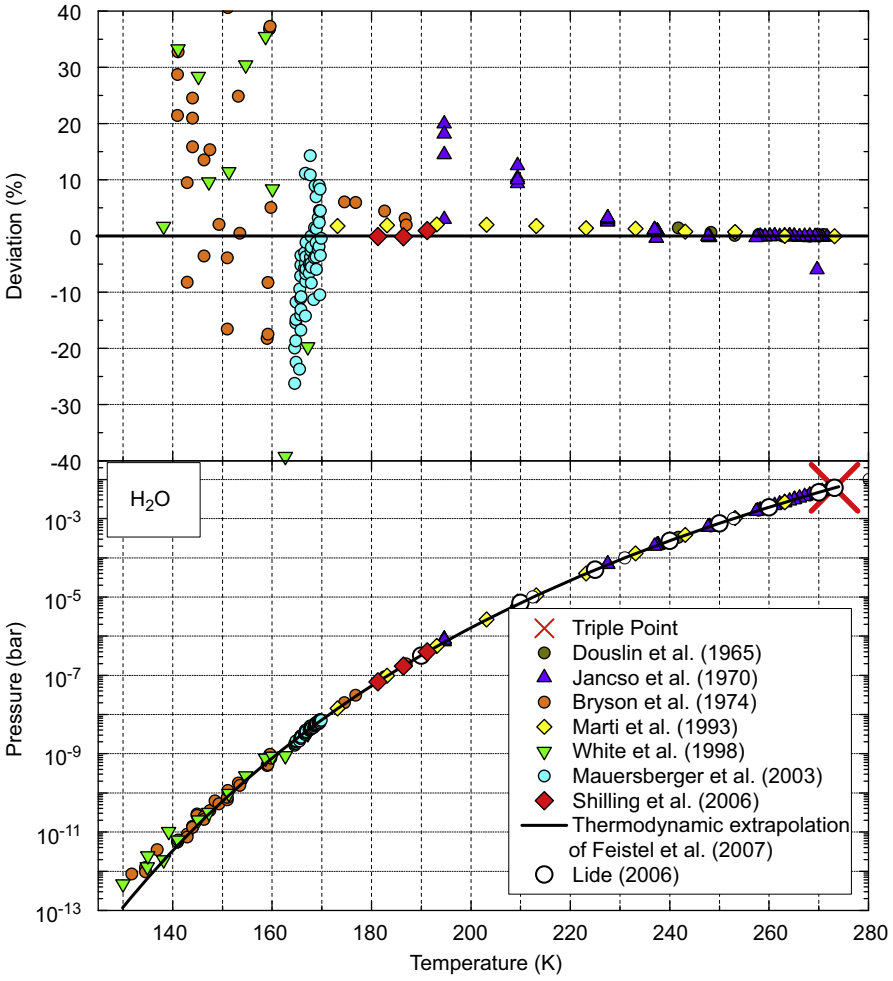

Fig. 3. Lower panel: sublimation vapour pressure of H_2O as a function of temperature. The experimental data are represented with different symbols, the triple point with a cross, and the thermodynamic relation of Feistel and Wagner (2007) with a black line. Upper panel: percentage deviation of the experimental data relative to the values calculated with the relation proposed by Feistel and Wagner (2007).

Table 6
Coefficients of the polynomial $\eta(T/T_t)$ (Eq. 6) of the semi-empirical relation (Eq. 5) for the sublimation pressure of crystalline Ih water ice (Feistel and Wagner, 2007).

I	e_i
0	20.996 966 510 789 7
1	3.724 374 782 713 62
2	−13.920 548 321 552 4
3	29.698 876 501 356 6
4	−40.197 239 263 594 4
5	29.788 048 105 021 5
6	−9.130 509 635 477 21

corresponds to that of the liquid–gas equilibrium (Fig. 6). In fact, this relation is an extrapolation of the liquid–gas equilibrium below the triple point temperature. In the astrophysical literature, two other empirical relations have been proposed by Yamamoto et al. (1983) and Huebner et al. (2006). The first does not reproduce correctly the experimental data (deviation of about 20% at 55 K) while the second relation proposed by Huebner et al. (2006) reproduces correctly the experimental data, but the slope below 55 K is not coherent with the measurements of heat capacity of the CO ices. Thus, we recommend the use of the thermodynamic relation proposed by Brown and Ziegler (1979) for the β phase ($T > 61.55$ K) and the one that we have computed for the α phase ($T < 61.55$ K; Tables 4 and 5).

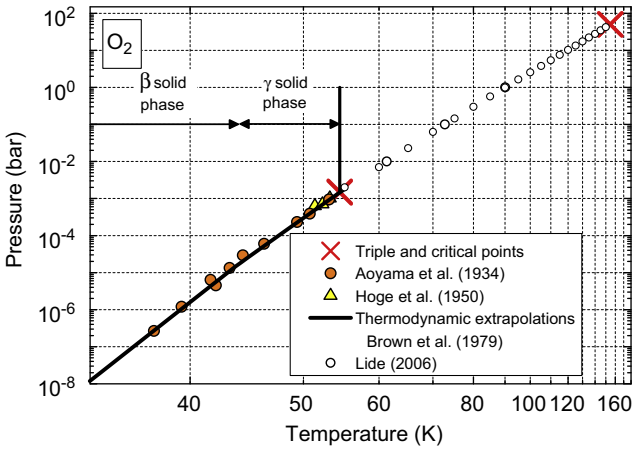

Fig. 4. Sublimation and evaporation pressures of O_2 as a function of temperature (reciprocal scale $1/T$). Vertical lines show the temperatures of the β–γ phase transition and of the triple point.

3.2.6. CO_2 (carbon dioxide)

The triple point of CO_2 is located at 216.58 ± 0.03 K and 5.185 ± 0.005 bar (Table 2). We have collected 207 experimental measurements ranging from 69.69 K (1.148×10^{-13} bar) to 216.56 K

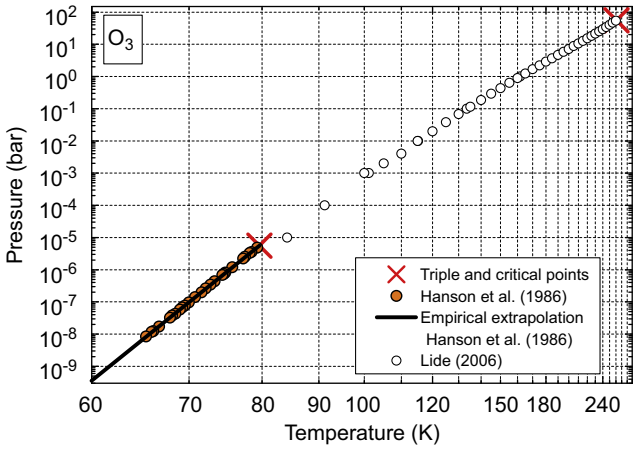

Fig. 5. Sublimation and evaporation pressures of O_3 as a function of temperature (reciprocal scale $1/T$).

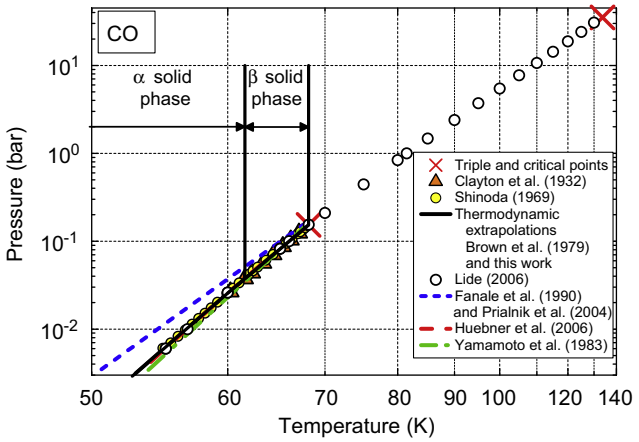

Fig. 6. Sublimation and evaporation pressures of CO as a function of temperature (reciprocal scale $1/T$). Vertical lines show the temperatures of the β–γ phase transition and of the triple point.

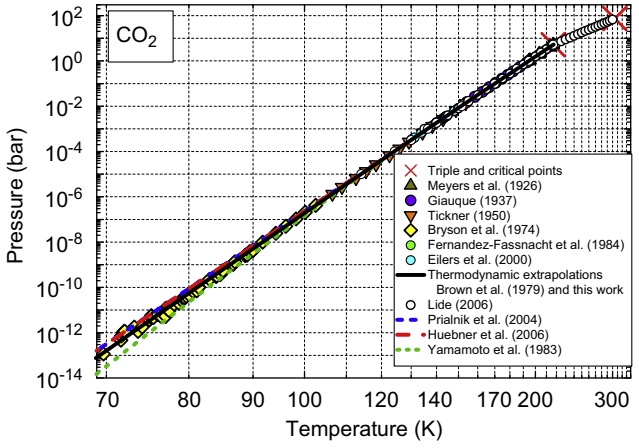

Fig. 7. Sublimation and evaporation pressures of CO_2 as a function of temperature (reciprocal scale $1/T$).

(5.174 bar; Meyers and Van Dusen, 1933; Giauque and Egan, 1937; Tickner and Lossing, 1951; Ambrose, 1956; Bryson et al., 1974; Fernandez-Fassnacht and Rio, 1984; Eiler et al., 2000; Table 3). Lide (2006) reports data for sublimation and evaporation equilibriums, which agree with previous experimental measurements. Brown and Ziegler (1979) have proposed a thermodynamic extrapolation for

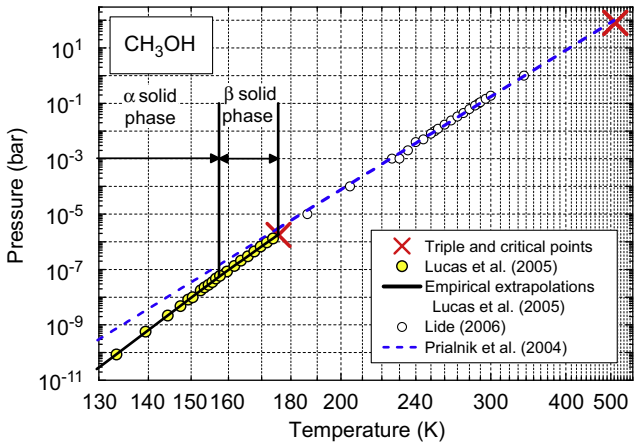

Fig. 8. Sublimation and evaporation pressures of CH_3OH as a function of temperature (reciprocal scale $1/T$). Vertical lines show the temperatures of the α–β phase transition and of the triple point.

temperatures ranging from 40 to 194.7 K (Tables 4 and 5), which fit with experimental measurements with an accuracy of $\pm 63\%$, reflecting the dispersion of the experimental data at $T < 120$ K. For $120\,\mathrm{K} < T < 194.7\,\mathrm{K}$, the accuracy of this relation is about $\pm 9\%$. For $194.7\,\mathrm{K} < T < 216.58\,\mathrm{K}$, we have performed an empirical interpolation of experimental data (Tables 4 and 5). Empirical extrapolation relations given by Yamamoto et al. (1983), Prialnik et al. (2004), and Huebner et al. (2006) reproduce very well experimental data for temperature higher than 120 K. Nevertheless, at lower temperature, Yamamoto et al. (1983) and Prialnik et al. (2004) overestimate the sublimation pressure (by a factor of ~ 2 at 80 K) whereas Huebner et al. (2006) underestimate it (factor ~ 0.4 at 80 K; Fig. 7). Thus, we recommend the use of the thermodynamic relation proposed by Brown and Ziegler (1979) below 194.7 K and our empirical relation above this temperature (Tables 4 and 5).

3.2.7. H_2CO (formaldehyde)

The triple point of H_2CO is located at 155.1 ± 0.3 K, but its pressure is unknown (Table 2). From the data of Spence and Wild (1935), concerning the evaporation equilibrium, we can estimate that the pressure at the triple point is about $(4 \pm 1) \times 10^{-4}$ bar. Lide (2006) reports data only for the evaporation equilibrium. No experimental data concerning the sublimation equilibrium have been found. Thus, no extrapolation is proposed here.

3.2.8. CH_3OH (methanol)

The triple point of CH_3OH is located at 175.5 ± 0.5 K (Table 2). The pressure at the triple point has not been directly measured. Nevertheless, thanks to the data of Lucas et al. (2005), we can estimate that it should be about $(1.8 \pm 0.2) \times 10^{-6}$ bar. We have collected 20 experimental measurements ranging from 133.4 K (8.6×10^{-11} bar) to 173.7 K (1.3×10^{-6} bar; Lucas et al., 2005; Table 3). Lide (2006) reports data only for the evaporation equilibrium. CH_3OH exists in two different crystalline phases (α and β); the temperature of the phase transition is 157.36 K (Lucas et al., 2005; Carlson and Westrum, 1971). Below this temperature, CH_3OH can also exist in a metastable form (Lucas et al., 2005), for which the sublimation pressure is slightly higher than for the stable phase. The heat capacity of methanol ice has been measured by Carlson and Westrum (1971) and Kelley (1929). Nevertheless, as the internal partition function of gaseous CH_3OH is not reported in the HITRAN database, we cannot calculate the heat capacity of the gas and consequently cannot propose any thermodynamic relation. In Tables 4 and 5, we give the coefficients of empirical extrapolation relations determined for

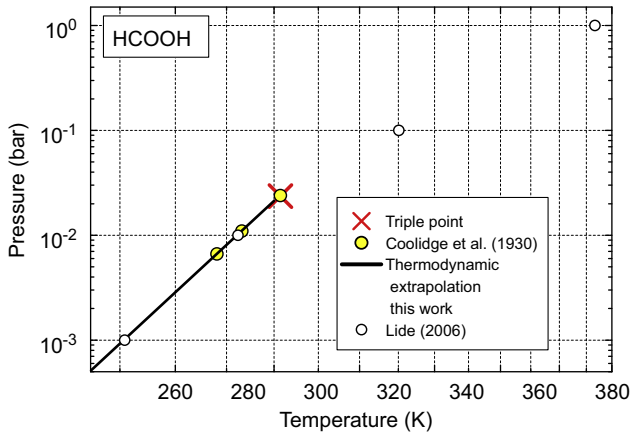

Fig. 9. Sublimation and evaporation pressures of HCOOH as a function of temperature (reciprocal scale $1/T$).

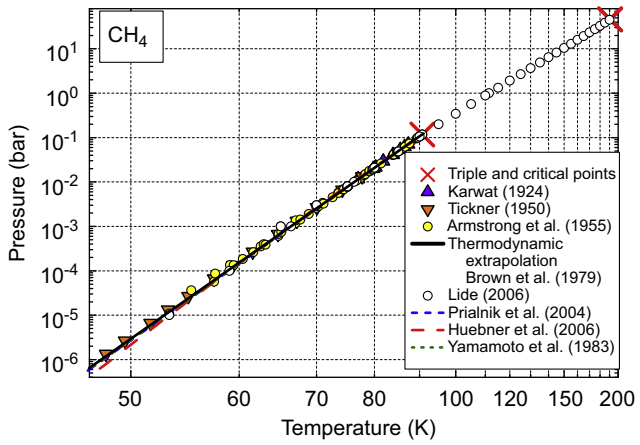

Fig. 10. Sublimation and evaporation pressures of CH_4 as a function of temperature (reciprocal scale $1/T$).

both crystalline phases by Lucas et al. (2005) from their own measurements. We can see in Fig. 8 that the empirical extrapolation proposed by Prialnik et al. (2004) is wrong as it is a direct extrapolation of the evaporation equilibrium curve for temperatures below the triple point, which is overestimated by a factor 1.7. Thus, we recommend the use of the empirical relations of Lucas et al. (2005) (Tables 4 and 5).

3.2.9. HCOOH (formic acid)

The triple point of HCOOH is located at 281.42 ± 0.07 K and 0.0236 ± 0.0001 bar (Table 2). We have collected only 3 experimental measurements ranging from 268.08 K (6.64×10^{-3} bar) to 281.40 K (2.39×10^{-2} bar: Coolidge, 1930; Table 3). Lide (2006) reports data for the sublimation and evaporation equilibriums, which agree with the previous experimental measurements. No extrapolation relation of HCOOH vapour pressure as a function of temperature has been proposed in the literature (Table 1). Nevertheless, the heat capacity of the solid has been measured from 15 K to the triple point by Stout and Fisher (1941) and the heat capacity of the gas can be calculated down to 15 K thanks to the internal partition function given in the HITRAN database (Rothman et al., 2005), which has been extrapolated using an $T^{1.5}$ dependence for $T < 70$ K. We have computed a thermodynamic relation from 15 K to the triple point temperature (Tables 4 and 5 and Fig. 9). This relation reproduces the 3 experimental measurements with an accuracy of $\pm 1.2\%$. However, due to their limited temperature range the validation of this relation may still be questionable. Nevertheless, we predict a sublimation enthalpy of 61.2 kJ mol^{-1} at 213.15 K, which is very close to the value of 62.1 ± 1.2 kJ mol^{-1} measured by Calis-Van Ginkel et al. (1978) at this temperature. Thus, our thermodynamic relation seems to be accurate. We have also performed an empirical extrapolation based on the 3 experimental data (Tables 4 and 5). The thermodynamic relation differs from this extrapolation by only 18% at 200 K and 66% at 150 K. We recommend the use of this thermodynamic relation but new experimental measurements are required to check the validity at low temperature.

3.2.10. $HCOOCH_3$ (methyl formate)

The location of the triple point of $HCOOCH_3$ is unknown. Lide (2006) reports data only for the evaporation–liquefaction equilibrium and no measurements concerning the sublimation pressure have been found. Thus, no vapour pressure relation is proposed.

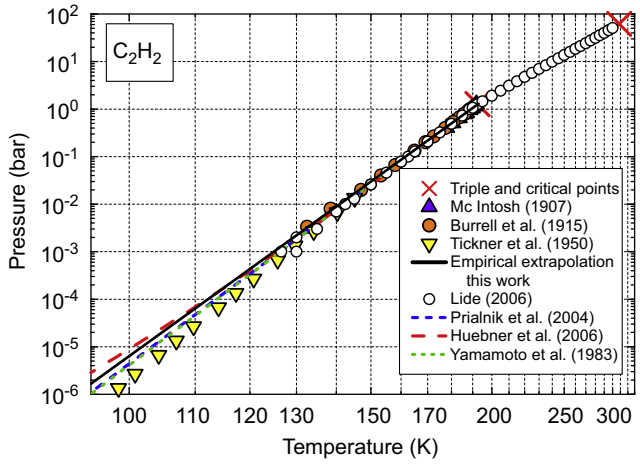

Fig. 11. Sublimation and evaporation pressures of C_2H_2 as a function of temperature (reciprocal scale $1/T$).

3.2.11. $HOCH_2CH_2OH$ (ethylene glycol)

The temperature of the $HOCH_2CH_2OH$ triple point is 258.8 ± 2.4 K and the pressure is unknown (Table 2). Lide (2006) reports data only for the evaporation equilibrium. No data concerning the sublimation equilibrium have been found.

3.2.12. CH_4 (methane)

Friend et al. (1989) have very accurately determined the location of the triple point of CH_4 (T_t=90.6854 $\pm$ 0.0003 K and P_t=0.11696 $\pm$ 0.00002 bar). We have collected 74 experimental measurements ranging from 48.15 K (1.33×10^{-6} bar) to 90.66 K (0.116 bar; Karwat, 1924; Tickner and Lossing, 1951; Armstrong et al., 1955; Table 3 and Fig. 10). Lide (2006) reports data for the sublimation and evaporation equilibriums, which agree with the previous experimental measurements. Vogt and Pitzer (1976) have shown that CH_4 can exist in two different crystalline forms (phases II and I); the transition between both forms occurs at 20.53 K. Brown and Ziegler (1979) have calculated the thermodynamic relation for phase I of CH_4 ice between 20.6 and 90.68 K. The experimental measurements are reproduced with an accuracy of $\pm 40\%$, reflecting the dispersion of experimental data at $T < 70$ K. For $70\,\text{K} < T < 90.68$ K, the uncertainty of this relation is about $\pm 3.5\%$. All empirical relations published in astrophysical literature by Yamamoto et al. (1983), Prialnik et al. (2004), and

Huebner et al. (2006) present higher deviations and therefore we recommend the use of the thermodynamic relation calculated by Brown and Ziegler (1979) (Tables 4 and 5).

3.2.13. C_2H_2 (acetylene)

The triple point of C_2H_2 is located at 192 ± 1 K and 1.275 ± 0.015 bar (Table 2). We have collected 39 experimental measurements ranging from 98.55 K (1.33×10^{-6} bar) to 191.95 K (1.263 bar; McIntosh, 1907; Burrell and Robertson, 1915a; Tickner and Lossing, 1951) (Table 3). We have excluded the measurements of Masterson et al. (1990), which differ significantly from all the other data. Moreover, close to 130 K, we can observe a discrepancy of about 40% between the data of Burrell and Robertson (1915a) and those of Tickner and Lossing (1951) (Fig. 11). As the measurements of Tickner and Lossing (1951) on C_2H_4 and C_2H_6 are also doubtful, we consider only the data of McIntosh (1907) and Burrell and Robertson (1915a). The different datasets which are reported by Lide (2006) are not in agreement (Fig. 11). No data concerning the heat capacity of the ice have been found and therefore we propose an empirical extrapolation relation (Tables 4 and 5). The empirical extrapolation relations proposed by Yamamoto et al. (1983), Prialnik et al. (2004), and Huebner et al. (2006) present higher deviations than our calculation. Hence we recommend our empirical relation (Tables 4 and 5). Further experimental studies are required to determine with more precision the sublimation pressure at temperatures lower than 180 K.

3.2.14. C_2H_4 (ethylene)

The triple point of C_2H_4 is located at 104.0 ± 0.1 K and $(1.2 \pm 0.1) \times 10^{-3}$ bar (Table 2). We have collected 25 experimental measurements ranging from 77.3 K (4.4×10^{-7} bar) to 103.78 K (1.17×10^{-3} bar; Tickner and Lossing, 1951; Menaucourt, 1982; Table 3 and Fig. 12). Lide (2006) reports data only for evaporation equilibrium. Brown and Ziegler (1979) have proposed a thermodynamic relation for temperatures ranging from 20 to 103.97 K (Tables 4 and 5). No other extrapolation relation has been proposed. The slopes of the curve related to the experimental data points of Tickner and Lossing (1951) and Menaucourt (1982) are different (Fig. 12). The measurements of Menaucourt (1982) agree with the calculation of Brown and Ziegler (1979) within $\pm 4\%$, which reflects the dispersion of these data. Thus, it seems that the sublimation relation proposed by Brown and Ziegler (1979) is reliable, whereas the data of Tickner and Lossing (1951), as for C_2H_2 and C_2H_6, are inaccurate. Here, we recommend the thermodynamic relation computed by Brown and Ziegler (1979).

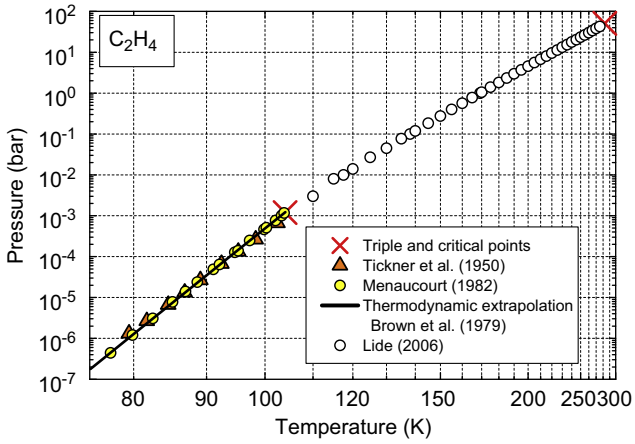

Fig. 12. Sublimation and evaporation pressures of C_2H_4 as a function of temperature (reciprocal scale $1/T$). A phase transition occurs near 50 K.

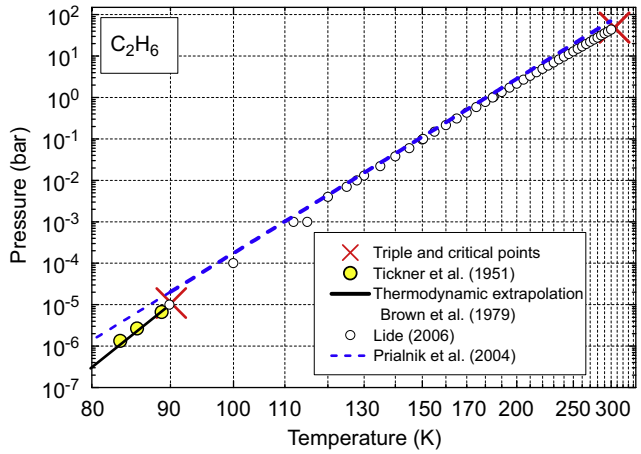

Fig. 13. Sublimation and evaporation pressures of C_2H_6 as a function of temperature (reciprocal scale $1/T$).

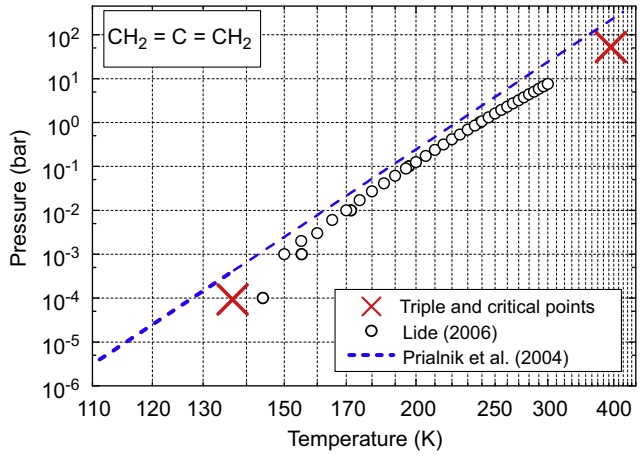

Fig. 14. Evaporation pressure of $CH_2{=}C{=}CH_2$ as a function of temperature (reciprocal scale $1/T$).

However, as there is a phase change occurring around 50 K (transition II–I; Rytter and Gruen, 1979), not taken into account in the calculations of Brown and Ziegler (1979), the validity of this relation may diverge below this temperature.

3.2.15. C_2H_6 (ethane)

The triple point of C_2H_6 is located at 90.34 ± 0.01 K and $(1.1 \pm 0.1) \times 10^{-5}$ bar (Table 2). We have collected only 3 experimental measurements ranging from 83.35 K (1.3×10^{-6} bar) to 88.75 K (6.7×10^{-6} bar; Tickner and Lossing, 1951; Table 3). Lide (2006) reports only data for evaporation equilibrium. Therefore, the sublimation properties of C_2H_6 are poorly known. C_2H_6 ice can exist in two different crystalline forms (phases II and I), and the transition temperature (89.77 ± 0.13 K) is very close to the triple point (Hans, 1976). Moreover, a metastable solid phase may also exist at lower temperatures (Wisnosky et al., 1983). Brown and Ziegler (1979) have computed a thermodynamic relation for temperatures ranging from 20 to 89.9 K (Tables 4 and 5), which does not reproduce correctly the experimental data of Tickner and Lossing (1951) (Fig. 13). However, as we saw earlier, in the cases of C_2H_2 and C_2H_4, the measurements of Tickner and Lossing (1951) do not seem accurate. Thus, we are rather confident in the relation proposed by Brown and Ziegler (1979), but experimental measurements are required to validate this relation. Prialnik et al. (2004) have proposed an empirical sublimation relation for C_2H_6, which is false. Indeed, at the triple point temperature, it

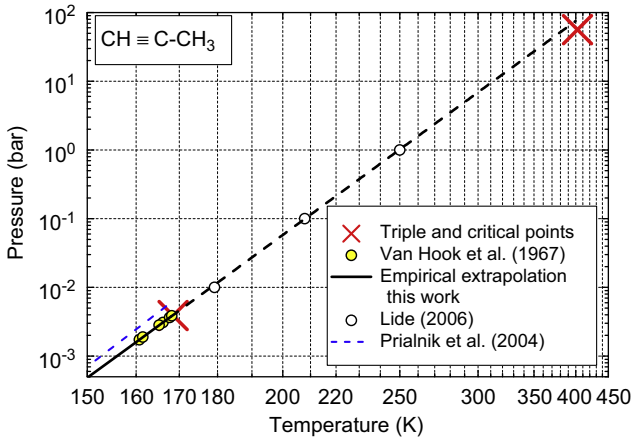

Fig. 15. Evaporation pressure of CH_3–C≡CH as a function of temperature (reciprocal scale $1/T$). The dashed black line represents the empirical relation that we have calculated from the experimental data of Van Hook (1967) for $T < 168.5$ K, which is extrapolated for $T > 168.5$ K.

overestimates the sublimation pressure by a factor 2 and the slope of this curve is approximately the same as the evaporation equilibrium curve (Fig. 13). Thus, we recommend the use of the thermodynamic relation computed by Brown and Ziegler (1979).

3.2.16. C_3H_4 (CH_2=C=CH_2) (allene)

The temperature at the triple point of CH_2=C=CH_2 is 136.59 ± 0.20 K and its pressure is unknown (Table 2). Nevertheless, by extrapolation of the evaporation data of Stull (1947a), we can estimate that the pressure at the triple point of CH_2=C=CH_2 is about $9.3 \pm 0.4 \times 10^{-5}$ bar. Lide (2006) reports data only for the evaporation equilibrium (Fig. 14) and no experimental data concerning sublimation have been found. Nevertheless, Prialnik et al. (2004) have proposed an empirical relation for the sublimation pressure, which has a slope close to that of the vaporization equilibrium curve (Fig. 14) and which overestimates the data of Lide (2006) by a factor of approximately 3. Thus, this relation is false and should not be used. Unfortunately, no other sublimation relation could be proposed as the sublimation vapour pressure of CH_2=C=CH_2 has never been measured, nor has the heat capacity of solid allene been measured.

3.2.17. C_3H_4 (CH_3–C≡CH) (propyne)

The triple point of CH_3–C≡CH is located at 168.5 ± 0.3 K and its pressure is unknown (Table 2). From the data of Van Hook (1967), we can estimate that the pressure at the triple point should be about $3.9 \pm 0.2 \times 10^{-3}$ bar. We have collected only 6 experimental measurements ranging from 160.7 K (1.73×10^{-3} bar) to 168.2 K (3.85×10^{-3} bar; Van Hook, 1967; Table 3). Lide (2006) reports data only for the evaporation–liquefaction equilibrium (Fig. 15). We have performed an empirical extrapolation of the sublimation data of Van Hook (1967), which reproduces also the data of the evaporation equilibrium (Fig. 15). So, we think that these measurements of Van Hook (1967) probably correspond to the vapour pressure of supercooling liquid propyne and not of ice. Thus, no measurement of the sublimation pressure of propyne is available. As for allene, Prialnik et al. (2004) have proposed an empirical relation for the sublimation pressure, which has a slope similar to that of the vaporization equilibrium but gives values higher by a factor of approximately 2 compared with the data of Van Hook (1967). Therefore, this sublimation relation is false and should not be used. Unfortunately, as for CH_2=C=CH_2, no other sublimation relation can be proposed as the vapour pressure of CH_3–C≡CH ice has never been reported.

3.2.18. C_3H_6 (propene)

The triple point of C_3H_6 is located at low temperature (87.8 ± 0.8 K) and its pressure has never been measured (Table 2). Nevertheless, the extrapolation of the evaporation data of Powell and Giauque (1939) and Stull (1947a) allows estimation of the C_3H_6 triple point pressure between 10^{-7} and 10^{-8} bar. Lide (2006) reports data only for the evaporation equilibrium and no data concerning the sublimation have been found. Thus no sublimation relation can be proposed.

3.2.19. C_3H_8 (propane)

The triple point of C_3H_8 is located at low temperature (85.47 ± 0.05 K) and at extremely low pressure ($(1.685 \pm 0.001) \times 10^{-9}$ bar; Younglove and Ely, 1987; Table 2). Lide (2006) reports data only for the evaporation equilibrium and no data concerning the sublimation have been found. Thus no sublimation relation can be proposed.

3.2.20. C_4H_2 (diacetylene)

The location of the triple point of C_4H_2 is not precisely known. According to Stull (1947a), its temperature and pressure are 235.6 ± 3.5 K and 0.1 ± 0.03 bar, respectively (Table 2). Khanna et al. (1990) have measured the vapour pressures of ice between 127 and 152 K (Table 3). These authors point out that their measurements are reliable only within a factor 2.5–3. Thus, these measurements seem doubtful, and we propose no empirical sublimation relation. Moreover Lide (2006) reports no data concerning the vapour pressure of C_4H_2. Thus, new experimental measurements are required to determine the vapour pressure of C_4H_2.

3.2.21. C_6H_2 (triacetylene)

The location of the triple point of C_6H_2 is unknown. Shindo et al. (2003) have measured the vapour pressure between 170.8 K (2.1×10^{-8} bar) and 198.1 K (1.1×10^{-6} bar) (Table 3). Nevertheless, it is not clear if their measurements correspond to the vaporization equilibrium or to the sublimation equilibrium. No other data have been published elsewhere. Thus no sublimation relation can be proposed.

3.2.22. C_6H_6 (benzene)

The triple point of C_6H_6 is located at 278.68 ± 0.02 K and $(4.785 \pm 0.005) \times 10^{-2}$ bar (Table 2; Goodwin, 1988). We have collected 49 experimental measurements ranging from 184.3 K (1.93×10^{-6} bar) to 278.68 K (4.78×10^{-2} bar; Deitz, 1933;

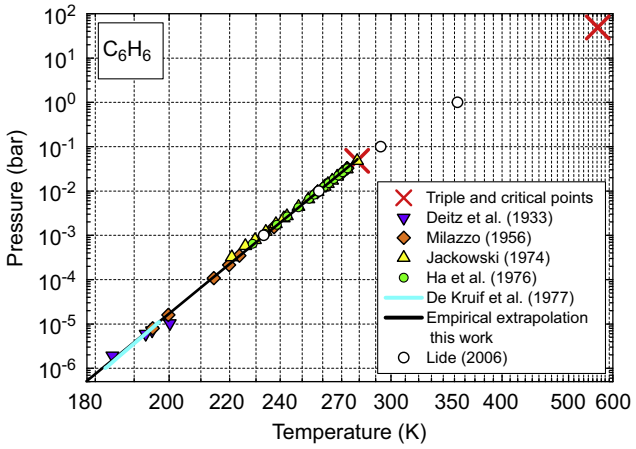

Fig. 16. Sublimation and evaporation pressures of C_6H_6 as a function of temperature (reciprocal scale $1/T$).

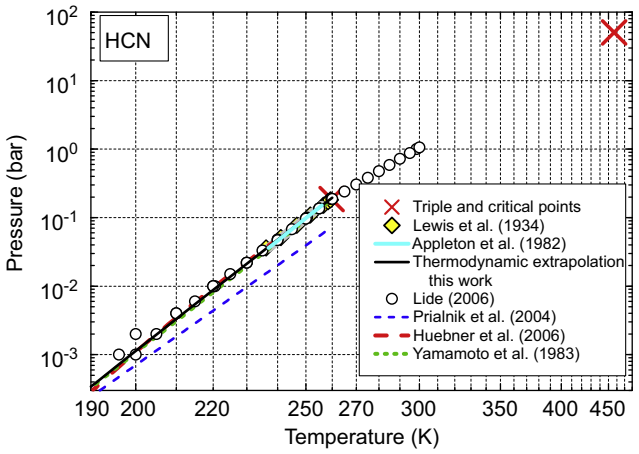

Fig. 17. Sublimation and evaporation pressures of HCN as a function of temperature (reciprocal scale $1/T$).

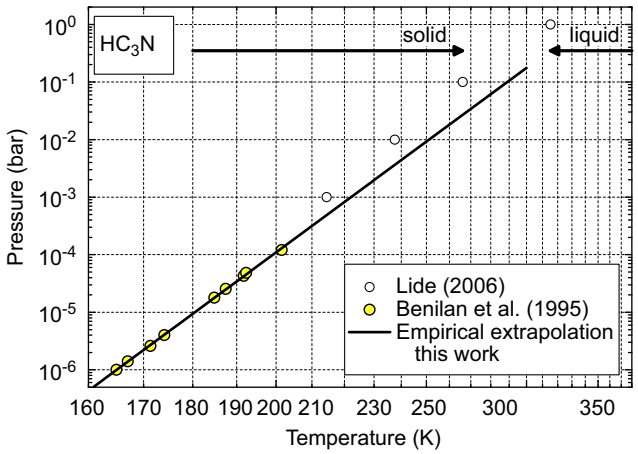

Fig. 18. Sublimation and evaporation pressures of HC_3N as a function of temperature (reciprocal scale $1/T$).

Milazzo, 1956; Jackowski, 1974; Ha et al., 1976; Table 3). De Kruif and Van Ginkel (1977) have also measured the vapour pressure of solid C_6H_6 between 183 and 197 K, but unfortunately their results are not tabulated; they give only an empirical relation of the form $\ln(P)=A+B/T$. As can be seen, in Fig. 16, this empirical relation and the data reported by Lide (2006) are in agreement with the other experimental measurements. So far, no other sublimation relation for C_6H_6 has been proposed. The heat capacity of solid C_6H_6 has been measured by Ziegler and Andrews (1942). Nevertheless, as the internal partition function of gaseous C_6H_6 is not reported in the HITRAN database, we cannot calculate the heat capacity of the gas and therefore cannot propose any thermodynamic relation. We can only propose an empirical extrapolation relation (Tables 4 and 5), which reproduces the experimental data with an accuracy of $\pm 41\%$, reflecting the dispersion of the measurements. We recommend the use of this empirical relation.

3.2.23. HCN (hydrogen cyanide)

The triple point of HCN is located at 259.85 ± 0.03 K and 0.1866 ± 0.0004 bar (Table 2). We have collected only 7 experimental measurements ranging from 235.2 K (3.6×10^{-2} bar) to 259.3 K (0.18 bar; Lewis and Schutz, 1934; Table 3). Appleton and Van Hook (1982) have also measured the vapour pressure of solid HCN between 237 and 256 K. Unfortunately their results are not tabulated. They give only an empirical relation of the form $\ln(P)=A+B/T$. Nevertheless, their results are in agreement with the measurements of Lewis and Schutz (1934) (Fig. 17). We can note in Fig. 17 that the different datasets reported by Lide (2006) are not in agreement around 200 K. The heat capacity of the solid has been measured from 15 K to the triple point by Giauque and Ruehrwein (1939) and the heat capacity of the gas can be calculated down to 15 K thanks to the internal partition function given in the HITRAN database (Rothman et al., 2005), which has been extrapolated using a linear dependence with temperature for $T<70$ K. From these data, we have computed a thermodynamic relation from 15 K to the triple point temperature (Tables 4 and 5). This relation reproduces the experimental data very well, with an accuracy of $\pm 3.5\%$, which reflects the dispersion of the measurements. Some other empirical relations have been proposed by Yamamoto et al. (1983), Prialnik et al. (2004), and Huebner et al. (2006). The relation proposed by Huebner et al. (2006) reproduces the experimental data with an accuracy of $\pm 3\%$. Nevertheless, its slope at $T<180$ K is not in agreement with the values of the heat capacities. The slope of the relation of Yamamoto et al. (1983) is too large and thus reproduces the experimental data with an accuracy of only $\pm 10\%$. The empirical relation proposed by Prialnik et al. (2004) underestimates all the measurements, including the triple point, by almost a factor of 2 (Fig. 17). Both relations should not be used, and we rather recommend the thermodynamic relation that we have computed.

3.2.24. HNC (hydrogen isocyanide)

The location of the triple point of HNC is unknown. No measurements concerning the vapour pressure of HNC have been found. Thus, no vapour pressure relation is proposed.

3.2.25. HC_3N (propiolonitrile)

It seems that the location of the triple point has never been determined directly. Nevertheless, Lide (2006) reports that at 266 K ($P_{vap}=0.1$ bar) HC_3N is solid, whereas at 315 K ($P_{vap}=1$ bar) it is liquid (Fig. 18). Thus, the triple point should be located between these two points. We have collected 9 experimental measurements ranging from 164.9 K (10^{-6} bar) to 201.5 K (1.2×10^{-4} bar; Benilan et al., 1994; Benilan, 1995; Table 3), which are not in agreement with Lide (2006). Nevertheless, we propose an empirical extrapolation relation (see Tables 4 and 5) based on the measurements of Benilan (1995), reproducing the experimental data with an accuracy of $\pm 8\%$, which reflects the dispersion of the measurements. As no other relation has been proposed, we recommend the use of this empirical relation. Further experimental studies are required to determine the sublimation pressure of HC_3N with more accuracy.

3.2.26. CH_3CN (acetonitrile)

The triple point of CH_3CN is located at low temperature, 229.32 ± 0.02 K, and its pressure is unknown (Table 2). Thanks to empirical extrapolation of the evaporation data of Stull (1947a), we can estimate that the pressure at the triple point is about $(2.0 \pm 0.1) \times 10^{-3}$ bar. Lide (2006) reports data only for the evaporation equilibrium. It has been shown that CH_3CN ice exists in two different crystalline form (phases II and I) with a transition temperature of 216.9 ± 0.1 K (Putnam et al., 1965). Nevertheless, no data concerning its sublimation have been found. Thus no sublimation relation can be proposed.

3.2.27. CH_3CH_2CN (propanenitrile)

The triple point of CH_3CH_2CN is located at low temperature, 180.37 ± 0.02 K, and its pressure is unknown (Table 2). Thanks to empirical extrapolation of the evaporation data of Stull (1947a), we can estimate that the pressure at the triple point is about

$(3.8 \pm 0.1) \times 10^{-6}$ bar. Lide (2006) reports data only for the evaporation equilibrium. It has been shown that CH_3CH_2CN ice exists in two different crystalline forms (phases II and I) with a transition temperature of 174.96 ± 0.01 K (Weber and Kilpatrick, 1962). Nevertheless, no data on the sublimation equilibrium have been found and no sublimation relation can be proposed.

3.2.28. C_2N_2 (cyanogen)

The triple point of C_2N_2 is located at 245.32 ± 0.02 K and 0.744 ± 0.009 bar (Table 2). We have collected 25 experimental measurements ranging from 156.3 K (5.2×10^{-5} bar) to 245.27 K (0.738 bar; Perry and Bardwell, 1925; Ruehrwein and Giauque, 1939; Benilan, 1995; Table 3). Lide (2006) reports data for the sublimation and evaporation equilibriums, which agree with the previous experimental measurements. The heat capacity of solid C_2N_2 has been measured by Ruehrwein and Giauque (1939). Nevertheless, as the internal partition function of gaseous C_2N_2 is not reported in the HITRAN database, we cannot calculated the heat capacity of the gas and so no thermodynamic relation is proposed. Therefore, we propose an empirical relation (Tables 4 and 5), reproducing the experimental data with an accuracy of $\pm 24\%$, which reflects the dispersion of the measurements (Fig. 19). The relation proposed by Huebner et al. (2006) reproduces also the experimental data with an accuracy of

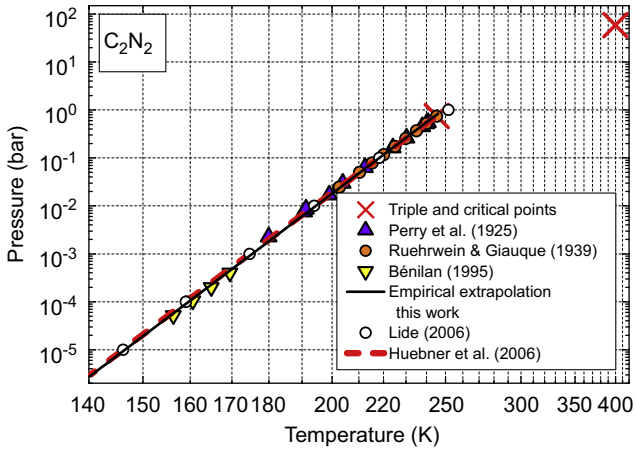

Fig. 19. Sublimation and evaporation pressures of C_2N_2 as a function of temperature (reciprocal scale $1/T$).

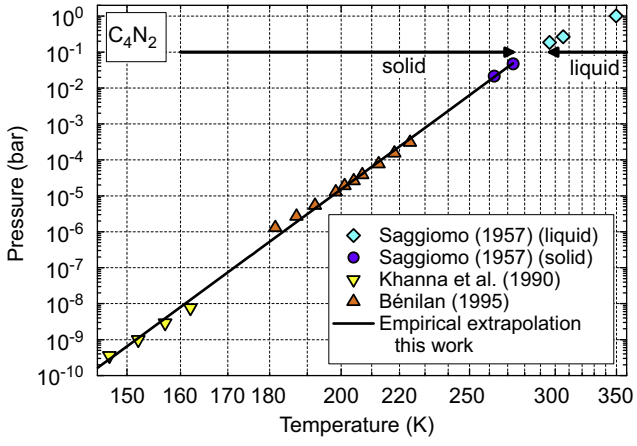

Fig. 20. Sublimation and evaporation pressures of C_4N_2 as a function of temperature (reciprocal scale $1/T$).

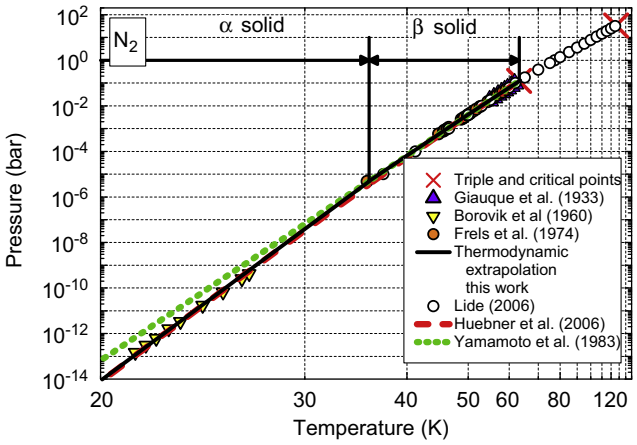

Fig. 21. Sublimation and evaporation pressures of N_2 as a function of temperature (reciprocal scale $1/T$). Vertical lines show the temperatures of the α–β phase transition and of the triple point.

$\pm 20\%$. Nevertheless, its slope for $T < 120$ K seems to be too high. Thus, we recommend the use of our empirical relation.

3.2.29. C_4N_2 (butynedinitrile)

It seems that the location of the triple point of C_4N_2 has never been determined directly. Nevertheless, Saggiomo (1957) reports that at 273.2 K (P_{vap}=0.047 bar) C_4N_2 is a solid, whereas at 296 K (P_{vap}=0.187 bar) it is a liquid (Fig. 20). Thus, the triple point should be located between these two points. We have collected 16 experimental measurements ranging from 147 K (3.6×10^{-10} bar) to 273.2 K (4.72×10^{-2} bar; Saggiomo, 1957; Khanna et al., 1990; Benilan, 1995; Table 3). Khanna et al. (1990) specify that their measurements are reliable only within a factor of 2.5–3. Lide (2006) reports no data concerning the vapour pressure of C_4N_2. We have calculated an empirical relation for the whole data set that reproduces the experimental measurements with an accuracy of $\pm 90\%$ (Tables 4 and 5 and Fig. 20). Nevertheless, the slopes of the data sets of Benilan (1995) and Khanna et al. (1990) are significantly different and lead to individual extrapolations differing by up to an order of magnitude. Thus, the empirical relation that we propose is uncertain. New measurements are required to more precisely define the vapour pressure of C_4N_2.

3.2.30. N_2 (nitrogen)

The triple point of N_2 is located at 63.14 ± 0.06 K and 0.1255 ± 0.0005 bar (Table 2). We have collected 38 experimental measurements ranging from 21.2 K (1.467×10^{-13} bar) to 60.67 K (7.367×10^{-2} bar; Giauque and Clayton, 1933; Borovik et al., 1960; Frels et al., 1974; Table 3 and Fig. 21). Lide (2006) reports data for the sublimation and evaporation equilibriums in agreement with previous experimental measurements. We have excluded the data of Atake and Chihara (1974), which are too different from the others. Solid N_2 has two different crystalline forms, α and β, with the temperature of solid–solid transition at 35.61 ± 0.05 K (Giauque and Clayton, 1933). Brown and Ziegler (1979) have proposed thermodynamic relations for each phase, which surprisingly do not accurately reproduce the experimental measurements. The relation for the α phase ($T < 35.6$ K) overestimates the experimental measurements by ~30%, whereas that for the β phase ($T > 35.61$ K) underestimates the experimental measurements by ~20%. We have thus computed our own thermodynamic relations for each phase (Table 4 and 5) using values of heat capacity of N_2 ices measured by Giauque and Clayton (1933) and the constant value $(7/2)R$ for the heat capacity

of the gas, which corresponds to the value of a perfect diatomic gas. Our relations for the α and β phases reproduce the experimental measurements with more accuracy ($\pm 28\%$ and $\pm 2.7\%$, respectively) than those of Brown and Ziegler (1979). In the astrophysical literature, empirical relations have been proposed by Yamamoto et al. (1983) and Huebner et al. (2006). Yamamoto et al. (1983) overestimate all measurements below 35 K and Huebner et al. (2006) reproduce experimental measurements with an accuracy of $\pm 40\%$. Thus, we recommend the use of both our thermodynamic relations.

3.2.31. NH_3 (ammonia)

The triple point of NH_3 is located at 195.41 ± 0.01 K and 0.0609 ± 0.0003 bar (Table 2). We have collected only 15 experimental measurements ranging from 162.39 K (1.27×10^{-3} bar) to 195.36 K (0.0608 bar; Karwat, 1924; Overstreet and Giauque, 1937; Table 3 and Fig. 22). The different dataset reported by Lide (2006) is not in agreement with them for T of about 170 K. The heat capacity of the solid has been measured by Overstreet and Giauque (1937) between 15 and 195 K and the heat capacity of the gas can be calculated down to 15 K thanks to the internal partition function given in the HITRAN database (Rothman et al., 2005), which has been extrapolated using a $T^{1.5}$ dependence for $T < 70$ K. From these data we have computed a thermodynamic relation from 15 K to the triple point temperature (Tables 4 and 5 and Fig. 22). This relation reproduces experimental data with an accuracy of $\pm 4.2\%$. In the astrophysical literature, empirical relations have been proposed by Yamamoto et al. (1983), Prialnik et al. (2004), and Huebner et al. (2006). The relation proposed by Yamamoto et al. (1983) is quasi-identical to our empirical relation. The relations proposed by Prialnik et al. (2004) and Huebner et al. (2006) overestimate all the measurements and their slopes are too small to be compatible with the values of heat capacities. Thus, we recommend the use of our thermodynamic relation.

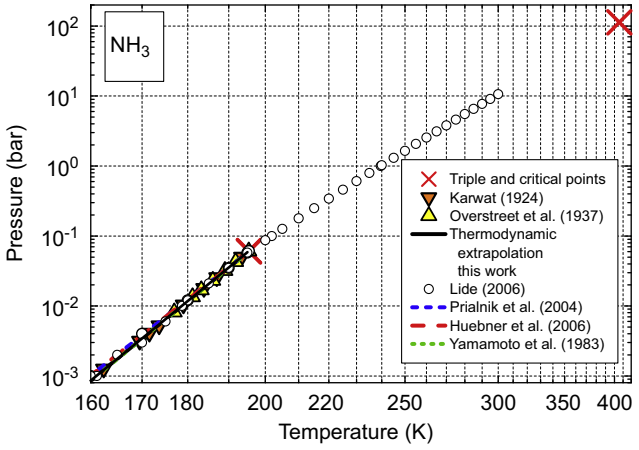

Fig. 22. Sublimation and evaporation pressures of NH_3 as a function of temperature (reciprocal scale $1/T$).

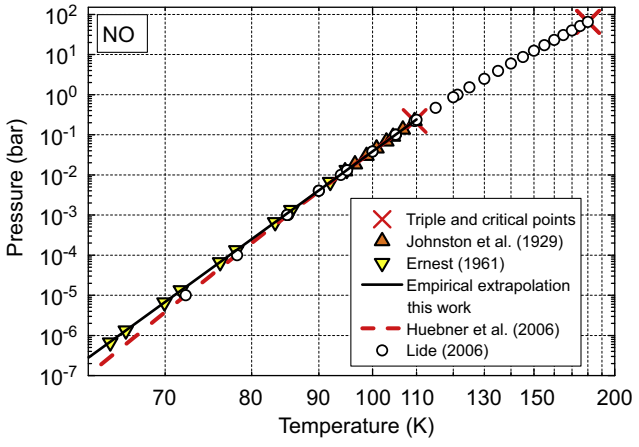

Fig. 23. Sublimation and evaporation pressures of NO as a function of temperature (reciprocal scale $1/T$).

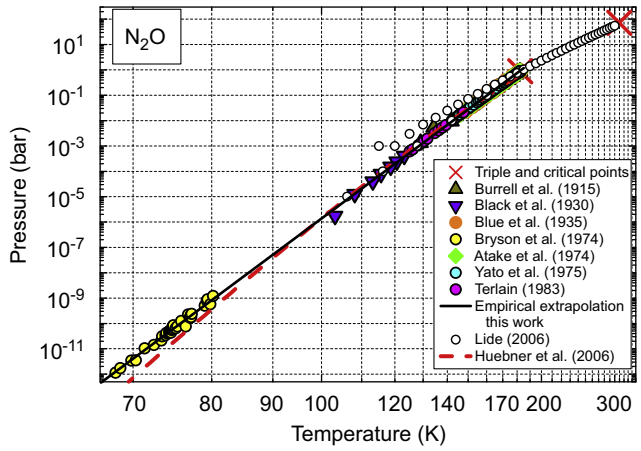

Fig. 24. Sublimation and evaporation pressures of N_2O as a function of temperature (reciprocal scale $1/T$).

3.2.32. NO (nitric oxide)

The triple point of NO is located at 109.5 ± 0.1 K and 0.219 ± 0.001 bar (Table 2). We have collected 18 experimental measurements ranging from 64.85 K (6.66×10^{-7} bar) to 109.49 K (0.219 bar; Johnston and Giauque, 1929; Ernest, 1961; Table 3). The data reported by Lide (2006) are not in accordance with the experimental measurements for $T < 80$ K (Fig. 23). The heat capacity of the NO ice has been measured between 15.6 and 108.4 K by Johnston and Giauque (1929) and the heat capacity of the gas can be calculated for $T > 70$ K thanks to the internal partition function given in the HITRAN database (Rothman et al., 2005). However, as some experimental measurements of the sublimation pressure are available for T lower than 70 K, the thermodynamic relation that we can compute did not provide any useful extrapolation of the data. So we have performed an empirical polynomial interpolation of the experimental measurements in the range $64.9\text{ K} < T < 109.5$ K, and a simple empirical extrapolation valid for $T < 64.9$ K (Tables 4 and 5). The first relation reproduces the experimental data with an accuracy of $\pm 1\%$ over the whole range but only $\pm 3\%$ for the second. In the astrophysical literature, an empirical relation has been proposed by Huebner et al. (2006), which underestimates by a factor of about 2 the experimental measurements at $T < 75$ K (Fig. 23). Thus, we recommend the use of our empirical interpolation relation for $64.9\text{ K} < T < 109.5$ K and our empirical extrapolation for $T < 64.9$ K.

3.2.33. NO_2 (nitrogen dioxide)

The location of the triple point of NO_2 is unknown. No measurement concerning the vapour pressure of NO_2 has been found. Some vapour pressure data attributed to NO_2 are given in the NIST database. Nevertheless, they correspond in fact to vapour pressure of N_2O_4 (dinitrogen tetroxide) measured by Giauque and Kemp (1938). Thus, no NO_2 vapour pressure relation is proposed.

3.2.34. N_2O (nitrous oxide)

The triple point of N_2O is located at 182.30 ± 0.05 K and 0.879 ± 0.001 bar (Table 2). We have collected 180 experimental measurements ranging from 68.1 K (1.14×10^{-12} bar) to 182.29 K (0.88 bar; Burrell and Robertson, 1915b; Black et al., 1930; Blue and Giauque, 1935; Atake and Chihara, 1974; Bryson et al., 1974; Yato et al., 1975; Terlain, 1983; Table 3). The different dataset reported by Lide (2006) is not in agreement for $T < 175$ K (Fig. 24). The heat capacity of solid N_2O has been measured between 15.2 and 180.7 K by Blue and Giauque (1935) and Atake and Chihara (1974) and the heat capacity of the gas can be calculated for $T > 70$ K thanks to the internal partition function given in the HITRAN database (Rothman et al., 2005). However, as the vapour pressure has been measured down to temperatures lower than 70 K, we prefer to interpolate all the collected data (Tables 4 and 5) rather than to compute a thermodynamic relation. This polynomial interpolation can be used for $T > 68.1$ K. For extrapolation at lower temperatures, we have determined a simple empirical relation. Our two relations reproduce the measurements of the vapour pressure with an accuracy of $\pm 50\%$, which reflects the dispersion of the measurements at low temperature. The relation proposed by Huebner et al. (2006) strongly underestimates the vapour pressure measurements for $T < 90$ K (Fig. 24); thus we recommend our empirical interpolation relation for $T > 68$ K and our empirical extrapolation relation for $T < 68$ K.

3.2.35. HNCO (isocyanic acid)

The location of the triple point of HNCO is unknown. No measurements concerning the vapour pressure of HNCO have been found. Thus, no vapour pressure relation is proposed.

3.2.36. NH_2CHO (formamide)

The triple point of NH_2CHO is located at 275.66 ± 0.8 K and its pressure is unknown (Table 2). Lide (2006) reports data only for the evaporation equilibrium. No data concerning the sublimation equilibrium have been found.

3.2.37. H_2S (hydrogen sulphide)

The triple point of H_2S is located at 187.57 ± 0.15 K and 0.229 ± 0.008 bar (Table 2). We have collected only 5 experimental measurements ranging from 164.9 K (3.21×10^{-2} bar) to 182.8 K (0.161 bar; Giauque and Blue, 1936) (Table 3). The different dataset reported by Lide (2006) is not in agreement at low temperatures (Fig. 25). H_2S exists in three different crystalline forms. Anderson et al. (1977) showed that phase III transforms to an intermediate phase II at 103.6 K and that a further transition occurs at 126.2 K to phase I. The heat capacity of the solid has been measured between 17 and 186.4 K by Giauque and Blue (1936) and the heat capacity of the gas can be calculated for $T > 70$ K thanks to the internal partition function given in the HITRAN database (Rothman et al., 2005). As a solid–solid transition exists at 126.2 K, we have computed a thermodynamic relation for the range $126.2\text{ K} < T < 187.57$ K corresponding to phase I and a simple empirical relation for lower T (Tables 4 and 5). These two relations reproduce the experimental data with an accuracy better than $\pm 0.3\%$. New experimental measurements are required to check the validity of these relations at $T < 164.9$ K. In astrophysical literature, empirical relations have been proposed by Huebner et al. (2006) and Prialnik et al. (2004). The relation of Prialnik et al. (2004) underestimates the experimental measurements by a factor of 2.5 (Fig. 25) and the relation of Huebner et al. (2006) reproduces the experimental data with an accuracy of $\pm 3\%$. Thus, we recommend the use of our thermodynamic relation for $127\text{ K} < T < 187.57$ K and our empirical relation for $T < 127$ K.

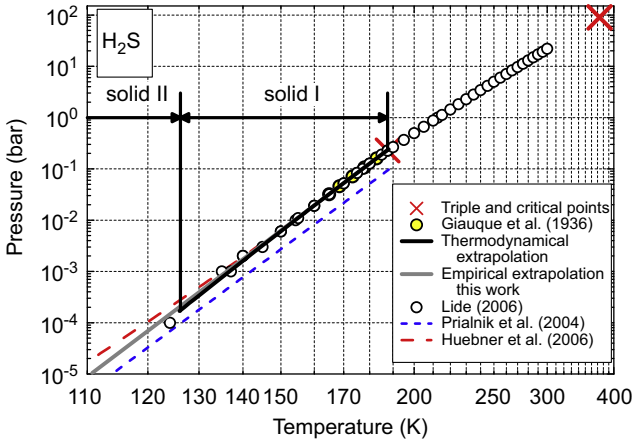

Fig. 25. Sublimation and evaporation pressures of H_2S as a function of temperature (reciprocal scale $1/T$). Vertical lines show the temperature of the phase transition (II–I) and of the triple point.

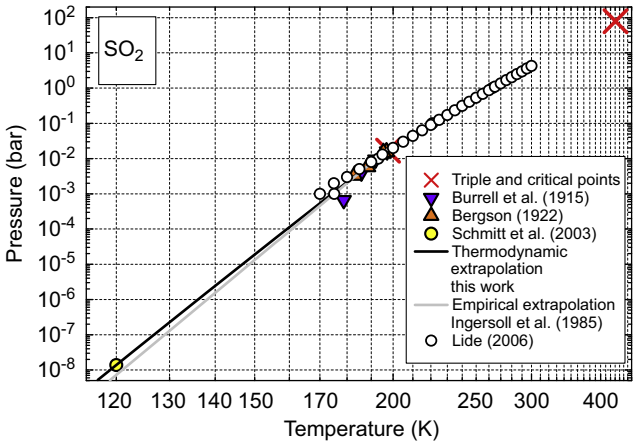

Fig. 26. Sublimation and evaporation pressures of SO_2 as a function of temperature (reciprocal scale $1/T$).

3.2.38. SO_2 (sulphur dioxide)

The triple point of SO_2 is located at 197.64 ± 0.05 K and 0.0167 ± 0.0001 bar (Table 2). We have collected only 9 experimental measurements ranging from 120 K (1.38×10^{-8} bar) to 197.15 K (1.6×10^{-2} bar; Burrell and Robertson, 1915b; Bergstrom, 1922; Schmitt and Rodriguez, 2003; Table 3). The different dataset reported by Lide (2006) is not in accordance with them for low temperatures and moreover these data for $T < 197.64$ K do not agree with the experimental data (Fig. 26). As can be seen in Fig. 26, the measurement at 179 K of Burrell and Robertson (1915b) seems to be false, and is therefore discarded in our extrapolation relation. The heat capacity of the solid that has been measured between 15.20 and 197.64 K by Giauque and Stephenson (1938) and the heat capacity of the gas have been calculated down to 15 K thanks to the internal partition function given in the HITRAN database (Rothman et al., 2005), which has been extrapolated using a $T^{1.5}$ dependence for $T < 70$ K. From these data, we have computed a thermodynamic relation (Tables 4 and 5), which reproduces the experimental data with an accuracy of $\pm 9.6\%$, reflecting the dispersion of the measurements. In the astrophysical literature, only Ingersoll et al. (1985) have proposed a sublimation relation (Fig. 26), which reproduces the experimental data with an accuracy of $\pm 90\%$ and for which the

slope is too weak to be compatible with the heat capacity values. New measurements of the vapour pressure of solid SO_2 are required to improve the proposed relations. We recommend the use of our thermodynamic relation.

3.2.39. CS_2 (carbondisulphide)

The triple point temperature of CS_2 is 161.45 ± 0.40 K and its pressure has never been directly determined (Table 2). From an extrapolation of the evaporation data of Stull (1947b) and Honig and Hook (1960), we can estimate that the triple point pressure is about $(2 \pm 1) \times 10^{-5}$ bar. Lide (2006) reports data only for evaporation equilibrium and no data concerning sublimation have been found. Thus, no sublimation relation can be proposed.

3.2.40. OCS (carbonyl sulphide)

The triple point temperature of OCS is 134.32 ± 0.20 K and its pressure has never been directly determined (Table 2). From an extrapolation of the evaporation data of Stull (1947b) and Honig and Hook (1960), we can estimate that the triple point pressure is about $(5 \pm 2) \times 10^{-4}$ bar. Lide (2006) reports data only for the evaporation equilibrium and no data concerning the sublimation have been found. Thus, no sublimation relation can be proposed.

3.2.41. H_2SO_4 (sulphuric acid)

The location of the triple point of H_2SO_4 is unknown. Lide (2006) reports data only for the evaporation–liquefaction equilibrium and no measurements concerning the sublimation pressure have been found. Thus, no vapour pressure relation is proposed.

3.2.42. NH_4SH (ammonium hydrogensulphide)

The location of the triple point of NH_4SH is unknown. Stull (1947b) reports data only for the evaporation–liquefaction equilibrium and no measurements concerning the sublimation pressure have been found. Thus, no vapour pressure relation is proposed.

3.2.43. H_2CS (thioformaldehyde)

The location of the triple point of H_2CS is unknown. No measurements concerning the vapour pressure of H_2CS have been found. Thus, no vapour pressure relation is proposed.

3.2.44. Cl_2 (chlorine)

The triple point of Cl_2 is located at 172.12 ± 0.15 K and $(1.39 \pm 0.01) \times 10^{-2}$ bar (Table 2). Honig and Hook (1960) and Lide (2006) report extrapolation for the sublimation equilibrium, whereas no experimental data concerning the sublimation have been found. Thus, we propose no sublimation relation.

3.2.45. ClS_2 (sulphur chloride)

The location of the triple point of ClS_2 is unknown. No measurements concerning the vapour pressure of ClS_2 have been found. Thus, no vapour pressure relation is proposed.

3.2.46. ClO (monochlorine monoxide)

The location of the triple point of ClO is unknown. No measurements concerning the vapour pressure of ClO have been found. Thus, no vapour pressure relation is proposed.

3.2.47. PH_3 (phosphine)

The triple point of PH_3 is located at 139.41 ± 0.20 K and $(3.6 \pm 0.1) \times 10^{-2}$ bar (Table 2). Lide (2006) reports data for the sublimation equilibrium. Nevertheless, it seems that these data have obtained by extrapolation of the liquid–gas equilibrium for temperatures below the triple point temperature. No experimental data concerning the sublimation have been found. Thus, we propose no sublimation relation.

3.2.48. AsH_3 (arsine)

The triple point of AsH_3 is located at 156.23 ± 0.02 K and $(2.98 \pm 0.02) \times 10^{-2}$ bar (Table 2). We have collected only 13 experimental measurements ranging from 136.15 K (2.67×10^{-3} bar) to 154.15 K (2.47×10^{-2} bar; Johnson and Pechukas, 1937; Table 3 and Fig. 27). Lide (2006) reports data for the sublimation and evaporation equilibriums. Sherman and Giauque (1955) showed the existence of a solid–solid transition occurring at $T = 105.5$ K from measurements of the heat capacity of the solid from 15.4 to 151.0 K. Unfortunately, as the internal partition function of gaseous AsH_3 is not reported in the HITRAN database, we cannot calculate the heat capacity of the gas and so no thermodynamic relation is proposed. Thus, we have calculated an empirical extrapolation relation (Tables 4 and 5), which reproduces the experimental data with an accuracy of $\pm 6\%$. No other extrapolation relation has been proposed in the literature, so we recommend the use of this empirical relation.

3.2.49. SiH_4 (silane)

The location of the triple point of SiH_4 is unknown. Nevertheless, Stull (1947b) reports that at $T = 94$ K ($P_{vap} = 1.4 \times 10^{-3}$ bar), SiH_4 is a liquid. Thus, the triple point of SiH_4 is located below this point. Lide (2006) reports data only for the evaporation

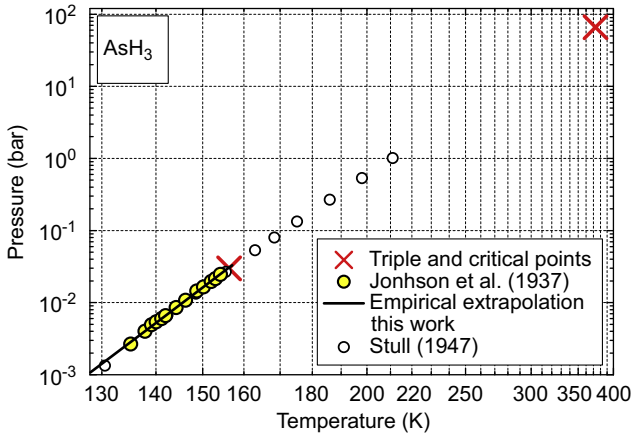

Fig. 27. Sublimation and evaporation pressures of AsH_3 as a function of temperature (reciprocal scale $1/T$).

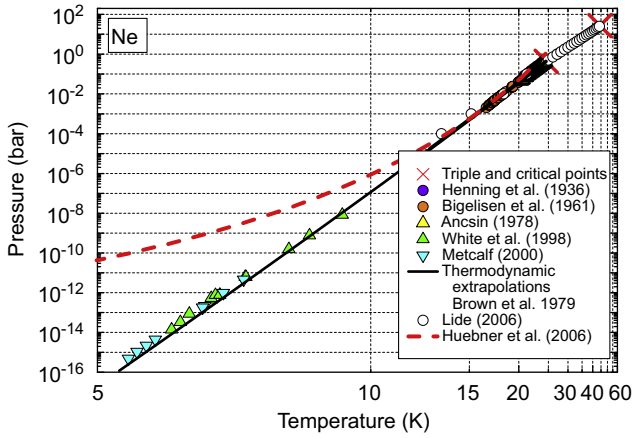

Fig. 28. Sublimation and evaporation pressures of Ne as a function of temperature (reciprocal scale $1/T$).

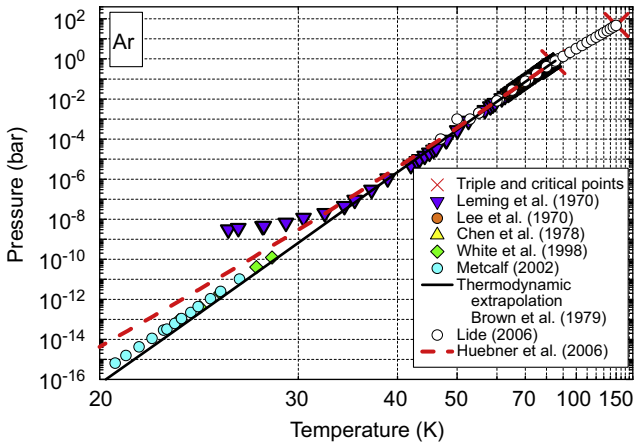

Fig. 29. Sublimation and evaporation pressures of Ar as a function of temperature (reciprocal scale $1/T$).

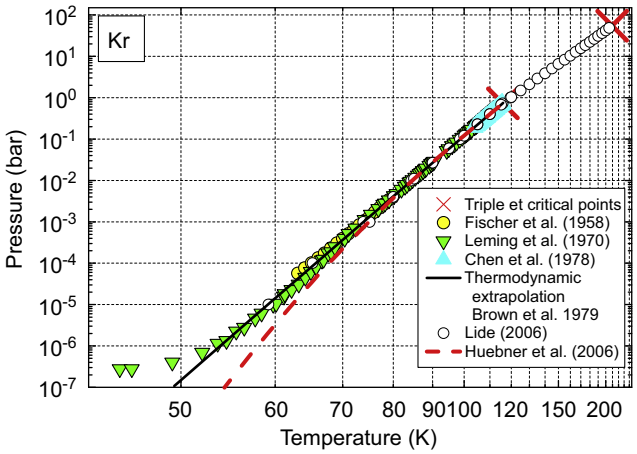

Fig. 30. Sublimation and evaporation pressures of Kr as a function of temperature (reciprocal scale $1/T$).

equilibrium and no data concerning the sublimation have been found. Thus no sublimation relation can be proposed.

3.2.50. Ne (neon)

The triple point of Ne is located at 24.56 ± 0.05 K and 0.433 ± 0.003 bar (Table 2). We have collected 156 experimental measurements ranging from 5.50 K (4.8×10^{-16} bar) to 24.50 K (0.418 bar; Henning and Otto, 1936; Bigeleisen and Roth, 1961; Ancsin, 1978; White et al., 1998; Metcalf, 2002; Table 3). The different dataset reported by Lide (2006) is not in accordance with them for T of about 14 K (Fig. 28). Ne ice exists in only one crystalline form. Nevertheless, Brown and Ziegler (1979) have calculated two thermodynamic relations (Table 4 and 5), first for $3.7\,\mathrm{K} < T < 12.5\,\mathrm{K}$ and then for $12.5\,\mathrm{K} < T < 24.56\,\mathrm{K}$. The second relation reproduces the experimental data with an accuracy of $\pm 9\%$, reflecting the dispersion of the measurements. The very low temperature relation underestimates the experimental measurements of White et al. (1998) and Metcalf (2002) by a factor of 2 at $T < 8$ K (Fig. 28). But we observe a similar problem with the experimental data of White et al. (1998) and Metcalf (2002) concerning argon. Therefore, we consider that these data at extremely low pressure are not accurate. An empirical relation has also been proposed by Huebner et al. (2006), but it overestimates all the measurements, especially below 15 K, where the relation strongly diverges. Thus we recommend the use of the thermodynamic relations proposed by Brown and Ziegler (1979).

3.2.51. Ar (argon)

The triple point of Ar is located at 83.8058 K and 0.68891 ± 0.00002 bar (Table 2). The triple point temperature of Ar was adopted as a defining fixed point on the present temperature scale ITS-90. We have collected 268 experimental measurements ranging from 20.53 K (6.56×10^{-16} bar) to 83.76 K (0.685 bar; Leming and Pollack, 1970; Lee et al., 1970; Chen et al., 1978; White et al., 1998; Metcalf, 2002; Table 3). The dataset reported by Lide (2006) diverges slightly from the experimental measurements for $T < 60$ K (Fig. 29). As for Kr and Xe, the data of Leming and Pollack (1970) present a strong discrepancy at low temperatures; thus we have excluded them below 33 K. Brown and Ziegler (1979) have proposed a thermodynamic relation (Tables 4 and 5), which reproduces experimental data above 55 K with an accuracy of $\pm 5\%$, reflecting the dispersion of the measurements. At lower temperatures, the relation of Brown and Ziegler (1979) underestimates the measurements of White et al. (1998) and Metcalf (2002) by a factor of 2 (Fig. 29). We are confident of the relation of Brown and Ziegler (1979) as the thermodynamic relation computed by Tegeler et al. (1999) is almost identical. Thus, we consider, as for Ne, that these extremely low-pressure data may have some systematic error. An empirical relation has also been proposed by Huebner et al. (2006), but it overestimates all the measurements, especially below 50 K. Thus we recommend the use of the thermodynamic relation proposed by Brown and Ziegler (1979).

3.2.52. Kr (krypton)

The triple point of Kr is located at 115.9 ± 0.2 K and 0.7315 ± 0.0006 bar (Table 2). We have collected 161 experimental measurements ranging from 45.13 K (2.8×10^{-7} bar) to 115.63 K (0.72 bar; Fisher and McMillan, 1958; Leming and Pollack, 1970; Chen et al., 1978; Table 3). The dataset reported by Lide (2006) diverges slightly from the experimental measurements for $T < 85$ K (Fig. 30). The measurements of Leming and Pollack (1970) for $T < 55$ K are very doubtful since their slope changes drastically below this temperature (Fig. 30). Moreover, for temperatures below 63 K the data of Leming and Pollack (1970) and Fisher and McMillan (1958) present a discrepancy of about 40%. We decided to exclude the data of Leming and Pollack (1970) below 65 K. The thermodynamic relation computed by Brown and Ziegler (1979) seems to be reliable (Tables 4 and 5 and Fig. 30) as it reproduces the experimental data for $T > 65$ K with an accuracy of $\pm 35\%$, reflecting only the dispersion of the measurements. The empirical relation proposed by Huebner et al. (2006) underestimates all the experimental results below 80 K (Fig. 30). Thus, we recommend the use of the thermodynamic relation computed by Brown and Ziegler (1979).

3.2.53. Xe (xenon)

The triple point of Xe is located at 161.4 ± 0.3 K and 0.816 ± 0.001 bar (Table 2). We have collected 197 experimental measurements ranging from 53.7 K (5.97×10^{-11} bar) to 161.33 K (0.813 bar; Leming and Pollack, 1970; Bryson et al., 1974; Chen et al., 1978; Tessier et al., 1982; Table 3). The dataset reported by Lide (2006) diverges slightly from the experimental measurements for $T < 120$ K (Fig. 31). As for Ar and Kr, the measurements of Leming and Pollack (1970) are very doubtful below 75 K since their slope changes drastically below this temperature (Fig. 31). Thus, we decided to exclude these data below 75 K. The thermodynamic relation computed by Brown and Ziegler (1979) seems to be reliable (Tables 4 and 5) as it reproduces the experimental data for $T > 75$ K with an accuracy of $\pm 20\%$, reflecting the dispersion of the

measurements. The empirical relation proposed by Huebner et al. (2006) strongly underestimates all the experimental results below 120 K (Fig. 31). Thus, we recommend the use of the thermodynamic relation computed by Brown and Ziegler (1979).

3.3. Summary of the bibliographic review

We have searched for experimental measurements of the sublimation pressure of 53 different species.

For 10 of these species (H_2O_2—hydrogen peroxide, $HCOOCH_3$—methyl formate, HNC—hydrogen isocyanide, HNCO—isocyanic acid, NO_2—nitrogen dioxide, H_2SO_4—sulphuric acid, NH_4SH—ammonium hydrogensulphide, H_2CS—thioformaldehyde, ClS_2—sulphur chloride, and ClO—monochlorine monoxide) the location of the triple point is unknown and no data concerning the sublimation equilibrium have been found. For some of these 10 species, measurements of the vapour pressure over the liquid phase can still be found in Stull (1947a, 1947b) or in Lide (2006).

For 13 other species (H_2CO—formaldehyde, NH_2CHO—formamide, $HOCH_2CH_2OH$—ethylene glycol, $CH_2{=}C{=}CH_2$—allene, C_3H_6—propene, C_3H_8—propane, CH_3CN—acetonitrile, CH_3CH_2CN—propanenitrile, CS_2—carbon disulphide, OCS—carbonyl sulphide, Cl_2—chlorine, PH_3—phosphine, and SiH_4—silane), the temperature of the triple point is known and in some cases the pressure of the triple point has also been measured. For these 13 molecules, no data concerning the sublimation equilibrium have been found, whereas results concerning the evaporation equilibrium can be found in Stull (1947a, 1947b) and in Lide (2006).

For the 30 remaining species, we have compiled 1842 experimental measurements of their sublimation pressure ranging from 4.8×10^{-16} to 5.2 bar. The intrinsic volatility of these species can be compared in Fig. 32, where the data have been summarized. Taking into account their abundances, their volatility in the solar nebula or in comet nuclei can be compared, as Yamamoto (1985) and Crovisier (1999) did. For species having very different abundances, their order of volatility can be reversed. Nevertheless, Yamamoto (1985) and Crovisier (1999) find qualitatively same results as we do. For 8 of these 30 species, the sublimation pressure has been measured only at relatively high pressures ($>10^{-3}$–10^{-2} bar), whereas it is possible to directly measure absolute pressures as low as 10^{-7} bar with a precision of 1%, thanks to variable-capacitance sensors (Baratron©, Barocell©). Moreover, for 3 simple hydrocarbons the

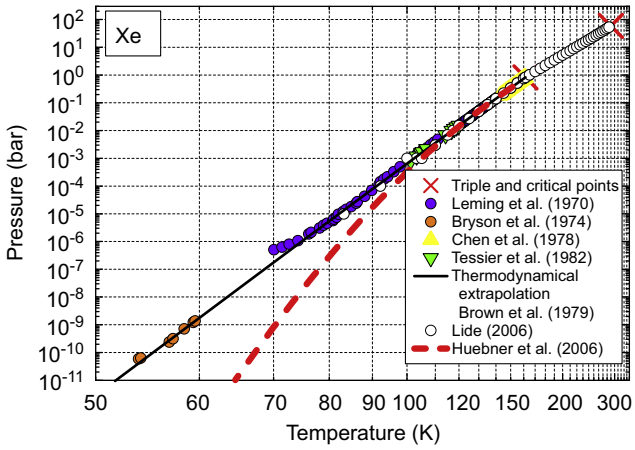

Fig. 31. Sublimation and evaporation pressures of Xe as a function of temperature (reciprocal scale $1/T$).

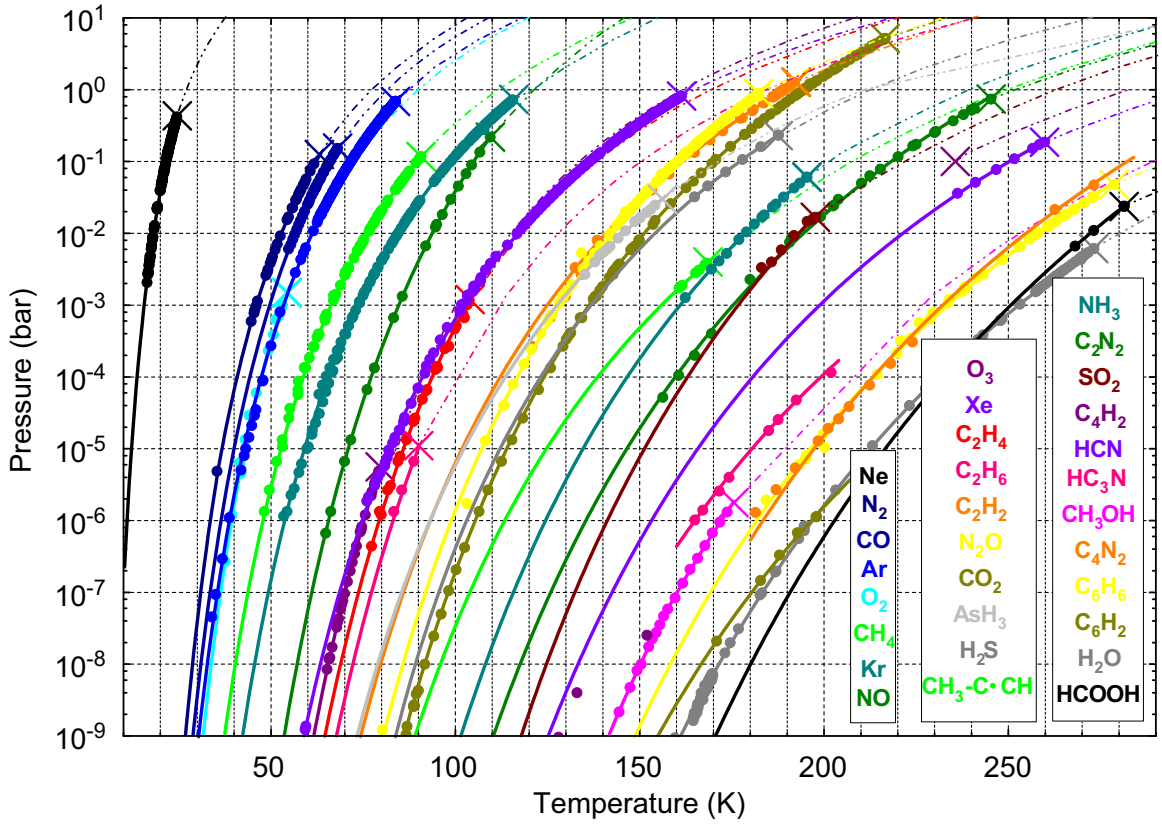

Fig. 32. Sublimation pressure as a function of temperature for the 30 species for which we have found some experimental data. Solid circles and the crosses represent the measurements and the triple points, respectively. The sublimation relations that we recommend (Table 6) are represented as solid lines, whereas dashed lines represent the liquid–gas equilibrium of these species derived from the compilations of Stull (1947a, 1947b) or Lide (2006).

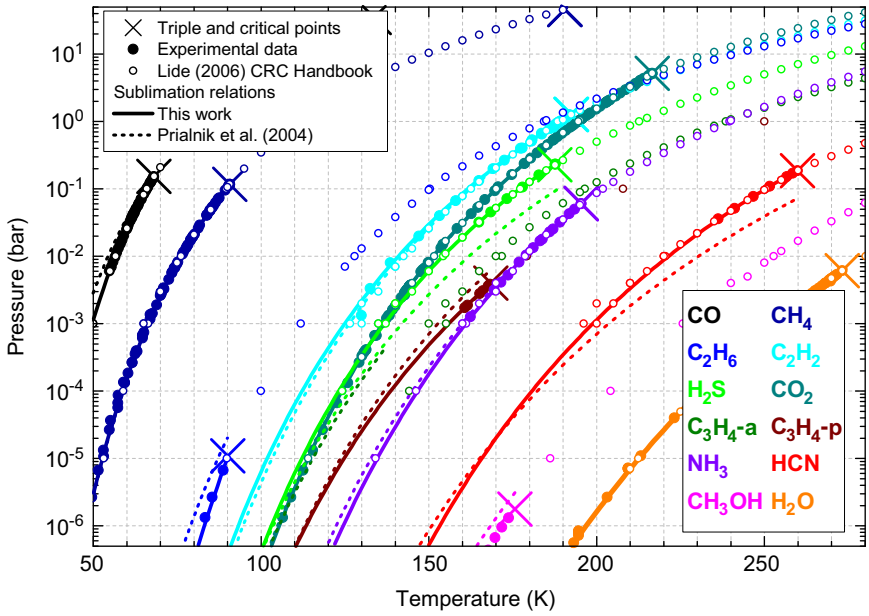

Fig. 33. Comparison between the sublimation relations that we propose and those of Prialnik et al. (2004): CO, CH_4, C_2H_6, C_2H_2, H_2S, CO_2, $CH_2{=}C{=}CH_2$, $CH_3{-}C{\equiv}CH$, NH_3, HCN, CH_3OH, and H_2O.

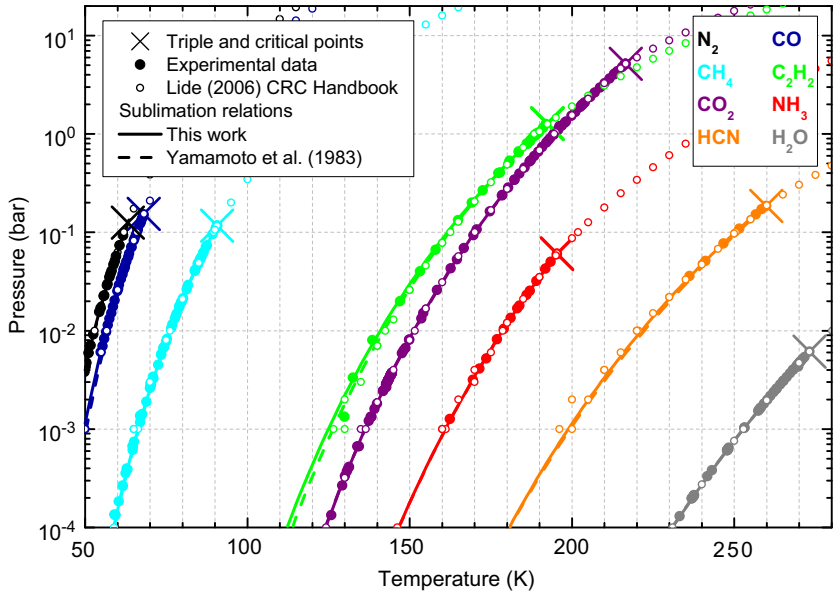

Fig. 34. Comparison between the sublimation relations that we propose and those of Yamamoto et al. (1983): N_2, CO, CH_4, C_2H_2, CO_2, NH_3, HCN, and H_2O.

existing experimental data are either very doubtful (C_4H_2) or not in agreement (C_2H_2 and C_2H_4). Thus, we consider that for 18 of these 30 species, the experimental measurements of their sublimation pressure should be improved. These 18 species are: CO—carbon monoxide, HCOOH—formic acid, CH_4—methane, C_2H_2—acetylene, C_2H_4—ethylene, C_2H_6—ethane, $CH_3{-}C{\equiv}CH$—propyne, C_4H_2—butadiyne C_6H_2—hexatriyne, C_6H_6—benzene, HCN—hydrogen cyanide, HC_3N—propiolonitrile, C_2N_2—cyanogen, NH_3—ammonia, NO—nitric oxide, H_2S—hydrogen sulphide, SO_2—sulphur dioxide, and AsH_3—arsine. The 12 remaining species for which we have found some reliable experimental sublimation curve at pressures lower than 3×10^{-7} bar are: H_2O—water, O_2—oxygen, O_3—ozone, CO_2—carbon dioxide, CH_3OH—methanol, C_4N_2—butynedinitrile, N_2—nitrogen, N_2O—nitric oxide, Ne—neon, Ar—argon, Kr—krypton, and Xe—xenon. For all of these 30 species (except $CH_3{-}C{\equiv}CH$, C_4H_2, and C_6H_2), we have proposed either thermodynamic or empirical sublimation relations, allowing us to calculate the sublimation pressure of these molecular solids at any temperatures.

3.4. Comparison between our results and the sublimation relations used in the astrophysical literature

In this section, we compare some empirical sublimation relations proposed by Prialnik et al. (2004), Yamamoto et al. (1983), and Huebner et al. (2006), widely used in the astrophysical literature and in our own work. As already discussed in Section 3.2, all the proposed relations, either thermodynamic or empirical (Tables 4 and 5), are more accurate than those proposed

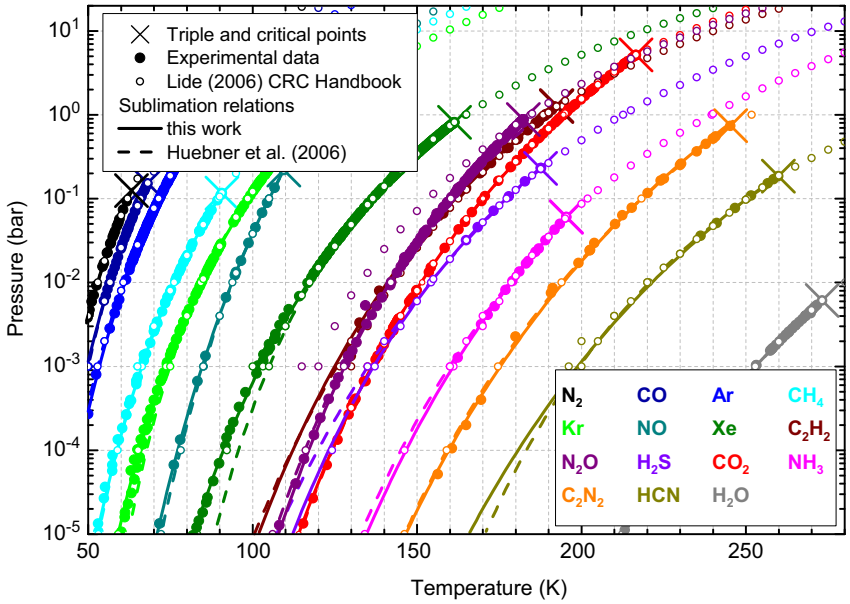

Fig. 35. Comparison between the sublimation relations that we propose and those of Huebner et al. (2006): N_2, CO, Ar, CH_4, Kr, NO, Xe, C_2H_2, N_2O, H_2S, CO_2, NH_3, C_2N_2, HCN, and H_2O.

by the above-mentioned authors. All the former relations are extrapolations of the values published in Lide (2006) or in previous editions of the CRC Handbook of Chemistry and Physics. As we saw in Section 3.2, the data reported by Lide (2006) are not always accurate and can lead to erroneous extrapolations. Yamamoto et al. (1983) and Prialnik et al. (2004) have used relations of the form $\ln(P)=A+B/T$, whereas Huebner et al. (2006) used a relation of the form $\log(P)=A+B/T+C\log(T)+DT$. Figs. 33–35 compare with the experimental data, the relations that we propose and those of Prialnik et al. (2004), Yamamoto et al. (1983), and Huebner et al. (2006), respectively.

As can be seen in Fig. 33, among the 12 sublimation relations proposed by Prialnik et al., (2004), 7 display the same slope as in the evaporation equilibrium curve (CO, C_2H_6, H_2S, $CH_2{=}C{=}CH_2$, $CH_3{-}C{\equiv}CH$, HCN, and CH_3OH). Thus, all these relations are false and should not be used at temperatures lower than the triple point temperature. The most problematic case is that of CO. Prialnik et al. (2004) used the relation that was originally proposed by Fanale and Salvail (1990) and which is used in most of the models simulating the activity of comet nuclei. For example, at 54 K this relation overestimates the sublimation pressure by a factor of two, and this error increases with decreasing temperature. Thus, using the relation that we propose could probably significantly change the results concerning the activity of comet nuclei at heliocentric distances greater than 4 AU. The other relations proposed by Prialnik et al. (2004) (for CH_4, C_2H_2, CO_2, NH_3, and H_2O) reproduce fairly well the experimental sublimation data at temperatures close to the triple point. Nevertheless, the accuracy of these relations decreases at lower temperatures. For example the sublimation pressure of CO_2 is already overestimated by a factor of two around 80 K.

The extrapolation relations proposed by Yamamoto et al. (1983) are quite accurate, but the slopes for CO, C_2H_2, NH_3, and HCN are not perfect, leading to moderate discrepancies at low temperatures (Fig. 34).

The relations proposed by Huebner et al. (2006) reproduce the data published in Lide (2006) very well. However, for several species, experimental data exist at temperatures lower than the lowest point published in Lide (2006). Thus, most of the relations proposed by Huebner et al. (2006) do not reproduce accurately the experimental data at low temperature. Moreover, as already discussed in Section 3.1, the empirical expression used by Huebner et al. (2006) does not allow us to control the slope of the curve at low temperature. Thus, as shown in Fig. 35, some of the extrapolation relations strongly diverge from the experimental data. This is particularly the case for Kr and Xe below 10^{-3} bar.

In conclusion, most of the relations that have been used in the astrophysical literature are quite accurate for temperatures close to the triple point. But, at lower temperatures, the accuracy of these relations decreases significantly and in some cases the error can reach one order of magnitude or more. The relations that we propose in Tables 4 and 5 are more accurate than all the sublimation relations published so far in the astrophysical literature, particularly at low temperature. Indeed, we have compiled a large number of experimental measurements at temperatures lower than the lowest point published in Lide (2006) and we have used, when possible, accurate thermodynamic calculations to extend the sublimation relations at even lower temperatures. As they are based on measurements of the heat capacity, the slopes of the thermodynamic relations that we propose are much more accurate.

4. Conclusion

We performed an extensive bibliographic search of 'all' published experimental measurements of the sublimation pressure for 53 different species. For 23 of these species, no experimental measurement has been found. For the 30 remaining species, we have compiled 1836 sublimation pressure measurements ranging from 4.8×10^{-16} to 5.2 bar, and we propose extrapolation relations at low temperatures that can be easily used for applications in different astrophysical environments, such as solar nebula, comet nuclei, or interstellar and circumstellar clouds. For 16 of these 30 species, we have calculated sublimation pressures at low temperature from thermodynamic formulae using measurements of heat capacities of the ice and the gas. Thus, the slope of these extrapolations should be very accurate. For the other species, we are able to propose empirical extrapolations that are more accurate than those generally used in the astrophysical literature.

This work concerns only pure ices. However, in several astrophysical environments, especially at very low temperature, the gases condense as a molecular mixture of different compounds. Good examples are the comet nuclei, which mostly contain water but are also made of numerous mixed compounds. Moreover, if the species are trapped in amorphous water ice, the mixture is not in thermodynamic equilibrium and it is impossible to define an 'equilibrium vapour pressure'. The species included at low temperature in the amorphous water ice structure will be released irreversibly during heating and crystallisation of the amorphous water ice (Bar-Nun et al., 1985; Schmitt et al., 1989). In the case when several compounds are mixed at equilibrium at the molecular level in ices, Henry's law can be used to estimate the vapour pressures of compounds having a very low abundance in the mixture, and Raoult's law for the dominant compound. Raoult's law states that the partial vapour pressure for the dominant compound of a condensed mixture is equal to the product of its molar fraction in the condensed mixture and its vapour pressure in the pure state. In the case of a non-ideal mixture, this law is valid only for molar fractions close to unity. However, for ideal mixtures (e.g. mixtures of compounds having similar chemical structures) it is valid for all possible values of molar fraction. Henry's law states that the vapour pressure of a minor compound of a binary mixture is proportional to its molar fraction in the condensed mixture. However, Henry's coefficient needs to be measured as a function of temperature for each couple of species. For ideal mixtures, a frequent situation with similar species, Raoult's law can also be used. This is the case in particular for isotopic species. If the isotopic composition of an ice is not the 'natural abundance' (all the sublimation curves presented in this paper are for ices with the natural isotopic abundance), then its vapour pressure can be corrected from that of the 'natural ice' by knowing this new isotopic composition. Both laws can be applied for several important planetary cases where one species strongly dominates the ice composition. For example part of the surfaces of Pluto and Triton are mainly composed of N_2 ice (Raoult's law) with minor inclusions ($<1\%$) of CH_4 and CO (Henry's law) in its crystalline structure.

It should be emphasized that there are also a large number of astrophysical situations where the 'mixed ice' is in fact made of a mixture of several types of pure ice grains, each with their own sublimation equilibrium. The bulk of the south permanent cap and the seasonal condensates on Mars, made of pure CO_2 ice mixed with trace amounts of pure H_2O ice grains (and dust) at the grain level, belong to this category of mixture.

Finally various species can also be trapped in clathrate hydrate, a water ice structure containing gas species within cages (Sloan and Koh, 2008). This type of structure, involving volatile species and water, is in thermodynamic equilibrium with the gas under specific conditions. The vapour pressure of a clathrate hydrate, (almost) always lower than that of the pure ice at a given temperature (Lunine and Stevenson, 1985), cannot be determined from the values of the pure ice and thus should be directly measured, or calculated with specific thermodynamic theories. In a number of astrophysical situations, these compounds may compete with pure or mixed ices, and may thus control the gas pressure and composition, and the exchanges between the gas and solid phases. Thus, a compilation of the existing data and an extrapolation of their equilibrium curves should also deserve strong attention.

Acknowledgements

N. Fray thanks CNES for a post-doctoral fellowship. We acknowledge A. Perrin, I. Kleiner, and Y. Benilan for helpful discussions concerning the HITRAN database, the internal partition function of molecules and the different empirical extrapolation relations, as well as D. Ferry, T. Metcalf, and R. Pohl for providing us their data under electronic form. We also acknowledge A. Jolly and F. Raulin for their help in revising the English. We thank J. Crovisier and an anonymous referee for their useful comments.

References

Ambrose, D., 1956. The vapour pressures and critical temperatures of acetylene and carbon dioxide. Trans. Faraday Soc. 52, 772–781.
Ancsin, J., 1978. Vapour pressures and triple point of neon and the influence of impurities on these properties. Metrologia 14, 1–7.
Anderson, A., Binbrek, O.S., Tang, H.C., 1977. Raman and infrared study of the low temperature phase of solid H_2S and D_2S. J. Raman Spectrosc. 6 (5), 213–220.
Aoyama, S., Kanda, E., 1934. Vapor pressures of solid O_2 and N_2. J. Chem. Soc. Japan 55, 23–29.
Appleton, G.T., Van Hook, W.A., 1982. Vapor pressures of some isotopic hydrogen cyanides. J. Chem. Eng. Data 27 (3), 363–365.
Armstrong, G.T., Brickwedde, F.G., Scott, R.B., 1955. Vapor pressures of methanes. J. Res. Natl. Bur. Stand. 55 (1), 39–52.
Atake, T., Chihara, H., 1974. A new condensed gas calorimeter. Thermodynamic properties of solid and liquid dinitrogen oxide. Bull. Chem. Soc. Japan 47 (9), 2126–2136.
Bar-Nun, A., Herman, G., Laufer, D., Rappaport, M.L., 1985. Trapping and release of gases by water ice and implications for icy bodies. Icarus 63 (3), 317–332.
Benilan, Y., 1995. Spectroscopie d'absorption UV à basse température et étude de l'atmosphère de Titan. Ph.D. Thesis, Université Paris VI.
Benilan, Y., Bruston, P., Raulin, F., Cossart-Magos, C., Guillemin, J.-C., 1994. Mid-UV spectroscopy of propynenitrile at low temperature: consequences on expected results from observations of Titan's atmosphere. J. Geophys. Res. 99, 17069–17074.
Bergstrom, F.W., 1922. The vapor pressure of sulfur dioxide and ammonia. J. Phys. Chem. 26 (4), 358–376.
Bigeleisen, J., Roth, E., 1961. Vapor pressures of the neon isotopes. J. Chem. Phys. 35 (1), 68–77.
Black, H.K., van Praagh, G., Topley, B., 1930. Note on the vapour pressure of solid nitrous oxide. Trans. Faraday Soc. 26, 196–197.
Blue, R.W., Giauque, W.F., 1935. The heat capacity and vapor pressure of solid and liquid nitrous oxide. The entropy from its band spectrum. J. Am. Chem. Soc. 57 (6), 991–997.
Bockelée-Morvan, D., Crovisier, J., Mumma, M.J., Weaver, H.A., 2004. The composition of cometary volatiles. In: Festou, M.C., Keller, H.U., Weaver, H.A. (Eds.), Comets II. University of Arizona Press, Tucson, USA, pp. 391–423.
Borovik, E.S., Grishin, S.F., Grishina, E.Y., 1960. The vapor pressure of nitrogen and hydrogen at low pressures. Sov. Phys. Tech. Phys. (Engl. Transl.) 5 (5), 506–511.
Boublik, T., Fried, V., Hala, E., 1984. The Vapour Pressures of Pure Substances, second ed Elsevier, Amsterdam, Netherlands.
Brown, G.N., Ziegler, W.T., 1979. Vapor pressure and heats of vaporization and sublimation of liquids and solids of interest in cryogenics below 1 atm pressure. Adv. Cryog. Eng. 25, 662–670.
Bryson, C.E., Cazcarra, V., Levenson, L.L., 1974. Sublimation rates and vapor pressures of water, carbon dioxide, nitrous oxide, and xenon. J. Chem. Eng. Data 19 (2), 107–110.
Burrell, G.A., Robertson, I.W., 1915a. The vapor pressures of acetylene, ammonia and isobutane at temperatures below their normal boiling points. J. Am. Chem. Soc. 37 (11), 2482–2486.
Burrell, G.A., Robertson, I.W., 1915b. The vapor pressures of sulfur dioxide and nitrous oxide at temperatures below their normal boiling points. J. Am. Chem. Soc. 37 (12), 2691–2697.
Calis-Van Ginkel, C.H.D., Calis, G.H.M., Timmermans, C.W.M., de Kruif, C.G., Oonk, H.A.J., 1978. Enthalpies of sublimation and dimerization in the vapour phase of formic, acetic, propanoic, and butanoic acids. J. Chem. Thermodyn. 10 (11), 1083–1088.
Carlson, H.G., Westrum, J.E.F., 1971. Methanol: heat capacity, enthalpies of transition and melting, and thermodynamic properties from 5 to 300 K. J. Chem. Phys. 54 (4), 1464–1471.
Chen, H.H., Lim, C.C., Aziz, R.A., 1978. The enthalpies of sublimation and internal energies of solid argon, krypton, and xenon determined from vapor pressures. J. Chem. Thermodyn. 10 (7), 649–659.
Clayton, J.O., Giauque, W.F., 1932. The heat capacity and entropy of carbon monoxide. Heat of vaporization. Vapor pressures of solid and liquid. Free energy to 5000 K from spectroscopic data. J. Am. Chem. Soc. 54 (7), 2610–2626.
Coolidge, A.S., 1930. The vapor pressure and heats of fusion and vaporization of formic acid. J. Am. Chem. Soc. 52 (5), 1874–1887.
Coustenis, A., Schmitt, B., Khanna, R.K., Trotta, F., 1999. Plausible condensates in Titan's stratosphere from Voyager infrared spectra. Planet. Space Sci. 47 (8–9), 1305–1329.
Crovisier, J., 1999. Solids and volatiles in comets. In: Greenberg, J.M., Li, A. (Eds.), Formation and Evolution of solids, NATO Science Series No. 523. Kluwer Academic Publishers, Dordrecht, Nethelands, pp. 389–426.
Cruikshank, D.P., Roush, T.L., Owen, T.C., Geballe, T.R., de Bergh, C., Schmitt, B., Brown, R.H., Bartholomew, M.J., 1993. Ices on the surface of Triton. Science 261, 742–745.

De Kruif, C.G., Van Ginkel, C.H.D., 1977. Torsion-weighing effusion vapour-pressure measurements on organic compounds. J. Chem. Thermodyn. 9 (8), 725–730.
de Pater, I., Romani, P.N., Atreya, S.K., 1991. Possible microwave absorption by H_2S gas in Uranus' and Neptune's atmospheres. Icarus 91 (2), 220–233.
Deitz, V.R., 1933. The vapor pressure of crystalline benzene and cyclohexene. J. Am. Chem. Soc. 55 (2), 472–475.
Douslin, D.R., Osborn, A., 1965. Pressure measurements in the 0.01–30 Torr range with an inclined-piston gauge. J. Sci. Instrum. 42, 369–373.
Douté, S., Schmitt, B., Quirico, E., Owen, T.C., Cruikshank, D.P., de Bergh, C., Geballe, T.R., Roush, T.L., 1999. Evidence for methane segregation at the surface of Pluto. Icarus 142 (2), 421–444.
Eiler, J.M., Kitchen, N., Rahn, T.A., 2000. Experimental constraints on the stable-isotope systematics of CO_2 ice/vapor systems and relevance to the study of Mars. Geochim. Cosmochim. Acta 64 (4), 733–746.
Encrenaz, T., 2001. The atmosphere of Mars as constrained by remote sensing. Space Sci. Rev. 96, 411–424.
Ernest, H.E., 1961. Purification and vapor pressure of nitric oxide. J. Chem. Phys. 35 (4), 1531–1532.
Espinasse, S., Klinger, J., Ritz, C., Schmitt, B., 1991. Modeling of the thermal behavior and of the chemical differentiation of cometary nuclei. Icarus 92 (2), 350–365.
Fanale, F.P., Salvail, J.R., 1984. An idealized short-period comet model: surface insolation, H_2O flux, dust flux, and mantle evolution. Icarus 60 (3), 476–511.
Fanale, F.P., Salvail, J.R., 1990. The influence of CO ice on the activity and the near-surface differentiation of comet nuclei. Icarus 84 (2), 403–413.
Feistel, R., Wagner, W., 2006. A new equation of state for H_2O ice Ih. J. Phys. Chem. Ref. Data 35 (2), 1021–1047.
Feistel, R., Wagner, W., 2007. Sublimation pressure and sublimation enthalpy of H_2O ice Ih between 0 and 273.16 K. Geochim. Cosmochim. Acta 71 (1), 36–45.
Fernandez-Fassnacht, E., Rio, F.D., 1984. The vapour pressure of CO_2 from 194 to 243 K. J. Chem. Thermodyn. 16 (5), 469–474.
Fisher, B.B., McMillan, W.G., 1958. The sublimation pressure of krypton below 80 K. J. Phys. Chem. 62 (4), 494–495.
Frels, W., Smith, D.R., Ashworth, T., 1974. Vapour pressure of nitrogen below the triple point. Cryogenics 14 (1), 3–7.
Friend, D.G., Ely, J.F., Ingham, H., 1989. Thermophysical properties of methane. J. Phys. Chem. Ref. Data 18 (2), 583–638.
Giauque, W.F., Clayton, J.O., 1933. The heat capacity and entropy of nitrogen. Heat of vaporization. Vapor pressures of solid and liquid. The Reaction $1/2\ N_2+1/2\ O_2=NO$ from spectroscopic data. J. Am. Chem. Soc. 55 (12), 4875–4889.
Giauque, W.F., Blue, R.W., 1936. Hydrogen sulfide. The heat capacity and vapor pressure of solid and liquid. The heat of vaporization. A comparison of thermodynamic and spectroscopic values of the entropy. J. Am. Chem. Soc. 58 (5), 831–837.
Giauque, W.F., Egan, C.J., 1937. Carbon dioxide. The heat capacity and vapor pressure of the solid. The heat of sublimation. Thermodynamic and spectroscopic values of the entropy. J. Chem. Phys. 5 (1), 45–54.
Giauque, W.F., Kemp, J.D., 1938. The entropies of nitrogen tetroxide and nitrogen dioxide. The heat capacity from 15 K to the boiling point. The heat of vaporization and vapor pressure. The equilibria $N_2O_4=2\ NO_2=2\ NO+O_2$. J. Chem. Phys. 6 (1), 40–52.
Giauque, W.F., Stephenson, C.C., 1938. Sulfur dioxide. The heat capacity of solid and liquid. Vapor pressure. Heat of vaporization. The entropy values from thermal and molecular data. J. Am. Chem. Soc. 60 (6), 1389–1394.
Giauque, W.F., Ruehrwein, R.A., 1939. The entropy of hydrogen cyanide. Heat capacity, heat of vaporization and vapor pressure. Hydrogen bond polymerization of the gas in chains of indefinite length. J. Am. Chem. Soc. 61 (10), 2626–2633.
Goodwin, R.D., 1988. Benzene thermophysical properties from 279 to 900 K at pressures to 1000 bar. J. Phys. Chem. Ref. Data 17 (4), 1541–1636.
Gottschal, A.J., Korvezee, A.E., 1953. An exact vapour pressure equation. Rec. Trav. Chim. 72, 465–472.
Grundy, W.M., Stansberry, J.A., 2000. Solar gardening and the seasonal evolution of nitrogen ice on Triton and Pluto. Icarus 148 (2), 340–346.
Ha, H., Morrison, J.A., Richards, E.L., 1976. Vapour pressures of solid benzene, cyclohexane and their mixtures. J. Chem. Soc. Faraday Trans. 1 (72), 1051–1057.
Hans, M.R., 1976. The heats of transition of solid ethane. J. Chem. Phys. 65 (4), 1371–1373.
Hanson, D., Mauersberger, K., 1986. The vapor pressures of solid and liquid ozone. J. Chem. Phys. 85 (8), 4669–4672.
Henning, F., Otto, J., 1936. Dampfdruckkurven und Tripelpunkte im Temperaturgebiet von 14° bis 90° abs. Phys. Z. 18, 633–638.
Hoge, H.J., 1950. Vapor pressure and fixed points of oxygen and heat capacity in the critical region. J. Res. Natl. Bur. Stand. 44, 321–345.
Honig, R.E., Hook, H.O., 1960. Vapor pressure data for some common gases. RCA Rev. 21, 360–368.
Huebner, W.F., Benkhoff, J., Capria, M.-T., Coradini, A., De Sanctis, C., Orosei, R., Prialnik, D., 2006. In: Battrick, B. (Ed.), Heat and Gas Diffusion in Comet Nuclei, The International Space Science Institute Report. ESA Publications, Noordwijk, The Netherlands.
Ingersoll, A.P., Summers, M.E., Schlipf, S.G., 1985. Supersonic meteorology of Io: sublimation-driven flow of SO_2. Icarus 64 (3), 375–390.
Jackowski, A.W., 1974. Vapour pressures of solid benzene and of solid cyclohexane. J. Chem. Thermodyn. 6 (1), 49–52.
Jancso, G., Pupezin, J., Van Hook, W.A., 1970. Vapor pressure of ice between $+10^{-2}$ and 10^{+2}. J. Phys. Chem. 74 (15), 2984–2989.
Johnson, W.C., Pechukas, A., 1937. Hydrogen compounds of arsenic. I. Preparation of arsine in liquid ammonia. Some physical properties of arsine. J. Am. Chem. Soc. 59 (10), 2065–2068.
Johnston, H.L., Giauque, W.F., 1929. The heat capacity of nitric oxide from 14 K to the boiling point and the heat of vaporization. Vapor pressures of solid and liquid phases. The entropy from spectroscopic data. J. Am. Chem. Soc. 51 (11), 3194–3214.
Karwat, E., 1924. Der dampfdruck des festen chlorwasserstoffs, methans und ammoniaks. Z. Phys. Chem. 112, 486–490.
Kelley, K.K., 1929. The heat capacity of methyl alcohol from 16 K to 298 K and the corresponding entropy and free energy. J. Am. Chem. Soc. 51 (1), 180–187.
Khanna, R.K., Allen, J.E., Masterson, C.M., Zhao, G., 1990. Thin-film infrared spectroscopic method for low-temperature vapor pressure measurements. J. Phys. Chem. 94 (1), 440–442.
Kouchi, A., 1987. Vapour pressure of amorphous H_2O ice and its astrophysical implications. Nature 330, 550–552.
Lee, M.W., Fuks, S., Bigeleisen, J., 1970. Vapor pressures of ^{36}Ar and ^{40}Ar. Intermolecular forces in solid and liquid argon. J. Chem. Phys. 53 (10), 4066–4076.
Leighton, R.R., Murray, B.C., 1966. Behavior of carbon dioxide and other volatiles on Mars. Science 153, 136–144.
Leming, C.W., Pollack, G.L., 1970. Sublimation pressures of solid Ar, Kr, and Xe. Phys. Rev. B 2 (8), 3323.
Lewis, G.N., Schutz, P.W., 1934. The vapor pressure of liquid and solid deutocyanic acid. J. Am. Chem. Soc. 56 (4), 1002.
Lewis, J.S., 1972. Low temperature condensation from the solar nebula. Icarus 16 (2), 241–252.
Lide, D.R., 2006. CRC Handbook of Chemistry and Physics, 87th ed CRC Press, Boca Raton, FL (2388pp.).
Lucas, S., Ferry, D., Demirdjian, B., Suzanne, J., 2005. Vapor pressure and solid phases of methanol below its triple point temperature. J. Phys. Chem. B 109 (38), 18103–18106.
Lunine, J.I., Stevenson, D.J., 1985. Thermodynamics of clathrate hydrate at low and high pressures with application to the outer solar system. Astrophys. J. Suppl. Ser. 58, 493–531.
Marti, J., Mauersberger, K., 1993. A survey and new measurements of ice vapor pressure at temperatures between 170 and 250 K. Geophys. Res. Lett. 20, 363–366.
Masterson, C.M., Allen, J.E., Kraus, G.F., Khanna, R.K., 1990. Vapor pressures of acetylene at low temperatures. In: Proceedings of the First International Conference on Laboratory Research for Planetary Atmospheres, NASA CP-3077, pp. 357–362.
Mauersberger, K., Krankowsky, D., 2003. Vapor pressure above ice at temperatures below 170 K. Geophys. Res. Lett. 30 (3), 21-1–21-3.
McIntosh, D., 1907. The physical properties of liquid and solid acetylene. J. Phys. Chem. 11 (4), 306–317.
Menaucourt, J., 1982. Pression de vapeur saturante de l'ethylene entre 77 K et 119 K. J. Chim. Phys. 79 (6), 531–535.
Merlin, F., Alvarez-Candal, A., Delsanti, A., Fornasier, S., Barucci, M.A., DeMeo, F.E., de Bergh, C., Doressoundiram, A., Quirico, E., Schmitt, B., 2009. Stratification of methane ice on Eris' surface. Astronom. J. 137, 315–328.
Metcalf, T.H., 2002. Elastic properties of quench condensed films of Neon and Argon. Ph.D. Thesis, Cornell University.
Meyers, C.H., Van Dusen, M.S., 1933. The vapor pressure of liquid and solid carbon dioxide. J. Res. Natl. Bur. Stand. 10, 381–412.
Milazzo, G., 1956. Tensioni di vapore di alcune sostanze organiche a bassa temperatura. Ann. Chim. Roma 46, 1105–1111.
Mosselman, C., Van Vugt, W.H., Vos, H., 1982. Exactly integrated Clapeyron equation. Its use to calculate quantities of phase change and to design vapor pressure–temperature relations. J. Chem. Eng. Data 27 (3), 246–251.
Mullins, J.C., Ziegler, W.T., Kirk, B.S., 1963. The thermodynamics properties of oxygen from 20 to 100 K. Adv. Cryog. Eng. 8, 123–134.
Murphy, D.M., Koop, T., 2005. Review of the vapour pressures of ice and supercooled water for atmospheric applications. Q. J. R. Meteorol. Soc. 131 (608), 1539–1565.
Overstreet, R., Giauque, W.F., 1937. Ammonia. The heat capacity and vapor pressure of solid and liquid. Heat of vaporization. The entropy values from thermal and spectroscopic data. J. Am. Chem. Soc. 59 (2), 254–259.
Owen, T.C., Roush, T.L., Cruikshank, D.P., Elliot, J.L., Young, L.A., de Bergh, C., Schmitt, B., Geballe, T.R., Brown, R.H., Bartholomew, M.J., 1993. Surface ices and the atmospheric composition of Pluto. Science 261, 745–748.
Perry, J.H., Bardwell, D.C., 1925. The vapor pressures of solid and liquid cyanogen. J. Am. Chem. Soc. 47 (11), 2629–2632.
Peter, T., 1998. Polar stratospheric clouds on Earth a review of particle thermodynamics, nucleation and growth kinetics. In: Schmitt, B., de Bergh, C., Festou, M. (Eds.), Solar System Ices. Kluwer Academic Publishers, Dordrecht, The Netherlands, pp. 443–476.
Powell, T.M., Giauque, W.F., 1939. Propylene. The heat capacity, vapor pressure, heats of fusion and vaporization. The third law of thermodynamics and orientation equilibrium in the solid. J. Am. Chem. Soc. 61 (9), 2366–2370.
Prialnik, D., Benkhoff, J., Podolak, M., 2004. Modeling the structure and activity of comet nuclei. In: Festou, M.C., Keller, H.U., Weaver, H.A. (Eds.), Comets II. University of Arizona Press, Tucson, USA, pp. 359–387.
Putnam, W.E., McEachern, D.M., Kilpatrick, J.E., 1965. Entropy and related thermodynamic properties of acetonitrile (methyl cyanide). J. Chem. Phys. 42 (2), 749–755.

Quirico, E., Doute, S., Schmitt, B., de Bergh, C., Cruikshank, D.P., Owen, T.C., Geballe, T.R., Roush, T.L., 1999. Composition, physical state, and distribution of ices at the surface of Triton. Icarus 139 (2), 159–178.

Rothman, L.S., Jacquemart, D., Barbe, A., Chris Benner, D., Birk, M., Brown, L.R., Carleer, M.R., Chackerian, J.C., Chance, K., Coudert, L.H., Dana, V., Devi, V.M., Flaud, J.M., Gamache, R.R., Goldman, A., Hartmann, J.M., Jucks, K.W., Maki, A.G., Mandin, J.Y., Massie, S.T., Orphal, J., Perrin, A., Rinsland, C.P., Smith, M.A.H., Tennyson, J., Tolchenov, R.N., Toth, R.A., Vander Auwera, J., Varanasi, P., Wagner, G., 2005. The HITRAN 2004 molecular spectroscopic database. J. Quant. Spectrosc. Radiat. Transfer 96 (2), 139–204.

Ruehrwein, R.A., Giauque, W.F., 1939. The entropy of cyanogen. Heat capacity and vapor pressure of solid and liquid. Heats of fusion and vaporization. J. Am. Chem. Soc. 61 (10), 2940–2944.

Rytter, E., Gruen, D.M., 1979. Infrared spectra of matrix isolated and solid ethylene. Formation of ethylene dimers. Spectrochim. Acta A: Mol. Spectrosc. 35 (3), 199–207.

Sack, N.J., Baragiola, R.A., 1993. Sublimation of vapor-deposited water ice below 170 K, and its dependence on growth conditions. Phys. Rev. B 48 (14), 9973–9978.

Saggiomo, A.J., 1957. The dinitriles of acetylenedicarboxylic and polyacetylenedicarboxylic Acids. I. Dicyanoacetylene and dicyanodiacetylene. J. Org. Chem. 22 (10), 1171–1175.

Samuelson, R., 1998. Atmospheric ices. In: Schmitt, B., de Bergh, C., Festou, M. (Eds.), Solar System Ices. Kluwer Academic Publishers, Dordrecht, The Netherlands, pp. 749–772.

Samuelson, R.E., Mayo, L.A., Knuckles, M.A., Khanna, R.J., 1997. C_4N_2 ice in Titan's north polar stratosphere. Planet. Space Sci. 45 (8), 941–948.

Schmitt, B., Rodriguez, S., 2003. Possible identification of local deposits of Cl_2SO_2 on Io from NIMS/Galileo spectra. J. Geophys. Res. (Planets) 108, 5104.

Schmitt, B., Quirico, E., Trotta, F., Grundy, W.M., 1998. Optical properties of ices from UV to infrared. In: Schmitt, B., de Bergh, C., Festou, M. (Eds.), Solar System Ices. Kluwer Academic Publishers, Dordrecht, The Netherlands, pp. 199–240.

Schmitt, B., Espinasse, S., Grim, R.J.A., Greenberg, J.M., Klinger, J., 1989. Laboratory studies of cometary ice analogues. ESA-SP 302, 65–69.

Sherman, R.H., Giauque, W.F., 1955. Arsine. Vapor pressure, heat capacity, heats of transition, fusion and vaporization. The entropy from calorimetric and from molecular data. J. Am. Chem. Soc. 77 (8), 2154–2160.

Shilling, J.E., Tolbert, M.A., Toon, O.B., Jensen, E.J., Murray, B.J., Bertram, A.K., 2006. Measurements of the vapor pressure of cubic ice and their implications for atmospheric ice clouds. Geophys. Res. Lett. 33 (71), L17801.

Shindo, F., Benilan, Y., Guillemin, J.C., Chaquin, P., Jolly, A., Raulin, F., 2003. Ultraviolet and infrared spectrum of C_6H_2 revisited and vapor pressure curve in Titan's atmosphere. Planet. Space Sci. 51 (1), 9–17.

Shinoda, T., 1969. Vapor pressure of carbon monoxide in condensed phases. Bull. Chem. Soc. Japan 42, 1815–1820.

Sloan, E.D., Koh, C.A., 2008. Clathrate hydrates of natural gases, third ed Taylor & Francis Group, New York.

Spence, R., Wild, W., 1935. The vapour pressure curve of formaldehyde and some related data. J. Chem. Soc. 138, 506–509.

Spencer, J.R., Stansberry, J.A., Trafton, L.M., Young, E.F., Binzel, R.P., Croft, S.K., 1997. Volatile transport, seasonal cycles, and atmospheric dynamics on Pluto. In: Stern, S.A., Tholen, D.J. (Eds.), Pluto and Charon. University of Arizona Press, Tucson, pp. 435–473.

Squires, R.E., Beard, D.B., 1961. Physical and orbital behavior of comets. Astrophys. J. 133, 657–667.

Stout, J.W., Fisher, L.H., 1941. The entropy of formic acid. The heat capacity from 15 to 300 K. Heats of fusion and vaporization. J. Chem. Phys. 9 (2), 163–168.

Stull, D.R., 1947a. Vapor pressure of pure substances. Organic compounds. Ind. Eng. Chem. 39 (4), 517–540.

Stull, D.R., 1947b. Vapor pressure of pure substances. Inorganic compounds. Ind. Eng. Chem. 39 (4), 540–550.

Tegeler, C., Span, R., Wagner, W., 1999. A new equation of state for argon covering the fluid region for temperatures from the melting line to 700 K at pressures up to 1000 MPa. J. Phys. Chem. Ref. Data 28 (3), 779–850.

Terlain, A., 1983. Sublimation pressure of nitrous oxide between 125 and 147 K. J. Chim. Phys. Physico-chim. Biol. 80 (11–12), 805–808.

Tessier, C., Terlain, A., Larher, Y., 1982. Sublimation pressure of Xe and zero temperature cohesion energy of Ar, Kr and Xe from sublimation pressure and heat capacity data. Physica A: Statist. Theoret. Phys. 113 (1–2), 286–292.

Tickner, A.W., Lossing, F.P., 1951. The measurement of low vapor pressures by means of a mass spectrometer. J. Phys. Chem. 55 (5), 733–740.

Trafton, L.M., Matson, D.L., Stansberry, J.A., 1998. Surface/atmosphere interactions and volatile transport (Triton, Pluto and Io). In: Schmitt, B., de Bergh, C., Festou, M. (Eds.), Solar System Ices. Kluwer Academic Publishers, Dordrecht, The Netherlands, pp. 773–812.

Van Hook, W.A., 1967. Vapor pressures of the methylacetylenes, H_3CCCH, H_3CCCD, D_3CCCH, and D_3CCCD. J. Chem. Phys. 46 (5), 1907–1918.

Vidler, M., Tennyson, J., 2000. Accurate partition function and thermodynamic data for water. J. Chem. Phys. 113 (21), 9766–9771.

Vogt, G.J., Pitzer, K.S., 1976. Entropy and heat capacity of methane; spin-species conversion. J. Chem. Thermodyn. 8 (11), 1011–1031.

Wagner, W., Pruss, A., 2002. The IAPWS formulation 1995 for the thermodynamic properties of ordinary water substance for general and scientific use. J. Phys. Chem. Ref. Data 31 (2), 387–535.

Wagner, W., Saul, A., Pruss, A., 1994. International equations for the pressure along the melting and along the sublimation curve of ordinary water substance. J. Phys. Chem. Ref. Data 23 (3), 515–527.

Washburn, E.W., 1924. The vapor pressure of ice and water below the freezing point. Mon. Weather Rev. 52 (10), 488–490.

Weber, L.A., Kilpatrick, J.E., 1962. Entropy and related thermodynamic properties of propionitrile. J. Chem. Phys. 36 (3), 829–834.

White, B.E., Hessinger, J., Pohl, R.O., 1998. Annealing and sublimation of noble gas and water ice films. J. Low Temp. Phys. 111 (3/4), 233–246.

Wisnosky, M.G., Eggers, D.F., Fredrickson, L.R., Decius, J.C., 1983. A metastable solid phase of ethane. J. Chem. Phys. 79 (7), 3513–3516.

Yamamoto, T., Nakagawa, N., Fukui, Y., 1983. The chemical composition and thermal history of the ice of a cometary nucleus. Astron. Astrophys. 122, 171–176.

Yamamoto, T., 1985. Formation environment of cometary nuclei in the primordial solar nebula. Astron. Astrophys. 142, 31–36.

Yato, Y., Lee, M.W., Bigeleisen, J., 1975. Phase equilibrium isotope effects in molecular solids and liquids. Vapor pressures of the isotopic nitrous oxide molecules. J. Chem. Phys. 63 (4), 1555–1563.

Younglove, B.A., Ely, J.F., 1987. Thermophysical properties of fluids. II. Methane, ethane, propane, isobutane, and normal butane. J. Phys. Chem. Ref. Data 16 (4), 577–798.

Ziegler, W.T., Andrews, D.H., 1942. The heat capacity of benzene-d6. J. Am. Chem. Soc. 64 (10), 2482–2485.

ARTICLE 2

Fray N., Marboeuf U., Brissaud O. And Schmitt B. (2010)

Equilibrium data of methane, carbon dioxide and xenon clathrate hydrates below the freezing point of water. Applications to astrophysical environments.

***Journal of Chemical and Engineering Data*, 55(11), 5101-5108.**

Equilibrium Data of Methane, Carbon Dioxide, and Xenon Clathrate Hydrates below the Freezing Point of Water. Applications to Astrophysical Environments

Nicolas Fray,*,†,‡ Ulysse Marboeuf,† Olivier Brissaud,† and Bernard Schmitt†

Laboratoire de Planétologie de Grenoble, Université Joseph Fourier, CNRS/INSU, Bâtiment D de Physique, BP 53, 38041 Grenoble Cedex 9, France, and LISA, Laboratoire Interuniversitaire des Systèmes Atmosphériques, UMR 7583 du CNRS, Universités Paris 7 et 12, 61 Avenue du Général de Gaulle, 94010 Créteil Cedex, France

This work reports new measurements of the three-phase (ice + clathrate hydrate + vapor) equilibrium in the systems of water and each of the following guest species: xenon from (167.20 to 246.16) K, carbon dioxide from (172.28 to 182.15) K, and methane from (145.75 to 195.74) K. The results are compared with the corresponding data reported in the literature and are used to determine empirical laws allowing the equilibrium pressure of these pure clathrates to be calculated at any temperature relevant to the astrophysical environments below the freezing point of water. These relations can be used in astrophysical models such as those devoted to the studies of the cooling and condensation of the solar nebula or to the ones of the physical evolution and gas production from cometary nuclei.

Introduction

Clathrate hydrates are water-based solid crystalline compounds stabilized by the inclusion of guest molecules inside cavities formed by the hydrogen-bonded network of water molecules.[1] They resemble ice in appearance, but they may form at temperatures higher than the freezing temperature of water. They are of great interest in the natural gas industry, as they can plug pipelines and flow channels. Some natural clathrate hydrates have also been discovered on Earth: in the seafloor, in permafrost, as well as in polar caps.[1,2] The amount of methane potentially trapped in natural methane clathrate hydrate deposits, mostly in seafloor sediments, may be very significant (from 1 to $5 \cdot 10^{15}$ m^3), which makes them of major interest as a potential energy resource. Although no clathrate hydrate has been detected so far in astrophysical environments, it has been proposed for a long time that clathrate hydrates could play a significant role in the chemistry of the solar nebula and in the physical evolution of numerous astrophysical objects.[3−7]

As it is of interest for the natural gas industry and for the studies of clathrate hydrates present in the seafloor, the L_W-H-V three-phase equilibrium (liquid water (L_W) + clathrate hydrate (H) + guest vapor (V)) of simple or mixed clathrate hydrates at temperatures higher than the freezing temperature of water has been extensively studied. Nevertheless, in the astrophysical environments, the temperature is very low compared to the freezing temperature of water. Thus, L_W-H-V equilibrium data are not relevant for most astrophysical applications. The I−H−V three-phase equilibrium (water ice (I) + clathrate hydrates (H) + guest vapor (V)) for clathrate hydrates at temperatures below the freezing temperature of water is important for most astrophysical studies such those of the cooling and condensation of the solar nebula, cometary nuclei, Titan hydrocarbon reservoirs, or Mars polar caps. Despite the importance of the phase equilibrium data at temperatures below the freezing temperature of water, there is a paucity of data in contrast to the ones at temperatures above the freezing temperature of water.

Delsemme and Swings[6] were the first to consider the presence of clathrate hydrates in the outer solar system and in cometary nuclei. Then, Miller[7] argued that clathrate hydrates could be present on most of the objects of the outer solar system as they incorporate molecular species at vapor pressures lower than those of the pure ices of those species. Lewis[8] and Sill and Wilkening[9] seem to be the first to investigate the possible formation of clathrate hydrates during the cooling of the solar nebula. Indeed when the temperature of the solar nebula decreases, water vapor condenses at about 150 K and forms microscopic icy particles. During the subsequent cooling, clathrate hydrates of H_2S, CH_4, Xe, CO, N_2, Kr, and Ar should form before these gaseous compounds could condense as pure ices.[10,11] Models of the cooling of the solar nebula taking into account the formation of clathrate hydrates succeed to reproduce the elemental enrichments observed in the four giant planets[10,12] as well as the nitrogen deficiency in comets.[11] So, if formed during the cooling of the solar nebula, clathrate hydrates could be indeed present in most objects of the outer solar system. Moreover, some clathrate hydrates could have been formed during the evolution of these objects; it could be the case of methane, ethane, and xenon clathrate hydrates at the surface of Titan,[13,14] carbon dioxide clathrate hydrates in polar caps of Mars,[15] and carbon monoxide clathrate hydrates in cometary nuclei.[16] We have to keep in mind that no clathrate hydrate has been detected so far in astrophysical environments and that all of the predictions concerning the possible presence of clathrates in astrophysical objects are based on extrapolations at very low temperatures of the few I−H−V equilibrium data.

In this paper, we report measurements of the I−H−V equilibrium pressure at low temperatures for single guest molecular (hereafter single) clathrate hydrates of xenon, carbon dioxide, and methane. We also determine empirical relations allowing

* Corresponding author. E-mail: nicolas.fray@lisa.u-pec.fr. Tel.: 00 33 (0)1 45 17 15 56. Fax: 00 33 (0)1 45 17 15 64.
† Laboratoire de Planétologie de Grenoble. E-mail: marboeuf@ujf-grenoble.fr, olivier.brissaud@obs.ujf-grenoble.fr, bernard.schmitt@obs.ujf-grenoble.fr.
‡ LISA.

10.1021/je1006604
Published on Web 09/24/2010

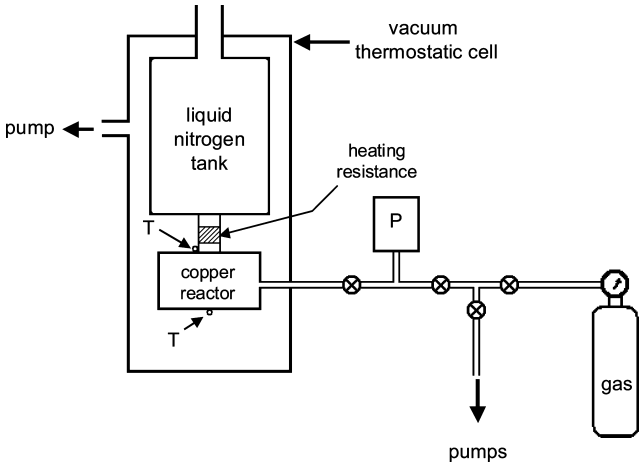

Figure 1. Schematic diagram of the apparatus used to measure the equilibrium pressure of xenon, carbon dioxide, and methane clathrate hydrates.

us to calculate the equilibrium pressure of clathrate hydrates at any temperatures relevant to the different astrophysical environments.

Experimental Section

Apparatus. A schematic diagram of our apparatus is shown in Figure 1. A cylindrical copper reactor of 26 mm internal diameter and of about 13 cm^3 inner volume is used to measure the equilibrium pressure of clathrate hydrates. It is composed of two parts connected by an indium gasket which ensures its sealing at low temperatures. It is located inside a thermostatic cell (ABT SORIME), evacuated to about 10^{-3} Pa thanks to a diffusion pump (Alcatel) backed by a diaphragm pump, and connected to a liquid nitrogen dewar via a copper finger. A heating resistance is fixed on this copper finger, and two silicon diodes, allowing us to measure the temperature from (70 to 300) K with an uncertainty of about 0.01 K, are glued on the lower and upper parts of the reactor. The heating resistance and both silicon diodes are connected to a temperature controller (model 331 of Lakeshore), which ensures a temperature stability of about ± 0.03 K.

The reactor is evacuated thanks to a turbo-molecular pump (TMU-071P, Pfeiffer) backed by a dry scroll vacuum pump (XDS 5, Edwards). The pressure is measured in the line located between the reactor and the pumping group using an absolute metal membrane pressure sensor (Baratron 690-A13T-RB, MKS) allowing us to measure the pressure between 1 Pa and 133.3 kPa with a resolution of 0.1 Pa and a relative uncertainty of 0.08 % of the reading value over most of the range over 100 Pa. Temperature and pressure are recorded as a function of time with a resolution of a few seconds thanks to a laboratory-made software.

Note that our reactor includes neither a stirrer nor a shaker contrary to most experimental setups devoted to the measurement of the I−H−V equilibrium.[17−20] Normally, these devices are used to crush the sample of ice and clathrate hydrates and to activate the kinetics of clathrate hydrate formation.[17]

Materials. The water used in the experiments was laboratory deionized and distilled and has a resistivity of 18.2 MΩ·cm. All of the gases have been purchased from Air Liquide; xenon, carbon dioxide, and methane have certified volume fraction purities of 99.998 %, 99.998 %, and 99.95 %, respectively.

Procedure. We have tried to reproduce in the laboratory the astrophysical process of clathrate hydrates formation, that is, we have tried to form clathrate hydrates directly from crystalline ice submitted to an overpressure of gas (but < 100 kPa). Nevertheless, as our reactor is neither equipped with a stirrer nor a shaker, our attempts of forming clathrate hydrates from crystalline ice have failed. We attribute this failure to a very long nucleation stage as already observed by Schmitt[21] and Moudrakovski et al.[22]

Thus, we choose to form clathrate hydrates in a second reactor in which we introduce about 5 cm^3 of liquid water and about 200 kPa of Xenon. This reactor is then immersed in a bath at 1 °C within a few minutes, and we obtain about 1 g of xenon clathrate hydrate which sinks in liquid water. These xenon clathrate hydrates are then transferred in the copper reactor, and the apparatus is reassembled. This transfer is performed under ambient atmosphere and in a cold room at −20 °C to slow down the decomposition of the Xe clathrate hydrate.

The study of the carbon dioxide or methane clathrate hydrates involves the conversion of our initial sample of xenon clathrate hydrate to carbon dioxide or methane clathrate hydrate. Such a transformation of one clathrate hydrate to another guest clathrate hydrate has already been performed and studied by Yoon et al.[23] In such a case, the copper reactor is thermostatted at the temperature corresponding to an equilibrium pressure of the desired clathrate hydrate of about 90 kPa. First, the gaseous xenon is evacuated, and we pump during about 1 min on the solid sample of clathrate hydrate. Second, we inject an overpressure of carbon dioxide or methane in the reactor. A rapid pressure decrease, due to the formation of clathrate hydrate of the guess molecule, is observed, and we wait for pressure stabilization. In this case, the nucleation stage is practically absent, and the clathrate hydrate growth begins very rapidly. This behavior was observed by Schmitt[21] and Moudrakovski et al.[22] and was interpreted as a preorganization of the ice surface. Indeed, after the evacuation of xenon, some cages should remain empty, and the overpressure of gas was injected before the transformation of the empty cages into crystalline water ice. This operation is repeated at least 10 times to ensure the removal of almost all of the initial xenon. If some xenon atoms remain after this, it should be only located deep inside the grains without contact with the gas phase and thus without influence on the equilibrium pressure of the newly formed clathrate nor contribution to the gas pressure.

When a sample of pure clathrate hydrate of the desired species (xenon, carbon dioxide, or methane) is obtained, the temperature of the copper cell is maintained constant, and an overpressure of gas is injected in the reactor. A pressure decrease is observed, as shown in Figure 2, due to the formation of clathrate hydrates and encapsulation of the gas molecules. The pressure should converge toward the equilibrium pressure; nevertheless, an apparent stabilization at higher pressures could be observed. This stabilization could be due either to the inclusion of all available water molecules into the clathrate hydrate structure and thus deviation of our measurements from the I−H−V equilibrium (no more ice) or to the formation of a thick impermeable layer of clathrate hydrate on the ice grains[21] also removing water ice from the I−H−V equilibrium. In such cases it is necessary to partially decompose the clathrate hydrates to form enough ice to go back to the I−H−V phase equilibrium. After obtaining the true clathrate equilibrium from a higher pressure, we reduce the pressure below the equilibrium pressure. A pressure increase is rapidly observed due to the decomposition of clathrate hydrates and the release of gas molecules. This procedure is repeated several times. A similar procedure has been used by different authors[24,25] at higher temperatures.

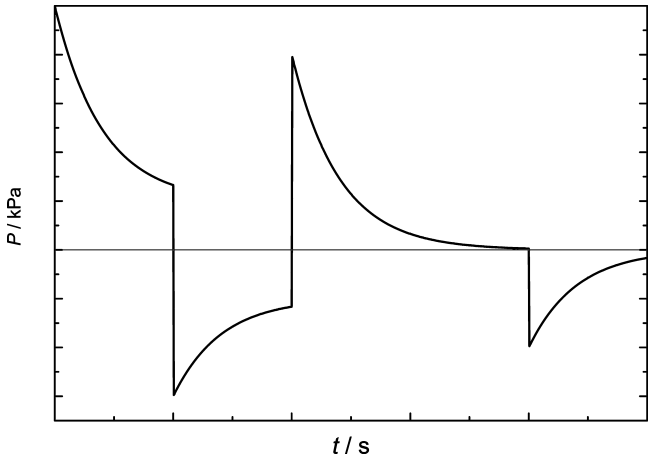

Figure 2. Schematic diagram of the experimental procedure at constant temperature.

At low temperatures such the ones that we have explored, the kinetic of clathrate hydrate formation or decomposition is extremely slow, and therefore it is very difficult to reach the equilibrium as schematized in Figure 2. Nevertheless, it has already been shown[21] that when the pressure comes close to its equilibrium value, it follows the following equation:

$$\frac{dP}{dt} = k(P - P_{eq}) \tag{1}$$

where k is the kinetic constant in s^{-1} and P_{eq} the equilibrium pressure. For the whole measured pressure evolution, we have determined the time range on which the slope (dP/dt) varies linearly against the pressure. Then, for this time range, the pressure evolution has been adjusted and extrapolated using the following equation:

$$P(t) = P_{eq} + \Delta P \cdot e^{-k(t-t_o)} \tag{2}$$

It allows us to determine the value to which the pressure tends. The equilibrium pressure is supposed to be the arithmetic average of the two closest values of decomposition and formation pressures, while the uncertainty is supposed to be the difference between these two values. An example of this procedure is given in Figure 3.

In most cases, the formation and the decomposition curves are observed for the same sample of clathrate hydrate. In these cases, the uncertainty on the temperature is about ± 0.03 K. In a few cases, the formation and decomposition curves were observed for different samples of clathrate hydrate with slightly different temperatures (ΔT < 0.5 K). In such a case, the formation (or decomposition) equilibrium pressure has been corrected to the measurement temperature of the other using the slope dP/dT of the whole equilibrium curve, before averaging both values.

Results and Discussion

All experimental equilibrium data measured in this work, as well as all the I−H−V experimental data already published in the literature for simple xenon, carbon dioxide, and methane clathrate hydrates are reported in Tables 1, 2, and 3 and are plotted in Figures 4, 5, and 6, respectively. Our measurements are also compared with the empirical laws used in astrophysical models and the pressure predicted by the CSMGem code

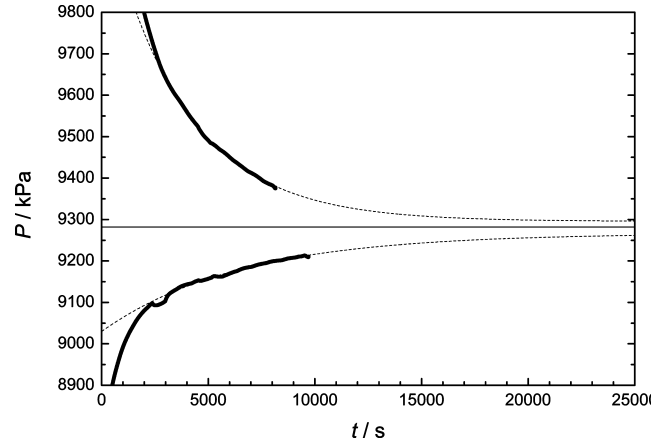

Figure 3. Temporal evolution of the pressure for a sample of xenon clathrate hydrates at $T = (219.53 \pm 0.03)$ K: solid lines, experimental measurements; dotted lines, adjustment and extrapolations of the experimental measurements; gray horizontal line, determined equilibrium pressure.

Table 1. Experimental Data for the HIV Equilibrium of Xenon Clathrate Hydrate

T/K	ΔT/K	P/kPa	ΔP/kPa	100 $\Delta P/P$	ref
268.2	0.1	121.3	0.7	0.6	18
253.3	0.1	64.8	0.7	1.1	18
238.2	0.1	30.8	0.7	2.3	18
229.4	0.1	19.4	0.7	3.6	18
223.0	0.1	13.5	0.7	5.2	18
211.2	0.1	6.5	0.7	10.8	18
273.15	0.2	155.1	7.0	4.5	25
228.15	0.3	16.2	7.0	43.2	25
246.16	0.03	43.67	$5\cdot10^{-2}$	0.1	this work
241.33	0.02	33.89	$3\cdot10^{-2}$	0.1	this work
228.17	0.02	16.21	$2\cdot10^{-2}$	0.1	this work
219.53	0.03	9.28	$1\cdot10^{-2}$	0.1	this work
216.60	0.04	7.50	$3\cdot10^{-2}$	0.4	this work
212.44	0.08	5.59	$8\cdot10^{-2}$	1.4	this work
207.17	0.05	3.85	$9\cdot10^{-2}$	2.3	this work
201.18	0.02	2.60	$2\cdot10^{-2}$	0.8	this work
191.17	0.02	1.11	$3\cdot10^{-3}$	0.5	this work
182.12	0.01	0.48	$3\cdot10^{-2}$	6.2	this work
175.84	0.01	0.264	$1.5\cdot10^{-3}$	0.6	this work
170.78	0.01	0.157	$1.5\cdot10^{-3}$	1.0	this work
167.47	0.03	0.099	$1\cdot10^{-3}$	1.0	this work

developed by Sloan and Koh[1] to compute the equilibrium conditions of clathrate hydrates.

All of the experimental measurements are used to determine empirical relations allowing us to calculate the equilibrium pressure of clathrate hydrates at any temperatures below the freezing temperature of water. To fit the experimental measurements, we use the following relation:

$$\ln P = A + B/T \tag{3}$$

in which P and T are the pressure (in kPa) and the absolute temperature. The parameters A and B are given in Table 4. This semiempirical formula can be derived from the Clausius−Clapeyron equation assuming that (i) the molar volume of the condensed phase is negligible against that of the gas, (ii) the gas is perfect, and (iii) the enthalpy of the phase change is independent of the temperature.

Clathrate Hydrate of Xenon. Concerning the xenon clathrate hydrate, we have performed 13 measurements ranging from 167.47 K (0.1 kPa) to 246.16 K (43.7 kPa) given in Table 1 and Figure 4. These data enlarge the temperature range on which the I−H−V equilibrium of xenon clathrate hydrate has been studied, since no data for T lower than 210 K has been reported

Table 2. Experimental Data for the HIV Equilibrium of Carbon Dioxide Clathrate Hydrate

T/K	Δ*T*/K	*P*/kPa	Δ*P*/kPa	100 Δ*P*/*P*	ref
271.8	unknown	1048	unknown	unknown	27
271.7	unknown	1041	unknown	unknown	27
271.4	unknown	1027	unknown	unknown	27
270.7	unknown	1000	unknown	unknown	27
270	unknown	972	unknown	unknown	27
268.9	unknown	924	unknown	unknown	27
267.4	unknown	869	unknown	unknown	27
264	unknown	752	unknown	unknown	27
256.8	unknown	545	unknown	unknown	27
192.54	unknown	21.88	unknown	unknown	15
186.75	unknown	14.49	unknown	unknown	15
182.15	unknown	10.27	unknown	unknown	15
176.86	unknown	6.77	unknown	unknown	15
171.54	unknown	4.20	unknown	unknown	15
167.07	unknown	2.808	unknown	unknown	15
162.37	unknown	1.765	unknown	unknown	15
151.52	unknown	0.535	unknown	unknown	15
200.96	unknown	36.3	unknown	unknown	54
200.58	unknown	37.8	unknown	unknown	54
198.99	unknown	33.4	unknown	unknown	54
196.78	unknown	29.3	unknown	unknown	54
218.2	unknown	104.3	unknown	unknown	58
217.8	unknown	101.3	unknown	unknown	58
213.8	unknown	81.6	unknown	unknown	58
203.2	unknown	43.3	unknown	unknown	58
194.5	unknown	24.8	unknown	unknown	58
213.6	0.1	80.4	0.4	0.50	21
208.1	0.1	59.0	0.3	0.50	21
203.1	0.1	43.7	0.2	0.46	21
198.6	0.1	33.8	0.2	0.59	21
195.2	0.1	26.0	0.1	0.38	21
195	0.1	25.7	0.1	0.39	21
271.14	0.1	102.6	5	4.9	33
269.4	0.1	963	11	1.1	19
266.4	0.1	864	11	1.3	19
263.9	0.1	790	11	1.4	19
262.7	0.1	755	11	1.5	19
258.8	0.1	652	11	1.7	19
256.4	0.1	593	11	1.9	19
253	0.1	516	11	2.1	19
249.8	0.1	454	11	2.4	19
247.1	0.1	406	11	2.7	19
244.5	0.1	364	11	3.0	19
271	0.1	1050	5	0.48	20
268.9	0.1	960	5	0.52	20
266.7	0.1	870	5	0.57	20
264.5	0.1	780	5	0.64	20
182.36	0.02	9.9	0.08	*0.8*	this work
176.91	0.02	6.46	0.13	*2.0*	this work
172.28	0.1	4.47	0.40	*8.9*	this work

Table 3. Experimental Data for the HIV Equilibrium of Methane Clathrate Hydrate

T/K	Δ*T*/K	*P*/kPa	Δ*P*/kPa	100 Δ*P*/*P*	ref
259.04	unknown	1647.7	unknown	unknown	55
270.9	0.03	2390	15	0.6	17
268.6	0.03	2220	15	0.7	17
266.5	0.03	2080	15	0.7	17
264.2	0.03	1900	15	0.8	17
262.4	0.03	1790	15	0.8	17
111	unknown	$1.87 \cdot 10^{-2}$	$5.3 \cdot 10^{-3}$	28	35
106	unknown	$8.67 \cdot 10^{-3}$	$2 \cdot 10^{-3}$	23	35
100	unknown	$2.13 \cdot 10^{-3}$	unknown	unknown	35
97	unknown	$1.23 \cdot 10^{-3}$	unknown	unknown	35
94	unknown	$6.27 \cdot 10^{-4}$	unknown	unknown	35
91	unknown	$2.67 \cdot 10^{-4}$	unknown	unknown	35
88	unknown	$1.40 \cdot 10^{-4}$	unknown	unknown	35
85	unknown	$7.33 \cdot 10^{-5}$	unknown	unknown	35
82	unknown	$2.13 \cdot 10^{-5}$	unknown	unknown	35
193.2	0.05	101.3	0.67	0.7	34
191.3	0.05	90.1	0.67	0.7	34
178.2	0.05	42	0.67	1.6	34
168.8	0.05	21.1	0.67	3.2	34
159.9	0.05	12.1	0.67	5.5	34
148.8	0.05	5.3	0.67	12.6	34
190.15	0.1	84.71	1.7	2.0	56
198.15	0.1	134.9	2.7	2.0	56
208.15	0.1	227.8	4.6	2.0	56
218.15	0.1	366.6	7.3	2.0	56
243.15	0.1	980.5	20	2.0	56
262.4	0.1	1847	37	2.0	56
272.2	0.1	2471	11	0.5	19
269.1	0.1	2236	11	0.5	19
265.5	0.1	2008	11	0.5	19
262.6	0.1	1829	11	0.6	19
259.1	0.1	1634	11	0.7	19
257.1	0.1	1518	11	0.7	19
256.3	0.1	1485	11	0.7	19
252.9	0.1	1324	11	0.8	19
248.8	0.1	1155	11	1.0	19
245.9	0.1	1041	3	0.3	19
244.2	0.1	971	3	0.3	19
272.6	0.1	2521	5	0.2	57
269.4	0.1	2269	5	0.2	57
265.2	0.1	1985	5	0.3	57
263.2	0.1	1842	5	0.3	57
195.74	0.02	103.2	1.2	1.1	this work
190.83	0.02	78.6	0.7	0.9	this work
180.82	0.02	41.7	0.8	1.9	this work
170.82	0.01	20.5	0.8	3.9	this work
160.87	0.05	8.8	0.2	2.3	this work
145.75	0.01	2.4	0.2	8.3	this work

before. Our measurements fit smoothly with the previous results of Makogon et al.,[25] but we observe a progressive deviation from the ones of Barrer and Edge[18] at lower temperature. No particular reason has been found to explain this deviation, except possibly a constant positive bias of about 1.5 kPa in their data (about two times their stated uncertainty). Whereas the data of Barrer and Edge[18] are not necessarily erroneous, we have rejected them, and we take into account only our measurements and the ones of Makogon et al.[25] for the determination of our empirical relation. It reproduces our experimental measurements and the two ones of Makogon et al.[25] with a relative deviation better than ± 6 %. The empirical relations previously used in astrophysical models[12,26] were based on the measurements of Barrer and Edge;[18] thus, they present the same erroneous deviation. At about 140 K, the predicted pressure is already twice than the one predicted using our empirical relation. The CSMGem code converges only for temperatures higher than 240 K. In the (240 to 273) K temperature range, the equilibrium pressures computed with this code display a slight relative deviation of ± 3 %, and the slope of this $P(T)$ curve seems to be too weak.

Because of the paucity of data about the L_W-H-V equilibrium for xenon clathrate hydrates, no determination of the Q1 quadruple point has been performed.

Clathrate Hydrate of Carbon Dioxide. Concerning carbon dioxide clathrate hydrates, we have performed three measurements ranging from 172.28 K (4.5 kPa) to 182.36 K (9.9 kPa) and shown in Figure 5 and Table 2. Our measurements fit smoothly with all of the previous results and particularly with the ones of Miller and Smythe[15] which have been performed in the same temperature range. This agreement shows that our experimental procedure is correct and that, if any xenon clathrate hydrate is remaining, it has no influence on the carbon dioxide clathrate hydrate equilibrium. To compute the empirical relation, we take into account all data reported in the literature. This relation reproduces all of the experimental measurements with a relative deviation better than ± 10 % and most of them within ± 4 %. It can be noted that the data set of Larson[27] and the one of Mohammadi and Richon[20] present a slope which seems to be much too large. We have checked that these data have not

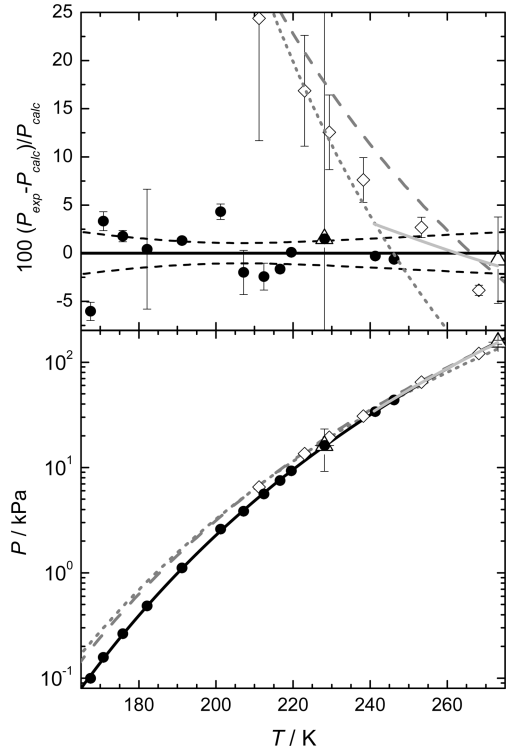

Figure 4. Equilibrium pressure of xenon clathrate hydrates as a function of the temperature for the HIV three-phase equilibrium (lower panel) and deviations of the experimental equilibrium pressures from those calculated by the empirical relation (upper panel): ●, this work; ◇, Barrer and Edge;[18] △, Makogon et al.;[25] solid black line, empirical relation determined in this work; dotted black line, confidence band at 95 % of our empirical relation; solid gray line, CSMGem prediction;[1] dashed gray line, empirical relation used by Hersant et al.;[12] dotted gray line, empirical relation used by Thomas et al.[26]

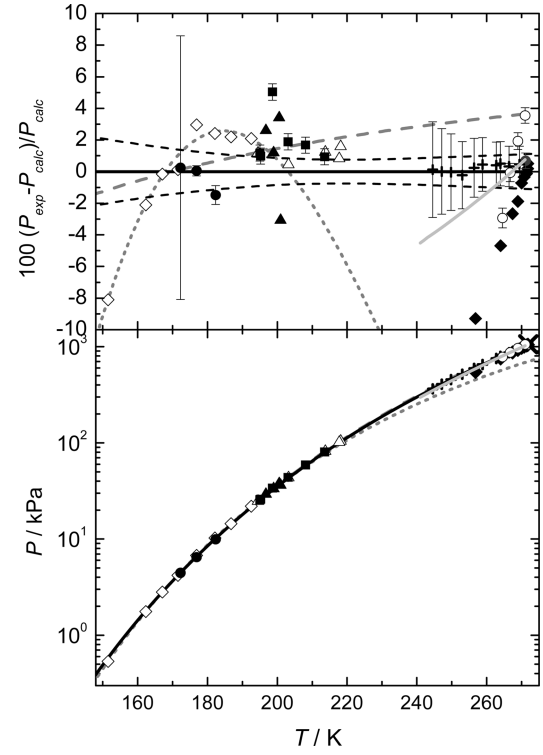

Figure 5. Equilibrium pressure of carbon dioxide clathrate hydrates as a function of the temperature for the HIV three-phase equilibrium (lower panel) and deviation of the experimental equilibrium pressures from those calculated by the empirical relation (upper panel): ●, this work; ×, Q1 quadruple point; ◆, Larson;[27] ◇, Miller and Smythe;[15] ▲, Adamson and Jones;[54] △, Falabella and Vanpee;[34] ■, Schmitt;[21] □, Wendland et al.;[33] +, Yasuda and Ohmura;[19] ○, Mohammadi and Richon;[20] solid black line, empirical relation determined in this work; dotted black line, confidence band at 95 % of our empirical relation; solid gray line, CSMGem prediction;[1] dashed gray line, empirical relation of Miller;[7] dotted gray line, empirical relation determined by Miller and Smythe.[15]

been acquired with liquid water in surfusion and correspond really to the I−H−V equilibrium. But our data are very consistent with those of Yasuda and Ohmura.[19] The empirical relations previously used in astrophysical models are the ones of Miller[7] and Miller and Smythe.[15] The first one is based on unpublished experimental measurements performed in the (140 to 273) K temperature range. Its relative deviation from our empirical relation is lower than 4 %. The second one is based on experimental data acquired between (151.52 and 192.54) K. It deviates significantly from the data at temperatures lower than 140 K and higher than 240 K. The CSMGem code provides data only for temperatures higher than 240 K. In the (240 to 273) K temperature range, the equilibrium pressure computed with this code presents a slight relative deviation of ± 4 %, but the slope of this curve seems to be too large.

At low temperatures, the curve of the clathrate hydrate equilibrium intersects the sublimation curve of carbon dioxide solid. Thus, as for propane,[28] the carbon dioxide clathrate hydrate presents a quadruple point at which carbon dioxide clathrate hydrates, water ice, solid carbon dioxide, and gaseous carbon dioxide are at thermodynamic equilibrium. Miller and Smythe[15] and Longhi[29] find respectively a temperature of (121 and 135) K for this quadruple point. Using our empirical relation for CO_2 clathrate hydrate and the one of Fray and Schmitt[30] for carbon dioxide solid, we find that this quadruple point of carbon dioxide clathrate hydrate is located at $T = (132.4 \pm 0.8)$ K and $P = (5.0 \pm 0.8)\ 10^{-2}$ kPa. For temperatures below 132.4 K, a mixture of pure water and carbon dioxide solid is more stable than the carbon dioxide clathrate hydrate.

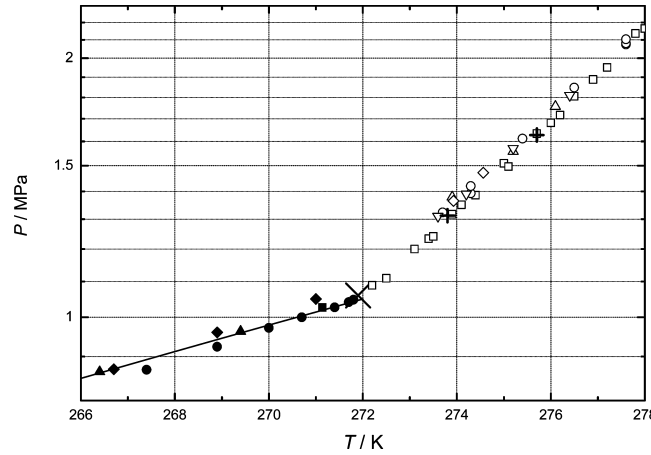

Figure 6. Equilibrium pressure of carbon dioxide clathrate hydrate as a function of the temperature for the HIV and HLV three-phase equilibria: ×, Q1 quadruple point determined in this study; ●, Larson;[27] ■, Wendland et al.;[33] ▲, Yasuda and Ohmura;[19] ♦, Mohammadi and Richon;[20] solid black line, empirical relation determined in this work for the HIV equilibrium; □, Larson;[27] ○, Deaton and Frost;[17] △, Robinson and Metha;[31] ▽, Fan and Guo;[32] ◇, Wendland et al.;[33] +, Yasuda and Ohmura.[19]

Considering the L_W−H−V equilibrium data measured by Larson,[27] Deaton and Frost,[17] Robinson and Metha,[31] Fan and Guo,[32] Wendland et al.,[33] and Yasuda and Ohmura,[19] we can determined that the Q1 quadruple point should be located at (271.9 ± 0.1) K and (1060 ± 20) kPa. This latter value is about

Table 4. Parameters of the Empirical Relations To Calculate the Equilibrium Pressure as a Function of the Temperature for the HIV Equilibrium of Simple Guest Clathrate Hydrates of Xenon, Carbon Dioxide, and Methane

	parameters of the empirical relation		temperature range of the experimental
compounds	*A*	*B*	data (K)
xenon	16.62	−3159	167.47 to 273.15
carbon dioxide	16.39	−2565	151.52 to 271.8
methane	15.78	−2176	82 to 272.2

200 kPa lower than the one published in Sloan and Koh.[1] Figure 6 shows the location of this quadruple point.

Clathrate Hydrate of Methane. Concerning methane clathrate hydrates, we have performed six measurements ranging from 145.75 K (2.4 kPa) to 195.74 K (103.2 kPa). These measurements are reported in Figure 7 and Table 3. The equilibrium pressures that we measured progressively diverge at low temperatures from the ones of Falabella and Vanpee[34] performed in the same temperature range. We find no reason to explain this deviation except possibly a constant positive bias of about 3 kPa in their data (four times their stated uncertainty). As the experimental data concerning the methane clathrate hydrate are quite dispersed, we take into account only our measurements as well as the ones of Delsemme and Wenger[35] and of Yasuda and Ohmura[19] to compute an empirical relation. This empirical relation reproduces the experimental measurements with a relative deviation of ± 10 %. The empirical relation previously used in astrophysical models is the one of Miller[7] which is based on unpublished results acquired over the (175 to 207) K temperature range. Its relative deviation from our first empirical relation is lower than 5 % between (80 and 270) K. On the contrary, the equilibrium pressures computed with the CSMGem code present a relative deviation reaching −35 % at 170 K. Furthermore, as for carbon dioxide, the slope of this curve seems to be too large.

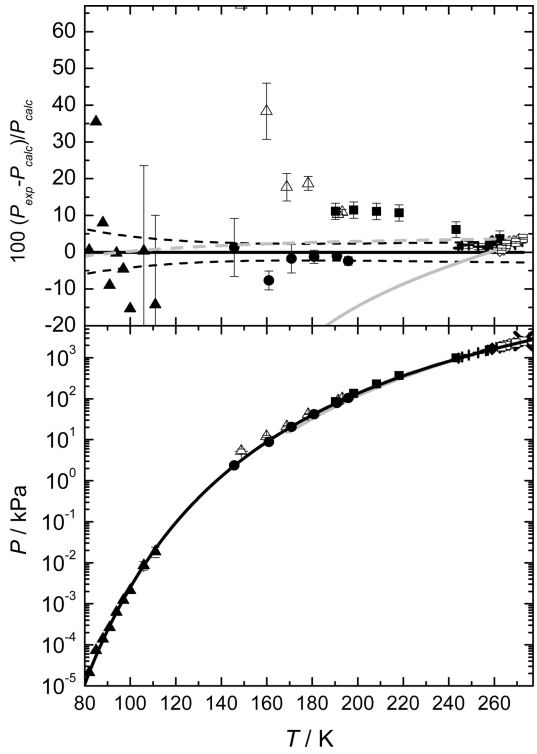

Figure 7. Equilibrium pressure of methane clathrate hydrates as a function of the temperature for the HIV equilibrium (lower panel) and deviation of the experimental equilibrium pressures from those calculated by the empirical relation (upper panel): ●, this work; ×, Q1 quadruple point; ◆, Roberts et al.;[55] ◇, Deaton and Frost;[17] ▲, Delsemme and Wenger;[35] △, Falabella and Vanpee;[34] ■, Makogon and Sloan;[56] +, Yasuda et al.;[19] □, Mohammadi and Richon;[57] solid black line, empirical relation determined in this work; dotted black lines, confidence band at 95 % of our empirical relation; solid gray line, CSMGem prediction;[1] dashed gray line, empirical relation determined by Miller.[7]

Considering the L_W-H-V equilibrium data measured by Deaton and Frost,[17] Snell et al.,[36] Jhaveri and Robinson,[37] De Roo et al.,[38] Adisasmito et al.,[39] Kang and Huen,[40] Nakamura et al.,[41] Ohmura et al.,[42] and Mohammadi et al.,[43] we can determine that the Q1 quadruple point should be located at (272.9 ± 0.2) K and (2540 ± 30) kPa. This latter value is in agreement with the one published by Sloan and Koh.[1]

Conclusion

We reported experimental I−H−V equilibrium data for xenon from (167.20 to 246.16) K, carbon dioxide from (172.28 to 182.15) K, and methane from (145.75 to 195.74) K. For xenon, we have shown that the data of Barrer and Edge[18] present a systematic deviation compared to our measurements and the ones of Makogon et al.[25] So far, the I−H−V equilibria for krypton and argon clathrate hydrates have only been measured by Barrer and Edge.[18] The discovery of the discrepancy for xenon casts some doubts on the validity of all of the measurements of these authors and therefore on the extrapolation law for krypton and xenon which are used in astrophysical models. For carbon dioxide, the different data sets present a very good agreement. Comparing the I−H−V equilibrium of carbon dioxide clathrate hydrate and the stability of carbon dioxide ice, we show that, for temperatures lower than (132.4 ± 0.8) K, a mixture of water and carbon dioxide ices should be thermodynamically more stable than carbon dioxide clathrate hydrate. For methane, the different data sets present a relative discrepancy reaching 70 %.

For these three molecular species, from our measurements as well as the ones already published in the literature, we derive empirical relations allowing us to calculate the equilibrium pressure of the clathrate phase at any temperature below the freezing point of water (see Table 4). Rigorously, these empirical relations have to be considered as interpolations in the temperature range of the experimental measurements. The validity of the extrapolations at very low temperatures, as the ones used in astrophysical models, could be questioned. Indeed, the empirical relation that we used derived from the Clausius−Clapeyron equation assumes that: (i) the molar volume of the condensed phase is negligible against that of gas, (ii) the gas is perfect, and (iii) the phase-change enthalpy is supposed to be independent of temperature. The first assumption is verified; nevertheless, the experimental measurements have been performed at pressures at which the perfect gas assumption is generally not verified, and the enthalpies of clathrate hydrate dissociation are known to vary at low temperatures.[44−46] Thus, the use of these empirical relations at very low temperatures has to be performed with caution. Moreover, these empirical relations are valid only for pure clathrate hydrates, whereas multiguest clathrate hydrates should be formed in an astrophysical environment. Unfortunately, there is a paucity of data concerning the composition and equilibrium of multiguest clathrate hydrates at temperatures below the freezing point of water. New measurements on the equilibrium of multiguest clathrate hydrates at low temperatures are welcome to constrain the partition of the considered molecules between the gaseous and the solid phases during the formation of these multiguest clathrate hydrates.

Concerning the possible formation and presence of clathrate hydrates in astrophysical objects, two issues remain unsolved: the

kinetics of clathrate hydrates formation from water ice crystals at low temperature and the direct detection of clathrate hydrates on astrophysical and planetary objects. Indeed, for the moment, natural clathrate hydrates have only been found on Earth, and no clathrate hydrate has been detected on others astrophysical objects. Thus, some spectroscopic studies, such as the ones of Dartois et al.,[47−49] specifically devoted to the search of clathrate hydrates on astrophysical objects have to be performed.

As the kinetics of clathrate hydrates formation and decomposition is not well-understood, it is generally not taken into account in astrophysical models. Indeed, the pioneering studies of Barrer and Edge[18] at low temperatures have already revealed that the formation rate of clathrate hydrates do not depend only on the temperature and pressure but also of the nature of the ice crystals. Sloan[50] states that clathrate hydrate kinetics is the largest challenge to future understanding of clathrate hydrates. Nevertheless, different authors[21,51−53] have already revealed that the mobility and the diffusion of water molecules at the surface of the ice crystals is a critical parameter controlling the formation kinetics of clathrate hydrates at low temperatures. Quantitative studies on the formation of clathrate hydrates from ice crystals would be welcome to introduce such considerations in astrophysical models.

Acknowledgment

We acknowledge E. Dartois for helpful discussions concerning the formation at low temperature and the infrared spectroscopy of clathrate hydrates as well as D. Gautier, D. Bockelée-Morvan, O. Mousis, D. Prianik, and M. Podolak for encouragement and discussions about their astrophysical models.

Literature Cited

(1) Sloan, E. D.; Koh, C. *Clathrate hydrates of Natural Gases*, 3rd ed.; CRC Press, Taylor & Francis Group: Boca Raton, FL, 2007.
(2) Max, M. D. *Natural Gas Hydrate in Oceanic and Permafrost Environments*; Kluwer Academic Publishers: Dordrecht, Netherlands, 2000.
(3) Lunine, J. I.; Stevenson, D. J. Thermodynamics of clathrate hydrate at low and high pressures with application to the outer solar system. *Astrophys. J., Suppl. Ser.* **1985**, *58*, 493–531.
(4) Miller, S. L. *Solar System Ices*; Schmitt, B., De Bergh, C., Festou, M., Eds.; Kluwer Academin Publishers: Dordrecht, Netherlands, 1998; pp 59−79.
(5) Kargel, J. S.; Lunine, J. I. *Solar System Ices*; Schmitt, B., De Bergh, C., Festou, M., Eds.; Kluwer Academin Publishers: Dordrecht, Netherlands, 1998; pp 97−118.
(6) Delsemme, A. H.; Swings, P. Gas hydrates in cometary nuclei and interstellar grains. *Ann. Astrophys.* **1952**, *15*, 1–6.
(7) Miller, S. L. The occurrence of gas hydrates in the solar system. *Proc. Natl. Acad. Sci. U.S.A.* **1961**, *47*, 1798–1808.
(8) Lewis, J. S. Low temperature condensation from the solar nebula. *Icarus* **1972**, *16*, 241–252.
(9) Sill, G. T.; Wilkening, L. L. Ice clathrate as a possible source of the atmospheres of the terrestrial planets. *Icarus* **1978**, *33*, 13–22.
(10) Gautier, D.; Hersant, F.; Mousis, O.; Lunine, J. I. Enrichments in Volatiles in Jupiter: A New Interpretation of the Galileo Measurements. *Astrophys. J.* **2001**, *550*, L227–L230.
(11) Iro, N.; Gautier, D.; Hersant, F.; Bockelée-Morvan, D.; Lunine, J. I. An interpretation of the nitrogen deficiency in comets. *Icarus* **2003**, *161*, 511–532.
(12) Hersant, F.; Gautier, D.; Lunine, J. I. Enrichment in volatiles in the giant planets of the Solar System. *Planet. Space Sci.* **2004**, *52*, 623–641.
(13) Osegovic, J. P.; Max, M. D. Compound clathrate hydrate on Titan's surface. *J. Geophys. Res., [Planets]* **2005**, *110*, 08004.
(14) Mousis, O.; Schmitt, B. Sequestration of Ethane in the Cryovolcanic Subsurface of Titan. *Astrophys. J.* **2008**, *677*, L67–L70.
(15) Miller, S. L.; Smythe, W. D. Carbon Dioxide Clathrate in the Martian Ice Cap. *Science* **1970**, *170*, 531–533.
(16) Marboeuf, U.; Mousis, O.; Petit, J.-M.; Schmitt, B. Clathrate Hydrates Formation in Short-Period Comets. *Astrophys. J.* **2010**, *708*, 812–816.
(17) Deaton, W. M.; Frost, E. M. Gas Hydrates and Their relation to Operation of Natural-Gas Pipelines. *U. S., Bur. Mines, Monogr.* **1946**, *8*, 1–101.
(18) Barrer, R. M.; Edge, A. V. J. Gas hydrates containing argon, krypon and xenon: kinetics and energetics of formation and equilibria. *Proc. R. Soc. London A* **1967**, *300*, 1–24.
(19) Yasuda, K.; Ohmura, R. Phase Equilibrium for Clathrate Hydrates Formed with Methane, Ethane, Propane, or Carbon Dioxide at Temperatures below the Freezing Point of Water. *J. Chem. Eng. Data* **2008**, *53*, 2182–2188.
(20) Mohammadi, A. H.; Richon, D. Equilibrium Data of Nitrous Oxide and Carbon Dioxide Clathrate Hydrates. *J. Chem. Eng. Data* **2008**, *54*, 279–281.
(21) Schmitt, B. La surface de la glace: structure, dynamique et interactions - Implications astrophysique. Ph.D. Thesis, University of Grenoble, Grenoble, France, 1986.
(22) Moudrakovski, I. L.; Sanchez, A. A.; Ratcliffe, C. I.; Ripmeester, J. A. Nucleation and growth of hydrates on ice surfaces: New insights from Xe-129 NMR experiments with hyperpolarized xenon. *J. Phys. Chem. B* **2001**, *105*, 12338–12347.
(23) Yoon, J. H.; Kawamura, T.; Yamamoto, Y.; Komai, T. Transformation of methane hydrate to carbon dioxide hydrate: In situ Raman spectroscopic observations. *J. Phys. Chem. A* **2004**, *108*, 5057–5059.
(24) Makogon, T. Y.; Sloan, E. D. Phase Equilibrium for Methane Hydrate from 190 to 262 K. *J. Chem. Eng. Data* **1994**, *39*, 351–353.
(25) Makogon, T. Y.; Mehta, A. P.; Sloan, E. D. Structure H and Structure I Hydrate Equilibrium Data for 2,2-Dimethylbutane with Methane and Xenon. *J. Chem. Eng. Data* **1996**, *41*, 315–318.
(26) Thomas, C.; Mousis, O.; Ballenegger, V.; Picaud, S. Clathrate hydrates as a sink of noble gases in Titan's atmosphere. *Astron. Astrophys.* **2007**, *474*, L17–L20.
(27) Larson, S. D. Phase Studies of the Two Component Carbon Dioxide-Water System, Involving the Carbon Dioxide Hydrate. Ph.D. Thesis, University of Illinois, Urbana, IL, 1955 (quoted in ref 1).
(28) Harmens, A.; Sloan, E. D. The Phase-Behavior of the Propane Water-System - a Review. *Can. J. Chem. Eng.* **1990**, *68*, 151–158.
(29) Longhi, J. Phase equilibria in the system CO_2-H_2O I: New equilibrium relations at low temperatures. *Geochim. Cosmochim. Acta* **2005**, *69*, 529–539.
(30) Fray, N.; Schmitt, B. Sublimation of ices of astrophysical interest: A bibliographic review. *Planet. Space Sci.* **2009**, *57*, 2053–2080.
(31) Robinson, D. B.; Metha, B. R. Hydrates in the Propane-Carbon Dioxide-Water System. *J. Can. Pet. Technol.* **1971**, *10*, 33–35.
(32) Fan, S. S.; Guo, T. M. Hydrate Formation of CO_2-Rich Binary and Quaternary Gas Mixtures in Aqueous Sodium Chloride Solutions. *J. Chem. Eng. Data* **1999**, *44*, 829–832.
(33) Wendland, M.; Hasse, H.; Maurer, G. Experimental Pressure-Temperature Data on Three- and Four-Phase Equilibria of Fluid, Hydrate, and Ice Phases in the System Carbon Dioxide-Water. *J. Chem. Eng. Data* **1999**, *44*, 901–906.
(34) Falabella, B. J.; Vanpee, M. Experimental Determination of Gas Hydrate Equilibrium below the Ice Point. *Ind. Eng. Chem. Fundam.* **1974**, *13*, 228–231.
(35) Delsemme, A. H.; Wenger, A. Physico-chemical phenomena in comets—I. Experimental study of snows in a cometary environment. *Planet. Space Sci.* **1970**, *18*, 709–715.
(36) Snell, L. E.; Otto, F. D.; Robinson, D. B. Hydrates in systems containing methane, ethylene, propylene, and water. *AIChE J.* **1961**, *7*, 482–485.
(37) Jhaveri, J.; Robinson, D. B. Hydrates in the Methane-Nitrogen System. *Can. J. Chem. Eng.* **1965**, *43*, 75–77.
(38) De Roo, J. L.; Peters, C. J.; Lichtenthaler, R. N.; Diepen, G. A. M. Occurrence of methane hydrate in saturated and unsaturated solutions of sodium chloride and water in dependence of temperature and pressure. *AIChE J.* **1983**, *29*, 651–657.
(39) Adisasmito, S.; Frank, R. J.; Sloan, E. D. Hydrates of carbon dioxide and methane mixtures. *J. Chem. Eng. Data* **1991**, *36*, 68–71.
(40) Kang, S.-P.; Huen, L. Clathrate phase equilibria for the water-phenol-methane system. *Fluid Phase Equilib.* **1998**, *146*, 339–349.
(41) Nakamura, T.; Makino, T.; Sugahara, T.; Ohgaki, K. Stability boundaries of gas hydrates helped by methane—structure-H hydrates of methylcyclohexane and cis-1,2-dimethylcyclohexane. *Chem. Eng. Sci.* **2003**, *58*, 269–273.
(42) Ohmura, R.; Uchida, T.; Takeya, S.; Nagao, J.; Minagawa, H.; Ebinuma, T.; Narita, H. Clathrate hydrate formation in (methane + water + methylcyclohexanone) systems: the first phase equilibrium data. *J. Chem. Thermodyn.* **2003**, *35*, 2045–2054.
(43) Mohammadi, A. H.; Anderson, R.; Tohidi, B. Carbon Monoxide Clathrate Hydrates: Equilibrium Data and Thermodynamic Modeling. *AIChE J.* **2005**, *51*, 2825–2833.
(44) Handa, Y. P. Calorimetric determinations of the compositions, enthalpies of dissociation, and heat capacities in the range 85 to 270 K for clathrate hydrates of xenon and krypton. *J. Chem. Thermodyn.* **1986**, *18*, 891–902.
(45) Handa, Y. P. Compositions, enthalpies of dissociation, and heat capacities in the range 85 to 270 K for clathrate hydrates of methane,

ethane, and propane, and enthalpy of dissociation of isobutane hydrate, as determined by a heat-flow calorimeter. *J. Chem. Thermodyn.* **1986**, *18*, 915–921.
(46) Anderson, G. K. Enthalpy of dissociation and hydration number of methane hydrate from the Clapeyron equation. *J. Chem. Thermodyn.* **2004**, *36*, 1119–1127.
(47) Dartois, E.; Deboffle, D. Methane clathrate hydrate FTIR spectrum. Implications for its cometary and planetary detection. *Astron. Astrophys.* **2008**, *490*, L19–L22.
(48) Dartois, E.; Schmitt, B. Carbon dioxide clathrate hydrate FTIR spectrum. Near infrared combination modes for astrophysical remote detection. *Astron. Astrophys.* **2009**, *504*, 869–873.
(49) Dartois, E.; Deboffle, D.; Bouzit, M. Methane clathrate hydrate infrared spectrum - II. Near-infrared overtones, combination modes and cages assignments. *Astron. Astrophys.* **2010**, *515*, A49–A54.
(50) Sloan, E. D. Clathrate hydrate measurements: microscopic, mesoscopic, and macroscopic. *J. Chem. Thermodyn.* **2003**, *35*, 41–53.
(51) Price, P. B. Kinetics of Conversion of Air Bubbles to Air Hydrate Crystals in Antarctic Ice. *Science* **1995**, *267*, 1802–1804.
(52) Pietrass, T.; Gaede, H. C.; Bifone, A.; Pines, A.; Ripmeester, J. A. Monitoring Xenon Clathrate Hydrate Formation on Ice Surfaces with Optically Enhanced ^{129}Xe NMR. *J. Am. Chem. Soc.* **1995**, *117*, 7520–7525.
(53) Jin, Y.; Nagao, J.; Hayashi, J.; Shimada, W.; Ebinuma, T.; Narita, H. Observation of Xe Hydrate Growth at Gas-Ice Interface by Microfocus X-ray Computed Tomography. *J. Phys. Chem. C* **2008**, *112*, 17253–17256.
(54) Adamson, A. W.; Jones, B. R. Physical Adsorption of Vapors on Ice. IV. Carbon Dioxide. *J. Colloid Interface Sci.* **1971**, *37*, 831–835.
(55) Roberts, O. L.; Brownscombe, E. R.; Howe, L. S.; Ramser, H. Constitution Diagrams and Composition of Methane and Ethane Hydrates. *Oil Gas J.* **1940**, *39*, 37–41.
(56) Makogon, T.; Sloan, J. E. Phase Equilibrium for Methane Hydrate from 190 to 262 K. *J. Chem. Eng. Data* **1995**, *40*, 344–344.
(57) Mohammadi, A. H.; Richon, D. Ice-Clathrate Hydrate-Gas Phase Equilibria for Air, Oxygen, Nitrogen, Carbon Monoxide, Methane, or Ethane plus Water System. *Ind. Eng. Chem. Res.* **2010**, *48*, 3976–3979.
(58) Falabella, B. J. A Study of Natural Gas Hydrates. Ph.D. Thesis, University of Massachusetts, Ann Arbor, MA, 1975 (quoted in ref 1).

Received for review June 17, 2010. Accepted September 9, 2010. N.F. thanks CNES for a postdoctoral fellowship. This work has been supported by the French "Centre National d'Etudes Spatiales" (CNES) and by the Research Network Program in Astrophysics from the The Israeli-French High Council for Science and Technology Research.

JE1006604

ARTICLE 3

Marboeuf U., Fray N., Brissaud O., Schmitt B., Bockelée-Morvan D. and Gautier D. (2012)

Equilibrium pressure of ethane, acetylene and krypton clathrate hydrates below the freezing point of water.

***Journal of Chemical and Engineering Data*, 57(12), 3408-3415**

Journal of chemical & engineering data

Article

pubs.acs.org/jced

Equilibrium Pressure of Ethane, Acetylene, and Krypton Clathrate Hydrates below the Freezing Point of Water

Ulysse Marboeuf,*[,†] Nicolas Fray,[‡] Olivier Brissaud,[†] Bernard Schmitt,[†] Dominique Bockelée-Morvan,[§] and Daniel Gautier[§]

[†]UJF-Grenoble 1/CNRS-INSU, Institut de Planétologie et d'Astrophysique de Grenoble (IPAG), UMR 5274, 38041 Grenoble, France

[‡]LISA, Laboratoire Interuniversitaire des Systèmes Atmosphériques, UMR CNRS 7583, Université Paris-Est Créteil (UPEC) et Université Paris Diderot (UPD), Créteil, France

[§]LESIA, CNRS UMR 8109, UPMC, Université Paris-Diderot, Observatoire de Paris, 5 pl. Jules Janssen, 92195 Meudon, France

ABSTRACT: We report measurements of the equilibrium pressure of single guest clathrate hydrates of C_2H_6, C_2H_2, and Kr at low temperatures (mainly in the range (150 to 230) K). The results are compared with other data reported in the literature and used to determine new empirical *correlation* laws allowing to calculate the equilibrium pressure of clathrates of these species at any temperature below the freezing point of water. Enthalpies of clathrate formation/dissociation for these molecules are estimated using the Clausius−Clapeyron equation and show good agreement with previous reported calorimetric measurements. These results are of particular interest for studies of extraterrestrial ice-rich environments such as comets and icy moons in the solar system.

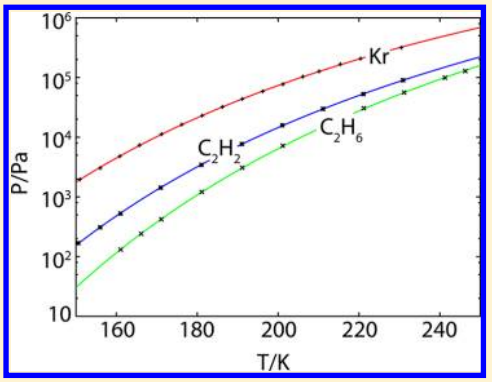

INTRODUCTION

Clathrate hydrates or *gas hydrates* (hereafter clathrates) are crystalline solids composed of water and gas. The lattice of water molecules is organized in the form of cages which are stabilized by the inclusion of gas molecules. This structure of water ice selectively retains and releases the gases trapped in cages and is of particular interest to explain the deficiency/enrichment of some molecular species in some astrophysical environments. For example, the presence of clathrates in comets[1−9] and icy moons of giant planets[10] has been discussed for a long time. Models of ice formation in the protoplanetary disk[11−18] show that icy bodies formed during the cooling of the solar nebula could be partially made up of clathrates. Several authors invoked the presence of clathrates to explain the anomalous relative abundances measured in solar system bodies.[14,15,19]

Characterizing C_2H_6, C_2H_2, and Kr clathrates is of particular interest for studying extraterrestrial environments. C_2H_6 and C_2H_2 have been detected in the gas phase of comets[20] and could be partially trapped in clathrates within these objects together with the main cometary volatile molecules.[9] Moreover, C_2H_6 could have been sequestrated by clathrates in the cryovolcanic subsurface of Titan, the largest satellite of Saturn,[10] thus explaining its deficiency in this moon. Kr, as other noble gases, has never been detected in cometary environments because its remote observation is very difficult.[20] However, its incorporation in cometary nuclei is suspected: noble gases of Earth could come partially from these objects,[21] and models of ice formation in protoplanetary disks show that this element could have been partially trapped in clathrates within icy bodies.[17]

In this paper, we report measurements of the equilibrium pressure of single guest clathrates of C_2H_6, C_2H_2, and Kr below the freezing point of water at temperatures relevant for extraterrestrial environments. The results are compared with other data reported in the literature and are used to determine new empirical correlation laws allowing to calculate the equilibrium pressure of these single guest clathrates at any temperature below the freezing point of water. These new empirical laws are then compared to laws currently used in astrophysical papers. Enthalpies of clathrate dissociation are also estimated using the Clausius−Clapeyron equation. The values derived in this work are in good agreement with previous published calorimetric measurements.

EXPERIMENTAL METHOD

Experimental System. Figure 1 shows the schematic diagram of the apparatus used in this study. This experimental system has already been described in a previous paper,[22] and we provide only a brief description in this section. The equilibrium pressure of clathrates is measured in a cylindrical copper reactor of about 13 cm^3 inner volume. This reactor is composed of two

Received: April 24, 2012
Accepted: November 9, 2012
Published: November 21, 2012

dx.doi.org/10.1021/je3004595 | *J. Chem. Eng. Data* 2012, 57, 3408−3415

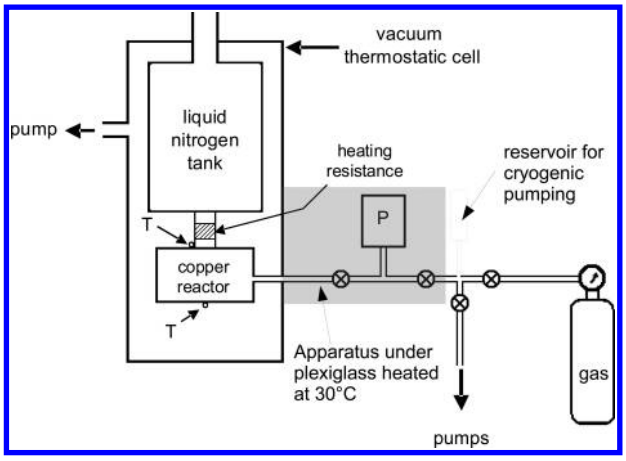

Figure 1. Schematic view of the experimental system used to measure the equilibrium pressure of single guest clathrates of C_2H_6, C_2H_2, and Kr.

parts connected by an indium gasket which ensures its sealing at low temperatures. It is located inside a thermostatic cell (ABT SORIME), evacuated to about 10^{-3} Pa using a diffusion pump (Alcatel) backed by a diaphragm pump, and connected to a liquid nitrogen dewar via a copper finger. A heating resistance is fixed on the upper copper finger, and two temperature sensors (silicon diodes) are glued on the lower and upper parts of the reactor. Resistance and temperature sensors are all connected to a temperature controller (model 331 of Lakeshore), which ensures a temperature stability of about ± 0.03 K. Finally, the apparatus allows us to measure temperatures from (77 to 300) K, with an uncertainty of about 0.01 K.

The reactor is evacuated using a turbo-molecular pump (TMU-071P, Pfeiffer) backed by a dry scroll vacuum pump (XDS 5, Edwards). The pressure is measured in the line located between the reactor and the pumping group using either (1) an absolute metal membrane pressure sensor (Baratron 690-A13T-RB, MKS) allowing us to measure the pressure between ($1.33 \cdot 10^2$ and $1.33 \cdot 10^5$) Pa with an accuracy 0.08 % of the reading value, or (2) a bonded strain gauge absolute pressure transducer (Teledyne Taber, model 2201) allowing us to measure pressures between (0 and $13.8 \cdot 10^5$) Pa with a measurement uncertainty of ± 10^2 Pa. Temperature and pressure are recorded as a function of time with a resolution of a few seconds using a laboratory-made software. Note that the reactor includes neither a stirrer nor a shaker. To avoid fluctuations of temperature (and hence pressure) induced by daily room temperature changes, we placed the apparatus (pressure sensors and tubing) under Plexiglas maintained at a regulated temperature of 30 °C.

Materials. Table 1 reports the purities and suppliers of the chemical species used in this work. C_2H_2 gas is mixed with N_2, which represents a volume fraction of 0.4 % of the total gas phase. To improve the purity of this gas before its injection into the reactor, we added a cooled reservoir between the entry of the reactor and the gas cylinder to eliminate N_2 (see Figure 1). The fractionation of the two gases is obtained by cryogenic pumping: the reservoir is immersed in liquid nitrogen at 77 K; then an amount of C_2H_2 gas from the bottle is introduced and condenses in the reservoir; by pumping the residual gas phase (N_2 essentially), only C_2H_2 remains in solid state in the reservoir. At least 99 % of N_2 impurity is eliminated in this operation. This step is controlled by measuring the initial and residual pressures with the first pressure sensor (Baratron). The reservoir is then heated at room temperature, then cooled and pumped again. This operation is repeated at least three times to ensure the removal of almost all of the initial N_2 in the gas phase. The final N_2 impurity level is then lower than 1 %. The water used to form clathrates in the experiments has been purchased from Merck and is produced for online analysis.

Table 1. Purities and Suppliers of Gas

chemical species	purity (molar fraction)	supplier
Xe	99.998 %	Air Liquide
Kr	99.998 %	Air Liquide
C_2H_6	99.95 %	Air Liquide
C_2H_2	99.6 %	Air Liquide

Procedure. The procedure used to form the clathrate structure is described in Fray et al. (2010),[22] and we briefly summarize the method in this section. We form single guest clathrates of Xe in a first reactor in which we introduce about 5 cm^3 of liquid water and about 200 kPa of Xe. This reactor is then immersed in a water bath at 1 °C during a few minutes, and we obtain about 1 g of clathrates of Xe. The sample is then transferred in the second reactor (copper reactor), in a cold room at about −20 °C, and the experimental system is assembled as in Figure 1. Air is then pumped.

To study the equilibrium pressure of clathrates of single guest species C_2H_6, C_2H_2, and Kr, we have to convert the initial sample of Xe to C_2H_6, C_2H_2, or Kr clathrates. For this, the reactor is maintained at a constant temperature of 220 K. The gaseous Xe is then evacuated by pumping the clathrate sample, leading to its partial decomposition, until gaseous Xe stops being released by the sample. In a second step, we inject in the reactor an amount of gas to a pressure larger than the expected equilibrium pressure of the desired species (C_2H_6, C_2H_2, or Kr). This pressure can reach several times the estimated (extrapolated) equilibrium pressure of the single species clathrate but is always lower than the corresponding vapor pressure of the pure species solid phase. The formation of the single guest clathrate results in a rapid decrease of the pressure in the isolated reactor. After pressure stabilization, the whole operation (decomposition/formation of clathrate) is repeated at least 10 times to ensure the removal of almost all of the initial Xe in the clathrate structure.

At this time of the procedure, we assume that we have obtained a sample of pure clathrate of the desired species. Some small Xe clathrate residues can remain deeply embedded in ice grains of the sample, but they do not interact with the gas phase. The temperature of the reactor is then maintained constant, and we reduce the pressure below the theoretical or experimental equilibrium pressure known in the literature. A pressure increase is then observed, as shown in Figure 2, due to the decomposition of clathrates and the release of gas molecules in the closed reactor. Once the pressure is stabilized, we obtain a first (under-)estimate of the clathrate equilibrium pressure from the partial decomposition of the clathrate structure. Then, we inject an overpressure of gas in the reactor and a pressure decrease is observed due to the formation of clathrates and encapsulation of the gas molecules. We obtain the second (over)estimate of the clathrate equilibrium pressure from reformation of the clathrate structure. This procedure is repeated several times at the same temperature until convergence of both pressures toward a common equilibrium pressure is achieved with a low relative error (as much as

dx.doi.org/10.1021/je3004595 | J. Chem. Eng. Data 2012, 57, 3408−3415

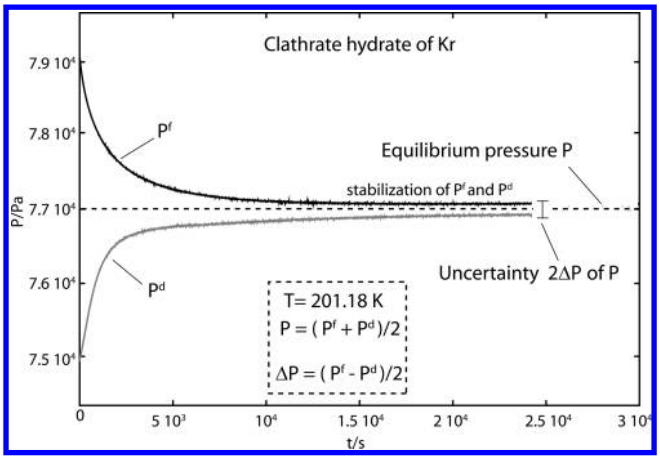

Figure 2. Procedure to obtain the clathrate equilibrium pressure P at temperature T. P is obtained by the arithmetic average of the two closest values of decomposition P^d and formation P^f pressures, while the total uncertainty is the difference between these two values divided by 2.

possible $\Delta P \leq 3$ %). The equilibrium pressure P is then supposed to be the arithmetic average of the two closest values of decomposition P^d and formation P^f pressures, while the maximum total uncertainty is supposed to be the difference ΔP between these two values (see Figure 2). This uncertainty is mostly determined by the kinetics of clathrate formation/decomposition that depends on temperature, the difference between the gas pressure and the equilibrium pressure of the clathrate, the availability of water molecules to form the cage structure, and on a number of uncontrolled parameters that can lead to the metastability of clathrates.[8,23−28] The equilibrium can be fast (≤ 1 day) at temperatures higher than 190 K. However at lower temperatures, several days are need to reach and measure the equilibrium pressure within a few percents. For all clathrate hydrates of the desired species (C_2H_6, C_2H_2, or Kr), both the formation and dissociation processes are made at a fixed temperature on the same sample of clathrate hydrate. The uncertainty on the temperature is then about ± 0.02 K.

RESULTS AND DISCUSSION

All experimental equilibrium data of single guest clathrates measured in this work, as well as the ones already published in the literature for species Kr, C_2H_6 and C_2H_2 are reported in Tables 4, 5, and 6 and are plotted in Figures 3, 5, and 7, respectively. The figures also display our empirical correlation laws and the deviation of the experimental data from these empirical laws.

Empirical correlation laws are determined by fitting our data with the following empirical relation:

$$\ln(P) = A + \frac{B}{T} \tag{1}$$

in which P and T are the pressure (in Pa) and the temperature (K). The parameters A and B for the three species C_2H_6, C_2H_2, and Kr are given in Table 2. These empirical correlation laws can be used at any temperature below the freezing point of water.

To assess the reliability of our data, we estimated the enthalpy of clathrate dissociation H_P^{cl} using the Clausius−Clapeyron equation given by the relation:

Table 2. Parameters[a] Describing the Equilibrium Pressure of Clathrates as a Function of the Temperature Using Equation 1

chemical species	A	B	T/K
Kr	22.3934	−2237.82	151 to 230
C_2H_6	24.8246	−3211.75	161 to 246
C_2H_2	23.20757	−2725.19	151 to 231

[a] A and B are the parameters of the empirical relation. A is dimensionless, and B is in kelvin.

$$\frac{d\ln(P)}{d(1/T)} = -\frac{H_P^{cl}}{R} \tag{2}$$

where R is the gas constant.

The values for the three species C_2H_6, C_2H_2, and Kr and their corresponding calorimetric measurements from Handa (1986)[31−40] are given in Table 3.

Table 3. Enthalpy of Clathrate Dissociation H^{cl} from Clausius−Clapeyron Equation 2 and Calorimetric Measurements

chemical species	H_p^{cl}[a] kJ·mol^{-1}	$H^{cl,\circ}$[b] kJ·mol^{-1}
Kr	18.6	19.54 ± 0.24[31]
C_2H_6	26.7	25.7 ± 0.24[40]
C_2H_2	22.66	no published data

[a] Enthalpy determined by Clausius−Clapeyron. [b] Enthalpy determined by calorimetric measurement.

These values are of particular interest to calculate the energy of phase change between water ice and clathrate in models of cometary nuclei[41] during their physicochemical evolution around the sun as well as for others applications to astrophysical models.

Clathrate of Krypton, Kr. We performed 16 measurements, ranging from (151 to 230.5) K, given in Table 4 and Figure 3. These data partially overlap and extend the temperature range of the experimental data of Jin et al. (2011)[29] and fully overlap those of Barrer and Edge (1967).[30] These latter values show a progressive deviation, from about 25 % at 202.9 K to about 300 % at 149 K, from our data and the ones of Jin et al. (2011).[29] One can note that a similar deviation from the data of Barrer and Edge (1967)[30] has already been observed for Xe clathrates (see Fray et al., 2010[22]).

Moreover, the data of Jin et al. (2011)[29] show a systematic positive deviation between 6 % and 8 % from our measurements. In summary, the three data sets that currently exist in the literature on the clathrate equilibrium pressure of Kr do not overlap and hence do not converge in a common relationship. So, although the data sets of other authors are not necessarily in error, we have taken into account only our measurements for the determination of the empirical relation of the equilibrium pressure of the single guest clathrate of Kr (see Table 2). It reproduces our nominal experimental measurements with a relative deviation of less than 2.5 % (without error bins, see Figure 3, upper panel).

From the slope of this $P(T)$ curve, H_P^{cl} is estimated to about 18.6 kJ·mol^{-1} in the temperature range (151 to 230) K. This value is in agreement with the one (18.5 kJ·mol^{-1}) obtained by Jin et al. (2011)[29] in the temperature range (204 to 270) K and the value $H^{cl,\circ}$ of 19.54 ± 0.24 kJ·mol^{-1} obtained at 273 K from

dx.doi.org/10.1021/je3004595 | J. Chem. Eng. Data 2012, 57, 3408−3415

Table 4. Experimental Data for the Equilibrium of Single Guest Clathrate of Kr below the Freezing Point of Water

T/K	ΔT/K	P/Pa	ΔP/Pa	$\Delta P/P$ (%)	reference
202.9	0.1	111191	unknown	unknown	30
191.0	0.1	62528	unknown	unknown	30
180.6	0.1	34264	unknown	unknown	30
173.7	0.1	22265	unknown	unknown	30
164.9	0.1	12012	unknown	unknown	30
149.0	1.0	6266	unknown	unknown	30
270.4	0.2	1420000	50000	3.52	29
269.2	0.2	1380000	50000	3.62	29
267.7	0.2	1300000	50000	3.85	29
265.2	0.2	1230000	50000	4.06	29
262.9	0.2	1140000	50000	4.39	29
260.2	0.2	1050000	50000	4.76	29
256.9	0.2	930000	5000	0.54	29
252.7	0.2	800000	5000	0.63	29
248.3	0.2	690000	5000	0.73	29
244.4	0.2	600000	5000	0.83	29
238.7	0.2	480000	5000	1.04	29
227.0	0.2	290000	5000	1.72	29
217.2	0.2	190000	5000	2.63	29
204.4	0.2	100000	5000	5	29
230.45	0.02	316535	1972	0.62	this work
220.38	0.02	206734	2802	1.36	this work
215.39	0.02	166777	3321	1.99	this work
210.14	0.02	126642	532	0.42	this work
206.12	0.02	103279	658	0.64	this work
201.18	0.02	77130	272	0.35	this work
196.19	0.02	58749	506	0.86	this work
191.14	0.02	43681	157	0.36	this work
186.22	0.02	32192	190	0.59	this work
181.22	0.02	22952	176	0.76	this work
176.19	0.02	16296	114	0.7	this work
171.17	0.02	11242	5	0.05	this work
165.73	0.02	7366	94	1.28	this work
160.86	0.02	4789	209	4.37	this work
156	0.02	3039	240	7.9	this work
150.98	0.02	1970	60	3.07	this work

earlier calorimetric measurements.[31] Considering this calorimetric value as the reference at 273 K for the enthalpy of dissociation of Kr clathrate, this leads to a relative difference/error of about 5 % relative to our value.

For a better accuracy, it is interesting to investigate the variation of the clathrate dissociation enthalpy $H^{cl}(T)$ with temperature to compare values published in the same temperature range as our data. $H^{cl}(T)$ varies following the relation:[32]

$$H^{cl}(T) = H^{cl,o} + \int_{T_0}^{T} \Delta C_x^{cl}(T)\mathrm{d}T \quad (3)$$

$\Delta C_x^{cl}(T)$ is the heat capacity difference between water ice and the clathrate structure of the species x (x = Kr here) at temperature T:

$$\Delta C_x^{cl}(T) = n_{hyd} C_{H_2O}^{i} + C_{p,x}^{g} - C_x^{cl} \quad (4)$$

where C_x^{cl} and $C_{H_2O}^{i}$ are the heat capacities of the clathrate of gas x and of pure water ice, respectively, and $C_{p,x}^{g}$ is the heat capacity of the gas x. Taking into account the values of the heat capacity of Kr clathrate measured by Handa (1986)[31] from (85 to 270) K, and assuming a heat capacity $C_{p,x}^{g}$ of the noble gas of $5/2R$, we obtain a clathrate dissociation enthalpy $H^{cl}(T)$ varying from (19 to 19.3) kJ·mol^{-1}. These values lead to a relative variation $(H_P^{cl} - H^{cl}(T))/H^{cl}(T)$ from (2 to 4) % between (151 and 230) K, the temperature range of our data (see Figure 4). So, our constant enthalpy of Kr clathrate dissociation obtained from the Clausius−Clapeyron eq 2 is in good agreement with the values determined by calorimetric analysis.

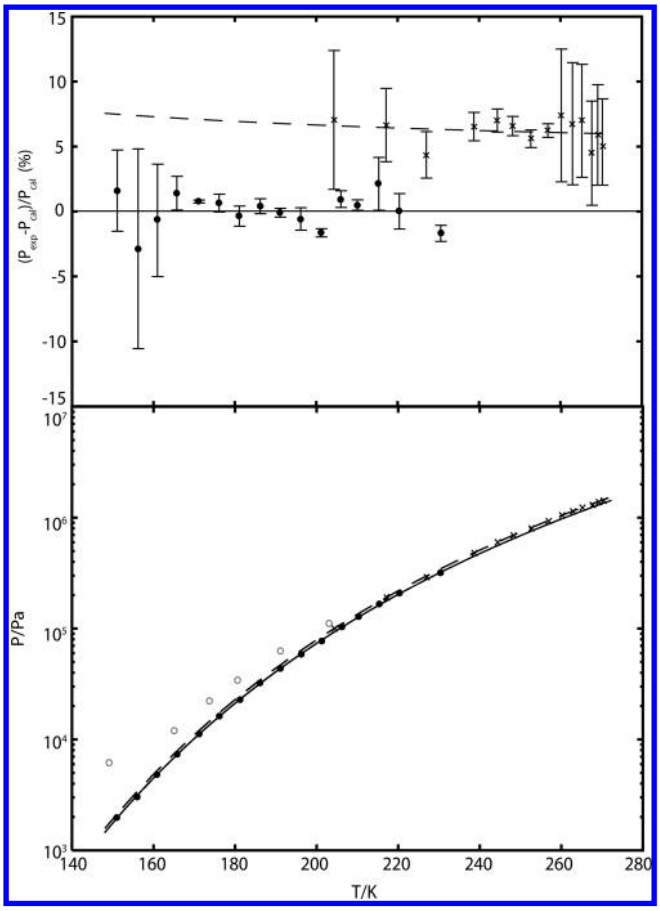

Figure 3. Equilibrium pressure of single guest clathrate of Kr (lower panel) and deviations of experimental data from our empirical relation (upper panel) as a function of the temperature: ●, this work; ×, Jin et al. (2011);[29] ○, Barrer and Edge (1967);[30] solid black line, our empirical relation; dashed black line, empirical relation from Jin et al. (2011).[29]

Clathrate of Ethane, C_2H_6. We performed 11 measurements ranging from (161.1 to 246.3) K which are given in Table 5 and Figure 5. There are five other papers providing experimental data of equilibrium pressure of C_2H_6 clathrate. Our data fully cover the range of temperatures of Falabella and Vanpee (1974)[33] data and extend all of the previous published data at lower temperatures. The data of Falabella and Vanpee (1974)[33] (temperature range from (200 to 240) K) and Roberts et al. (1940)[34] (260 to 270 K) show systematic positive deviations up to 23 % compared to the empirical relation derived from our values only. However, our data fit fairly well those of Deaton and Frost (1946),[35] Yasuda and Ohmura (2008),[36] and Mohammadi and Richon (2010).[37] We have then taken into account only these data together with our measurements for the determination of the empirical relation of the equilibrium pressure of the single guest clathrate of C_2H_6

dx.doi.org/10.1021/je3004595 | J. Chem. Eng. Data 2012, 57, 3408−3415

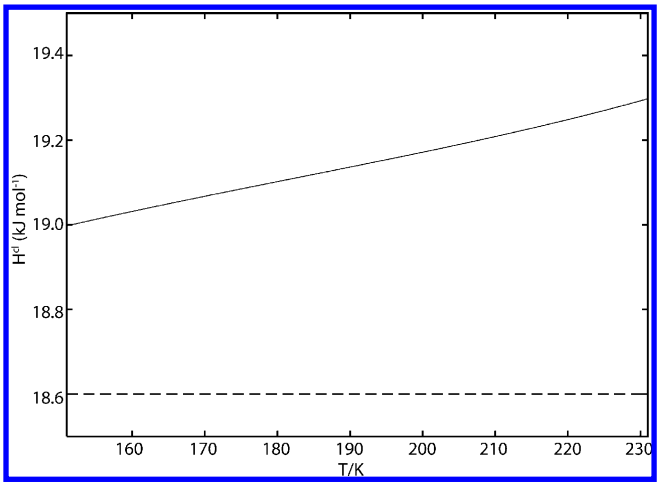

Figure 4. Enthalpy of clathrate dissociation of Kr as a function of temperature in the temperature range (151 to 230) K of our data: dashed black line, our value; black line, relation from Handa (1986).[31] Our value is obtained from the $P(T)$ slope of our data and by using eq 3.

(see Table 2). This relation reproduces the measurements with a relative deviation of ± 2.5 % (see Figure 5, upper panel). The expression of Miller (1961),[39] an interpolation of unpublished experimental measurements performed from (161 to 243) K, shows a progressive deviation from our relation with a maximum of about 8 % at 160 K.

From the slope of this empirical law, H_P^{cl} is approximately 26.7 kJ·mol^{-1} in the temperature range (161 to 246.3) K. Our value is in very good agreement with the one (26.4 kJ·mol^{-1}) obtained from the slope of Miller (1961)[39] in the temperature range (161 to 243) K and the value $H^{cl,o}$ (25.7 ± 0.24 kJ·mol^{-1}) obtained at 273 K from calorimetric measurements.[40] Taking into account the calorimetric value $H^{cl,o}$ as the reference at 273 K for the enthalpy of clathrate dissociation of C_2H_6, this leads to a relative difference value of about 3.9 %.

We can now investigate the variation of clathrate dissociation enthalpy with temperature using eq 3. By taking into account values of the heat capacity of clathrate C_x^{cl} measured by Handa (1986)[40] from (85 to 270) K, and assuming the heat capacity of the gas $C_{p,x}^{g}$ given by Chao et al. (1973),[42] we obtain a clathrate dissociation enthalpy $H^{cl}(T)$ varying from (26.9 to 26.0) kJ·mol^{-1}. These values lead to a relative variation $(H_P^{cl} - H^{cl}(T))/H^{cl}(T)$ from (−0.6 to 2.7) % between (161 and 246) K, the temperature range of our data set (see Figure 6). Our calculation of a constant enthalpy of clathrate dissociation of C_2H_6 using the Clausius−Clapeyron equation is then in good agreement with the calorimetric analysis.

Clathrate of Acetylene, C_2H_2. We performed 10 measurements ranging from (150.5 to 231) K given in Table 6 and Figure 7. To our knowledge only Stackelberg and Müller (1954)[38] published two experimental data of equilibrium pressure of acetylene clathrate, but the value at 257.75 K shows a very large deviation of about a factor of 3 compared to our values. On the other hand, Miller (1961)[39] published an equilibrium pressure empirical law based on unpublished experimental data performed from (158 to 231) K that confirms this deviation. We have then taken into account only our data for the determination of the empirical relation of the equilibrium pressure of the single guest clathrate of C_2H_2 (see Table 2). It reproduces our experimental measurements with a relative deviation of ± 2 % (see Figure 7, upper panel). The

Table 5. Experimental Data for the Equilibrium Pressure of Single Guest Clathrate of C_2H_6

T/K	ΔT/K	P/Pa	ΔP/Pa	ΔP/P (%)	reference
269.3	unknown	441000	unknown	unknown	34
260.9	unknown	290000	unknown	unknown	34
260.8	unknown	294000	unknown	unknown	34
272.0	unknown	457000	unknown	unknown	35
269.3	unknown	405000	unknown	unknown	35
266.5	unknown	357000	unknown	unknown	35
263.6	unknown	313000	unknown	unknown	35
240.8	0.1	101300	666	0.7	33
240.4	0.1	98100	666	0.7	33
230.2	0.1	56400	666	1.2	33
215.7	0.1	22100	666	3	33
200.8	0.1	8300	666	8	33
271.9	0.1	443000	3000	0.7	36
269.7	0.1	403000	3000	0.7	36
267.3	0.1	360000	3000	0.8	36
264.3	0.1	315000	3000	1	36
261.8	0.1	281000	3000	1	36
258.4	0.1	241000	3000	1.3	36
255.6	0.1	209000	3000	1.4	36
252.3	0.1	177000	3000	1.7	36
248.4	0.1	145000	3000	2.1	36
244.9	0.1	122000	3000	2.5	36
272.2	0.1	462000	5000	1	37
268.3	0.1	385000	5000	1.3	37
265.2	0.1	336000	5000	1.5	37
262.5	0.1	290000	5000	1.7	37
246.30	0.02	127973	968	0.8	this work
241.25	0.02	99163	965	1	this work
231.16	0.02	55950	187	0.3	this work
221.19	0.02	30610	861	2.8	this work
211.22	0.02	15038	193	1.3	this work
201.14	0.02	7172	144	2	this work
191.12	0.02	3081	59	1.9	this work
181.13	0.02	1211	25	2	this work
171.12	0.02	422	12	2.8	this work
166.13	0.02	241	7.9	3.3	this work
161.08	0.02	131	8.5	6.5	this work

pressure empirical law expression of Miller (1961)[39] shows a progressive deviation from our relation with a maximum of about 10 % at 151 K.

From the slope of our empirical law, ΔH is approximately 22.65 kJ·mol^{-1}, while the value obtained from the slope of Miller (1961)[39] is 22.3 kJ·mol^{-1}. As no calorimetric data are available in the literature, we cannot assess the reliability of our data.

Comparison with the Empirical Correlation Laws Used in Astrophysical Models. In this section, we compare the empirical laws used in astrophysical models from (40 to 270) K (temperature range of applications of these laws) to our empirical correlation laws for clathrates of Kr, C_2H_6, and C_2H_2. Figure 8 shows the extrapolations of equilibrium pressure empirical laws of single guest clathrates of Kr, C_2H_6, and C_2H_2 given in astrophysical papers (lower panel) and presents absolute deviations from our empirical relations (upper panel) as a function of the temperature from (40 to 270) K. For the clathrate of Kr, the expression used in astrophysical models[16] show a deviation from our relation of (4 to 21000) % in this temperature range. For the clathrate of C_2H_2, the pressure

dx.doi.org/10.1021/je3004595 | J. Chem. Eng. Data 2012, 57, 3408−3415

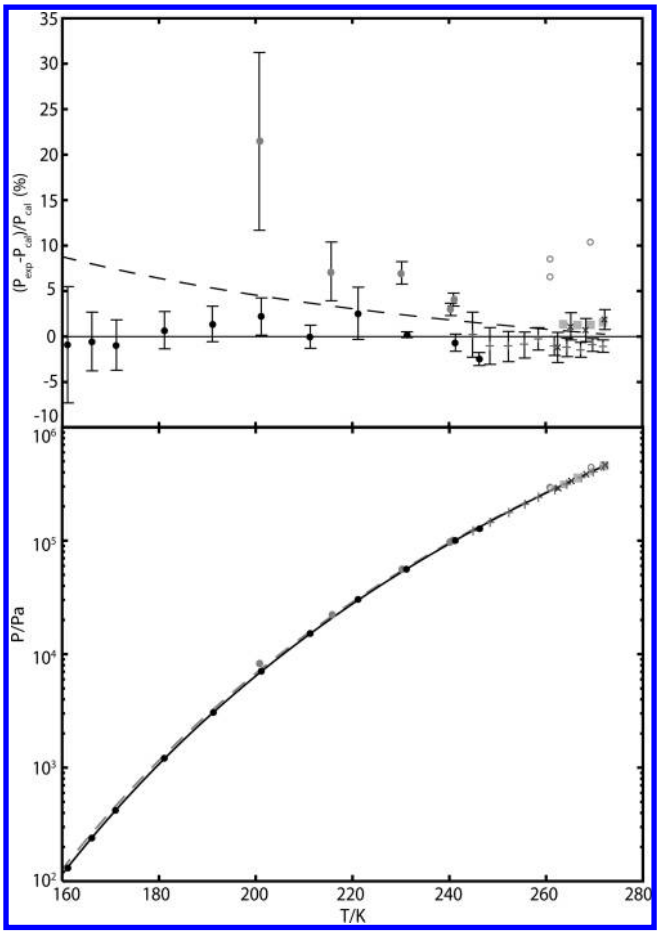

Figure 5. Equilibrium pressure of single guest clathrate of C_2H_6 (lower panel) and deviations of experimental data from our empirical relation (upper panel) as a function of the temperature: ●, this work; ×, Mohammadi and Richon (2010);[37] +, Yasuda and Ohmura (2008);[36] gray ●, Falabella and Vanpee (1974);[33] gray ■, Deaton and Frost (1946);[35] ○, Roberts et al. (1940);[34] solid black line, our empirical relation; dashed gray line, empirical relation from Miller (1961).[39]

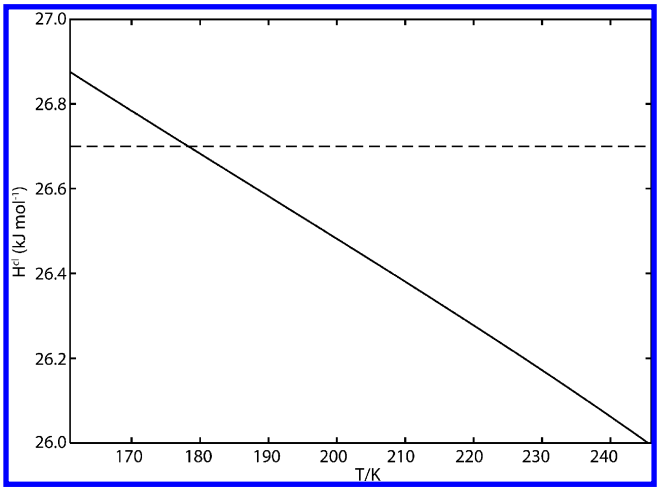

Figure 6. Enthalpy of clathrate dissociation of C_2H_6 as a function of temperature in the temperature range (151 to 230) K of our data: dashed black line, our value; black line, relation from Handa (1986).[40] Our value is obtained from the $P(T)$ slope of our data and by using eq 3.

Table 6. Experimental Data for the Equilibrium Pressure of Single Guest Clathrate of C_2H_2

T/K	ΔT/K	P/Pa	ΔP/Pa	$\Delta P/P$ (%)	reference
273.15	unknown	570000	unknown	unknown	38
257.75	unknown	100000	unknown	unknown	38
230.90	0.02	89845	92	0.1	this work
221.09	0.02	52795	213	0.4	this work
211.12	0.02	29835	299	1	this work
201.05	0.02	15794	105	0.67	this work
191.04	0.02	7683.7	64	0.84	this work
181.04	0.02	3436.4	94	2.74	this work
170.97	0.02	1427.5	22	1.52	this work
161.03	0.02	526.5	14	2.66	this work
156.00	0.02	309.8	8	2.54	this work
150.56	0.02	168.4	5	2.94	this work

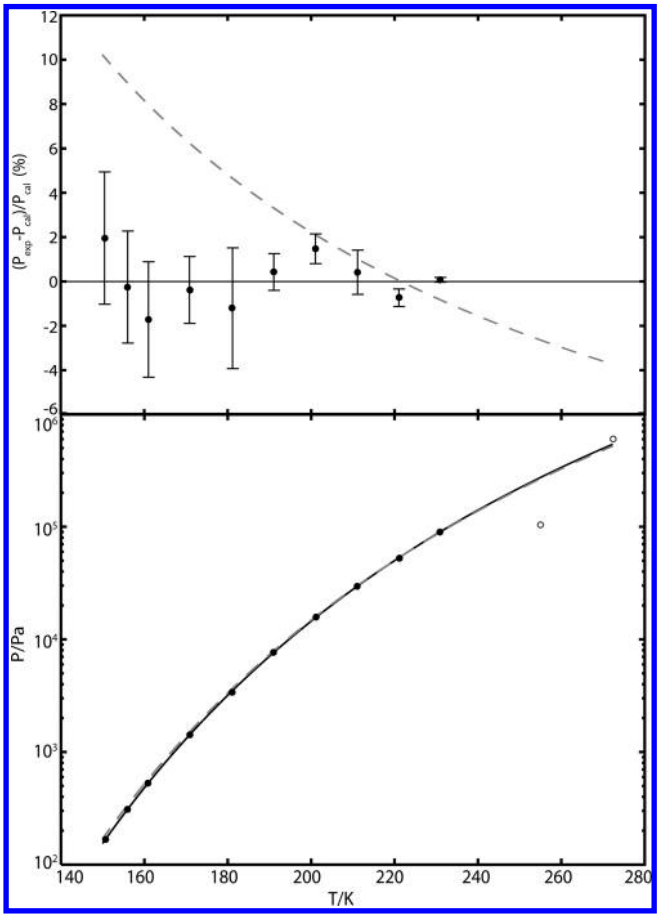

Figure 7. Equilibrium pressure of single guest clathrate of C_2H_2 (lower panel) and deviations of experimental data from our empirical relation (upper panel) as a function of the temperature: ●, this work; ○, Stackelberg and Müller (1954);[38] solid black line, our empirical relation; dashed gray line, empirical relation from Miller (1961).[39]

empirical law expression of Miller (1961)[39] shows a progressive deviation from our relation of (0 to 150) % in the same range of temperature. For the clathrate of C_2H_6, the expression of Miller (1961)[39] and the law used by Mousis and Schmitt (2008)[10] show a deviation from our relation of (0.3 to 100) % and (5 to 320) %, respectively.

dx.doi.org/10.1021/je3004595 | J. Chem. Eng. Data 2012, 57, 3408−3415

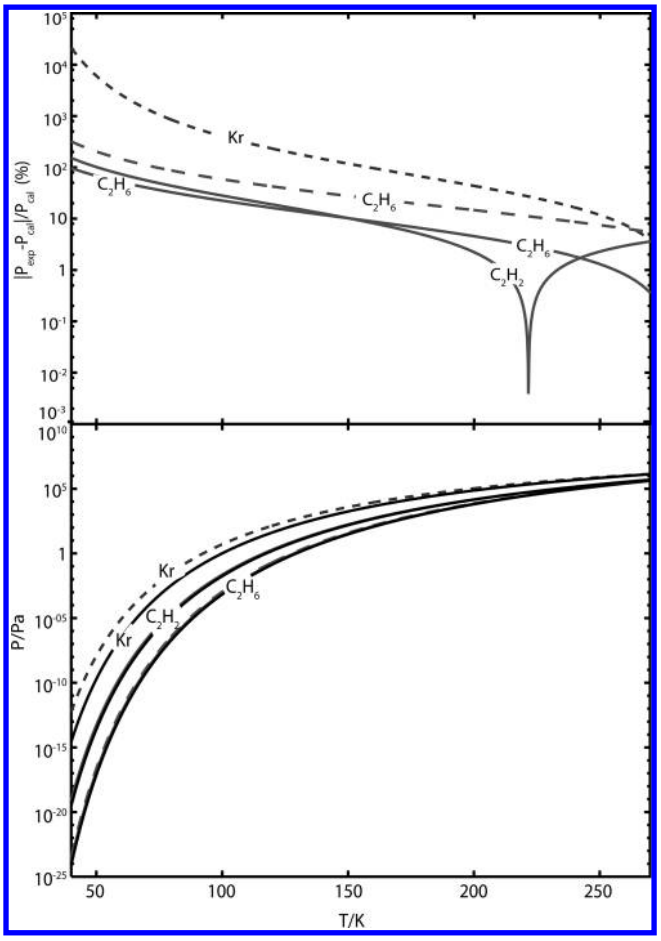

Figure 8. Extrapolations of equilibrium pressure empirical laws of single guest clathrate of Kr, C_2H_6, and C_2H_2 given in astrophysical papers (lower panel) and their deviations from our empirical relation (upper panel) as a function of the temperature from (40 to 270) K. Solid black line, empirical relations determined in this work for Kr, C_2H_6, and C_2H_2 species; solid gray lines, empirical relation from Miller (1961)[39] for C_2H_6 and C_2H_2 molecules; dashed black line, empirical relation used by Hersant et al. (2004)[16] for Kr species; dashed gray line, empirical relation used by Mousis and Schmitt (2008)[10] for C_2H_6 molecule.

CONCLUSION

We performed measurements of the equilibrium pressure of single guest clathrates of krypton from (150.97 to 230.45) K, ethane from (161.08 to 246.3) K, and acetylene from (150.56 to 230.90) K. We derived empirical correlation laws allowing to calculate the equilibrium pressure of single guest clathrates of these three species at any temperature below the freezing point of water.

For krypton, our clathrate equilibrium pressures are lower than those published in the literature. We have shown that the data of Barrer and Edge (1967)[30] present a progressive deviation from our measurements and those of Jin et al. (2011).[29] This discrepancy with data of Barrer and Edge (1967)[30] has already been observed with the clathrate of Xe,[22] indicating that their data are not reliable. Moreover, our data and those of Jin et al. (2011)[29] show a systematic deviation so that the three data sets available for the krypton clathrate equilibrium pressure do not converge in a common relationship. Consequently, we have taken into account only our measurements for the determination of the empirical relation for the equilibrium pressure of this clathrate. For C_2H_6, our data set is in good agreement with those of Deaton and Frost (1946),[35] and recent papers of Yasuda and Ohmura (2008),[36] and Mohammadi and Richon (2010),[37] and demonstrates also the reliability of our experimental method. The empirical correlation law of Miller (1961),[39] from unpublished experimental data, shows a progressive deviation from our relation. For C_2H_2, the data of Stackelberg and Müller (1954)[38] show a large deviation from our measurements and the equilibrium empirical law given by Miller (1961).[39] We have then taken into account only our measurements for the determination of the equilibrium pressure of this clathrate. The expression of Miller (1961),[39] from unpublished measurements, also shows a low progressive deviation from our data.

For the three species, we calculated the enthalpy of clathrate dissociation ΔH using the Clausius−Clapeyron equation. Our results agree well with the ΔH values obtained from calorimetric measurements of ethane[40] and krypton,[31] but there are no published data for acetylene. These new empirical laws could affect theoretical studies on the clathrate formation/dissociation in extraterrestrial environments (e.g., comets and icy moons of the solar system) since the laws currently used in astrophysical models show significant deviations from our results.

AUTHOR INFORMATION

Corresponding Author

*E-mail: marboeuf@ujf-grenoble.fr.

Funding

U.M. thanks CNES for a postdoctoral fellowship. This work has been supported by the French "Centre National d'Etudes Spatiales" (CNES), the French "Programme National de Planétologie", and by the Research Network Program in Astrophysics from The Israeli-French High Council for Science and Technology Research.

Notes

The authors declare no competing financial interest.

ACKNOWLEDGMENTS

We thank F. Grisolle concerning the help of the filling up of the dewar with liquid nitrogen.

REFERENCES

(1) Delsemme, A. H.; Swings, P. Hydrates de gaz dans les noyaux cométaires et les grains interstellaires. *Ann. Astrophys.* **1952**, *15*, 1−6.
(2) Klinger, J.; Ocampo, J.; Schmitt, B. On clathrate hydrates in comets. *Asteroids, Comets, Meteors II* **1986**, 241−243.
(3) Schmitt, B.; Klinger, J. Different trapping mechanisms of gases by water ice and their relevance for comet nuclei. in Diversity and Similarity of Comets. *ESA Spec. Publ.* **1987**, *278*, 613−619.
(4) Smoluchowski, R. Clathrate hydrates in cometary nuclei and porosity. *Month, Not. Roy. Astrom. Soc.* **1988**, *235*, 343−348.
(5) Mousis, O.; Gautier, D.; Bockelée-Morvan, D.; Robert, F.; Dubrulle, B.; Drouart, A. Constraints on the Formation of Comets from D/H Ratios Measured in H_2O and HCN. *Icarus* **2000**, *148*, 513−525.
(6) Prialnik, D.; Benkhoff, J.; Podolak, M. Modeling the structure and activity of comet nuclei. *Comets II* **2004**, 359−387.
(7) Huebner, W. F. Origins of Cometary Materials. *Space Sci. Rev.* **2008**, *138*, 5−25.
(8) Marboeuf, U.; Mousis, O.; Petit, J.-M.; Schmitt, B. Clathrate Hydrates Formation in Short-Period Comets. *Astrophys. J.* **2010**, *708*, 812−816.

(9) Marboeuf, U.; Mousis, O.; Petit, J.-M.; Schmitt, B.; Cochran, A. L.; Weaver, H. A. On the stability of clathrate hydrates in comets 67P/Churyumov-Gerasimenko and 46P/Wirtanen. *Astronomy Astrophys.* **2011**, *525*, A144.
(10) Mousis, O.; Schmitt, B. Sequestration of Ethane in the Cryovolcanic Subsurface of Titan. *Astrophys. J.* **2008**, *677*, L67−L70.
(11) Lewis, J. S. Low Temperature Condensation from the Solar Nebula. *Icarus* **1972**, *16*, 241−252.
(12) Gautier, D.; Hersant, F.; Mousis, O.; Lunine, J. I. Enrichments in Volatiles in Jupiter: A New Interpretation of the Galileo Measurements. *Astrophys. J.* **2001**, *550*, L227−L230.
(13) Gautier, D.; Hersant, F.; Mousis, O.; Lunine, J. I. Erratum: Enrichments in Volatiles in Jupiter: A New Interpretation of the Galileo Measurements. *Astrophys. J.* **2001**, *559*, L183−L183.
(14) Iro, N.; Gautier, D.; Hersant, F.; Bockelée-Morvan, D.; Lunine, J. I. An interpretation of the nitrogen deficiency in comets. *Icarus* **2003**, *161*, 511−532.
(15) Loveday, J. S.; Nelmes, R. J.; Guthrie, M.; Belmonte, S. A.; Allan, D. R.; Klug, D. D.; Tse, J. S.; Handa, Y. P. Stable methane hydrate above 2 GPa and the source of Titan's atmospheric methane. *Nature* **2001**, *410*, 661−663.
(16) Hersant, F.; Gautier, D.; Lunine, J. I. Enrichment in volatiles in the giant planets of the Solar System. *Planet. Space Sci.* **2004**, *52*, 623−641.
(17) Mousis, O.; Lunine, J. I.; Picaud, S.; Cordier, D. Volatile inventories in clathrate hydrates formed in the primordial nebula. *Faraday Discuss.* **2010**, *147*, 509−525.
(18) Mousis, O.; Marboeuf, U.; Lunine, J. I.; Alibert, Y.; Fletcher, L. N.; Orton, G. S.; Pauzat, F.; Ellinger, Y. Determination of the Minimum Masses of Heavy Elements in the Envelopes of Jupiter and Saturn. *Astrophys. J.* **2009**, *696*, 1348−1354.
(19) Blake, D.; Allamandola, L.; Sandford, S.; Hudgins, D.; Freund, F. Clathrate Hydrate Formation in Amorphous Cometary Ice Analogs in Vacuo. *Science* **1991**, *254*, 548−551.
(20) Bockelée-Morvan, D.; Crovisier, J.; Mumma, M. J.; Weaver, H. A. The Composition of Cometary Volatiles. *Comets II* **2004**, 391.
(21) Dauphas, N. The dual origin of the terrestrial atmosphere. *Icarus* **2003**, *165*, 326−339.
(22) Fray, N.; Marboeuf, U.; Brissaud, O.; Schmitt, B. Equilibrium Data of Methane, Carbon Dioxide, and Xenon Clathrate Hydrates below the Freezing Point of Water. Applications to Astrophysical Environments. *J. Chem. Eng. Data* **2010**, *55*, 5101−5108.
(23) Barrer, R. M.; Ruzicka, D. J. Non-stoichiometric clathrate compounds of water. Part 4.-Kinetics of formation of clathrate phases. *Trans. Faraday Soc.* **1962**, *58*, 2262−2271.
(24) Bar-Nun, A.; Dror, J.; Kochavi, E.; Laufer, D. Amorphous water ice and its ability to trap gases. *Phys. Rev. B* **1987**, *35*, 2427−2435.
(25) Kim, H. C.; Bishnoi, P. R.; Heidemann, R. A.; Rizvi, S. S. H. Kinetics of methane hydrate decomposition. *Chem. Eng. Sci.* **1987**, *42*, 1645−1653.
(26) Englezos, P.; Kalogerakis, N.; Dholabhai, P. D.; Bishnoi, P. R. Kinetics of formation of methane and ethane gas hydrates. *Chem. Eng. Sci.* **1987**, *42*, 2647−2658.
(27) Clarke, M. A.; Bishnoi, P. R. Determination of the intrinsic rate constant and activation energy of CO_2 gas hydrate decomposition using in-situ particle size analysis. *Chem. Eng. Sci.* **2004**, *59*, 2983−2993.
(28) Sun, X.; Mohanty, K. K. Kinetic simulation of methane hydrate formation and dissociation in porous media. *Chem. Eng. Sci.* **2006**, *61*, 3476−3495.
(29) Jin, Y.; Matsumoto, K.; Nagao, J.; Shimada, W. Phase Equilibrium Conditions for Krypton Clathrate Hydrate below the Freezing. *J. Chem. Eng. Data* **2011**, *56*, 58−61.
(30) Barrer, R. M.; Edge, A. V. J. Gas hydrates containing argon, krypon and xenon: kinetics and energetics of formation and equilibria. *Proc. R. Soc. London A* **1967**, *300*, 1−24.
(31) Handa, Y. P. Calorimetric determinations of the compositions, enthalpies of dissociation, and heat capacities in the range 85 to 270 K for clathrate hydrates of xenon and krypton. *J. Chem. Thermodyn.* **1986**, *18*, 891−902.
(32) Makogon, T. Y.; Sloan, E. D. Phase Equilibrium for Methane Hydrate from 190 to 262 K. *J. Chem. Eng. Data* **1994**, *39*, 351−353.
(33) Falabella, B. J.; Vanpee, M. Experimental Determination of Gas Hydrate Equilibrium below the Ice Point. *Ind. Eng. Chem. Fundam.* **1974**, *13*, 228−231.
(34) Roberts, O. L.; Brownscombe, E. R.; Howe, L. S.; Ramser, H. Constitution Diagrams and Composition of Methane and Ethane Hydrates. *Oil Gas J.* **1940**, *39*, 37−41.
(35) Deaton, W. M.; Frost, E. M. Gas Hydrates and Their relation to Operation of Natural-Gas Pipelines. *U. S. Bur. Mines, Monogr.* **1946**, *8*, 1−101.
(36) Yasuda, K.; Ohmura, R. Phase Equilibrium for Clathrate Hydrates Formed with Methane, Ethane, Propane, or Carbon Dioxide at Temperatures below the Freezing Point of Water. *J. Chem. Eng. Data* **2008**, *53*, 2182−2188.
(37) Mohammadi, A. H.; Richon, D. Ice-Clathrate Hydrate-Gas Phase Equilibria for Air, Oxygen, Nitrogen, Carbon Monoxide, Methane, or Ethane plus Water System. *Ind. Eng. Chem. Res.* **2010**, *48*, 3976−3979.
(38) Stackelberg, M. v.; Müller, H. R. Feste Gashydrate II struktur und Raumchemie. *Z. Elektrochem.* **1954**, *58*, 25−39.
(39) Miller, S. L. The occurrence of gas hydrates in the solar system. *Proc. Natl. Acad. Sci. U.S.A.* **1961**, *47*, 1798−1808.
(40) Handa, Y. P. Compositions, enthalpies of dissociation, and heat capacities in the range 85 to 270 K for clathrate hydrates of methane, ethane, and propane, and enthalpy of dissociation of isobutane hydrate, as determined by a heat-flow calorimeter. *J. Chem. Thermodyn.* **1986**, *18*, 915−921.
(41) Marboeuf, U.; Schmitt, B.; Petit, J.-M.; Mousis, O.; Fray, N. A cometary nucleus model taking into account all phase changes of water ice: amorphous, crystalline, and clathrate. *Astonomy Astrophys.* **2012**, *542*, A82.
(42) Chao, J.; Wilhoit, R. C.; Zwolinski, B. J. Ideal gas thermodynamic properties of Ethane and Propane. *J. Phys. Chem. Ref. Data* **1973**, *2*, 427−437.

ARTICLE 4

Marboeuf U., Schmitt B., Petit J.-M., Mousis O. and Fray N. (2012)

A cometary nucleus model taking into account all phase changes of water ice: amorphous, crystalline, and clathrate.

***Astronomy and Astrophysics,* 542, A82**

A&A 542, A82 (2012)
DOI: 10.1051/0004-6361/201118176

Astronomy & Astrophysics

A cometary nucleus model taking into account all phase changes of water ice: amorphous, crystalline, and clathrate⋆

U. Marboeuf[1], B. Schmitt[1], J.-M. Petit[2], O. Mousis[2], and N. Fray[3]

[1] UJF-Grenoble 1/CNRS-INSU, Institut de Planétologie et d'Astrophysique de Grenoble (IPAG), UMR 5274, 38041 Grenoble, France
e-mail: marboeuf@obs.ujf-grenoble.fr
[2] Institut UTINAM, CNRS-UMR 6213, Observatoire de Besançon, BP 1615, 25010 Besançon Cedex, France
[3] CNRS, UMR 7583, Université Paris-Est et Paris Diderot, Laboratoire Inter-Universitaire des Systèmes Atmosphériques, LISA/IPSL, Créteil, France

Received 29 September 2011 / Accepted 13 March 2012

ABSTRACT

Context. Current theories, models of cometary nuclei and of ice formation in the protoplanetary disk, and laboratory studies suggest that cometary materials could be formed of pure crystalline water ice, amorphous water ice, clathrate hydrate, or a mixture of these structures of water ice. However, current models of cometary nuclei consider only two forms of ice during the thermodynamic evolution of comets: amorphous and crystalline water ices.

Aims. In this work, we have developed a model of cometary nucleus that takes into account all water ice structures and phase changes in order to predict the outgassing profile of volatile molecules that could be measured by the Rosetta mission and can be used to constrain the structural type of ice existing in the interior of the Comet 67P/Churyumov-Gerasimenko, the target comet of the Rosetta mission, and, hopefully, its initial composition.

Methods. We added the physic of formation/dissociation of clathrate hydrates in addition to others physical processes that are taken into account in models without clathrate hydrates. All thermal changes, as well as the release and trapping of gas with water phase changes are taken into account.

Results. This model describes heat transmission, latent heat exchanges, all water ices structures and transitions (amorphous-to-pure crystalline, amorphous-to-clathrate hydrates and pure crystalline-to-clathrate hydrates and vise versa), sublimation/recondensation of volatile molecules in the nucleus, gas diffusion, gas released and trapped by crystallization and clathrate formation/dissociation processes, as well as gas and dust release and mantle formation at the surface. Applying this model to the comet 67P/Churyumov-Gerasimenko, results show different outgassing profiles of volatiles molecules from the nucleus depending on the water ice structure, the distribution of volatile molecules between the "trapped" and "condensed" states in the nucleus and the thermal inertia of its porous matrix.

Conclusions. Given these results, we pretend that this model is able to constrain the water ice structure and chemical composition in comets from outgassing profiles of volatile molecules, and especially those of the target comet of the Rosetta mission.

Key words. comets: general – comets: individual: 67P/Churyumov-Gerasimenko

1. Introduction

Comets are currently supposed to be the most primitive objects in the solar system. Their chemical composition suggest that cometary material is formed at low temperature in colder regions of the protoplanetary disk or in the interstellar medium (ISM), where most volatile molecules can condensate. The chemical composition and water ice structure included in cometary material are mainly affected by temperature and molecular composition of the surrounding environment both during their formation and their thermodynamical evolution in the protoplanetary disk and solar system after their incorporation in comets. Experimental and theoretical studies have shown that cometary material could be formed of pure crystalline or amorphous water ice, clathrate hydrates, or a mixture of these structures of water ice, depending of the location of formation of the comet in the solar system. The amorphous water ice structure could have been formed in the solar nebula that gave birth to the solar system, or in the ISM. This structure of ice could have been preserved in colder region of solar system (Heliocentric distance $R_h \geq 12$ UA, Kouchi et al. 1994) before their incorporation in comets. In the frame of this hypothesis, the water ice structure of comets is currently assumed to be initially amorphous in numerical models (Espinasse et al. 1991; Mekler & Podolak 1994; Enzian et al. 1997; Orosei et al. 1999; Capria et al. 2003; Prialnik et al. 2004; Mousis et al. 2005; Huebner et al. 2006). The amorphous ice structure becomes crystalline in subsurface layers as the comet nucleus is progressively and repeatedly heated by turning around the Sun. Up to now only these two icy structures are considered by current models of cometary nuclei. However, models of ice formation in the protoplanetary disk (Lewis 1972; Gautier et al. 2001a,b; Iro et al. 2003; Hersant et al. 2004; Marboeuf et al. 2008; Mousis et al. 2008, 2009, 2010) show that comets formed beyond 15 UA could be fully made up of crystalline water ice and clathrate hydrates. Moreover, as shown by Marboeuf et al. (2010, 2011), this structure of water ice could form within all cometary nuclei, whatever the initial water ice structure considered in comets (amorphous or pure crystalline).

The clathrates are crystalline solids composed of water and gas. The water molecules structure is organized in the form of

⋆ Appendix A is only available in electronic form at http://www.aanda.org

cages which are stabilized by the inclusion of gas molecules. Each cage contains a single gas molecule trapped thanks to van der Waals interactions. The formation and decomposition of this structure of ice inside cometary nuclei would add sinks and sources of volatile molecules and of energy. In addition, the thermodynamic properties of clathrate differs from those of the pure crystalline and amorphous water ice structures and can strongly change the thermal behavior of cometary nuclei. As a result, their formation and decomposition inside the nucleus can generate an outgassing profile of volatile molecules at the surface that differ markedly from that expected from models without formation of clathrate since this structure selectively retains and releases the gases trapped inside. The existence of clathrate inside comets has been discussed since a long time (Delsemme & Swings 1952; Klinger et al. 1986; Schmitt & Klinger 1987; Smoluchowski 1988; Mousis et al. 2000; Prialnik et al. 2004; Huebner 2008; Marboeuf et al. 2010, 2011). The authors proposed that the presence of clathrate in extraterrestrial ices might account for their anomalous volatile molecules retention and release (Blake et al. 1991; Iro et al. 2003). Thus, the existence of this structure of ice has often been invoked in order to account for the appearance of various molecules at particular heliocentric distances before or after perihelion of a comet (Smoluchowski 1988). The possible formation/dissociation of clathrate in cometary nuclei and their implication for the thermal evolution and the degassing of these objects have been poorly studied in numerical models. Only a couple of models of comets including such a structure of ice have already been developed (Houpis et al. 1985; Flammer et al. 1998), but unfortunately the hypotheses about the nucleus composition as well as the physics on which they are based are incorrect: they considered that the icy matrix of the cometary nucleus is initially entirely composed of clathrate and that their dissociation occurs only during the sublimation of H_2O ice at the nucleus surface.

The present work aims to present a model of cometary nucleus, which takes into account all structural water ices and phase changes during the thermal evolution of the comet. All initial water ice structures (amorphous, pure crystalline, clathrate hydrates or a mixture of these structures of water ice) can be taken into account in this model following assumptions considered on the formation location of the comet in the solar system. So, all phases changes of water ice (amorphous $\longrightarrow$ pure crystalline, amorphous $\longrightarrow$ clathrate hydrates and pure crystalline $\longleftrightarrow$ clathrate hydrates) are taken into account following the thermodynamical evolution of the comet around the sun and initial physical assumptions considered in the model. In addition to physical processes that are also taken into account by most other models, we added the physics of formation/dissociation of clathrate within the porous network of the nucleus icy matrix. All thermodynamic changes and gas trapping/release induced by clathrate formation/dissociation are included in this cometary nucleus model. The goal of this model is to be able to interpret the outgassing observations of comets, and in particular the future detailed observations that will be made by the Rosetta mission in order to constrain the chemical composition and the water ice structure in the interior of the target comet 67P/Churyumov-Gerasimenko (hereafter 67P/C-G). This article is organized as follows: in a first step, we present the model and describe the physical processes taken into account. In a second step, we discuss the physical assumptions and the thermodynamic parameters adopted. In a third step, we present the outgassing profiles as a function of heliocentric distance of volatile molecules for a model with the same orbit parameters as 67P/C-G and for different initial water ice structures.

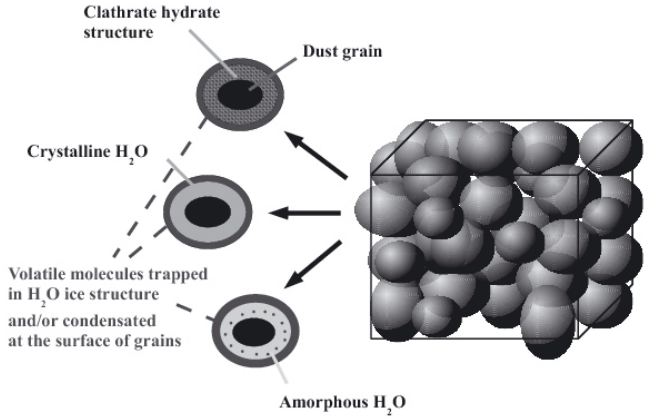

Fig. 1. Schematic view of the interior of a homogeneous comet nucleus composed of icy grains. The matrix of the nucleus can be formed of icy grains with amorphous, crystalline water ice structures, clathrate hydrates or a mixture of these icy grains and water ice structures.

2. Description of the physical nucleus model

The original comet nucleus model we use is the one developed by Marboeuf et al. (2008). This model considers a sphere composed of a porous predefined mixture of water ice, volatile molecules (in gas and solid states) and dust grains in specified proportions. It describes heat transmission, latent heat exchanges, amorphous-to-crystalline ice transition, sublimation/recondensation of volatiles in the nucleus, gas diffusion, as well as gas and dust release and mantle formation at the surface. The comet matter modeled here is composed of refractory grains with an icy mantle composed of water and some other volatile molecules (see Fig. 1). Water ice can be initially amorphous or pure crystalline, depending on the formation location of the body in the solar system. When the ice is amorphous, a fraction of the other volatile molecules can be trapped in the amorphous icy matrix, while the remaining is condensed in the pores as pure ices. When heated, the fraction of volatiles condensed in the pores sublimates first, and then the other fraction trapped within the ice matrix is released during the transition from amorphous to crystalline water ice. The gas released diffuses through the porous matrix and eventually escapes to space at the surface of the object.

In addition to these physical processes that are also taken into account by most other models, our model is able to take into account the clathrate structure, or a mixture of amorphous, pure crystalline water ice and clathrate hydrate, as the initial water ice structure in comets depending on assumptions on the formation of cometary material in the ISM or/and protoplanetary disk, and the formation location of the comet in the solar system. Moreover, we added the physics of clathrate formation and dissociation within the icy porous matrix of our comet nucleus model whatever the initial ice structure considered in the model[1]. Hence, all phase changes of water ice structure are taken into account in this model. All these processes are presented below. The clathrates are ice-like solids formed from

[1] If the initial water ice structure is amorphous, clathrate formation occurs only when water ice is fully crystalline or when the amorphous ice begins to crystallize. We assume that it doesn't occur when water ice is amorphous whatever the volatile molecule considered, although Notesco & Bar-Nun (2000) showed that a clathrate of CH_3OH can be formed when amorphous mixture of water ice with trapped CH_3OH is warmed to about 120 K, before the crystallization of the water structure.

a nonstoichiometric mixture of water and low-molecular mass gases. The water molecules structure is organized in the form of cages which are stabilized by the inclusion of gas molecules. Each cage contains a single gas molecule trapped thanks to van der Waals interactions but it is possible to trap several different molecules in a structure composed of several cages. There are mainly two types of structure of clathrates whose formation depends on the size of the trapped molecules (Handa 1986a; Sloan & Fleyfel 1992; Sloan 1998; Rydzy et al. 2007). The formation/dissociation of clathrate hydrates occurs by the direct gas-ice interaction between gas phase molecules and crystalline water ice or clathrate hydrate, respectively. The formation of cages becomes possible, and the clathrate is stabilized, when the gas pressure is greater than the equilibrium pressure of the clathrate of this gas. At lower pressure, the cages dissociate. Thus, depending on the sign and amplitude of the difference between the gas pressure in the pores and the clathrate equilibrium pressure (temperature dependent), the volatile molecules can be trapped in, or released by, clathrate at rates determined by the kinetic laws of their formation or dissociation. The possible ranges of formation/dissociation rates are determined from laboratory works. We consider that gas and crystalline water ice or clathrate hydrate can always interact together (see footnote 1). All thermal changes induced by clathrate formation/decomposition are also included in this model, such as the exchange of latent heat during their formation/dissociation and their change in thermal conductivity. Along the orbital evolution of comets, clathrate formation provides a third internal source of energy in addition to the ones of crystallization and gas recondensation and a second sink for volatile molecules (aside gas recondensation). On the other side clathrate dissociation supplies a third source of gas into the porous matrix (with pure volatile ices sublimation and gas released during crystallization) as well as a second sink of energy, in addition to ices sublimation. The transfers of mass and heat in the nucleus that take into account these physical effects are described by the heat diffusion (Sect. 2.1 and Eq. (1)) and gas diffusion (Sect. 2.2 and Eq. (22)) equations given below. In Appendix A, we describe the numerical model of the nucleus to solve the heat and mass equations of conservation. To help the reader to find his/her way through the equations and tables, a list of the principal symbols used in this paper is given in Appendix B. Moreover, in order to facilitate reading of the paper, we have chosen to insert a bullet • in front of paragraphs that define and explain the main physical parameters and assumptions related to the conservation Eqs. (1) and (22).

2.1. Equations of conservation of energy

The heat diffusion through the nucleus is described by the energy conservation equation:

$$\rho c \frac{\partial T}{\partial t} = \nabla \left(K^m \frac{\partial T}{\partial r} \right) - \sum_x H_x^{\rm s} (Q_x^{\rm s} + Q_x^{\rm cr}) + Y^{\rm cr} + Y^{\rm chs} + Y^{\rm cl} \quad \left({\rm J\,m^{-3}\,s^{-1}} \right) \tag{1}$$

with

$$\rho c = \sum_l \rho^l c^l = \sum_x \rho_x^i c_x^i + \rho^d c^d + \rho^{\rm cl} c^{\rm cl} \qquad \left({\rm J\,m^{-3}\,K^{-1}} \right) \tag{2}$$

- T is the temperature (K), t the time (s), r the distance (m) from the center of the nucleus and ρ^l the density (kg m^{-3}) of the solid component l of the comet nucleus ($l = d$ for dust, cl for clathrate or i for pure ices of elements x).
- c^l is the specific heat capacity (J kg^{-1} K^{-1}) of the solid component l of the comet nucleus ($l = d$ for dust, cl for clathrate or i for pure ices of elements x).

The specific heat capacity of clathrate is assumed to be the sum of the specific heat capacity of pure water ice and the one of the gas molecules trapped in the clathrate structure as described (Handa 1986a; Handa & Tse 1986) by:

$$\rho^{\rm cl} c^{\rm cl} = \rho_{\rm H_2O}^{\rm cl} c_{\rm H_2O}^i + \sum_x \rho_x^{\rm cl} c_x^{\rm g} \qquad \left({\rm J\,m^{-3}\,K^{-1}} \right) \tag{3}$$

where $\rho_{\rm H_2O}^{\rm cl}$ is the mass density (kg m^{-3}) of water molecules that form the clathrate hydrate structure and $c_{\rm H_2O}^i$ the specific heat capacity (J kg^{-1} K^{-1}) of water ice. $\rho_x^{\rm cl}$ is the mass density (kg m^{-3}) of volatile molecules x that are trapped in the clathrate and $c_x^{\rm g}$ their gas mass heat capacity (J kg^{-1} K^{-1}) at constant volume. Equation (3) assumes that the heat capacity of the empty hydrate lattice is essentially equal to that of water crystalline ice (Handa & Tse 1986). The contribution of the enclathrated guest to the clathrate heat capacity is then given by the constant volume heat capacity of the guest molecule (see Sect. 3.3 for details).

When water ice is amorphous, a fraction of other volatile molecules is trapped inside. The specific heat capacity of this agglomerate becomes then:

$$\rho^{\rm am} c^{\rm am} = \rho_{\rm H_2O}^{\rm am} c_{\rm H_2O}^{\rm am} + \sum_x \rho_x^{\rm tp} c_x^i \qquad \left({\rm J\,m^{-3}\,K^{-1}} \right) \tag{4}$$

where $\rho_{\rm H_2O}^{\rm am}$ is the mass density (kg m^{-3}) of amorphous water ice, $c_{\rm H_2O}^{\rm am}$ its specific heat capacity (J kg^{-1} K^{-1}) and $\rho_x^{\rm tp}$ the mass density (kg m^{-3}) of the volatile molecules trapped in amorphous ice.

- $H_x^{\rm s}$ is the molar latent heat of sublimation of ice x (J mol^{-1}) and $Q_x^{\rm cr}$ (mol m^{-3} s^{-1}) the rate of moles of gas x per unit volume released ($\geq$0) by amorphous ice during the process of crystallization. Note that the energy needed to release the volatile molecules initially trapped in amorphous ice remains unknown and we assume in this work that it is the same as the latent heat of sublimation (see Eq. (1)). $Q_x^{\rm s}$ represents the rate of volatile molecule x (mol m^{-3} s^{-1}) that sublimates/condenses ($\geq$0/$\leq$0) in the pores of the matrix. Its expression is given by the inversion of the gas diffusion Eq. (22) given in Sect. 2.2. This term is present only if the volatile x is condensed, or condenses, in the layer as pure ice otherwise it takes the value 0.
- $Y^{\rm cr}$ is the power per unit volume released during the crystallization process of amorphous water ice, and is described by (Espinasse et al. 1991):

$$Y^{\rm cr} = \frac{H^{\rm cr} \rho_{\rm H_2O}^{\rm am}}{M_{\rm H_2O} \tau^{\rm cr}(T)} \qquad \left({\rm J\,m^{-3}\,s^{-1}} \right) \tag{5}$$

where $H^{\rm cr}$ is the latent heat of crystallization (J mol^{-1}), $M_{\rm H_2O}$ the molar mass of water (kg mol^{-1}), and $\tau^{\rm cr}$ the time (s) of crystallization of the amorphous water ice, as given by Schmitt et al. (1989):

$$\tau^{\rm cr}(T) = 9.54 \times 10^{-14} e^{\frac{5370}{T}} \qquad (s) \tag{6}$$

- $Y^{\rm chs}$ is the power per unit volume exchanged between the gas phase of molecules, which diffuse in the porous network, and the solid matrix described by:

$$Y^{\rm chs} = \sum_x \frac{\partial \rho_x^{\rm g}}{\partial t} c_x^{\rm g} \Delta T \qquad \left({\rm J\,m^{-3}\,s^{-1}} \right) \tag{7}$$

$\frac{\partial \rho_x^g}{\partial t}$ is the change of mass density of the gas x per unit time (kg m^{-3} s^{-1}) and ΔT is the difference of temperature of the gas that diffuse through the matrix from the previous deeper layer at the temperature T_{i+1} (i is the index of the layer, see Appendix A) to current layers at the temperature T_i.

- $Y^{\rm cl}$ is the power per unit volume released/taken during the formation/dissociation of cages (H_2O molecules structure in addition of trapped volatile molecules) of clathrates described by:

$$Y^{\rm cl} = -\sum_x H_x^{\rm cl} Q_x^{\rm cl} \qquad \left(\mathrm{J\,m^{-3}\,s^{-1}}\right) \tag{8}$$

$Q_x^{\rm cl}$ is the number of moles of gas x trapped/released ($\leq 0/\geq 0$) per units volume and time (mol m^{-3} s^{-1}) described in Sect. 2.3 and $H_x^{\rm cl}$ (J mol^{-1}) is the enthalpy of formation/dissociation of clathrate per mole of gas x trapped/released. Although $H_x^{\rm cl}$ is only function of the volatile molecule x trapped/released in/from the clathrate structure, this term takes also into account the energy to form/dissociate the cages of H_2O molecules which trap/release the volatile molecule x. Here, $H_x^{\rm cl}$ is assumed to be constant with temperature (see Sect. 3.3 for details).

Note that, in the process of clathrate formation by crystallization of an amorphous ice mixture, the energy taken or released remains unknown. We assume, from Eq. (1), that the energy taken or released during this process is equal to the latent heat of formation of clathrate of gas x minus the molar latent heat of sublimation of ice $x'' - \sum_x Q_x^{\rm cl}(H_x^{\rm cl} - H_x^{\rm s})''$ since $Q_x^{\rm cl} = -Q_x^{\rm cr}$.

- K^m is the heat conduction coefficient (J s^{-1} m^{-1} K^{-1}) of the porous matrix. This parameter is linked to the porosity and to the contact of icy grains with other. It influences directly, with the porosity, the thermal inertia of the nucleus. Groussin et al. (2007) estimate a low thermal inertia ($\leq$50 W K^{-1} m^{-2} s$^{\frac{1}{2}}$) for the comet 9P/Tempel 1, implying a low heat conductivity ($\leq 3 \times 10^{-3}$ W K^{-1} m^{-1}). Davidsson et al. (2009) re-evalued IR spectra of comet 9P/Tempel 1 obtained by the Deep Impact spacecraft and find a thermal inertia generally high (1000–3000 W K^{-1} m^{-2} s$^{\frac{1}{2}}$), although it may be substantially lower (40–380 W K^{-1} m^{-2} s$^{\frac{1}{2}}$) in specific areas. Using the assumed thermal inertia ($I = \sqrt{\rho c K^m}$) given by Davidsson et al. (2009), the high thermal inertia induces a thermal conductivity between 1 and 10 W K^{-1} m^{-1} while the low thermal inertia induces values between 10^{-2} and 1. Due to the uncertainty of the thermal conductivity of the porous icy matrix, the model is able to take into account either the Russel's formula (1935) expressed below (see Espinasse et al. 1993), and which gives heat conductivity of about 1 W K^{-1} m^{-1}, or the Hertz factor h expressed below (see Kossacki et al. 1999; Davidsson & Skorov 2002; Prialnik et al. 2004; Huebner et al. 2006), used to correct the effective area of the matrix material through which heat flows, and which can impose heat conductivity between 10^{-3} and 1 W K^{-1} m^{-1}.

Russel's formula (1935) (see Espinasse et al. 1993):

$$K^m = \frac{K^{\rm s}[\Psi^{2/3}K^p + (1-\Psi^{2/3})K^{\rm s}]}{K^{\rm s}[\Psi - \Psi^{2/3} + 1] - K^p\Psi^{2/3}[\Psi^{1/3} - 1]} \qquad \left(\mathrm{W\,m^{-1}K^{-1}}\right) \tag{9}$$

where Ψ is the porosity of the matrix and K^p the radiative conductivity across the pores described by Squyres et al. (1985):

$$K^p = 4\epsilon\sigma r_{\rm p} T^3 \qquad \left(\mathrm{W\,m^{-1}K^{-1}}\right) \tag{10}$$

where ϵ is the infrared surface emissivity of the nucleus, σ the Stefan-Boltzmann constant and $r_{\rm p}$ the radius of the pores.

$K^{\rm s}$ is the conductivity of the solid phase of the components (dust and ices) described by:

$$K^{\rm s} = \frac{\sum_l f^l k^l}{\sum_l f^l} = \frac{\sum_x f_x^i k_x^i + f^d k^d + f^{\rm cl} k^{\rm cl}}{\sum_l f^l} \qquad \left(\mathrm{W\,m^{-1}K^{-1}}\right) \tag{11}$$

where f^l is the volume fraction of the component l (with $l = i$ for the solid phase of the icy components x, d for the dust grains and cl for the clathrate) in the solid matrix and k^l its conductivity. Note that the term $f^{\rm cl}k^{\rm cl}$ of the conductivity of clathrate includes the water structure and the gases trapped inside. In this study, the thermal conductivity of the clathrate structure is set independent of the quantity and composition of gases trapped inside because we are missing experimental data to constrain these dependencies (See Sect. 3.3). f^l is given by:

$$f^l = \frac{\rho^l}{(1-\Psi)\rho^{{\rm b},\,l}} \tag{12}$$

where ρ^l is the mass density of the element l by nucleus unit volume and $\rho^{{\rm b},\,l}$ the bulk density of the non-porous solid phase of the component l. For clathrates, $f^{\rm cl}$ gives:

$$f^{\rm cl} = \frac{\rho^{\rm cl}}{(1-\Psi)\rho^{{\rm b,\,cl}}} \tag{13}$$

with $\rho^{\rm cl} = \rho_{\rm H_2O}^{\rm cl} + \sum_x \rho_x^{\rm cl}$.
$\rho_{\rm H_2O}^{\rm cl}$ and $\rho_x^{\rm cl}$ are the masses of H_2O and gas x molecules that form the clathrate per unit volume of nucleus. $\rho^{{\rm b,\,cl}}$ is defined (Tonnet 2007; Thiam 2008) by:

$$\rho^{{\rm b,\,cl}} = \rho_{\rm H_2O}^{{\rm b,\,cl}}\left(1 + \frac{M_{\rm gas}^{\rm cl}}{M_{\rm H_2O} n_{\rm hyd}}\right) \qquad \left(\mathrm{kg\,m^{-3}}\right) \tag{14}$$

$\rho_{\rm H_2O}^{{\rm b,\,cl}}$ is the bulk mass density of water molecules in clathrate (kg m^{-3}) and $M_{\rm gas}^{\rm cl}$ the mean molar mass of gases trapped in the clathrate (kg mol^{-1}) defined as:

$$M_{\rm gas}^{\rm cl} = \sum_x y_x^{\rm cl} M_x^{\rm cl} \qquad \left(\mathrm{kg\,mol^{-1}}\right) \tag{15}$$

$M_x^{\rm cl}$ is the molar mass of the gas x and $y_x^{\rm cl}$ the molar fraction of gas x trapped in the clathrate. $n_{\rm hyd}$ is the hydrate number defined as the molecular ratio $\frac{H_2O}{\rm gas}$ in the clathrate:

$$n_{\rm hyd} = \frac{N_{\rm H_2O}^{\rm cl}}{N_{\rm gas}^{\rm cl}} = \frac{M_{\rm gas}^{\rm cl}}{M_{\rm H_2O}} \frac{\rho_{\rm H_2O}^{\rm cl}}{\rho_{\rm gas}^{\rm cl}} \tag{16}$$

where $N_{\rm gas}^{\rm cl}$ and $\rho_{\rm gas}^{\rm cl}$ are respectively the number and the mass density (kg m^{-3}) of gas molecules that are trapped in the clathrate structure, and $N_{\rm H_2O}^{\rm cl}$ the number of water molecules forming the bulk clathrate structure. This term gives the number of water molecules for each gas molecule trapped (see Sect. 3.3 for its value).

Hertz factor formula: If the area of contact between adjoining grains is small, the resultant conductivity of the medium will be reduced even further by a Hertz factor h (Davidsson & Skorov 2002; Prialnik et al. 2004):

$$K^m = hK^s \qquad \left(\mathrm{W\,m^{-1}K^{-1}}\right) \tag{17}$$

K^s is the conductivity of the solid phase of the components (dust and ices) described by Eq. (11). h is expressed by considering two spheres of radius R that are pressed together and have a contact area of radius r_c, so $h \approx \frac{r_c^2}{R^2}$ (Kossacki et al. 1999). Its value can vary between 10^{-3} and 1 (see Davidsson & Skorov 2002; Huebner et al. 2006; Volkov & Lukyanov 2008).

2.1.1. Conservation of energy at the surface of the nucleus

At the surface, the local temperature is given by a thermal balance between the solar energy absorbed by the surface on one side and on the other side, from left to right, its thermal emission, the heat diffusion towards the interior and the energy of sublimation of the ice species existing at the surface:

$$\frac{C_s(1-A_b)}{R_h^2}\max(\cos\,\xi, 0) = \epsilon\sigma T^4 + K\frac{\partial T}{\partial r} + \sum_x \alpha_x^i H_x^s \varphi_x + \sum_x y_x^{cl} H_x^{cl} \alpha_{H_2O}^{cl} \varphi_{H_2O} \qquad (\mathrm{W\,m^{-2}}) \tag{18}$$

where C_s is the solar constant (W m^{-2}), A_b the bolometric Bond albedo, R_h the heliocentric distance (UA), and ξ the solar zenith distance calculated as (see Sekanina 1979; Fanale & Salvail 1984; Prialnik 2004; Gortsas et al. 2011):

$$\cos\,\xi = \cos\,\theta\,\cos\left(\omega\,(t-t_0)\right)\,\cos\,\theta_s + \sin\,\theta\,\sin\,\theta_s \tag{19}$$

θ is the latitude on the comet, t the time since the beginning of the computation (s), t_0 the initial time of computation (s), and $\omega = \frac{2\pi}{P_r}$ where P_r is the nucleus rotation period of the comet (s). θ_s is the cometocentric latitude of the sub-solar point given by:

$$\sin\,\theta_s = \sin\,\delta\,\sin\left(\phi+\gamma\right) \tag{20}$$

δ is the obliquity, ϕ the argument of the sub-solar meridian at perihelion. The true anomaly γ of the comet is calculated by using Kepler's equations.

Note that using a 1D model, the insertion of the term $\cos\,\theta\,\cos\left(\omega\,(t-t_0)\right)$ in the left hand side of Eq. (18) assumes that the lateral transfers of energy are negligible in the comet. Also, using this formula, we study the thermodynamic and outgassing behavior of the comet only on one point on it surface.

ϵ is the infrared surface emissivity, σ the Stefan-Boltzmann constant (W m^{-2} K^{-4}), α_x^i the surface fraction covered by the pure ice species x (including H_2O) and $\alpha_{H_2O}^{cl}$ the one covered by water molecules that form the clathrate structure. y_x^{cl} is the molar fraction of the volatile x (relative to water) initially trapped in the clathrate structure. φ_x is the free sublimation rate of the species x (mol m^{-2} s^{-1}) given by the expression of Delsemme & Miller (1971):

$$\varphi_x(T) = \frac{P_x^s(T)}{\sqrt{2\pi M_x RT}} \qquad \left(\mathrm{mol\,m^{-2}\,s^{-1}}\right) \tag{21}$$

where M_x is the molar mass of the corresponding gas specie, $P_x^s(T)$ its vapor sublimation pressure (Pa), and R the perfect gas constant (J mol^{-1} K^{-1}). Here, the last term of Eq. (18) assumes that the water molecules still present in the clathrate structure at the surface of the nucleus (if not dissociated before) are subjected to the same rate of sublimation as for pure crystalline ice.

2.2. Equation of conservation of mass

For each molecule x the diffusion of gas through the matrix pores is described by the mass conservation equation:

$$\frac{\partial \rho_x^g}{\partial t} = M_x\left(\nabla.\left(\Phi_x\right) + Q_x^{cr} + Q_x^s + Q_x^{cl}\right) \qquad \left(\mathrm{kg\,m^{-3}\,s^{-1}}\right) \tag{22}$$

- Q_x^{cr} is the the net sources of gas x released in the pores during water ice crystallization:

$$Q_x^{cr} = J_x^{am}\frac{\rho_{H_2O}^{am}}{M_{H_2O}\tau^{cr}(T)} \qquad \left(\mathrm{mol\,m^{-3}\,s^{-1}}\right) \tag{23}$$

  where J_x^{am} is the initial x/H_2O mole fraction of the gas x trapped in amorphous ice.
- Q_x^s and Q_x^{cl} are respectively the pure ice sublimation/condensation (see part 2.1) and clathrate dissociation/formation (see part 2.3) rates. ρ_x^g is the mass density of gas x.
- Φ_x its molar flow given by:

$$\Phi_x = G_x\frac{\partial P_x}{\partial r} \qquad \left(\mathrm{mol\,m^{-2}\,s^{-1}}\right) \tag{24}$$

  where P_x is the partial pressure of gas x (Pa) and G_x its diffusion coefficient (mol m^{-1} s^{-1} Pa^{-1}).

The flux of gas diffusing through the porous matrix can be a free molecular (Knudsen) flow (see 1. below), a visquous flow (see 2. below), or a mixture of them (see 3. below). The mechanism governing the diffusion of volatile molecules is determined by the Knudsen number K^n of the gas mixture:

$$K^n = \frac{\lambda}{2r_p} \tag{25}$$

r_p is the average radius of the pores (m) and λ the mean free path of molecules from kinetic theory:

$$\lambda = \frac{k_B T}{\sqrt{2}\pi d^2 P_t} \qquad (\mathrm{m}) \tag{26}$$

k_B is the Boltzmann constant (J K^{-1}), P_t the total pressure of the gas (Pa) and d the mean diameter of gas molecules defined as:

$$d = \sum_x \frac{P_x}{P_t} d_x \qquad (\mathrm{m}) \tag{27}$$

where d_x is the diameter of molecule x (m) and P_x its partial pressure (Pa).

1. When K^n is greater than 1, molecule-wall collisions predominate over molecule-molecule collisions (Knudsen 1909; Kast & Hohenthanner 2000). The gradient of the partial pressure is the driving force and each specie can diffuse independently of others. The gas diffusion through the porous matrix is then described by Knudsen (free-molecule) flow and the coefficient of diffusion G_x of the molecule x in a single cylindrical pore is (Mekler et al. 1990):

$$G_x^k(T) = \frac{8}{3\pi}\frac{r_p}{\tau}\sqrt{\frac{\pi}{2M_x RT}} \qquad \left(\mathrm{mol\,m^{-1}\,s^{-1}\,Pa^{-1}}\right) \tag{28}$$

   with τ the tortuosity that is defined as the ratio of the length of a pore to the distance between its ends. Further on, we adopt the appropriate value $\sqrt{2}$ for the tortuosity of an unconsolidated medium (Carman 1956; Mekler et al. 1990; Kossacki & Szutowicz 2006).

2. When K^n is less than 10^{-2}, the mean free path of molecules is much lower than the diameter of pores: molecule-molecule collisions predominate over molecule-wall collisions. The gas diffusion is then viscous and the coefficient of diffusion G_x for a single cylindrical pore becomes (see Espinasse et al. 1991):

$$G_x^v(T, P_t) = \frac{r_p^2}{\tau}\frac{P_t}{8\eta RT} \qquad \left(\mathrm{mol\,m^{-1}\,s^{-1}\,Pa^{-1}}\right) \tag{29}$$

with η the dynamic viscosity of gas derived from kinetic theory of gases as:

$$\eta = \frac{1}{3}\rho_t v^t \lambda \qquad \left(\mathrm{kg\,m^{-1}\,s^{-1}}\right) \tag{30}$$

ρ_t is the total gas density (kg m^{-3}) and v^t the thermal velocity of molecules:

$$v^t = \sqrt{\frac{8RT}{\pi M_{gas}}} \qquad \left(\mathrm{m\,s^{-1}}\right) \tag{31}$$

where M_{gas} is the molar mass of the gas (kg mol^{-1}).

3. For values of K^n between 10^{-2} and 1 (transition region between the free-molecule flow and the viscous flow), the mean free path of molecules is of the size of the pore diameter. In this region, there are molecule-molecule collisions as well as molecule-wall collisions: mass transfer occurs due to Knudsen flow and viscous flow. The total flux can then be described as the sum of the fluxes due to viscous flow and due to Knudsen flow (Knudsen 1909; Kast & Hohenthanner 2000). Fanale & Salvail (1987) used, for the transition regime of CO_2 in porous material, the following equation:

$$G_x(T) = 0.9G_x^k(T) + 0.5G_x^v(T) \qquad \left(\mathrm{mol\,m^{-1}\,s^{-1}\,Pa^{-1}}\right). \tag{32}$$

Coefficients 0.9 and 0.5 are issue from an adaptation of an equation presented by Scheidegger (1974). These coefficients are valid only for CO_2 since they may be different for other chemical species (Bouziani & Fanale 1998). However, they have been used by Espinasse et al. (1991) for the transition regimes of CO, CO_2 and H_2O. In this work, we will use it regardless of the chemical specie that diffuse in the porous matrix in this transition region since no experimental data concerning the flow of other species has been reported in the literature.

In the case of a parallel network arrangement of cylindrical pores[2], the total molar flux of gas x perpendicular to the surface can be written as:

$$Z_x^{tot} = N_p \Phi_x \pi r_p^2 \qquad \left(\mathrm{mol\,m^{-2}\,s^{-1}}\right) \tag{33}$$

where N_p is the number of cylindrical pores per unit of surface (m^{-2}) defined as:

$$N_p = \frac{\Psi}{\pi r_p^2 \tau} \qquad \left(\mathrm{m^{-2}}\right). \tag{34}$$

[2] A randomly arranged pore network which opens and closes during the physico-chemical differention of the nucleus would be definitely a better physical representation of the cometary environment but the use of the 1D model forces us to use a parallel arrangement.

We finally obtain:

$$Z_x^{tot} = \frac{\Psi}{\tau}\Phi_x \qquad \left(\mathrm{mol\,m^{-2}\,s^{-1}}\right) \tag{35}$$

Note that the gas is always supposed to be perfect so we can link the pressure P to the gas density following the ideal gas equation of state $P_x = \rho_x^g \frac{RT}{M_x}$.

All ices in a cell of the matrix are at the same temperature. Similarly, all gases are in thermal equilibrium at the temperature of the corresponding cell. When the volatile species x is condensed in the pores, we impose equilibrium between the gas and solid phases. Hence the partial gas pressure equals the vapor saturation pressure: $P_x = P_x^s(T)$. Otherwise the value of the pressure is obtained by solving the gas diffusion equation (Eq. (22)).

2.3. Term of formation/dissociation of clathrates Q_x^{cl}

The presence of several volatile molecules in the gas phase of the porous network can generate the formation of multiple guest (hereafter MG) clathrates whose equilibrium pressure varies as a fonction of the gas phase composition and the temperature. The equilibrium pressure of the MG clathrate P_{MG}^{cl} is given by (Lipenkov & Istomin 2001; Hand et al. 2006):

$$P_{MG}^{cl} = \left(\sum_x \frac{y_x^g}{P_x^{cl}}\right)^{-1} \qquad (\mathrm{Pa}) \tag{36}$$

where y_x^g is the mole fraction of the volatile x in the gas phase and P_x^{cl} the equilibrium pressure of the corresponding single guest clathrate. This equation is only valid when the fractions of volatile molecules in the gas phase and trapped in clathrate are identical, but we will use it regardless, in the absence of a current better and well established model. Indeed some statistical thermodynamic models aims at determining the clathrate equilibrium pressure and the composition of the gas trapped inside MG clathrates in equilibrium with the gas phase (van der Waals & Platteeuw 1959; Parrish & Prausnitz 1972; Lunine & Stevenson 1985; Thomas et al. 2009) but they depend on several parameters that are poorly constrained or unknown for some molecules. So we decided here, as a first step, to use the equilibrium pressure of clathrates given by Eq. (36) whatever the difference in composition between the gas phase and the gas in MG clathrates.

When the total gas pressure P_t in the pores is higher than the equilibrium pressure of the MG clathrate P_{MG}^{cl}, the water ice and the gas phase can combine to form cages of clathrate at the surface of the pores. Below the equilibrium pressure, the cages become unstable leading to their dissociation into crystalline water ice and to the release of the trapped gases.

The molar amount of volatile molecules trapped or released by unit of nucleus volume and per second during the formation/dissociation ($\leq 0/\geq 0$) of clathrate is given by the term Q_{gas}^{cl}:

$$Q_{gas}^{cl} = -(1-\Psi) f^l q_k^{cl} \qquad \left(\mathrm{mol\,m^{-3}\,s^{-1}}\right) \tag{37}$$

f^l is the volume ratio (see Eq. (12)) of water ice ($l = i$ when formation of clathrate occurs) or of clathrate in the solid matrix ($l = cl$ when dissociation of clathrate occurs), q_k^{cl} is the number of moles of gas trapped ($k = f$ for formation of clathrate) or released ($k = d$ for dissociation of clathrate) by the clathrate per unit volume of solid water ice (formation) or of clathrate (dissociation) and per second described by

(Sun & Mohanty 2006; Clarke & Bisnoi 2004; Englezos et al. 1987; Kim et al. 1987; Schmitt 1986):

$$q_k^{\rm cl} = \lambda_k^{\rm cl} A_{\rm s} \left(P_{\rm t} - P_{\rm MG}^{\rm cl}\right) \qquad \left({\rm mol\,m^{-3}\,s^{-1}}\right) \tag{38}$$

$\lambda_k^{\rm cl}$ (mol m^{-2} Pa^{-1} s^{-1}) is the kinetic parameter of formation ($k = f$) or dissociation ($k = d$) of clathrate, $P_{\rm t}$ the total gas pressure, $P_{\rm MG}^{\rm cl}$ the equilibrium pressure of MG clathrate given by Eq. (36) and $A_{\rm s}$ (m^{-1}) the reaction surface area per unit of volume of solid reactant defined as the total surface area of the pores $S_{\rm p}$ divided by the volume of solid:

$$A_{\rm s} = \frac{S_{\rm p}}{(1-\Psi)V} = \frac{\Psi}{1-\Psi}\frac{2}{r_{\rm p}} \qquad \left({\rm m^{-1}}\right). \tag{39}$$

Note that, when water ice undergoes crystallization, we assume that the rate of clathrate formation is the one of crystallization. This assumption is justified as the mobility of the water molecules, the limiting factor of clathrate formation, is high during crystallization. It is only taken into account if the equilibrium pressure of MG clathrate $P_{\rm MG}^{\rm cl}$ is lower than the total gas pressure $P_{\rm t}$ and if the volatile molecules needed to form cages are in sufficient amount. The number of moles of gas that form clathrate per unit of volume and per second given previously by Eq. (37) becomes then:

$$Q_{\rm gas}^{\rm cl} = -\frac{\rho_{\rm H_2O}^{\rm am}}{M_{\rm H_2O} n_{\rm hyd} \tau^{\rm cr}(T)} \qquad \left({\rm mol\,m^{-3}\,s^{-1}}\right). \tag{40}$$

The number of moles of molecule x trapped/released ($\leq 0/\geq 0$) in/by clathrate per unit of nucleus volume and per second is defined as:

$$Q_x^{\rm cl} = \Gamma_x^l Q_{\rm gas}^{\rm cl} \qquad \left({\rm mol\,m^{-3}\,s^{-1}}\right) \tag{41}$$

where Γ_x^l is the molar fraction of the molecule x trapped in the case of formation of MG clathrate ($l = f$) or released in the case of dissociation of MG clathrate ($l = d$). The calculation of this parameter being somewhat complex and uncertain at low temperature and low pressure, we decided to use here a simple law that gives with a good approximation (see Sect. 3.3 for details) the mole fraction of gas trapped during the formation of cages:

$$\Gamma_x^f = y_x^{\rm g} \frac{P_{\rm MG}^{\rm cl}}{P_x^{\rm cl}} \tag{42}$$

with $\sum_x \Gamma_x^f = 1$. We assume in this model that this equation remains valid whatever the total gas pressure $P_{\rm t}$ of the gas phase in the porous network provided it is greater to the MG clathrate equilibrium pressure $P_{\rm MG}^{\rm cl}$. So, the mole fraction of gas trapped doesn't directly depend of the total gas pressure $P_{\rm t}$ but on the gas composition $y_x^{\rm g}$ and on the equilibrium pressure curves $P_x^{\rm cl}$ of single guest clathrates of molecules x present in the gas phase.

When the clathrate equilibrium pressure is greater than the total gas pressure, the gas trapped in the cages can be released and its composition is then given by:

$$\Gamma_x^d = y_x^{\rm cl} \tag{43}$$

with $\sum_x \Gamma_x^d = 1$. $y_x^{\rm cl}$ is the molar fraction, averaged over the layer, of the volatile x trapped in the clathrate structure (see Sect. 3.3 for details).

In order to help the reader to follow kinetic law adopted and power exchanged during water ice transitions, a resume is given in Fig. 2.

2.4. Porosity and pore radius changes

At the end of each time step Δt, we calculate the variation of mass density of species x in each layer using Q_x^l ($l = i$ for solid phase and cl for clathrates of elements x):

$$\Delta\rho_x^l = M_x Q_x^l \Delta t \qquad \left({\rm kg\,m^{-3}}\right). \tag{44}$$

For a more realistic physical representation of the nucleus, the porosity and the radius of the pores are also recomputed for each layer:

$$\Psi = 1 - \sum_l \frac{\rho^l}{\rho^{{\rm b},\,l}} \tag{45}$$

$$r_{\rm p} = r_{\rm p}^i \sqrt{\frac{\Psi}{\Psi^i}} \qquad ({\rm m}) \tag{46}$$

where ρ^l and $\rho^{{\rm b},l}$ are the mass density of the solid phase and bulk density of the component l, and Ψ^i and $r_{\rm p}^i$ the initial porosity and pores radius.

2.5. Dust ejection and mantle formation at the surface of the nucleus

The radius a of dust grains in the cometary nucleus is given by a power law size distribution (Rickman et al. 1990):

$$N(a){\rm d}a = N_0 a^\beta {\rm d}a \tag{47}$$

β is the power law of the size distribution and N_0 a normalization factor. The grains are initially encased in H_2O ice and can be freed from it by its sublimation at the surface. At this time, the grains can either be ejected from the nucleus or accumulate at its surface thus forming a dust mantle covering the icy layers. A critical radius gives the largest dust grain a^* that can be ejected from the comet. It is computed by comparing the sum of gas drag and centrifugal force with the gravitational attraction of the nucleus (see Orosei et al. 1999):

$$a^* = \frac{3}{4}\frac{\sum_x M_x \Phi_x V_x}{\rho^{{\rm b},\,d}\left(G_{\rm c}\frac{M_n}{R_n^2} - R_n\omega^2\cos^2\theta\right)} \qquad ({\rm m}) \tag{48}$$

where Φ_x is the flux of the gas x at the surface of the comet (kg m^{-2} s^{-1}) and V_x its velocity (m s^{-1}). $\rho^{{\rm b},d}$ is the bulk mass density of the non porous dust grain (kg m^{-3}), $G_{\rm c}$ is the gravitational constant (m^3 kg^{-1} s^{-2}), M_n is the comet nucleus mass (kg) and R_n its radius (m). Dust grains whose radius is smaller than r^* are immediately lost to space, while the larger grains stay at the surface and contribute to the formation of a dust mantle. In this model, no cohesive forces between grains (see description in Huebner et al. 2006) are taken into account. The exact value of a cohesive force would remain very uncertain although it is possible that a cohesive energy between particles dominates compared to gravitational energy of the nucleus (see Huebner et al. 2006). This choice is at least consistent with the assumption that the dust flux is proportional to the gas flux in models and observations (Jewitt et al. 1999; Prialnik et al. 2004; Rosenberg & Prialnik 2009).

3. Discussion about the physical assumptions and thermodynamic parameters adopted

3.1. Volatile molecules considered in the model

At the beginning of the computation the cometary nucleus has a homogeneous composition made of ices and dust. The initial

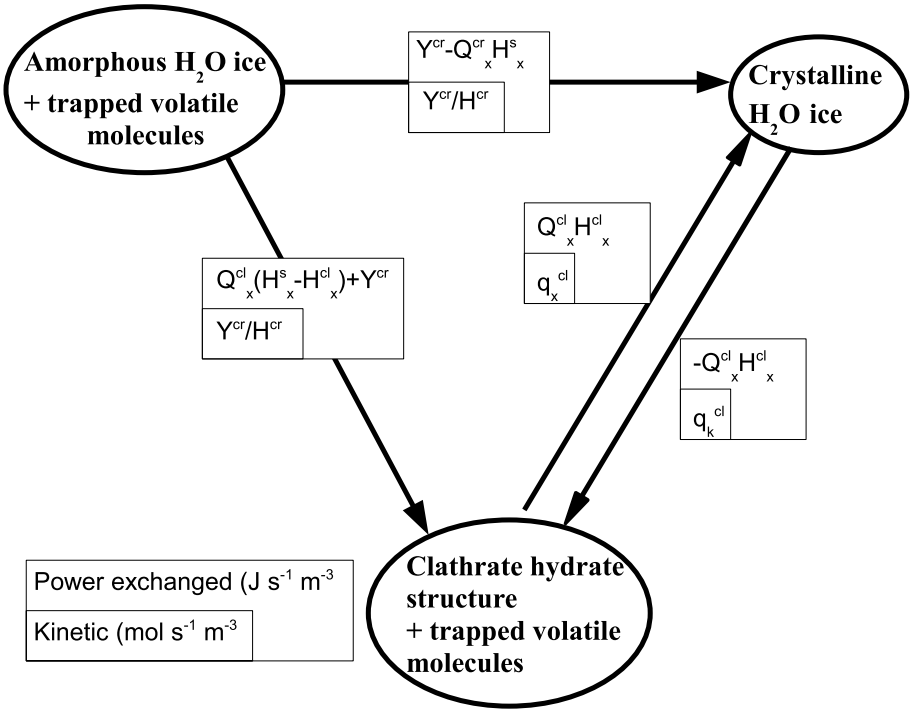

Fig. 2. Schematic view resuming the kinetic law adopted and the power released or taken by water ice structure during its transition.

ice phase of our model can be any type of water ice (amorphous, crystalline, clathrate or a mixture of these structures) mixed with CO, CO_2, CH_4 and H_2S, either as pure ice phases, or trapped in amorphous ice or in clathrate. These four molecules are the most abundant volatile species (production rates relative to water greater than 1%) observed in cometary comas (Bockelée-Morvan et al. 2004) whose data on the equilibrium pressure of single guest clathrates exist. The other equally abundant molecules H_2CO, CH_3OH and NH_3 are not considered in this model for the following reasons. H_2CO is not mostly produced in the nucleus of comets but is rather the result of a distributed source in the coma, which could be provided by the photo and thermal degradation of dust (Fray et al. 2004; Fray et al. 2006; Cottin & Fray 2008). Moreover, no data is available on its stability curves either in the form of clathrate or as a pure condensate (Fray & Schmitt 2009) and thus this molecule cannot be considered in the mixture of ices of our comet nucleus model. In addition, to our best knowledge, no experimental data concerning the stability curve of the CH_3OH clathrate has been reported in the literature (Marboeuf et al. 2008) and the conditions under which it forms stoichiometric hydrates or clathrate (Blake et al. 1991; Notesco & Bar-Nun 2000) is still unclear. Finally, NH_3 doesn't form clathrate, but rather stoichiometric hemihydrates ($2NH_3{-}H_2O$) and/or monohydrates ($NH_3{-}H_2O$) under some conditions (Lewis 1972; Bertie & Shehata 1984; Lunine & Stevenson 1987; Kargel 1998; Moore et al. 2007). The volatile molecules considered in the model can be condensed as pure ices in the porous nucleus network and/or trapped in the amorphous water ice or in the clathrate hydrate structure. Their initial distribution between these states strongly depends on the environment temperature, the molecule (equilibrium pressure, size, polarizability) and their initial abundance in the molecular cloud (Kouchi et al. 1994; Bar-Nun et al. 2007) or in the protoplanetary disk, leading to a very large diversity among trapping efficiencies of various gases in amorphous water ice (Bar-Nun et al. 2007) and clathrate hydrates. However there are some constraints on these trapping efficiencies. Schmitt et al. (1989) showed that amorphous ice can firmly trap other volatile molecules inside its structure only up to a total of 8% (in mole, relative to water) until crystallization occurs (Schmitt et al. 1992). The clathrate hydrate structures can trap until $n_{\rm hyd}$ volatile molecules (hereafter $n_{\rm hyd} = 6$, see Sect. 3.3). However, up to now no general agreement exists on the respective amounts of trapped gas (in amorphous water ice or clathrate hydrate) and gas condensed as pure ices in the initial comet nucleus material. A sensitivity study of the model on different initial scenarios of repartition between species trapped and condensed should thus be conducted (Paper II).

3.2. Thermodynamic parameters

The thermodynamic parameters of the materials are given in Table 1. The modeling of the thermodynamical processes depends on several hypotheses that we will explain here in more details. We also provide the assumptions we made on the values of their parameters.

Assumptions on the phase transition from pure amorphous to crystalline water ice: the phase transition from pure amorphous to crystalline water ice is exothermic and irreversible but, as it has been shown experimentally by Kouchi & Sirono (2001), the crystallization of amorphous mixtures made of water and some other volatile molecules can become endothermic. This is fully included in our model as the overall energy liberated, or absorbed, during the crystallization process is assumed to be the crystallization energy of the water ice minus the sublimation energy of each of the trapped species:

$$Y^{\rm cr} - \sum_x H_x^{\rm s} Q_x^{\rm cr} \text{ (from Eq. (1))} \qquad \left(\mathrm{J\,m^{-3}\,s^{-1}}\right). \tag{49}$$

This assumes that (1) the crystallization energy of the amorphous water structure is the same for mixed H_2O-dominated ices as for pure water ice and that (2) the energy required to expel the guest molecules from the amorphous water lattice is the same as the sublimation energy from its pure solid. Both these energies are possibly larger for mixed ices, and should partly compensate

Table 1. Thermodynamic parameters of the materials.

Symbol	Name	Unity	Value
$\rho^{b,l}$	Bulk density of solid l	kg m^{-3}	
$\rho^{b,d}$	Dust		3000
$\rho_x^{b,i}$	Ices x		
	H_2O		920
	CO		950[a]
	CO_2		1562[b]
	CH_4		507[c]
	H_2S		1100[d]
c^l	Heat capacities of solids	J kg^{-1} K^{-1}	
c^d	Dust		770[e]
c_x^i	Ices x		
	H_2O		
	crystalline		$7.49\ T + 90$[f]
	amorphous		$7.49\ T + 201$[g]
	CO		
	Valid temperature range for values		
	$T \leq 61.55$ K		$36.8\ T - 242.52$[h]
	61.55 K $\leq T \leq$ 68.1 K		1817.49[h]
	CO_2		$484 \log(T) - 1325.03$[i]
	H_2S		
	Valid temperature range for values		
	$T \leq 126.22$ K		$8.91 \times 10^{-2}\ T^2 - 5514.46/T + 406.45$[d]
	$T \geq 126.22$ K		$85.12\ T - 1.623 \times 10^6/T - 2.335 \times 10^4 \log(T) + 1.167 \times 10^5$[d]
k	Heat conductivities k of solids	J s^{-1} m^{-1} K^{-1}	
k^d	Dust		4.2[j]
	Mantle of dust in surface		0.01[k]
k_x^i	Ices x		
	H_2O		
	amorphous		$7.1 \times 10^{-3}\ T^l$
	crystalline		$567/T^l$
	CO		$-1.43 \times 10^{-2}\ T + 8.3 \times 10^{-1}$[m]
	CO_2		$167\,600\ T^{-3.48} + 91/T^n$
	CH_4		$-8.73 \times 10^{-3}\ T \log(T) + 4.25 \times 10^{-2}\ T^o$
H^{cr}	Crystallization latent heat of water ice	J mol^{-1}	1620[p]
P_x^s	Equilibrium pressure of sublimation of ices	Pa	
	CO		
	Valid temperature range for values		
	$T \leq 61.55$ K		$e^{10.43-721.3T^{-1}-1.07410^4T^{-2}+2.34110^5T^{-3}-2.39210^6T^{-4}+9.47810^6T^{-5}} \times 10^5$[q]
	61.55 K $\leq T \leq$ 68.1 K		$e^{10.25-748.2T^{-1}-5.84310^3T^{-2}+3.93910^4T^{-3}} \times 10^5$[q]
	CO_2		
	Valid temperature range for values		
	$T \leq 194.7$ K		$e^{14.76-2571T^{-1}-7.78110^4T^{-2}+4.32510^6T^{-3}-1.20710^8T^{-4}+1.3510^9T^{-5}} \times 10^5$[q]
	194.7 K $\leq T \leq$ 216.58 K		$e^{18.61-4154T^{-1}+1.04110^5T^{-2}} \times 10^5$[q]
	CH_4		$e^{10.51-1110T^{-1}-4341T^{-2}+1.03510^5T^{-3}-7.9110^5T^{-4}} \times 10^5$[q]
	H_2S		
	Valid temperature range for values		
	$T \leq 126.2$ K		$e^{12.98-2707T^{-1}} \times 10^5$[q]
	126.2 K $\leq T \leq$ 187.57 K		$e^{8.933-726T^{-1}-3.50410^5T^{-2}+2.72410^7T^{-3}-8.58210^8T^{-4}} \times 10^5$[q]

References. [a] Shinoda (1969) ; [b] Air liquide ; [c] Stewart (1960) ; [d] Giauque & Blue (1936) ; [e] Prialnik et al. (2004) ; [f] Giauque & Stout (1936) ; [g] Handa & Klug (1988) ; [h] Clayton & Giauque (1932) ; [i] Giauque & Egan (1937) ; [j] Ellsworth & schubert (1983) ; [k] Grun et al. (1993) and Huebner et al. (2006) ; [l] Klinger (1980) ; [m] data fit of Stachowiak et al. (1998) ; [n] data fit of Koloskova et al. (1974) ; [o] data fit of Manzhelii & Krupskii (1968) ; [p] Ghormley (1968) ; [q] expressions given in Fray & Schmitt (2009) .

in the sum, but without experimental knowledge of their values and dependences they cannot be taken into account in our model.

Densities, saturation pressure and enthalpy of sublimation of volatile ices: the density and saturation pressure of all the pure volatile ices taken into account in the model are given in Table 1. Expressions of saturation pressure are taken from the critical compilation by Fray & Schmitt (2009). Enthalpy of sublimation of volatile ices are determined using the Clausius-Clapeyron equation given by:

$$H_x^s = \frac{RT^2}{P_x^s(T)} \frac{dP_x^s(T)}{dT} \qquad \left(\mathrm{J\,mol^{-1}}\right). \tag{50}$$

This equation supposes that the gas is considered as perfect and that the molar volume of the corresponding solid ice phase can be neglected against that of the gas phase.

Heat capacities of volatile ices: the heat capacities of CO, CO_2 and H_2S ices and their variation with temperature are obtained from fits of the data from Clayton & Giauque (1932), Giauque & Egan (1937) and Giauque & Blue (1936) respectively. CO has two crystalline phases (Clayton & Giauque 1932) with a discontinuity of its heat capacity at 61.55 K (temperature of the phase transition). The heat capacity of CH_4 ice is assumed to be the same as the one of CO because of the lack of data. This discontinuity for solid phases of CO and CH_4 does not generate numerical instability in the model, since these volatile ices remain minor elements in relation to water ice and dust in comets. The heat capacity of crystalline water ice comes from Giauque & Stout (1936). The one of amorphous water ice is assumed to be about 111 J kg^{-1} K^{-1} higher than the values for crystalline water ice below the glass transition temperature, this increase being probably due in part to the slightly weaker hydrogen bonding in low-density amorphous ice (Handa & Klug 1988).

Heat conductivities of volatile ices: the heat conductivity of CO ice is obtained by fiting data from Stachowiak et al. (1998) between 20 and 37 K. We assume here that the extrapolation of this law is valid between 37 and 60 K. Thoses of CO_2 and CH_4 ices are obtained by fitting the data from Koloskova et al. (1974) and Manzhelii & krupskii (1968). The heat conductivity of H_2S is assumed to be the same as CO because of the lack of data. The heat conductivity of amorphous ice containing trapped molecules is assumed to be the same as that of pure amorphous ice. The heat conductivity of dust grains is from Ellsworth & schubert (1983). For a dust mantle at the surface of the nucleus, laboratory experiments (see Grün et al. 1993; and Huebner et al. 2006 for a review), showed that the thermal conductivity of dust layers composed by silicate particles is very low (about 10^{-2} to 10^{-3} W m^{-1} K^{-1}). Following these results, we assigned a value of 0.01 W m^{-1} K^{-1} to the thermal conductivity of the dust mantle.

3.3. Modeling parameters of clathrates

The physical parameters for modeling the formation of clathrates are given in Tables 2 and 3. There are mainly two types of structure of clathrate whose cages number and size differ and depend on the size of the trapped molecules. The volatile molecules we consider (CO, CH_4, CO_2, H_2S) can be trapped in clathrates, and all create single guest clathrates of structure I individually (Davidson et al. 1987, Dartois 2011; Handa 1986b; Anderson 2003; Miller 1961). So, we consider in this model that only the structure I is formed inside the comet nucleus during the formation of MG clathrates. The unit cell of structure I is cubic, of volume $V^{\rm cl}$ equal to 1.741×10^{-27} m^3 and contains 46 water molecules ($N^{\rm cl}_{\rm H_2O}$). This structure can trap up to 8 gas molecules respectively in 6 large and 2 small cavities. The ideal hydrate number $n_{\rm hyd}$ (see Eq. (16)) in the case of a maximum occupancy of the cages is then equal to $46/8 = 5.75$. In reality, the occupancy rate of cages depends on the thermodynamic conditions (temperature, gas pressure), and on the size, shape and abundance of the gas molecules trapped. If only the large cages are filled, the hydration number is $46/6 = 7.67$. However, the occupation of the cages by molecules depends on their size but also on their relative abundance for mixed clathrates. It is currently impossible to determine the occupancy of the cages in the thermodynamic conditions existing within cometary nuclei and we therefore fix the hydrate number to 6, closer to real values (Handa 1986a,b; Sloan 1998; Sun & Mohanty 2006), as the nominal value of the number of hydration. This assumption is in good agreement with Avlonitis et al. (2005) who showed that the hydration number decreases slowly with temperature if both types of cavities are occupied by gas.

Table 2. Parameters of the equilibrium curves of single-guest clathrates used in Eq. (51).

Molecule	A	B	Reference (exp. data)
CO	−1890.39	23.3818	Mohammadi & Richon (2010)
CO_2	−2565	23.294	Fray et al. (2010)
CH_4	−2176.2	22.6864	Fray et al. (2010)
H_2S	−3111	22.8931	Hersant et al. (2004)

Notes. A is in K and B is dimensionless. For CO, values of data fit by Mohammadi & Richon (2010).

3.3.1. Heat capacity of clathrates

The heat capacity of the clathrate hydrate structure is assumed, in this model (see Eq. (3)), equal to the sum of the heat capacity of pure crystalline water ice and of the constant volume heat capacity of the guest molecule (the contribution of the enclathrated guest to the crystalline water ice structure). This model predicted successfully the heat capacity of clathrates of small molecules such as Ar, Kr, N_2, O_2, CO and CH_4 (Parsonage & Staveley 1984; Handa 1986c; Handa & Tse 1986; Avlonitis 1994). However, for larger molecules and multicomponent systems trapped in clathrate structure, Eq. (3) is no more accurate since the heat capacity of the empty hydrate lattice differs from that of crystalline water ice (Avlonitis 1994). Calculations show that the heat capacity of the hydrate lattice alone can be either higher or lower than the heat capacity of crystalline water ice, depending on the guest molecule. Similarly, the partial molar heat capacity of the enclathrated gases can be higher or lower than the corresponding experimental ideal gas heat capacity. These differences depend on the size of the guest relative to the two clathrate cavities, the hydrate number (see Eq. (16)), and the temperature (Avlonitis 1994). Since there is not yet enough experimental data for a better estimation of the heat capacity of MG clathrates, we choose to keep the law given by Eq. (3) for MG clathrates, irrespective of the nature of the guest molecules trapped in the clathrate structure.

3.3.2. Equilibrium pressure of single and multiple guest clathrates

The equilibrium pressure curves $P^{\rm cl}_x$ of single guest clathrates of molecules x (with x = CO, CO_2, CH_4 or H_2S) required to calculate the equilibrium pressure of the MG clathrate $P^{\rm cl}_{\rm MG}$ given by Eq. (36), are fits of experimental data by a semi-empirical law:

$$\ln\ P^{\rm cl}_x = A/T + B \tag{51}$$

where A and B are constants (Miller 1961), $P^{\rm cl}_x$ is in Pa and T in K. Their values are given in Table 2.

Table 3. Parameters for clathrate formation/dissociation.

Symbol	Name	Unity	Value
$n_{\rm hyd}$	Hydrate number		6^{α}
$\rho^{\rm cl}_{\rm H_2O}$	Bulk density of water structure of clathrate	kg m^{-3}	790
$k^{\rm cl}$	Heat conductivity of clathrate	W m^{-1} K^{-1}	
	Valid temperature range for values		
	$T \leq 80$ K		$5.47954 \times 10^{-2}\ T - 3.13102 \times 10^{-3}\ T^2$ $+9.40412 \times 10^{-5}\ T^3 - 1.29299 \times 10^{-6}\ T^4$ $+6.38159 \times 10^{-9}\ T^{5\beta}$
	$T \geq 80$ K		$2.1 \times 10^{-4}\ T + 0.43^{\chi}$
$H^{\rm cl}_x$	Absolute enthalpy of dissociation of guest trapped in clathrate	J mol^{-1}	
	CO		$15\,720^{\delta}$
	CO_2		$21\,327^{\delta}$
	CH_4		$18\,130^{\epsilon}$
	H_2S		$25\,404^{\delta}$
$\lambda^{\rm cl}_{n,\,f}$	Nominal kinetics constant of formation of clathrate	mol m^{-2} Pa^{-1} s^{-1}	$3 \times 10^{-13\phi}$
$\lambda^{\rm cl}_{n,\,d}$	Nominal kinetics constant of dissociation of clathrate	mol m^{-2} Pa^{-1} s^{-1}	$30 \times \lambda^{\rm cl}_{n,\,f}{}^{\phi}$

Notes. $^{(\alpha)}$ Sloan (1998); Sun & Mohanty (2006) ; $^{(\beta)}$ data fit of Krivchikov et al. (2005a,b, 2008) ; $^{(\chi)}$ Krivchikov et al. (2005a,b) ; $^{(\delta)}$ provided by the Clausius-Clapeyron equation from data given by references in Table 2 ; $^{(\epsilon)}$ Handa (1986b) ; $^{(\phi)}$ Englezos et al. (1987); Schmitt (1986) .

3.3.3. Enthalpy of formation and dissociation of clathrates

The enthalpy of the clathrate formation reaction $H^{\rm cl}_x$ per mole of encaged gas x, is the heat released when one mole of gas and $n_{\rm hyd}$ moles of crystalline water ice are converted into clathrate at the prevailing conditions of thermodynamic equilibrium. It 's effective value can strongly influence the thermal behavior and the physical evolution of the nucleus. Experimental measurements of the enthalpy of formation/dissociation are not easily obtained and such data are very scarce (Avlonitis 2005). Only the enthalpy of formation of clathrate hydrates of structure I as Xe, CH_4, C_2H_6 (Handa 1986a,b), and clathrate hydrates of structure II as tetrahydrofuran, ethylene oxide (Leaist et al. 1982), Kr, C_3H_8 and iC_4H_{10} (Handa 1986a,b) have been measured, but in a limited temperature range for each molecule, all around or above 200 K. Avlonitis (2005) developed and implemented a method for predicting enthalpies of clathrate formation and demonstrated that a major energetic component in hydrate formation is the heat of enclathration, defined as the residual enthalpy of the enclathrated gas, and that the enthalpy of transformation of crystalline ice into the empty clathrate structure is comparatively small. So, the enthalpy of formation/dissociation of single guest clathrates below the ice point is mainly a property of the gas itself: it depends solely on the nature of the enclathrated molecule. The enthalpy of formation of single guest clathrates is then independent of the clathrate structure, the hydration number $n_{\rm hyd}$, the gas distribution between cavities, the temperature and the pressure (Avlonitis 2005). His model corroborates in every case the experimental data of Handa (1986a,b) and Anderson (2003) as well as the results of Yoon et al. (2003), which were derived by application of the Clausius-Clapeyron equation (See Eq. (50)). This equation is a good approximation to calculate the formation/dissociation heat of single guest clathrates and show fair agreements with experimental data (Handa 1986a,b). Roberts et al. (1940), Barrer & Edge (1967), and Skovborg & Rasmussen (1994) derived analytically this Clausius-Clapeyron equation for simple gas hydrates. Furthermore, the values of enthalpy of clathrate dissociation obtained from the equilibrium pressure data of CH_4 and Xe clathrates measured by Fray et al. (2010), using the Clausius-Clapeyron equation, fit very well the data from Handa (1986a,b), with a relative difference of only 0.2% and 0.9% respectively. Given, the simplicity of the Clausius-Clapeyron equation and the good correlation with experimental values, we can use this equation to obtain approximate values of the enthalpy of dissociation of single guest clathrate hydrates. Moreover, the model of Avlonitis (2005) showed that the values of enthalpy of all of the seven simple gas hydrates (N_2, CH_4, CO_2, Xe, C_2H_6, C_3H_8 and iC_4H_{10}) he studied in the range 180−270 K are so slightly decreasing with temperature that they may be considered approximately constant. However, Anderson (2004), by using the Clausius-Clapeyron equation, has shown a decrease of about 10% of the enthalpy of dissociation of the CH_4 clathrate at 150 K compared to its value at 200−220 K. It is also known that $H^{\rm cl}_x(T)$ vary with T as follows (Makogon & Sloan 1994):

$$H^{\rm cl}_x(T) = H^{\rm cl}_x(T_0) + \int_{T_0}^{T} \Delta C^{\rm cl}_x(T)\mathrm{d}T \qquad \left(\mathrm{J\,mol^{-1}}\right) \tag{52}$$

with $\Delta C^{\rm cl}_x(T)$ the heat capacity difference between the ice and clathrate structures at temperature T:

$$\Delta C^{\rm cl}_x(T) = n_{\rm hyd} C^{i}_{\rm H_2O} + C^{\rm g}_{p,x} - C^{\rm cl}_x \qquad \left(\mathrm{J\,mol^{-1}\,K^{-1}}\right) \tag{53}$$

where $C^{\rm cl}_x$ and $C^{i}_{\rm H_2O}$ are the heat capacities of the clathrate of gas x and of pure water ice, respectively, and $C^{\rm g}_{p,x}$ the heat capacity of the gas x. However, $\Delta C^{\rm cl}_x(T)$ vary with temperature and the guest molecules in the clathrate structure. These variations depend on the size of the guest relative to the cavity, the hydrate number $n_{\rm hyd}$ (see Eq. (14)), and the temperature (Avlonitis 1994). Unfortunately, there is no experimental data allowing to an estimate $\Delta C^{\rm cl}_x(T)$ and hence $H^{\rm cl}_x(T)$ in the 100−200 K range temperature for the guest molecules CO, CO_2 and H_2S used in this paper. However, the heat capacities of clathrate hydrates have been measured over a wide temperature range, moslty from 85 K to 270 K, for clathrate hydrates of structure I as Xe, CH_4, C_2H_6 (Handa 1986a,b), and for structure II as tetrahydrofuran (Leaist et al. 1982; Handa et al. 1984; Yamamuro et al. 1988a), ethylene oxide (Leaist et al. 1982; Yamauro et al. 1990), propylene oxide, 1.3-dioxolane, 2.5-dihydrofuran, 1.3-dioxane (Handa 1985), acetone (Kuratomi et al. 1991), Ar (Yamamuro et al. 1988b), Kr, C_3H_8 and iC_4H_{10} (Handa 1986a,b). Using the gas heat capacities $C^{\rm g}_{p,x}$ of CH_4 (McDowell & Kruse 1963), C_3H_8 and C_2H_6

(Chao et al. 1973), tetrahydrofuran (Chao et al. 1986) and assuming the values of $\frac{5}{2}$R for the noble gases Xe and Kr, we obtain a ratio $\frac{\int_{T_0}^{T} \Delta C_x^{\rm cl}(T)\mathrm{d}T}{H_x^{\rm cl}(T_0)}$ that doesn't exceed 5% between 85 and 270 K for all these single guest clathrates. Given the small variation of $H_x^{\rm cl}(T)$ with temperature, we assume hereafter that it remains constant in the model (see Table 3). Moreover, this assumption is justified since the simple law adopted for the equilibrium pressure of single guest clathrates (Eq. (51)) assumes implicitly that $H_x^{\rm cl}(T)$ provided by using the Clausius-Clapeyron equation (Eq. (50)) remains constant over its valid temperature range.

An additional difficulty remains with the calculation of the enthalpy of MG clathrates since it depends on the type and abundance of the different molecules trapped inside. Recently, Rydzy et al. (2007) studied the influence of incorporation of guest molecules such as C_2H_6, C_3H_8 and CO_2 in methane clathrate on its thermal behavior. They concluded that the enthalpy of formation of MG clathrates increases with increasing size of the guest molecules or more precisely with increasing guest-to-cavity size ratios for the guests in the large cages (and hence the cavity occupation of molecules). This is contradictory to the hypothesis proposed by Sloan & Fleyfel (1992) that the heat of dissociation should be, within size constraints, independent of the type and concentration of the mixed guest gas molecules. In addition, Hachikubo et al. (2008) showed that the dissociation enthalpy of MG clathrates composed of CH_4 and C_2H_6 increases with ethane concentration. To conclude, the value of the enthalpy of formation/dissociation of MG clathrates remains difficult to predict as it depends on temperature, molecular abundances and guest to cavity size ratios. We thus use in our model the simple relation given by Eq. (8) that provides the energy released/taken per unit volume of clathrate formed/dissociated as a linear combination of the single guest clathrate values, following the abundance and type of gas molecule trapped/released in/from the clathrate structure. The values of the enthalpy of formation of the single guest clathrates listed in Table 3 are mostly provided by the Clausius-Clapeyron equation.

3.3.4. Thermal conductivity of clathrates

The thermal conductivity of clathrates differs drastically from that of crystalline water ice both in magnitude and temperature dependence (Krivchikov et al. 2007) because their cages are very poor thermal conductors. In contrast to the crystalline structure of H_2O ice, in which the thermal conductivity falls with increasing temperature following a T^{-1} dependence (for $T > 100$ K), the thermal conductivity of clathrate hydrates mostly increases slightly with increasing temperature (Tse & White 1988). This is a behavior very similar to the ones of the thermal conductivity of amorphous solids (Tse & White 1988; Krivchikov et al. 2005a,b) but with smaller values than for amorphous H_2O ice. There are limited data on the conductivity of clathrates at low temperatures. Their thermal conductivity has been measured on gas hydrates of structure I as CH_4 (Krivchikov et al. 2005a), Xe (Handa & Cook 1987; Krivchikov et al. 2006) and ethylene oxide (Cook & Laubitz 1983), and gas hydrates of structure II as tetrahydrofuran (Ross & Andersson 1982; Tse & White 1988; Andersson & Suga 1996; Krivchikov et al. 2005b), dioxolane (Andersson & Ross 1983; Ahmad & Phillips 1987) and cyclobutanone (Andersson & Ross 1983) in a wide range of temperatures. It is very challenging to measure the bulk thermal conductivity of a homogeneous continuous solid (Krivchikov et al. 2007). This bulk value is thus deduced from the measured effective thermal conductivity of powders using simple models of heat transfer (parallel layers model, Jagjiwanram model, Adler model, Rayleigh model, geometric model or Maxwell model; see Krivchikov et al. 2007, for a brief description) in inhomogeneous media disregarding the thermal resistance of the boundary between the two media. This results in a dispersion of the thermal conductivities values obtained for each guest molecule, but by less than one order of magnitude. Moreover, the thermal conductivity of clathrates depends on the guest molecules trapped inside and decreases when its size increases (Andersson & Ross 1983). However, at high temperature (170 K), the thermal conductivities of clathrates of CH_4, Xe and tetrahydrofuran differ by only 20% (Krivchikov et al. 2007). The temperature dependences of the thermal conductivity of structure I of Xe and CH_4 are similar (Krivchikov et al. 2006) but are different from the ones of structure II of tetrahydrofuran, dioxolane and cyclobutanone. The temperature dependence of the thermal conductivity of Xe and CH_4 is divided into four (I–IV) distinct temperature regimes. The temperature dependences in the intervals I–II (below 54 K) and IV (greater than 95 K) are similar to what is observed in tetrahydrofuran and dioxolane clathrate hydrates of structure II (Krivchikov et al. 2006). The thermal conductivity grows with temperature and the curve has a shape typical for amorphous substances. In the intervals I–II (below 54 K), the temperature dependence of clathrate hydrate is only weakly dependent on the type of clathrate structure (Krivchikov et al. 2006). In these intervals the thermal conductivity is practically independent on the nature of the guest molecules. In the interval IV (above 95 K), the thermal conductivity is approximately proportional to T. In the interval III (54–95 K) the thermal conductivity of the clathrates of Xe and CH_4 exhibits an anomalous behavior: the thermal conductivity decreases by more than 50% as the temperature increases for Xe but is less pronounced for CH_4. For temperatures greater than 80 K (mainly in the interval IV), Krivchikov et al. (2005a,b) fited the thermal conductivity of the single guest clathrate of CH_4 with a good accuracy by a linear dependence with T (law given in Table 3). Moreover, the thermal conductivity of the CH_4 hydrate coincides within the experimental error with the thermal conductivity of the dioxolane clathrate (Krivchikov et al. 2005a,b). At present there is no theoretical model permitting a quantitative description and prediction of the thermal conductivity of clathrate hydrates in a wide range of temperatures (Krivchikov et al. 2006). Thus, in the absence of more data on the thermal conductivity of single and MG clathrates, we adopt the temperature-dependent thermal conductivity of the methane clathrate given in Table 3 and use it independently of the clathrate composition. The thermal conductivity of methane clathrate between 10 and 80 K is obtained by fitting the data from Krivchikov et al. (2005a,b, 2007). Above 80 K, it is approximated by a linear temperature dependence (Krivchikov et al. 2005a,b).

3.3.5. Kinetics of formation and dissociation of clathrates

The kinetics parameters, $\lambda_f^{\rm cl}$, $\lambda_d^{\rm cl}$, of formation/dissociation of clathrates from/to crystalline water ice and gas are poorly constrained at low temperature. Conventionally, two main stages of the clathrate formation process are distinguished (Kuhs et al. 2006). The first stage, relatively rapid, corresponds to the formation of a clathrate film over the crystalline ice surfaces (stage I), and the second, wich dominates when the whole ice grain is covered by a clathrate layer, is the growth of the shell of clathrate

phase around ice grains (stage II). This last stage includes two steps: (1) the clathration reaction itself at the inner (ice-clathrate) as well as external (clathrate-gas) interfaces and (2) gas and water mass transports (diffusion) through the clathrate layer. In this paper, we assume that the first stage mainly dominates the kinetics of formation of the cages at the surface of the pores because the ice matrix is very porous and the grains diameter very small. It means that we consider that the maximum thickness of the clathrate shell that can be formed during this first stage is always larger than the radius of our micron sized grains. The second, much slower, stage of grain growth by diffusion of water molecules and gas through the clathrate shell is then neglected. For the first stage, Schmitt (1986) determined values between 3×10^{-13} and 10^{-12} mol m^{-2} Pa^{-1} s^{-1} for the formation rate of CO_2 clathrate from CO_2 gas and crystalline water ice at temperatures around 200 K. Staykova (2004) and Kuhs et al. (2006) determined values of the kinetics parameter of methane clathrate formation between 245 and 272 K starting from hydrogenated and deuterated ices. They showed a temperature dependence with values ranging between about 9×10^{-14} mol m^{-2} Pa^{-1} s^{-1} at 245 K and 5×10^{-13} mol m^{-2} Pa^{-1} s^{-1} at 263 K. These authors and others (Wang et al. 2002; Staykova et al. 2003; Genov & Kuhs 2003) assumed that the value of the kinetics parameter of formation/dissociation of clathrates follows an Arrhenius-type function of temperature:

$$\lambda_f^{\rm cl} = \lambda_0^{\rm cl} \exp \frac{-E_{\rm a}}{RT} \qquad \left(\text{mol m}^{-2}\,\text{s}^{-1}\,\text{Pa}^{-1}\right) \tag{54}$$

where $\lambda_0^{\rm cl}$ is a constant kinetics parameter and $E_{\rm a}$ the activation energy of the process. Kuhs et al. (2006) calculated $E_{\rm a}$ and find a value (92.8 kJ mol^{-1}) two times greater than the ones of Staykova et al. (2003) and Genov et al. (2004) for the formation of CH_4 and CO_2 clathrates respectively. In the case of CO_2-clathrate, Genov et al. (2004) estimated the activation energies to be 5.5 kJ mol^{-1} at low temperatures and 31.5 kJ mol^{-1} above 220 K, indicating that water molecule mobility plays a considerable role in the clathration reaction. Furthermore, Falenty et al. (2011) find a value of 72.5 kJ mol^{-1} for CO_2 and temperatures between 185 and 195 K. Thus, the physical parameters that may affect the value of $\lambda_f^{\rm cl}$ are multiple: temperature, activity of the ice surface (mobility of water molecules), type of gas molecule, thickness of clathrate formed, thermal history, ... (Schmitt 1986). In the absence of more detailed knowledge of the kinetics laws at low temperature, we assume in this work that the kinetics parameter $\lambda_f^{\rm cl}$ of clathrate formation is constant (no temperature dependence). We also adopt the minimum value measured by Schmitt (1986) and called hereafter the "nominal value", $\lambda_{n,\,f}^{\rm cl}$(3×10^{-13} mol m^{-2} Pa^{-1} s^{-1}). Concerning their decomposition, Schmitt (1986) has experimentally shown that the dissociation of clathrates can be much faster than their formation (up to 30 times faster). However, under some conditions a few monolayers of pure crystalline water ice can form above the clathrate structure, leading to its isolation from the gas phase in the porous network and preventing its dissociation for same time even in the presence of a gas pressure well below the equilibrium pressure (metastability). We thus assume in this model, when the gas pressure is lower than the one of MG clathrate, a nominal kinetics parameter $\lambda_{n,\,d}^{\rm cl}$ for dissociation equal to 30 times the one adopted for the formation of clathrate. However, the influences of the values of $\lambda_f^{\rm cl}$ and $\lambda_d^{\rm cl}$ (and of a possible "decomposition latency time") on the formation/dissociation of clathrates will be studied in next paper. Note that the values of the kinetics parameters used to determine the number of moles of gas trapped or released by the clathrate (Eq. (38)) are valid only in the nucleus layers where water ice is crystallized and not completely converted into clathrate, whatever their temperature. When clathrate formation occurs in layers where amorphous ice is undergoing crystallization, then the crystallisation rate of ice is used (see Eq. (40)).

3.3.6. Composition of volatile molecules both trapped and released in/by clathrate

The main difficulty with the modeling of clathrates is to accurately determine the abundance of molecules trapped inside the clathrate structure (Γ_x^f) in equilibrium with their abundance in the gas phase. For this, it is necessary to know the fractionation factors between the gas and solid phases. Many statistical thermodynamic models (Van der Waals & Platteeuw 1959; Parrish & Prausnitz 1972; Lunine & Stevenson 1985; Sun & Duan 2005; Anderson 2007; Thomas et al. 2009) predict the molecular abundances trapped in the cages of clathrates formed from a gas phase of known composition. They are mostly based on the Van der waals & Platteeuw (1959) statistical model, with some variations. However, these models depend on several parameters that are not well known yet for all molecules. Moreover, these models are fairly well constrained near the triple point of ice but were never validated in the 100−200 K temperature range because there is no experimental data to our knowledge which gives both the composition of guest molecules and that of the gas phase in this range of temperature. So we decided, as a first step, to calculate the molecular abundances trapped during the formation of clathrates by a simple law given by Eq. (42). This equation is determined from the analysis of the data from Kang et al. (2001) and Rydzy et al. (2007). It shows fair agreements (within few %) at the triple point of ice (Kang et al. 2001) and below (Rydzy et al. 2007) with both the molecular abundances in the gas phase and trapped in the clathrate. Secondly, we compared the molecular abundances obtained from this equation with those from the model of Thomas et al. (2009), which is derived from a statistical model of Van der Waals & Platteeuw (1959). The results show that the relative difference between the abundances of molecules trapped in cages calculated by Eq. (42) and the ones determined by the model of Thomas et al. (2009) is about or less than 1% for the most abundant species trapped, which is sufficient for the purposes of our calculations. However, this relative difference increases strongly when the abundance of the molecules trapped becomes low. But in such cases, larger uncertainty also remains about the results obtained by this type of model. Since the calculation of this fractionation parameter is somewhat complex and uncertain at low temperature and low pressure with such statistical models, we decided to use in this paper the law we determined, given by Eq. (42), that provides a good approximation of the main molecular abundances trapped in cages and also strongly simplifies the calculation.

An other difficulty remains with the molar fraction of volatile molecules x released (Γ_x^d, see Eq. (43)) in the gas phase of the porous network when the clathrate structure dissociates (for total pressure $P_{\rm t}$ of the gas phase lower than the MG clathrate equilibrium pressure $P_{\rm MG}^{\rm cl}$). Unfortunately, there is no experimental or theoretical data that allows us to predict the behavior of MG clathrate during its dissociation in the presence of a gas phase out of equilibrium with clathrate, and hence the molar fraction of volatile molecules released. We thus assumed in this model that the molar fraction of the volatile x released by the clathrate structure is the average over the layer of the volatile

Table 4. Initial parameters of the comet nucleus.

Parameter	Name	Unity	Value			
a	Semimajor axis	AU	3.511			
e	Eccentricity		0.632			
R	Radius	km	2^a			
P	Rotational period	h	12.3^a			
θ	Latitude on nucleus surface	degree °	0			
T	Initial temperature	K	30			
ϵ	Infrared surface emissivity		1			
A_l	Bolometric Bond's albedo		0.05			
Ψ^i	Initial porosity	%	70			
τ	Tortuosity		$\sqrt{2}^{a,b}$			
r_p	Average pore radius	m	10^{-4}			
β	power law size distribution of dust grains		-3.5^c			
J_{dust}	dust/ice mass ratio		1			
J_x	Volatile x/H_2O molar ratio	%				
	Initial H_2O ice structure in the model		crystalline	amorphous	clathrate	mixed
J_{CO}	condensed || trapped amorphous | clathrate		14||0|0	11||3|0	1||0|13	8.6||4.33|1
J_{CO_2}	condensed || trapped amorphous | clathrate		5||0|0	2||3|0	2||0|0	4||1|0
J_{CH_4}	condensed || trapped amorphous | clathrate		2||0|0	1.2||0.8|0	1.2||0|1.66	1.2||0.3|0.3
J_{H_2S}	condensed || trapped amorphous | clathrate		2||0|0	0.8||1.2|0	1||0|1.83	1||0.4|0.6

References. [(a)] Kossacki & Szutowicz (2006), [(b)] Carman (1956), Mekler et al. (1990), [(c)] McDonnell et al. (1986), Huebner et al. (2006).

x trapped in the clathrate structure (Eq. (43)). This assumption can be justified as follows: the clathrate structure is stable as long as the volatile molecules trapped remain inside. If some of these molecules are released, they will destabilize the clathrate structure and the resulting dissociation of the cages will expel the remainder of the volatile molecules, whatever the total gas pressure P_t ($P_t \leq P_{MG}^{cl}$) and the molar fraction of the volatile molecules in the gas phase of the porous network. However the assumption that the mole fraction released is simply the average of all the volatile molecules trapped in clathrate in a given nucleus layer is not exact because MG clathrate with variable composition may form by layers depending on the gas composition (if $P_t \geq P_{MG}^{cl}$). The resultant onion-like clathrate grains will not equilibrate between layers, or extremely slowly, due to the extremely slow diffusivity of molecules inside the clathrate structure. Ideally it would thus be necessary to manage the formation/decomposition of each clathrate layer at the grain scale inside each nucleus layer but in a first step the averaging hypothesis allows us to strongly simplify the calculation in the model.

4. Outgassing behavior of four different models of a comet

In this section, we study the outgassing profile of volatile molecules of the comet 67P/C-G, for four models made respectively fully of crystalline ice, amorphous ice, clathrate or a mixture of the three. The goal is to show that the outgassing behavior of the comet strongly depend on the initial water ice structure and that the model is able to constrain the chemical composition and the water ice structure from the analysis of the temporal profiles of gas production of 67P/C-G that will be observed by the Rosetta mission.

4.1. orbital and physical parameters adopted

The orbital and physical parameters adopted in this paper for the nucleus are the ones of the comet 67P/C-G given in Table 4. At the beginning of the computation, the cometary nucleus is assumed to have a homogeneous composition made of ices and dust. In this section, we consider four models whose initial ice phase is assumed to be composed respectively of crystalline water ice, amorphous water ice, clathrate hydrates or a mixture of the three (called hereafter respectively crystalline, amorphous, clathrate and mixed models), all mixed with pure solid CO, CO_2, CH_4 and H_2S. In this study, it is assumed that no clathrate formation/dissociation occurs in the amorphous and crystalline models. Table 4 gives the initial x/H_2O (J_x) mole fractions of the species x (x = CO, CO_2, CH_4 or H_2S) condensed either as pure ices in the porous network or trapped in the water ice following its structure: amorphous or clathrate[3]. The values of J_X (sum of the three states) of all models are consistent with the observations in cometary comae of molecular species that are released directly from the nucleus (Bockelée-Morvan et al. 2004).

Whatever the model, we adopt only one nominal global initial composition of the nucleus with about 14% of CO, 5% of CO_2, 2% of CH_4 and H_2S relative to water molecules. As discussed in the Sect. 3.1, the abundance of trapped species in amorphous water ice depends on many parameters. As no reliable experimental data exists on the composition of mixed gas trapped in amorphous ice, we therefore choose, for the amorphous model, one nominal arbitrary set of plausible distribution of the volatile molecules between the states "trapped inside amorphous water ice" (up to a total of 8% in mole, Schmitt et al. 1992) and "condensed as pure ice" (thus segregated from water ice) in the porous network, considering the equilibrium pressure of species at very low temperature (hereafter 30 K) and our current knowledge on trapping processes. For the crystalline model, the volatile molecules are only in the state "condensed as pure ice". For the clathrate model, the distribution between the states "trapped inside clathrate structure" (up to about 17% in mole) and "condensed as pure ice" come from Mousis et al. (2010). CO, CH_4 and H_2S represent respectively 79%, 10% and 11% of the molecules trapped in the clathrate structure. The "mixed" model is arbitrarily composed of 33% of each of the three water ice structures presented before.

[3] No volatile molecule is trapped in crystalline ice since no experiment has shown this possibility.

The value of the dust/ice ratio $J_{\rm dust}$ is assumed to be equal to 1 in all models, about the value indicated for 1P/Halley by the Giotto-DIDSY measurements (McDonnell et al. 1987) and prescribed by Greenberg's (1982) interstellar dust model (Tancredi et al. 1994). In this work, we assume a power of order −3.5 for the size distribution of dust grains (McDonnell et al. 1986; Huebner et al. 2006) with a cut-off at a radius of 1 cm (Prialnik 1997). The initial temperature is assumed to be equal to 30 K. Davidsson & Gutierrez (2005) give a density of 100−600 kg m^{-3} for the comet 67P/Churyumov-Gerasimenko, leading to porosities greater than 60%. Lamy et al. (2007) estimated the mean nucleus density at ≈370 kg m^{-3}. Note that these values should be taken with caution, since most of these estimates are based on many assumptions and are generally regarded as very uncertain (Richardson et al. 2007; Weissman et al. 2004). Here, we have chosen to test a porosity of 70% leading to a density of about 430 kg m^{-3}.

An important parameter that remains unknown is the thermal inertia I, i.e. the thermal conductivity K^m by using the relation ($I = \sqrt{\rho c K^m}$), of the porous icy matrix in comets (see Sect. 2.1). A low thermal inertia could limit the depletion of volatile molecules and the differentiation of the nucleus by thermal diffusion only to close subsurface layers. The comet would remain almost intact until the sublimation of water ice and other solid volatile molecules occurs near the surface during its perihelion passage. Conversely, a large thermal inertia could induce a great and deep differentiation of the nucleus. The temporal outgassing profile of the volatile molecules of the comet would be thereby quite different between these two extremes thermal inertia scenarios since the interfaces of sublimation of ices and the surface positions would be different. Due to the uncertainty in the thermal conductivity of the porous icy matrix, we test heat conductivities of about 1 and 0.01 W K^{-1} m^{-1} using Russel formula, i.e. high thermal inertia, and Hertz factor (hereafter value of 10^{-2}), i.e. low thermal inertia, given in Sect. 2.1 of the paper. Using the Russel formula, this leads to a thermal inertia of the nucleus of about 350 W K^{-1} m^{-2} s$^{\frac{1}{2}}$ for clathrate and mixed models, and about 500 W K^{-1} m^{-2} s$^{\frac{1}{2}}$ for crystalline and amorphous models. Using the Hertz factor, this leads to thermal inertia of 40 W K^{-1} m^{-2} s$^{\frac{1}{2}}$ for clathrate and mixed models, and 60 W K^{-1} m^{-2} s$^{\frac{1}{2}}$ for crystalline and amorphous models.

4.2. results

Figure 3 represents the thermodynamic evolution of the nucleus of 67P/C-G as a function of distance to the sun, during one revolution and after about 50 years of revolution around the sun, for the crystalline model and for the two types of thermal conductivity. The lines represent the nucleus surface and the minimum depths at which solid CO_2, H_2S, CH_4 and CO exist (hereafter called interfaces of sublimation of solid ices). Below, the gas phase of a given molecule is in equilibrium with its pure condensed phase. Above, only the gas phase exists in the porous network.

The lower thermal inertia (Hertz factor used) induces a limited physical differentiation of the nucleus within only about 3 m of depth. At each perihelion passage, the ablation of the surface (about 6 m) reaches the interfaces of the volatile ices phases, leading to a strong sublimation of volatile molecules. After each passage, the comet is like new. For greater thermal inertia (Russel formula used), the depth of the physical differentiation is about 80 m. The ablation of the surface, about 2 m per revolution, never reaches the interfaces of the volatile ices in the interior of the comet. So, with such a high thermal inertia, the interfaces of sublimation of the volatile ices are only slightly affected by the ablation of the surface of the nucleus. The nucleus remains then differentiated in subsurface layers.

Figure 4 represents the outgassing profiles of CO, CO_2, CH_4 and H_2S, in molecules per second and per unit of surface, of the nucleus as a function of distance to the sun, during one revolution after about 50 years of revolution around the sun, for the four models and for the two types of thermal conductivity. As the water ice production doesn't change as a function of the initial state of the water ice, we plot its curve only for the crystalline model with high thermal inertia.

Let's start the description by the models with a high thermal conductivity given by Russell's formula. For the crystalline model, the maximum productions in the outgassing profiles of CO_2 and H_2S are shifted compared to perihelion (at about 1.3 AU). The outgassing profiles of CO and CH_4 remain approximately constant whatever the position of the comet around the sun. For all the molecules, their outgassing comes from the sublimation of their pure ice phase. The deeper the interface of sublimation of a volatile molecule inside the nucleus is, more shifted relative to perihelion its outgassing peak is.

For the amorphous model, the crystallization of amorphous H_2O ice only slightly changes the production of CO and CH_4 during the perihelion passage. The main difference with the crystalline model, i.e. the global decrease in gas production, especially of CO, comes from the distribution of the volatile molecules between the "trapped" and "condensed" states in the icy matrix.

For the clathrate model, the outgassing profiles of all molecules (except CO_2 since this molecule is not trapped in the clathrate structure at low temparature) are changed compared to the others models. The maximum of outgassing of CO, CH_4 and H_2S occurs at perihelion passage, with some strong fluctuations of the outgassing (hereafter spikes). The spikes represent the release, close to the surface, of these molecules initially trapped in the clathrate structure. They are related to the day/night changes of insolation, and hence to sublimation of H_2O, at the surface of the nucleus.

For the mixed model, the outgassing profiles of molecules are as the ones of the crystalline and clathrate models together, with a thermal inertia close to this last one. As in the clathrate model, the maximum outgassings of CO, CH_4 and H_2S molecules occur at perihelion passage.

For models using a low thermal inertia determined by the Hertz factor, the outgassing profiles of the volatile molecules change compared to the above models with high thermal inertia. In most cases, the outgassing of molecules increases strongly just before and during perihelion passage since the ablation of the surface reaches the interfaces of sublimation of the volatile ices. The global production of all molecules is increased compared to models with greater thermal conductivity. For the crystalline model, the maximum of outgassing of CO_2 and H_2S occurs at perihelion passage. For these two molecules, which have their interface close to the surface, their outgassing fluctuates in phase with H_2O due to the day/night insolation variation. The maximum of the outgassing profiles of CO and CH_4 are shifted compared to the ones of CO_2 and H_2S since the depth of their interface of sublimation are deeper in the nucleus (see Fig. 3).

For the amorphous model, the crystallization of amorphous H_2O ice fully changes the production of all the molecules during the perihelion passage. The outgassing of molecules increases significantly during perihelion passage since the ablation of the surface reaches both the interfaces of crystallization

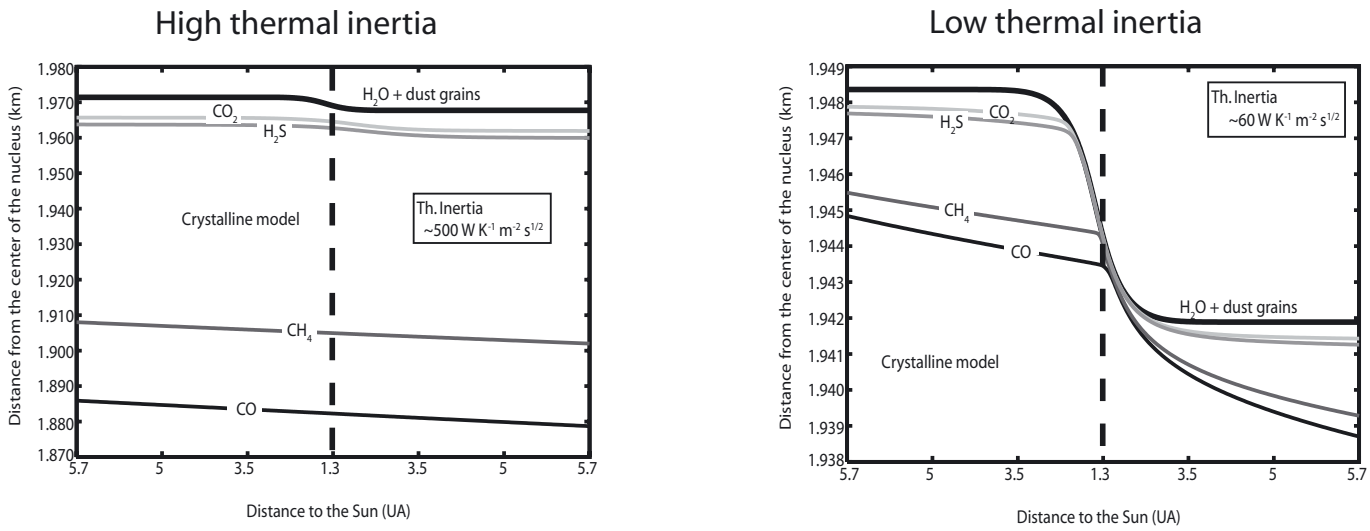

Fig. 3. Physical differentiation of 67P/C-G as a function of distance to the sun, during one revolution and after about 50 years of revolution around the sun, for crystalline model and for the two types of thermal inertia. The vertical dashed line represents the perihelion passage. Scale of the two figures is different.

of amorphous water ice and of sublimation of volatile ices. For all the molecules, the outgassing fluctuates with the day/night insolation variation, but with a variable amplitude reflecting their abundance close to the surface.

For the mixed and clathrate models, the outgassing of all molecules (including CO_2) is concentrated during the perihelion passage with fluctuations due to the day/night insolation variation. The differences between the outgassing profiles of these two models come from the different distributions of molecules between the "trapped" and "condensed" states in the nucleus.

To summarize, the outgassing profiles of the volatile molecules is function of the distribution of these molecules between the "trapped" and "condensed" states, the nature of the trapping (amorphous ice or clathrate structure), the thermal conductivity of the icy matrix and hence the depth of the interfaces of phase change of the volatile ices. Knowing the outgassing profiles of several molecules from a comet nucleus, we expect that this model, by inversion, should be able to determine its water ice structure and the abundances of volatile molecules between the "trapped" and "condensed" states. In the case of the 67P/C-G comet, the target of the Rosetta mission, which will be monitored all along its orbit such an inversion of the actual and initial states and compositions of the nucleus is very promising.

5. Conclusion

The chemical composition and water ice structure of the cometary nuclei remain currently unknown. For a better insight into these witnesses of the origins of comets, we have developed a model that takes into account all water ice structures (amorphous, crystalline, clathrate hydrate or any mixture of these structures of ice) and all their phase changes (amorphous water ice to pure crystalline water ice, amorphous water ice to clathrate hydrate, pure crystalline water ice to clathrate hydrate and vice-versa), as well as sublimation/condensation of volatile molecules in the porous network. This model describes the heat transfer, latent heat exchanges, gas diffusion, and the gas releases and trapping by crystallization and clathrate formation/dissociation processes. Taking into account all these physico-chemical processes, this model has been applied to the comet 67P/Churyumov-Gerasimenko with four initial different ices structures: crystalline ice, amorphous ice, clathrate and a mixture of the three. Results showed that the outgassing profile of volatile molecules from the nucleus is mainly function of the structure of water ice, the distribution of the volatile molecules between the "trapped" and "condensed" states in the icy matrix, and the thermal inertia of the icy matrix. We expect that this model will be able to constrain the chemical composition and the water ice structure in cometary nuclei from the outgassing profiles of volatile molecules observed during comet activity, and especially those of the 67P/Churyumov-Gerasimenko, the target comet of the Rosetta mission.

In the process of building this model, we did a complete review of all physical processes and thermodynamic properties of ices below the freezing point of water. We have identified several gaps to be filled by experimentals studies, essentially linked with the lacks of data in the thermodynamic properties of ices and clathrates, the pressure equilibrium conditions of clathrates, and the trapping and release processes of volatile molecules in the water ice structures (amorphous water ice and clathrate hydrate). these limitations are one of the reasons why we have considered only four volatile molecules (CO, CO_2, CH_4 and H_2S) in addition to H_2O although more than twenty volatile molecules have been identified in comets (Bockelée-Morvan et al. 2004). Since all these four molecules create single guest clathrates of structure I, only this structure of clathrate hydrate has been taken into account in the model. The presence of molecules in comets such as C_2H_2, C_2H_6 (observed in comets) or as Ar, Kr, N_2,... (not yet observed) could lead to the formation of structure II or a mixture of structure I and II as shown in Rydzy et al. (2007). In these conditions, the formation and decomposition of clathrate hydrate during the physico-chemical evolution of comets could then be more complex in terms of energy and trapping/release of volatile molecules than the simpler case presented in this model. Moreover, the main difficulty, taking into account all phases changes in the model, remains the correct estimate of the abundances of volatile molecules trapped and released by amorphous water ice and clathrate hydrate, at and far from equilibrium pressure conditions, as well as the fractionation between the gas phase and the clathrate compositions. The trapping of volatile molecules during amorphous water ice condensation and clathrate hydrate structure formation,

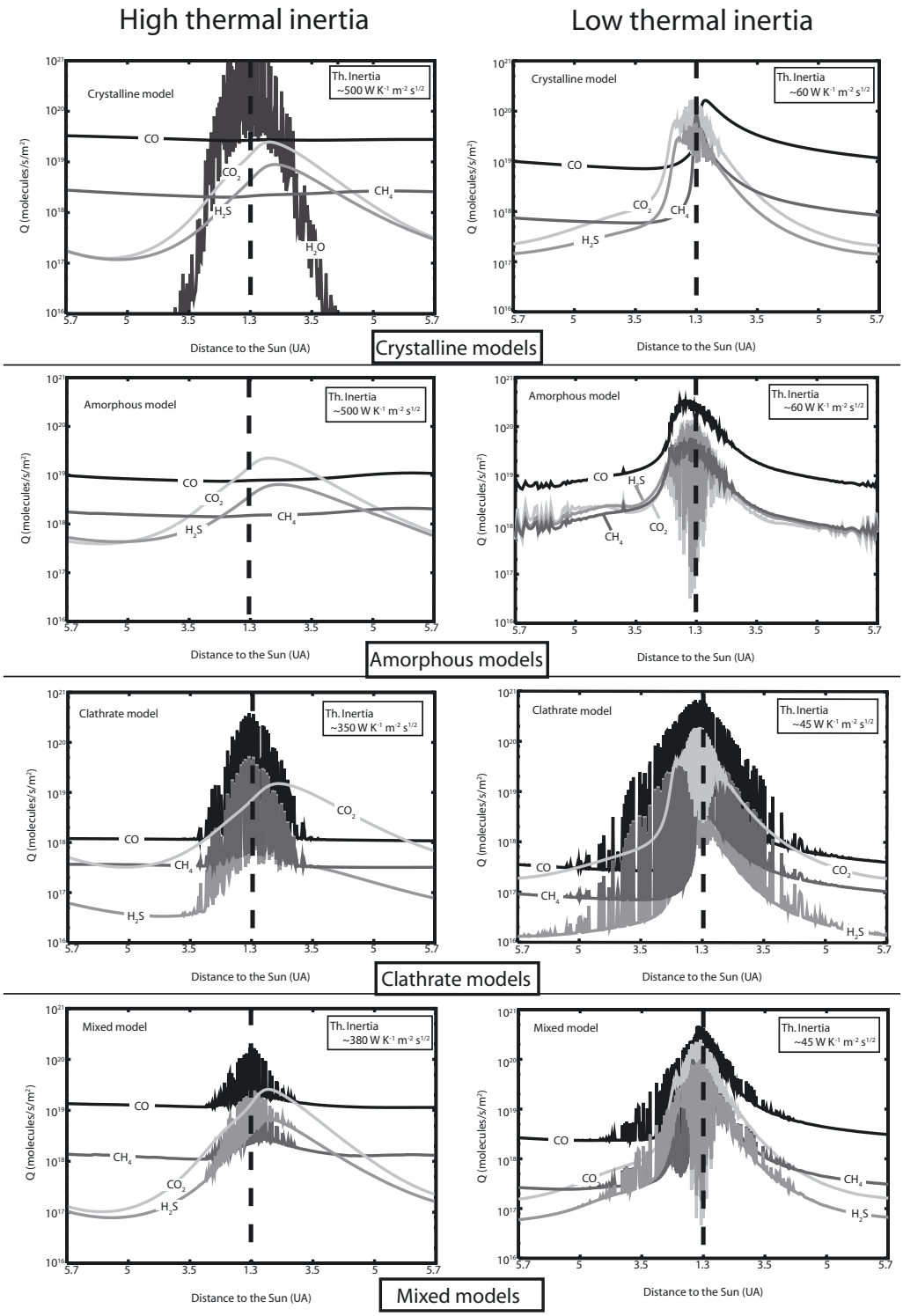

Fig. 4. Outgassing profiles, in molecule per second and per unit of surface, of 67P/C-G as a function of the distance to the sun, during one revolution and after about 50 years of revolution around the sun, for the four models and for the two types of thermal inertia (high on *the left* and low on *the right*). The vertical dashed line represents the perihelion passage.

and their release during the amorphous-to-crystalline water ice transition and the dissociation of the clathrate structure, out of equilibrium pressure conditions, should be more deeply studied experimentally. This will allow to better constrain the models of cometary nuclei which currently adopt arbitrary initial abundances of volatile molecules and poorly constrained processes for their release in the porous network. Currently, the remaining uncertainties about the behavior of water ice and the trapping/release processes of molecules inside the nucleus are problematic, without experimental and theoretical data, for the interpretation of the outgassing profiles of the volatile molecules that will be observed by the Rosetta spacecraft. In order to assess the uncertainties about the behavior of the different water ice structures, especially during the various phase transitions, this model will be submitted to a sensitivity study on the influences of the physical parameters that are poorly constrained.

We will devote a particular attention to issues of the kinetic rates of formation/dissociation of clathrates and of the degree of release, or not (metastability), of the volatile molecules trapped in water ice (amorphous or clathrate hydrate). This study will be presented separately in a next paper whose the objective is to determine whether the formation of clathrate is physically viable, thermodynamically and kinetically in the 67P/Churyumov-Gerasimenko comet without clathrate structure at the origin.

Acknowledgements. This work has been supported by the French Centre National d'Études Spatiales (CNES) and by the University Joseph Fourier – Grenoble 1 through post-doctoral fellowships (U.M.). All the computations presented in this paper were performed at the Service Commun de Calcul Intensif de l'Observatoire de Grenoble (SCCI) and using the UTINAM Cluster thanks to the grant of Franche-Comté region.

References

Ahmad, N., & Phillips, W. A. 1987, Solid State Commun., 63, 167
Anderson, G. K. 2003, J. Chem. Thermodyn., 35, 1171
Anderson, G. K. 2004, J. Chem. Thermodyn., 36, 1119
Anderson, B. J. 2007, Fluid Phase Equilibria, 254, 144
Andersson, O. P., & Ross, R. G. 1983, J. Phys. C, 16, 1423
Andersson, O. P., & Suga, H. 1996, J. Phys. Chem. Solids, 57, 125
Avlonitis, D. 1994, Ind. Eng. Chem. Res., 33, 3247
Avlonitis, D. 2005, Am. Inst. Chem. Eng., 51, 1258
Bar-Nun, A., Notesco, G., & Owen, T. 2007, Icarus, 190, 655
Barrer, R. M., & Edge, A. V. J. 1967, Roy. Soc. London Proc. Ser. A, 300, 1
Barrer, R. M., & Ruzicka, D. J. 1962, Trans. Faraday Soc., 58, 2262
Bertie, J. E., & Refaat Shehata, M. 1984, J. Chem. Phys., 81, 27
Blake, D., Allamandola, L., Sandford, S., Hudgins, D., & Freund, F. 1991, Science, 254, 548
Bockelée-Morvan, D., Crovisier, J., Mumma, M. J., & Weaver, H. A. 2004, Comets II, 391
Bouziani, N., & Fanale, F. P. 1998, ApJ, 499, 463
Capria, M. T., Coradini, A., & de Sanctis, M. C. 2003, Adv. Space Res., 31, 2543
Carman, P. C. 1956, Flow of gases through porous media (London: Butterworths Scientific Publications)
Chao, J., Wilhoit, R. C., & Zwolinski, B. J. 1973, J. Phys. Chem. Ref. Data, 2, 427
Chao, J., Hall, K. R., Marsh, K. N., & Wilhoit, R. C. 1986, J. Phys. Chem. Ref. Data, 15, 1369
Clarke, M. A., & Bishnoi, P. R. 2004, Chem. Eng. Sci., 59, 2983
Clayton, J. O., & Giauque, W. F. 1932, J. Am. Chem. Soc., 54, 2610
Cook, J. G., & Laubitz, M. J. 1983, In Thermal Conductivity, ed. J. G. Hust (New York: Plenum), 17, 745
Cottin, H., & Fray, N. 2008, Space Sci. Rev., 138, 179
Dartois, E. 2011, Icarus, 212, 950
Davidsson, B. J. R., & Gutiérrez, P. J. 2005, Icarus, 176, 453
Davidsson, B. J. R., & Skorov, Y. V. 2002, Icarus, 159, 239
Davidson, D. W., Desando, M. A., Gough, S. R., et al. 1987, Nature, 328, 418
Davidsson, B. J. R., Gutiérrez, P. J., & Rickman, H. 2009, Icarus, 201, 335
Delsemme, A. H., & Miller, D. C. 1971, Planet. Space Sci., 19, 1229
Delsemme, A. H., & Swings, P. 1952, Ann. Astrophys., 15, 1
Ellsworth, K., & Schubert, G. 1983, Icarus, 54, 490
Englezos, P., Kalogerakis, N., Dholabhai, P. D., & Bishnoi, P. R. 1987, Chem. Eng. Sci., 42, 2647
Enzian, A., Cabot, H., & Klinger, J. 1997, A&A, 319, 995
Espinasse, S., Klinger, J., Ritz, C., & Schmitt, B. 1991, Icarus, 92, 350
Espinasse, S., Coradini, A., Capria, M. T., et al. 1993, Planet. Space Sci., 41, 409
Falenty, A., Genov, G., Hansen, T. C., Kuhs, W. H., & Salamatin, A. N. 2011, J. Phys. Chem. C, 115, 4022
Fanale, F. P., & Salvail, J. R. 1984, Icarus, 60, 476
Fanale, F. P., & Salvail, J. R. 1987, Icarus, 72, 535
Flammer, K. R., Mendis, D. A., & Houpis, H. L. F. 1998, ApJ, 494, 822
Fray, N., & Schmitt, B. 2009, Planet. Space Sci., 57, 2053
Fray, N., Bénilan, Y., Cottin, H., & Gazeau, M.-C. 2004, J. Geophys. Res. (Planets), 109, 7
Fray, N., Bénilan, Y., Biver, N., et al. 2006, Icarus, 184, 239
Fray, N., Marboeuf, U., Brissaud, O., Schmitt, B. 2010, J. Chem. Eng. Data, 55, 5101
Gautier, D., Hersant, F., Mousis, O., & Lunine, J. I. 2001a, ApJ, 550, L227
Gautier, D., Hersant, F., Mousis, O., & Lunine, J. I. 2001b, ApJ, 559, L183
Genov, G., & Kuhs, W. F. 2003, Sixth International Conference on Mars, 3098
Genov, G., Kuhs, W. F., Staykova, D. K., Goreshnik, E., & Salamatin, A. N. 2004, Am. Mineral., 89, 1228
Ghormley, J. A. 1968, J. Chem. Phys., 48, 503
Giauque, W. F., & Blue, R. W. 1936, Contribution from the chemical Laboratory of the University of California
Giauque, W. F., & Egan, C. J. 1937, J. Chem. Phys., 5, 45
Giauque, W. F., & Stout, J. W. 1936, J. Am. Chem. Soc., 58, 1144
Gortsas, N., Kührt, E., Motschmann, U., & Keller, H. U. 2011, Icarus, 212, 858
Greenberg, J. M. 1982, Comet Discoveries, Statistics, and Observational Selection, IAU Colloq. 61, 131
Groussin, O., A'Hearn, M. F., Li, J.-Y., et al. 2007, Icarus, 187, 16
Grün, E., Gebhard, J., Bar-Num, A., et al. 1993, J. Geophys. Res., 98, 15
Hachikubo, A., Nakagawa, R., Kubota, D., et al. 2008, Proc. 6th Int. Conf. Gas Hydrates (ICGH)
Hand, D. P., Chyba, C. F., Carlson, R. W., & Cooper, J. F. 2006, Astrobiology, 6, 463
Handa, Y. P. 1985, J. Chem. Thermodynamics, 17, 201
Handa, Y. P. 1986a, J. Chem. Thermodynamics, 18, 891
Handa, Y. P. 1986b, J. Chem. Thermodynamics, 18, 915
Handa, Y. P. 1986c, J. Phys. Chem., 90, 5497
Handa, Y. P., & Cook, J. G. 1987, J.. Phys. Chem., 91, 6327
Handa, Y. P., & Klug, D. D. 1988, J. Phys. Chem., 92, 3323
Handa, Y. P., & Tse, J. S. 1986, J. Phys. Chem., 90, 5917
Handa, Y. P., Hawkins, R. E., & Murray, J. J. 1984, J. Chem. Thermodyn., 16, 623
Hersant, F., Gautier, D., & Lunine, J. I. 2004, Planet. Space Sci., 52, 623
Houpis, H. L. F., Mendis, D. A., & Ip, W.-H. 1985, ApJ, 295, 654
Huebner, W. F. 2008, Space Sci. Rev., 138, 5
Huebner, W. F., Benkhoff, J., Capria, M.-T., et al. 2006, Heat and Gas Diffusion in Comet Nuclei, The International Space Science Institute (Bern, Switzerland, Noordwijk, The Netherlands: ESA Publications Division)
Iro, N., Gautier, D., Hersant, F., Bockelée-Morvan, D., & Lunine, J. I. 2003, Icarus, 161, 511
Jewitt, D., & Matthews, H. 1999, AJ, 117, 1056
Kang, S. P., Lee, H., & Ryu, B.-J. 2001, J. Chem. Thermodyn., 33, 513
Kargel, J. S. 1998, Sol. Syst. Ices, 227, 3
Kast, W., & Hohenthanner, C.-R. 2000, Int. J. Heat Mass Transfer, 43, 807
Kim, H. C., Bishnoi, P. R., Heidemann, R. A., & Rizvi, S. S. H. 1987, Chem. Eng. Sci., 42, 1645
Klinger, J. 1980, Science, 209, 271
Klinger, J., Ocampo, J., & Schmitt, B. 1986, Asteroids, Comets, Meteors II, 241
Knudsen, M. 1909, Annalen der Physik, 75
Koloskova, L. A., Krupskii, I. N., Manzhelii, V. G., Gorodilov, B. Ya., & Kravchenko, Yu. G. 1974, Institute for Low Temperature Physics and Engineering, Kharkov, USSR, 31, 69
Kossacki, K. J., & Szutowicz, S. 2006, Planet. Space Sci., 54, 15
Kossacki, K. J., Szutowicz, S. Ł., & Leliwa-Kopystyński, J. 1999, Icarus, 142, 202
Kouchi, A., Yamamoto, T., Kozasa, T., Kuroda, T., & Greenberg, J. M. 1994, A&A, 290, 1009
Krivchikov, A. I., Gorodilov, B. Ya., Korolyuk, O. A., et al. 2005a, J. Low Temp. Phys., 139, 693
Krivchikov, A. I., Manzhelii, V. G., Korolyuk, O. A., Gorodilov, B. Ya., & Romantsova, O. O. 2005b, Phys. Chem. Chem. Phys., 7, 728
Krivchikov, A. I., Gorodilov, B. Ya., Korolyuk, O. A., et al. 2006, Phys. Rev. B, 73, 064203
Krivchikov, A. I., Korolyuk, O. A., & Romantsova, O. O. 2007, Low Temp. Phys., 33, 612
Kuhs, W. F., Staykova, D. K., & Salamatin, A. N. 2006, J. Phys. Chem. B, 110, 13283
Kuratomi, N., Yamamuro, O., Matsuo, T., & Suga, H. 1991, J. Chem. Thermodyn., 23, 485
Lamy, P. L., Toth, I., Davidsson, B. J. R., et al. 2007, Space Sci. Rev., 128, 23
Leaist, D. G., Murray, J. J., Post, M. L., & Davidson, D. W. 1982, J. Phys. Chem., 86, 4175
Lewis, J. S. 1972, Icarus, 16, 241
Lipenkov, V. Y., & Istomin, V. A., 2001, Mater. Glyatsiol. Issled, 91, 1
Lowry, S., Fitzsimmons, A., Lamy, P., & Weissman, P. 2008, The Solar System Beyond Neptune, 397
Lunine, J. I., & Stevenson, D. J. 1987, Icarus, 70, 61
Makogon, T. Y., & Sloan, E. D. 1994, J. Chem. Eng. Data, 39, 351
Manzhelii, V. G., & Krupskii, I. N. 1968, Physicotechnical Institute for Low Temperatures, Kharkov, USSR, No. 1, 10, 284
Marboeuf, U. 2008, Ph.D. Thesis, Univ. de Franche-Comté
Marboeuf, U., Mousis, O., Ehrenreich, D., et al. 2008, ApJ, 681, 1624
Marboeuf, U., Mousis, O., Petit, J.-M., & Schmitt, B. 2010, ApJ, 708, 812
Marboeuf, U., Mousis, O., Petit, J.-M., et al. 2011, A&A, 525, A144

McDowell, R. S., & Kruse, F. H. 1963, J. Chem. Eng. Data, 8, 547
McDonnell, J. A. M., Alexander, W. M., Burton, W. M., et al. 1986, Nature, 321, 338
McDonnell, J. A. M., Evans, G. C., Evans, S. T., et al. 1987, A&A, 187, 719
Mekler, Y., & Podolak, M. 1994, Planet. Space Sci., 42, 865
Mekler, Y., Prialnik, D., & Podolak, M. 1990, ApJ, 356, 682
Miller, S. L. 1961, PNAS, 47, 1798
Mohammadi, A. H., & Richon, D. 2010, Ind. Eng. Chem. Res., 49, 3976
Moore, M. H., Ferrante, R. F., Hudson, R. L., & Stone, J. N. 2007, Icarus, 190, 260
Mousis, O., Gautier, D., Bockelée-Morvan, D., et al. 2000, Icarus, 148, 513
Mousis, O., Marboeuf, U., Petit, J.-M., & Klinger, J. 2005, MNRAS, 362, L40
Mousis, O., Alibert, Y., Hestroffer, D., et al. 2008, MNRAS, 383, 1269
Mousis, O., Marboeuf, U., Lunine, J. I., et al. 2009, ApJ, 696, 1348
Mousis, O., Lunine, J. I., Picaud, S., & Cordier, D. 2010, Faraday Discussions, 147, 509
Notesco, G., & Bar-Nun, A. 2000, Icarus, 148, 456
Orosei, R., Capaccioni, F., Capria, M. T., et al. 1999, Planet. Space Sci., 47, 839
Parrish, W. R., & Prausnit, J. M. 1972, Ind. Eng. Chem. Process Des. Develop., 11, 26
Parsonage, N. G., & Staveley, L. A. K. 1984, Thermodynamic studies of clathrates and inclusion compounds (London: Academic Press), 3, 1
Patankar, S. V. 1980, Numerical heat transfer and fluid flow (Washington, DC: Hemisphere Publishing Corp.)
Prialnik, D. 1997, ApJ, 478, L107
Prialnik, D., Benkhoff, J., & Podolak, M. 2004, Comets II, 359
Richardson, J. E., Melosh, H. J., Lisse, C. M., & Carcich, B. 2007, Icarus, 190, 357
Rickman, H., Fernandez, J. A., & Gustafson, B. A. S. 1990, A&A, 237, 524
Roberts, O. L., Brownscombe, E. R., & Howe, L. S. 1940, Oil and Gas J., 30, 37
Rosenberg, E. D., & Prialnik, D. 2009, Icarus, 201, 740
Ross, R. G., & Andersson, P. 1982, Can. J. Chem., 60, 881
Russel, H. W. 1935, J. Am. Ceram. Soc. 18, 1
Rydzy, M. B., Schicks, J. M., Naumann, R., & Erzinger, J. 2007, J. Phys. Chem. B, 111, 9539
Scheidegger, A. E. 1974, The physics of Flow through Porous Media (Toronto: Univ. Toronto Press)
Schmitt, B. 1986, Ph.D. Thesis, Univ. Joseph Fourier, Grenoble, France
Schmitt, B., & Klinger, J. 1987, in Diversity and Similarity of Comets, ESA Spec. Publ., 278, 613
Schmitt, B., Espinasse, S., Grim, R. J. A., Greenberg, J. M., & Klinger, J. 1989, Phys. Mech. Cometary Mat., ESA Spec. Publ., 302, 65
Schmitt, B., Grim, R. J. A., Greenberg, J. M., & Klinger, J. 1992, in Physics and Chemistry of Ice (Sapporo: Hokkaido Univ. Press), 344
Sekanina, Z. 1979, Icarus, 37, 420
Shinoda, T. 1969, Bull. Chem. Soc. Japan, 42, 1815
Skovborg, P., & Rasmussen, P. 1994, Fluid Phase Equilib., 96, 223
Sloan, E. D. 1998, Clathrate Hydrates of Natural Gases (New York: Marcel Dekker Inc.)
Sloan, E. D., & Fleyfel, F. 1992, Fluid Phase Equilib., 76, 123
Smoluchowski, R. 1988, MNRAS, 235, 343
Squyres, S. W., McKay, C. P., & Reynolds, R. T. 1985, J. Geophys. Res., 90, 12381
Stachowiak, P., Sumarokov, V. V., Mucha, J., & Jezowski A. 1998, J. Low Temp. Phys., 111, 379
Staykova, D. K. 2004, Ph.D. Thesis, Universität Göttingen
Staykova, D. K., Kuhs, W. F., Salamatin, A. N., & Hansen, T. 2003, J. Phys. Chem. B, 107, 10299
Stewart, J. W. 1959, J. Phys. Chem. Solids, 12, 122
Sun, R., & Duan, Z. 2005, Geochim. Cosmochim. Acta, 69, 4411
Sun, X., & Mohanty, K. K. 2006, Chem. Eng. Sci., 61, 3476
Tancredi, G., Rickman, H., & Greenberg, J. M. 1994, A&A, 286, 659
Thiam, A. 2008, Ph.D. Thesis, École Nationale Supérieure des Mines, Saint-Etienne
Thomas, C., Mousis, O., Picaud, S., & Ballenegger, V. 2009, Planet. Space Sci., 57, 42
Tonnet, N. 2007, Ph.D. Thesis, École Nationale Supérieure des Mines, Saint-Etienne
Tse, J. S., & Klug, D. D. 2002, J. Supramolecul. Chem., 2, 467
Tse, J. S., & White, M. A. 1988, J. Phys. Chem., 92, 5006
Van der Waal, J. H., & Platteeuw, J. C. 1959, Advances in Chemical Physics (New-York: Interscience)
Volkov, A. N., & Lukyanov, G. A. 2008, Sol. Sys. Res., 42, 209
Wang, X., Schultz, A. J., & Halpern, Y. 2002, J. Phys. Chem. A, 106, 7304
Weissman, P. R., Asphaug, E., & Lowry, S. C. 2004, Comets II, 337
Yamamuro, O., Oguni, M., Matsuo, T., & Suga, H. 1988a, J. Phys. Chem. Solids, 49, 425
Yamamuro, O., Oguni, M., Matsuo, T., & Suga, H. 1988b, J. Incl. Phen. Mol. Recognit. Chem., 6, 307
Yamamuro, O., Handa, Y. P., & Suga, H. 1990, J. Incl. Phen. Mol. Recognit. Chem., 8, 45
Yoon, J.-H., Yamamoto, Y., Komai, T., & Haneda, H. 2003, Ind. Eng. Chem. Res., 42, 1111

Pages 20 to 24 are available in the electronic edition of the journal at http://www.aanda.org

Appendix A: The numerical scheme

In this section, we describe the numerical comet nucleus model used to solve the heat and mass diffusion equations and developed originally by Marboeuf et al. (2008). In order to ensure perfect conservation of mass and energy in the model, we use finite volume method (Patankar 1980) for the discretisation of Eqs. (1) and (22). For illustrative purpose, we detail below the space and time integration of Eq. (1) which is the most complex equation.

Our numerical model of comet nucleus is a one-dimensional grid with N_C layers (see Fig. A.1). We define r_i as the position of the top of each layer from $r_1 = R_{\rm nucleus}$ at the surface to r_{N_c+1} at the center of the nucleus.

The layers are spherical shells and the temperature and other state variables are assumed constant inside each layer, a common approximation in discretization schemes.

We note Δr_i the thickness of each layer i:

$$\Delta r_i = r_i - r_{i+1}. \tag{A.1}$$

The initial thickness of the layers increases with depth following a geometric progression $\Delta r_i = a\Delta r_{i-1}$, where a is a constant factor slightly larger than 1.

The variable L in Fig. A.1 represents either the temperature T, the pressure P, the coefficient of diffusion of mass G or the coefficient of diffusion of heat K^m that we calculate at the center of each layer: this corresponds to the physical conditions in the center of each cell.

When a chemical species begins to sublimate, i.e. the temperature is such that the vapor saturation pressure is equal to the partial gas pressure of the species x in the pores, the sublimation front of the species divides the nucleus into two zones. In the first one, from the surface down to the interface, species x is only present in the gas form and simply obeys Eq. (22) without the source/well terms. In the second zone, from the interface down to the center of the nucleus, the gas x is in equilibrium with its ice, its pressure is the vapor saturation pressure, a function of temperature, and all the other variables are adjusted by the model to account for gas flow due to gradients.

The two Eqs. (1) and (22) are solved in this structure following the method of Orosei et al. (1999). In order to increase the numerical stability, both the fluxes of heat and mass are solved together in the resolution of Eq. (1) for the layers where chemical species are condensed. For a more realist treatment of the gas diffusion through the porous matrix between the interface and the surface, each chemical species can diffuse following its own time step of diffusion.

When the total time of gas diffusion $t_{\rm tot}$, between the interface of species x and the surface, is smaller than $f_{\rm tg}\ \Delta t$ ($f_{\rm tg}$ is an accuracy parameter that we impose and Δt is the time step for integration of Eq. (1)), the gas diffusion of species x is assumed to be in a steady state and the right term of the mass conservation Eq. (22) is taken equal to zero. In the following simulations, we use $f_{\rm tg} = 0.1$.

A.1. Spatial integration

The finite volume method, described first by Patankar (1980), consists in integrating the equations of conservation (1) and (22) on each volume of control. The main advantage of this method is that the divergence term present in both equations of conservation is integrated analytically, leading to a simple algebraic difference equation of terms at the surface of the control volume, which can be easily solved numerically.

Hereafter, we develop successively the different terms of the spatial integration of the conservation energy Eq. (1), which is the most interesting equation:

A.1.1. Spatial integration of the first terms of Eq. (1)

Term of the left hand side of Eq. (1). Performing the spatial integration of the left hand side term of Eq. (1) over the control volume yields:

$$\iiint_v \rho c \frac{\partial T}{\partial t} {\rm d}v = \rho c \frac{\partial T_i}{\partial t} V_i \qquad \left({\rm J\,s^{-1}}\right) \tag{A.2}$$

with $V_i = \frac{4}{3}\pi[r_i^3 - r_{i+1}^3]$ and i the index of the layer. Here we make use of the underlying assumption in discretization schemes that the temperature in constant inside a cell. One can also consider the temperature used in the model as an average of the real temperature over the cell.

First term of the right hand side of Eq. (1). In the following, we will always use spherical coordinates, assuming spherical symmetry, so that only the radial component of the equations remains.

In order that two cells see the same flux on both sides of the interface of the volumes, we choose to express the coefficients of diffusion G_i and conduction $K_i^{\rm pm}$ at the surface of each volume of control, i.e. each radial cell, and denote g_i and $k_i^{\rm pm}$ their value at the limit between cells $i-1$ and i. Figure A.1 shows the variable L_i that represents the coefficients of diffusion G_i and conduction K_i^m at the center of the cell i and its corresponding variable l_i on each interface for the coefficients of diffusion g_i and conduction k_i^m. In this way, each layer possesses a set of coefficients of diffusion (G, K^m) defined in the center of the cell and an other set of coefficients (g, k^m) defined at its surface. The coefficients l_i can be written as functions of the coefficients L_{i-1} and L_i located above and below the interface of the layers. We consider that theses coefficients form a parallel network defined by equation:

$$l_i = \frac{\Delta r_{i-1} + \Delta r_i}{\frac{\Delta r_{i-1}}{L_{i-1}} + \frac{\Delta r_i}{L_i}}. \tag{A.3}$$

The result of replacing the coefficients L_i by l_i in the divergence terms of Eqs. (1) and (22) is the exact conservation of the flux of mass and energy through the interface. Note that the interpolation in divergence terms of the coefficients at the boundary of the cells must be applied to all, but only, the coefficients of the gradient terms (see below Eqs. (A.9) and (A.10)).

The spatial integration of the divergence becomes then:

$$\begin{aligned}\iiint_v \nabla\left(k^m \frac{\partial T}{\partial r}\right){\rm d}v &= \iiint_v \frac{1}{r^2}\frac{\partial}{\partial r}\left(r^2 k^m \frac{\partial T}{\partial r}\right){\rm d}v \\ &= 4\pi\left[r_i^2 k_i^m \frac{\partial T_i}{\partial r} - r_{i+1}^2 k_{i+1}^m \frac{\partial T_{i+1}}{\partial r}\right]\left({\rm J\,s^{-1}}\right)\end{aligned} \tag{A.4}$$

where the gradient of temperature $\frac{\partial T_i}{\partial r}$ is written as:

$$\frac{\partial T_i}{\partial r} = 2\frac{T_{i-1} - T_i}{\Delta r_{i-1} + \Delta r_i} \qquad \left({\rm K\,m^{-1}}\right). \tag{A.5}$$

Second term of the right hand side of Eq. (1). The term Q_x only exists in Eqs. (1) and (22) if the chemical species x is condensed in the pores. It is derived from Eq. (22) and the integration of

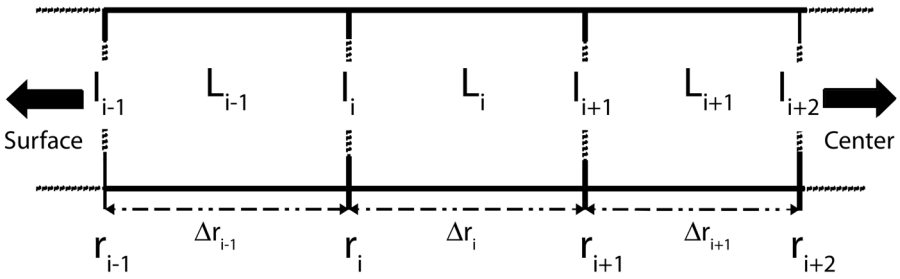

Fig. A.1. Schematic view of the numerical nucleus. Pressure P_i and temperature T_i are defined at the center of each cell i and are represented by the coefficient L_i. The coefficients of heat conduction $K_i^{\rm pm}$ and gas diffusion G_i are defined at the center and at the edge of each cell i. They are here represented by the coefficients L_i at the center and l_i at the edge of each cell i. The parameters r_i and Δr_i are the distance from the center of the nucleus and the thickness of each cell i.

this term becomes:

$$\iiint_v Q_x^{\rm s} {\rm d}v = \iiint_v \left(\frac{\partial \rho_x^{\rm g}}{\partial t} - \nabla \left(G_x \frac{\partial P_x^{\rm s}(T)}{\partial r} \right) - Q_x^{\rm cr} - Q_x^{\rm cl} \right) {\rm d}v \ \left({\rm mol\,s^{-1}} \right) \quad \text{(A.6)}$$

with $\rho_x^{\rm g} = \frac{\Psi P_x^{\rm s}(T)}{RT}$ (mol m^{-3} s^{-1}). Here we have used $P_x^{\rm s}$ in place of P_x because the species x exists in condensed form and hence the gas is in thermodynamic equilibrium at pressure $P_x^{\rm s}$.

A.1.2. Spatial integration of the Eq. (A.6) (source/well term $Q_x^{\rm s}$)

We expand below the different terms of the spatial integration of Eq. (A.6):

First term of the right hand side of Eq. (A.6):

$$\iiint_v \frac{\partial \rho_x^{\rm g}}{\partial t} {\rm d}v = \frac{\partial \rho_{i,x}^{\rm g}}{\partial t} V_i = \frac{\Psi_i}{RT_i} \frac{\partial P_x^{\rm s}(T_i)}{\partial t} V_i \qquad \left({\rm mol\,s^{-1}} \right) \quad \text{(A.7)}$$

where T is assumed to be constant during the gas pressure variation. Finally, because $P_x^{\rm s}(T)$ is only a function of T, we can write:

$$\iiint_v \frac{\partial \rho_x^{\rm g}}{\partial t} {\rm d}v = \frac{\Psi_i}{RT_i} \frac{\partial P_x^{\rm s}(T_i)}{\partial T} \frac{\partial T_i}{\partial t} V_i \qquad \left({\rm mol\,s^{-1}} \right). \quad \text{(A.8)}$$

Second term of the right hand side of Eq. (A.6): since we know $P_x^{\rm s}(T)$ analytically, we express this gradient in terms of the temperature gradient $\frac{\partial P_x^{\rm s}(T_i)}{\partial r} = \frac{\partial P_x^{\rm s}(T_i)}{\partial T} \frac{\partial T_i}{\partial r}$. Similarly to what we did for the heat and gas diffusion coefficients, using Eq. (A.3), we interpolate the quantity $\Theta_{i,x} = G_{i,x} \frac{\partial P_x^{\rm s}(T_i)}{\partial T}$, that appears in the divergence term, and which is known only at the centers of the control volumes, to its value $\theta_{i,x}$ at the edge of the cells, in order to ensure proper conservation.

The radial component of the integration gives then for each volatile molecule:

$$\iiint_v \nabla \left(g_x \frac{\partial P_x^{\rm s}(T)}{\partial r} \right) {\rm d}v = 4\pi \left[r_i^2 g_{i,x} \frac{\partial P_x^{\rm s}(T_i)}{\partial r} - r_{i+1}^2 g_{i+1,x} \frac{\partial P_x^{\rm s}(T_{i+1})}{\partial r} \right] \left({\rm mol\,s^{-1}} \right) \quad \text{(A.9)}$$

where $\frac{\partial P_x^{\rm s}(T_i)}{\partial r}$ is the gradient of vapor saturation pressure of species x.

The spatial integration over the control volume of the remaining terms $Y^{\rm cr}$, $Y^{\rm chs}$, and $Y^{\rm cl}$ is straightforward. $Q_x^{\rm cr}$ from Eqs. (1) and (A.6) vanishes.

A.1.3. Final spatial integration of the energy Eq. (1)

Finally, as a result of the spatial integration of Eq. (1), we obtain the conservation of the energy at a given time step:

$$\rho_i c_i \frac{\partial T_i}{\partial t} = \frac{4\pi}{V_i} \left[r_i^2 \Phi_i \frac{\partial T_i}{\partial r} - r_{i+1}^2 \Omega_{i+1} \frac{\partial T_{i+1}}{\partial r} \right] - \sum_x H_{i,x}^{\rm s} \left(\frac{\Psi_i}{RT_i} \frac{\partial P_x^{\rm s}(T_i)}{\partial T} \frac{\partial T_i}{\partial t} \right) + Y_i^{\rm cr} + Y_i^{\rm chs} + \sum_x Q_{i,x}^{\rm cl} \left(H_{i,x}^{\rm s} - H_{i,x}^{\rm cl} \right) \ \left({\rm J\,s^{-1}} \right) \quad \text{(A.10)}$$

with

$$\Phi_i = k_i^m + \sum_x H_{i,x}^{\rm s} \theta_{i,x} \qquad \left({\rm J\,s^{-1}\,m^{-1}\,K^{-1}} \right) \quad \text{(A.11)}$$

and

$$\Omega_{i+1} = k_{i+1}^m + \sum_x H_{i,x}^{\rm s} \theta_{i+1,x} \qquad \left({\rm J\,s^{-1}\,m^{-1}\,K^{-1}} \right) \quad \text{(A.12)}$$

where $\theta_{i,x}$ and k_i are defined at the interface of the layers i and $i-1$, as explained above.

A.2. Temporal integration

Equations (1) and (22) are nonlinear and the best method to solve them would be to use an iterative fully implicit method for each spatial step in order to find the exact value of T and P for each time step. However, such a method is very time consuming. We choose then to follow Espinasse et al. (1991) in using the predictor-corrector method and imposing a slow evolution with time. The different choices of integration methods for both the space and time derivative equations of conservation, in the finite difference framework, have been already discussed in Huebner et al. (2006) and Prialnik et al. (2004). Here we recall only the principles of the integration scheme and give more details. The idea of the predictor-corrector scheme is to first estimate the values of T and P at the middle of the time step Δt for each cell and time step (predictor). The knowledge of $P^{\Delta t/2}$ and $T^{\Delta t/2}$ permits us to calculate the values of the non-linear coefficients (G, g), (K, k) and $(G_x \frac{\partial P_x^{\rm s}}{\partial T})$ at the middle of the current time step. These last values are then used to solve Eqs. (1) and (22) with the current time step Δt at the corrector. Now, we give, as an example, the time integration of Eq. (A.10) on a time step $n\Delta t$, with $n = \frac{1}{2}$

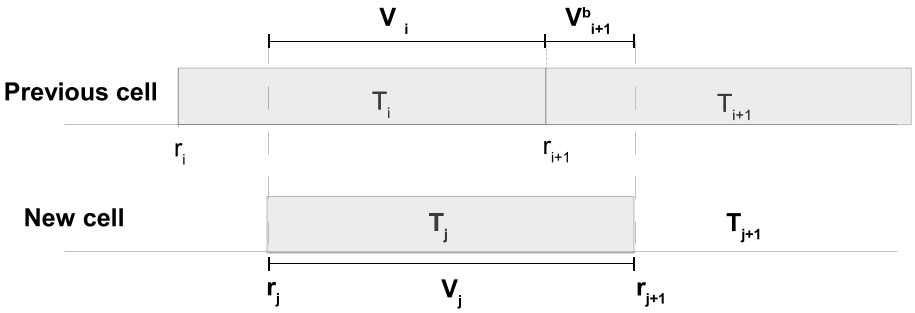

Fig. A.2. Reconstruction of a cell after removal of the interface. The new temperature T_j and pressure P_j of each cell j are calculated from the previous values T_i and P_i by interpolation. V_i^a and V_{i+1}^b are respectively the volume fractions of cell i and $i+1$ that give the volume V_j of the new cell j.

for the predictor and 1 for the corrector:

$$\int_t^{t+n\Delta t} \rho c \frac{\partial T_i}{\partial t} \mathrm{d}t = \frac{4\pi}{V_i} \int_t^{t+n\Delta t} \left[r_i^2 \Phi_i \frac{\partial T_i}{\partial r} - r_{i+1}^2 \Omega_{i+1} \frac{\partial T_{i+1}}{\partial r} \right] \mathrm{d}t - \int_t^{t+n\Delta t} \left[\sum_x H_{i,x}^{\mathrm{s}} \left(\frac{\Psi_i}{RT_i} \frac{\partial P_x^{\mathrm{s}}(T_i)}{\partial T} \frac{\partial T_i}{\partial t} \right) \right] \mathrm{d}t + \int_t^{t+n\Delta t} \left[Y_i^{\mathrm{cr}} + Y_i^{\mathrm{chs}} \right] \mathrm{d}t + \int_t^{t+n\Delta t} \left[\sum_x Q_{i,x}^{\mathrm{cl}} \left(H_{i,x}^{\mathrm{s}} - H_{i,x}^{\mathrm{cl}} \right) \right] \mathrm{d}t \ (\mathrm{J}). \quad (A.13)$$

To solve this equation, we need to know the temporal evolution of the temperature gradient on the time step $n\Delta t$. To this end, we replace it by a linear combination of the known and unknown temperature gradients balanced by a parameter f that takes values between 0 and 1 according to the type of resolution scheme we choose:

$$\Gamma_i = \left[f \left(\frac{\partial T_i}{\partial r} \right)^{t+n\Delta t} + (1-f) \left(\frac{\partial T_i}{\partial r} \right)^{t} \right] \quad \left(\mathrm{K\,m^{-1}} \right). \quad (A.14)$$

As a result of the time integration, we obtain the final equation:

$$\rho_i c_i [T_i^{t+n\Delta t} - T_i^t] = \frac{4\pi}{V_i} \left[r_i^2 \Phi_i^{t+m\Delta t} \Gamma_i - r_{i+1}^2 \Omega_{i+1}^{t+m\Delta t} \Gamma_{i+1} \right] n\Delta t - \sum_x H_{i,x}^{\mathrm{s},\ t+m\Delta t} \left[\frac{\Psi_i}{RT_i^{t+m\Delta t}} \frac{\partial P_x^{\mathrm{s}}(T_i^{t+m\Delta t})}{\partial T} \left[T_i^{t+n\Delta t} - T_i^t \right] \right] + \left(Y_i^{\mathrm{cr},\ t+m\Delta t} + Y_i^{\mathrm{chs},\ t+m\Delta t} \right) n\Delta t + \sum_x Q_{i,x}^{\mathrm{cl},\ t+m\Delta t} \left(H_{i,x}^{\mathrm{s},\ t+m\Delta t} - H_{i,x}^{\mathrm{cl},\ t+m\Delta t} \right) n\Delta t \quad (\mathrm{J}) \quad (A.15)$$

with $m = 0$ for the predictor and $\frac{1}{2}$ for the corrector.

For the predictor we choose to take a fully implicit scheme ($f = 1$), while for the corrector, we use a Cranck-Nicolson scheme which is a semi-implicit method ($f = 1/2$). Both numerical schemes are totally mathematically stable. The predictor scheme is accurate at the first level order in time step Δt and predicts a good value of the variables as long as the time step is short[4] (Huebner et al. 2006; Prialnik et al. 2004). The corrector is accurate to second order in Δt. This last scheme is restricted by a boundary condition on the time step if anyone wants fair physical solutions (Patankar 1980): $\frac{\alpha \Delta t}{\Delta x^2} \leq 1$. Hence, mixing the fully implicit and the semi-implicit schemes improve the stability and accuracy of the overall scheme.

[4] Its actual size is up to the user. The method is stable for all time steps, but the error on each time step is of order $(\Delta t)^2$.

After expanding each term in Eq. (A.15), we obtain a tridiagonal matrix which takes the form:

$$a_i T_{i-1}^{t+n\Delta t} + b_i T_i^{t+n\Delta t} + c_i T_{i+1}^{t+n\Delta t} = d_i. \quad (A.16)$$

For each layer i we can solve Eq. (A.16) with a tri-diagonal matrix algorithm (TDMA, Patankar 1980). Following the same scheme, Eq. (22) for species x is transformed into a tridiagonal system, with pressure P_x in place of T.

Remember that the sublimation interface of species x separates the nucleus into two different regions. Below the interface, the full Eq. (1) is solved with all source terms, while the pressure in Eq. (22) is the vapor saturation pressure P_x^{s}, a function of T. The source term Q_x in Eq. (22) is then explicitly computed from T and P_x^{s} and its gradient. Above the interface, the source term Q_x in Eq. (22) vanishes and hence the full Eq. (A.6) disappears from Eq. (A.15). Then Eq. (22) is solved between the surface and the sublimation interface of species x, while Eq. (1) is solved from the surface to the center of the nucleus, with the change of terms mentioned above at the sublimation interface.

To apply the TDMA, we need to impose boundary conditions at each end of the integration space, both for Eq. (1) and Eq. (22). At the surface, the temperature is given by Eq. (18) (Dirichlet boundary condition). At the center of the nucleus, we impose the flux of heat equal to zero (Neumann boundary condition):

$$\frac{\partial T}{\partial r} = 0. \quad (A.17)$$

If species x is present in condensed form everywhere in the nucleus, then we never solve Eq. (22), and $P_x = P_x^{\mathrm{s}}(T)$ even at the surface. If, on the contrary, there exists a sublimation interface for species x, then Eq. (22) is solved between the surface of the nucleus and the sublimation interface. Here, we impose a Dirichlet boundary condition at both ends. At the surface, we impose

$$P_x = 0,$$

and at the sublimation interface, we have

$$P_x = P_x^{\mathrm{s}}(T).$$

At the end of the corrector, when all the variables are recalculated, the interface front of sublimation of each specie is moved towards the center of the nucleus. In order to avoid instabilities during the computation, each interface is moved continuously towards the center following the prescription of Orosei et al. (1999). The size and the number of cells are then recalculated at each time step (see Fig. A.2). We do this so that the size of the cells do not change too much with time at a given location, therefore avoiding abrupt changes in the gradients of P_x and T and ensuring stability of the computation. In order to ensure the exact conservation of energy and mass in the nucleus, the new

Table B.1. Greek symbols.

Parameter	Unity	Description
$\alpha_x^{\rm cl}$		Surface fraction of the porous network covered by water molecules that form the clathrate structure
α_x^i		Surface fraction of the porous network covered by the pure ice species x
β		Power law of the size distribution of dust grains
Δr_i	m	Thickness of each layer i
Δt	s	Time step
δ		Obliquity
ϵ		Infrared surface emissivity of the nucleus
φ_x	mol m^{-2} s^{-1}	Free sublimation rate of the specie x
Φ_x	mol m^{-2} s^{-1}	Molar flow of gas x
ϕ		Argument of the sub-solar meridian at perihelion
Γ_x^l		Molar fraction of the molecule x trapped during formation of MG clathrate ($l = f$) or released during dissociation of MG clathrate ($l = d$)
γ		The true anomaly of the comet
λ	m	Mean free path of molecules in the porous network
$\lambda_k^{\rm cl}$	mol m^{-2} Pa^{-1} s^{-1}	Kinetic parameter of formation ($k = f$) or dissociation ($k = d$) of clathrate
$\lambda_{n,\,k}^{\rm cl}$	mol m^{-2} Pa^{-1} s^{-1}	Nominal kinetic parameter of formation ($k = f$) or dissociation ($k = d$) of clathrate
θ		Latitude on the comet surface
$\theta_{\rm s}$		Cometocentric latitude of the sub-solar point
$\rho_{\rm H_2O}^{\rm am}$	kg m^{-3}	Mass density of amorphous water ice
$\rho_{(x)}^l$	kg m^{-3}	Mass density of the solid or gas component l ($l = d$ for dust, cl for clathrate, i for pure ices of elements x, or g for gas)
$\rho_x^{\rm tp}$	kg m^{-3}	Mass density of the volatile molecule x trapped in amorphous ice
$\rho_{(x)}^{{\rm b},\,l}$	kg m^{-3}	Bulk density of the solid component l ($l = d$ for dust, cl for clathrate or i for pure ices of elements x
$\rho_x^{\rm g}$	kg m^{-3}	Mass density of gas x
σ	J s^{-1} m^{-2} K^{-4}	Stefan-Boltzmann constant
$\tau^{\rm cr}$	s	Time of crystallization of the amorphous water ice
τ		Tortuosity that is defined as the ratio of the length of a pore to the distance between its ends
ω	s^{-1}	Spin rotation period of the comet nucleus
ξ		Solar zenith distance
Ψ, Ψ^i		Porosity and initial porosity of the matrix

temperature T_j and pressure P_j of each new cell j are calculated from the previous values by interpolation.

For illustration, let us consider a new cell j that overlaps with previous cells i and $i + 1$ (see Fig. A.2). The new temperature T_j is computed so that the internal energy of the cell does not change, i.e. the energy change of the fraction of mass from cell i changing from T_i to T_j is exactly the opposite of that due to the fraction of mass from cell $i + 1$ changing from T_{i+1} to T_j, throught their respective heat capacities following the equation:

$$\int_{T_i}^{T_j}\left(\rho_i c(T) - \sum_x H_x^{\rm s}\frac{\partial\rho_{i,x}^{\rm g}}{\partial T}\right)V_i^a {\rm d}T = - \int_{T_{i+1}}^{T_j}\left(\rho_{i+1} c(T) - \sum_x H_x^{\rm s}\frac{\partial\rho_{i+1,x}^{\rm g}}{\partial T}\right)V_{i+1}^b {\rm d}T \quad \text{(A.18)}$$

where V_i^a and V_{i+1}^b are respectively the volume fractions of cell i and $i + 1$ that give the volume V_j of the new cell j.

Similarly the total mass of each constituent (dust, water, molecules in gas and condensed forms) is strictly conserved by recomputing the condensed mass density and keeping either the same amount of gas when there is no condensed molecule or forcing the pressure to the vapor saturation pressure at the temperature of the cell.

Appendix B: Symbols used in the paper

In this section, we present tables with principal symbols used in the model (Tables B.1 and B.2).

Table B.2. Latin symbols.

Parameter	Unity	Description
A_b		Bolometric Bond albedo of the nucleus surface
A_s	m^{-1}	Reaction surface area per unit of volume of solid reactant
a^*	m	Critical radius that gives the largest dust grain that can be ejected from the comet
a	m	Radius of dust grains in the comet
c^l	J kg^{-1} K^{-1}	Specific heat of the solid component l ($l = d$ for dust, cl for clathrate or i for pure ices of elements x) or of the gas component ($l = g$ of gas)
$c^{am}_{H_2O}$	J kg^{-1} K^{-1}	Specific heat capacity of amorphous ice
C_s	J m^{-2} s^{-1}	Solar constant
d	m	Mean diameter of gas molecules
d_x	m	Diameter of the molecule x
f^l		Volume ratio in the solid matrix of water ice ($l = i$ when formation of clathrate occurs) or of clathrate ($l = cl$ when dissociation of clathrate occurs)
G_c	m^3 kg^{-1} s^{-2}	Gravitational constant
G_x	mol m^{-1} Pa^{-1} s^{-1}	Diffusion coefficient of gas x in the porous network
G^k_x	mol m^{-1} Pa^{-1} s^{-1}	Knudsen gas coefficient diffusion ($K^n > 1$)
G^v_x	mol m^{-1} Pa^{-1} s^{-1}	Viscous gas coefficient diffusion ($K^n < 10^{-2}$)
H_{cl}	J mol^{-1}	Enthalpy of formation/dissociation of clathrate per mole of gas trapped/released
H_{cr}	J mol^{-1}	Latent heat of crystallization per mole of water
H^s_x	J mol^{-1}	Enthalpy of sublimation of ice x
h		Hertz factor
I	J K^{-1} m^{-2} $s^{-\frac{1}{2}}$	Thermal inertia
J^{am}_x		Initial x/H_2O mole fraction of the gas x trapped in amorphous ice
J^{ip}_x		Mole fraction x/H_2O of the gas x trapped in amorphous ice
K^m	J s^{-1} m^{-1} K^{-1}	Heat conduction coefficient of the porous matrix
K^n		Knudsen number
k^l	J s^{-1} m^{-1} K^{-1}	Heat conductivity of the solid l ($l = i$ for the solid phase of the icy components x, d for the dust grains and cl for the clathrate)
K^s	J $^{-1}$ m^{-1} K^{-1}	Conductivity of the solid phase of the components (dust and ices)
K^p	J $^{-1}$ m^{-1} K^{-1}	Radiative conductivity across the pores
(m, n)		$(0, \frac{1}{2})$ for the predictor and $(\frac{1}{2}, 1)$ for the corrector
M_n	kg	Comet nucleus mass
M_{H_2O}	kg mol^{-1}	Molar mass of water
M^{cl}_x	kg mol^{-1}	Molar mass of the species x trapped in the clathrate
M_x	kg mol^{-1}	Molar mass of the species x
n_{hyd}		Hydrate number of clathrate
$N^{am}_{H_2O}$	mol m^{-3}	Number of moles of amorphous water ice per unit volume
N_p	m^{-2}	Number of cylindrical pores per unit of surface
P_r	s	Nucleus rotation period of the comet
P_t	Pa	Total gas pressure
P_x	Pa	Partial pressure of gas x
P^{cl}_x	Pa	Equilibrium pressure of the corresponding single guest clathrate
P^s_x	Pa	Sublimation vapor pressure of the species x
P^{cl}_{MG}	Pa	Equilibrium pressure of the MG clathrate
Q^{cl}_{gas}	mol m^{-3} s^{-1}	Rate of trapping/release of volatile molecules x per unit of nucleus volume during the formation/dissociation of clathrate
q^{cl}_k	mol m^{-3} s^{-1}	Number of moles of gas trapped ($k = f$ for formation of clathrate) or released ($k = d$ for dissociation of clathrate) by the clathrate
Q^{cl}_x	mol m^{-3} s^{-1}	Rate of trapping/release of gas x in/by clathrate per unit of nucleus volume
Q^{cr}_x	mol m^{-3} s^{-1}	Rate of release of gas x by amorphous water ice per unit of nucleus volume
Q^s_x	mol m^{-3} s^{-1}	Rate of sublimation/condensation volatile molecule x per unit of nucleus volume
R	J mol^{-1} K^{-1}	The perfect gas constant
R_h	UA	Heliocentric distance
R_n	m	Radius of the nucleus
r_i	m	Distance of the layer i from the center of the nucleus
r_p, r^i_p	m	Radius and initial radius of the pores
T	K	Temperature
t	s	Time
V_i	m^3	Spherical volume of the layer
v^t	m s^{-1}	Thermal velocity of molecules
Y^{cl}	J s^{-1} m^{-3}	Power per unit volume released/taken during the formation/dissociation of clathrates
Y^{cr}	J s^{-1} m^{-3}	Power per unit volume released during the crystallization process of amorphous water ice
Y^{chs}	J s^{-1} m^{-3}	Power per unit volume exchanged between the gas phase of molecule x and the solid matrix
y^g_x		Molar fraction of the volatile x in the gas phase
y^{cl}_x		Molar fraction of the volatile x trapped in the clathrate structure
Z^{tot}_x	mol m^{-2} s^{-1}	Total molar flux of gas x

ARTICLE 5

Ferradaz T., Bénilan Y., Fray N., Jolly A., Schwell M., Gazeau M.-C., Jochims H.-W. and Guillemin J.-C. (2009)

Temperature dependant photoabsorption cross sections of cyanoacetylene and diacetylene in the mid- and vacuum-UV: Application to Titan's Atmosphere.

***Planetary and Space Science*, 57(1), 10-22.**

Available online at www.sciencedirect.com
ScienceDirect
Planetary and Space Science 57 (2009) 10–22
Planetary and Space Science
www.elsevier.com/locate/pss

Temperature-dependent photoabsorption cross-sections of cyanoacetylene and diacetylene in the mid- and vacuum-UV: Application to Titan's atmosphere

T. Ferradaz[a,*], Y. Bénilan[a], N. Fray[a], A. Jolly[a], M. Schwell[a], M.C. Gazeau[a], H.-W. Jochims[b]

[a]*LISA, Laboratoire Interuniversitaire des Systèmes Atmosphériques, UMR 7583, Universités Paris 7 et Paris 12, 61 avenue du Général de Gaulle, 94010 Créteil Cedex, France*
[b]*Institut für Physikalische und Theoretische Chemie der Freien Universität Berlin, Takustr. 3, 14195 Berlin, Germany*

Received 11 July 2008; received in revised form 8 October 2008; accepted 8 October 2008
Available online 25 October 2008

Abstract

Cyanoacetylene (HC_3N) and diacetylene (C_4H_2) play an important role in the photochemistry of Titan's atmosphere, in part because of their strong absorption between 110 and 180 nm. Accurate photoabsorption cross-sections at temperatures representative of Titan's atmosphere are required to interprete Cassini observations and to calculate photolysis rates used in photochemical models. Using synchrotron radiation as a tunable vacuum ultraviolet (VUV) light source, we have measured absolute photoabsorption cross-sections of C_4H_2 and HC_3N with a spectral resolution of 0.05 nm in the region between 80 and 225 nm and at different temperatures between 173 and 295 K. The measured cross-sections are used to model transmission spectra of Titan atmosphere in the VUV.

Keywords: Cyanoacetylene; Diacetylene; Absorption cross-sections; Vacuum ultraviolet; Low temperatures; Titan

1. Introduction

Titan, the largest satellite of Saturn, is the only body in the Solar System besides the Earth with a dense atmosphere mainly composed of dinitrogen (N_2). It also contains a large amount of methane (CH_4), around 5% in the troposphere and 1.5% in the stratosphere (Niemann et al., 2005; Flasar et al., 2005). High-energy electrons from Saturn's magnetosphere and solar UV photons induce the dissociation of N_2 and CH_4 in the upper atmosphere. The recombination of the fragments initiates an organic chemistry that leads to the production of numerous saturated and unsaturated hydrocarbons and nitriles. Many of those molecules have been detected from the analysis of ultraviolet and infrared spectra recorded by the Voyager missions (Hanel et al., 1981; Kunde et al., 1981; Smith et al., 1981) and confirmed by ISO observations (Coustenis et al., 2003). Some more complex and heavier molecules up to C_6 have been revealed in situ in Titan's upper atmosphere by the Cassini ion and neutral mass spectrometer (INMS) (Waite et al., 2005). Recent spectroscopic observations by the composite infrared spectrometer (CIRS) (Teanby et al., 2007; Coustenis et al., 2007) and the ultraviolet imaging spectrograph (UVIS) (Shemansky et al., 2005) onboard the Cassini spacecraft have confirmed the chemical diversity of Titan's atmosphere.

Two of the minor and heaviest constituents detected in Titan's atmosphere are cyanoacetylene (HC_3N) and diacetylene (C_4H_2) (also called propynenitrile and butadiyne). They have been identified for the first time by Voyager infrared measurements (Kunde et al., 1981). The stratospheric abundance of both compounds shows a significant increase from southern to northern latitudes (Coustenis et al., 2007; Coustenis and Bézard, 1995).

HC_3N is a member of the cyanopolyyne series with the general formula H–(C≡C)n–C≡N, $n>1$, while C_4H_2 ($n=2$) is the first member of the polyynes with the general

*Corresponding author. Tel.: +33 01 45 17 15 38; fax: +33 01 45 17 15 64.
E-mail addresses: ferradaz@lisa.univ-paris12.fr (T. Ferradaz), benilan@lisa.univ-paris12.fr (Y. Bénilan).

0032-0633/$ - see front matter © 2008 Elsevier Ltd. All rights reserved.
doi:10.1016/j.pss.2008.10.005

formula H–(C≡C)n–H. Cyanopolyynes are easily observable in the interstellar medium (ISM) by microwave observations because they have a strong permanent dipole moment. HC_3N has been detected for the first time in the ISM by microwave spectrocopy (Turner, 1971). Since then, longer chains, up to $HC_{11}N$, have been observed too (Bell et al., 1997). On the contrary, polyynes have no permanent dipole moment and are much more difficult to observe. C_4H_2 and C_6H_2 are the only polyynes observed so far. They have been identified in the infrared range in the circumstellar envelope of CRL618 by ISO (Cernicharo et al., 2001). The study of polyynes and cyanopolyynes are of special interest for Titan since they are predicted by photochemical models to be possible haze precursors (Yung et al., 1984; Lavvas et al., 2008). Thick layers of haze are observed in Titan's atmosphere and are responsible for the satellite's orange color. HC_3N is also important from an exobiological point of view since it is an intermediate in a prebiotic synthesis of cytosine proposed by Orgel (2002).

Complementary to infrared and microwave spectroscopy, UV spectroscopy is also a powerful diagnostic tool in the study of organic composition and chemical process in planetary atmospheres. Vacuum ultraviolet (VUV) spectroscopy sounds the upper atmosphere, from the thermosphere down to the upper stratosphere. The UVIS instrument on board the Cassini spacecraft is able to acquire spectra in Titan's atmosphere in the Far UV range (110–190 nm) with a resolution of 0.275 nm (Esposito et al., 2004). During Titan flyby labeled T_B, stellar occultation absorption spectra have shown the presence of several species including C_4H_2 (Shemansky et al., 2005).

The interpretation of spectra in the VUV range is critically dependent on the knowledge of the absorption coefficients of the molecules in the same temperature conditions as in the planetary environment (Jolly and Bénilan, 2008). Cross-sections in this wavelength range are also needed to calculate photolysis rates which are essential parameters for photochemical models. Unfortunately, for many organic compounds of planetological interest, ultraviolet spectra are not well known or even unavailable, especially at low temperatures.

The absolute absorption coefficient of HC_3N between 105 and 165 nm has already been measured by Connors et al. (1974) at room temperature. In the mid-UV domain (185–230 nm), temperature dependent studies have been carried out before (Bénilan et al., 1994; Andrieux et al., 1995) and it is interesting to note that significant differences have been observed (Bénilan et al., 1996).

The VUV spectrum of C_4H_2 has been obtained by Kloster-Jensen et al. (1974) at room temperature, in the wavelength range 122–276 nm, but only the relative intensities have been measured in this work. Absolute cross-sections values at room temperature have been obtained by Okabe (1981) and Glicker and Okabe (1987), in the 120–260 nm region. The temperature dependence of the ultraviolet absorption cross-sections has also been measured, but only between 160 and 220 nm with a resolution of 0.1 nm for temperatures ranging from about 220–330 K (Fahr and Nayak, 1994). In another study in the mid-UV range (195–265 nm), at 0.02 nm resolution, absolute absorption cross-sections were determined at various temperature between 193 and 293 K (Smith et al., 1998). Both studies have demonstrated significant effects of the temperature on cross-sections, in particular variation of band intensities.

It appears that for both molecules, temperature dependent studies are lacking below 160 nm where both molecules have their strongest absorption. Therefore, we have measured the temperature dependent absorption cross-sections of HC_3N and C_4H_2 in the gas phase between 80 and 225 nm at various temperatures between 170 and 298 K.

In Section 2, we present the experimental setup and the data reduction procedure used to determine cross-sections from synchrotron radiation absorption. In the Section 3, we show the results and discuss the effects of temperature on the absorption coefficients. Finally, we discuss in Section 4 the influence of our new laboratory measurements on the interpretation of Titan's atmospheric ultraviolet spectra.

2. Experimental method and procedures

C_4H_2 was prepared by dehydrochlorination of 1,4-dichloro-2-butyne ($C_4H_4Cl_2$) (Khlifi et al., 1995) in tetraethylene diethyl ether to which 40% aqueous sodium hydroxide solution was slowly added. Once formed, the compound was carried away in a stream of nitrogen, dried over calcium chloride and was trapped with an acetone/liquid nitrogen slush (−25 to −30 °C). It has then been distilled at −70 °C in order to eliminate impurities. This process was monitored using infrared spectroscopy.

HC_3N was synthesized according to the method of Moureu and Bongrand (1920) modified later by Miller and Lemmon (1967). In this procedure, ammonia is added on methylpropiolate and the corresponding amide is dehydrated to yield HC_3N. The purity of the final product was also checked by infrared spectroscopy. Both compounds were stored at liquid nitrogen temperature to avoid any polymerization.

Tunable VUV light was obtained from the synchrotron radiation facility BESSY in Berlin. A first set of measurements was made in the 80–200 nm spectral region at 0.3 nm resolution with the 10 m focal length normal incidence monochromator (NIM) at the U125/2 undulator beamline. A linear dispersion of 0.08 nm mm^{-1} was reached by using the first order of a 1200 lines/mm spherical grating. The recorded data were self-calibrated in wavelength by a stepwise system inside the monochromator (Reichardt et al., 2001a). To allow for measurements below windows cutoffs, the window (cf. Fig. 1) was replaced by a micro chanel plate (MCP) and a differential pumping system. An MCP allows for VUV light transmission and at the same

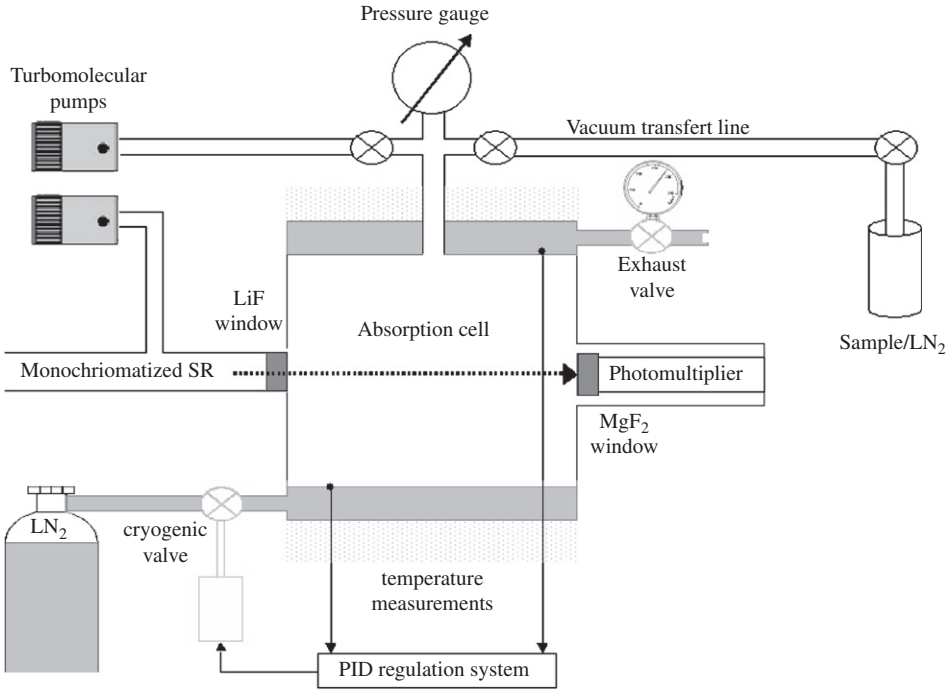

Fig. 1. Experimental setup used for measuring the ultraviolet absorption spectra at low temperatures.

time, a pressure gap of three orders of magnitude is realized, permitting application of the Beer–Lambert Law. Light detection was performed by a photomultiplier tube sensitive to visible light produced by fluorescence of sodium salicylate deposited on the exit BK7 glass window when excited by VUV photons. All results presented in this paper for the 80–115 nm range have been obtained with this configuration.

A second set of measurements have been taken between 115 and 225 nm using a 3 m focal length NIM equipped with a 600 lines/mm holographically ruled grating giving a linear dispersion of 0.56 nm mm^{-1}, connected to a dipole magnet beamline (DIP 12-1B) (Reichardt et al., 2001b). In these experiments, we reached an instrumental bandwidth (FWHM) of 0.05 nm. Wavelength calibration was obtained by using the first self-calibrated set of measurements as a reference. The VUV radiation intensity was measured directly with a solar blind photomultiplier tube closed by a MgF_2 window (Electron Tubes Limited 9402B with caesium telluride photocathode). The absorption cell is a cylinder (volume = 940 cm^3) with an optical pathlength of 11.77 cm (Fig. 1). In the second set of measurements, a LiF window was placed at the entrance of the cell instead of the MCP as presented in Fig. 1. The use of an holographically ruled grating with aluminum/MgF_2 coating provides low diffused light and the LiF window suppresses second order emission. Low temperatures in the cell were obtained by flowing liquid nitrogen in the double wall surrounding the cell. During the experiments, the temperature is measured continuously at two diametrically opposite positions with Type-K thermocouples fixed on the inside wall of the cell. The cell temperature is regulated by controlling the flow of liquid nitrogen through a cryogenic valve, making use of a standard proportional, integral, and derivative (PID) controller. The stability of the temperature is ± 1 K over a period of 8 h and thermal equilibrium is usually obtained after 1 h with a measured temperature gradient of <2 K over the absorption path. The cooling system allows us to reach almost liquid nitrogen temperatures but no experiment have been done below 170 K, since at such a temperature, the vapour pressure of the studied molecules drops below 1 μbar which is close to the current limit of our pressure measurement system.

The signal was recorded through a picoamperemeter (Keithley) using an integration time of 1 s per sample. Absolute photoabsorption cross-sections are calculated using the Beer–Lambert law:

$$\sigma = (1/l) \times \ln(I_0/I) \times (1013/P) \times (T/273) \quad (1)$$

σ corresponds to the absolute absorption coefficient (in cm^{-1} amagat^{-1}), I_0 is the light intensity transmitted with an empty cell, I is the light intensity transmitted through the gas sample, l the absorption path length (cm) and T (K) and P (mbar) are respectively the temperature and the pressure of the sample. Since the intensity of the light flux decreases with time, due to the decay of the storage ring current, I_0 is estimated by an interpolation between empty cell scans recorded before and after the spectra.

In the second data set, the use of an MgF_2 window to protect the solar blind photomultiplier prevents measurement of any flux below about 113 nm due to the transparency cut-off. Note that, similarly to previous studies (Hunter and Malo, 1969), we observe a shift of the short-wavelength cut-off as the temperature decreases (Fig. 4).

For each recorded spectrum, the sample is vaporized into the cell at the desired pressure which is monitored with an MKS baratron capacitance manometer (10^{-4} to 1 mbar). In the VUV domain, all measurements were made at pressures between 3 and 20 μbars to avoid any saturation of absorption features. In the mid-UV range, pressures of up to 100 μbars were used. For a given spectral region, at least four different pressures are used to check the reproducibility of the measurements and to make sure that the data are free from saturation. We verified that the data follow the Beer–Lamber law over the studied pressure range.

Experimental uncertainties on the cross-section determinations are estimated to be about 10%. This is mainly due to pressure measurements uncertainties and errors in the determination of the I_0 continuum level. In the mid-UV domain, uncertainties may reach 20% because of incident light fluctuations caused by the weakness of the synchrotron radiation above 200 nm. The consequence is a larger error on the determination of the I_0 continuum value. Also, a small path length is not well adapted in this spectral domain where small absorption coefficients are observed and hence large pressures are needed. In fact, the molecules' saturation vapour pressure values at low temperature are in fact limiting our ability to work at higher pressures.

3. Results and discussion

3.1. Cyanoacetylene

3.1.1. Photoabsorption by HC_3N at room temperature

Fig. 2 shows the absolute photoabsorption coefficient of HC_3N in the spectral region from 80 to 220 nm determined at room temperature (298 K). The experimental resolution is 0.3 nm below 115 and 0.05 nm from 115 to 225 nm. For the sake of completeness, we also show absorption cross-sections.

The absorption spectra of HC_3N exhibits a complex vibrational structure from 180 to 230 nm assigned to the forbidden electronic transition $^1\Delta_u \leftarrow {}^1\sum_g{}^+$ (Job and King, 1966; Bruston et al., 1989). The vibronic bands arise from the Herzberg-Teller effect: the intensity is borrowed from the allowed transitions by π-type vibrations. In this wavelength domain, the absolute absorption coefficient and its temperature dependency has already been studied by Bénilan et al. (1994).

Between 105 and 165 nm, Connors et al. (1974) room temperature study is the only one that reports absolute absorption cross-section measurements. The first transition extending from 151–164 nm has been assigned to a $^1\prod_u \leftarrow {}^1\sum_g{}^+$ transition by these authors. This system shows two doublets separated by about 2060 cm^{-1}, which implies the active $\nu'_3(\sigma^+)$ vibration mode measured at 2079 cm^{-1} in the $^1\sum_g{}^+$ electronic ground state (Jolly et al., 2007). A strong and diffuse intravalence shell band is observed with an origin at 145 nm. It has been assigned to a $^1\sum_u{}^+ \leftarrow {}^1\sum_g{}^+$ transition by Connors et al. (1974). A second peak is present at 141 nm separated by 1910 cm^{-1} from the previous one corresponding most likely again to excitation of the $\nu'_3(\sigma^+)$ vibration. This diffuse system is followed by several strong and sharp transitions which have been assigned by Connors et al. (1974) to Rydberg series converging to the first ionization energy at 11.6 eV (106.9 nm). As seen in Fig. 2, the absorption coefficient varies by 3 orders of magnitude in the entire UV region, with a maximum of 6125 cm^{-1} am^{-1} at 145 nm.

Our cross-section values below 165 nm are in very good agreement with those of Connors et al. (1974) for the larger

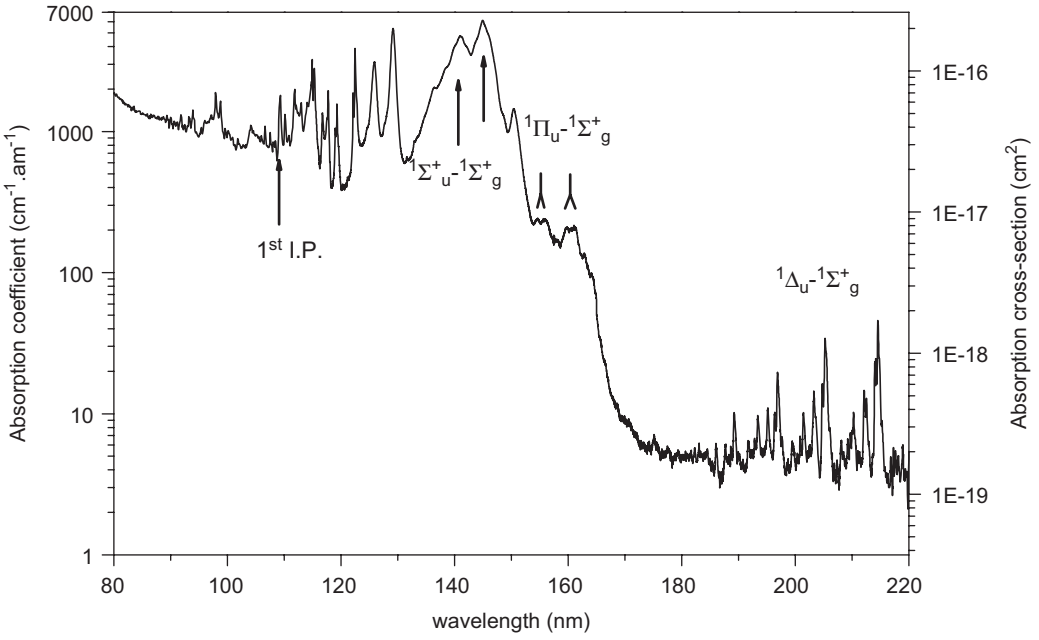

Fig. 2. Absolute photoabsorption cross-section of HC_3N between 80 and 225 nm at room temperature. The main electronic transitions are shown.

Table 1
Absorption cross-sections (in $cm^{-1} am^{-1}$) for selected peaks of HC_3N measured in this work and in previous work and the percentage changes $P_{c,203\,K}$ and $P_{c,243\,K}$.

λ (nm)	Connors et al. (1974) ($cm^{-1} am^{-1}$)	$\sigma_{298\,K}$ ($cm^{-1} am^{-1}$)	$\sigma_{243\,K}$ ($cm^{-1} am^{-1}$)	$\sigma_{203\,K}$ ($cm^{-1} am^{-1}$)	$P_{c,\ 243\,K}$	$P_{c,\ 203\,K}$
114.5		1584	1559	1599	−1.6	0.9
114.8		2192	2176	2233	−0.7	1.9
114.9		3235	3373	3553	4.3	9.8
115.1		2120	2198	2322	3.7	9.5
115.3	2800	2798	2975	3038	6.3	8.6
116.3	–	671	730	783	8.7	16.6
116.7	1095	1356	1408	1456	3.8	7.4
117.5	–	1245	1293	1309	3.8	5.1
117.7	1257	1950	2133	2235	9.4	14.6
119.0	–	1057	1110	1161	5.1	9.8
119.3	1113	1566	1728	1846	10.3	17.9
122.1	–	1878	2036	2186	8.4	16.4
122.4	2658	3886	4525	4890	16.4	25.8
125.9	2727	3104	3266	3364	5.2	8.4
129.2	5053	5361	5635	5769	5.1	7.6
131.6	–	661	684	727	3.5	10
132.9	–	860	879	930	2.3	8.1
136.5	2109	2042	2056	2108	0.7	3.2
141.1	4857	4738	4845	4872	2.3	2.8
145.0	6055	6125	6334	6315	3.4	3.1
150.4	1386	1452	1442	1437	−0.7	−1
154.6	307	242	200	202	−17.5	−16.8
155.9	–	240	212	198	−11.5	−17.2
159.8	–	209	164	123	−21.7	−41.3
161.0	236	217	186	142	−14.1	−34.3
162.9	–	135	94	61	−30.5	−55

and most diffuse bands: only 1% difference at 145 nm and 6% at 129.2 nm. On the contrary, large differences arise when comparing sharper peaks, for instance at 122.4 and 117.7 nm where we find peak intensities 50% higher than Connors et al.'s (see Table 1). The observed differences in the intensities of the sharpest peaks can be explained by the different spectral resolution used in both studies. The resolution is not given explicitly by Connors et al. (1974), but our HC_3N spectrum is clearly better resolved since it shows more detailed structure. For example, several new peaks can be distinguished at 119, 122.1 nm and between 114.4 and 118.2 nm.

Our mid-UV range measurements can be compared with those of Bénilan et al. (1994) in Table 2. Discrepancies of up to about 20% appear at room temperature and even more for some features at lower temperature. This clearly shows that our setup is much less precise in the mid-UV compared to the VUV, mainly due to the fluctuations of the synchrotron radiation above 200 nm and the small size of our cell as evoked earlier. In their study, Bénilan and colleagues used a deuterium lamp as light source and a 3 m long cell, specially adapted for the mid-UV domain.

3.1.2. Temperature dependence of the absorption coefficient of HC_3N between 170 and 225 nm

Fig. 3 shows the absolute absorption coefficient of HC_3N between 170 and 225 nm at the resolution of 0.05 nm at three different temperatures: 298, 243 and 203 K. Our measurements confirm the temperature dependency highlighted by Bénilan et al. (1994, 1996). In particular, we observe an increase of the most intense bands and a decrease of the width of the bands when the temperature decreases. Temperature effects can be quantified by calculating the fractional change in cross-section value $P_{c,T}$. The change of cross-section values σ_T as a function of temperature T may be defined as the percent change $P_{c,T}$ which can be given as

$$P_{c,T} = 100 \times \frac{\sigma_T - \sigma_{298}}{\sigma_{298}} \quad (2)$$

A negative or a positive $P_{c,T}$ value means that the absorption coefficient at a temperature T is respectively smaller or larger than that at 298 K.

The absolute absorption coefficients versus temperature at different peak positions is shown in Table 2, together with the percentage change $P_{c,T}$. The absorption coefficient for the intense absorption peak at 224.7 nm increases by 31% from 40.9 to 53.6 $cm^{-1} am^{-1}$ when the temperature decreases from 298 to 203 K. A similar increase, between 20% and 34%, is observed for the other three main peaks at 196.9, 205.2 and 214.6 nm. Our $P_{c,T}$ values are very close to those obtained by Bénilan and colleagues (see Table 2).

Table 2
Mid-UV absorption coefficients (in $cm^{-1} am^{-1}$) of cyanoacetylene for various features measured at selected temperatures in this work and in previous work (Bénilan et al., 1994) with the percentage changes $P_{c,\ 203\,K}$ and $P_{c,\ 243\,K}$.

λ (nm)	Bénilan et al. (1994) at 293 K	Bénilan et al. (1994) at 213 K	σ (298 K)	σ (243 K)	σ (203 K)	$P_{c,243\,K}$	$P_{c,203\,K}$
189.2	–	–	10.2	8.9	11.7	−12.8	15.3
193.4	9.0	8.3	9.7	9.3	11.5	−3.7	18.7
195.2	11.8	16.8	11.0	11.6	14.5	5.7	31.5
196.4	10.5	10.0	10.2	10.3	12.1	1	18
196.9	19.8	20.5	19.7	22.0	25.9	11.8	31.4
200.8	7.4	6.9	6.9	6.4	10.0	−7.8	43.6
201.4	9.9	10.5	10.2	11.1	14.4	9	41.1
203.3	13.5	15.5	14.5	15.2	19.6	4.7	35.3
204.8	14.8	19.0	16.4	18.3	22.5	12	37.7
205.2	28.4	38.5	34.3	37.5	45.9	9.5	34
210.3	9.4	8.9	10.2	9.3	10.5	−9	2.3
212.1	14.1	16.5	14.6	16.2	18.2	10.8	24.3
212.5	12.0	13.3	12.9	13.1	14.9	1.9	16.3
214.0	19.7	26.8	23.5	25.4	31.0	8	32
214.2	24.3	31.8	24.6	28.1	33.4	14.3	35.9
214.2	21.4	25.8	23.7	24.1	28.4	1.8	19.9
214.6	37.9	48.3	45.8	49.2	55.0	7.4	19.9
221.9	7.8	9.8	8.6	11.2	12.8	30.2	49.1
222.4	8.4	10.8	8.8	11.8	13.3	34.7	51.7
224.1	14.0	20.1	16.2	19.2	20.0	18.3	23
224.2	17.1	22.9	19.5	21.5	22.2	10.5	14.1
224.7	33.7	47.6	40.9	47.6	53.6	16.5	31

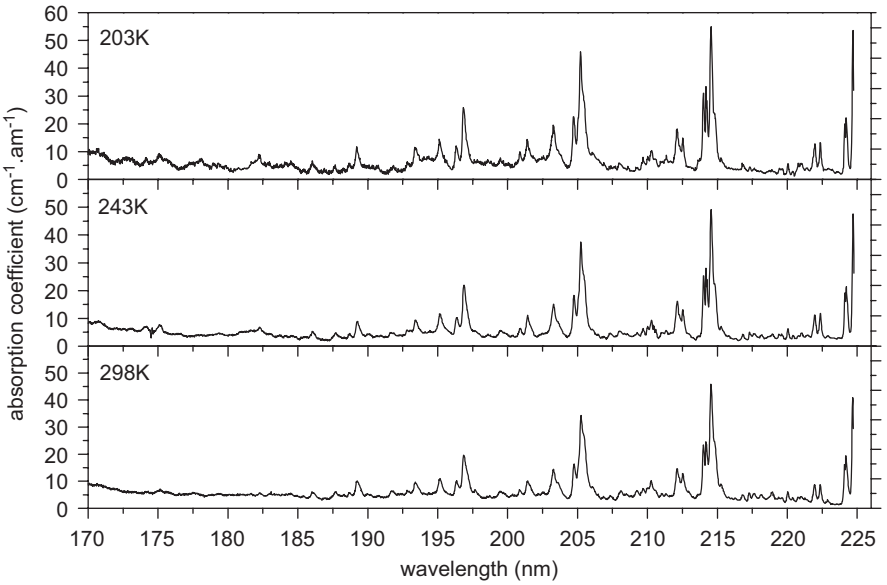

Fig. 3. Absolute absorption coefficient of HC_3N between 170 and 225 nm measured at 203, 243 and 298 K.

3.1.3. Temperature dependence of the absorption coefficient of HC_3N between 115 and 170 nm

The photoabsorption cross-section of HC_3N at low temperature has been measured for the first time in the VUV region. As seen in Fig. 4, the spectra obtained at different temperatures are not significantly different. The absorption coefficients of the main bands at 298, 243 and 203 K are listed in Table 1, together with the $P_{c,T}$ values. For the large and diffuse bands at 125.9, 129.2, 141.1 and 145 nm, the variation of the peak absorption coefficient is $<10\%$ in the studied temperature range. This is within the quoted experimental error. Only the sharpest absorption features show significant temperature effects. For example, the band at 122.4 nm shows an increase from 3886 to 4890 $cm^{-1} am^{-1}$ for a temperature change from 298 to 203 K. This variation can be explained by a rearrangement

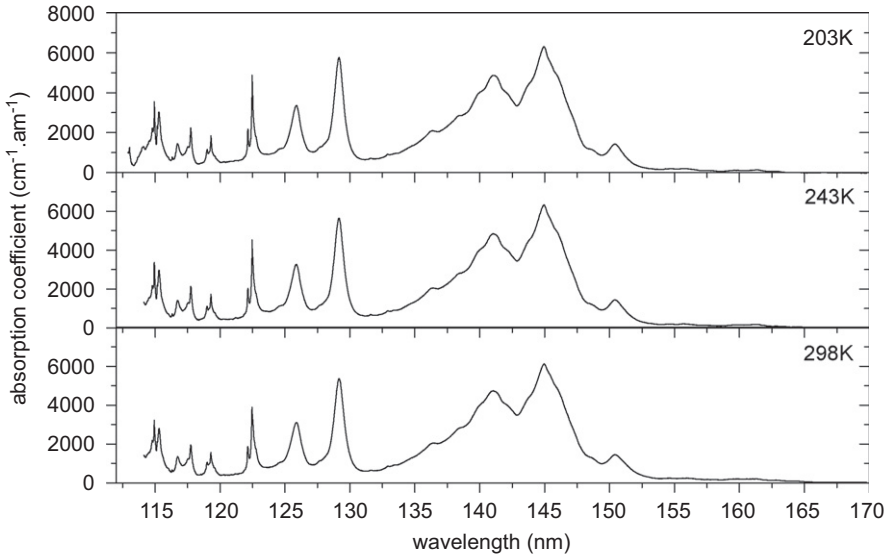

Fig. 4. Absolute absorption coefficient of HC_3N between 112 and 170 nm measured at 203, 243 and 298 K.

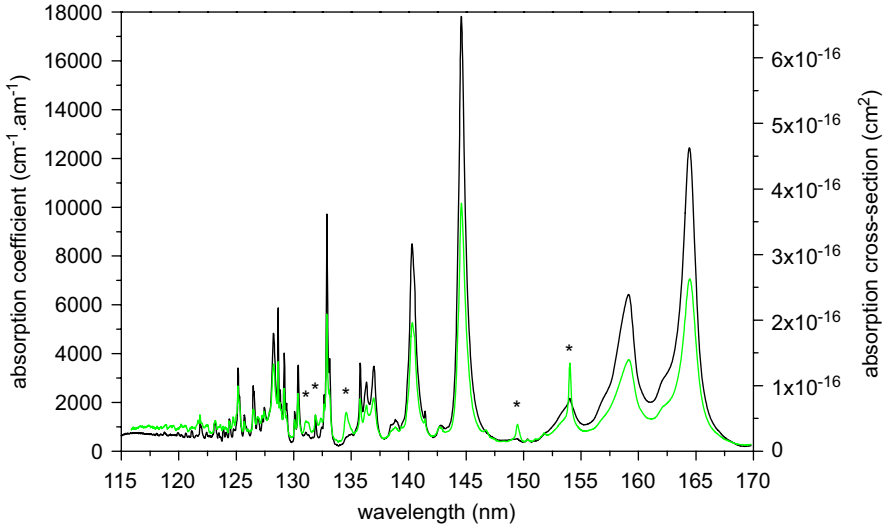

Fig. 5. The absorption spectrum of C_4H_2 between 115 and 170 nm at 268 K obtained with a pure sample (black line) compared to the one at room temperature (green line). The comparison shows the C_4H_2 sample at 293 K contains an impurity, its the main features being identified by stars.

of the rovibrational population distribution that favours sharper band profiles when the gas temperature is reduced. Since the transition moment must be conserved, larger cross-sections peaks are usually observed at low temperatures. The broadening of the bands, caused by the predissociation of the molecule, prevents observation of this phenomenon in the large and diffuse bands. This explains qualitatively the greater variations observed for the sharper peaks as compared to the broad ones. It also explains the minor role of the temperature in the 112–170 nm domain, compared to the mid-UV where predissociation is less strong. We also observe large negative $P_{c,T}$ values between 152 and 164 nm. This is very likely an indication that the absorption originates from an excited vibrational level of the ground electronic state.

3.2. Diacetylene

3.2.1. Preliminary remarks on the purity of the sample

In spite of all precautions that were taken during the synthesis of C_4H_2 (including IR spectral control of the sample) the presence of an impurity has been revealed in spectra between 115 and 170 nm. The impurity is possibly 2-chloro-1-butene-3-yne (C_4H_3Cl), a compound that could have formed by the elimination of only one equivalent HCl from the compound 1,4-dichloro-2-butyne ($C_4H_4Cl_2$) (Khlifi et al., 1995). It has been observed by several other groups (Georgieff and Richard, 1958; Smith et al., 1998). The contamination is identified by one peak at 154.3 nm and several other smaller features (134.8, 149.7 and 131–133 nm) which vary in intensity due to the evolving composition of our sample. In fact, outgasing enhanced the

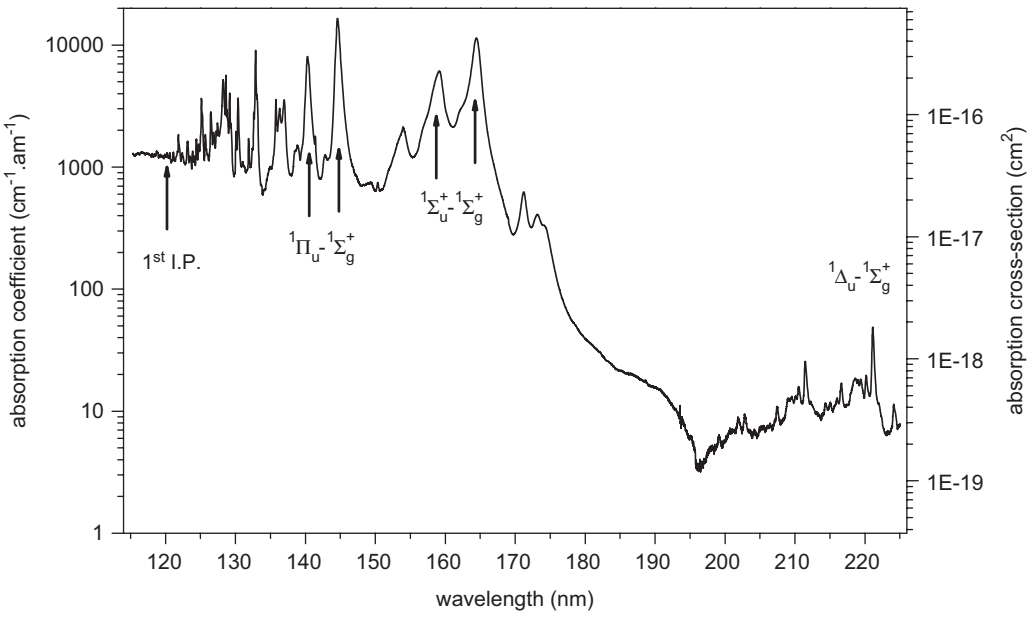

Fig. 6. The photoabsorption cross-section of C_4H_2 on a logarithmic scale in the 115–225 nm at ambient temperature (293 K). The main electronic transitions are shown.

purity of our sample during the measurements. Finally, our last spectrum, obtained at 268 K, does not show any impurity absorption peaks unlike the spectrum obtained at 293 K, as seen in Fig. 5. By considering the latter as free of impurity, the spectrum of the impurity could be estimated by subtraction and the partial pressure of the impurity contained in each sample can be calculated. Assuming that the impurity spectrum does not vary with temperature, the pressure corrections that have been applied to obtain the C_4H_2 absorption coefficients are 15% at 298 and 243 K, 5% at 203 K and 20% at 173 K.

3.2.2. *Photoabsorption by C_4H_2 at 293 K*

The absorption coefficient of C_4H_2 measured at 293 K and 0.05 nm resolution in the 115–225 nm range is shown in Fig. 6, together with the cross-section values.

As it is the case for HC_3N, the absorption spectrum of C_4H_2 can be clearly divided into two parts. The first one, between 195 and 225 nm, shows structured vibrational progressions which were assigned to a $^1\Delta_u \leftarrow {}^1\sum_g{}^+$ forbidden electronic transition by Haink and Jungen (1979). The second region, between 115 and 175 nm, shows a succession of several strong absorption features. The spectrum consists mainly of two allowed electronic transitions with vibrational progressions. An intense and diffuse band, assigned to the origin of the $^1\sum_u \leftarrow {}^1\sum_g{}^+$ transition, is observed at 164.4 nm (Smith, 1967). Two peaks at 159.1 and 154 nm corresponding to a vibrational progression with spacings of about 2000 cm^{-1} are assigned to the excitation of the ν_2 vibrational C≡C stretching. The prominent peak at 144.6 nm is assigned to the origin of the $^1\prod_u \leftarrow {}^1\sum_g{}^+$ transition (Smith, 1967). This transition also shows a vibrational progression with peaks at 140.3 and 136.4 nm. Almost all the strong peaks belong to the R and R' Rydberg series leading both to the first ionization energy at 10.18 eV (121.9 nm). At shorter wavelength a third Rydberg R'' series, with associated ν_2 vibration progressions, was identified by Smith (1967).

Table 3
Relative absorption coefficients at low temperatures of diacetylene for the two main peaks in mid-UV, in this work and in previous works.

λ (nm)	$\sigma_{223}/\sigma_{295\,K}$ Fahr and Nayak (1994)	$\sigma_{193}/\sigma_{293\,K}$ Smith (1967)	$\sigma_{203}/\sigma_{293\,K}$ from this work
211.3	1.03	1.31	1.16
221	1.05	1.38	1.33

3.2.3. *Temperature dependence of the absorption coefficient of C_4H_2 between 195 and 225 nm*

The absorption coefficient of C_4H_2 has been measured from 180 to 225 nm at two temperatures, 293 and 203 K. As shown in Table 3, we measure a significant temperature effect for the strongest peaks at 211.3 and 221 nm. In order to compare this temperature dependence with that observed with previous studies by Fahr and Nayak (1994) and Smith et al. (1998), we list in Table 3 the ratio between low- and room-temperature cross-sections. Fahr and Nayak saw almost no change from 295 to 223 K, but according to Smith et al. (1998), the presence of an impurity (C_4H_3Cl) biased their study of the temperature dependence. On the contrary, the results of these authors (Smith et al., 1998) are comparable to ours, considering experimental errors (see Table 3).

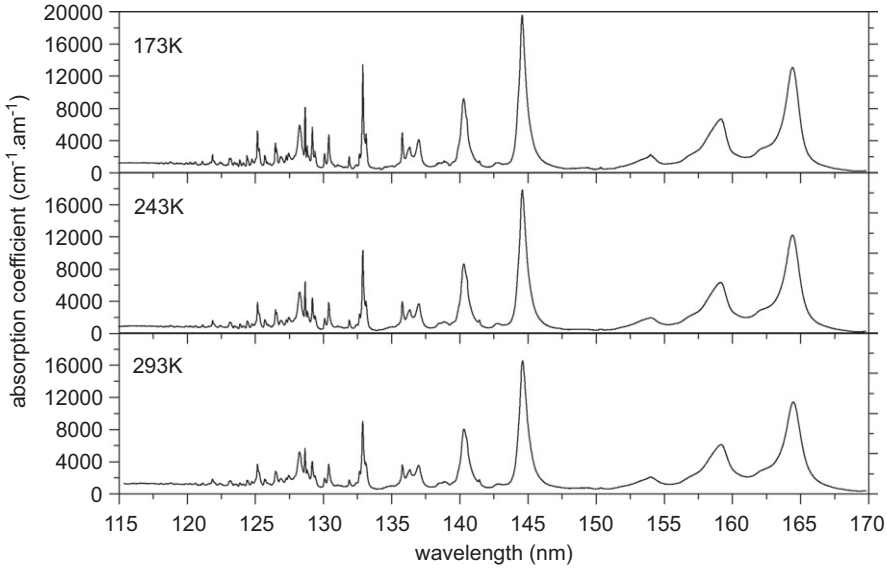

Fig. 7. Absorption coefficient of C_4H_2 between 115 and 170 nm at different temperatures: 293, 243 and 173 K.

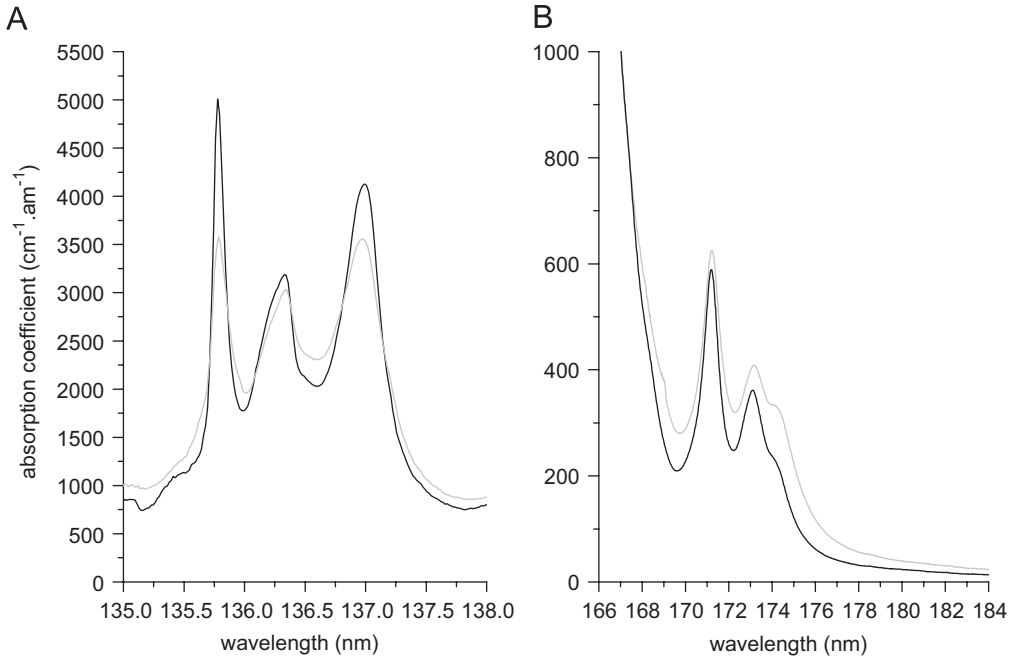

Fig. 8. Variation in the structure of the absorption coefficient of C_4H_2 in the regions 135–138 nm (panel A) and 166–184 nm (panel B) against temperature for 293 K (gray line) and 173 K (dark line).

3.2.4. Temperature dependence of the absorption coefficient of C_4H_2 between 115 and 170 nm

Here, we present the first VUV low temperatures absorption coefficients for C_4H_2 in the 115–170 nm wavelength range (268, 243, 203 and 173 K). The corresponding spectra are presented in Fig. 7 for 173, 243 and 293 K. Most of the peaks show an intensity enhancement at low temperature compared to room temperature. The sharpest feature at 132.9 nm shows the strongest variation. It increases by 50% when the temperature decreases from room temperature to 173 K. Narrowing of the band width is also clearly observed for this band. In Fig. 8, we show an example of the influence of the temperature on the line shape of three overlapping transitions between 135 and 138 nm (Fig. 8A) and in the 166–184 nm interval (Fig. 8B). In the 135–138 nm interval, as the temperature decreases, the background continuum decreases and the band profile becomes narrower. Furthermore, the maxima of the three band increase. This effect is due to the redistribution of the population towards lower rotational energy levels with decreasing temperature. This is expected in the case of cold bands originating from the vibrational ground state. In the

Table 4
Absorption cross-section (in $cm^{-1}\,am^{-1}$) of C_4H_2 for selected peaks at different temperatures and comparison with the work of Okabe (1981).

λ (nm)	σ_{293}	Okabe (1981)	$\sigma_{293}/\sigma_{Okabe}$	σ_{268}	σ_{243}	σ_{203}	σ_{173}
125.2	3661	2767	1.3	3416	3892	4229	5179
128.7	5655	3573	1.6	5873	6429	7036	8116
129.2	4034	2260	1.8	4027	4425	4850	5694
130.4	3692	2010	1.8	3531	3852	4078	4737
132.9	9022	2767	3.3	9723	10 317	11 617	13 464
135.8	3580	2139	1.7	3616	3961	4350	5009
137.0	3556	ind.	–	3487	3687	3783	4127
140.3	8284	5964	1.4	8495	8655	9053	9572
144.6	16 548	6153	2.7	17 820	17 829	18 956	19 560
159.1	6117	4621	1.3	6428	6365	6680	6691
164.4	11 418	5695	2	12,435	12 226	13 135	13 082

region 166–184 nm, we also observe a decrease of the background continuum as the temperature decreases. The band maxima decrease, however. This effect is certainly due to the combination of the redistribution over rotational levels for the cold bands and the presence of hot bands originating from excited vibrational levels (Table 4).

The absorption coefficient of C_4H_2 has been measured by Okabe (1981) and by Fahr and Nayak (1994). Okabe has measured the absorption cross-sections between 120 and 180 nm at 0.08 nm resolution and room temperature. Our values are approximately a factor of two higher than those determined by Okabe, for the most intense bands. Our absorption coefficient at 132.9 nm is even three times higher than the value reported by Okabe. These discrepancies are mainly due to saturation problems in Okabe's study as already mentioned by Shemansky et al. (2005) and Jolly and Bénilan (2008). Indeed, Okabe has used an absorption cell ten times longer than ours and a minimum pressure of 60 μbars which leads to zero transmission for the most intense bands. Fahr and Nayak (1994) have measured the absorption cross-section between 160 and 260 nm at a resolution of 0.2 nm, as well as the temperature dependence between 220 and 300 K. They took great care of avoiding saturation and showed a significant temperature dependence of the absorption cross-section. Our results at room temperature show a good agreement between 160 and 175 nm: our values are slightly lower, by 5% for the 164.4 nm and larger, by 15%, for the weak band at 171 and 173 nm. These differences are possibly due to a better resolution in the present study.

Temperature effects are presented in Fig. 9 where the percentage changes $P_{c,T}$ are presented for various peaks at four different temperatures. Except for the two sharpest features (132.9 and 129.7 nm) where the relative variation reaches 50%, we observe effects of 8–18% for the most intense bands when the temperature decreases from 293 to 173 K. For the band at 164.4 nm, which is the only one for which we can make a comparison with the results of Fahr and Nayak (1994), we find a 15% increase when lowering the temperature from 300 to 203 K whereas they found a

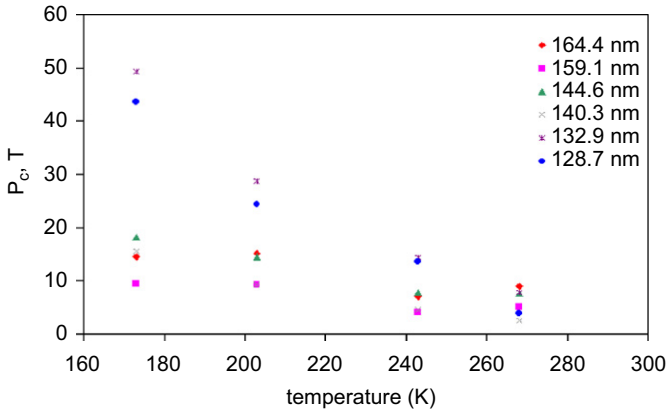

Fig. 9. The percentage change $P_{c,T}$ for C_4H_2 for different temperatures and for selected wavelengths.

30% increase for the absorption coefficient measured at 223 K. Fahr and Nayak do not give experimental errors, however their results are reproducible within 2%. Thus, there seems to be a significant difference compared to our measurements. This remains to be clarified in the future.

4. Implications for the interpretation of Titan's atmospheric spectra

From observations of a stellar occultation, the Cassini UVIS experiment (Esposito et al., 2004) was able to measure transmission spectra of Titan's atmopshere in the far ultraviolet (Shemansky et al., 2005). Absorption cross-sections at low temperatures are necessary to interpret satisfactorily these observations which sound the upper atmosphere of Titan. By analysing the atmospheric transmission spectra, Shemansky et al. (2005). were able to infer the vertical distribution of the absorbing species. Whereas HC_3N was not detected, in the case of C_4H_2, difficulties appeared in the analysis due to Okabe's erroneous absorption cross-section data, as concluded by Shemansky et al. (2005)

In order to test the influence on the analysis of UVIS data of our new absorption cross-sections obtained at low

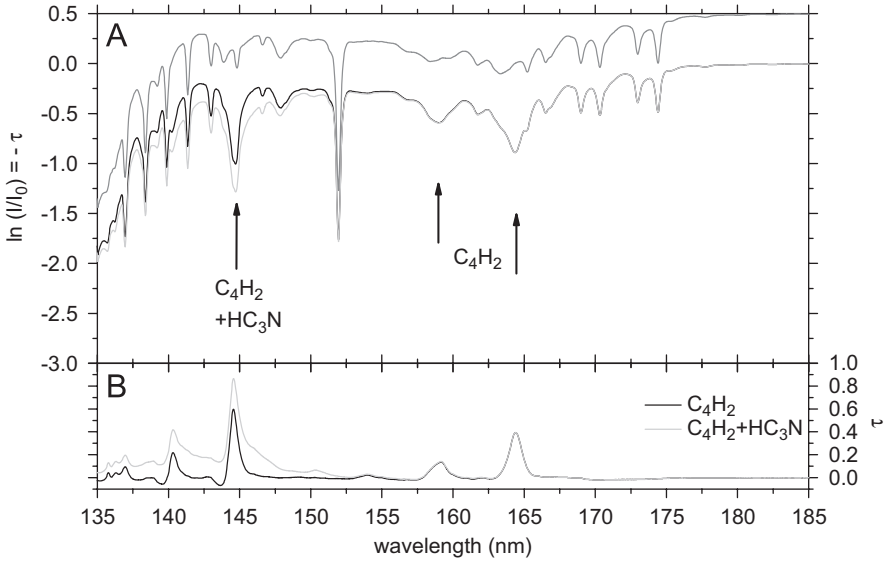

Fig. 10. Expected Titan's transmission spectra simulated in the 135–185 nm range (in panel A). The first one (gray line shifted upward by 0.5 for clarity) is obtained using the last available absorption spectra for CH_4, C_2H_2, C_2H_2, C_2H_6 and HCN with the following column densities (cm^{-2}): $CH_4 = 1.9 \times 10^{17}$, $C_2H_2 = 1.1 \times 10^{16}$, $C_2H_4 = 8.2 \times 10^{15}$, $C_2H_6 = 7.3 \times 10^{15}$, $HCN = 1.9 \times 10^{16}$. A second simulation (black line) integrates absorption from C_4H_2 reported in this present work with an abundance value of $1.3 \times 10^{15}\,cm^{-2}$. The transmission spectrum in light gray line incorporates absorption from HC_3N with the same abundance value as the one of C_4H_2. Panel B shows the optical densities corresponding to the last two cases.

temperatures for C_4H_2 and HC_3N, we have simulated transmission spectra to be expected at high altitude in Titan's atmosphere (cf. Fig. 10).

Considering the available absorption cross-sections for the main molecular species, CH_4, C_2H_6 (Chen and Wu, 2004), C_2H_2 (Wu et al., 2001), C_2H_4 (Wu et al., 2004) and HCN (Nuth and Glicker, 1982), the expected transmission spectra can be calculated using the column densities values given by Shemansky et al. (2005) in Fig. 2 of their paper. The calculated transmission spectrum is then convoluted by a boxcar function with a width of 0.275 nm to match UVIS resolution. It is shown as a gray line in Fig. 10A.

We obtain a second transmission spectrum (black line in Fig. 10A) by adding our absorption cross-section of C_4H_2 and taking an abundance value of $1.3 \times 10^{15}\,cm^{-2}$ as proposed by Shemansky et al. (2005). As seen in Fig. 10, strong C_4H_2 absorption features appear at 144.6 and 164.4 nm due to C_4H_2. These features are clearly observed in the UVIS transmission spectra of Titan's atmosphere as can be seen in Fig. 2 of Shemansky's paper, but they were lacking in their model which uses Okabe's saturated absorption data for C_4H_2. Our measured absorption cross-sections for C_4H_2 should significantly improve the analysis of the transmission spectra and the determination of its column densities at different altitudes and latitudes. Since absorption maxima in the main bands are enhanced as compared to previous reference data and since they increase with decreasing temperature, we can expect a lower abundance of C_4H_2 than the proposed value by Shemansky et al. (2005).

A third simulation (light gray line) is done by adding our HC_3N absorption cross-sections at the same abundance like C_4H_2 ($1.3 \times 10^{15}\,cm^{-2}$) because recent results from photochemical models (Hébrard et al., 2007) predict that these two compounds are present in Titan's atmosphere at approximately the same concentration. Unlike in the low-resolution Voyager observations (Vervack et al., 2004), the contribution of the two species HC_3N and HCN in the region 135–150 nm, can be well separated with UVIS which have a resolving power ten times higher. However, it is now the similarity of the spectral features of HC_3N and C_4H_2 which makes them difficult to separate. Nevertheless, as can be seen in Fig. 10B, the optical depth at 144.6 nm increases when HC_3N is present. This leads to a change in the relative intensity of the two main absorption bands of C_4H_2 at 145 and 165 nm. These effects should be easily visible in the observed transmission spectra taken by UVIS if the signal to noise ratio is good enough. This could lead to the first UV detection and quantification of HC_3N in the upper atmosphere of Titan.

5. Conclusion

We have determined the absorption coefficients for two gaseous organic species, HC_3N and C_4H_2, from the vacuum UV spectral region up to the mid UV. The absorption cross-sections were determined at 0.05 nm resolution in the 80–225 nm range for HC_3N, and between 115 and 225 nm for C_4H_2. The resolution that we have used has allowed us to observe several sharp features which had not been observed before. Special care has been taken to ensure that the absorption coefficients were not obtained from saturated spectra. Thus, in the case of C_4H_2, significantly higher absorption coefficients were obtained as compared to the previously reported values by Okabe (1981). To a lesser extent, absorption coefficients measured

for HC_3N are also generally larger than the values of Connors et al. (1974).

The study in the 180–225 nm region has confirmed the temperature dependence of the absorption coefficient reported by earlier studies. No significant temperature dependencies for the cross-sections in the 112–170 nm domain over the 203–298 K temperature range have been observed for HC_3N. However, in the same wavelength range, the absorption coefficient of C_4H_2 clearly increases by 50% for sharp peaks when the temperature is changed from 296 to 173 K. Under low-temperature conditions, we note an almost linear increase of both the absorption maxima and the narrowing of the band profile. This is interpreted in terms of the change of the population of the rovibrational levels. Since the mid-UV and VUV measurements were obtained in the same experimental conditions, and since the results in the mid-UV agree with previous studies, it confirms that in the VUV the temperature effects are important in the case of C_4H_2 but not for HC_3N. The absorption bands of C_4H_2 are much narrower than those of HC_3N in the same wavelength range explaining the different behavior observed for these compounds.

These new results will improve the interpretation of Titan transmission spectra. Detection of HC_3N by UVIS and a more accurate determination of the vertical profile of C_4H_2 are expected.

More data at low temperature would be needed to improve the modeled transmission of limb spectra obtained by UVIS. For example, the model still uses room temperature cross-sections for HCN. The determination of HCN cross-sections at low temperature is clearly needed.

All the spectra presented here can be found in our spectroscopic data base at the following internet link: http://www.lisa.univ-paris12.fr/GPCOS/SCOOPweb/SCOOP.html.

Acknowledgements

The authors wish to thank Dr. Gerd Reichardt for his excellent assistance during the synchrotron radiation beam time periods. We acknowledge the financial support of the European Commision Programme "Access to Research Infrastructures" in providing access to the synchrotron BESSY at Berlin. We also acknowledge the financial support of the French CNRS program PNP.

References

Andrieux, D., Bénilan, Y., de Vanssay, E., Paillous, P., Khlifi, M., Raulin, F., Bruston, P., Guillemin, J.-C., 1995. Absorption coefficient of propynenitrile in the mid-UV range for the study of Titan's atmosphere: solution to sample contaminations. J. Geophys. Res. 100, 9455–9460.

Bell, M.B., Feldman, P.A., Travers, M.J., McCarthy, M.C., Gottlieb, C.A., Thaddeus, P., 1997. Detection of $HC_{11}N$ in the cold dust cloud TMC-1. Astrophys. J. 483, L61.

Bénilan, Y., Bruston, P., Raulin, F., Cossart-Magos, C., Guillemin, J.-C., 1994. Mid-UV spectroscopy of propynenitrile at low temperature: consequences on expected results from observations of Titan's atmosphere. J. Geophys. Res. 99, 17069–17074.

Bénilan, Y., Andrieux, D., Khlifi, M., Bruston, P., Raulin, F., Guillemin, J.-C., Cossart-Magos, C., 1996. Temperature dependence of HC_3N, C_6H_2, and C_4N_2 mid-UV absorption coefficients. Application to the interpretation of Titan's atmospheric spectra. Astrophys. Space Sci. 236, 85–95.

Bruston, P., Poncet, H., Raulin, F., Cossart-Magos, C., Courtin, R., 1989. UV spectroscopy of Titan's atmosphere, planetary organic chemistry, and prebiological synthesis: I. Absorption spectra of gaseous propynenitrile and 2-butynenitrile in the 185- to 250-nm region. Icarus 78, 38–53.

Cernicharo, J., Heras, A.M., Tielens, A.G.G.M.P., Pardo, J.R., Herpin, F., Guélin, M., Waters, L.B.F.M., 2001. Infrared space observatory's discovery of C_4H_2, C_6H_2, and Benzene in CRL 618. Astrophys. J. 546, L123–L126.

Chen, F.Z., Wu, C.Y.R., 2004. Temperature-dependent photoabsorption cross sections in the VUV-UV region. I. Methane and ethane. J. Quant. Spectrosc. Radiat. Transfer 85, 195–209.

Connors, R.E., Roebber, J.L., Weiss, K., 1974. Vacuum ultraviolet spectroscopy of cyanogen and cyanoacetylenes. J. Chem. Phys. 60, 5011–5024.

Coustenis, A., Bézard, B., 1995. Titan's atmosphere from voyager infrared observations: IV. Latitudinal variations of temperature and composition. Icarus 115, 126–140.

Coustenis, A., Salama, A., Schulz, B., Ott, S., Lellouch, E., Encrenaz, T., Gautier, D., Feuchtgruber, H., 2003. Titan's atmosphere from ISO mid-infrared spectroscopy. Icarus 161, 383–403.

Coustenis, A., Achterberg, R.K., Conrath, B.J., Jennings, D.E., Marten, A., Gautier, D., Nixon, C.A., Flasar, F.M., Teanby, N.A., Bézard, B., Samuelson, R.E., Carlson, R.C., Lellouch, E., Bjoraker, G.L., Romani, P.N., Taylor, F.W., Irwin, P.G.J., Fouchet, T., Hubert, A., Orton, G.S., Kunde, V.G., Vinatier, S., Mondellini, J., Abbas, M.M., Courtin, R., 2007. The composition of Titan's stratosphere from Cassini/CIRS mid-infrared spectra. Icarus 189, 35–62.

Esposito, L.W., Barth, C.A., Colwell, J.E., Lawrence, G.M., McClintock, W.E., Stewart, A.I.F., Keller, H.U., Korth, A., Lauche, H., Festou, M.C., Lane, A.L., Hansen, C.J., Maki, J.N., West, R.A., Jahn, H., Reulke, R., Warlich, K., Shemansky, D.E., Yung, Y.L., 2004. The Cassini ultraviolet imaging spectrograph investigation. Space Sci. Rev. 115, 299–361.

Fahr, A., Nayak, A.K., 1994. Temperature dependent ultraviolet absorption cross sections of 1,3-butadiene and butadiyne. Chem. Phys. 189, 725–731.

Flasar, F.M., Achterberg, R.K., Conrath, B.J., Gierasch, P.J., Kunde, V.G., Nixon, C.A., Bjoraker, G.L., Jennings, D.E., Romani, P.N., Simon-Miller, A.A., Bézard, B., Coustenis, A., Irwin, P.G.J., Teanby, N.A., Brasunas, J., Pearl, J.C., Segura, M.E., Carlson, R.C., Mamoutkine, A., Schinder, P.J., Barucci, A., Courtin, R., Fouchet, T., Gautier, D., Lellouch, E., Marten, A., Prangé, R., Vinatier, S., Strobel, D.F., Calcutt, S.B., Read, P.L., Taylor, F.W., Bowles, N., Samuelson, R.E., Orton, G.S., Spilker, L.J., Owen, T.C., Spencer, J.R., Showalter, M.R., Ferrari, C., Abbas, M.M., Raulin, F., Edgington, S., Ade, P., Wishnow, E.H., 2005. Titan's atmospheric temperatures, winds, and composition. Science 308, 975–978.

Georgieff, K.K., Richard, Y., 1958. Diacetylene: preparation, purification, and ultraviolet spectrum. Can. J. Chem. 36, 1280–1283.

Glicker, S., Okabe, H., 1987. Photochemistry of diacetylene. J. Phys. Chem. 91, 437–440.

Haink, H.-J., Jungen, M., 1979. Excited states of the polyacetylenes. Analysis of the near ultraviolet spectra of diacetylene and triacetylene. Chem. Phys. Lett. 61, 319–322.

Hanel, R., Conrath, B., Flasar, F.M., Kunde, V., Maguire, W., Pearl, J.C., Pirraglia, J., Samuelson, R., Herath, L., Allison, M., Cruikshank, D.P., Gautier, D., Gierasch, P.J., Horn, L., Koppany, R., Ponnamperuma, C., 1981. Infrared observations of the Saturnian system from voyager 1. Science 212, 192–200.

Hébrard, E., Dobrijevic, M., Bénilan, Y., Raulin, F., 2007. Photochemical kinetics uncertainties in modeling Titan's atmosphere: first consequences. Planet. Space Sci. 55, 1470–1489.

Hunter, W.R., Malo, S.A., 1969. The temperature dependence of the short wavelength transmittance limit of vacuum ultraviolet window materials—I. Experiment. J. Phys. Chem. Solids 30, 2739–2745.

Job, V.A., King, G.W., 1966. The electronic spectrum of cyanoacetylene: part II. Analysis of the 2300-Å system. J. Mol. Spectrosc. 19, 178–184.

Jolly, A., Bénilan, Y., 2008. Review of quantitative spectroscopy of polyynes. J. Quant. Spectrosc. Radiat. Transfer 109, 963–973.

Jolly, A., Bénilan, Y., Fayt, A., 2007. New infrared integrated band intensities for HC_3N and extensive line list for the n_5 and n_6 bending modes. J. Mol. Spectrosc. 242, 46–54.

Khlifi, M., Paillous, P., Delpech, C., Nishio, M., Bruston, P., Raulin, F., 1995. Absolute IR band intensities of diacetylene in the 250–4300 cm^{-1} region: implications for Titan's atmosphere. J. Mol. Spectrosc. 174, 116–122.

Kloster-Jensen, E., Haink, H.-J., Christen, H., 1974. The electronic spectra of unsubstituted Mono- to pentaacetylene in the gas phase and in solution in the range 1100–4000 Å. Helv. Chim. Acta 57, 1731–1744.

Kunde, V.G., Aikin, A.C., Hanel, R.A., Jennings, D.E., Maguire, W.C., Samuelson, R.E., 1981. C_4H_2, HC_3N and C_2N_2 in Titan's atmosphere. Nature 292, 686–688.

Lavvas, P.P., Coustenis, A., Vardavas, I.M., 2008. Coupling photochemistry with haze formation in Titan's atmosphere, part I: model description. Planet. Space Sci. 56, 27–66.

Miller, F.A., Lemmon, D.H., 1967. The infrared and Raman spectra of dicyanodiacetylene. Spectrochim. Acta 23A, 1415–1423.

Moureu, C., Bongrand, J.C., 1920. Le cyanoacetylene C_3NH. Ann. Chim. 14, 47.

Niemann, H.B., Atreya, S.K., S.J. Bauer, G.R.C., Demick, J.E., Frost, R.L., Gautier, D., Haberman, J.A., Harpold, D.N., Hunten, D.M., Israel, G., Lunine, J.I., Kasprzak, W.T., Owen, T.C., Paulkovich, M., Raulin, F., Raaen, E., Way, S.H., 2005. The abundances of constituents of Titan's atmosphere from the GCMS instrument on the Huygens probe. Nature 438, 779–784.

Nuth, J.A., Glicker, S., 1982. The vacuum ultraviolet spectra of HCN, C_2N_2 and CH_3CN. J. Quant. Spectrosc. Radiat. Transfer 28, 223–231.

Okabe, H., 1981. Photochemistry of acetylene at 1470 Å. J. Photochem. 17, 172–184.

Orgel, L.E., 2002. Is cyanoacetylene prebiotic? Origins Life Evol. Biosphere 32, 279–281.

Reichardt, G., Bahrdt, J., Schmidt, J.-S., Gudat, W., Ehresmann, A., Müller-Albrecht, R., Molter, H., Schmoranzer, H., Martins, M., Schwentner, N., Sasaki, S., 2001a. A 10 m-normal incidence monochromator at the quasi-periodic undulator U125-2 at BESSY II. Nucl. Instrum. Methods Phys. Res., Sect. A 467–468, 462–465.

Reichardt, G., Noll, T., Packe, I., Rotter, P., Schmidt, J.-S., Gudat, W., 2001b. Adaption of the BESSY I-3 m normal incidence monochromators to the BESSY II source. Nucl. Instrum. Methods Phys. Res. Sect. A 467–468, 458–461.

Shemansky, D.E., Stewart, A.I.F., West, R.A., Esposito, L.W., Hallett, J.T., Liu, X., 2005. The Cassini UVIS stellar probe of the Titan atmosphere. Science 308, 978–982.

Smith, W.L., 1967. The absorption spectrum of diacetylene in the vacuum ultraviolet. In: Proceedings of the Royal Society of London. Series A Mathematical and Physical Sciences. Vol. 300, pp. 519–533.

Smith, B.A., Soderblom, L., Beebe, R.F., Boyce, J.M., Briggs, G., Bunker, A., Collins, S.A., Hansen, C., Johnson, T.V., Mitchell, J.L., Terrile, R.J., Carr, M.H., Cook, A.F., Cuzzi, J.N., Pollack, J.B., Danielson, G.E., Ingersoll, A.P., Davies, M.E., Hunt, G.E., Masursky, H., Shoemaker, E.M., Morrison, D., Owen, T., Sagan, C., Veverka, J., Strom, R., Suomi, V.E., 1981. Encounter with Saturn—Voyager 1 imaging science results. Science 212, 163–191.

Smith, N.S., Bénilan, Y., Bruston, P., 1998. The temperature dependent absorption cross sections of C_4H_2 at mid ultraviolet wavelengths. Planet. Space Sci. 46, 1215–1220.

Teanby, N.A., Irwin, P.G.J., de Kok, R., Vinatier, S., Bézard, B., Nixon, C.A., Flasar, F.M., Calcutt, S.B., Bowles, N.E., Fletcher, L., Howett, C., Taylor, F.W., 2007. Vertical profiles of HCN, HC_3N, and C_2H_2 in Titan's atmosphere derived from Cassini/CIRS data. Icarus 186, 364–384.

Turner, B.E., 1971. Detection of interstellar cyanoacetylene. Astrophys. J. 163, L35–L39.

Vervack, R.J., Sandel, B.R., Strobel, D.F., 2004. New perspectives on Titan's upper atmosphere from a reanalysis of the voyager 1 UVS solar occultations. Icarus 170, 91–112.

Waite, J.J., Niemann, H., Yelle, R.V., Kasprzak, W.T., Cravens, T.E., Luhmann, J.G., McNutt, R.L., Ip, W.H., Gell, D., De La Haye, V., Müller-Wordag, I., Magee, B., Borggren, N., Ledvina, S., Fletcher, G., Walter, E., Miller, R., Scherer, S., Thorpe, R., Xu, J., Block, B., Arnett, K., 2005. Ion neutral mass spectrometer results from the first flyby of Titan. Science 308, 90.

Wu, C.Y.R., Chen, F.Z., Judge, D.L., 2001. Measurements of temperature-dependent of temperature cross sections of C_2H_2 in the VUV-UV region. J. Geophys. Res. 106, 7629–7636.

Wu, C.Y.R., Chen, F.Z., Judge, D.L., 2004. Temperature-dependent photoabsorption cross sections in the VUV–UV region: Ethylene. J. Geophys. Res. 109, E07S15.

Yung, Y.L., Allen, M., Pinto, J.P., 1984. Photochemistry of the atmosphere of Titan—comparison between model and observations. Astrophys. J. Suppl. Ser. 55, 465–506.

ARTICLE 6

Fray N., Bénilan Y., Gazeau M.-C., Jolly A., Schwell M., Arzoumanian E., Ferradaz T., Es-Sebbar E. And Guillemin J.-C. (2010)

Temperature-dependant photoabsorption cros-section of cyanoacetylene in the vacuum UV.

Journal of Geophysical Research (Planets), **115, E06010**

JOURNAL OF GEOPHYSICAL RESEARCH, VOL. 115, E06010, doi:10.1029/2009JE003518, 2010

Temperature-dependent photoabsorption cross section of cyanodiacetylene in the vacuum UV

N. Fray,[1] Y. Bénilan,[1] M.-C. Gazeau,[1] A. Jolly,[1] M. Schwell,[1] E. Arzoumanian,[1] T. Ferradaz,[1] Et. Es-Sebbar,[1] and J.-C. Guillemin[2,3]

Received 29 September 2009; accepted 28 December 2009; published 23 June 2010.

[1] Using synchrotron radiation as a tunable VUV light source, we have measured, for the first time, the absolute photoabsorption cross sections of HC_5N with a spectral resolution of 0.05 nm in the region between 80 and 205 nm from 233 to 298 K. The measured cross sections are used to predict the HC_5N photodestruction rate in the solar system and to model a transmission spectrum in Titan's atmosphere. Comparing the latter with that acquired by the Ultraviolet Imaging Spectrograph on board the Cassini spacecraft, we have determined an upper limit of 2.7×10^{-5} on the HC_5N abundance at 1100 km.

Citation: Fray, N., Y. Bénilan, M.-C. Gazeau, A. Jolly, M. Schwell, E. Arzoumanian, T. Ferradaz, Et. Es-Sebbar, and J.-C. Guillemin (2010), Temperature-dependent photoabsorption cross section of cyanodiacetylene in the vacuum UV, *J. Geophys. Res.*, *115*, E06010, doi:10.1029/2009JE003518.

1. Introduction

[2] Cyanobutadiyne (H-C≡C-C≡C-C≡N, also called 2, 4-pentadiynenitrile or cyanodiacetylene) is the simplest cyanopolyyne. Numerous members of the (H-(C≡C)$_n$-C≡N) family, up to $n = 5$, have been detected in dark clouds [*Bell et al.*, 1997]. HC_5N was detected for the first time in the molecular cloud Sgr B2 by *Avery et al.* [1976]. Since then, it has also been observed in numerous cold dark clouds [*Suzuki et al.*, 1992] and in hot circumstellar environments such as CRL 618 [*Cernicharo et al.*, 2001; *Pardo et al.*, 2005]. We also note that the isotopologues DC_5N [*MacLeod et al.*, 1981], $HC^{13}CCCCN$, as well as $HCCCC^{13}CN$ [*Takano et al.*, 1998] have been detected in Taurus Molecular Cloud 1 (TMC-1).

[3] In the cometary environment, a very low upper limit on the production rate of HC_5N has been determined [*Crovisier et al.*, 2004]. The upper limit on the relative abundance ratio of $[HC_5N]/[HCN]$ is thus <0.012, which is lower than that in CRL 618 (0.1 [see *Cernicharo et al.*, 2001]) and in TMC-1 (0.14 [see *Irvine et al.*, 1987]). HC_5N has been found to be a product of laboratory simulations of Titan's atmosphere [*de Vanssay et al.*, 1995; *Coll et al.*, 1995]. Traces of HC_5N have also been observed after the irradiation of a mixture of cyanoacetylene (HC_3N) and acetylene (C_2H_2) as well as a mixture of dicyanoacetylene (C_4N_2) and acetylene (C_2H_2) [*Trolez and Guillemin*, 2005]. Recently, HC_5N has been predicted to be present at an altitude of 1100 km with an abundance of 10^{-6} by *Vuitton et al.* [2007]. Attempts to detect this molecule in Titan's atmosphere were unsuccessful in the submillimeter range [*Marten et al.*, 2002], and no detection or upper limits have been reported using infrared or in the UV range.

[4] Until recently, quantitative spectroscopic studies were hindered by the lack of an efficient method to form pure samples of HC_5N. This situation has changed recently with the development of a new chemical synthesis by *Trolez and Guillemin* [2005] that allows the isolation of very pure samples. This approach enabled *Bénilan et al.* [2007] to measure the vibrational band intensities in the mid-IR range (from 3500 to 400 cm^{-1}) and *Coupeaud et al.* [2007] to record relative cross sections of HC_5N in the 200–320 nm spectral range.

[5] In this article we present, for the first time, the absolute photoabsorption cross sections of HC_5N in the VUV spectral range from 80 to 205 nm and with a temperature dependence between 233 and 298 K. This information enables us to calculate the photodestruction rate, which is an essential parameter to constrain photochemical models of planetary atmospheres. Our cross sections can also be used to determine an upper limit of HC_5N abundance in Titan's upper atmosphere by using the data recorded in the VUV range by the Ultraviolet Imaging Spectrograph (UVIS) on board the Cassini spacecraft.

2. Experimental Methods and Procedures

[6] The samples of HC_5N have been prepared by the reaction of 1, 3-butadiynyltri-*n*-butylstannane with *p*-toluenesulfonyl cyanide [*Trolez and Guillemin*, 2005]. They were distilled at low temperature and this process was monitored using IR spectrometry. At the end of the distillation, no band of any impurities was seen in the IR spectra. The

[1]Laboratoire Interuniversitaire des Systèmes Atmosphériques, UMR 7583 du CNRS, Universités Paris 7 et 12, Créteil, France.
[2]École Nationale Supérieure de Chimie de Rennes, UMR 6226, CNRS, Rennes, France.
[3]Also at Université européenne de Bretagne, Rennes, France.

0148-0227/10/2009JE003518

resulting pure samples were stored in solid form at liquid nitrogen temperature to avoid any polymerization.

[7] As all the details of the experimental methods and procedures have already been described by *Ferradaz et al.* [2009], we give only a brief summary of the experimental protocols. To measure the VUV spectra of HC_5N, we used two spectroscopic cells. The first has a very short optical path length (10 cm) and is enclosed by a MgF_2 window at the entrance and by a VUV photomultiplier at the exit. The second cell is longer (120 cm) and the entrance window has been replaced by a microchannel plate (MCP), which allows photons of short wavelengths (in principle, down to 50 nm) to penetrate into the cell and thus provides precise knowledge of the optical path length. The exit window was covered with sodium salicylate on the inside, transforming VUV light into visible light to be detected by a visible photomultiplier.

[8] Both cells have double walls allowing the flow of liquid nitrogen, which is controlled through a cryogenic valve at the entrance. A standard proportional, integral, and derivative control loop is used to stabilize the temperature within ±1 K. Although the cell can, in principle, reach liquid nitrogen temperature (77 K), no experiments could be performed below 220 K because the vapor pressure of HC_5N drops below the detection limit of our pressure measurement system at that point.

[9] Tunable VUV light is obtained from the synchrotron radiation facility in Berlin (BESSY). A first set of measurements was obtained at the U125/2 undulator beamline equipped with a 10 m focal length normal incidence monochromator (NIM). This undulator allows us to overcome problems associated with high-order radiation from the grating, and the stepwise system in the monochromator provides spectra that are self-calibrated in wavelength [*Reichardt et al.*, 2001a]. During this first campaign, we used the long cell equipped with the MCP to record spectra below the cutoff of MgF_2 windows. With this setup, spectra were acquired in the 80–180 nm spectral region at a resolution of 0.3 nm. A second set of measurements was performed at the DIP 12-1B dipole magnet beamline equipped with a 3 m focal length NIM [*Reichardt et al.*, 2001b]. The short cell, closed by MgF_2 windows that allowed high-order the radiation of the grating to be cut off, was used to record spectra in the 115–205 nm spectral range, at a resolution of 0.05 nm. We calibrated wavelength by using the first self-calibrated set of measurements as a reference.

[10] For each recorded spectrum, the solid sample of HC_5N was vaporized to the desired pressure, which was monitored by an MKS Baratron capacitance manometer (range 10^{-4} to 1 mbar). Most spectra were taken for at least at three different pressures in the 2–200 μbar range to check the reproducibility of our measurements. Comparing all the spectra we have acquired, we restricted the influence of the stray light by selecting only spectra that were free from any saturation and had low absorption.

[11] To account for the steady decrease of the incident VUV light intensity, which is caused by the decay of BESSY's storage ring current, two "empty-cell" spectra were recorded just before and right after each HC_5N spectrum. A synthetic empty-cell spectrum was then interpolated by considering a linear decrease of the incident light intensity. Comparing the spectra we have acquired at different pressures, we estimate that this procedure leads to an uncertainty of 10% on the absorption cross section and that this error dominates all other sources of errors.

3. Results and Discussion

3.1. Photoabsorption Cross Section at Room Temperature

[12] Figure 1 shows the absolute photoabsorption coefficient of HC_5N in the 80–300 nm range measured at room temperature (298 K). The spectral resolution of our measurements (80–205 nm) is 0.3 nm below 115 nm and 0.05 nm for wavelengths between 115 and 205 nm (see Table 1). In the 115–205 nm spectral region, at least three spectra have been taken with different pressures between 2 and 200 μbar. The uncertainty on the absorption cross sections is about 10% (see section 2). For wavelengths lower than 115 nm, this uncertainty is estimated to be about 40% because only one spectrum has been taken in this spectral range.

[13] Between 150 and 205 nm, the absorption spectrum of HC_5N exhibits a very large and intense band structure (Figure 1). We assign this structure to the transition from the ground state to the first symmetry-allowed electronic state ($^1\Sigma^+ \leftarrow {}^1\Sigma^+$ transition), in agreement with the semiempirical calculation of electronic absorption of cyanopolyynes performed by *Scemama et al.* [2002]. Indeed, the wavelength of this transition has been predicted at 175.45 nm [*Scemama et al.*, 2002] and we observe a maximum of absorption at 175.24 nm. Note that this agreement between the theoretical prediction and our subsequent experimental measurement is remarkably good. In this range, the spectrum exhibits numerous local maxima. These substructures, spaced by about 650 and 2300 cm^{-1}, can tentatively be assigned to the ν_7 and ν_2 vibrational modes, which are very intense in the infrared range [*Bénilan et al.*, 2007].

[14] Between 115 and 150 nm, numerous sharp and intense bands are observed (Figure 1). They are presumably due to Rydberg series and seem to converge toward a broad structure located between 114 and 116 nm. Unfortunately, the first ionization energy of HC_5N has never been measured, so we do not know exactly where the Rydberg series should converge. The individual bands of the series are therefore difficult to identify properly. For wavelengths shorter than 115 nm, an intense continuum is observed with some weak superimposed bands.

[15] The spectrum of HC_5N between 200 and 300 nm has been measured by *Coupeaud et al.* [2007] in the gas phase (Figure 1). These authors tentatively assigned the observed bands to the $B^1\Delta \leftarrow X^1\Sigma^+$ transition. Since *Coupeaud et al.* [2007] measured only optical densities, we used our absolute cross sections in the 200–205 nm range to calibrate the intensity of their spectrum.

3.2. Temperature Dependence of the Absorption Coefficient

[16] The VUV spectrum of HC_5N has been measured at 233, 250, and 298 K to study the temperature dependence of the absorption coefficient (Figure 2). At 233 and 250 K, at least three spectra have been recorded at different pressures ranging from 2 to 90 μbars. The resolution of both spectra varies between 0.05 and 0.1 nm (Table 1).

[17] Significant differences are observed between the spectra obtained at the three different temperatures. First, the

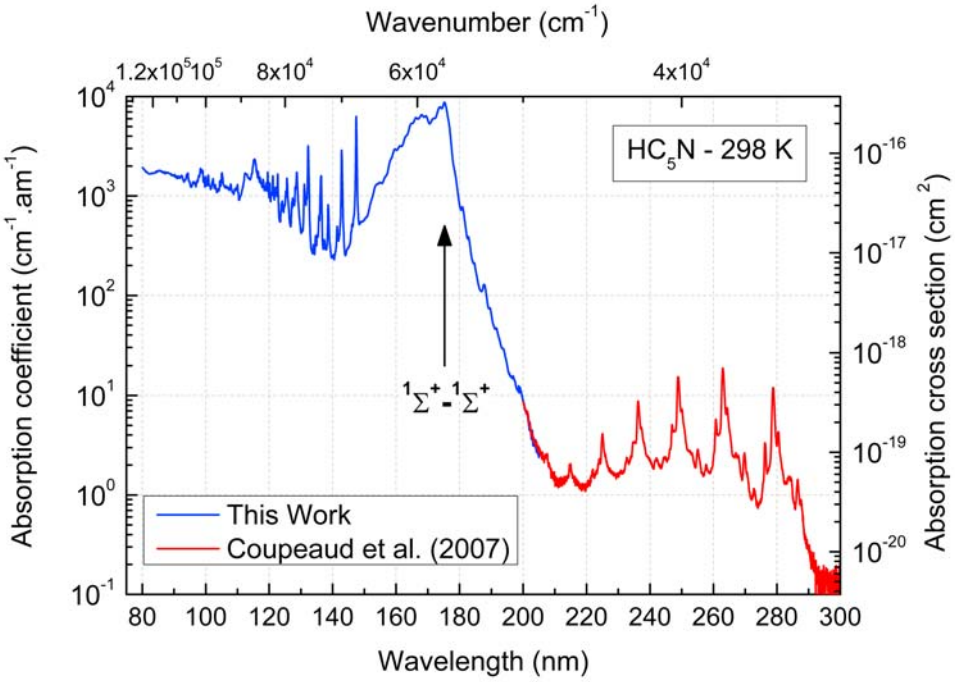

Figure 1. Absolute photoabsorption coefficient of HC_5N between 80 and 300 nm at room temperature. Our measurement at 298 K, in blue, ranges from 80 to 205 nm; for longer wavelengths, the spectrum of *Coupeaud et al.* [2007] is shown in red. The origin of the $^1\Sigma^+ \leftarrow {}^1\Sigma^+$ electronic transition is indicated.

absorption coefficient of the transition $^1\Sigma^+ \leftarrow {}^1\Sigma^+$ shows an increase of 25% when the temperature decreases from 298 to 233 K. Second, as can be seen in the inset of Figure 2, some of the sharpest bands show typical temperature effects. The band maximum increases and the full width at half maximum decreases when the temperature decreases from 298 to 233 K, as already observed for C_4N_2 and C_2H_2 in the mid-UV range [*Bénilan et al.*, 1996, 2000]. These effects are due to the change in the population distribution that favors the low J rotational levels when the gas temperature is reduced.

4. Astrophysical Implications

4.1. Photodestruction Rate

[18] Very few photolysis studies of HC_5N exist. In the gas phase, attempts to detect products of HC_5N photolysis at 254 nm have been unsuccessful, but dust attributed to the formation of oligomeric compounds was observed [*Guillemin et al.*, 2008]. In an Ar matrix at 10 K, *Coupeaud et al.* [2007] demonstrated that photolysis at 267 nm of HC_5N leads to the formation of isocyanodiacetylene (H-C≡C-C≡C-N=C) with no other products being observed.

[19] The photodestruction rate, denoted J (in s^{-1}), determines the lifetime of molecules in environments subject to solar UV radiation. Knowledge of its value is a requisite for predicting molecular abundances from chemical modeling of atmospheres. This important parameter can be calculated using the following formula:

$$J = \int_{\lambda_1}^{\lambda_2} \Phi(\lambda)\sigma(\lambda)S(\lambda)d\lambda,$$

where $\Phi(\lambda)$, $\sigma(\lambda)$, and $S(\lambda)$ are the photodestruction quantum yield, the absorption cross section (in cm^2), and the solar irradiance spectra (in photons cm^{-2} s^{-1} nm^{-1}), respectively. Because the exact dissociation limit is unknown, we have chosen to include all wavelengths up to 290 nm for calculating J, using the spectrum of *Coupeaud et al.* [2007] (see section 3.1). The wavelength of 290 nm corresponds to the origin of the absorption system observed in their study (included here in Figure 1). Another important assumption concerns the photodestruction quantum yield Φ taken as equal to unity for all the wavelengths, in the absence of any further information. Given these hypotheses, the values of J calculated have to be considered upper limits.

[20] We have further considered two solar irradiance reference spectra, ATLAS 1 and ATLAS 3, which have been measured during moderately high and low activity levels, respectively, of the Sun [*Thuillier et al.*, 2004a, 2004b]. If we consider that the photodestruction of HC_5N occurs for wavelengths ranging from 80 to 290 nm, the HC_5N photodestruction rate at 1 AU from the Sun is equal to $(4.2 \pm 0.4) \times 10^{-4}$ and $(4.0 \pm 0.4) \times 10^{-4}$ s^{-1} for moderately high and low solar activity levels, respectively. Note that the variation

Table 1. Experimental Details of the HC_5N Spectra

	Spectral Range (nm)	Resolution (nm)	Sampling (nm)	Uncertainty (%)
298 K	80–115	0.3	0.1	40
	115–205	0.05	0.015	10
250 K	115–150	0.05	0.015	10
	150–181.5	0.1	0.015	10
233 K	115–184	0.05	0.015	10

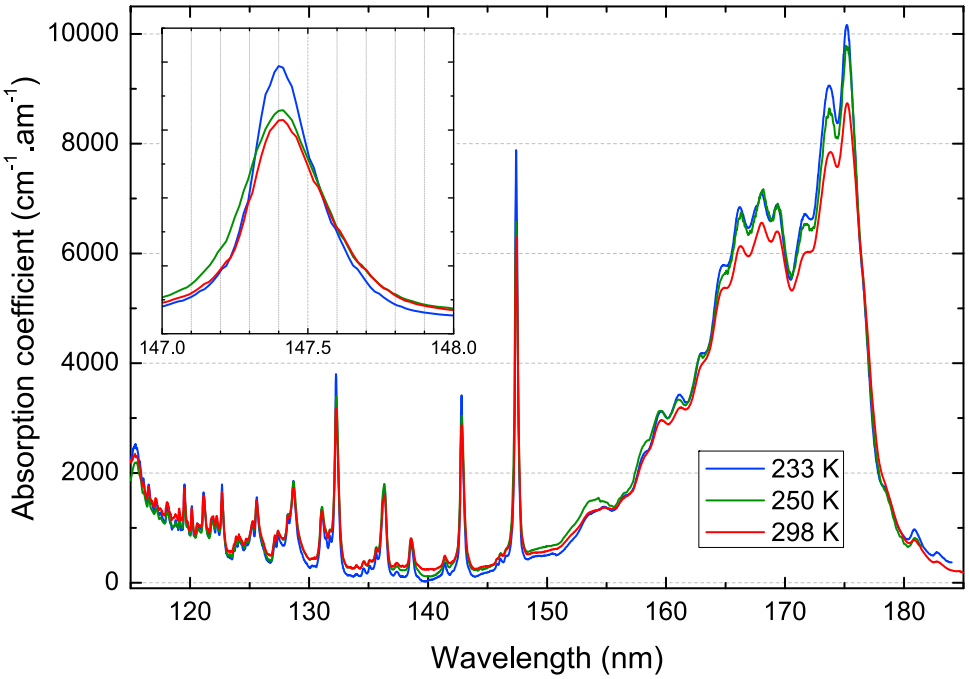

Figure 2. Absolute photoabsorption coefficient of HC_5N between 115 and 185 nm at 233, 250, and 298 K. A magnification of the sharp band located at 147.4 nm is shown in the inset.

attributable to the solar cycle is lower than the uncertainties of the absorption spectrum.

[21] Because of the very low solar flux in this domain, the 80–115 nm spectral range accounts for less than 1% of the HC_5N photodestruction rate. In contrast, the 115–180 nm spectral range accounts for 70% of the J value, which emphasizes the importance of our measurements in this spectral region. The 180–290 nm spectral range, despite its very low absorption cross section, accounts for about 30% of the photodestruction rate of HC_5N. The solar flux in this domain is quite high and perhaps is overestimated since we suppose $\Phi = 1$.

[22] The J calculations were performed for the spectra at 233, 250, and 298 K. Because the absorption cross sections are slightly higher for $T = 233$ and 250 K than for 298 K, the photodestruction rate increases by about 5% when the gas temperature decreases. Thus, the temperature dependence is not significant in comparison with the uncertainties of our spectra.

[23] Comparing our J value with those for HCN (1.5×10^{-5} s^{-1}) and HC_3N (6.6×10^{-5} s^{-1}) given by *Crovisier* [1994], we can conclude that the lifetime of HC_5N is about 25 and 6 times shorter than HCN and HC_3N, respectively. We note that the abundances of these three molecules in comets and in Titan's atmosphere decrease when the photodissociation rate increases [*Crovisier et al.*, 2004; *Vuitton et al.*, 2007].

[24] In *Krasnopolsky*'s [2009] photochemical model of Titan's upper atmosphere, the photodestruction rate of HC_5N was considered to be equal to that of HC_3N. Our preceding result suggests that the HC_5N rate may be significantly higher than that for HC_3N.

4.2. Interpretation of Titan's Atmospheric Spectra

[25] A first attempt to detect HC_5N in Titan's atmosphere in the submillimeter wavelength range was unsuccessful and only an upper limit for the mixing ratio (4×10^{-10}) could be determined in the lower stratosphere [*Marten et al.*, 2002]. More recently, *Vuitton et al.* [2007] predicted an abundance of 1×10^{-6} at 1100 km. At such a high altitude, one way to firmly detect HC_5N is to use the UVIS instrument [*Esposito et al.*, 2004] on board the Cassini spacecraft. From stellar occultations, the Cassini UVIS experiment was able to measure transmission spectra through Titan's atmosphere in the far UV [*Shemansky et al.*, 2005]. Figure 2 of Shemansky et al.'s publication presented a spectrum acquired at a southern latitude of −36° and for a tangent altitude of 868 km; although many compounds could be detected, no signature of HC_5N was observed. At the wavelength of the strongest feature of HC_5N, the optical density of the UVIS spectrum is close to zero with a noise of ±0.2. To reproduce this observation, we calculated the logarithm of the transmission, taking into account the cross sections and the column densities for CH_4, C_2H_2, C_2H_4, C_2H_6, C_4H_2, HCN, and HC_3N given in Table 2 and discussed by *Ferradaz et al.* [2009]. The calculated transmission spectrum has been convoluted by a boxcar function with a width of 0.275 nm to mach the UVIS resolution (Figure 3). To determine an upper limit of HC_5N in the upper atmosphere, we considered a noise level of 0.2, which corresponds to a column density of 5×10^{14} cm^{-2} (Figure 3, bottom).

[26] We recalculated the logarithm of the transmission by including the contribution of HC_5N (Figure 3, top). The strong $^1\Sigma^+ \leftarrow {}^1\Sigma^+$ transition around 175 nm appears as a small bump close to a C_2H_4 structure, whereas the sharp peak around 147 nm appears as a subtle shoulder close to a

Table 2. Column Densities and Characteristics of the Spectra Used to Calculate Titan's Transmission Spectra Presented in Figure 3

Species	Column density (cm^{-2})	Reference used for the column density	Reference VUV spectrum	Temperature of the reference spectrum (K)
CH_4	1.9×10^{17}	*Shemansky et al.* [2005]	*Chen and Wu* [2004]	150
C_2H_2	4.0×10^{15} [a]	*Ferradaz et al.* [2009]	*Wu et al.* [2001]	150
C_2H_4	8.2×10^{15}	*Shemansky et al.* [2005]	*Wu et al.* [2004]	200
C_2H_6	7.3×10^{15}	*Shemansky et al.* [2005]	*Chen and Wu* [2004]	150
HCN	1.9×10^{16}	*Shemansky et al.* [2005]	*Nuth and Glicker* [1982]	300
C_4H_2	1.3×10^{15}	*Ferradaz et al.* [2009]	*Ferradaz et al.* [2009]	173
HC_3N	1.3×10^{15}	*Ferradaz et al.* [2009]	*Ferradaz et al.* [2009]	243
HC_5N	5.0×10^{14} [b]	This work	This work	233

[a]This value was printed incorrectly as 1.1×10^{16} cm^{-2} in the work published by *Ferradaz et al.* [2009].
[b]The HC_5N column density is the upper limit that we have determined from the transmission spectrum published by *Shemansky et al.* [2005].

C_2H_2 band. We conclude that the $^1\Sigma^+ \leftarrow {}^1\Sigma^+$ transition is the most favorable structure for the detection of HC_5N in this spectral range.

[27] To convert our HC_5N column density upper limit to abundance takes two assumptions: to suppose that the HC_5N density (cm^{-3}) varies exponentially with the altitude, and to consider that the scale height of HC_5N is equal to that of C_4H_2. The scale height of C_4H_2 can be determined from the density measurements of the Ion Neutral Mass Spectrometer (INMS) [*Cui et al.*, 2009] and is close to 40 km. This leads to a maximum density of 1.2×10^4 cm^{-3} at 1100 km. Because the interpolated N_2 density measured by *Cui et al.* [2009] is 1.7×10^9 cm^{-3} at the same altitude, we determine a maximum abundance of 7×10^{-6} for HC_5N at 1100 km. The principal hypothesis of this calculation is the value of the HC_5N scale height. When this value varies between 30 and 50 km, the upper limit of the HC_5N abundance varies between 1.6×10^{-6} and 2.7×10^{-5}. Considering this range of variation, even if the HC_5N abundance is expected to depend on at least latitude, we note that both our upper limits are consistent with the value of 1×10^{-6} predicted by *Vuitton et al.* [2007] from INMS measurements.

5. Conclusions

[28] We have determined, for the first time, the absolute absorption coefficient of HC_5N in the 80–205 nm spectral range at ambient temperature with a resolution of 0.05 nm for wavelength longer than 115 nm and of 0.3 nm for shorter wavelengths. We found that the position of the $^1\Sigma^+ \leftarrow {}^1\Sigma^+$ transition was predicted accurately by *Scemama et al.* [2002]. For wavelengths ranging from 115 to 180 nm, we recorded three spectra at 233, 250, and 298 K to determine the temperature dependence of the main absorption bands. The intensities of the main absorption bands increased by about 25% and the band profiles narrowed when the temperature decreased from 298 to 233 K.

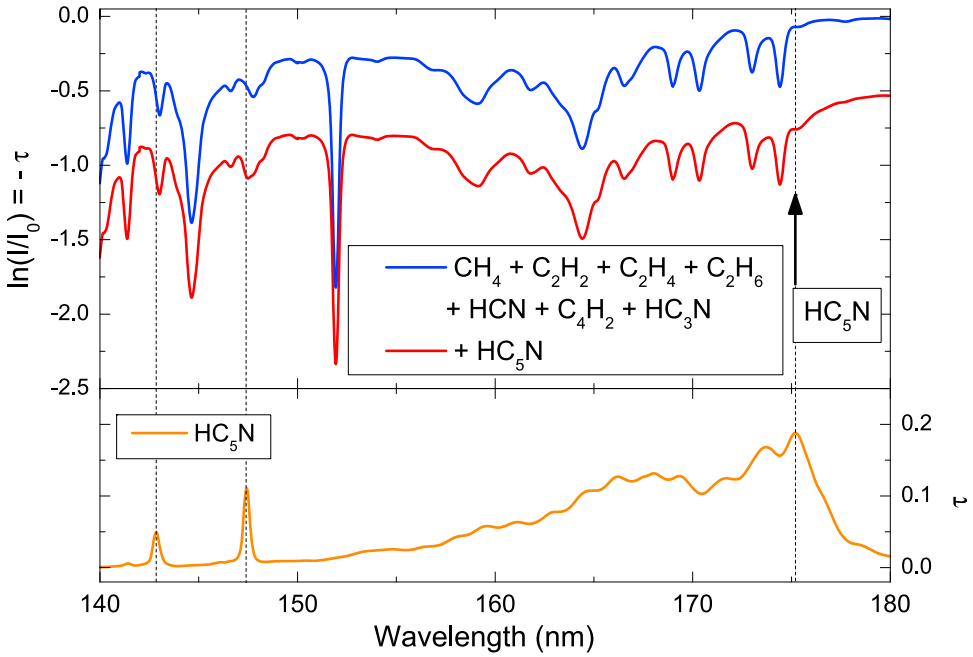

Figure 3. (top) Titan's expected transmission spectra simulated in the 140–180 nm spectral range. The blue line was obtained considering CH_4, C_2H_2, C_2H_4, C_2H_6, C_4H_2, HCN, and HC_3N and the red line (shifted downward by 0.5 for clarity) includes the absorption of HC_5N. (bottom) Optical density of HC_5N assuming a column density of 5×10^{14} cm^{-2}.

[29] The spectra at room temperature allowed us to calculate the photodestruction rate of HC_5N at 1 AU from the Sun to be 4×10^{-4} s^{-1}, which is 25 and 6 times larger than for HCN and HC_3N, respectively. The intense absorption features of HC_5N between 115 and 180 nm account for 70% of the total photodestruction rate. Finally, we determined an upper limit for HC_5N in the upper atmosphere of Titan, which is higher than the value predicted by *Vuitton et al.* [2007].

[30] **Acknowledgments.** The authors wish to thank Gerd Reichard for his excellent assistance during the synchrotron radiation beam time periods, Hans-Werner Jochims for judicious advice concerning the VUV spectroscopy with synchrotron radiation, and Gérard Thuiller for providing a file of the solar spectra. We thank V. Vuitton and an anonymous referee for their useful comments. We acknowledge the financial support of the European Commission Programme "Access to Research Infrastructures" for providing access to the synchrotron facility BESSY in Berlin. We also acknowledge the financial support of the French program PNP (INSU-CNRS).

References

Avery, L. W., N. W. Broten, J. M. MacLeod, T. Oka, and H. W. Kroto (1976), Detection of the heavy interstellar molecule cyanodiacetylene, *Astrophys. J.*, *205*, L173–L175, doi:10.1086/182117.

Bell, M. B., P. A. Feldman, M. J. Travers, M. C. McCarthy, C. A. Gottlieb, and P. Thaddeus (1997), Detection of $HC^{11}N$ in the cold dust cloud TMC-1, *Astrophys. J.*, *483*, L61, doi:10.1086/310732.

Bénilan, Y., D. Andrieux, M. Khlifi, P. Bruston, F. Raulin, J.-C. Guillemin, and C. Cossart-Magos (1996), Temperature dependence of HC_3N, C_6H_2, and C_4N_2 mid-UV absorption coefficients. Application to the interpretation of Titan's atmospheric spectra, *Astrophys. Space Sci.*, *236*(1), 85–95, doi:10.1007/BF00644323.

Bénilan, Y., N. Smith, A. Jolly, and F. Raulin (2000), The long wavelength range temperature variations of the mid-UV acetylene absorption coefficient, *Planet. Space Sci.*, *48*(5), 463–471, doi:10.1016/S0032-0633(00)00019-2.

Bénilan, Y., A. Jolly, Y. Trolez, F. Raulin, and J.-C. Guillemin (2007), Infrared band intensities of cyanobutadiyne (HC_5N) between 400 and 4000 cm^{-1}, *J. Mol. Spectrosc.*, *245*(2), 109–114, doi:10.1016/j.jms.2007.07.006.

Cernicharo, J., A. M. Heras, A. G. G. M. Tielens, J. R. Pardo, F. Herpin, M. Guélin, and L. B. F. M. Waters (2001), Infrared Space Observatory's discovery of C_4H_2, C_6H_2, and benzene in CRL 618, *Astrophys. J.*, *546*, L123–L126, doi:10.1086/318871.

Chen, F. Z., and C. Y. R. Wu (2004), Temperature-dependent photoabsorption cross sections in the VUV-UV region. I. Methane and ethane, *J. Quant. Spectrosc. Radiat. Transf.*, *85*(2), 195–209, doi:10.1016/S0022-4073(03)00225-5.

Coll, P., D. Coscia, M.-C. Gazeau, E. de Vanssay, J.-C. Guillemin, and F. Raulin (1995), Organic chemistry in Titan's atmosphere: New data from laboratory simulations at low temperature, *Adv. Space Res.*, *16*(2), 93–103, doi:10.1016/0273-1177(95)00197-M.

Coupeaud, A., M. Turowski, M. Gronowski, N. Piétri, I. Couturier-Tamburelli, R. Kolos, and J.-P. Aycard (2007), Spectroscopy of cyanodiacetylene in solid argon and the photochemical generation of isocyanodiacetylene, *J. Chem. Phys.*, *126*(16), 164301, doi:10.1063/1.2720842.

Crovisier, J. (1994), Photodestruction rates for cometary parent molecules, *J. Geophys. Res.*, *99*(E2), 3777–3781, doi:10.1029/93JE02088.

Crovisier, J., D. Bockelée-Morvan, P. Colom, N. Biver, D. Despois, D. C. Lis, and the Team for Target-of-Opportunity Radio Observations of Comets (2004), The composition of ices in comet C/1995 O1(Hale-Bopp) from radio spectroscopy. Further results and upper limits on undetected species, *Astron. Astrophys.*, *418*, 1141–1157, doi:10.1051/0004-6361:20035688.

Cui, J., et al. (2009), Analysis of Titan's neutral upper atmosphere from Cassini Ion Neutral Mass Spectrometer measurements, *Icarus*, *200*, 581–615, doi:10.1016/j.icarus.2008.12.005.

de Vanssay, E., M.-C. Gazeau, J.-C. Guillemin, and F. Raulin (1995), Experimental simulation of Titan's organic chemistry at low temperature, *Planet. Space Sci.*, *43*(1–2), 25–31, doi:10.1016/0032-0633(94)00146-I.

Esposito, L. W., et al. (2004), The Cassini Ultraviolet Imaging Spectrograph investigation, *Space Sci. Rev.*, *115*, 299–361, doi:10.1007/s11214-004-1455-8.

Ferradaz, T., Y. Bénilan, N. Fray, A. Jolly, M. Schwell, M.-C. Gazeau, and H. W. Jochims (2009), Temperature-dependent photoabsorption cross-sections of cyanoacetylene and diacetylene in the mid- and vacuum-UV: Application to Titan's atmosphere, *Planet. Space Sci.*, *57*(1), 10–22, doi:10.1016/j.pss.2008.10.005.

Guillemin, J.-C., Y. Trolez, and A. Moncomble (2008), Synthesis, chemistry and photochemistry of cyanobutadiyne (HCCCCCN), *Adv. Space Res.*, *42*(12), 2002–2007, doi:10.1016/j.asr.2007.08.013.

Irvine, W. M., P. F. Goldsmith, and Å. Hjalmarson (1987), *Interstellar Processes*, D. Reidel, Dordrecht, Netherlands.

Krasnopolsky, V. A. (2009), A photochemical model of Titan's atmosphere and ionosphere, *Icarus*, *201*, 226–256, doi:10.1016/j.icarus.2008.12.038.

MacLeod, J. M., L. W. Avery, and N. W. Broten (1981), Detection of deuterated cyanodiacetylene DC_5N in Taurus Molecular Cloud 1, *Astrophys. J.*, *251*, L33–L36, doi:10.1086/183687.

Marten, A., T. Hidayat, Y. Biraud, and R. Moreno (2002), New millimeter heterodyne observations of Titan: Vertical distributions of nitriles HCN, HC_3N, CH_3CN, and the isotopic ratio $^{15}N/^{14}N$ in its atmosphere, *Icarus*, *158*, 532–544, doi:10.1006/icar.2002.6897.

Nuth, J. A., and S. Glicker (1982), The vacuum ultraviolet-spectra of HCN, C_2N_2, and CH_3CN, *J. Quant. Spectrosc. Radiat. Transf.*, *28*(3), 223–231, doi:10.1016/0022-4073(82)90025-5.

Pardo, J. R., J. Cernicharo, and J. R. Goicoechea (2005), Observational evidence of the formation of cyanopolyynes in CRL 618 through the polymerization of HCN, *Astrophys. J.*, *628*, 275–282, doi:10.1086/430774.

Reichardt, G., et al. (2001a), A 10 m-normal incidence monochromator at the quasi-periodic undulator U125–2 at BESSY II, *Nucl. Instrum. Methods Phys. Res., Sect. A*, *467–468*, 462–465, doi:10.1016/S0168-9002(01)00359-X.

Reichardt, G., T. Noll, I. Packe, P. Rotter, J. S. Schmidt, and W. Gudat (2001b), Adaption of the BESSY I-3m normal incidence monochromators to the BESSY II source, *Nucl. Instrum. Methods Phys. Res., Sect. A*, *467–468*, 458–461, doi:10.1016/S0168-9002(01)00357-6.

Scemama, A., P. Chaquin, M.-C. Gazeau, and Y. Bénilan (2002), Semi-empirical calculation of electronic absorption wavelengths of polyynes, monocyano- and dicyanopolyynes. Predictions for long chain compounds and carbon allotrope carbyne, *Chem. Phys. Lett.*, *361*(5–6), 520–524, doi:10.1016/S0009-2614(02)00988-0.

Shemansky, D. E., A. I. F. Stewart, R. A. West, L. W. Esposito, J. T. Hallett, and X. Liu (2005), The Cassini UVIS stellar probe of the Titan atmosphere, *Science*, *308*, 978–982, doi:10.1126/science.1111790.

Suzuki, H., S. Yamamoto, M. Ohishi, N. Kaifu, S.-I. Ishikawa, Y. Hirahara, and S. Takano (1992), A survey of CCS, HC_3N, HC_5N, and NH_3 toward dark cloud cores and their production chemistry, *Astrophys. J.*, *392*, 551–570, doi:10.1086/171456.

Takano, S., A. Masuda, Y. Hirahara, H. Suzuki, M. Ohishi, S.-I. Ishikawa, N. Kaifu, Y. Kasai, K. Kawaguchi, and T. L. Wilson (1998), Observations of ^{13}C isotopomers of HC_3N and HC_5N in TMC-1: Evidence for isotopic fractionation, *Astron. Astrophys.*, *329*, 1156–1169.

Thuillier, G., L. Floyd, T. N. Woods, R. Cebula, E. Hilsenrath, M. Hersé, and D. Labs (2004a), Solar irradiance reference spectra, in *Solar Variability and Its Effects on Climate*, *Geophys. Monogr. Ser.*, vol. 141, edited by J. M. Pap et al., pp. 171–194, AGU, Washington, D. C.

Thuillier, G., L. Floyd, T. N. Woods, R. Cebula, E. Hilsenrath, M. Hersé, and D. Labs (2004b), Solar irradiance reference spectra for two solar active levels, *Adv. Space Res.*, *34*, 256–261, doi:10.1016/j.asr.2002.12.004.

Trolez, Y., and J.-C. Guillemin (2005), Synthesis and characterization of 2,4-pentadiynenitrile—A key compound in space science, *Angew. Chem. Int. Ed.*, *44*, 7224–7226, doi:10.1002/anie.200502122.

Vuitton, V., R. V. Yelle, and M. J. McEwan (2007), Ion chemistry and *N*-containing molecules in Titan's upper atmosphere, *Icarus*, *191*(2), 722–742, doi:10.1016/j.icarus.2007.06.023.

Wu, C. Y. R., F. Z. Chen, and D. L. Judge (2001), Measurements of temperature-dependent absorption cross sections of C_2H_2 in the VUV-UV region, *J. Geophys. Res.*, *106*(E4), 7629–7638, doi:10.1029/2000JE001292.

Wu, C. Y. R., F. Z. Chen, and D. L. Judge (2004), Temperature-dependent photoabsorption cross sections in the VUV-UV region: Ethylene, *J. Geophys. Res.*, *109*, E07S15, doi:10.1029/2003JE002180.

E. Arzoumanian, Y. Bénilan, Et. Es-Sebbar, T. Ferradaz, N. Fray, M.-C. Gazeau, A. Jolly, and M. Schwell, Laboratoire Interuniversitaire des Systèmes Atmosphériques, UMR 7583 du CNRS, Universités Paris 7 et 12, 61 Avenue du Général de Gaulle, 94010 Créteil Cedex, France. (nicolas.fray@lisa.univ-paris12.fr)

J.-C. Guillemin, École Nationale Supérieure de Chimie de Rennes, UMR 6226, CNRS, Avenue du Général Leclerc, CS 50837, 35708 Rennes Cedex 7, France.

ARTICLE 7

Venot O., Fray N., Bénilan Y., Gazeau M.-C., Hébrard E., Larcher G., Schwell M., Dobrijevic M. and Selsis F. (2013)

High-temperature measurements of VUV absorption cross sections of CO2 and application to exoplanets.

Astronomy & Astrophysics, 551, A131

A&A 551, A131 (2013)
DOI: 10.1051/0004-6361/201220945

Astronomy & Astrophysics

High-temperature measurements of VUV-absorption cross sections of CO_2 and their application to exoplanets

O. Venot[1,2], N. Fray[3], Y. Bénilan[3], M.-C. Gazeau[3], E. Hébrard[12], G. Larcher[3], M. Schwell[3], M. Dobrijevic[1,2], and F. Selsis[1,2]

[1] Univ. Bordeaux, LAB, UMR 5804, 33270 Floirac, France
e-mail: venot@obs.u-bordeaux1.fr
[2] CNRS, LAB, UMR 5804, 33270 Floirac, France
[3] Laboratoire Interuniversitaire des Systèmes Atmosphériques, UMR CNRS 7583, Universités Paris Est Créteil (UPEC) et Paris Diderot (UPD), Créteil, France

Received 18 December 2012 / Accepted 28 January 2013

ABSTRACT

Context. Ultraviolet (UV) absorption cross sections are an essential ingredient of photochemical atmosphere models. Exoplanet searches have unveiled a large population of short-period objects with hot atmospheres, very different from what we find in our solar system. Transiting exoplanets whose atmospheres can now be studied by transit spectroscopy receive extremely strong UV fluxes and have typical temperatures ranging from 400 to 2500 K. At these temperatures, UV photolysis cross section data are severely lacking.
Aims. Our goal is to provide high-temperature absorption cross sections and their temperature dependency for important atmospheric compounds. This study is dedicated to CO_2, which is observed and photodissociated in exoplanet atmospheres. We also investigate the influence of these new data on the photochemistry of some exoplanets.
Methods. We performed these measurements with synchrotron radiation as a tunable VUV light source for the 115–200 nm range at 300, 410, 480, and 550 K. In the 195–230 nm range, we used a deuterium lamp and a 1.5 m Jobin-Yvon spectrometer and we worked at seven temperatures between 465 and 800 K. We implemented the measured cross section into a 1D photochemical model.
Results. For $\lambda > 170$ nm, the wavelength dependence of $\ln(\sigma_{CO_2}(\lambda, T) \times \frac{1}{Q_v(T)})$ can be parametrized with a linear law. Thus, we can interpolate $\sigma_{CO_2}(\lambda, T)$ at any temperature between 300 and 800 K. Within the studied range of temperature, the CO_2 cross section can vary by more than two orders of magnitude. This, in particular, makes the absorption of CO_2 significant up to wavelengths as high as 230 nm, while it is negligible above 200 nm at 300 K.
Conclusions. The absorption cross section of CO_2 is very sensitive to temperature, especially above 160 nm. The model predicts that accounting for this temperature dependency of CO_2 cross section can affect the computed abundances of NH_3, CO_2, and CO by one order of magnitude in the atmospheres of hot Jupiter and hot Neptune. This effect will be more important in hot CO_2-dominated atmospheres.

Key words. molecular data – planets and satellites: atmospheres – methods: laboratory

1. Introduction

Exoplanets exhibit a wide variety of mass, radius, orbits, and host stars. Because of observational biases, most transiting exoplanets are very close to their parent stars and are highly irradiated, implying large UV fluxes and high atmospheric temperatures. The atmosphere of transiting hot Jupiters and hot Neptunes can be studied by spectroscopy at the primary transit (Tinetti et al. 2007b,a; Swain et al. 2008; Beaulieu et al. 2010, 2011; Tinetti et al. 2010) and at the secondary eclipse (Swain et al. 2009a,b; Stevenson et al. 2010, 2012). Photochemistry has an important influence on the atmospheric composition of these exoplanets, from the top of the atmosphere down to 100 mbar (Moses et al. 2011; Line et al. 2011; Venot et al. 2012). For these exoplanets and within this large pressure range, the temperature can vary roughly from 400 to 2500 K. To model correctly the photochemistry of these planets, we need to use absorption cross sections consistent with these temperatures for all the species whose photolysis plays an important role in either the formation/destruction of molecules or in the penetration of the UV flux into the atmosphere. Carbon dioxide (CO_2) is one of these species. It has been observed in extrasolar giant planet atmospheres (Swain et al. 2009a,b), but cross section measurements ($\sigma_{CO_2}(\lambda, T)$) are extremely sparse above room temperature.

Some high-temperature measurements have been performed in the past but only at a few wavelengths. For instance, Koshi et al. (1991) measured the production of $O(^3P)$ in the photodissociation of CO_2 at 193 nm by using atomic resonance absorption spectroscopy behind reflected shock waves between 1500 and 2700 K. They saw that the production of oxygen atoms increases with the temperature. Before that, Generalov et al. (1963) measured $\sigma_{CO_2}(\lambda, T)$ behind a shock wave at temperatures up to 6300 K at 238 and 300 nm, and observed absorption up to 355 nm at 5000 K. These measurements, because of the technique employed, are limited to a narrow range of wavelengths and do not provide complete spectra. Nevertheless, they showed that the absorption of CO_2 increases at high temperature.

The first experiments dedicated to the determination of absorption cross sections of CO_2 at temperatures different from 298 K were motivated by solar system planetary studies (Mars, Titan, Venus, primitive Earth). Lewis & Carver (1983) measured $\sigma_{CO_2}(\lambda, T)$ between 120 and 197 nm at 202 and 367 K. They observed an enhancement of $\sigma_{CO_2}(\lambda, T)$ for the longer

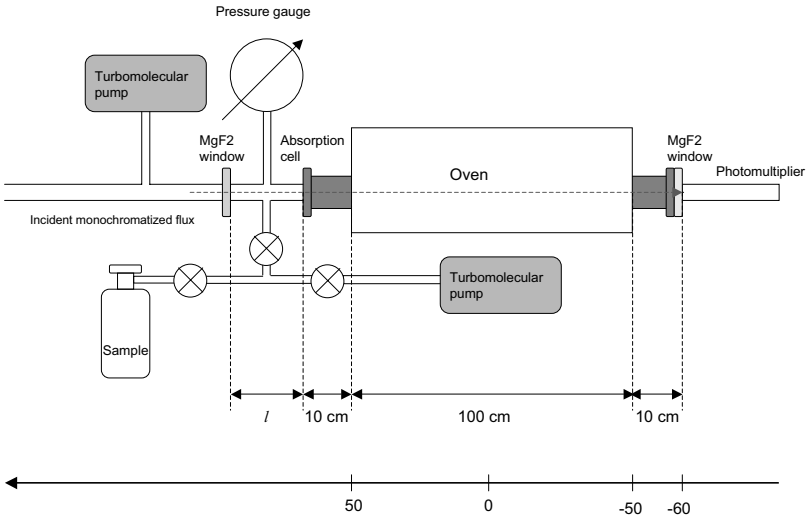

Fig. 1. Experimental setup used for measuring the ultraviolet absorption spectra at high temperatures. The length l changed during the different set of measurements. For the 115–200 nm experiments, l = 13.3 cm. For the 195–230 nm range, l = 27.0 cm. Finally, for the temperature calibration, l = 20 cm.

wavelengths when the temperature increases. This trend was confirmed by Yoshino et al. (1996), who measured the absorption cross section of CO_2 at 195 and 295 K, between 118.7 and 175.5 nm. Parkinson et al. (2003) extended these measurements up to 192.5 nm for 195 K, and up to 200 nm for 295 K. They observed that the cross sections at 195 K were smaller than those at 295 K. Finally, still in the frame of Mars and Venus studies, Stark et al. (2007) explored a lower wavelength range and measured $\sigma_{CO_2}(\lambda, T)$ between 106.1 and 118.7 nm at 295 and 195 K.

During the same period, Jensen et al. (1997) used a heated cell traversed by a tunable laser to measure the absorption cross section of CO_2 at high temperatures. They obtained spectra from 230 to 355 nm at 1523, 1818, 2073, and 2273 K. In the frame of combustion studies, Schulz et al. (2002) measured the absorption cross section in shock-heated CO_2 between 190 and 320 nm, and for temperatures ranging from 900 to 3050 K. They fit the strong temperature dependence of $\sigma_{CO_2}(\lambda, T)$ with an empirical function. Oehlschlaeger et al. (2004) extended these data to higher temperatures (up to 4500 K). They measured the absorption of shock-heated carbon dioxide at four different laser wavelengths (216.5, 244, 266, and 306 nm). They also fit the variation of $\sigma_{CO_2}(\lambda, T)$ with a semi-empirical formula. Jeffries et al. (2005) showed that the temperature dependence of CO_2 absorption in the UV could be used to determine the gas temperature, making this parameter a useful tool in combustion applications.

To our best knowledge, no measurements exist of the absorption cross section of CO_2 between 300 and 900 K in the wavelength range useful for exoplanetary studies (<190 nm). Here we report measurements of this parameter at 300, 410, 480, 550 K between 115 and 200 nm, as well as between 195 and 230 nm at seven temperature values between 465 and 800 K. We determine a semi-empirical formula to fit the temperature dependence for wavelengths longer than 170 nm. Finally, we study the effect of these new data on the atmospheric composition predicted by a 1D photochemical model of hot exoplanet atmospheres.

2. Experimental methods and procedures

2.1. Measurements

We used gaseous CO_2 of 99.995% purity. Tunable VUV light between 115 and 200 nm was obtained from the synchrotron radiation facility BESSY in Berlin. Measurements in this spectral range were performed using a three-meter focal length normal incidence monochromator (NIM) equipped with a 600 lines/mm holographically ruled grating with a linear dispersion of 0.56 nm.mm^{-1} and connected to a dipole magnet beamline (DIP12-1B) (Reichardt et al. 2001). We recorded spectra of CO_2 with a resolution of 0.05 nm. Wavelength calibration was obtained by using the set of measurements of Yoshino et al. (1996), Parkinson et al. (2003), and Stark et al. (2007) as a reference. The VUV radiation intensity was measured directly with a solar blind photomultiplier tube closed by a MgF_2 window (Electron Tubes Limited 9402B with caesium-telluride photocathode, see Fig. 1). The entrance of the cell was also closed by a MgF_2 window. With this configuration, the absorption cell is a cylinder with an optical path length of 133 cm. The signal coming from the photomultiplier was recorded through a pico ampere meter (Keithley) using an integration time of 1 s per point. We recorded three points per resolution interval.

To account for the steady decrease of the incident VUV light intensity, which is caused by the decay of BESSY's storage ring current, two "empty-cell" spectra were recorded just before and right after each CO_2 spectrum. A synthetic empty-cell spectrum was then interpolated by considering a linear decrease of the incident light intensity in accordance with the recorded ring current decrease during our experiment time (1/2 h approximately). Comparing the spectra we have acquired at different pressures, we estimate that this procedure leads to an uncertainty of 10% on the absorption cross section and that this error dominates over all other sources of errors.

Measurements in the 195–230 nm range were performed at the Laboratoire Interuniversitaire des Systèmes Atmosphériques (LISA) in Créteil, France. We used a UV deuterium lamp and a 1.5 m Jobin-Yvon spectrometer. The experimental setup was the same as for the lower wavelength range (see Fig. 1), except that the optical path length was 147 cm. In this spectral range, we recorded spectra with a resolution of 0.3 nm. In both cases, an oven (Nabertherm) was used to heat the cell to a temperature of 1400 K. The temperature of the oven was constant and measured continuously at three fixed points along the tube.

Gaseous carbon dioxide was introduced into the cell at the desired pressure, which was monitored by two MKS Baratron®

manometers (range 10^{-4} to 1 mbar and 1 to 1000 mbar). All spectra were taken for at least three different pressures in the 0.2–1000 mbar range to check the reproducibility of our measurements. Comparing all the spectra we have acquired, we restricted the influence of the stray light by selecting only spectra that were free from any saturated absorption, i.e., with transmission greater than 10%.

2.2. Temperature calibration

Even if the temperature of the oven is controlled at three different points, the temperature distribution of the gas inside the cell is not homogeneous along the optical pathway. Moreover, the temperature set by the oven (T_{set}) does not correspond to the effective temperature of the gas (T_{gas}). We calibrated the temperature of the gas in two steps. First, with a thermocouple type E, we measured the temperature at the center of the absorption cell, without gas. Figure 2 shows the relation between the set temperature and the temperature measured inside the cell at the center T_{max}. As we can see, for $T_{set} = 1273$ K, the temperature at the center of the oven is only 856 K. We find that the maximum temperature in the cell is given by

$$T_{max} = 0.53 \times T_{set} + 181. \quad (1)$$

We then measured the temperature gradient inside the absorption cell at different points in the cell (see Fig. 3). Figure 3 also shows that there is a middle area where the temperature is relatively constant, and the temperature decreases towards the extremities of the absorption cell. The temperature in the cell $T_{gas}(x)$ can be modeled using a symmetrized inverse exponential function with two limits

$$T_{gas}(x) = T_{max} + \frac{T_{amb} - T_{max}}{1 + \exp\left(-\frac{|x|-|x_0|}{\Delta x}\right)}, \quad (2)$$

where T_{max} (K) is calculated from Eq. (1), and T_{amb} is the ambient temperature (298 K); x_0 (cm) and Δx (cm) are determined by minimizing the χ^2 function using the measured data. x_0 corresponds to the position where $T_{gas}(x_0) = (T_{amb} + T_{max})/2$. The cell is heated by the oven and cooled by conduction from the part at ambient temperature outside the oven. An equilibrium is reached by the two processes that fix x_0. Figure 4 shows the relation between x_0 and T_{set}. We find that x_0 is given by

$$x_0 = 25 \times \exp\left(-\frac{T_{set} - 273}{300}\right) - 56 \quad (3)$$

with x_0 in cm and T_{set} in Kelvin. As we can see in Fig. 4, $|x_0|$ varies by 30%, from 40 cm to 56 cm, in our temperature range. The fact that x_0 increases with temperature means that the cooling process becomes less efficient when the temperature increases. The value of Δx is found to be constant for the whole temperature range and is equal to 9 cm.

2.3. Calculation of the absorption cross section

When the temperature is constant in the cell, absolute photoabsorption cross sections can be calculated using the Beer-Lambert law

$$\sigma = \left(\frac{1}{nL}\right) \times \ln\left(\frac{I_0}{I}\right), \quad (4)$$

where σ corresponds to the absorption cross section (cm^2), I_0 is the light intensity transmitted with an empty cell, I is the light intensity transmitted through the gas sample, L is the absorption path length (cm), and n is the volume density of the gas (cm^{-3}), following the relation $P = nk_BT$, where T (K) and P (Pa) are, respectively, the temperature and the pressure of the sample and k_B the Boltzmann constant.

As explained in Sect. 2.2, in our experiments the temperature is not constant along the optical pathway, so we can not use the Eq. (4) since the density depends on T. Consequently, the light transmitted through the cell should be integrated step by step along the optical pathway and the data should be inverted in order to retrieve the absorption cross sections. In order to simplify the problem, we consider a mean temperature T_{mean} for the

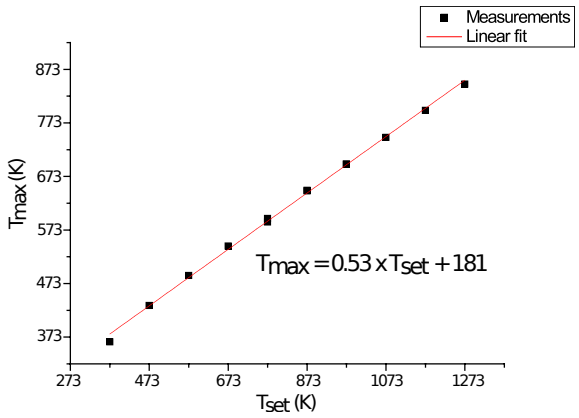

Fig. 2. Relation between the set temperature (T_{set}) and the temperature measured at the center of the oven (T_{max}).

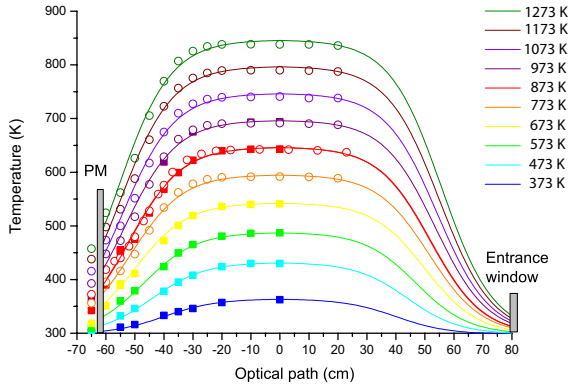

Fig. 3. Temperature gradient inside the cell. 0 cm is the middle of the oven, where the temperature is the highest (T_{max}).

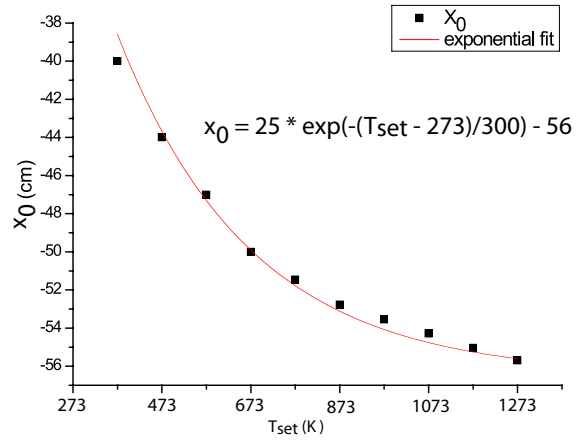

Fig. 4. Relation between x_0 and the order temperature T_{set}.

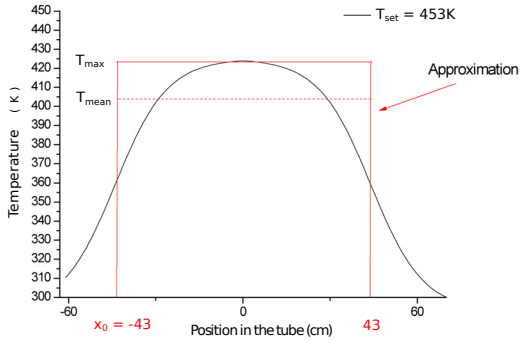

Fig. 5. Temperature inside the absorption cell for $T_{\rm set}$ = 453 K. The maximum temperature $T_{\rm max}$ is 420 K and the mean temperature $T_{\rm mean}$ is (410 ± 15) K. The portion of gas out of the range $[-x_0; x_0]$ is considered at ambient temperature.

gas along the pathway $-x_0$ to x_0 (Fig. 5). This way, we can assign one spectrum to one temperature. The mean temperature is calculated by integrating Eq. (2) from $-x_0$ to x_0 and normalizing by $2x_0$. The portion of gas out of the range $[-x_0; x_0]$ is considered to be at ambient temperature. The mean temperature calculated is then used to calculate the absorption cross section. For instance, with $T_{\rm set}$ = 453 K, the maximum temperature reached is in fact $T_{\rm max}$ = 420 K and we determined an absorption cross section for a mean temperature $T_{\rm mean}$ = (410 ± 15) K. In our case, the intensity I is attributable partly to the section at the ambient temperature and partly to the section at the mean temperature.

The absorbance of the portion of gas at ambient temperature is subtracted from the overall absorbance measured with the heated gas. We calculate the absorption cross section at the mean temperature with the formula

$$\sigma(T_{\rm mean}) = \frac{1}{n_{\rm mean} \times L_{\rm mean}} \times \left[\ln\left(\frac{I_0}{I}\right) - \sigma(T_{\rm amb}) \times n_{\rm amb} \times L_{\rm amb}\right], \quad (5)$$

where $\sigma(T_{\rm amb})$ and $\sigma(T_{\rm mean})$ (cm^2) are the absorption cross sections at ambient temperature and at the mean temperature of the gas, $n_{\rm amb}$ and $n_{\rm mean}$ (cm^{-3}) are the volume densities of the gas in the portion at $T_{\rm amb}$ and at $T_{\rm mean}$, respectively. $L_{\rm mean} = 2x_0$ and $L_{\rm amb} = L - 2x_0$ (cm) are the portion of gas at $T_{\rm mean}$ and at $T_{\rm amb}$, respectively. We validated a posteriori this approximation by comparing measured transmissions at different temperatures and pressures, with the transmissions obtained from the complete radiative transfer through the cell taking into account the temperature variation along the optical path and the temperature variation of the absorption cross section presented in the next section. Results are generally in agreement to better than one percent (see Fig. 6).

3. Results and discussion

3.1. Photoabsorption cross section from 115 nm to 200 nm

Before heating the gas, we measured ambient temperature (300 K) spectra of CO_2 in order to calibrate and compare it with the previously published data (Yoshino et al. 1996; Parkinson et al. 2003; Stark et al. 2007); our measurements agree very closely with these measurements with a difference of less than a few percentage points for all wavelengths. Our measurements at room temperature did not go up to 200 nm, so between 170 and 200 nm we use the data of Parkinson et al. (2003).

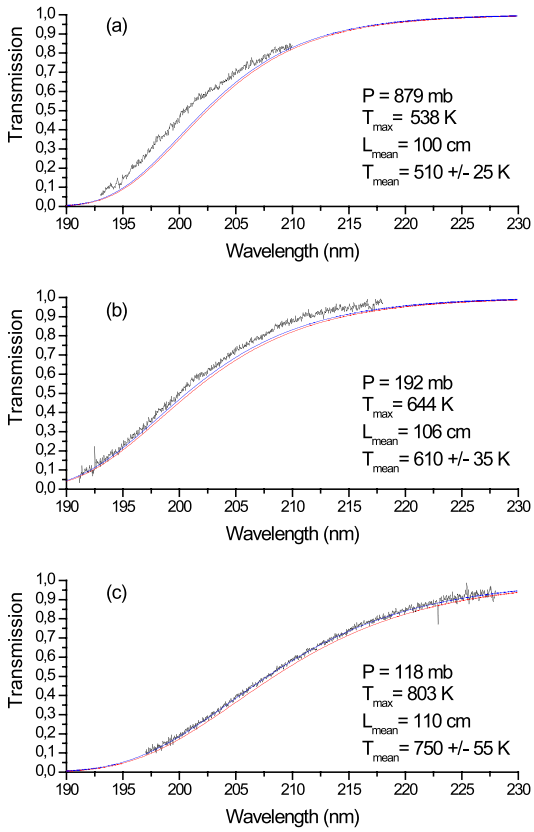

Fig. 6. Transmission of the flux as a function of the wavelength determined by the measurements (black lines) compared to the measurements obtained from the complete radiative transfer through the cell, taking into account the real temperature variation along the optical path, **a)** 538 K; **b)** 644 K; and **c)** 803 K (red line), and the measurements obtained when considering the mean temperature **a)** 510 K; **b)** 610 K; and **c)** 750 K (blue line).

Then, we measured $\sigma_{CO_2}(\lambda, T)$ at three different temperatures: 410 (±15) K, 480 (±25) K, and 550 (±30) K. We show these data in Fig. 7. Between 115 and 120 nm we see a change of the cross section which depends on the temperature. At 120 nm, the absorption cross section is ten times higher at 550 K than at 300 K and an increase of a factor of 2.5 is observed at 121.6 nm between the lower and the upper temperature. Slight differences of up to 50% can be observed between 125 and 140 nm while between 140 and 150 nm differences are minor. After 160 nm, we clearly observe large differences between the different temperatures. The slope of the cross section varies with the temperature. The higher the temperature is, the less steep is the slope. At 195 nm, there is a factor ~200 between $\sigma_{CO_2}(\lambda, 300\ {\rm K})$ and $\sigma_{CO_2}(\lambda, 550\ {\rm K})$.

3.2. Photoabsorption cross section from 195 nm to 230 nm

We measured $\sigma_{CO_2}(\lambda, T)$ at seven different temperatures: 465 (±20) K, 510 (±25) K, 560 (±30) K, 610 (±35) K, 655 (±45) K, 750 (±55) K and 800 (±60) K. As for the cross section at shorter wavelengths, we clearly see the dependence on the temperature in this wavelength range and the increase of the cross section for high temperatures (Fig. 8). As we plotted the data obtained previously at shorter wavelengths in this figure, we see good agreement between the two ranges. Especially, we see that $\sigma_{CO_2}(\lambda < 200\ {\rm nm}, 550\ {\rm K})$ matches almost perfectly with $\sigma_{CO_2}(\lambda > 195\ {\rm nm}, 560\ {\rm K})$.

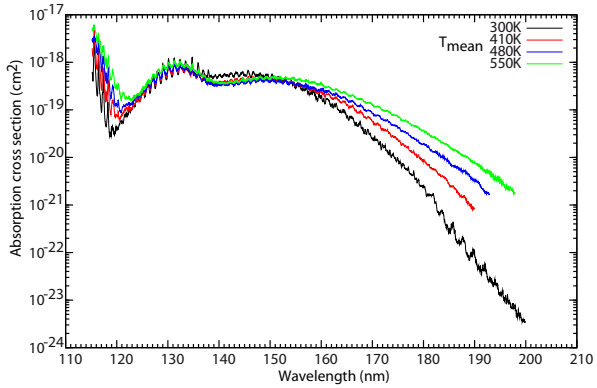

Fig. 7. Absorption cross section of CO_2 at T_{mean} = 300 K (black), 410 K (red), 480 K (green) and 550 K (blue) for wavelengths between 115 and 200 nm.

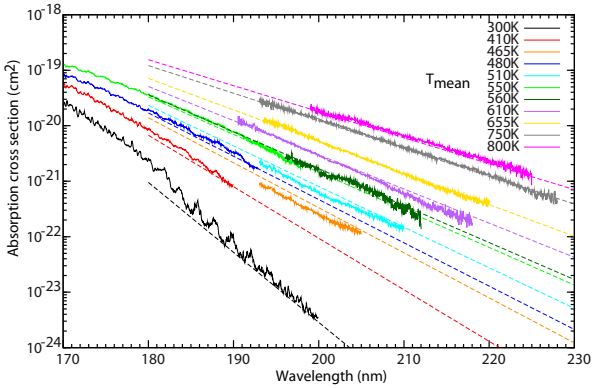

Fig. 8. Absorption cross section of CO_2 for wavelengths longer than 195 nm at 465 K, 510 K, 560 K, 610 K, 655 K, 750 K, and 800 K, plotted with the cross section at ambient temperature (black) and the absorption cross sections measured at shorter wavelengths and presented in Fig. 7 (300 K, 410 K, 480 K, and 550 K). The absorption cross sections calculated with Eq. (6) are plotted with the same color coding.

3.3. Determination of an empirical law

For wavelengths longer than 170 nm, we parametrize the variation of $\ln(\sigma_{CO_2}(\lambda,T)\times\frac{1}{Q_v(T)})$ with a linear regression

$$\ln\left(\sigma_{CO_2}(\lambda,T)\times\frac{1}{Q_v(T)}\right)=a(T)+b(T)\times\lambda \quad (6)$$

with T in K and λ in nm and where
$a(T)=-42.26+(9593\times1.44/T)$,
$b(T)=4.82\times10^{-3}-61.5\times1.44/T$,
and
$Q_v(T)=(1-\exp(-667.4\times1.44/T))^{-2}\times(1-\exp(-1388.2\times1.44/T))^{-1}\times(1-\exp(-2449.1\times1.44/T))^{-1}$
is the partition function. Figure 8 compares the absorption cross sections obtained with this calculation to the measurements. We can see that the parametrization is very good.

In this wavelength region, measurements at ambient temperature have been obtained with high resolution (Cossart-Magos et al. 1992, 2005). The narrow bands that have been identified in this study allow us to make the assumption that the continuum is made of the superposition of bands corresponding to transitions from high vibrational states of the electronic ground state to different vibrational states of the upper electronic states $^1B_2$, $^1A_2$, or $^3B_2$ (see Cossart-Magos et al. 2005). If we suppose that at each wavelength we associate only one transition coming from a defined vibrational level having an effective energy, the cross sections which are proportional to the population of the lower level should have a Boltzmann like temperature dependence ($\ln\sigma_{CO_2}(\lambda,T)\times Q_v(T)=-hc\nu/k_BT+$Cste). So, the coefficients $a(T)$ and $b(T)$ plotted as a function of $hc/k_BT(=1.44/T)$ should give a straight line from which we could obtain the ground state frequency of the vibration mode involved in the electronic transition. Trying to use this model did not give a good parametrization of our data. Consequently, we chose to keep our parametrization given by Eq. (6) which has no physical meaning but simply allows us to parametrize our data with only four parameters. This greatly simplifies the implementation of the temperature dependency of the absorption cross sections in the radiative transfer codes.

Our results are not compatible with the data of Schulz et al. (2002). We used their formulation $\ln\sigma(\lambda,T)=a+b\lambda$ with the coefficients a and b given in their paper, to determine the absorption cross section of CO_2 for some temperatures in the range 900–3500 K. The absorption cross section calculated for T = 940 K falls in between our data for 655 K and 750 K. Also, the value found with their calculation for T = 1160 K is only slightly higher than our data at 800 K. Schulz et al. (2002) may have overestimated the temperature in their measurements. Or, another possible problem in their measurement is that their background signal (I_0) is measured at ambient temperature. Thermal emission is therefore not taken into account when their samples are heated. This could lead to an underestimation of their absorbance, and consequently to lower absorption cross sections compared to ours.

4. Application to exoplanets

We investigated the impact of the temperature dependency of the CO_2 cross section on a prototype planet whose characteristics are similar to those of the hot Neptune GJ 436b. We chose this planet because the temperature of its upper atmosphere is around ~500 K which corresponds to the highest temperature for which we measured the cross section between 115 and 200 nm. This exoplanet was discovered in 2004 by Butler et al. (2004). Its semi-major axis is a = 0.02887 (±0.00095) AU and its mass is $M\sin i$ = 0.0737 (±0.0052) M_J (Southworth 2010).We considered three different types of host stars: an M, a G, and an F star. We used the spectra of GJ 644 (M3V, Segura et al. 2005), the Sun (G2V, Gueymard 2004), and HD 128167 (F2V, Segura et al. 2003), scaled to get the bolometric flux received by GJ436b. Figure 9 compares the flux received at the top of the atmosphere of a GJ 436b-like planet with the different stars.

We used the model described in Venot et al. (2012) and the same temperature profile as Line et al. (2011) calculated by Lewis et al. (2010). Although this is not a realistic assumption, we used the same temperature for all three host stars. To model the vertical mixing, we considered an eddy diffusion coefficient constant K_{zz} = 10^8 cm^2 s^{-1}. Elemental abundances of the atmosphere of this planet are highly uncertain (Stevenson et al. 2010; Madhusudhan & Seager 2011). So we assumed a heavy elemental enrichment of 100 compared with solar abundances (Grevesse & Sauval 1998), which is arbitrary but higher only by a factor of 2 than the carbon enrichment of Uranus and Neptune (Hersant et al. 2004, and references therein). Consequently we obtained a high abundance of CO_2.

CO_2 has two routes to photodissociate:

$CO_2+h\nu \longrightarrow CO + O(^3P)$ $\quad J4$
$CO_2+h\nu \longrightarrow CO + O(^1D)$ $\quad J5.$

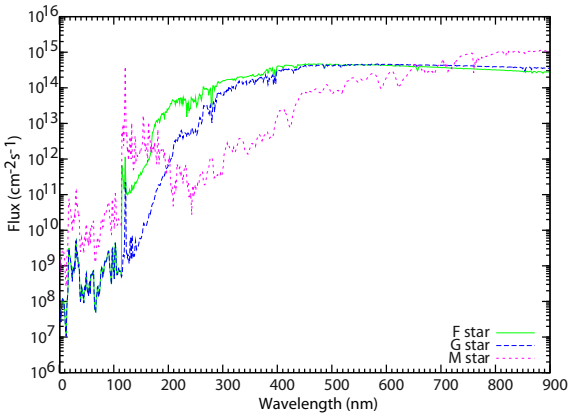

Fig. 9. UV flux received at the top of the atmosphere of a GJ 436b-like planet with the M star (dotted line pink), G star (dashed line blue) and F star (full line green).

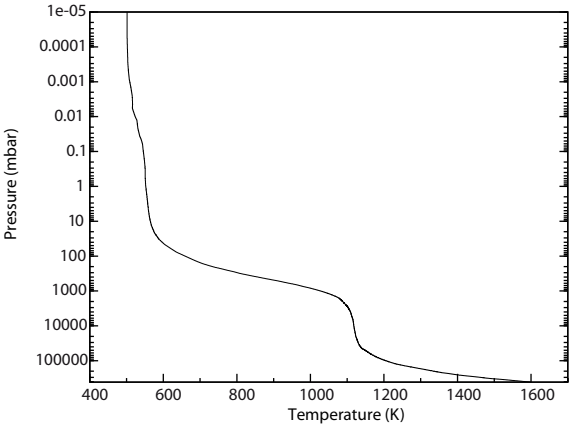

Fig. 10. Temperature profile of GJ 436b (Lewis et al. 2010).

Table 1. Quantum yields for the photodissociations of CO_2.

Quantum yield	Values [wavelength range]
$q_4(\lambda)$	1 [167–227]
$q_5(\lambda)$	variable [50–107] ; 1 [108–166]

Depending on the energy of the photons, one route is favored over the other. The quantum yield for these two photolyses, $q_4(\lambda)$ and $q_5(\lambda)$, are presented in Table 1 (Huebner et al. 1992). We see that at longer wavelengths, CO_2 photodissociates through the route $J4$. We assume that it remains the same at high temperature.

The loss rate of a photolysis Jk corresponds to the loss of CO_2 because of this photolysis. It is given by

$$\frac{\partial n_{CO_2}}{\partial t} = -J^k_{CO_2} n_{CO_2}, \quad (7)$$

where n_{CO_2} is the density of CO_2 (cm^{-3}) and $J^k_{CO_2}$ is the photodissociation rate of CO_2 by the photodissociation Jk

$$J^k_{CO_2}(z) = \int_{\lambda_1}^{\lambda_2} \sigma_{CO_2}(\lambda) F(\lambda, z) q_k(\lambda) \mathrm{d}\lambda, \quad (8)$$

where $[\lambda_1; \lambda_2]$ is the spectral range on which CO_2 absorbs the UV flux, $\sigma_{CO_2}(\lambda)$ the absorption cross section of CO_2 at the wavelength λ (cm^2), $F(\lambda, z)$ the UV spectral irradiance at λ and the altitude z (cm^{-2} s^{-1} nm^{-1}), and $q_k(\lambda)$ the quantum yield corresponding to the photodissociation Jk.

First, we find the steady-state composition of these atmospheres using the absorption cross sections available in the literature, which means at ambient temperature. Then, we replace the "ambient cross section" of CO_2 ($\sigma_{CO_2}(300\ \mathrm{K})$) by the cross section measured at 550 K, between 115 and 200 nm ($\sigma_{CO_2}(550\ \mathrm{K})$). For wavelengths between 200 and 230 nm, we use Eq. (6) to determine $\sigma_{CO_2}(550\ \mathrm{K})$.

As we see in Fig. 11 (left), changing the absorption cross section of CO_2 has consequences on the abundances of some species. For instance, when considering an M star at 5×10^{-4} mbar with $\sigma_{CO_2}(300\ \mathrm{K})$, CO_2 has an abundance of 1.5×10^{-2}, whereas with $\sigma_{CO_2}(550\ \mathrm{K})$, its abundance is only 0.82×10^{-2}, which corresponds to a reduction of 45%. The compounds $O(^3P)$, CO, and NH_3 are also affected by the change of $\sigma_{CO_2}(T)$ at the same pressure. There is almost no difference in the case of the G star. But for the F star at 0.01 mbar, CO_2 is nearly eight times less abundant with $\sigma_{CO_2}(550\ \mathrm{K})$ than with $\sigma_{CO_2}(300\ \mathrm{K})$. Consequently, because CO_2 absorbs more photons, less NH_3 is destroyed and is 40 times more abundant than with $\sigma_{CO_2}(300\ \mathrm{K})$. We see that other species are also affected by the change of CO_2 absorption cross section, such as CH_4, HCN, H_2, and N_2. To see these variations, we represented in Fig. 11 (right) the differences of abundances of the major species (i.e., for species with an abundance superior to 10^{-10}) between the two models. We see that the differences in abundances can reach almost 10^5%, even for species which are not directly linked to $\sigma_{CO_2}(T)$, such as HCN in the case of the M star.

These differences are easily comprehensible. We chose the case of NH_3 to illustrate it. At high temperature, the absorption cross section of CO_2 is higher around 120 nm and for wavelengths superior to 150 nm, so CO_2 absorbs more UV flux than with the ambient cross section. Consequently, more CO_2 is photolysed. The UV photons that are now absorbed by CO_2 were absorbed by NH_3 when using $\sigma_{CO_2}(300\ \mathrm{K})$. Now NH_3 absorbs fewer UV photons, so less is destroyed. This can be generalized to the other species. Indeed, the general behavior of these curves can be explained in terms of the various opacity sources that peak at slightly different altitudes. Because of the competition among the different opacity sources in the atmosphere, all the species absorbing in the same range of wavelength as CO_2 are affected.

We see in Fig. 12 that for pressures higher than ~50 mbar, the total loss rate is not altered by the change of absorption cross section. For pressures lower than that, the total loss rate of CO_2 is ~10 times more important with $\sigma_{CO_2}(550\ \mathrm{K})$ than with $\sigma_{CO_2}(300\ \mathrm{K})$. Between 10 and 5×10^{-4} mbar, the loss rate of the photolysis process $J4$ is approximately equal to the total loss rate when we use $\sigma_{CO_2}(550\ \mathrm{K})$, whereas it is far from the case with $\sigma_{CO_2}(300\ \mathrm{K})$. Indeed, between 10^{-3} and 10 mbar, the loss rate of $J4$ increases by a factor of 10–100 when we use $\sigma_{CO_2}(550\ \mathrm{K})$. At around 5×10^{-4} mbar with $\sigma_{CO_2}(550\ \mathrm{K})$, the photodissociation process $J5$ is about 10 times less efficient in destroying CO_2 than with $\sigma_{CO_2}(300\ \mathrm{K})$. Nevertheless, we do not see any change in the abundance of $O(^1D)$. In both cases, with the M star we see a peak of destruction of CO_2 around 3×10^{-4} mbar.

It is with the G star that the difference of composition is the least important when we change σ_{CO_2}. This is quite normal because the flux received by the planet before 200 nm is lower than with the M star and the F star (see Fig. 11). On the contrary, the

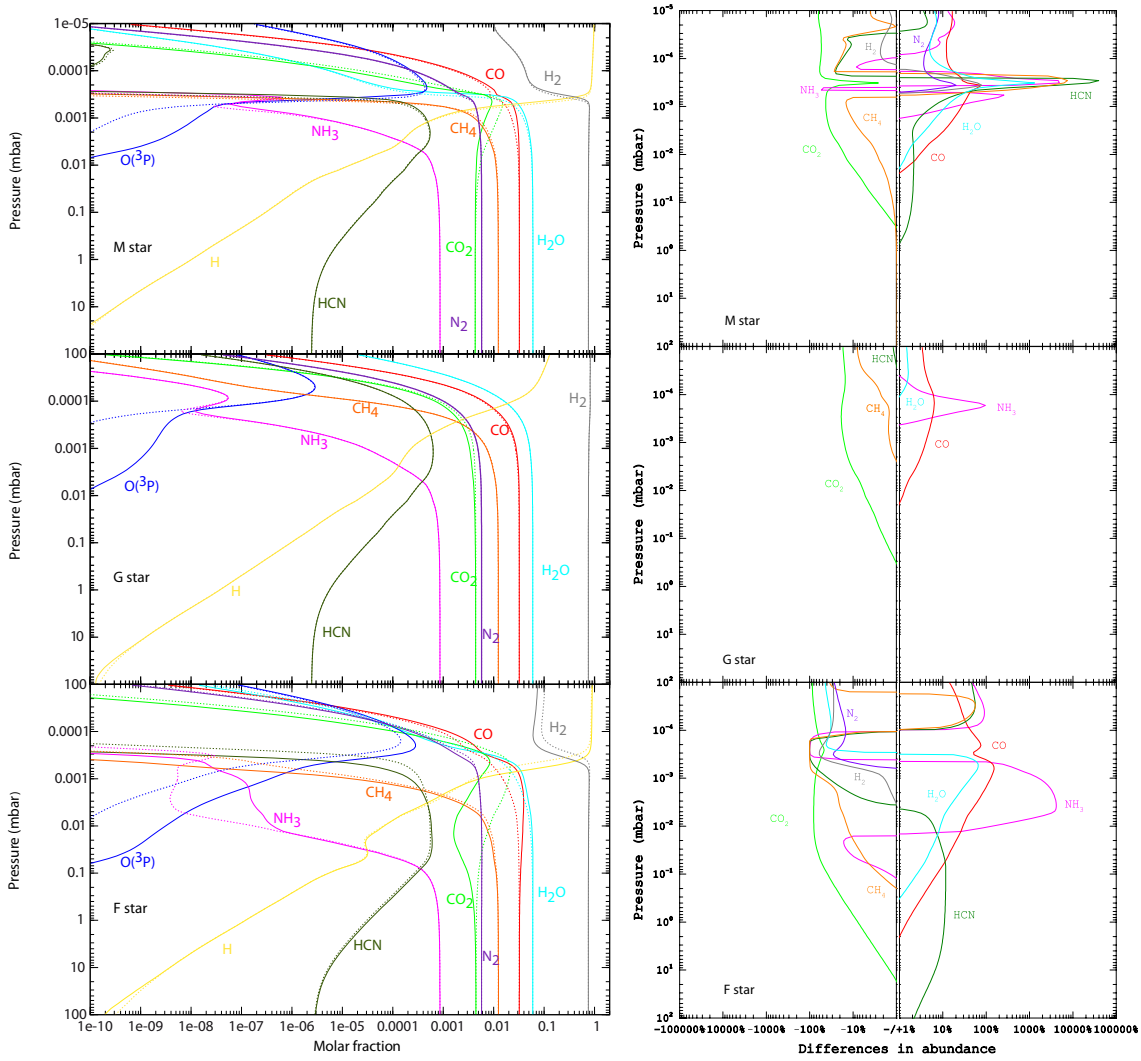

Fig. 11. *Left*: comparison of the atmospheric composition of GJ 436b using σ_{CO_2}(300 K) (dotted line) and σ_{CO_2}(550 K) (full line) when the planet orbits an M star (*top*), a G star (*middle*) and an F star (*bottom*). *Right*: differences in abundances (in %) between the results obtained with σ_{CO_2}(300 K) and σ_{CO_2}(550 K) for species that have an abundance superior to 10^{-10}, for an M star (*top*), a G star (*middle*), and an F star (*bottom*).

difference of composition is the most important in the case F star, because it is the most important flux between 115 and 230 nm.

Since the VUV flux is more important with the F star than with the two previous cases, we observe in Fig. 12 that the total loss rate of CO_2 is approximately two times more important than for the G star case in the whole atmosphere. The total loss rate of CO_2 in the F star case is roughly twice as high as than in the M star case in the entire atmosphere, except for pressures around 10^{-3} mbar, where it is more than three times lower. As for the two other cases, we observe that with σ_{CO_2}(550 K), the photodissociation rate of *J*4 is much more important.

5. Conclusion

We measured absorption cross sections of carbon dioxide at high temperatures for the first time, in the range 115–200 nm with a resolution of 0.05 nm and in the range 195–230 nm with a resolution of 0.3 nm. Between 115 and 200 nm, we measured $\sigma_{CO_2}(\lambda, T)$ at four temperatures: 300, 410, 480, and 550 K. For longer wavelengths, we made measurements at the following temperatures: 465, 510, 560, 610, 655, 750, and 800 K. For $\lambda > 160$ nm, we clearly see that the absorption cross section increases with the temperature. Thanks to the quasi-linear variation of $\ln(\sigma_{CO_2}(\lambda, T) \times \frac{1}{Q_v(T)})$ after 170 nm, we parametrize the variation of $\ln(\sigma_{CO_2}(\lambda, T) \times \frac{1}{Q_v(T)})$ with a linear regression which allows us to calculate $\sigma_{CO_2}(\lambda, T)$ at any temperature in the range 170–230 nm. As we show for GJ 436b, these new data have a considerable influence on the loss rate of CO_2, and on the atmospheric composition of exoplanets that possess high atmospheric temperatures. Placing a hot Neptune around different stars (M, G, and F), we find that the F star is the star for which the change of absorption cross section has the most influence. This information is important to model other planets, like HD 221287b (Naef et al. 2007), HD 31253b (Meschiari et al. 2011), or HD 153950b (Moutou et al. 2009) which are orbiting F stars around 1.26 AU, so receive approximatively the same UV fluxes as in our simulations.

To model hot exoplanets, we recommend using cross sections relevant to the atmospheric temperature when available, or at least, as close as possible to the atmospheric temperature. Carbon dioxide is not the only absorbing species of exoplanet atmospheres. The influence of the absorption cross section of CO_2 on the atmospheric composition of GJ 436b is only illustrative because the photochemistry results from the fact

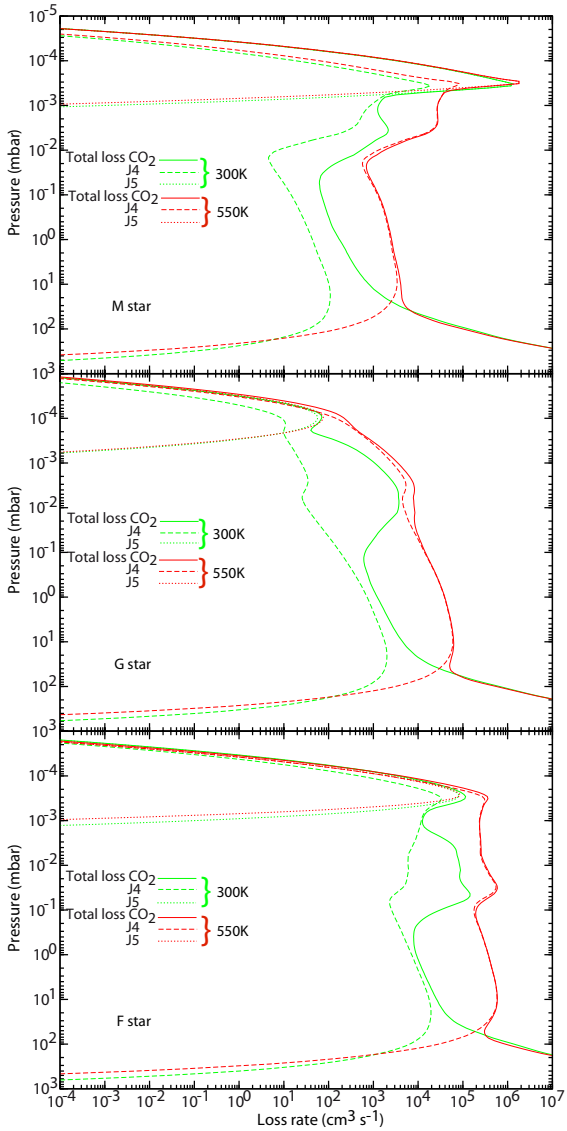

Fig. 12. Total loss rate and photodissociation rates of CO_2 when using $\sigma_{CO_2}(300\ K)$ (green) and $\sigma_{CO_2}(550\ K)$ (red) in the atmosphere of GJ 436b when the planet orbits an M star (*top*), a G star (*middle*), and an F star (*bottom*).

that species shield each other according to their abundances and their cross sections. We expect that the effect of $\sigma_{CO_2}(\lambda, T)$ will be more important on other types of atmospheres, in particular CO_2-rich atmospheres. But the real impact of the temperature dependence of $\sigma_{CO_2}(\lambda, T)$ can be evaluated only by taking into account the temperature dependence of all the other cross sections. Here, we simply show that it is necessary to establish this dependence for all species that absorb UV radiation. This work on CO_2 is a first step towards this goal. Because Venot et al. (2012) show that NH_3 is an important absorber around 200 nm and that it absorbs UV flux very deep in the atmosphere (in pressure regions that can be probed with observations), we plan to measure the absorption cross section of this molecule at temperatures higher than 300 K. Finally, a great deal of work remains to be done in this area which is essential for the photochemical modeling of hot exoplanet atmospheres, whether terrestrial or gaseous.

Acknowledgements. The authors wish to thank Gerd Reichard and Peter Baumgärtel for their excellent assistance during the synchrotron radiation beam time periods. We acknowledge the financial support of the European Commission Programme "Access to Research Infrastructures" for providing access to the synchrotron facility BESSY in Berlin. We also acknowledge the financial support of the program PIR EPOV and of the European Cooperation in Science and Technology – Chemistry and Molecular Sciences and Technologies (COST-CMST). O.V., F.S. and E.H. acknowledge support from the European Research Council (ERC Grant 209622: E_3ARTHs).

References

Beaulieu, J., Kipping, D., Batista, V., et al. 2010, MNRAS, 409, 963
Beaulieu, J.-P., Tinetti, G., Kipping, D. M., et al. 2011, ApJ, 731, 16
Butler, R., Vogt, S., Marcy, G., et al. 2004, ApJ, 617, 580
Cossart-Magos, C., Launay, F., & Parkin, J. 1992, Mol. Phys., 75, 835
Cossart-Magos, C., Launay, F., & Parkin, J. 2005, Mol. Phys., 103, 629
Generalov, N., Losev, S., & Maksimenko, V. 1963, Opt. Spectrosc., 15, 12
Grevesse, N., & Sauval, A. 1998, Space Sci. Rev., 85, 161
Gueymard, C. 2004, Solar Energy, 76, 423
Hersant, F., Gautier, D., & Lunine, J. 2004, Planet. Space Sci., 52, 623
Huebner, W., Keady, J., & Lyon, S. 1992, Solar photo rates for planetary atmospheres and atmospheric pollutants (Kluwer Academic Pub)
Jeffries, J., Schulz, C., Mattison, D., et al. 2005, Proc. Combustion Institute, 30, 1591
Jensen, R., Guettler, R., & Lyman, J. 1997, Chem. Phys. Lett., 277, 356
Koshi, M., Yoshimura, M., & Matsui, H. 1991, Chem. Phys. Lett., 176, 519
Lewis, B., & Carver, J. 1983, J. Quant. Spectrosc. Rad. Transf., 30, 297
Lewis, N., Showman, A., Fortney, J., et al. 2010, ApJ, 720, 344
Line, M., Vasisht, G., Chen, P., Angerhausen, D., & Yung, Y. 2011, ApJ, 738, 32
Madhusudhan, N., & Seager, S. 2011, ApJ, 729, 41
Meschiari, S., Laughlin, G., Vogt, S., et al. 2011, ApJ, 727, 117
Moses, J., Visscher, C., Fortney, J., et al. 2011, ApJ, 737, 15
Moutou, C., Mayor, M., Lo Curto, G., et al. 2009, A&A, 496, 513
Naef, D., Mayor, M., Benz, W., et al. 2007, A&A, 470, 721
Oehlschlaeger, M., Davidson, D., Jeffries, J., & Hanson, R. 2004, Chem. Phys. Lett., 399, 490
Parkinson, W. H., Rufus, J., & Yoshino, K. 2003, Chem. Phys., 290, 251
Reichardt, G., Noll, T., Packe, I., et al. 2001, Nucl. Instrum. Meth. Phys. Res. Sect. A, 467, 458
Schulz, C., Koch, J., Davidson, D., Jeffries, J., & Hanson, R. 2002, Chem. Phys. Lett., 355, 82
Segura, A., Krelove, K., Kasting, J., et al. 2003, Astrobiology, 3, 689
Segura, A., Kasting, J., Meadows, V., et al. 2005, Astrobiology, 5, 706
Southworth, J. 2010, MNRAS, 408, 1689
Stark, G., Yoshino, K., Smith, P. L., & Ito, K. 2007, J. Quant. Spectrosc. Rad. Transf., 103, 67
Stevenson, K., Harrington, J., Nymeyer, S., et al. 2010, Nature, 464, 1161
Stevenson, K., Harrington, J., Lust, N., et al. 2012, ApJ, 755, 9
Swain, M., Vasisht, G., & Tinetti, G. 2008, Nature, 452, 329
Swain, M., Tinetti, G., Vasisht, G., et al. 2009a, ApJ, 704, 1616
Swain, M., Vasisht, G., Tinetti, G., et al. 2009b, ApJ, 690, L114
Tinetti, G., Liang, M., Vidal-Madjar, A., et al. 2007a, ApJ, 654, L99
Tinetti, G., Vidal-Madjar, A., Liang, M., et al. 2007b, Nature, 448, 169
Tinetti, G., Deroo, P., Swain, M. R., et al. 2010, ApJ, 712, L139
Venot, O., Hébrard, E., Agundez, M., et al. 2012, A&A, 546, A43
Yoshino, K., Esmond, J. R., Sun, Y., et al. 1996, J. Quant. Spectrosc. Rad. Transf., 55, 53

ARTICLE 8

Cottin H., and Fray N. (2008)

Distributed sources in comets.

***Space Science Reviews,* 138(1-4), 179-197.**

Space Sci Rev (2008) 138: 179–197
DOI 10.1007/s11214-008-9399-z

Distributed Sources in Comets

Hervé Cottin · Nicolas Fray

Received: 8 April 2007 / Accepted: 5 June 2008 / Published online: 1 July 2008

Abstract The distribution of some molecules and radicals (H_2CO, CO, HNC, CN, ...) in the atmosphere of several comets cannot be explained only by a direct sublimation from the nucleus, or by gas phase processes in the coma. Such molecules are in part the result of a distributed source in the coma, which could be the photo and thermal degradation of dust. We present a review of the degradation processes and discuss possible interpretations of the observations in which the degradation of solid complex organic material in dust particles seems to play a major role. The knowledge of such gas production mechanisms provides important clues on the chemical nature of the refractory organic material contained in comet nuclei.

Keywords Comets · Distributed source · Extended source · Composition · Organic chemistry · Modelling

Introduction

Our current knowledge of the composition of the comet nuclei derives from observations made in their atmospheres, and from our understanding of the physico-chemical processes governing the emission of material into the atmosphere (sublimation of ices contained in the nucleus releasing gaseous molecules and dragging along solid particles), and its evolution once out-gassed or lifted. Recently, Stardust spacecraft captured cometary grains in the atmosphere of Comet 81P/Wild 2. Those grains were brought back to Earth in 2006 and were analysed in the laboratory where it has been shown they were made of a complex mineral and organic mixture (Brownlee et al. 2006). The grains collected during this mission are representative of the most refractory component of comets, emitted from the nucleus, that survived the collection process. Until the *Rosetta* mission succeeds in landing the *Philae* probe at the surface of Comet 67P/Churyumov–Gerasimenko in 2014, the only way to study

H. Cottin (✉) · N. Fray
Laboratoire Interuniversitaire des Systèmes Atmosphériques, Universités Paris 12 et Paris 7,
UMR CNRS 7583, 61 Av. du Général de Gaulle, Créteil 94010, France
e-mail: cottin@lisa.univ-paris12.fr

the whole unaltered molecular composition of cometary nuclei will be in an indirect way, reconstructing the composition of the nuclei from what we can probe in their atmospheres.

The simplest way to describe chemistry within cometary atmospheres is the application of Haser's model which supposes that 'parent molecules' are released only by the nucleus ices sublimating and that 'daughter molecules' are produced solely by the photodissociation of a single gaseous species. Moreover, this simple model requires many hypotheses: radial expansion of molecules at constant velocity, stationary state of the gas production, spherical symmetry around the nucleus, and destruction of the 'parent' species by photodissociation (Haser 1957). More advanced hypothesis have to be introduced into models to take into account a chemistry more elaborated than simple photolysis (proton transfer, dissociative recombination, etc.), and more elaborated physics than radial transport at constant velocity (hydrodynamic models, magnetohydrodynamic & Monte Carlo models (Rodgers et al. 2004; Ip 2004; Combi et al. 2004)). However, approaching the distribution of parent molecules in comets via a Haser distribution is usually sufficient, while the study of species formed in the coma requires the other kind of modelling.

The present paper focuses specifically on distributed sources, also called sometimes 'extended' sources in the literature. Properly speaking, this term could apply to any compound formed in the coma from a parent molecule by any kind of process (photolysis, electron impact, charge exchange reactions, dissociative electron recombination . . .). However, such mechanisms are considered as normal coma chemistry, and do not require the introduction of an additional term. In common cometary terminology, the use of "distributed sources" or "extended sources" can be confusing as it is not really associated to a clear and self consistent definition. It often refers to the production of a molecule in the coma through an unknown process, with no associated known parent. In the book Comets II (Festou et al. 2004), the following definition is given in the glossary:

> Extended source – Most stable molecular species (as opposed to radicals, atoms and ions) appear to be emitted directly from the nucleus. Some stable molecular species appear to have at least one component that is produced in the coma from another source. Processes that have been suggested are sublimation from grains or large polymerized molecules, photon-induced desorption or photo-sputtering from grains or large molecules, gas-phase chemistry in the coma, or photodissociation of other parent molecules. Well known examples in comets are extended source components of H_2CO and CO. The term "distributed source" is also often used.

We do not endorse this definition as it excludes radicals while CN, C_2 and C_3 radicals are also often associated with a distributed source, and including these species in the present definition would also include any compound produced in the coma through the mechanisms mentioned above. Moreover, the term "extended source" is rather ambiguous as it is also used to describe the extended nature of the gas and dust release across the nucleus surface (for example in Thomas et al. 1988). This problem is clarified by using the word *distributed.* It also makes sense to favour this term since it is the common mathematical word used to describe inhomogeneous terms in differential equations, e.g., the right-hand-sides of the conservation equations presented later in this paper. Therefore, using the word *distributed* causes less confusion and is more consistent with common science/mathematics usage.

Taking into account the previous discussion, we propose the following definition:
A *distributed source* is an additional source of a gaseous species being produced in the coma from the grains. It is an exchange of mass between the dust and the gas inventory of the coma. Henceforth, we restrict the expression "distributed source" to the production of gaseous species in the coma from solid materials. In this usage, mechanisms that simply

change one gaseous molecule to another, keeping the mass budget unchanged, are understood as chemistry, and not distributed sources. We propose the use of the term "secondary source" in this case as opposed to distributed to avoid any confusion and the use of "additional source" to cover both distributed and secondary sources. The present definition of the distributed sources seems rather consistent, for future use and with its historical use in the literature. Of course, it may not be known from observations alone whether an enhancement in the density of a species in the coma is due to a dust (distributed) source, but such a situation can't be avoided at present.

To date, the origins of observed species tagged as "distributed" are unknown or at least uncertain. The first section of this paper is a review of the observations of distributed species while interpretations of these observations are discussed in the second section.

1 Observations

The best way to reveal the origin of the production of a gaseous species detected in the atmosphere of a comet, and whether it is directly released from the nucleus, produced by chemistry in the gas phase, or by a distributed source, is to determine its radial distribution in the coma. Moreover, to make a distinction between a production by chemistry or a distributed source, the spatial distributions have to be carefully analysed. In some cases, densities of gaseous species as a function of the distance from the nucleus were measured in-situ by mass spectroscopy. This technique has revealed for the first time the existence of distributed sources in the coma of Comet 1P/Halley (Meier et al. 1993). Nevertheless, the spatial distribution of gas species is generally determined by long-slit spectroscopy at infrared, visible and ultraviolet wavelengths as well as by coarse mapping or interferometry at millimeter wavelengths (Bockelée-Morvan et al. 2004).

Others observational clues on the existence of distributed sources can be found. Indeed generally, the heliocentric evolution of the production rates of molecules produced by a distributed source is steeper than the one of molecules produced from the nucleus (Bockelée-Morvan and Rickman 1997). Moreover, the line shape at millimeter wavelengths, which is characteristic of the motion of gas species in the coma, could give clues on the production mechanism (Gunnarsson et al. 2002; Womack et al. 1997).

In this chapter, we review the observational evidences for some of the distributed source for H_2CO, CO, HNC, CN and some sulfur compounds. Concerning C_2 and C_3 radicals, for which the nature of the parents is uncertain, some information can be found in Combi and Fink (1997), Festou (1999) and Helbert et al. (2005).

1.1 Distributed Source for H_2CO

The radial distribution of H_2CO in the coma of 1P/Halley has been deduced from in-situ measurements by the Neutral Mass Spectrometer (NMS) onboard the Giotto spacecraft (Meier et al. 1993; Eberhardt 1999). It has been shown that its density profile cannot be reconciled with its only source in the nucleus. The additional source for the H_2CO production has been confirmed by coarse mapping at radio wavelengths in Comets C/1990 K1 (Levy), C/1989 X1 (Austin) (Colom et al. 1992) and C/1996 B2 (Hyakutake) (Biver et al. 1999). In Comet C/1995 O1 (Hale-Bopp), interferometric observations have also shown that H_2CO had an additional source (Wink et al. 1997; Bockelée-Morvan and Crovisier 2000; Milam et al. 2006). All these observations suggest that the production scale length for H_2CO is about 7000 km at 1 AU, which does not fit with the photodissociation of any known

possible gaseous parent (see Sect. 2). These observations have been performed for heliocentric distances lower than 1.5 AU. Moreover, the H_2CO production rates measured in C/1995 O1 (Hale-Bopp) present a very steep heliocentric evolution which suggests that the origin of some H_2CO is distributed out to 4 AU (in and outbound) (Biver et al. 2002a; Bockelée-Morvan and Rickman 1997).

1.2 Distributed Source for CO

In a similar manner than for H_2CO, an additional and potentially distributed source for CO has been discovered in the coma of 1P/Halley thanks to in situ measurements by mass-spectrometry (Eberhardt et al. 1987; Eberhardt 1999). These measurements indicate that approximately one third of the total CO is produced directly from the nucleus, while the remainder of CO comes from an additional source located in the innermost 25 000 km of the coma (Eberhardt 1999). Determination of the CO spatial distribution by infrared long-slit spectroscopy has confirmed the existence of a CO additional source in Comet C/1996 B2 (Hyakutake) (DiSanti et al. 2003). This observation suggests a parent scale length of about 1000 km and a release rate from nucleus that accounts for about 80% of total observed CO. A coarse map of the CO spatial distribution has also been obtained at millimetre wavelengths in this comet (Biver et al. 1999). Both observations are compatible with most of the CO being released from the nucleus, at least within the innermost 1000 km in the coma. As these observations do not extend farther than 7000 km in the coma, they are not sensitive to other sources with a scale length as large as the one observed in Comet 1P/Halley. In Comet C/1995 O1 (Hale-Bopp), the spatial distribution of CO has been determined by infrared long slit spectroscopy by numerous authors (Brooke et al. 2003; Disanti et al. 2001, 1999; Weaver et al. 1997) for heliocentric distances smaller than 2 AU. These observations suggest that the production of additional CO reaches its terminal value at a distance of about 7000 km from the nucleus at 1.49 AU and 5000 km at 1.06 AU (Brooke et al. 2003; Disanti et al. 2001). The ratio of nucleus to additional sources release rates determined from these infrared observations remains controversial. Indeed, according to different authors, the release of CO from additional source could represent 50% (Disanti et al. 2001) or 90% (Brooke et al. 2003) of the total. Beyond 2 AU from the Sun, only the nucleus source was seen by infrared long slit spectroscopy (Disanti et al. 2001). Nevertheless, this observation seems to be contradictory with the ones performed in the radio domain, which probe larger fractions of the coma than the infrared observations. The radio observations show that at large heliocentric distances, the profiles of the CO radio lines in Comet C/1995 O1 (Hale-Bopp) could be fitted assuming a production by a distributed source (Gunnarsson et al. 2003). Interferometric maps of the CO spatial distribution have been obtained when the comet was close to perihelion (Henry et al. 2002). They show strong deviations from those expected for an isotropic distribution of CO, probably caused by the existence of CO jets. One may also note that the heliocentric evolution of the CO production rates in Comet C/1995 O1 (Hale-Bopp) is not as steep as for H_2CO, HNC or CS (Biver et al. 2002a) as one might expect from distributed sources. First coarse mapping at millimeter wavelengths of CO in Comet 29P/Schwassmann–Wachmann 1 at 6.2 AU seems to reveal a strong additional source at such heliocentric distances (Gunnarsson et al. 2002). Nevertheless, new observations and analysis of the CO line profile indicate that the additional source, if present, is very weak (Gunnarsson et al. 2008). Since the observations seem to be inconsistent, a summary of them is given in Table 1.

Table 1 Summary of the observations of the CO additional source

Comet	References	Observational method	R_H (AU)	Remarks
1P/Halley	Eberhardt et al. 1987	(1)	0.9	• Production of CO at $\rho < 20\,000$ km
	Eberhardt 1999	(1)	0.9	• $Q_{nucleus}(CO)/Q_{nucleus}(H_2O) = 3.5\%$
				• $Q_{total}(CO)/Q_{nucleus}(H_2O) = 11\%$
				• Production of CO at $\rho < 25\,000$ km
C/1996 O2 (Hyakutake)	DiSanti et al. 2003	(2)	0.64–1.06	• $Q_{nucleus}(CO) = 14.9\%$
				• $Q_{total}(CO) = 19.1\%$
				• Production of CO at $\rho < 10^3$ km for $R_H = 0.64$ AU
				• Production of CO at $\rho < 2$–$3 \cdot 10^3$ km for $R_H = 1.06$ AU
	Biver et al. 1999	(4)	1.24	• $Q_{nucleus}(CO) \approx Q_{total}(CO)$
				• $L_P \approx 400$ km (*)
C/1995 O1 (Hale-Bopp)	Weaver et al. 1997	(2)	1.1	• Detection of a CO distributed source
	Disanti et al. 1999 and 2001	(2)	0.93–4.11	• Detection of a CO distributed source only for $R_H < 2$ AU
				• $Q_{nucleus}(CO)/Q_{total}(CO) \approx 50\%$ for $R_H < 2$ AU
				• Production of CO at $\rho < 6$–$7 \cdot 10^3$ km for $R_H = 1.49$ AU and at $\rho < 5 \cdot 10^3$ km for $R_H = 1.06$ AU
	Brooke et al. 2003	(2)	1.02–1.05	• Detection of a CO distributed source
				• $Q_{nucleus}(CO)/Q_{total}(CO) \approx 10\%$
				• $L_P \approx 5000$ km (*)
	Gunnarsson et al. 2003	(3)	3.7–10.8	• Detection of a CO distributed source
				• $Q_{nucleus}(CO)/Q_{total}(CO) \approx$ 10–60%
	Henry et al. 2002	(5)		• Presence of a spiral CO jet
	Biver et al. 2002a	(6)		• No steep heliocentric evolution of $Q(CO)$

(1) In-situ mass spectrometry
(2) Long slit spectroscopy at infrared wavelengths
(3) Analysis of the radio line profile
(4) Coarse mapping at radio wavelengths
(5) Interferometry at radio wavelengths
(6) Determination of the production rates at radio wavelengths
(*) L_p: production scale length of the distributed molecule. See precisions in Sect. 2.1

1.3 Distributed Source for HNC

HNC, which is an isomeric form of HCN, was detected for the first time in Comet C/1996 B2 (Hyakutake) (Irvine et al. 1996) at millimeter wavelengths. It was then observed in C/1995

O1 (Hale-Bopp) (Biver et al. 2002a; Irvine et al. 1998a) and in other comets (Biver et al. 2002b, 2006). In Comet C/1995 O1 (Hale-Bopp), interferometric observations made it possible to measure the HNC spatial distribution (Wink et al. 1997), which deviates from that of HCN in the innermost coma, and indicates production of HNC in the coma. Nevertheless, the main indication of an HNC distributed source is the heliocentric dependence of the HNC/HCN ratio. Indeed, as for the H_2CO production rates, this ratio increases with decreasing heliocentric distance in Comet C/1995 O1 (Hale-Bopp) (Biver et al. 2002a), C/2002 C1 (Ikeya-Zhang) (Irvine et al. 2003) as well as for other comets (Biver et al. 2006).

1.4 Distributed Source for CN

Reviews about the existence of the CN additional source have already been published (Festou 1999; Fray et al. 2005). It is clear that at least some of the CN radicals are produced in the coma through HCN photodissociation. Nevertheless, it is not clear if this mechanism could solely explain the abundance of CN. Indeed CN and HCN production rates have the same order of magnitude in most of the comets and considering the uncertainties in their production rates, we cannot conclude if HCN is the only parent molecule of CN or not in most of the comets. In comets, the $^{14}N/^{15}N$ isotopic ratios in CN is about two times lower than on Earth (Hutsemékers et al. 2005). First measurements of the $^{14}N/^{15}N$ in HCN (Jewitt et al. 1997; Ziurys et al. 1999) lead to values close to the terrestrial one. This was a major indication that HCN could not be the unique parent molecule of CN radicals until new measurements in comet 17P/Holmes and reanalysis of the older observations show that the $^{14}N/^{15}N$ isotopic ratio in CN and HCN are about the same (Bockelée-Morvan et al. 2008). Nevertheless, from this new result, we cannot exclude that CN has other major progenitors, than HCN, sharing the same low $^{14}N/^{15}N$ isotopic ratio (Bockelée-Morvan et al. 2008). The spatial distribution of CN has been measured in numerous comets by long-slit spectroscopy at UV wavelengths. From these observations, it seems that CN radicals could be entirely produced by the HCN photodissociation for heliocentric distances greater than 3 AU. Nevertheless, closer to the Sun, the CN spatial distribution is too narrow to be explained only by this process (Bockelee-Morvan and Crovisier 1985; Fray et al. 2005). Indeed for heliocentric distance less than 3 AU, the CN parent scale length is lower than the HCN photodissociation scale lengths (see Fig. 1).

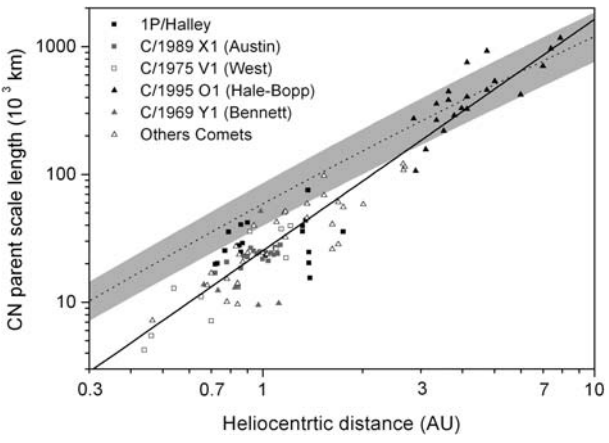

Fig. 1 Measured CN parent scale lengths as a function of the heliocentric distance. The CN parent scale lengths have been normalized to the minimum of solar flux and the *black line* is the best fit to these data. The *dashed line* is the effective CN parent scale length assuming that CN is produced exclusively by photodissociation of HCN. The *grey region* represents the error on the effective CN parent scale lengths due to uncertainties in the photodissociation rate of HCN and in the expansion velocity (figure from Fray et al. 2005)

1.5 Distributed Sources for Other Species

The radial distribution of OCS has been determined in Comet C/1995 O1 (Hale-Bopp) at about 1 AU from the Sun by infrared long-slit spectroscopy (Dello Russo et al. 1998). This observation suggests that about 70% of the total production of OCS comes from an additional source having a parent scale length of 3000–3500 km. The fact that most sulfur is contained in the refractory CHON grains suggests that OCS may be derived from refractory grains by a distributed source. However, as the mechanism for a distributed source for OCS is unknown, an additional contribution from other gaseous species cannot be ruled out.

CS has been observed in different comets at millimeter and ultraviolet wavelengths. The CS/HCN and CS/H_2O production rate ratios increase with decreasing heliocentric distance in all the comets for which CS has been observed (Biver et al. 2000, 2002a, 2006). The spatial distribution of CS has been determined thanks to coarse mapping at millimeter wavelengths in Comet C/1996 B2 (Hyakutake) at 0.7 AU (Biver et al. 1999) suggesting a parent scale length of about 1200 km. Whereas this value is roughly in agreement with the photodissociation scale length of CS_2, which has been tentatively detected in Comet P/122 de Vico (Jackson et al. 2004), the increase of CS abundance with decreasing heliocentric distance suggests that CS is also produced by an additional mechanism (Biver et al. 2006).

In Comet C/1995 O1 (Hale-Bopp), the SO spatial distribution has been measured by interferometry at millimeter wavelengths (Wink et al. 1997). This observation shows clearly that SO is a daughter species. SO is at least produced in part by the photodissociation of SO_2. Nevertheless, its production rate is greater than the one of SO_2, suggesting an additional production mechanism of SO (Bockelée-Morvan et al. 2000; Boissier et al. 2007).

First detection of radical NS is reported in Comet C/1995 O1 (Hale-Bopp) (Irvine et al. 2000). In their paper, the authors state that whether NS itself is present in the nucleus or has a distributed source in the coma is unknown.

2 Interpretations

2.1 General Discussion

Understanding the chemistry of comets is quite a difficult task. The additional sources, including distributed and secondary sources, do not have an origin based on the same mechanism. Some physical and chemical mechanisms which could explain the origin of secondary and distributed (i.e. additional) sources are summarized in Fig. 2. Some production of gaseous species may result from the dissociation (photolysis or other chemical processes including electron impact (Helbert et al. 2005)) of several gaseous parents (among which some may not have been detected to date) or chemistry between two gaseous compounds in the innermost coma. Distributed sources include sublimation of icy grains in the coma or the production of gaseous compounds during the degradation of solid organic material contained in cometary dust particles.

Indeed, it is now established that the organic content of comets is more complex than what is seen in the gaseous phase alone. Most of the detections presented in the above section are all remote sensing observations, probing the gaseous phase of comets, leading to the detection of about 20 stable gaseous molecules (Bockelée-Morvan et al. 2004). However in 1986, Vega 1 & 2 and Giotto spacecrafts probed the atmospheres of Comet 1P/Halley. Molecular analyses of solid particles in the coma were conducted by mass spectrometry and resulted in the detection of solid organic compounds much more complex than the gaseous

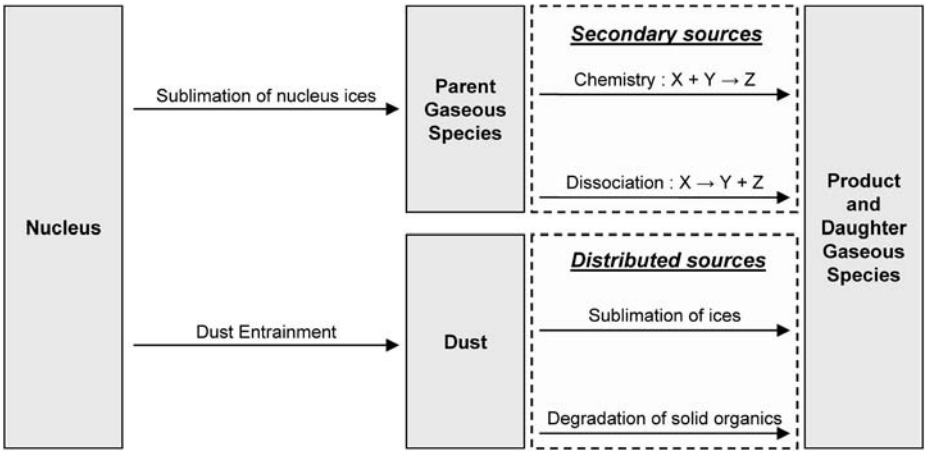

Fig. 2 Chemical mechanisms of production of the gaseous species in the cometary environment. The 'secondary' and 'distributed' sources have been clearly distinguished

ones securely detected from the Earth. It showed that more organic material is present, in the solid state, and that its molecular mass can reach value above 150 amu (Kissel and Krueger 1987; Mitchell et al. 1992). In-situ results from the Stardust mission (with the CIDA mass spectrometer) have confirmed these observations (Kissel et al. 2004). Recently, the analysis of grains captured from Comet 81P/Wild 2 by the Stardust spacecraft has also enabled the detection of complex organic material made of aliphatic and aromatic hydrocarbons, and molecules bearing a large range of organic functions (hydroxyl, carbonyl, amide, nitrile . . .) with high molecular weight (up to 300 amu) (Keller et al. 2006; Sandford et al. 2006).

For an even better insight into the most complex and less volatile material, one can turn to experimental laboratory work. The principle of such experiments is the following: from observations of the most abundant species in comae and in the interstellar medium, one can infer probable compositions of the nucleus ices. A gaseous sample of the key species is condensed under near vacuum conditions on a cold substrate and irradiated by UV photons or charged particles. Sometimes, condensed ices are also simply warmed up slowly without irradiation. These processes are similar to the ones precometary ices may have encountered in the Solar Nebula or in the interstellar medium and they allow the synthesis of complex organic compounds from the initial simple ice. When the sample is warmed up for analysis, a refractory organic residue remains on the substrate at ambient temperature. The diversity of organic compounds synthesized during those experiments is remarkable (Greenberg 1982; Colangeli et al. 2004; Despois and Cottin 2005), and this mixture of molecules can be considered as an analogue of the solid organic component of comets.

In the frame of the study of distributed sources, a new generation of cometary laboratory experiments has been developed. Proceeding in an opposite direction than the 'classical' ice experiments, they study the production of gaseous compounds during the photo-degradation (induced by the solar UV flux) and the thermal-degradation (induced by dust particles heating) of complex solid molecules suspected to be present in cometary dust particles, once they are ejected in the coma. Such experiments are described in Cottin et al. (2000), Fray et al. (2004a, 2004b) and an example is given in Fig. 3.

These experiments are not actually meant to *simulate* the cometary environment, but rather to measure physico-chemical data, such as production quantum yields (photo-

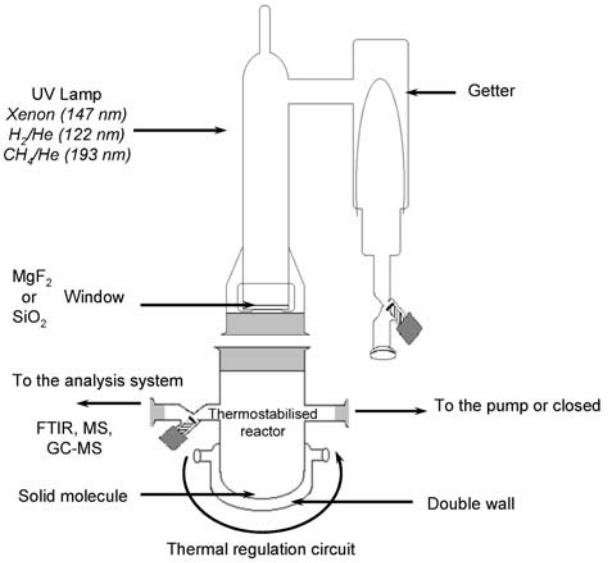

Fig. 3 Experimental setup dedicated to the study of the degradation of solid organic material into gaseous fragments. The solid organic molecule is deposited at the bottom of a Pyrex reactor where it can be heated with a thermal regulation circuit or photolyzed (at different wavelengths) with a UV lamp located at the top of the reactor. Gaseous degradation products can then be analyzed by infrared spectroscopy, direct mass spectrometry or gas chromatography coupled with a mass spectrometer (more details in Cottin et al. 1999, 2000)

degradation), Arrhenius constants and activation energies (thermal-degradation), characteristic of the gaseous production resulting from the decomposition of some specific targeted solid material. Results obtained after that kind of experiments, which were not necessarily conducted in a cometary context, are summarized in Table 2.

These quantitative data are then included into numerical models simulating the production of gaseous species during the degradation of solid compounds ejected in the cometary atmosphere on dust particles. The purpose of these models is to calculate the spatial distribution of the gaseous species produced by these mechanisms. With hypotheses similar to the classical Haser's approach, these models are based on the equation of conservation.

If a gaseous species is produced solely by the photodissociation of a unique parent molecule, then the conservation equation can be written:

$$\frac{\partial n_D}{\partial t} + div(n_D.v_{gas}) = \beta_P.n_P - \beta_D.n_D. \tag{1}$$

Here n_P and n_D are the number density (m^{-3}) of the parent and daughter molecules respectively, β_P and β_D the photodissociation rates (s^{-1}) of the parent and daughter molecules and v_{gas} the gas expansion velocity in the coma ($m\,s^{-1}$) assumed to be constant. In the frame of the Haser's model, the parent (l_P) and daughter (l_D) scale lengths are defined as the product of the gas expansion and the photo-lifetime (reciprocal of the photodissociation rate). The distribution of daughter molecules produced by the photo processes of a single gaseous parent is shown in (2), where Q_P and Q_D are the spherically symmetric production rates of parent and daughter molecules (s^{-1}).

$$n_D(r) = \frac{1}{r^2}\left(\frac{Q_P}{4\pi v_{gas}}\frac{l_D}{l_P - l_D}(e^{-r/l_P} - e^{-r/l_D}) + \frac{Q_D}{4\pi v_{gas}}e^{-r/l_D}\right). \tag{2}$$

In most cases, the parent and daughter scale lengths are measured by adjustment of the observations with (2). This parent scale length is then compared to the photodestruction rate of a candidate parent molecule. This comparison gives important clues on the nature

Table 2 Summary of data available on the degradation of potential precursors of distributed sources

	Photodegradation				Thermal degradation		
POM	Products and production quantum yields for various wavelength from Cottin et al. (2000)				H_2CO is the only product. Kinetic parameters for its production as a parameters for its production as a function of T (Arrhenius law) for two different POM polymers are given below. From Fray et al. (2004a).		
	λ (nm)	122	147	193		Ea (J mol^{-1})	A (molec g^{-1} s^{-1}
	H_2CO	0.75 ± 0.21	0.96 ± 0.19	<0.16	POM 1	81×10^3 ±0.76%	1.2×10^{30} +28%/−22%
	HCOOH	0.13 ± 0.05	0.26 ± 0.10	ε			
	CO	NE	∼ 1	ε	POM 2	99×10^3 ±2.3%	7.2×10^{32} +140%/−60%
	CO_2	NE	∼ 0.3	ε			
	CH_3OH	∼ 0.05	∼ 0.05	ε			
	NE : Present but not estimated						
HMT	Some HCN detected at 147 nm but at level too low to be quantified (Cottin et al. 2002)				No thermal degradation. HMT sublimates when heated under vacuum (Fray 2004)		
HCN polymer	Some HCN, CH_4 and C_2H_2 are produced with quantum yields lower than 0.03 at 122 and 147 nm (Fray 2004; Fray et al. 2004b)				NH_3 and HCN are the major products of the thermal degradation (Fray et al. 2004b). The production kinetics have been measured for $T > 420$ K (Fray 2004). Nevertheless, for lower T, the production declines to very low value (unpublished results)		
C_3O_2 polymer	No data available				For $T > 400$ K: release of CO_2 For $T > 500$ K: increased efficiency in the degradation, with release of CO_2 and CO. CO/CO_2 ratio increases with T. From Blake and Hyde (1964) and Smith et al. (1963)		

of the gaseous parent molecule. Nevertheless, one should keep in mind that the ejection velocity acquired by the daughter species during the photolysis of the parent is neglected. This actually changes the physical meaning of the parent scale length (Combi and Delsemme 1980), but as a first approximation this results in estimations usually sufficient to suggest a possible parent.

In the case of a production from the degradation of solid material in cometary dust particles, the conservation equation is:

$$\frac{\partial n_D(r)}{\partial t} + div(n_D(r) \cdot v_{gaz}) = \left(n_{grain}(r) \cdot \sigma_\alpha(r) \cdot C_D\right) + \left(n_{grain}(r) \cdot m_\alpha(r) \cdot k_D(T)\right) - \left(\beta_D \cdot n_D(r)\right). \quad (3)$$

In the right side of this equation, the first two terms are the production of the considered gaseous species by the photo- and the thermal-degradation of the solid material. In this equation, n_{grain} is the grain density in the coma (m^{-3}), σ_α the surface of material exposed to the

Solar flux and C_D the production rate of gaseous species by photo-degradation ($m^{-2}\,s^{-1}$), m_α the mass of solid material in each particles and k_D the production rate of the gaseous species by thermal-degradation ($kg^{-1}\,s^{-1}$).

With classical Haser's hypotheses regarding the dynamics in the coma, two scale lengths related respectively to the thermal- (l_T) and photo-degradation (l_P) can be defined (Cottin et al. 2004; Fray et al. 2006) and (3) is integrable analytically. Then, n_D can be written:

$$n_D(r) = \frac{1}{4\pi r^2 v_{gas}} \left\{ \begin{array}{l} \frac{3Q_{grain}\beta^3 m_\alpha}{m_D l_T X} \left[\begin{array}{l} l_D(1-X)(1-e^{-\frac{r}{l_D}}) \\ +\frac{(3X-2)(1+1/\beta)}{(1/l_D-1/l_T)}(e^{-\frac{r}{l_T}}-e^{-\frac{r}{l_D}}) \\ +\frac{(1-3X)(1+1/\beta)^2}{(1/l_D-2/l_T)}(e^{-\frac{2r}{l_T}}-e^{-\frac{r}{l_D}}) \\ +\frac{X(1+1/\beta)^3}{(1/l_D-3/l_T)}(e^{-\frac{3r}{l_T}}-e^{-\frac{r}{l_D}}) \end{array} \right] \\ +Q_D\, e^{-\frac{r}{l_D}} \end{array} \right\}. \quad (4)$$

Where Q_{grain} is the production of grains of a specific size and composition, β is the ratio l_T/l_P, m_D the mass of the daughter molecule, X is related to the photoproduction of the daughter compound, and Q_D the contribution from the nucleus to the production of the molecule (more details can be found in Cottin et al. (2004)).

Even if this equation can be simplified in the case that either thermal or photo degradation is not relevant (one being negligible compared to the other), (4) has to be integrated over the whole size distribution of dust particles, taking into account the velocity and temperature for each size range. Moreover, the scale lengths related to the degradation of solid material depend on the initial composition of the cometary dust particles: they are not characteristic for a specific solid material. Therefore, parent scale length, as the one used with gaseous parents (2) has no direct equivalent here and a discussion about this parameter is useless for identifying a parent compound in the solid phase. As an example, measuring the scale length of the parent of formaldehyde, which is about 7000 km at 1 AU as mentioned in Sect. 1.1, is purely formal and unfortunately of no help in assessing the nature of the parent if it is in the solid phase.

2.2 Origin of H_2CO

Adjusting the spatial distribution of formaldehyde in Comet 1P/Halley would be quite simple considering the photodissociation of CH_3OH. If H_2CO is considered as the main CH_3OH photoproduct (for rate coefficients see Huebner et al. 1992), methanol would have to be produced from the nucleus at a level of 16% relative to water to obtain a good fit to measurements (Cottin et al. 2004). But methanol is only produced in amounts ranging from ~ 1 to 6% in comets (Bockelée-Morvan et al. 2004). Moreover, as discussed in Bockelée-Morvan et al. (1994), formaldehyde is not the main dissociation product of methanol, but rather the CH_3O methoxy radical. Thus, the additional source of cometary H_2CO is not consistent with a production from the CH_3OH photodissociation.

Formaldehyde is known to polymerize into long linear molecules (–$(CH_2$–O$)_n$–) called polyoxymethylene (POM) (Fig. 4). This polymer was invoked in the cometary context to interpret a mass spectrum obtained with the PICCA instrument on board the Giotto spacecraft, between 8200 and 12600 km from the nucleus of Comet 1P/Halley. Indeed, Huebner (1987) suggested that the alternation of patterns with $\Delta m/z = 14$ and 16 shown in the PICCA spectrum is consistent with a sequence of –CH_2– ($m = 14$) and –O– ($m = 16$). But few years later, Mitchell et al. (1992) showed that the PICCA mass spectrum is not

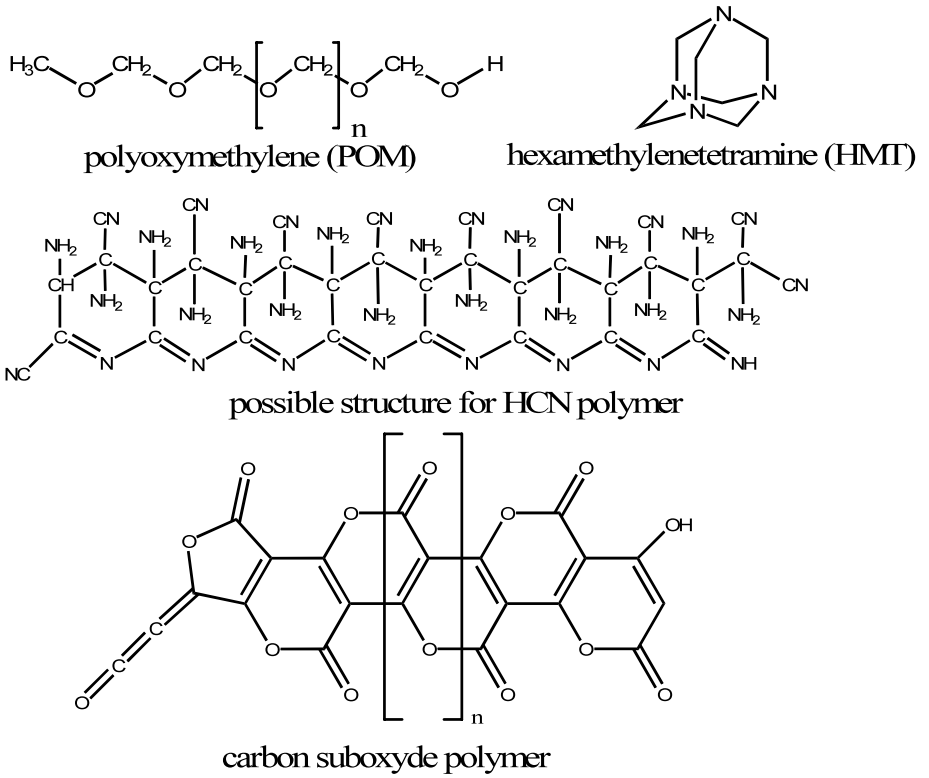

Fig. 4 Molecular structures of molecules evoked in this paper as possible parents for observed distributed sources. Structure of HCN polymer is one possible among others (see Minard et al. 1998 for more structures). Structure of carbon suboxide polymers proposed by Ballauff et al. (2004)

specifically characteristic of POM: the regular pattern observed is only the signature of a mixture of organic molecules composed of C, H, O, N atoms. Thus, even if the observed spectrum is not sufficient to establish its presence definitively, the presence of POM in cometary nucleus and dust particles cannot be ruled out at this stage. Furthermore, its production is possible under certain conditions in laboratory simulated interstellar and precometary ices (Schutte et al. 1993). Therefore, polyoxymethylene has often been suggested as the H_2CO distributed source (see, e.g. Boice et al. 1989, 1990; Meier et al. 1993; Eberhardt 1999). Boice et al. (1990) tried to estimate the production of formaldehyde from POM, but with the hypothesis that short polymer chains are emitted from dust particles and photodissociated in the gas phase. Because of the lack of experimental data, photodissociation rates were estimated from formaldehyde and related molecular bond strengths, without any direct laboratory measurement. Meier et al. (1993) showed that this does not fit the *Giotto* measurements.

First quantitative data considering the production of gaseous H_2CO by photo- and thermal-degradation of solid polyoxymethylene have been measured with the experimental setup shown Fig. 3 and described by Cottin et al. (2000) and Fray et al. (2004a). It has been shown that the major gaseous species produced by the photo-degradation of POM at 122 and 147 nm was H_2CO and CO and their production quantum yields have been measured (Cottin et al. 2000 and Table 2). Moreover, H_2CO is the sole gaseous species produced

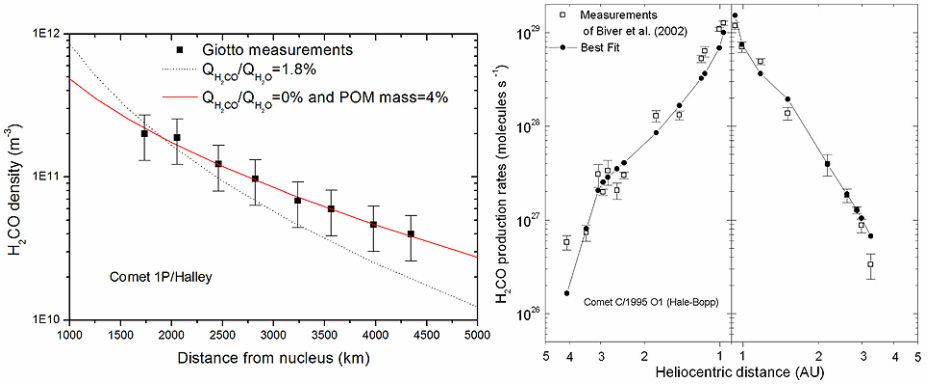

Fig. 5 *On the left*: H_2CO density profile in Comet 1P/Halley: measured by Giotto spacecraft (*squares*), and calculated considering a distributed source from solid polyoxymethylene (*continuous line*). This fit is obtained if POM represents 4% in mass of dust particles and H_2CO is not released from the nucleus. *Dotted line* is the best fit with no distributed source, obtained if 1.8% of H_2CO (relative to H_2O) is released from the nucleus. *On the right*: H_2CO production rates as a function of heliocentric distance in Comet C/1995 O1 (Hale-Bopp). The measurements of H_2CO are represented as open squares and the computed values as *black circles*. The latter have been obtained considering a POM mass fraction in the dust particles of 3.1% and H_2CO production at the surface of the nucleus equal to 3% of HCN production (i.e. $Q(H_2CO)/Q(H_2O) = 0.0075\%$)

by the thermal-degradation of POM. Its production kinetics follows an Arrhenius law and the Arrhenius constants and activation energies have been measured (Fray et al. 2004a and Table 2).

The production of gaseous formaldehyde in the coma from solid polyoxymethylene has been modelled using these quantitative data. If we consider that a few percent in mass of POM is present on dust particles when they are ejected from the nucleus, the spatial distribution of H_2CO in 1P/Halley as well as the steep heliocentric evolution of the H_2CO production rates in Comet C/1995 O1 (Hale-Bopp) are quite well reproduced (Cottin et al. 2004; Fray et al. 2006) (Fig. 5).

The fact that POM can account for the distributed source of formaldehyde in two comets, within the same abundance range, and for observations as a function of the nucleus distance and also as a function of the heliocentric distance, strengthens the probability of its presence without being an actual detection of the polymer in comets. The presence of POM (or POM-like polymers) in the solid state on cometary dust particles is to date the best interpretation of observations.

2.3 Origin of CO

The case of the additional source for CO is more controversial than for H_2CO. As shown in Sect. 1.2, not all the observations are consistent. The photodissociation of several gaseous molecules (C_3O_2, H_2CO and CO_2) have been proposed to explain the origin of CO in the coma.

In Comet 1P/Halley, it has been proposed that gaseous carbon suboxide (C_3O_2) could be a precursor for CO by photodissociation (Huntress et al. 1991). If present in the atmosphere of comets, C_3O_2 would be photodissociated into CO and C_2O, C_2O being photodissociated into CO and C, and be a parent molecule at least for some CO (Crovisier 1994). Nevertheless, its upper limit in this comet ($< 0.1\%$) is far from the amount required to produce the CO from secondary sources (7.5%) (Crovisier et al. 1991). Thus,

photodissociation of gaseous C_3O_2 cannot alone explain the formation of CO, even if it has been shown in the laboratory that it can be present in cometary ices (Brucato et al. 1997; Gerakines and Moore 2001). Looking for another gaseous parent, Meier et al. (1993) suggests that H_2CO is a precursor of 2/3 of the CO from an additional source, while later reanalysis of the data led to the conclusion that distributed formaldehyde produced from degradation of polyoxymethylene could fully explain all of the additional CO under certain assumptions such as the kinetics of POM degradation which were not known at that time (Eberhardt 1999). A comprehensive modelling with current knowledge of POM properties has yet to be done to settle this question for Comet 1P/Halley. If one considers CO_2 as a parent for CO, the CO Cameron system in the UV wavelength domain would be expected. It has been observed in several comets (Biermann 1976; Weaver et al. 1994; Bockelée-Morvan et al. 2004). This structure is thought to be produced mainly by prompt emission following the photodissociation of CO_2. Therefore it is clear that the photodissociation of CO_2 also contributes to the CO production in the coma. Nevertheless, as the photodissociation rate of CO_2 is very low ($\beta_{CO_2} = 2 \cdot 10^{-6}$ s^{-1}) (Huebner et al. 1992), this mechanism cannot explain the observed scale length of the CO distributed source. In Comet 1P/Halley, it is not yet settled whether a mechanisms different than the photodissociation of other gaseous molecules has to be considered to explain the CO additional source.

In Comet C/1995 O1 (Hale-Bopp), the additional source of the CO in the atmosphere seems to be triggered at 2 AU (Disanti et al. 2001). The photolysis of a gaseous parent would not result in the same kind of observation, which suggests some thermal threshold from which a solid precursor might start to decompose and release CO in the gas phase. Looking for a solid precursor leads one to consider if POM could also be the origin of the additional CO. But even if photo-degradation of POM yields a small amount of CO (about the same order of magnitude than for H_2CO (Cottin et al. 2000), no CO is produced by thermal-degradation, which is the dominant degradation mechanism of POM for most of dust particles. Also, if CO from distributed sources in C/1995 O1 (Hale–Bopp) originated from POM degradation, then one should expect H_2CO production from distributed sources to at least equal that for CO, and more probably be larger by perhaps as much as one or two orders of magnitude. This would result in more H_2CO than CO in the coma, which is not the case. Thus, POM cannot be the main precursor for carbon monoxide.

As we already discussed in this section, gaseous carbon suboxide is not sufficient to produce the observed amount of CO from additional sources. But its polymer (carbon suboxide polymer, shown in Fig. 4) is known to decompose into CO_2 and CO when pyrolysed. The polymer starts to release some gas (CO_2) at about 400 K, but only due to structural changes, the mass loss is low. Above 500 K the polymer degrades with increased efficiency as the temperature rises and with an additional production of CO. The CO/CO_2 ratio tends to 1/1 above 700 K and with increasing time (Blake and Hyde 1964; Smith et al. 1963). These studies show that if the same kind of polymers is present in comets, a distributed CO_2 source should also be observed, which, to date, is not the case. But laboratory synthesised polymer are extremely unstable as the compound is extremely hygroscopic (Schmedt auf der Günne et al. 2005). Exposed to air, it takes up atmospheric water within seconds and undergoes chemical modifications. Therefore, before reaching final conclusions about the relevance of this molecule in the cometary environment, new laboratory measurements have to be undertaken in controlled environment. Furthermore, no data about the photo-degradation of C_3O_2 polymers in VUV are currently available.

In Comet 29P/Schwassmann–Wachmann, located at large heliocentric distance , the temperature of the grains is so low that the distribution of CO in the coma can be explained by the slow sublimation of CO frozen on grains ejected from the nucleus (Gunnarsson et al. 2002, 2008). In this case, sublimation of the CO ice is a distributed source.

Because of the potential for multiple precursors, understanding the origin of CO from secondary and/or distributed sources requires probably a complete modelling work taking into account several gaseous and solid parents. Different compositions between comets, resulting in comets enriched or depleted in one or several precursors, and the use of different measurement methods probing different regions of the coma at different scales, could be an explanation for the contradictory observations.

2.4 Origin of HNC

In Comet C/1995 O1 (Hale-Bopp), Rodgers and Charnley (1998, 2005) and Irvine et al. (1998a, 1998b) show that the additional source for HNC could be accounted for by superthermal chemistry driven by fast hydrogen atoms ($HCN + H_f \rightarrow HNC + H$, with H_f = fast H). This would then be a secondary source. But this mechanism is only efficient in the relatively dense environment of Comet C/1995 O1 (Hale-Bopp), and due to the failure of such superthermal reactions to produce efficiently HNC in less active comets (Irvine et al. 2003; Rodgers and Charnley 2001, 2005), it seems more reasonable to look for other processes for the origin of HNC from additional sources.

Therefore, these authors propose the degradation of an unknown solid organic parent as the origin for the HNC from distributed sources. Candidates are the same as the ones presented and discussed in the next section for the parents of CN from distributed sources. However, quantitative and even qualitative data about its production by thermal or photo-degradation of refractory parents are rather difficult to obtain, since HNC is not easy to detect because of its rapid isomerisation into HCN in laboratory.

2.5 Origin of CN

The CN radicals may be produced by HCN photodissociation and another unknown mechanism. As the observed spatial distribution of CN is less distributed than the predicted distribution of CN produced solely by HCN photodissociation (Fig. 1), the scale length of the unknown production process has to be shorter than the observed production scale lengths (Fray et al. 2005). If the unknown mechanism is the photodissociation of a gaseous molecule, its lifetime has to be shorter than that of HCN. This is the case for HC_3N and C_2N_2. Nevertheless, the HC_3N production rate measured in Comet C/1995 O1 (Hale-Bopp) does not seem to be sufficient to explain the CN distribution and C_2N_2 has never been detected in comets (Fray et al. 2005). Another hypothesis is a direct production of CN radical by degradation of complex refractory organic compounds present on cometary dust particles. This hypothesis has originally been proposed by A'Hearn et al. (1986) and Lamy and Perrin (1988). Hexamethylenetetramine (HMT) could be a candidate since it is easily synthesized from H_2CO and NH_3 during laboratory simulations of interstellar and precometary ices (Bernstein et al. 1995; Cottin et al. 2001; Muñoz Caro et al. 2004). But it has been shown that this compound is quite stable when photolyzed (Cottin et al. 2002) and no degradation has been observed when heated (HMT sublimates when heated) (Fray 2004). Thus HMT is surely not the parent molecule of CN. It has also been shown that HCN polymers, which have been proposed to be present in cometary nuclei (Rettig et al. 1992), produce HCN and NH_3 when heated (Fray et al. 2004b). Under certain circumstances, such polymers can be synthesized in interstellar or precometary ices (Gerakines et al. 2004). If one turns to other candidates, it must be noted that thermal-degradation of polyacrylonitrile leads to the formation of HCN, NH_3 and CH_4 (Xue et al. 1997) and that thermal-degradation of numerous synthetic nitrogen polymers also leads to

the formation of HCN (Michal 1982). As numerous nitrogenated compounds can produce HCN by thermal-degradation, more experiments have to be implemented to measure quantitative data needed for proper modelling.

Nevertheless, one should keep in mind that since CN parent scale length is shorter than the HCN photodissociation scale length (Fig. 1), CN has to be directly produced from the dust particles without HCN as an intermediary species (Fray et al. 2005). So far, all the experimental studies investigating the volatile compounds produced during photo- or thermal-degradation of nitrogenated organic matter have been performed in conditions in which CN radicals were not detectable, even if it was produced. Indeed, in laboratory conditions CN radicals are very reactive species turning very rapidly into HCN.

2.6 Origin of Sulfur Compounds

A recent analysis of SO interferometric observations in Comet C/1995 O1 (Hale-Bopp) concludes that the discrepancy between measured and computed values of the SO photodissociation rate may indicate that SO_2 is not the sole parent of SO, or that SO_2 is itself created by an additional source in the coma (Boissier et al. 2007). Whether this results from coma chemistry or a distributed source remains unknown.

Concerning NS detection in the same comet, Canaves et al. (2002, 2007), have published a detailed modelling of the chemistry of NS in cometary comae. Their most recent results conclude that the amount of detected NS in Comet C/1995 O1 (Hale-Bopp) can be explained by gas phase chemistry in the atmosphere. They call it a distributed source, but it would rather be a secondary source if we stick to the definitions proposed in the present paper.

Very limited interpretation can be given for distributed sources of sulfur bearing species. Indeed, except the recent references given hereabove, the literature lacks discussion about the origin of these species. If, much work remains to be done in the laboratory for C, H, O, N molecules, almost everything has to be done for C, H, S (and possibly O and N) molecules.

3 Conclusions

We are far from being able to understand the origin of distributed sources in comets. They are for sure a signature of complex chemistry in both gaseous and solid phases, but we still lack crucial data characterizing the physico-chemical properties of candidate parent compounds to reach final interpretations. More laboratory work is needed, mostly to measure how the complex refractory organic component of comets behaves on dust particles (photo- and thermal-degradation).

The discussions developed in the present paper should not leave the impression that all the distributed sources could be explained evoking the convenient degradation of some unknown solid material. If this process seems to be quite adapted to the case of formaldehyde, it is possible that it actually hides our current ignorance of some other chemical processes in the atmosphere of comets. Work remains before a conclusion can be formed. However, as our knowledge of the composition of the nucleus of comets derives from what we observe in their atmosphere, distributed sources are precious, though tangled, Ariadne's threads to follow.

Acknowledgements The authors wish to thanks the two referees for their extensive work on the paper. Their valuable reviews greatly help to improve its clarity as well for the English than for its science content.

References

M.F. A'Hearn, S. Hoban, P.V. Birch, C. Bowers, R. Martin, D.A. Klinglesmith, Nature **324**, 649–651 (1986). doi:10.1038/324649a0

M. Ballauff, S. Rosenfeldt, N. Dingenouts, J. Beck, P. Krieger-Beck, Angew. Chem. Int. Ed. **43**(43), 5843–5846 (2004). doi:10.1002/anie.200460263

M.P. Bernstein, S.A. Sandford, L.J. Allamandola, S. Chang, M.A. Scharberg, Astrophys. J. **454**, 327–344 (1995). doi:10.1086/176485

L. Biermann, NASA STI/Recon technical report N 77, 22023 (1976)

N. Biver, D. Bockelée-Morvan, J. Crovisier, J.K. Davies, H.E. Matthews, J.E. Wink et al., Astron. J. **118**, 1850–1872 (1999). doi:10.1086/301033

N. Biver, D. Bockelée-Morvan, J. Crovisier, F. Henry, J.K. Davies, H.E. Matthews et al., Astron. J. **120**, 1554–1570 (2000). doi:10.1086/301529

N. Biver, D. Bockelée-Morvan, P. Colom, J. Crovisier, F. Henry, E. Lellouch et al., Earth Moon Planets **90**, 5–14 (2002a). doi:10.1023/A:1021599915018

N. Biver, D. Bockelée-Morvan, J. Crovisier, P. Colom, F. Henry, R. Moreno et al., Earth Moon Planets **90**, 323–333 (2002b). doi:10.1023/A:1021530316352

N. Biver, D. Bockelée-Morvan, J. Crovisier, D.C. Lis, R. Moreno, P. Colom et al., Astron. Astrophys. **449**, 1255–1270 (2006). doi:10.1051/0004-6361:20053849

A.R. Blake, A.F. Hyde, Trans. Faraday Soc. **60**, 1775–1782 (1964). doi:10.1039/tf9646001775

D. Bockelee-Morvan, J. Crovisier, Astron. Astrophys. **151**, 90–100 (1985)

D. Bockelée-Morvan, J. Crovisier, P. Colom, D. Despois, Astron. Astrophys. **287**(2), 647–665 (1994)

D. Bockelée-Morvan, H. Rickman, Earth Moon Planets **79**, 55–77 (1997). doi:10.1023/A:1006225030955

D. Bockelée-Morvan, J. Crovisier, Earth Moon Planets **89**, 53–71 (2000). doi:10.1023/A:1021530016410

D. Bockelée-Morvan, D.C. Lis, J.E. Wink, D. Despois, J. Crovisier et al., Astron. Astrophys. **353**, 1101–1114 (2000)

D. Bockelée-Morvan, J. Crovisier, M.J. Mumma, H.A. Weaver, in *Comets II*, ed. by M. Festou, H.U. Keller, H.A. Weaver (University of Arizona Press, Tucson, 2004), p. 391

D. Bockelée-Morvan, N. Biver, E. Jehin, A.L. Cochran, H. Wiesemeyer, J. Manfroid et al., Astrophys. J. **679**, L49–L52 (2008). doi:10.1086/588781

D.C. Boice, D.W. Naegeli, W.F. Huebner, Physics and mechanics of cometary materials. ESA SP **302**, 83–88 (1989)

D.C. Boice, W.F. Huebner, M.J. Sablik, I. Konno, Geophys. Res. Lett. **17**, 1813–1816 (1990). doi:10.1029/GL017i011p01813

J. Boissier, D. Bockelee-Morvan, N. Biver, J. Crovisier, D. Despois, B.G. Marsden et al., Astron. Astrophys. **475**, 1131–1144 (2007). doi:10.1051/0004-6361:20078380

T.Y. Brooke, H.A. Weaver, G. Chin, D. Bockelée-Morvan, S.J. Kim, L.H. Xu, Icarus **166**, 167–187 (2003). doi:10.1016/j.icarus.2003.08.008

D. Brownlee, P. Tsou, Aléon et al., Science **314**, 1711–1716 (2006). doi:10.1126/science.1135840 Medline

J.R. Brucato, A.C. Castorina, M.E. Palumbo, M.A. Satorre, G. Strazzulla, Planet. Space Sci. **45**(7), 835–840 (1997). doi:10.1016/S0032-0633(97)00071-8

M.V. Canaves, A.A. De Almeida, D.C. Boice, G.C. Sanzovo, Earth Moon Planets **90**, 335–347 (2002). doi:10.1023/A:1021582300423

M.V. Canaves, A.A. de Almeida, D.C. Boice, G.C. Sanzovo, Adv. Space Res. **39**, 451–457 (2007). doi:10.1016/j.asr.2006.09.040

L. Colangeli, J.R. Brucato, A. Bar-Nun, R.L. Hudson, M.H. Moore, in *Comets II*, ed. by M. Festou, H.U. Keller, H.A. Weaver (University of Arizona Press, Tucson, 2004), pp. 695–717

P. Colom, J. Crovisier, D. Bockelee-Morvan, D. Despois, G. Paubert, Astron. Astrophys. **264**, 270–281 (1992)

M.R. Combi, A.H. Delsemme, Astrophys. J. **237**, 633–640 (1980). doi:10.1086/157909

M.R. Combi, U. Fink, Astrophys. J. **484**, 879–890 (1997). doi:10.1086/304349

M.R. Combi, W.M. Harris, W.H. Smyth, in *Comets II*, ed. by M. Festou, H.U. Keller, H.A. Weaver (University of Arizona Press, Tucson, 2004), pp. 523–552

H. Cottin, M.C. Gazeau, J.F. Doussin, F. Raulin, Phys. Chem. Earth **24**, 597–602 (1999)

H. Cottin, M.-C. Gazeau, J.-F. Doussin, F. Raulin, J. Photochem. Photobiol. Chem. **135**(1), 53–64 (2000). doi:10.1016/S1010-6030(00)00274-4

H. Cottin, C. Szopa, M.H. Moore, Astrophys. J. Lett. **561**(1), L139–L142 (2001). doi:10.1086/324575

H. Cottin, S. Bachir, F. Raulin, M.C. Gazeau, Adv. Space Res. **30**(6), 1481–1488 (2002). doi:10.1016/S0273-1177(02)00508-2

H. Cottin, Y. Bénilan, M.-C. Gazeau, F. Raulin, Icarus **167**, 397–416 (2004). doi:10.1016/j.icarus.2003.10.009

J. Crovisier, T. Encrenaz, M. Combes, Nature **353**, 610 (1991). doi:10.1038/353610a0 Medline
J. Crovisier, J. Geophys. Res. **99**(E2), 3777–3781 (1994). doi:10.1029/93JE02088
N. Dello Russo, M.A. Disanti, M.J. Mumma, K. Magee-Sauer, T.W. Rettig, Icarus **135**, 377–388 (1998). doi:10.1006/icar.1998.5990
D. Despois, H. Cottin, in *Lectures in Astrobiology*, ed. by M. Gargaud, B. Barbier, H. Martin, J. Reisse (Springer, Berlin, 2005), pp. 289–352
M.A. Disanti, M.J. Mumma, N. dello Russo, K. Magee-Sauer, R. Novak, T.W. Rettig, Nature **399**, 662 (1999). doi:10.1038/21378 Medline
M.A. Disanti, M.J. Mumma, N. Dello Russo, K. Magee-Sauer, Icarus **153**, 361–390 (2001). doi:10.1006/icar.2001.6695
M.A. DiSanti, M.J. Mumma, N. Dello Russo, K. Magee-Sauer, D.M. Griep, J. Geophys. Res. Planets **108f**, 15–11 (2003)
P. Eberhardt, D. Krankowsky, Schulte et al., Astron. Astrophys. **187**, 481–484 (1987)
P. Eberhardt, Space Sci. Rev. **90**(1/2), 45–52 (1999). doi:10.1023/A:1005221309219
M.C. Festou, Space Sci. Rev. **90**, 53–67 (1999). doi:10.1023/A:1005225426057
M.C. Festou, H.U. Keller, H.A. Weaver, *Comets II* (University of Arizona Press, Tucson, 2004)
N. Fray, PhD thesis. Université Paris 12 (2004)
N. Fray, Y. Bénilan, H. Cottin, M.-C. Gazeau, J. Geophys. Res. Planets **109**, E07S12 (2004a). doi:10.1029/2003JE002191
N. Fray, Y. Bénilan, H. Cottin, M.-C. Gazeau, R.D. Minard, F. Raulin, Meteorit. Planet. Sci. **39**, 4 (2004b)
N. Fray, Y. Bénilan, H. Cottin, M.C. Gazeau, J. Crovisier, Planet. Space Sci. **53**, 1243–1262 (2005). doi:10.1016/j.pss.2005.06.005
N. Fray, Y. Bénilan, N. Biver, D. Bockelée-Morvan, H. Cottin, J. Crovisier et al., Icarus **184**(1), 239–254 (2006). doi:10.1016/j.icarus.2006.04.014
P.A. Gerakines, M.H. Moore, Icarus **154**(2), 372–380 (2001). doi:10.1006/icar.2001.6711
P.A. Gerakines, M.H. Moore, R.L. Hudson, Icarus **170**, 202–213 (2004). doi:10.1016/j.icarus.2004.02.005
J.M. Greenberg, in *Comets*, ed. by L.L. Wilkening (University of Arizona Press, Tuscon, 1982), pp. 131–163
M. Gunnarsson, H. Rickman, M.C. Festou, A. Winnberg, G. Tancredi, Icarus **157**, 309–322 (2002). doi:10.1006/icar.2002.6839
M. Gunnarsson, D. Bockelée-Morvan, A. Winnberg et al., Astron. Astrophys. **402**, 383–393 (2003) doi:10.1051/0004-6361:20030178
M. Gunnarsson, D. Bockelée-Morvan, N. Biver, J. Crovisier, H. Rickman, Astron. Astrophys. **484**, 537–546 (2008)
L. Haser, Bulletin de l'académie royale de Belgique **43**, 740–750 (1957)
J. Helbert, H. Rauer, D.C. Boice, W.F. Huebner, Astron. Astrophys. **442**, 1107–1120 (2005). doi:10.1051/0004-6361:20041571
F. Henry, D. Bockelée-Morvan, J. Crovisier, J. Wink, Earth Moon Planets **90**, 57–60 (2002). doi:10.1023/A:1021508216836
W.F. Huebner, Science **237**(August), 628–630 (1987). doi:10.1126/science.237.4815.628 Medline
W.F. Huebner, J.J. Keady, S.P. Lyon, Astrophys. Space Sci. **195**, 1–294 (1992). doi:10.1007/BF00644558
W.T. Huntress Jr., M. Allen, M. Delitsky, Nature **352**, 316–318 (1991). doi:10.1038/352316a0
D. Hutsemékers, J. Manfroid, E. Jehin, C. Arpigny, A. Cochran, R. Schulz et al., Astron. Astrophys. **440**, L21–L24 (2005). doi:10.1051/0004-6361:200500160
W.H. Ip, in *Comets II*, ed. by M. Festou, H.U. Keller, H.A. Weaver (University of Arizona Press, Tucson, 2004), pp. 605–629
W. Irvine, D. Bockelee-Morvan, Lis et al., Nature **382**, 418–420 (1996). doi:10.1038/383418a0
W.M. Irvine, E.A. Bergin, J.E. Dickens, D. Jewitt, A.J. Lovell, H.E. Matthews et al., Nature **393**, 547 (1998a). doi:10.1038/31171 Medline
W.M. Irvine, J.E. Dickens, A.J. Lovell, F.P. Schloerb, M. Senay, E.A. Bergin et al., Faraday Discuss. **109**, 475–492 (1998b). doi:10.1039/a709289j Medline
W.M. Irvine, M. Senay, A.J. Lovell, H.E. Matthews, D. McGonagle, R. Meier, Icarus **143**(2), 412–414 (2000). doi:10.1006/icar.1999.6281 Medline
W.M. Irvine, P. Bergman, T.B. Lowe, H. Matthews, D. McGonagle, A. Nummelin et al., Orig. Life Evol. Biosph. **33**, 609–619 (2003). doi:10.1023/A:1025791101127 Medline
W.M. Jackson, A. Scodinu, D. Xu, A.L. Cochran, Astrophys. J. **607**, L139–L141 (2004). doi:10.1086/421995
D.C. Jewitt, H.E. Matthews, T. Owen, R. Meier, Science **278**, 90–93 (1997). doi:10.1126/science.278.5335.90 Medline
L.P. Keller, S. Bajt, G.A. Baratta et al., Science **314**, 1728–1731 (2006). doi:10.1126/science.1135796 Medline
J. Kissel, F.R. Krueger, J. Silén, B.C. Clark, Science **304**, 1774–1776 (2004). doi:10.1126/science.1098836 Medline

J. Kissel, F.R. Krueger, Nature **326**, 755–760 (1987). doi:10.1038/326755a0
P.L. Lamy, J.-M. Perrin, Icarus **76**, 100–109 (1988). doi:10.1016/0019-1035(88)90142-X
R. Meier, P. Eberhardt, D. Krankowsky, R.R. Hodges, Astron. Astrophys. **277**, 677–690 (1993)
J. Michal, Fire Mater. **6**(1), 13–15 (1982). doi:10.1002/fam.810060105
S.N. Milam, A.J. Remijan, Womack et al., Astrophys. J. **649**, 1169–1177 (2006). doi:10.1086/506501
R.D. Minard, P.G. Hatcher, R.C. Gourley, C.N. Matthews, Orig. Life Evol. Biosph. **28**, 461–473 (1998). doi:10.1023/A:1006566125815 Medline
D.L. Mitchell, R.P. Lin, C.W. Carlson, A. Korth, H. Reme, D.A. Mendis, Icarus **98**, 125–133 (1992). doi:10.1016/0019-1035(92)90213-Q
G.M. Muñoz Caro, U. Meierhenrich, W.A. Schutte, W.H.-P. Thiemann, J.M. Greenberg, Astron. Astrophys. **413**, 209–216 (2004). doi:10.1051/0004-6361:20031447
T.W. Rettig, S.C. Tegler, D.J. Pasto, M.J. Mumma, Astrophys. J. **398**, 293–298 (1992). doi:10.1086/171857
S.D. Rodgers, S.B. Charnley, Astrophysical J. Lett. **501**(2), L227–L230 (1998). doi:10.1086/311459
S.D. Rodgers, S.B. Charnley, Mon. Not. R. Astron. Soc. **323**(1), 84–92 (2001). doi:10.1046/j.1365-8711.2001.04099.x
S.D. Rodgers, S.B. Charnley, W.F. Huebner, D.C. Boice, in *Comets II*, ed. by M. Festou, H.U. Keller, H.A. Weaver (University of Arizona Press, Tucson, 2004), pp. 505–522
S.D. Rodgers, S.B. Charnley, Mon. Not. R. Astron. Soc. **356**(4), 1542–1548 (2005). doi:10.1111/j.1365-2966.2004.08606.x
S.A. Sandford, J. Aléon, C.M.O.D. Alexander et al., Science **314**, 1720 (2006)
J. Schmedt auf der Günne, J. Beck, W. Hoffbauer, P. Krieger-Beck, Chem. Eur. J. **11**, 4429–4440 (2005). doi:10.1002/chem.200401133
W.A. Schutte, L.J. Allamandola, S.A. Sandford, Icarus **104**, 118–137 (1993). doi:10.1006/icar.1993.1087 Medline
R.N. Smith, D.A. Young, E.N. Smith, C.C. Carter, Inorg. Chem. **2**(4), 829–838 (1963). doi:10.1021/ic50008a041
N. Thomas, D.C. Boice, W.F. Huebner, H.U. Keller, Intensity profiles of dust near extended sources on comet Halley. Nature **332**(6159), 51–52 (1988) doi:10.1038/332051a0
H.A. Weaver, P.D. Feldman, J.B. McPhate, M.F. A'Hearn, C. Arpigny, T.A. Smith, Astrophys. J. **422**, 374–380 (1994). doi:10.1086/173732
H.A. Weaver, T.Y. Brooke, G. Chin, S.J. Kim, D. Bockelée-Morvan, J.K. Davies, Earth Moon Planets **78**, 71–80 (1997). doi:10.1023/A:1006227530238
J. Wink, D. Bockelée-Morvan, D. Despois, P. Colom, N. Biver, J. Crovisier et al., Earth Moon Planets **78**, 63–63 (1997). doi:10.1023/A:1006263026604
M. Womack, M.C. Festou, S.A. Stern, Astron. J. **114**, 2789–2796 (1997). doi:10.1086/118687
T.J. Xue, M.A. McKinney, C.A. Wilkie, Polym. Degrad. Stabil. **58**(1–2), 193–202 (1997). doi:10.1016/S0141-3910(97)00048-7
L.M. Ziurys, C. Savage, M.A. Brewster, A.J. Apponi, T.C. Pesch, Wyckoff, Astrophys. J. Lett. **527**(1), L67–L71 (1999). doi:10.1086/312388

ARTICLE 9

Le Roy L., Briani G., Briois C., Cottin H., Fray N., Thirkell L., Poulet, G. and Hilchenbach, M. (2012)

On the prospective detection of polyoxymethylene in comet 67P/Churyumov-Gerasimenko with the COSIMA instrument onboard Rosetta.

***Planetary and Space Science,* 65(1), 83-92.**

Planetary and Space Science 65 (2012) 83–92

Contents lists available at SciVerse ScienceDirect

Planetary and Space Science

journal homepage: www.elsevier.com/locate/pss

On the prospective detection of polyoxymethylene in comet 67P/Churyumov–Gerasimenko with the COSIMA instrument onboard Rosetta

Léna Le Roy [a,b], Giacomo Briani [b,1], Christelle Briois [a], Hervé Cottin [b,*], Nicolas Fray [b], Laurent Thirkell [a], Gilles Poulet [a], Martin Hilchenbach [c]

[a] Laboratoire de Physique et Chimie de l'Environnement et de l'Espace (LPC2E), UMR 6115 CNRS – Université d'Orléans, 3A Avenue de la Recherche Scientifique, 45071 Orléans Cedex 2, France

[b] Laboratoire Interuniversitaire des Systèmes Atmosphériques, LISA, UMR CNRS 7583, Université Paris Est Créteil et Université Paris Diderot, Institut Pierre Simon Laplace, 61 Avenue du Général De Gaulle, 94010 Créteil Cedex, France

[c] Max Planck Institute for Solar System Research (MPS), Max-Plank-Str. 2, 37191 Katlenburg-Lindau, Germany

ARTICLE INFO

Article history:
Received 4 August 2011
Received in revised form
23 January 2012
Accepted 25 January 2012
Available online 7 February 2012

Keywords:
Polyoxymethylene
Cometary grains
COSIMA
Rosetta
TOF SIMS

ABSTRACT

The presence of polyoxymethylene (POM) in cometary grains has been debated years ago. Although never proven, its presence can not be excluded. Rosetta, the ESA mission to comet 67P/Churyumov–Gerasimenko, may answer this question. On board the spacecraft, COSIMA (COmetary Secondary Ion Mass Analyzer) will analyze the grains ejected from the nucleus using a Time Of Flight Secondary Ion Mass Spectrometer (TOF-SIMS). In this paper we report the extent to which COSIMA will be able to detect POM if this compound is present on cometary grains. We have analyzed two kinds of POM polymers with a laboratory model of COSIMA. Positive mass spectra display alternating sequence of peaks with a separation of 30.011 Da between 1 and 600 Da related to formaldehyde and its oligomers but also to the fragmentation of these oligomers. The separation of 30.011 Da of numbers peaks, corresponding to the fragmentation into H_2CO is characteristic of POM and we show that it could be highlight by mathematical treatment. POM lifetime on COSIMA targets have also been studied as POM is thermally instable. It can be concluded that the cometary grains analysis have to be planned not too long after their collection in order to maximize the chances to detect POM. This work was supported by the Centre National d'Etudes Spatiales (CNES).

1. Introduction

Comets are considered as the most pristine remainders of the Solar System formation, and they could have delivered water and organic molecules on the primitive Earth (Delsemme, 1999; Oro et al., 2006). Thus, the study of comets is interesting for planetology and astrobiology: their analysis can provide insights into physical and chemical conditions in the early Solar nebula (Irvine and Lunine, 2004) and on the nature of organic molecules delivered on the early Earth (Anders, 1989; Chyba and Sagan, 1992; Oro, 1961). The knowledge of the chemical composition of comets is therefore important for our understanding of the Solar System formation and the emergence of life on Earth.

The volatile phase of the cometary environment has been extensively studied by remote sensing instruments. More than twenty five gaseous species have already been identified in their coma (Bockelée-Morvan et al., 2004; Feldman et al., 2004), from which models regarding the composition of nuclei ices can be derived. Numerous minerals have been detected in cometary grains thanks to remote infrared spectroscopy (Crovisier et al., 1997) and to the analysis of the cometary grains returned on Earth by the Stardust mission (Zolensky et al., 2006). The presence of refractory organic compounds on cometary grains has been revealed by the Giotto and Vega mission (Kissel et al., 1986a, b), and confirmed by the Stardust mission (Sandford et al., 2006). But their exact nature is still uncertain due to the difficulty to analyze the organic phase of cometary grains or the nucleus directly.

Several in-situ missions have taken measurements related to the composition of solid organic compounds in cometary grains. To date, four missions (Vega 1 & 2, Giotto and Stardust) have provided results: in 1986 the time-of-flight mass spectrometers PUMA 1 & 2 and PIA, respectively onboard the Soviet missions Vega 1 & 2 and onboard the European Space Agency (ESA) mission Giotto, have made the first in situ analysis of grains ejected from the nucleus of the comet 1P/Halley (Kissel et al., 1986a, b). The mass spectra collected by PUMA highlighted the presence of

* Corresponding author. Tel.: +33 1 45 17 15 63; fax: +33 1 45 17 15 64.
E-mail address: Herve.Cottin@lisa.u-pec.fr (H. Cottin).

[1] Present address: Centre de Spectrométrie Nucléaire et de Spectrométrie de Masse (CSNSM), UMR 8609, Université Paris Sud/CNRS, Bat. 104, F-91405 Orsay Campus, France.

0032-0633/$ - see front matter © 2012 Elsevier Ltd. All rights reserved.
doi:10.1016/j.pss.2012.01.011

different kind of grains: rocky grains, CHON grains (i.e., grains constituted of C, H, O and N atoms) and grains made of rocky elements and organics, which could be intermixed on the submicron scale (Jessberger et al., 1988). The organic part in the grains is important in Halley's dust. It represents about 50% in mass, the remaining 50% being due to the minerals (Fomenkova et al., 1994). It also appeared that these organic compounds are more complex than expected (i.e., mass spectra displayed features for mass greater than 100 Da) (Kissel et al., 1986a). However, only assumptions about the nature of those compounds can be made due to the very short observation duration of the comet (1.5 h), the break-up of the parent compounds on high-velocity impacts on the metal targets and the limited mass resolution of instruments (Krueger and Kissel, 1987). The mass resolution is defined as $m/\Delta m$; here Δm is the Full Width at Half Maximum (FWHM) of a peak centered at the mass m. It was about 100 and 200 at $m/z=100$ for PUMA 1 & 2 and PIA, respectively (Lawler et al., 1989).

In 2006, the analysis of the samples returned by the NASA's Stardust spacecraft highlighted the presence of crystalline silicates as well as complex organic matter (aromatic, aliphatic and N-containing functional groups) in grains of comet 81P/Wild 2 (Sandford et al., 2006; Sandford et al., 2010; Zolensky et al., 2006). Since these preliminary results, more analyses have been performed and revealed the presence of glycine, the simplest amino acid (Elsila et al., 2009). The Stardust spacecraft also made in situ measurements, with CIDA (Cometary Interstellar Dust Analyser), an onboard particle impact time-of-flight mass spectrometer. Its measurements highlighted that nitrogen-containing species are an important part of the cometary dust particles (Kissel et al., 2004).

The forthcoming space mission related to cometary studies is the Rosetta mission. This ESA mission, launched in March 2004, will perform the most exhaustive study ever done of a comet after a ten years journey (Glassmeier et al., 2007). Its target is the Jupiter family comet 67P/Churyumov–Gerasimenko (67P/CG). The probe consists of two parts: an orbiter, to study the comet for at least one year and a half during its approach to the Sun, and a lander, to perform analyses directly on the nucleus during at least five days.

Onboard the probe, several instruments will measure the chemical composition of refractory organic material:

- COSIMA (COmetary Secondary Ion Mass Analyzer) is a mass spectrometer designed to collect and analyze the cometary grains (Kissel et al., 2007). COSIMA is a TOF-SIMS (Time of Flight Secondary Ion Mass Spectrometry), which analyzes the first few atomic layers of a solid sample and then enables the measure of the chemical composition of grains and notably of refractory organic matter. Its mass resolution ($m/\Delta m$) better than 1500 at $m/z=100$, is at least 10 time better than the one of the mass spectrometers on board the Stardust, Giotto and Vega missions. The grains will be collected on metallic targets at about 100 m/s (Kissel et al., 2007). Thus the cometary matter will not be vaporized and turned into a hot plasma as for previous missions, for which the impact velocity of grains was 6, 69 and 78 km/s for Stardust, Giotto and Vega 1 & 2, respectively (Brownlee et al., 2006; Langevin et al., 1987).
- VIRTIS (Visible InfraRed thermal Imaging spectrometer) is a spectral imager, onboard the orbiter, which covers the 0.25 to 5 μm wavelength range. It will detect and characterize spectral bands of minerals and molecules arising from surface and from grains dispersed in the coma (Coradini et al., 2007).
- COSAC (COmetary Sampling and Composition experiment) is a gas chromatograph coupled with a time of flight mass spectrometer ($m/\Delta m=350$ at the peak FWHM at $m/z=70$) on board the lander PHILAE. It will analyze samples from the surface and subsurface of 67P/CG nucleus and allow the characterization and quantification of organic compounds including large and chiral molecules by heating them up to 327 K (Goesmann et al., 2007).
- MODULUS-Ptolemy (Methods of Determining and Understanding Light elements from Unequivocal Stable isotope compositions) is an instrument onboard the lander centered around an ion trap mass spectrometer ($m/\Delta m=66$ at the peak FWHM at $m/z=44$, this mass resolution has been calculated from the mass spectrum of Ptolemy qualification model; it could be improved, if required, but the intensity of the signal will decrease). Its aim is to determine the nature and isotopic compositions of gases and refractory compounds at the surface and sub-surface of the nucleus. These measurements will be done directly for gaseous species and by converting solid compounds into gases using various thermal and chemical techniques. Gases can be analyzed directly by the mass spectrometer, or via gas chromatography columns or through chemical processing modules before the mass spectrometer analysis (Wright et al., 2007).

In this paper, we focus on the detection of the formaldehyde polymer polyoxymethylene (POM, $(H_2CO)_n$) with COSIMA. The presence of POM on grains of comet 1P/Halley has been claimed in 1987 by Huebner (1987). Indeed mass spectra acquired by the PICCA instrument displayed a regular pattern of peaks with alternations of 14 and 16 Da (Da) that Huebner (1987) linked this to the sequence of $-CH_2-$($m=14$ Da) and $-O-$($m=16$ Da) fragments, and then to POM. However Mitchell et al. (1992) have shown that this pattern can be relevant of any kind of complex mixture made of C, H, O, N atoms. Thus the presence of POM has never been confirmed, or excluded. Nevertheless some clues point towards its presence:

- POM or POM-like polymers are synthesized during thermal processing or UV irradiation of cometary ice analogs (Bernstein et al., 1995; Schutte et al., 1993a, b; Vinogradoff et al., 2011).
- Its presence in cometary grains and its thermal decomposition into gaseous formaldehyde is an efficient way to explain the observation of the distributed source (i.e., production of gaseous product by photo and/or thermal degradation of refractory carbonaceous matter in coma) of gaseous formaldehyde in cometary atmospheres. Indeed only a few percent in mass of POM in grains could explain this distributed source (Cottin et al., 2004; Cottin and Fray, 2008; Fray et al., 2006).

COSIMA is surely the most appropriate instrument to detect directly POM in comet 67P/CG. Indeed the major infrared spectral features of POM are close to 10 μm, whereas VIRTIS will probe the coma only up to 5 μm. COSAC and MODULUS-Ptolemy will involve indirect detection of POM because solid samples have to be heated to temperatures at which POM decomposes into formaldehyde. So, only a formaldehyde excess can be measured with these two instruments.

The goal of this paper is to study the extent to which COSIMA could detect POM if this organic compound is present in the grains of comet 67P/CG.

The polyoxymethylene has specific chemical properties, which could enhance or decrease the possibility of its detection. POM is a generic name for formaldehyde polymers. Usually, its terminal group is an hydroxyl group (OH) which gives the general formula: $HO-(CH_2O)_n-H$ with n the number of monomers (Walker, 1964). Two other common terminal functions are: the methylether function (CH_3O) and the acetate function (CH_3CO), which lead, respectively to $CH_3O-(CH_2O)_n-CH_3$ and $CH_3CO-(CH_2O)_n-COCH_3$ (Bevington and May, 1964; Pchelintsev et al., 1988).

POM has different designations as a function of chain length (number of monomers) and of terminal group. These differences confer to POM specific chemical properties such as difference on its thermal stability. POM thermal decomposition proceeds by a zipper mechanism initiated at chain end, up to about 530 K, producing gaseous formaldehyde as the only reaction product (Zimmermann and Behnisch, 1982). For instance, POM with OH as terminal group is thermally less stable than POM with an acetate function as a terminal group.

Obviously, if there is some POM in the grains of 67P/CG, its exact nature is unknown. COSIMA would give us some hints. Due to POM instability, the temperatures that cometary grains can reach in COSIMA have to be considered in order to propose optimal tasks to detect POM.

Fig. 1 represents a schematic view of COSIMA. COSIMA contains several units: (i) a storage area for 72 targets, (ii) a target manipulator unit (TMU) to handle the transport of targets between individual stations, (iii) a dust collection position where cometary grains could be collected onto targets, (iv) an optical microscope system (COSISCOPE) to image each target and locate precisely the grains, (v) a chemistry station, in which a target can be heated up to 403 K and (vi) the TOF-SIMS.

Depending on its location, targets are submitted to different temperatures. In the storage area, the temperature should be below 303 K (Kissel et al., 2007). When they are brought to the dust collection position, temperature can drop to about 253 K (the coldest one that targets can reach). After the collection, they are moved to the microscope position to localize the grains and then in front of the TOF-SIMS. Temperature at microscope and analysis position should be below 303 K. The target could also be brought inside a chemistry station where the samples can be heated up to 403 K.

Rosetta trajectories and timelines after lander delivery in 2014 are currently being discussed and planned by ESA. Therefore all COSIMA operations are not yet planned, such as the time between the collection of a grain and its analysis. Another critical parameter has to be taken into account: a delay of about a week between new programming operation from Earth and its application in space. As POM is thermally unstable, long storage duration without any analysis could compromise its detection if POM disappears from the grains before the analysis.

In this paper, TOF-SIMS analysis (with a ground analog instrument of COSIMA) and decomposition kinetics studies of different kind of POMs are reported. Our goals are to measure reference spectra to enable POM identification with COSIMA, and to estimate POM lifetime to define a COSIMA operational strategy allowing a clear detection of POM if present in cometary grains.

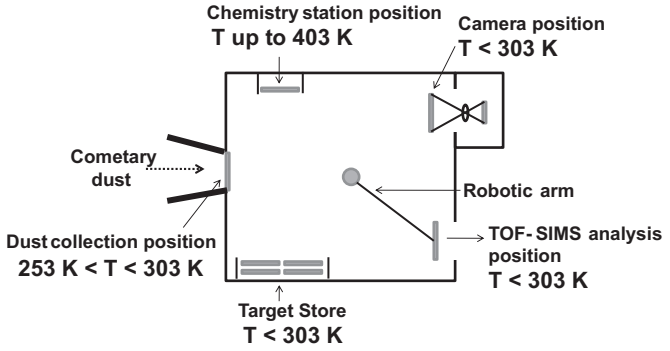

Fig. 1. Schematic view of COSIMA based on Kissel et al. (2007). The temperatures that cometary dust could encounter in COSIMA are reported.

2. Experimental

2.1. Analytical techniques

2.1.1. FTIR spectroscopy

Fourier Transform InfraRed (FTIR) spectroscopy has been operated to compare the two kinds of POM used in this study (commercial and synthesized), to check the repeatability of laboratory analog syntheses and to follow the evolution of the POM as a function of time during kinetic studies.

The spectrum of the commercial product ("POM Com") has been analyzed in KBr pellets at a resolution of 4 cm^{-1}, whereas the spectra of the laboratory analogs ("POM Lab") have been measured inside a high vacuum chamber on a CsI or MgF_2 window, where they are synthesized, at a resolution of 0.5 cm^{-1}.

2.1.2. TOF-SIMS

The TOF-SIMS used in this study is a laboratory model of COSIMA developed and located in LPC2E (Orléans), having similar instrumental characteristics such as the mass resolution ($m/\Delta m=$ 2000 at the peak FWHM at $m/z=100$) and having the same Primary Ion Beam System (PIBS).

The instrument consists of a pulsed primary indium ion beam ($^{115}In^{+}$) which is focused onto the sample. This bombardment induces the release of atoms, neutral molecules, positive and negative secondary ions from the first three monolayers of the sample. The secondary ions are then focused on the detector which is a micro-chanel plate.

The output cumulated signal gives the number of detected secondary ions versus time. This time corresponds to the flight duration that ions take to go from the target to the detector. The conversion of time into mass is calculated using the assumption that some peaks measured in the spectrum (e.g., H, C, Na, In or Au) are known.

As both positive and negative secondary ions are released from the sample, spectra are measured in both modes (positive & negative). The measurement of the secondary ions is made between 1 and 600 Da (Da) but can be extended to higher mass ranges (up to 19,440,000 Da) if needed. The mass spectra sampling is smaller than the width of the observed peaks (For instance Hydrogen peak has a FWHM of 0.039 Da and the sampling of this peak is 0.009 Da). During all the experiments, the vacuum pressure inside the analysis chamber is about 1×10^{-9} mbar.

2.1.3. Sample preparation and control spectra analysis

For the analysis, gold targets (purity 99.95%, Goodfellows) were cleaned in ultrasonic bath of *n*-hexane and then acetone to remove any kind of contamination. For each sample, two sets of TOF-SIMS analysis were performed. A first set of spectra is acquired before sample deposition to reference the nature and the level of the surface contamination. After this step, POM samples are deposited on the cleaned target and gently crushed with an agate pestle to obtain thin deposit. The second series of spectra is then measured.

2.2. Samples

If any, the exact nature of POM in comets is unknown. It must be rather fragile and easily decomposed into formaldehyde to account for the observed distributed formaldehyde source. Therefore, we have selected two kinds of POM for our analyses. The first one is a paraformaldehyde ($(HO–(CH_2O)_n–H$) with n ranging from 6 to 100) (Prolabo, purity > 99.5%). Later in this paper, it will be referred as "POM Com". The second one ("POM Lab") is a laboratory analog synthesized under conditions relevant to

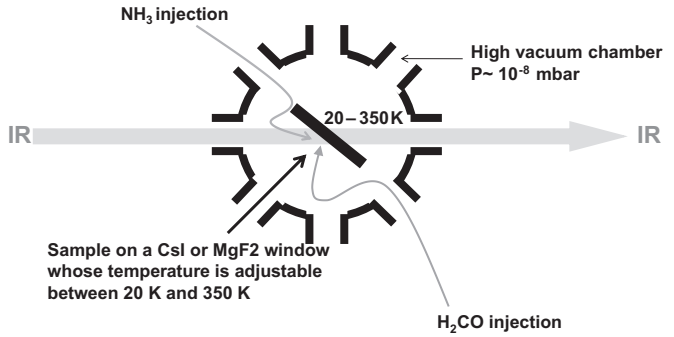

Fig. 2. Schematic view of OREGOC setup. The sample is deposited on a CsI or MgF_2 window whose temperature is adjustable between 20 and 350 K.

chemistry of interstellar and cometary ices (see details of synthesis in Section 2.3).

2.3. Laboratory analog synthesis

To synthesize POM under representative conditions of giant molecular clouds or presolar nebula, an experimental setup named OREGOC (French acronym for origin and evolution of ices and cometary organic compounds) (Fig. 2) similar to those described in Allamandola et al. (1988), Gerakines et al. (1995), Hagen et al. (1979) and Hudson and Moore (1995) is used. A CsI or a MgF_2 window is cooled down at about 20 K thanks to a closed-cycle helium cryostat (Advanced Research Systems, Inc.). Its temperature, measured by two thermocouples (type E and Au–Fe–Cr), is adjustable by means of a resistive heater driven with a temperature controller (Lakeshore). This window is located inside a high vacuum stainless steel chamber evacuated by a turbo pump (Varian turbo-V 301) backed up by a primary pump (Varian SH110). The pressure at room temperature is about 1×10^{-8} mbar. The ice evolution is monitored by FTIR.

POM is synthesized by the polymerization of formaldehyde catalyzed by ammonia (Schutte et al., 1993a). Ammonia (Air liquid, 99.995%) and formaldehyde[2] are deposited as ices on the cooled window through two independent tubes in order to prevent early reaction at ambient temperature. Once the H_2CO:NH_3 ices mixture is deposited at 20 K (Fig. 3), it is heated at 2 K/min. POM is produced during ice warming-up as already shown by Schutte et al. (1993a). At 293 K, the remaining sample is made only of POM (Fig. 4).

The synthesized POM is removed from the cryostat for further TOF-SIMS analysis, or kept inside the cryostat and heated at various temperatures (Table 1) in order to measure its lifetime as a function of temperature.

If only H_2CO ice is deposited on the window, no POM can be observed during the subsequent heating. The synthesis of POM requires a catalyst such as NH_3 (Schutte et al., 1993b). A H_2CO:NH_3 ratio close to 0.5 is used, as in this case the conversion of the initial H_2CO to POM is efficient (Schutte et al., 1993b).

The initial molecular ratio is derived from the IR spectra by integrating vibrational bands to estimate the column density of H_2CO and NH_3 according to their band strengths provided by the literature. For NH_3, the band strengths of the "umbrella" mode at $1070\,cm^{-1}$ is 1.7×10^{-17} cm/molecule (D'Hendecourt and Allamandola, 1986) and for H_2CO, the band strength at $2820\,cm^{-1}$ is 3.7×10^{-18} cm/molecule (Schutte et al., 1993b). We have tried to reproduce similar gas ratio deposition for each experiment to obtained similar POM (see Table 1).

[2] Formaldehyde is produced by the thermal decomposition of commercial POM (Prolabo, >99.5%) because commercial formaldehyde is never sold as desired (i.e., with a purity > 99%) and it always contains water or water and methanol. POM thermal degradation allows us to produce pure gaseous formaldehyde.

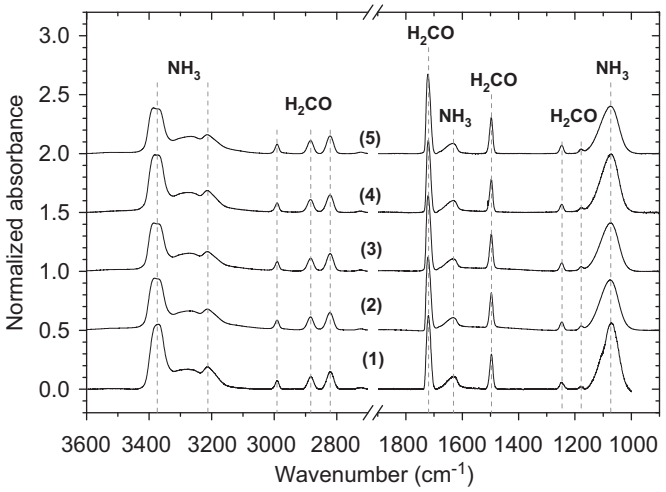

Fig. 3. FTIR spectra of ice deposit at 20 K for the five experiments presented in Table 1. All absorbances have been normalized to 0.15 at $2822\,cm^{-1}$ to compare the H_2CO:NH_3 ratio.

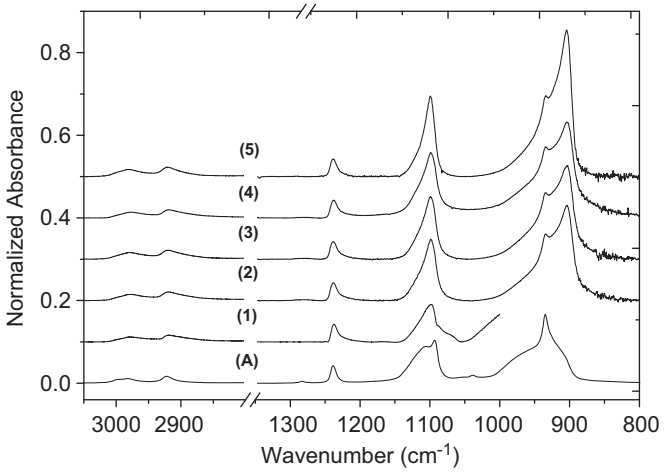

Fig. 4. FTIR spectra of POM at 293 K for the "POM Com" (A) and the five experiments (1–5) presented in Table 1. All absorbances have been normalized to 0.043 at $1238\,cm^{-1}$. Experiment no 1 has been performed on a MgF_2 substrate, which absorbs the IR beam below $1000\,cm^{-1}$.

2.3.1. POM characterization by FTIR spectroscopy

Fig. 4 shows infrared spectra of the "POM Com" (A) and of the "POM Lab" samples (1–5). Table 2 lists the position of the infrared solid bands of the two kinds of POM as well as their attributions by Tadokoro et al. (1963) and Schutte et al. (1993b).

Some differences can be noticed between "POM Com" and "POM Lab" (Fig. 4). For instance, the major feature is located at 903 and $935\,cm^{-1}$ for "POM Lab" and "POM Com", respectively. This difference may be interpreted by the solid state reorganization of "POM Com" structure induced by the pressure of the sample inside KBr pellets (Terlemezyan et al., 1978).

Four intense bands of POM, located at 903, 1099, 1238 and $2900\,cm^{-1}$, have been integrated. Between 3025 and $2850\,cm^{-1}$, IR spectra of POM display two features which are very close. So the integrated area at $2900\,cm^{-1}$ corresponds to the integration of both IR bands. The ratios of these areas are given in Table 1 and enlighten that the different "POM Lab" samples that we have synthesized are quite similar.

Table 1
Parameters of the experiments, H_2CO:NH_3 ratio for the ice mixture and also some properties of the synthesized POM.

N°	Comment		Ice mixture H_2CO:NH_3	POM features: IR band ratio		
	POM nature	Experiment		903/1238	1099/1238	2900/1238
A	Commercial POM	TOF SIMS analysis	NA	16.7	7.4	1.8
1	POM Lab	TOF SIMS analysis	0.35	NA	8.2	2.6
2	POM Lab	Decomposition T=320 K	0.55	17.7	6.9	2.4
3	POM Lab	Decomposition T=330 K	0.57	18.1	6.9	2.5
4	POM Lab	Decomposition T=340 K	0.50	17.2	6.7	2.5
5	POM Lab	Decomposition T=350 K	0.63	24.8	7.9	2.7

Table 2
Assignments of POM FTIR features (Schutte et al., 1993b; Tadokoro et al., 1963); s, m and w correspond to strong, medium and weak intensity, respectively.

Vibrational mode	POM Com ν (cm^{-1})	POM Lab ν (cm^{-1})	Intensity
CH_2 (rock.)–COC (sym. stretch.)		903	s
COC (sym. stretch.)+CH_2 (rock.)	935	935	s
Unassigned	980		w
Unassigned	1038		s
COC (antisym. stretch.)–OCO (bend.)	1093		s
COC (sym. stretch.)+CH_2 (rock.)		1099	s
Unassigned	1106		s
CH_2 (rock.)+COC (bend.)–COC (sym. stretch.)	1238	1238	w
CH_2 (twist)	1283	1283	w
CH_2/CH_3 deformation	1382	1382	w
CH_2/CH_3 deformation	1433	1433	w
CH_2/CH_3 deformation	1469	1469	w
CH stretch.	2789	2790	m
CH stretch.	2922	2920	m
CH_2 (antisym. stretch.)	2982	2979	m
Unassigned	2998		m

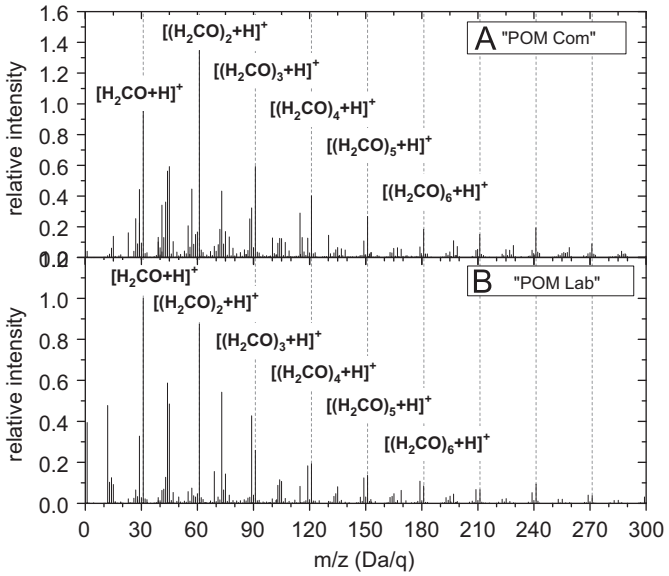

Fig. 5. Positive SIMS spectra of "POM Com" (A) and "POM Lab" (B). The figures present the relative intensities versus mass to charge ratio (m/z, inDa/q). Mass spectra are normalized to the intensity of peaks close to m/z=30.

3. Results and discussion

The following section presents reference TOF-SIMS spectra, and their interpretation, of the two kinds of POM and their lifetimes for the temperature that cometary grains could encounter inside COSIMA. These data allow us to determine the best strategy to identify POM in cometary grains from observations of the COSIMA instrument.

3.1. POM characterization by a ground analog of COSIMA

3.1.1. Positive mode of the instrument

Fig. 5 displays the positive spectra of the "POM Com" and of a "POM Lab" sample from 1 to 300 Da, whereas both POMs show features from 1 to 600 Da. From each peak position, we have attributed the most likely molecular formula. Nevertheless it must be noted that with the resolving power of the instrument, each peak could be matched to several molecular formulae. Indeed the higher the mass is, the more molecular formulae possibility increases. In the present case, as the nature of the sample is known before measuring its mass spectrum, the molecular formula attribution is easier and relatively reliable. However due to the limited number of secondary ions and the broad shape of the peaks beyond 300 Da, the molecular formula attributions with exact mass measured are very difficult. Nevertheless we assume that all these peaks belong to Polyoxymethylene.

Most intense peaks of both spectra are related to the monomer $[(H_2CO)+H]^+$ and its oligomers at mass $[(H_2CO)_n+H]^+$. Peaks related to oligomers fragmentation are also detected such as $[(H_2CO)_n–H]^+$, $[(H_2CO)_n+H–H_2O]^+$, $[(H_2CO)_n+H–OH]^+$, $[(H_2CO)_n+H–O]^+$, $[(H_2CO)_n+H–CH_2]^+$ and $[(H_2CO)_n+H–C]^+$ (Table 3). The different families of peaks are presented in Table 3. The peaks belonging to a family are separated by a mass of 30.011 Da, which is characteristic of POM positive spectra.

Both POMs share common features but the relative intensities of similar peaks are different. For instance, the intensities of peaks related to $[(H_2CO)_n–H]^+$ are higher for "POM Lab" than for the "POM Com". This could be due to different chemical structure of the two POMs. POM Lab structure might facilitate the production of $[(H_2CO)_n–H]^+$ under the primary ion beam.

3.1.2. Negative mode of the instrument

Fig. 6 shows negative spectra of "POM Com" (A) and of "POM Lab" (B). Both spectra are quite similar. Their major peaks are those of hydrogen, oxygen and of hydroxyl ions. They also display features related to C^-, CH^- and HCO_2^- at m/z=44.999. In the "POM Lab" spectrum (B), a peak related to Fluor anion can be observed. It comes from the MgF_2 substrate on which "POM Lab" has been synthesized. In "POM Com" spectrum (A), some peaks of cyanide and chloride (CN^- and Cl^-) are also present. They are linked to the contamination of the target.

Apart for F^-, CN^- and Cl^-, all peaks detected could be characteristic of any oxygenated compounds. They cannot allow an unambiguous identification of POM. So, by itself, a negative spectrum of POM is not sufficient to identify clearly the presence of this compound.

However, it must be highlighted that negative spectra of POM provided by the Static SIMS Library 4 (2006), have a quite different appearance: the major peak is HCO_2^- anion at m/z= 44.999 and it displays features with an alternating sequence of mass from 45 to 435 Da.

Table 3
List of the major spectral features identified thanks to their measured mass and classified in families. Only peaks between 1 and 300 Da are taken into account in this table because beyond 300 Da molecular formula attributions are very difficult due to the limited number of secondary ions and also to the broad shape of these peaks. The number of members corresponds to the number of molecules that the family contains. This table is adapted from the one presented in Bonnet et al. (submitted) for HCN polymers.

Family	POM Com			POM Lab		
	Number of members	*n* range for clearly identified molecules	*n* for most intense molecules	Number of members	*n* range for clearly identified molecules	*n* for most intense molecules
$[(H_2CO)_n+H]^+$	10	1 to 10	2	10	1 to 10	1
$[(H_2CO)_n-H]^+$	10	1 to 10	1	10	1 to 10	3
$[(H_2CO)_n+H-C]^+$	10	1 to 10	1	8	1 to 9	1
$[(H_2CO)_n+H-CH2]^+$	10	1 to 10	1	10	1 to 10	1
$[(H_2CO)_n+H-O]^+$	10	1 to 10	1	10	1 to 10	1
$[(H_2CO)_n+H-OH]^+$	10	1 to 10	1	10	1 to 10	1
$[(H_2CO)_n+H-H_2O]^+$	10	1 to 10	1	10	1 to 10	1

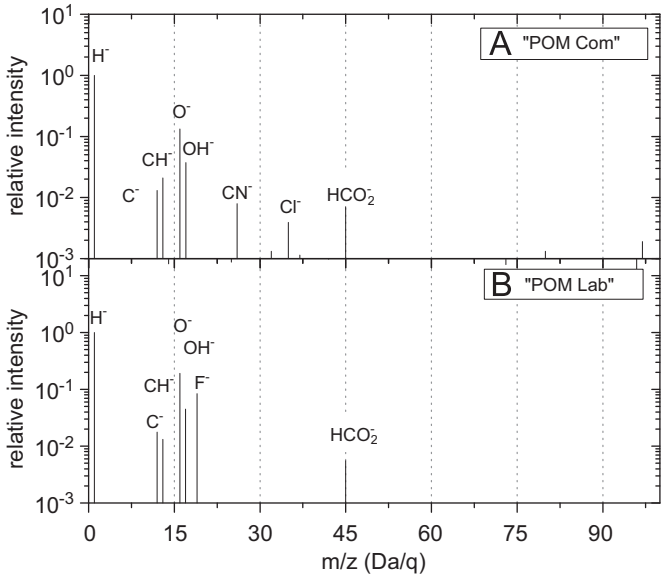

Fig. 6. Negative SIMS spectra of "POM Com" (A) and "POM Lab" (B). The figures show the relative intensity (in logarithm scale) versus mass to charge ratio (m/z). They have been normalized to the intensity of the peak at $m/z=1.008$.

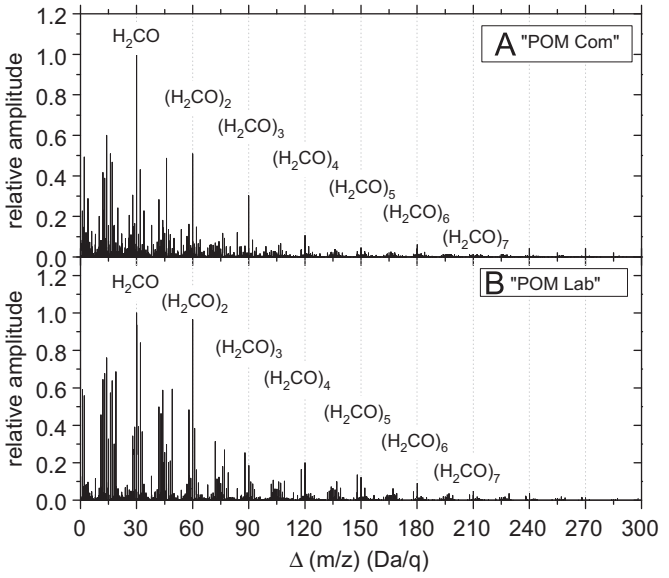

Fig. 7. Sum of peak intensity product as a function of the centroid difference $\Delta(m/z)$ with class interval width of 0.005 Da/q for commercial POM (A) and POM Lab (B). (A) ("POM Com") is normalized to the intensity at $\Delta(m/z)=30.013$. (B) ("POM Lab") is normalized to the intensity at $\Delta(m/z)=30.008$.

In fact these differences between our spectra and the one from the Static SIMS library are hardly surprising as a different primary ion beam has been used for the two experiments. Our analysis are made with an Indium ion gun whereas the spectrum from the static SIMS library has been performed with a Cesium ion gun, which enhances the production of negative secondary ions from the sample (Hill, 2001). The sample preparation was also different: Polyoxymethylene has been washed in *n*-hexane and methanol before being mounted under a grid (no feature of *n*-hexane and methanol are observed in these spectra).

3.2. Detection of POM with COSIMA

The grains of 67P/CG are expected to be a complex mixture of minerals and organic compounds. Therefore the detection of POM in COSIMA spectra will not be easy even if as a pure compound it presents distinctive features.

In order to enhance the ability to detect POM presence in COSIMA spectra, mathematical methods for handling spectra could be useful. As observed, positive spectrum of POM displays a sequence of peaks with an alternation of mass 30.011. We now present a strategy to highlight this specific characteristic of the POM positive spectrum.

From the original mass spectrum, a peak detection algorithm is used to determine the centroid $(m/z)_i$ and the intensity (I_i) of each peak having intensity higher than 100 counts. After this step, centroid differences $\Delta(m/z)$ between each pair of peaks in the spectrum are calculated as well as the product of the intensities of both considered peaks. The histogram showing the sum of peak intensity product as a function of the centroid difference $\Delta(m/z)$ with class interval width of 0.005 Da/q can be plotted. This procedure allows strengthening mass difference of the intense peaks present in the original mass spectrum. The histogram is shown in Fig. 7.

Those histograms present peaks up to 270 Da and most of them are, as for the spectra, separated from 30.011 Da. For both histograms, the most intense peak is located close to 30 Da. Some differences between these two histograms can be highlighted. For instance, the intensity of the peak at $\Delta(m/z)=60$ is higher in the "POM Lab" histogram than in the "POM Com" one (Fig. 7).

The major insight that brings the data treatment is that the peak widths in histograms are smaller than the corresponding peak widths in mass spectra. The decrease of the peak width is

illustrated in Fig. 8 for the peaks at 30 and 31 Da in histograms and in original mass spectra, respectively.

The peak close to 31 Da in the "POM Lab" mass spectrum is characterized by a centroid at $m/z=31.017$ and a FWHM of 0.030 whereas the peak close to 30 in the "POM Lab" histogram is characterized by a centroid at $\Delta(m/z)=30.012$ and a FWHM of 0.016. This treatment improves artificially the mass resolution by a factor 2 for "POM Lab" and by a factor of 4.4 for "POM Com". Therefore it allows easier molecular formula attributions. For instance, the peak related to the monomer of POM in the mass spectrum ($m/z=31.017$) could be linked to 7 ions (CH_3O^+: pseudo-molecular ion of POM monomer, SiH_3^+, CH_5N^+…) considering the mass resolution, whereas the one from the data treatment could be associated only to 2 molecules (POM or aluminum hydride polymer).

The polymer of aluminum hydride $(AlH_3)_n$, named alane, is used as reducing agent in organic chemistry. Its monomer structure ($m/z=30.005$ Da) could interfere with formaldehyde at the instrumental resolution. Nevertheless this compound is currently only found under two forms: the monomer and the dimer structure. But Kawamura et al. (2003) show that $(AlH_3)_n$ with n up to 4 can form stable cyclic or polymeric structures. Therefore with only 3 oligomers, there is little chance to find a sequence of peaks alternating from 30.005 up to 270 Da provided by $(AlH_3)_n$.

So POM is the best candidate to explain these specific peaks alternation. These characteristic features on histograms could be easily interpreted by the loss of the same fragments (H, C, CH_2, O, OH, H_2O and H_2CO) for all POM oligomers under the primary ion bombardment. The difference noticed at $\Delta(m/z)=60$ for the two histograms could be due to the preferential dimer loss during the fragmentation of the "POM Lab". For "POM Lab", an alternating sequence of peaks at $\Delta(m/z)$ equals $[(H_2CO)_n–2H]$ is also observed. It could be due to the high intensity of peaks at mass $[(H_2CO)_n–H]^+$ in the "POM Lab" mass spectrum.

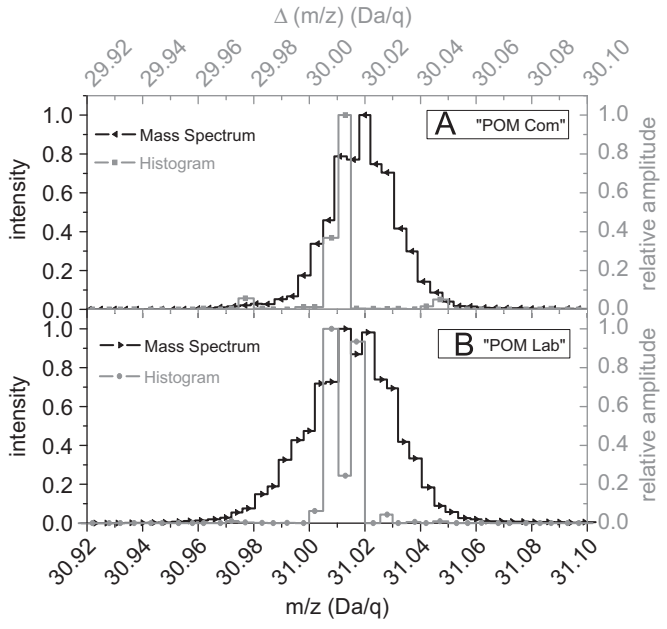

Fig. 8. Superposition of data treatment results (gray) and mass spectra (black) for "POM Com" (A) and "POM Lab" (B). The figures are focused on the peak linked to formaldehyde. Mass spectrum figures show the relative intensity versus mass to charge ratio (m/z). Mass spectra are normalized to the intensity at $m/z=30.020$ for "POM Com" and at $m/z=30.013$ for "POM Lab". Histograms show the sum of peak intensity product as a function of the centroid difference $\Delta(m/z)$ with class interval width of 0.005 Da/q. Histograms are normalized to the intensity at $\Delta(m/z)=30.013$ for "POM Com" and at $\Delta(m/z)=30.008$ for "POM Lab". The figure shows that the data treatment reduces the FWHM of peaks.

We have tested our method just with a spectrum of pure polyoxymethylene and it seems to allow its identification. But to really check its validity for COSIMA, it shall be tested on spectra of complex mixture containing POM. This point is however beyond the scope of this paper.

3.3. POM lifetime parameterization

POM in the solid phase can undergo a thermal decomposition into gaseous H_2CO at temperatures as low as 255 K (Grassie and Roche, 1968; Zimmermann and Behnisch, 1982; Fray et al., 2004). Between the cometary grain collection and their analysis, grains will be stored at a temperature close to 303 K (Kissel et al., 2007). Thus, if present in cometary grains, POM could undergo decomposition inside the COSIMA instrument. The thermal decomposition kinetics of POM samples, synthesized by heating H_2CO:NH_3 ice mixtures, has been parameterized to constrain when cometary grains have to be analyzed after their collection to maximize the chances to detect POM.

After being synthesized, four "POM Lab" samples have been kept at constant temperature (320, 330, 340 and 350 K) and monitored by FTIR (see Table 1). For each experiment, infrared spectra have been acquired with a time resolution of about 100 s and for each spectra the area of four infrared bands (903, 1099, 1238 and 2900 cm^{-1}) have been calculated. The initial time of decomposition is the time at which the temperature of the sample becomes constant. The temporal evolution of these four band's area is shown in Fig. 9.

In Fig. 9, the POM decay predicted from the data published by Fray et al. (2004) is plotted using a first order kinetic law. It can be concluded that our experimental data do not follow first order kinetics, as commercial POM would. Indeed the rate of "POM Lab" disappearance decreases with time. A similar behavior has already been observed on POM thermal decomposition by Grassie and Roche (1968).

As previously mentioned, POM is a general name for formaldehyde polymers. It has been shown by Grassie and Roche (1968) that the kinetic of the thermal decomposition of POM depends on the average molecular weight of POM. Our samples are not

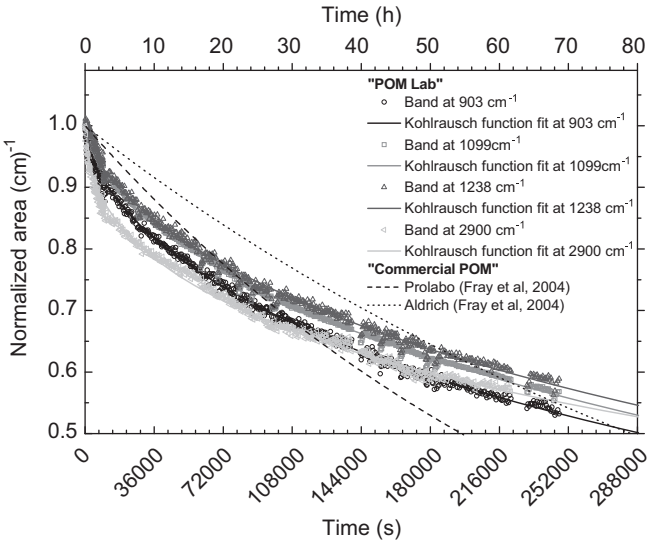

Fig. 9. Normalized area of four POM infrared bands as a function of time when submitted at 320 K. The bands at 903, 1099, 1238 and 2900 cm^{-1} are plotted in black, gray, dark gray and light gray, respectively. For each infrared band, a Kohlrausch relaxation function fit is shown. The temporal evolution predicted from Fray et al. (2004) on two different commercial POM provided by Prolabo (black dashed line) and Aldrich (black dotted line) is also plotted. These latter predictions have been calculated assuming a first order kinetic.

controlled in term of chain length and are most probably a mixture of polymers with various molecular weights.

For each POM molecule, if the thermal degradation follows first order kinetics, with a kinetic rate being a function of the chain length, the kinetic of decay of the whole POM sample should follow a Kohlrausch relaxation function (Plonka and Paszkiewicz, 1996). This function can be written:

$$N(t) = N_0 e^{-(kt)^{\alpha}} = N_0 e^{-(t/\tau_0)^{\alpha}} \quad (3)$$

$N(t)$ and N_0 being the number of molecules in the sample as a function of time and at initial time, respectively, α the dispersion parameter ranging from 0 to 1, k the mean kinetic rate (s^{-1}) and τ_0 the mean characteristic time (s) of decomposition.

The Kohlrausch relaxation function (Eq. (3)), related to dispersive kinetics, is fitted by "stretched" exponential curves (Plonka, 2001). These curves are characterized by two parts: at the beginning a sharp decrease and afterwards a much slower decline. This behavior could be explained either by chemical or physical processes such as not truly elementary reaction (i.e., species diffusion before reaction) or parallel reaction with different kinetics yielding to the same product, α reflecting the dispersion of the reaction rates compared to a mean value of k (Andraos, 2000; Plonka and Paszkiewievcz, 1992, 1996; Siebrand and Wildman, 1986).

The time evolution of each studied band can be fitted with this model (Fig. 9). The parameters k and α, as well as their uncertainties, for each infrared band and for each experiment are reported in Table 4.

Grassie and Roche (1968) have shown that there is an inverse relationship between the thermal decomposition of POM kinetics and the average molecular weight of the sample. Therefore, the observed temporal evolution of POM could be due to the faster decomposition of the lighter polymers at the beginning of the experiment. It is then possible that the average molecular weight of the sample increases during the thermal degradation. Moreover, whereas it is very difficult to link the molecular weight of the polymer to its infrared spectrum, this interpretation could explain the fact that the time evolution of the infrared bands is different.

The mean kinetic constant (k, in s^{-1}) should follow the Arrhenius law (Eq. (4)). It is equal to the inverse of the characteristic time of degradation (τ_0, in s)

$$k(T) = Ae^{-\mathrm{Ea}/RT} \quad (4)$$

Table 4
Results of the fits with the Kohlrausch relaxation function (Eq. (3)) on the temporal evolution of each infrared band and for each experiment.

POM decomposition temperature (K)	IR band (cm^{-1})	k (s^{-1})	Δk (s^{-1})	A	$\Delta\alpha$	R^2
320	903	1.9E−06	2E−07	0.592	0.002	0.996
	1099	1.7E−06	1E−07	0.624	0.002	0.998
	1238	1.6E−06	2E−07	0.624	0.003	0.997
	2900	1.3E−06	1E−07	0.467	0.002	0.997
330	903	5.0E−06	6E−07	0.600	0.003	0.996
	1099	3.9E−06	3E−07	0.589	0.002	0.998
	1238	3.4E−06	3E−07	0.521	0.002	0.997
	2900	4.4E−06	4E−07	0.469	0.002	0.997
340	903	4.9E−05	1.2E−05	0.513	0.006	0.984
	1099	3.9E−05	7E−06	0.545	0.005	0.992
	1238	3.5E−05	6E−06	0.565	0.005	0.993
	2900	2.2E−05	8E−06	0.461	0.008	0.968
350	903	6.4E−05	1.1E−05	0.619	0.006	0.983
	1099	6.3E−05	5E−06	0.612	0.002	0.997
	1238	6.1E−05	9E−06	0.619	0.004	0.990
	2900	1.6E−05	6E−06	0.368	0.006	0.940

where A is the frequency factor (s^{-1}), E_a the activation energy (J mol^{-1}) and R the universal gas constant (J mol^{-1} K^{-1}) and T the temperature (K). Fig. 10 displays the natural logarithm of the mean kinetic constant as a function of the inverse of the temperature. These measurements are well fitted using an Arrhenius law (Fig. 10). This fit allows to estimate E_a=113 ($\pm$4%) kJ mol^{-1} and Ln A=29 ($\pm$41%). Since the kinetic constants derived from the Kohlrausch relaxation function are actually average values, E_a and A values are relevant to the parameterization of the mean kinetic constant as a function of the temperature.

Knowing these values, the mean characteristic time of POM decomposition can be estimated for any temperature. Whatever the kinetic parameterization is, we can define the characteristic time of decomposition as the inverse of k (see Eq. (3)). It corresponds to the duration after which 37% of the initial sample of POM is remaining (diminution by a factor e).

COSIMA samples can encounter temperature between 253 and 303 K. Fig. 11 displays the mean characteristic time of POM decomposition as a function of the temperature calculated from

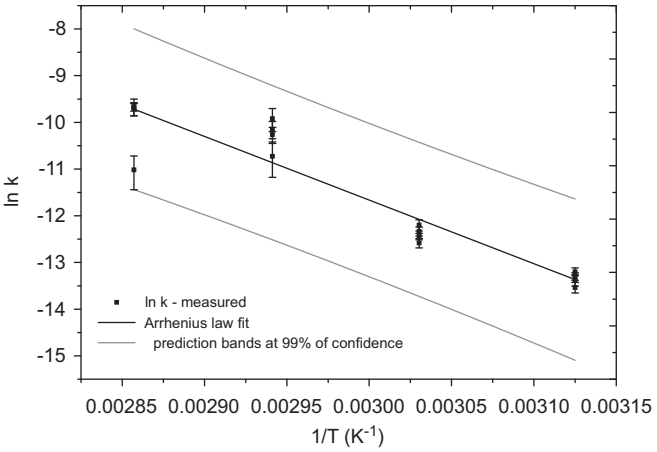

Fig. 10. Natural logarithm of the POM decomposition kinetic rate as a function of the inverse of the temperature. The black dots are experimental measurements and the black line is the best fit with a linear function allowing us to measure the activation energy (E_a) and the frequency factor (A) of the Arrhenius law. The gray lines are the predictions bands of Arrhenius law at a level of 99% of confidence.

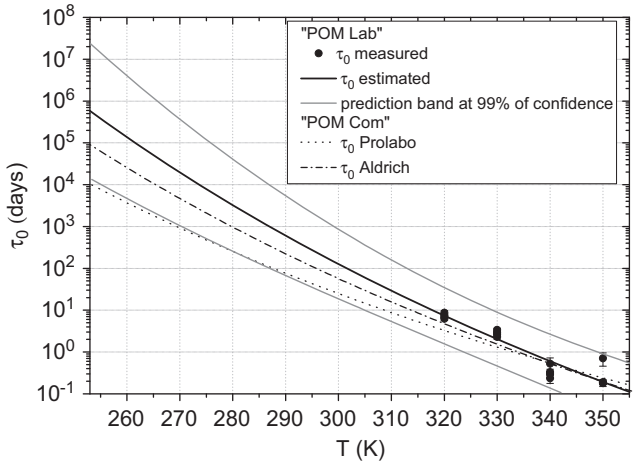

Fig. 11. Mean characteristic times of POM decomposition as a function of the temperature. The black dots are experimental measurements and the black curve is the extrapolation of our measurements using the Arrhenius law measured in this work. The gray curves are the predictions bands at a level of 99% of confidence. The dotted and dash-dotted curves are the characteristic times of POM decomposition calculated from Fray et al. (2004).

our measurements using a Kohlrausch relaxation function (see Eq. (3)) and from the measurements published by Fray et al. (2004) on two different commercial samples using a first order kinetics for the temperature range that cometary grains could encounter inside COSIMA.

The characteristic times calculated using the data of Fray et al. (2004) fall in the interval of 99% of confidence except below 280 K for the "Commercial POM" from Prolabo (Fig. 11). Our measurements are in quite good agreement with these previous data, even if the parameterization of the kinetics depends on the source of POMs, and although characteristic times of POM decomposition could differ by almost an order of magnitude when extrapolated at low temperature.

After grain collection, the COSIMA target can be stored before analysis. During this storage, the temperature of the target and then of the collected cometary grains can reach 303 K (Kissel et al., 2007). At this temperature, according to our parameterization, the mean characteristic time of POM decomposition is at least 15 days. Thus, if during the storage stage the cometary grains do not encounter temperature higher than 303 K, the POM, if present in cometary grains, will decompose slowly. In such case the storage of the target will not prevent the detection of POM. It must be kept in mind that the delay between new programming operations from Earth and their application in space is about 1 week. Thus, the decomposition of POM has to be taken into account to decide the space operation of COSIMA. In order to maximize the chance to detect POM in cometary grains, the analysis of the collected grains has to be done as quickly as possible.

To check the presence of POM on cometary grains, the chemistry station integrated in COSIMA could also be used. Indeed, in the chemistry station, the target and the collected grains can be heated up to 403 K. At this temperature, the mean lifetime of POM is lower than 17 min. Therefore if two analyses are made, one just after the sample collection, the second one after the sample heating, then confirmation of the presence of POM can be highlighted by the disappearance of specific POM features in the mass spectra.

4. Conclusion

COSIMA is a decisive instrument for the characterization of solid compounds ejected from the nucleus of comet 67P/CG and more especially of refractory organic molecules. If there is some POM in the grains of 67P/CG, it is feasible to detect it in the positive mode of the instrument, provided that its signature is not drowned by the other cometary organic compounds. Mathematical treatment of the data will be a useful tool to highlight the presence of POM in mass spectra of complex mixture. POM can be identified thanks to its specific alternation in mass (30.011 Da) of these peaks and also thanks to its specific fragmentation pattern. As POM is a thermally unstable compound, cometary grains have to be analyzed within a fortnight after their collection in order to maximize chances to observe the features of this polymer.

COSIMA has one of the best resolutions for a spaceborne mass spectrometer since the beginning of cometary space exploration. It will allow an easier identification of compounds compared to the mass spectrometers onboard Vega 1 & 2, Giotto and Stardust. However, current specifications of such instruments are far from resolving all the ambiguities in mass spectra of complex organic mixture. Only instruments with very high resolution capabilities, such as the one achieved with the commercial Orbitrap instrument in the laboratory, at about 100 000 (Hu et al., 2005), are fully adapted to in situ analysis of complex organic mixtures in the Solar System. Such instruments should be adapted to space and considered as being part of the payload of future space missions.

Acknowledgment

This work has been supported by CNES (Centre National des Etudes Spatiales – French space agency) and region Centre, L.L.R. is the recipient of a CNES/Région Centre fellowship.

References

Allamandola, L.J., Sandford, S.A., Valero, G.J., 1988. Photochemical and thermal evolution of interstellar/precometary ice analogs. Icarus 76, 225–252.

Anders, E., 1989. Pre-biotic organic matter from comets and asteroids. Nature 342, 255–257.

Andraos, J., 2000. Biomolecular kinetics at low temperature using FTIR matrix isolation spectroscopy: some caveats. Thermokinetic parameters for the reaction of fulveones with pyridine in pyridine matrixes. Journal of Physical Chemistry 104, 1532–1543.

Bernstein, M.P., Sandford, S.A., Allamandola, L.J., Chang, S., Scharberg, M.A., 1995. Organic compounds produced by photolysis of realistic interstellar and cometary ice analogs containing methanol. Asia Pacific Journal 454, 327–344.

Bevington, J.C., May, H., 1964. aldehyde polymers. Encyclopedia of polymer science and technology, 609–628.

Bockelée-Morvan, D., Crovisier, J., Mumma, M.J., Weaver, H.A., Keller, H.U., Weaver, H.A., 2004. The composition of cometary volatiles. In: Festou, M.C., Keller, H.U., Weaver, H.A. (Eds.), Comets II. the University of Arizona Press, Tucson, USA, pp. 391–423.

Bonnet, J.-Y., Thissen, R., Frisari, M., Vuitton, V., Quirico, E., Orthous-Daunay, F.-R., Dutuit, O., Le Roy, L., Fray, N., Cottin, H., Hörst, S.M., Yelle, R.V., submitted. Structure and composition of HCN polymer through high resolution mass spectrometry. International Journal of Mass Spectrometry.

Brownlee, D., Tsou, P., Aleon, J., Alexander, C., Araki, T., Bajt, S., Baratta, G., Bastien, R., Bland, P., Bleuet, P., Borg, J., Bradley, J., Brearley, A., Brenker, F., Brennan, S., Bridges, J., Browning, N., Brucato, J., Bullock, E., Burchell, M., Busemann, H., Butterworth, A., Chaussidon, M., Cheuvront, A., Chi, M., Cintala, M., Clark, B., Clemett, S., Cody, G., Colangeli, L., Cooper, G., Cordier, P., Daghlian, C., Dai, Z., D'Hendecourt, L., Djouadi, Z., Dominguez, G., Duxbury, T., Dworkin, J., Ebel, D., Economou, T., Fakra, S., Fairey, S., Fallon, S., Ferrini, G., Ferroir, T., Fleckenstein, H., Floss, C., Flynn, G., Franchi, I., Fries, M., Gainsforth, Z., Gallien, J.-P., Genge, M., Gilles, M., Gillet, P., Gilmour, J., Glavin, D., Gounelle, M., Grady, M., Graham, G., Grant, P., Green, S., Grossemy, F., Grossman, L., Grossman, J., Guan, Y., Hagiya, K., Harvey, R., Heck, P., Herzog, G., Hoppe, P., Horz, F., Huth, J., Hutcheon, I., Ignatyev, K., Ishii, H., Ito, M., Jacob, D., Jacobsen, C., Jacobsen, S., Jones, S., Joswiak, D., Jurewicz, A., Kearsley, A., Keller, L., Khodja, H., Kilcoyne, A., Kissel, J., Krot, A., Langenhorst, F., Lanzirotti, A., Le, L., Leshin, L., Leitner, J., Lemelle, L., Leroux, H., Liu, M.-C., Luening, K., Lyon, I., MacPherson, G., Marcus, M., Marhas, K., Marty, B., Matrajt, G., McKeegan, K., Meibom, A., Mennella, V., Messenger, K., Messenger, S., Mikouchi, T., Mostefaoui, S., Nakamura, T., Nakano, T., Newville, M., Nittler, L., Ohnishi, I., Ohsumi, K., Okudaira, K., Papanastassiou, D., Palma, R., Palumbo, M., Pepin, R., Perkins, D., Perronnet, M., Pianetta, P., Rao, W., Rietmeijer, F., Robert, F., Rost, D., Rotundi, A., Ryan, R., Sandford, S., Schwandt, C., See, T., Schlutter, D., Sheffield-Parker, J., Simionovici, A., Simon, S., Sitnitsky, I., Snead, C., Spencer, M., Stadermann, F., Steele, A., Stephan, T., Stroud, R., Susini, J., Sutton, S., Suzuki, Y., Taheri, M., Taylor, S., Teslich, N., Tomeoka, K., Tomioka, N., Toppani, A., Trigo-Rodriguez, J., Troadec, D., Tsuchiyama, A., Tuzzolino, A., Tyliszczak, T., Uesugi, K., Velbel, M., Vellenga, J., Vicenzi, E., Vincze, L., Warren, J., Weber, I., Weisberg, M., Westphal, A., Wirick, S., Wooden, D., Wopenka, B., Wozniakiewicz, P., Wright, I., Yabuta, H., Yano, H., Young, E., Zare, R., Zega, T., Ziegler, K., Zimmerman, L., Zinner, E., Zolensky, M., 2006. Comet 81P/Wild 2 under a microscope. Science 314, 1711–1716.

Chyba, C., Sagan, C., 1992. Endogenous production, exogenous delivery and impact-shock synthesis of organic molecules: an inventory for the origins of life. Nature 355, 125–132.

Coradini, A., Capaccioni, F., Drossart, P., Arnold, G., Ammannito, E., Angrilli, F., Barucci, A., Bellucci, G., Benkhoff, J., Bianchini, G., Bibring, J., Blecka, M., Bockelee-Morvan, D., Capria, M., Carlson, R., Carsenty, U., Cerroni, P., Colangeli, L., Combes, M., Combi, M., Crovisier, J., Desanctis, M., Encrenaz, E., Erard, S., Federico, C., Filacchione, G., Fink, U., Fonti, S., Formisano, V., Ip, W., Jaumann, R., Kuehrt, E., Langevin, Y., Magni, G., McCord, T., Mennella, V., Mottola, S., Neukum, G., Palumbo, P., Piccioni, G., Rauer, H., Saggin, B., Schmitt, B., Tiphene, D., Tozzi, G., 2007. Virtis: an imaging spectrometer for the Rosetta Mission. Space Science Reviews 128, 529–559.

Cottin, H., Bénilan, Y., Gazeau, M.-C., Raulin, F., 2004. Origin of cometary extended sources from degradation of refractory organics on grains: polyoxymethylene as formaldehyde parent molecule. Icarus 167, 397–416.

Cottin, H., Fray, N., 2008. Distributed sources in comets. Space Science Reviews 138, 179–197.

Crovisier, J., Leech, K., Bockelée-Morvan, D., Brooke, T.Y., Hanner, M.S., Altieri, B., Keller, H.U., Lellouch, E., 1997. The spectrum of comet Hale–Bopp (C/1995 O1)

observed with the infrared space observatory at 2.9 astronomical units from the Sun. Science 275, 1904–1907.
D'Hendecourt, L., Allamandola, L.J., 1986. Time dependant chemisty in dense molecular cloud. III. Infrared band cross section of molecules in the solid state in 10 K. Astronomy and Astrophysics Supplement 64, 453–467.
Delsemme, A.H., 1999. The deuterium enrichment observed in recent comets is consistent with the cometary origin of seawater. Physica Status Solidi 47, 125–131.
Elsila, J.E., Glavin, D.P., Dworkin, J.P., 2009. Cometary glycine detected in samples returned by Stardust. Meteoritics & Planetary Science 44, 1323–1330.
Feldman, P.D., Cochran, A.L., Combi, M.R., 2004. Spectroscopic investigation of fragment species in the coma. In: Festou, M.C., Keller, H.U., Weaver, H.A. (Eds.), Comets II. The University of Arizona Press, Tucson, USA, pp. 425–447.
Fomenkova, M., Chang, S., Mukhin, L.M., 1994. Carbonaceous components in the comet Halley dust. Geochimica et Cosmochimica Acta 58, 4503–4512.
Fray, N., Bénilan, Y., Biver, N., Bockelée-Morvan, D., Cottin, H., Crovisier, J., Gazeau, M.-C., 2006. Heliocentric evolution of the degradation of polyoxymethylene: application to the origin of the formaldehyde (H_2CO) extended source in comet C/1995 O1 (Hale–Bopp). Icarus 184, 239–254.
Gerakines, P.A., Schutte, W.A., Greenberg, J.M., Van Dishoeck, E.F., 1995. The infrared band strengths of H_2O, CO and CO_2 in laboratory simulations of astrophysical ice mixture. Astronomy & Astrophysics 296, 810–818.
Glassmeier, K.-H., Boehnhardt, H., Koschny, D., Kührt, E., Richter, I., 2007. The Rosetta mission: flying towards the origin of the solar system. Space Science Reviews 128, 1–21.
Goesmann, F., Rosenbauer, H., Roll, R., Szopa, C., Raulin, F., Sternberg, R., Israel, G., Meierhenrich, U., Thiemann, W., Munoz-Caro, G., 2007. COSAC, the cometary sampling and composition experiment on philae. Space Science Reviews 128, 257–280.
Hagen, W., Allamandola, L.J., Greenberg, J.M., 1979. Insterstellar molecule formation in grains mantles: the laboratory analog experiments, results and implication. Astrophysics and Space Science 65, 215–240.
Hill, R., 2001. Primary ion beam systems. In: Vickerman, J.C., Briggs, D. (Eds.), TOF-SIMS. surface analysis by mass spectrometry. IM Publications & SurfaceSpectra Limited, pp. 95–113.
Hu, Q., Noll, R.J., Li, H., Makarov, A., Hardman, M., Graham Cooks, R., 2005. The orbitrap: a new mass spectrometer. Journal of Mass Spectrometry 40, 430–443.
Hudson, R.L., Moore, M.H., 1995. Far-IR spectral changes accompanying proton irradiation of solids of astrochemical interest. Radiation Physics and Chemistry 45, 779–789.
Huebner, W.F., 1987. First polymer in space identified in comet Halley. Science 237, 628–630.
Irvine, W.M., Lunine, J.I., 2004. The cycle of matter in our galaxy: from clouds to comets. In: Festou, M.C., Keller, H.U., Weaver, H.A. (Eds.), Comets II. University of Arizona Press, Tucson, USA, pp. 25–31.
Jessberger, E.K., Cristoforidis, A., Kissel, J., 1988. Aspects of the major element composition of Halley's dust. Nature 332, 691–695.
Kawamura, H., Kumar, V., Sun, Q., Kawazoe, Y., 2003. Cyclic and linear polymeric structures of Al_nH_{3n} (n=3_7) molecules. Physical Review A 67, 063205. id.
Kissel, J., Altwegg, K., Clark, B.C., Colangeli, L., Cottin, H., Czempiel, S., Eibl, J., Engrand, C., Fehringer, H.M., Feuerbacher, B., Fomenkova, M., Glasmachers, A., Greenberg, J.M., Grün, E., Haerendel, G., Henkel, H., Hilchenbach, M., von Hoerner, H., Höfner, H., Hornung, K., Jessberger, E.K., Koch, A., Krüger, H., Langevin, Y., Parigger, P., Raulin, F., Rüdenauer, F., Rynö, J., Schmid, E.R., Schulz, R., Silén, J., Steiger, W., Stephan, T., Thirkell, L., Thomas, R., Torkar, K., Utterback, N.G., Varmuza, K., Wanczek, K.P., Werther, W., Zscheeg, H., 2007. Cosima: high resolution time-of-flight secondary ion mass spectrometer for the analysis of cometary dust particles onboard Rosetta. Space Science Reviews 128, 823–867.
Kissel, J., Brownlee, D.E., Buchler, K., Clark, B.C., Fechtig, H., Grun, E., Hornung, K., Igenbergs, E.B., Jessberger, E.K., Krueger, F.R., Kuczera, H., McDonnell, J.A.M., Morfill, G.M., Rahe, J., Schwehm, G.H., Sekanina, Z., Utterback, N.G., Volk, H.J., Zook, H.A., 1986a. Composition of comet Halley dust particles from Giotto observations. Nature 321, 336–337.
Kissel, J., Krueger, F.R., Silen, J., Clark, B.C., 2004. The cometary and interstellar dust analyser at comet 81P/Wild2. Science 304, 1774–1776.
Kissel, J., Sagdeev, R.Z., Bertaux, J.L., Angarov, V.N., Audouze, J., Blamont, J.E., Buchler, K., Evlanov, E.N., Fechtig, H., Fomenkova, M.N., von Hoerner, H., Inogamov, N.A., Khromov, V.N., Knabe, W., Krueger, F.R., Langevin, Y., Leonasv, B., Levasseur-Regourd, A.C., Managadze, G.G., Podkolzin, S.N., Shapiro, V.D., Tabaldyev, S.R., Zubkov, B.V., 1986b. Composition of comet Halley dust particles from VEGA observations. Nature 321, 280–282.
Krueger, F.R., Kissel, J., 1987. The chemical composition of the dust of comet P/Halley as mesured by PUMA on board VEGA-1. Naturwissenschaften 74, 312–316.
Langevin, Y., Kissel, J., Bertaux, J.L., Chassefière, E., 1987. First statistical analysis of 5000 mass spectra of cometary grains obtain by PUMA 1 (Vega 1) and PIA (Giotto) impact ionization mass spectrometers in the compressed modes. Astronomy and Astrophysics 187, 761–766.
Lawler, M.E., Brownlee, D.E., Temple, S., Wheelock, M.M., 1989. Iron, magnesium, and silicon in dust from comet Halley. Icarus 80, 225–242.
Mitchell, D.L., Lin, R.P., Carlson, C.W., Korth, A., Rème, H., Mendis, D.A., 1992. The origin of complex organic ions in the coma of comet Halley. Icarus 98, 125–133.
Oro, J., 1961. Comets and formation of biochemical compounds on the primitive Earth. Nature 190, 389–390.
Oro, J., Lazcano, A., Ehrenfreund, P., 2006. In: Thomas, P.J., Hicks, R.D., Chyba, C.F., Mckay, C.P. (Eds.), Comets and the Origin and Evolution of Life, 2nd edn. Springer, pp. 1–18.
Pchelintsev, V.V., Sokolov, A.Y., Zaikov, G.E., 1988. Kinetic principles and mechanisms of hydrolytic degradation of mono- and polyacetals – A review. Polymer Degradation and Stability 21, 285–310.
Plonka, A., 2001. Dispersive kinetics. Annual Reports on the Progress of Chemistry, Section C: Physical Chemistry 97, 91–147.
Plonka, A., Paszkiewievcz, A., 1992. Kinetics in dynamically disorder systems: time scale dependence of reacrion patterns in condensed media. Journal of Chemical Physics 96, 1128–1133.
Plonka, A., Paszkiewievcz, A., 1996. Phenmenological interpretation of kinetics with time dependent specific reaction rates. Chemical Physics 212, 1–8.
Sandford, S.A., Aleon, J., Alexander, C.M.O.D., Araki, T., Bajt, S., Baratta, G.A., Borg, J., Bradley, J.P., Brownlee, D.E., Brucato, J.R., Burchell, M.J., Busemann, H., Butterworth, A., Clemett, S.J., Cody, G., Colangeli, L., Cooper, G., D'Hendecourt, L., Djouadi, Z., Dworkin, J.P., Ferrini, G., Fleckenstein, H., Flynn, G.J., Franchi, I.A., Fries, M., Gilles, M.K., Glavin, D.P., Gounelle, M., Grossemy, F., Jacobsen, C., Keller, L.P., Kilcoyne, A.L.D., Leitner, J., Matrajt, G., Meibom, A., Mennella, V., Mostefaoui, S., Nittler, L.R., Palumbo, M.E., Papanastassiou, D.A., Robert, F., Rotundi, A., Snead, C.J., Spencer, M.K., Stadermann, F.J., Steele, A., Stephan, T., Tsou, P., Tyliszczak, T., Westphal, A.J., Wirick, S., Wopenka, B., Yabuta, H., Zare, R.N., Zolensky, M.E., 2006. Organics captured from comet 81P/Wild 2 by the Stardust Spacecraft. Science 314, 1720–1724.
Sandford, S.A., Bajt, S., Clemett, S.J., Cody, G.D., Cooper, G., Degregorio, B.T., de Vera, V., Dworkin, J.P., Elsila, J.E., Flynn, G.J., Glavin, D.P., Lanzirotti, A., Limero, T., Martin, M.P., Snead, C.J., Spencer, M.K., Stephan, T., Westphal, A., Wirick, S., Zare, R.N., Zolensky, M.E., 2010. Assessment and control of organic and other contaminants associated with the Stardust sample return from comet 81P/Wild 2. Meteoritics & Planetary Science 45, 406–433.
Schutte, W., Allamandola, L., Sandford, S., 1993a. Formaldehyde and organic molecule production in astrophysical ices at cryogenic temperatures. Science 259, 1143–1145.
Schutte, W.A., Allamandola, L.J., Sandford, S.A., 1993b. An experimental study of the organic molecules produced in cometary and interstellar ice analogs by thermal formaldehyde reactions. Icarus 104, 118–137.
Siebrand, W., Wildman, T.A., 1986. Dispersive kinetics: a structural approach to nonexponential processes in disordered media. Accounts of Chemical Research 19, 238–243.
Tadokoro, H., Kobayashi, M., Kawaguchi, Y., Kobayashi, A., Murahashi, S., 1963. Normal vibration of the polymer molecules of helical configuration. III. Polyoxymethylene and polyoxymethylene-d_2. Journal of Chemical Physics 38, 703–721.
Terlemezyan, L., Mihailov, M., Schmidt, P., Schneider, B., 1978. Conformational changes of poly(oxymethylene) induced by pressure and mechanical treatment. Makromolekulare Chemie 179, 807–813.
The Static SIMS Library, 2006. In: Vickerman, J.C., Briggs, D., Henderson, A. (Eds.), SurfaceSpectra, 4. Manchester, UK.
Vinogradoff, V., Duvernay, F., Danger, G., Theulé, P., Chiavassa, T., 2011. New insight into the formation of hexamethylenetetramine (HMT) in interstellar and cometary ice analogs. Astronomy and Astrophysics 530. id.A128.
Walker, J., 1964. Formaldehyde, 3rd edn. Reinhold, New York.
Wright, I.P., Barber, S.J., Morgan, G.H., Morse, A.D., Sheridan, S., Andrews, D.J., Maynard, J., Yau, D., Evans, S.T., Leese, M.R., Zarnecki, J.C., Kent, B.J., Waltham, N.R., Whalley, M.S., Heys, S., Drummond, D.L., Edeson, R.L., Sawyer, E.C., Turner, R.F., Pillinger, C.T., 2007. Ptolemy an instrument to measure stable isotopic ratios of key volatiles on a cometary nucleus. Space Science Reviews 128, 363–381.
Zimmermann, H., Behnisch, J., 1982. Thermogravimetric investigations on the kinetics of thermal degradation of polyoxymethylenes. Thermochimica Acta 59, 1–8.
Zolensky, M.E., Zega, T.J., Yano, H., Wirick, S., Westphal, A.J., Weisberg, M.K., Weber, I., Warren, J.L., Velbel, M.A., Tsuchiyama, A., Tsou, P., Toppani, A., Tomioka, N., Tomeoka, K., Teslich, N., Taheri, M., Susini, J., Stroud, R., Stephan, T., Stadermann, F.J., Snead, C.J., Simon, S.B., Simionovici, A., See, T.H., Robert, F., Rietmeijer, F.J.M., Rao, W., Perronnet, M.C., Papanastassiou, D.A., Okudaira, K., Ohsumi, K., Ohnishi, I., Nakamura-Messenger, K., Nakamura, T., Mostefaoui, S., Mikouchi, T., Meibom, A., Matrajt, G., Marcus, M.A., Leroux, H., Lemelle, L., Le, L., Lanzirotti, A., Langenhorst, F., Krot, A.N., Keller, L.P., Kearsley, A.T., Joswiak, D., Jacob, D., Ishii, H., Harvey, R., Hagiya, K., Grossman, L., Grossman, J.N., Graham, G.A., Gounelle, M., Gillet, P., Genge, M.J., Flynn, G., Ferroir, T., Fallon, S., Ebel, D.S., Dai, Z.R., Cordier, P., Clark, B., Chi, M., Butterworth, A.L., Brownlee, D.E., Bridges, J.C., Brennan, S., Brearley, A., Bradley, J.P., Bleuet, P., Bland, P.A., Bastien, R., 2006. Mineralogy and petrology of comet 81P/Wild 2 nucleus samples. Science 314, 1735–1739.

ARTICLE 10

Vinogradoff V., Fray N., Duvernay F., Briani G., Danger G., Cottin H., Theulé P. and Chiavassa T. (2013)

Importance of the thermal reactivity for hexamethylenetetramine (HMT) formation from simulated interstellar ices.

***Astronomy and Astrophysics*, 551, A128**

A&A 551, A128 (2013)
DOI: 10.1051/0004-6361/201220870

Astronomy & Astrophysics

Importance of thermal reactivity for hexamethylenetetramine formation from simulated interstellar ices

V. Vinogradoff[1], N. Fray[2], F. Duvernay[1], G. Briani[3], G. Danger[1], H. Cottin[2], P. Theulé[1], and T. Chiavassa[1]

[1] Université Aix-Marseille, PIIM: Laboratoire de Physique des Interactions Ioniques et Moléculaires, UMR CNRS 7345, Centre de St-Jérôme, Avenue Escadrille Normandie-Niemen, 13397 Marseille, France
e-mail: vassilissa.vinogradoff@etu.univ-amu.fr
[2] Université Paris Est Créteil (UPEC), Université Paris Diderot (UPD), LISA: Laboratoire Interuniversitaire des Systèmes Atmosphériques, UMR CNRS 7583, 61 Avenue du Général de Gaule, 94010 Créteil Cedex, France
e-mail: nicolas.fray@lisa.u-pec.fr
[3] Université Paris Sud, CSNSM: Centre de Spectrométrie Nucléaire et de Spectrométrie de Masse, UMR 8609 CNRS/IN2P3, bâtiment 104, 91405 Orsay Campus, France

Received 7 December 2012 / Accepted 23 January 2013

ABSTRACT

Context. Complex organic molecules are observed in a broad variety of astrophysical objects, but little is known about their formation mechanism. Laboratory simulations on interstellar ice analogues are therefore crucial for understanding the origin of these complex organic molecules. In this context, we focus on the thermal reactivity for the formation of the organic residue obtained after photolysis at 25 K of the interstellar ice analogue (H_2O:CH_3OH:NH_3) warmed to 300 K.
Aims. We determine the formation mechanism of one major product detected in the organic residue: hexamethylenetetramine (HMT). We compare the warming of the photolysed interstellar ice analogue with the warming of the two non-photolysed specific ice mixtures H_2CO:NH_3:HCOOH and CH_2NH:HCOOH, which are used as references. Using both general and specific approaches, we show the precise role of the UV photons and the thermal processing in the HMT formation.
Methods. We used Fourier transform infrared spectroscopy (FTIR) to monitor the chemical changes induced by the heating of the photolysed ice analogue and characterize some important species that will subsequently evolve in the formation of HMT in the residue.
Results. We show that the thermal processes play a key role in the HMT formation in photolysed ice analogues heated at 300 K. We identify the stable intermediates in the HMT formation that are formed during the warming: the aminomethanol (NH_2CH_2OH) and the protonated ion trimethyletriamine ($TMTH^+$, $C_3H_{10}N_3^+$). We also identify for the first time a new product in the organic residue, the polymethylenimine PMI (-(CH_2 -NH)$_n$). Results from this study will be interesting for the analysis of the forthcoming Rosetta mission.

Key words. astrochemistry – ISM: molecules

1. Introduction

Dense molecular clouds in the interstellar medium (ISM) are the sites of star formation. Within them, due to the low temperature, atoms and molecules from the gas phase condense on dust particles and form an icy mantle. In young stellar objects (YSOs) and molecular clouds, the composition of the icy mantle is dominated by H_2O, while CO, CO_2, CH_3OH, NH_3, and H_2CO are also commonly observed (Gibb et al. 2001, 2004; Knez et al. 2005; Boogert et al. 2008). In these environments, the icy mantle is exposed to energetic processing such as cosmic rays, UV photons, and thermal processes that trigger the chemical evolution of the ice composition, which leads to the formation of complex molecules. This is confirmed by several astronomical observations. Organic molecules are observed in a broad variety of ISM environments and in the solar system. For example, glycolaldehyde and formamide have been detected in the gas phase of hot cores by radio astronomy. There the temperature is high enough to allow ice sublimation, releasing molecules formed within interstellar (IS) ices (Danger et al. 2012a). Carbonaceous chondrites contain carboxylic acids, aromatic hydrocarbons, alcohols, and other organic molecules (Pizzarello et al. 2006). Comets are formed by agglomeration of dust particles from an interstellar and/or solar nebula origin in the outer parts of the solar nebula. They are also rich in organic molécules. Indeed, organic molecules have been detected in cometary grains by in-situ mass spectrometry (Kissel & Krueger 1987; Fomenkova et al. 1994; Kissel et al. 2004). The delivery of these organic species to the surface of the early Earth by comets may have provided the basic ingredients required for the origin of life (Oró 1961; Bernstein et al. 2002; Muñoz Caro et al. 2002).

Laboratory experiments that simulate the energetic and thermal processing of IS ice analogues show the formation of complex organic molecules. A small fraction of new refractory species is of high molecular mass, up to 4000 amu at room temperature (Danger et al. 2012b), this material is generally called refractory organic residue, or simply residue. Large organic compounds are produced either by ice photoprocessing (Agarwal et al. 1985; Briggs et al. 1992; Bernstein et al. 1995; Muñoz Caro & Schutte 2003; Muñoz Caro et al. 2004), by ion bombardment (Cottin et al. 2001; Strazzulla & Baratta 1992; Kobayashi et al. 1995; Kaiser & Roessler 1998), or by thermal processes (Bossa et al. 2009; Vinogradoff et al. 2011; Danger et al. 2011; Vinogradoff et al. 2013, 2012a).

Among the complex organic molecules that have been detected in this organic residue produced in the laboratory, hexamethylenetetramine (HMT, $C_6H_{12}N_4$, Fig. 1) has been observed by numerous authors (Bernstein et al. 1995; Muñoz Caro & Schutte 2003; Muñoz Caro et al. 2004; Cottin et al. 2001). It can reach up to 50% of residue mass. This molecule seems to

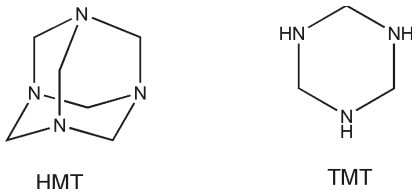

Fig. 1. Structures of HMT (hexamethylenetetramine $C_6H_{12}N_4$) and TMT (trimethylenetriamine $C_3H_9N_3$).

be of prime interest because its acid hydrolysis forms ammonia, formaldehyde, and amino-acids (Hulett et al. 1971). Thus, HMT may be a significant source of prebiotic compounds on the early Earth. HMT was proposed as a good tracer of photochemical processing in the pre-cometary phase (Bernstein et al. 1995) because it is supposed to be formed through the photolysis of the IS ice. However, it has already been shown that HMT could be formed after proton irradiation of H_2O:CO:CH_3OH:NH_3 ices (Cottin et al. 2001), or by only heating at room temperature, without any energetic processing (photons or particles), of H_2CO:NH_3:HCOOH ices (Vinogradoff et al. 2011, 2012b). Furthermore, Vinogradoff et al. (2011, 2012b) suggested that HMT formation could not be explained only by UV photolysis processes, but rather by UV and thermal activations from canonical H_2O:CO:CH_3OH:NH_3 ice mixture. Indeed, HMT would be an indicator of thermal processed ice rather than a photochemically processed one because of its formation mechanism.

The classical experimental approach in laboratory studies mainly focuses on residue composition (Bernstein et al. 1995; Muñoz Caro et al. 2004) but rarely on the chemistry induced during the reaction between 10 K and room temperature. The aim of this work is to understand the chemical changes during the warming of the photolysed ice mixture and especially the HMT formation, using two non-photolysed specific ice mixtures as comparative references. The idea is not to fully identify all species that are produced during the warming, but rather to focus on processes and intermediates that are crucial in the HMT formation from a H_2O:CH_3OH:NH_3 ice mixture. The molecular ratios we used here, between methanol and ammonia, are consistent with IS and cometary ice composition. H_2O is the main oxygen-bearing component, NH_3 is the main nitrogen-bearing component (around 10% with respect to water) and CH_3OH the most abundant organic molecule containing carbon, hydrogen, and oxygen (around 10% with respect to water) (Gibb et al. 2001, 2004; Knez et al. 2005; Boogert et al. 2008). We chose to exclude another important molecule, carbon dioxyde (CO_2), to simplify the analysis. Indeed, carbon dioxyde is known to thermally react in interstellar ice analogues with ammonia, forming carbamate (Bossa et al. 2008; Bertin et al. 2009).

In this study, we monitor the chemical changes induced by the heating of the photolysed ice and characterise some important species that subsequently evolve into the residue containing HMT. For the first time, we identify in a photolysed ice mixture, the major stable intermediates that lead to the formation of HMT at room temperature: the aminomethanol molecule (NH_2CH_2OH) and the protonated ion of trimethylenetriamine ($TMTH^+$, $C_3H_{10}N_3^+$) (see Fig. 1). We compare the thermal evolution after the photolysis of H_2O:CH_3OH:NH_3 ice mixtures (EXP1) with the warming of two non-photolysed specific ice mixtures H_2CO:NH_3:HCOOH (EXP2) and CH_2NH:HCOOH (EXP3), used as references (Vinogradoff et al. 2011, 2012b). Using both general and specific approaches, we show the precise role of the UV photons and the thermal processing in the HMT formation.

2. Experimental

To study the thermal evolution after the photolysis of an H_2O:CH_3OH:NH_3 ice mixture (EXP1), an experimental device similar to the one described in Allamandola et al. (1988), which was previously described in Le Roy et al. (2012), was used. A CsI window was cooled down to 25 K with a closed-cycle helium cryostat (Advanced Research Systems, Inc.). Its temperature, measured with two thermocouples (type E and Au-Fe-Cr), is adjustable by means of a resistive heater driven with a temperature controller (Lakeshore). This window is located inside a high-vacuum stainless steel chamber evacuated at about 10^{-8} mbar. In this device the infrared beam, for the analysis of the solid thin film, and the VUV beam for the photolysis are perpendicular to each other, and the CsI window is oriented at 45° of each beam, allowing simultaneous photolysis and analysis. Basically, gas mixtures can be injected to the vacuum chamber to be condensed on the CsI window cooled to 25 K and be simultaneously photolysed. The mixtures are prepared by filling two bulbs while their partial pressures are monitored.

The gas mixtures prepared for our experiments contain H_2O triply distilled, CH_3OH from Sigma-Aldrich 99.9% and NH_3 from Air Liquid 99.995%. In the first bulb, we prepared the H_2O:CH_3OH mixture in 10:1 proportions, which were then injected into the vacuum chamber to form ices with a condensation rate at about 10^{15} molecules $cm^{-2}\,s^{-1}$. The second bulb was filled only with ammonia. This was injected at the same time as the H_2O:CH_3OH mixture with a condensation rate of about 10^{14} molecules $cm^{-2}\,s^{-1}$, resulting in an ice mixture of H_2O:CH_3OH:NH_3 in 10:1:1 proportions. The condensation rates were calibrated according to preliminary experiments. The VUV photolysis was performed at the same time as the injection with a microwave-powered hydrogen-flow discharge lamp. This lamp was equipped with an MgF_2 window. The typical emission spectrum of this type of lamp is composed of the Lyman-α line of atomic hydrogen at 121.6 nm and of a broad emission band centred at about 160 nm generated by molecular hydrogen. Preliminary chemical actinometry experiments, performed with the protocol provided by Cottin et al. (2003), allowed us to measure a flux of about 10^{14} photons $cm^{-2}\,s^{-1}$ in our experimental setup. Thus, in this experiment we have a photon-to-molecule ratio of about 0.1. Each injection lasted approximately nine hours. After that time, injection and photolysis were stopped. Then, the two bulbs were refilled to prepared a new injection. This procedure was repeated six times to achieve an injection and photolysis time of 56 hours. After the photolysis, the ice mixture was warmed to 175 K, the heating rate being 2 K/min. Afterwards, to obtain a gentle ice sublimation, the heating rate was changed to 0.4 K/min, until the temperature reached 300 K. The infrared spectra were measured simultaneously to the warming and each spectrum was averaged on 256 scans between 4000 and 600 cm^{-1}.

For the two specific ice mixtures (EXP2 and EXP3), the experimental device is precisely described in Vinogradoff et al. (2012b). EXP2 is composed of H_2CO (heating of paraformaldehyde from Aldrich) NH_3 (99.9995% pure gas from Air Liquide) and HCOOH (from Acros Organics, 99% purity) molecules, the EXP3 mixtures contain CH_2NH (synthesized in the laboratory) and HCOOH molecules. The ice mixtures are deposited at 25 K and then warmed with a 4 K min^{-1} temperature rate up to 330 K with a temperature controller. Pure HMT was bought from Aldrich to register a pure HMT infrared spectrum and PMI (polymetheleneimine) was formed in situ in the ice mixture by

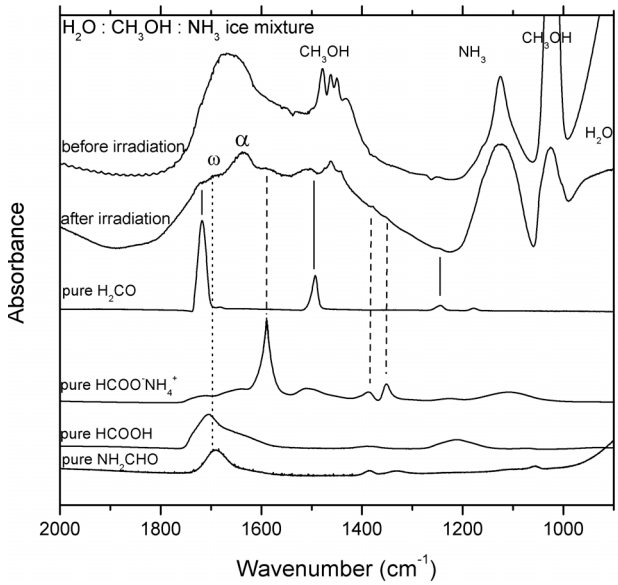

Fig. 2. Infrared spectra between 900 and 2000 cm^{-1} of the EXP1 ice mixture (H_2O:CH_3OH:NH_3=10:1:1). The spectrum before irradiation was measured after 10 min of ice deposition at 25 K without photolysis. Afterwards, we started the simultaneous ice deposition and photolysis for 56h at 25 K. The two spectra are compared with pure ice of H_2CO, $NH_4^+HCOO^-$, pure HCOOH, and pure NH_2CHO. ω is assigned to the broad band at 1710 cm^{-1} that could be a combination of the HCOOH and NH_2CHO bands, whereas α is tentatively assigned to the bending (OH) of water.

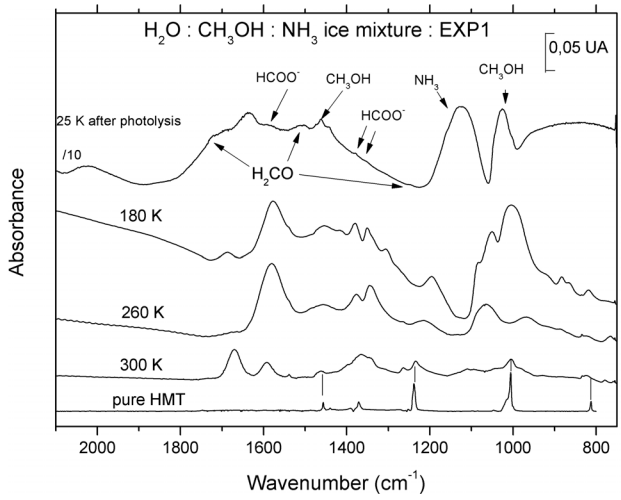

Fig. 3. Infrared spectra of the EXP1 ice mixture (H_2O:CH_3OH:NH_3 = 10:1:1) photolysed at 25 K (56h) followed by a warming at 180 K, 260 K, and 300 K, compared with pure HMT at 300 K.

sublimation of HMT (produced by the experiments) at 400 K, because PMI is more refractory, see Vinogradoff et al. (2012b).

3. Results and discussion

3.1. Photolysis of an interstellar/cometary ice mixture: H_2O:CH_3OH:NH_3 (EXP1)

Figure 2 shows infrared spectra of the EXP1 ice mixture composed of H_2O:CH_3OH:NH_3 = 10:1:1. The first spectrum was recorded after 10 min of ice deposition without irradiation at 25 K, while the second spectrum was measured after deposition and photolysis during 56 h at 25 K. We assigned most of the bands that are observed after photolysis at 25 K (Table 1). Two products can be securely assigned, formaldehyde, H_2CO, at 1723, 1502, and 1246 cm^{-1} (Schutte et al. 1993), and formate ion, $HCOO^-$, at 1585, 1378, and 1353 cm^{-1} (Schutte et al. 1999). No cations were securely attributed, nevertheless, ammonium ions (NH_4^+) are expected to be present and be the counter ion of $HCOO^-$, and could contribute to the structure at 1460 cm^{-1}. Indeed, it has been shown previously that at low temperature, the features of the formate ion are clearly observable, whereas those of NH_4^+ are too weak to be clearly discernible (Gálvez et al. 2010). An individual spectrum of each product is displayed in Fig. 2 for comparison. The formation of these compounds can be explained by the photo-dissociation of CH_3OH and H_2O and recombination of photoproducts. The photolysis of pure methanol at low temperature has been previously investigated by Öberg et al. (2009). They reported three photodissociation channels: CH_2OH+H, OCH_3 +H, and CH_3+OH with a photodissociation branching ratio of 5:1: < 1:

$CH_3OH + h\nu \longrightarrow CH_2OH^\bullet + H^\bullet$
$CH_3OH + h\nu \longrightarrow CH_3O^\bullet + H^\bullet$
$CH_3OH + h\nu \longrightarrow CH_3^\bullet + {}^\bullet OH.$

Subsequent photolysis and bond breaking form the formaldehyde, the HCO radical, and finally the carbon monoxyde:

$CH_3O^\bullet + h\nu \longrightarrow H_2CO + H^\bullet$
$H_2CO + h\nu \longrightarrow HCO^\bullet + H^\bullet$
$HCO^\bullet + h\nu \longrightarrow CO + H^\bullet.$

Ammonium formate is formed through low-temperature reaction of HCOOH and NH_3 (Schutte et al. 1999):

$HCOOH + NH_3 \longrightarrow NH_4^+HCOO^-.$

Although detecting of the formate ion is an indirect evidence of HCOOH formation, the bands of HCOOH cannot be unambiguously identified because they overlap with bands of formaldehyde, ammonia, and water in the 1800–1600 cm^{-1} region. Several solid-phase reaction channels have been proposed in the past decades to explain HCOOH formation from atomic recombinations (Tielens & Hagen 1982; Garrod & Herbst 2006). An alternative formation route has been experimentally proposed by Ioppolo et al. (2011). They observed the formation of HCOOH at low temperature mainly through hydrogenation of the HO-CO complex:

$CO + {}^\bullet OH \longrightarrow HO\text{-}CO \xrightarrow{H} HCOOH.$

This way to form HCOOH is the most likely here due to H_2O photolysis in the EXP1 experiment, and could explain why CO is not detected in our ice mixture. Another way to form HCOOH in solid phase has been shown by Hudson & Moore (1999), which invokes recombination of OH, produced by the photolysis of water, and HCO, coming from methanol via formaldehyde photolysis:

$HCO^\bullet + {}^\bullet OH \longrightarrow HCOOH.$

In the 1800–1600 cm^{-1} range we also observed bands of formamide NH_2CHO produced by the photolysis of ammonia and $HCO^\bullet$ radicals, leading to the contribution of the bands at 1710 cm^{-1}.

The ice mixture was then warmed and monitored by FTIR spectroscopy. After the H_2O, CH_3OH, and NH_3 sublimation, the infrared spectrum and the chemical composition of the ice mixture are greatly changed (Fig. 3), indicating that chemistry is occurring during the warming. At 180 K, we observe two strong bands, located at 1573 and 1002 cm^{-1} (Table 2). This could

Table 1. Assigned features of the infrared spectrum of the EXP1 ice mixture H_2O:CH_3OH:NH_3: = 10:1:1 after 56 h of VUV photolysis at 25 K.

		EXP1 25 K	
Wavenumber (cm^{-1})	Assignments	Species	References
1723	ν(CO)	H_2CO	Schutte et al. (1993)
1710	ν(CO)	HCOOH/NH_2CHO	Schutte et al. (1999)/Brucato et al. (2006)
1638	δ(OH)	H_2O	Palumbo (2005)*
1585	ν_{as}(COO^-)	$HCOO^-$	Schutte et al. (1999)
1502	δ(CH_2)	H_2CO	Schutte et al. (1993)
1460	δ(OH) / δ(NH)	CH_3OH / NH_4^+?	Schutte et al. (1999)
1378	δ_s (CH)	$HCOO^-$	Schutte et al. (1999)
1353	δ_{as} (CH)	$HCOO^-$	Schutte et al. (1999)
1246	ρ(CH_2)	H_2CO	Schutte et al. (1993)
1122	ω(NH)	NH_3	Kerkhof et al. (1999)
1024	ν(C-O)	CH_3OH	Kerkhof et al. (1999)
840 b	libration	H_2O	Palumbo (2005)*

Notes. Vibration mode: stretching (ν), bending (δ), rocking (ρ), inversion (ω). *as*: asymmetric mode, *s*: symmetric mode. * Tentatively assigned to water bands in a complex environment changing the position bands from pure water ice.

be associated to C-O/C-N stretching modes, while the band at 1573 cm^{-1} is assigned to the (COO^-) antisymmetric stretching mode of the formate ion $HCOO^-$. At 260 K the band at 1002 cm^{-1} disappears, leaving new products with bands at 1068, 1341, 1376, and 1580 cm^{-1} (Table 3). As the thermal processing continues, the most volatile compounds sublimate and leave at 300 K an organic residue characterised by a complex infrared spectrum. Nevertheless, some bands in the EXP1 residue agree well with characteristic bands of HMT ($C_6H_{12}N_4$), at 812, 1006, 1235, 1366, and 1462 cm^{-1} (Bernstein et al. 1994). This is not surprising because HMT is known to be one of the main components of organic residues formed from a canonical IS ice analogue (composed of H_2O:CH_3OH:NH_3:CO:CO_2) photolysed at low temperature and warmed to room temperature (Bernstein et al. 1995; Schutte 2002; Bernstein et al. 1997; Cottin et al. 2001; Muñoz Caro & Schutte 2003; Muñoz Caro et al. 2004). Knowing that the warming of the different molecules of the ice mixture CH_3OH:NH_3/H_2O sublime without any reaction, we deduce that the photolysis products are the precursors of HMT. In the following section we show each step of the formation of the intermediates needed for the HMT production during the warming of the photolysed IS ice analogue.

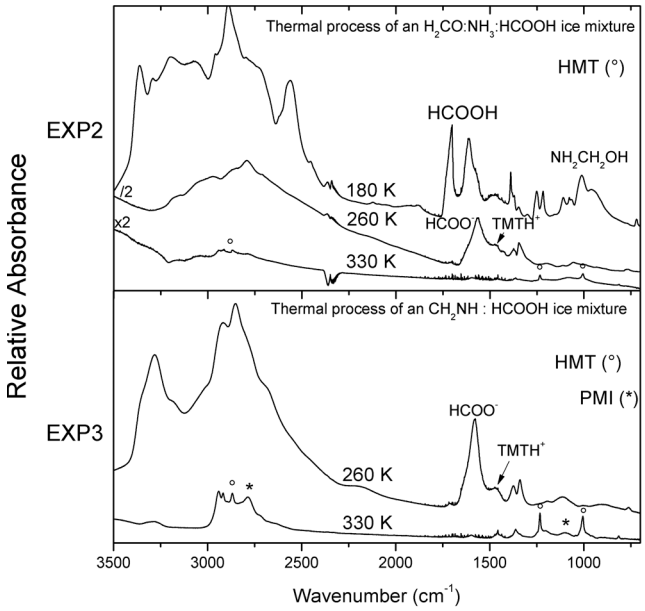

Fig. 4. Infrared spectra of the EXP2 ice mixture (H_2CO:NH_3:HCOOH) warmed at 180, 260, and 330 K and the EXP3 ice mixture (CH_2NH:HCOOH) warmed at 260 and 330 K, no photolysis.

3.2. HMT precursor identification

3.2.1. Formation of HMT from the precursors by thermal processes: dedicated experiments EXP2, and EXP3

HMT can be synthesised by thermal processes if specific ice compositions are selected (Vinogradoff et al. 2011). The reactant molecules were chosen on the basis of the molecules formed after the photolysis of the H_2O:CH_3OH:NH_3 ice mixture described above (Table 1). We report in Fig. 4 the thermal evolution of the two dedicated experiments.

The first dedicated experiment (EXP2) is the heating of an H_2CO:NH_3:HCOOH ice mixture (Fig. 4). After warming at 180 K, the formation of aminomethanol (NH_2CH_2OH) and formate ion ($HCOO^-$) is observed. The aminomethanol is formed from the nucleophilic addition reaction of ammonia and formaldehyde (Bossa et al. 2009), and is detected in two bands at 1002 and 3366 cm^{-1}. The formate ion is formed via acid-base reaction between formic acid (HCOOH) and ammonia. Then, the methylenimine (CH_2NH) should be formed through a dehydration process of the aminomethanol in the presence of HCOOH (Vinogradoff et al. 2012b). Unfortunately, this latter intermediate is never observed due to its high reactivity, but instead polymerises, giving a new intermediate: the cyclic trimer of CH_2NH, the trimethylenetriamine (TMT, $C_3H_9N_3$, Fig. 1), the first cycle of HMT structure, in its protonated form $TMTH^+$ (Vinogradoff et al. 2012b). Indeed, at 260 K, almost pure $TMTH^+HCOO^-$ species stay on the substrate since the volatile compounds have desorbed (see Fig. 4). Finally, at 330 K $TMTH^+HCOO^-$ is converted into HMT. The first dedicated experiment (EXP2) points out the expected presence of methylenimine as a chemical intermediate. To confirm this hypothesis, a second dedicated experiment (EXP3) dealt with this expected intermediate: the heating of a CH_2NH:HCOOH ice mixture. At 260 K, as for the first experiment, after the warming we observed $TMTH^+HCOO^-$ salt. At 330 K, we observed not only the features of HMT but also another product, the PMI, polymethylenimine polymer (Fig. 4). PMI is a polymer identified by Danger et al. (2011) and Vinogradoff et al. (2012b) in ice mixtures containing methylenimine, CH_2NH. Interestingly, the pure imine (CH_2NH) does not

Table 2. Assigned features of the infrared spectrum of the EXP1 ice mixture H_2O:CH_3OH:NH_3 = 10:1:1 after 56 h of VUV photolysis at 25 K and warmed at 180 K.

EXP1 180 K			
Wavenumber (cm^{-1})	Assignments	Species	References
3366	ν(NH)	NH_2CH_2OH	Bossa et al. (2009)
1686	ν(C=O)	RCOOH	
1573	$\nu(COO^-)$	$HCOO^-$	Schutte et al. (1999)
1454 b	δ(NH)	NH_4^+	Vinogradoff et al. (2012b)
1380	δ_s(CH)	$HCOO^-$	Schutte et al. (1999)
1351	δ_{as}(CH)	$HCOO^-$	Schutte et al. (1999)
1002	ν(C-N)	NH_2CH_2OH	Bossa et al. (2009)

Notes. Vibration mode: stretching (ν), bending: δ_s. broad (b).

Table 3. Assigned features of the infrared spectrum of the EXP1 ice mixture (H_2O:CH_3OH:NH_3 = 10:1:1) after 56 h of VUV photolysis at 25 K and warmed at 260 K.

EXP1 260 K			
Wavenumber (cm^{-1})	Assignments	Species	References
1580	$\nu(COO^-)$	$HCOO^-$	Vinogradoff et al. (2012b)
1464	δ(CNH)	$TMTH^+$	Vinogradoff et al. (2012b)
1376	ρ_s(CH)	$HCOO^-$	Vinogradoff et al. (2012b)
1341	ν_s(C=O)/ρ_{as}(CH)	$HCOO^-$	Vinogradoff et al. (2012b)
1215	ν(C-N)	unknown	
1068	ν(C-N)	unknown	
964	?	unknown	
766	$\rho_s(NH_2)$/ δ(OCO)	$HCOO^-$/$TMTH^+$	Vinogradoff et al. (2012b)

Notes. Vibration mode: stretching (ν), bending (δ), rocking (ρ), *as*: asymmetric mode, *s*: symmetric mode.

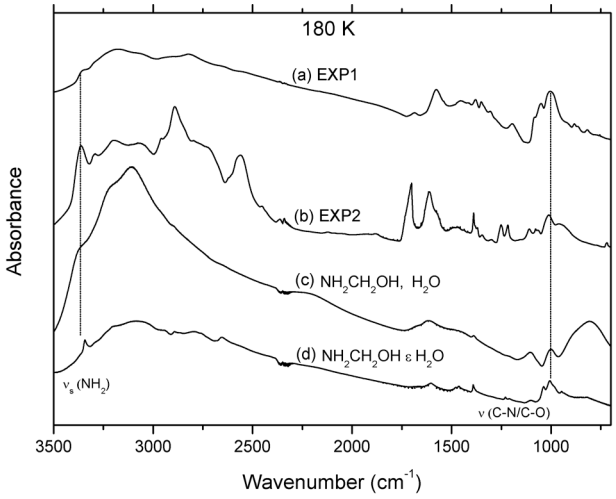

Fig. 5. Infrared spectra of: **a)** EXP1 ice mixture (H_2O:CH_3OH:NH_3= 10:1:1) after photolysis and warmed at 180 K, **b)** EXP2 ice mixture (H_2CO:NH_3:HCOOH) warmed at 180 K, compared with infrared spectrum of NH_2CH_2OH formed from warming of the H_2CO:NH_3:H_2O ice mixture at **c)** 180 K and **d)** 190 K (with some residual water).

lead to HMT in the interstellar-like conditions (Vinogradoff et al. 2012b) and has to be catalysed by the formic acid. Thus HCOOH plays a double catalytic role in HMT formation, (i) for the dehydration of aminomethanol, and (ii) for the cyclisation until HMT (Vinogradoff et al. 2011, 2012b).

3.2.2. Warming the EXP1 ice mixture at 180 K: identification of NH_2CH_2OH

Four spectra are shown in Fig. 5: a) the photolysed ice mixture (EXP1) warmed at 180 K; b) the first specific ice mixture H_2CO:NH_3:HCOOH (EXP2) warmed at 180 K; c) NH_3:H_2CO:H_2O ice mixture warmed at 180 K, and d) NH_3:H_2CO:H_2O ice mixture warmed at 190 K. Spectra c) and d) in Fig. 5 refer to the aminomethanol formation from the warming of NH_3:H_2CO:H_2O ice mixture, according to the procedure described by Bossa et al. (2009), before and after water sublimation. These two spectra are considered as reference spectra of aminomethanol below. They show that the ice environment has a significant influence on the aminomethanol infrared spectrum. Indeed, the two characteristic bands of aminomethanol located around 3366 and 1002 cm^{-1} are significantly broader in water environment than in the pure solid (Fig. 5c,d). Both these features at 1002 cm^{-1} and 3366 cm^{-1} are clearly defined in the spectra of EXP1 and EXP2 (see Fig. 5, Table 2), showing that the warming process of the different ice mixtures leads to the aminomethanol formation.

It is worth mentioning that both EXP1 and EXP2 do contain other products. In the photolysed ice mixture (EXP1) spectrum (Fig. 5a), we observe a strong band at 1573 cm^{-1} corresponding to the $HCOO^-$ ion (Schutte et al. 1999) as well as a feature at 1686 cm^{-1}, which could be tentatively assigned to a carboxylic acid (perhaps to formic acid (HCOOH) – Table 2). This ion could be associated with NH_4^+, which is consistent with the broad band at 1454 cm^{-1} (Table 2). The warming of the photolysed ice mixture (EXP1) has enabled the aminomethanol formation through the thermal reaction between formaldehyde generated during the UV photolysis and ammonia. NH_2CH_2OH is the first intermediate in the HMT mechanism (Vinogradoff et al. 2011), and as mentioned above, since HCOOH is also tentivately detected at 180 K, a road toward HMT is opened.

$$\left.\begin{matrix}CH_3OH\\NH_3\\H_2O\end{matrix}\right\} \xrightarrow{h\nu} H_2CO{+}HCOOH{+}NH_3 \xrightarrow{T>70\ K} NH_2CH_2OH.$$

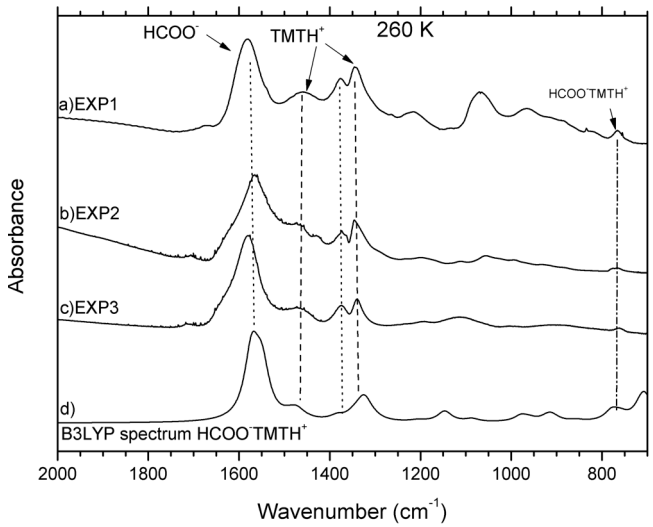

Fig. 6. Infrared spectra of the three mixtures at 260 K, between 2000−700 cm^{-1}: **a)** EXP1 (H_2O:CH_3OH:NH_3) ice mixture after photolysis and warmed at 260 K, **b)** H_2CO:NH_3:HCOOH ice mixture only warmed at 260 K, and **c)** CH_2NH:HCOOH ice mixture only warmed at 260 K, compared with the B3LYP spectrum of $HCOO^-TMTH^+$ salt (from Vinogradoff et al. 2012b).

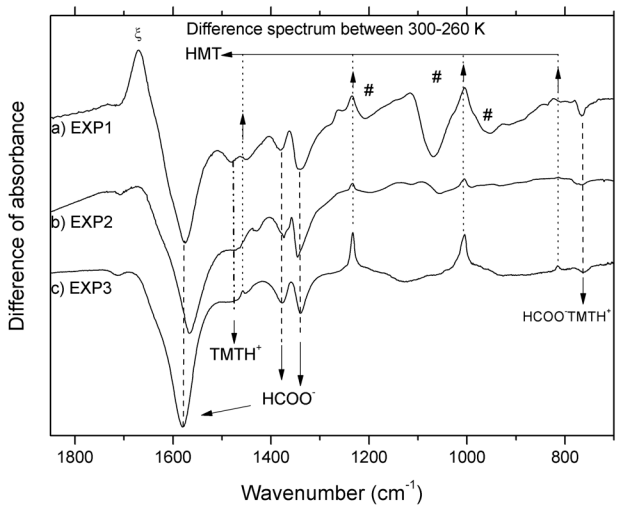

Fig. 7. Infrared spectra of the difference 300 K (presented in Fig. 8) minus 260 K (presented in Fig. 6) (1/1), **a)** H_2O:CH_3OH:NH_3 ice mixture, **b)** H_2CO:NH_3:HCOOH ice mixture, and **c)** CH_2NH:HCOOH ice mixture. # and ξ refer to unknown compounds in the EXP1 ice mixture, photolysed and warmed.

3.2.3. Warming the EXP1 ice mixture at 260 K: identification of the $TMTH^+$ ion

As the temperature is increased from 180 K to 260 K, the infrared spectrum of the photolysed ice mixture (EXP1) is greatly modified, indicating changes in the ice composition due to both sublimation of volatiles and reactivity induced by thermal activation. Between 180 and 260 K, the aminomethanol features disappear. The features of the formate ion, detected at lowest temperatures, are still clearly observed although they have slightly shifted. This shift could be due in part to the warming but it is mainly assigned to a change of the counter ion of $HCOO^-$. Indeed, the nature of the new counter ion has been revealed using quantum calculation (Vinogradoff et al. 2012b). In Fig. 6d, the calculated infrared spectrum of the $TMTH^+HCOO^-$ is shown. The $TMTH^+HCOO^-$ infrared spectrum is dominated by strong bands located at 1580, 1464, 1376, 1341, and 766 cm^{-1} (Fig. 6, Table 3). These bands are clearly seen in the spectrum of the photolysed ice mixture (EXP1) recorded at 260 K attesting the $TMTH^+$ formation during the warming of the photolysed ice mixture. The attribution of the 1464 cm^{-1} band to the $TMTH^+$ is consolidated by the observation of the same band in the infrared spectra recorded at 260 K after the warming of the HCOOH:CH_2NH ice mixture (EXP3). Furthermore, $TMTH^+$ is also detected in the spectrum at 260 K of the first dedicated experiment (EXP2), starting with an H_2CO:NH_3:HCOOH ice mixture. Because we already detected NH_2CH_2OH in these experiments, it shows that CH_2NH comes from the dehydration of NH_2CH_2OH by HCOOH. This dehydration was verified using mass spectrometry (see Vinogradoff et al. 2012b, for details). Some additional bands are observed in the photolysed EXP1 ice mixture, at 964, 1068, and 1215 cm^{-1} and are certainly due to other products in ice mixture (Table 3).

$$NH_2CH_2OH \xrightarrow[HCOOH]{T>180\ K} [CH_2NH] \rightarrow TMTH^+HCOO^- + ?$$

3.2.4. HMT formation at 300 K and comparison between the three residues

The thermal evolutions between 260 K and 300 K (or 330 K) of the three ice mixtures (EXP1, EXP2, and EXP3) are reported in Fig. 7. The difference spectra were obtained by subtracting spectra recorded at 300 K (EXP1) or 330 K (EXP2 and EXP3) and the one at 260 K, with a 1/1 ratio. In Fig. 7, spectrum a) refers to the photolysed ice mixture (H_2O:CH_3OH:NH_3), spectra b) and c) refer to the two specific ice mixtures H_2CO:NH_3:HCOOH and CH_2NH:HCOOH. The negative bands attest to the loss of the compounds (by chemical reaction or their sublimation), while the positive bands attest to the formation of new compounds that occur in this temperature range. The positive bands observed at 812, 1006, 1235, and 1462 cm^{-1} are due to the HMT formation (dotted line) while negative bands at 1580, 1464, 1376, 1341, and 766 cm^{-1} indicate the disappearance of $TMTH^+HCOO^-$ between 260 K and 300 K (Fig. 7a, dashed line).

The infrared spectrum of the organic residue remaining at 300 K, after the photolysis and the warning of the ice, is very complex and its evolution between 260 and 300 K is not fully understood. As an example, an unknown product with a feature at 1670 cm^{-1} appeared while at least one molecule with bands at 950, 1050 and 1210 cm^{-1} disappeared. However, the thermal evolution between 260 K and 300 K of the three experiments presented here follows the same trend: HMT formation and the decrease of the $TMTH^+HCOO^-$ species. This observation shows that HMT is synthetised from $TMTH^+$ and the chemistry leading to HMT in this three experiments is identical:

$$TMTH^+HCOO^- \xrightarrow{T > 290\ K} HMT(s) + HCOOH\ (g).$$

The HCOOH release has been verified by mass spectrometry for EXP2 and EXP3 (see Vinogradoff et al. 2012b).

We report in Fig. 8 the infrared spectra of the three organic residues at room temperature. In this figure, the first residue (a) is formed from the photolysed ice mixture. The second (b) and the third one (c) are obtained from the heating of the specific ice mixtures, H_2CO:NH_3:HCOOH and CH_2NH:HCOOH. These residues are compared to pure HMT (d) and pure PMI (e) in the same experimental conditions. Infrared bands as well as

Table 4. Assigned features of the infrared spectrum of the EXP1 ice mixture (H_2O:CH_3OH:NH_3 = 10:1:1) after 56 h of VUV photolysis at 25 K and warmed at 300 K.

EXP1 300 K			
Wavenumber (cm^{-1})	Assignments	Species	References
2872	ν(CH)	HMT	Bernstein et al. (1994)
1670	ν(C=O)	Amide, RCOOH	
1592	ν(COO^-)	$HCOO^-$	Schutte et al. (1999)
1462	δ(CH,NH)	HMT	Bernstein et al. (1994)
1366	δ(CH)	HMT	Bernstein et al. (1994)
1235	ν(C-N)	HMT	Bernstein et al. (1994)
1209	ν(C-N)	PMI	Vinogradoff et al. (2012b)
1091	ν(C-N)	PMI	Vinogradoff et al. (2012b)
1006	ν(C-N)	HMT	Bernstein et al. (1994)
970	ν(C-N)	PMI	Vinogradoff et al. (2012b)
812	ωNH	HMT	Bernstein et al. (1994)
779	δ(OCO)	$HCOO^-$	Schutte et al. (1999)

Notes. Vibration mode: stretching (ν), bending (δ), inversion (ω).

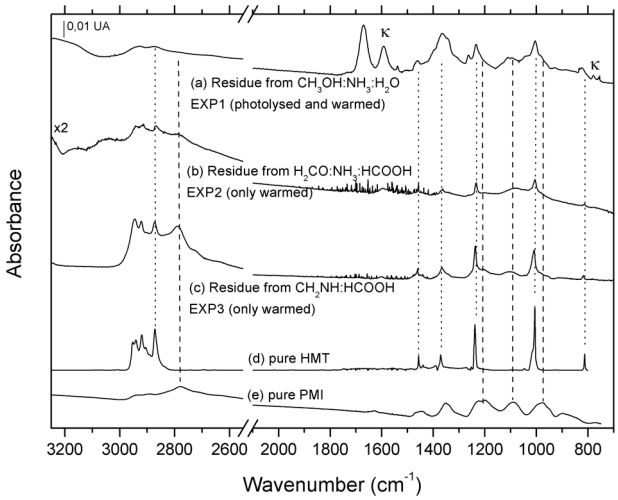

Fig. 8. Infrared spectra of three residues at 300 K, **a)** from H_2O:CH_3OH:NH_3 ice mixture photolysed at 25 K and warmed until 300 K, **b)** from H_2CO:NH_3:HCOOH ice mixture only warmed until 330 K, and **c)** from CH_2NH:HCOOH ice mixture only warmed until 330 K, compared with **d)** pure HMT in the same experimental conditions at 260 K, and **e)** pure PMI in the same experimental conditions at 500 K. κ sign to remaining $HCOO^-$ in the ice mixture.

vibrational assignments of the residue produced from the photolysed and subsequent warming of the EXP1 ice mixture are reported in Table 4. In the spectrum of this residue, we unambiguously observed the characteristic bands of HMT (dotted lines) located at 812, 1006, 1235, 1366, 1462, and 2872 cm^{-1} (Bernstein et al. 1994). We can say without doubt that a part of this organic residue is composed of HMT. Moreover, the broad bands at 970, 1091, and 1209 cm^{-1} can be assigned to PMI. Because PMI is a polymer of CH_2NH (inevitable molecule in the HMT formation), it is not surprising to observe it. We also observed two bands at 1592 and 779 cm^{-1} (Fig. 8a) that might be assigned to the remaining formate ion (κ sign) trapped in the ice mixture. Unfortunately, we cannot attribute the band at 1670 cm^{-1} to a specific molecule; it could be due to amides, carboxylic acid, or carbamate, see Bossa et al. (2008). We can note that a similar band has already been observed by Bernstein et al. (1995).

Despite the different starting material and different energetic processing, the warming of the photolysed ice mixture leads to HMT and PMI as well as to the two dedicated experiments in which H_2CO:NH_3:HCOOH and CH_2NH:HCOOH ice mixtures are only warmed (see Fig. 8). It has to be noted that pure HMT sublimates in our experimental conditions at around 260 K, while the HMT observed in the three residues is still present at 300 K. The formation of highly refractory compounds such as PMI trap the HMT in a complex refractory matrix that delays the sublimation of HMT.

3.3. Discussion

Laboratory experiments simulating the energetic and thermal processing of interstellar ice analogues are crucial for understanding the chemical evolution of materials from the ISM to planetary systems. In this work, an H_2O:CH_3OH:NH_3 10:1:1 ice mixture was submitted to VUV photons and was subsequently warmed, with the intention to simulate the interstellar ice evolution. Such processes could happen for the IS ice during the collapse and formation of proto-stellar cores or in the solar system. When warmed to room temperature, the photolysed IS ice analogues produces an organic residue, which is assumed to be a close analogue of organic compounds present in comets.

The thermal processes are often neglected but they affect the bulk and the surface composition of ice, although UV photons affect only the surface composition.

In this study, we chose to focus on the chemical mechanisms induced by thermal processes that lead to the formation of only one precise molecule, unambiguously detected in these residues: HMT. To understand the chemical evolution induced by the warming, we used two dedicated experiments in which ice mixtures were only warmed, leading to a simpler chemical evolution than in the photolysis experiment. These two dedicated experiments started with a deposit of H_2CO:NH_3:HCOOH and CH_2NH:HCOOH ice mixtures at low temperature. With these dedicated experiments, we showed that two intermediates, aminomethanol (NH_2CH_2OH) and $TMTH^+$ (protonated form of the trimethylenetriamine, $C_3H_{10}N_3$), are formed during the warming of the photolysed ice analogue. HMT is only formed at about 280–290 K from the last stable intermediate, the $TMTH^+$. The neutral form of this intermediate was postulaled by Bernstein but was never characterised due to the lack of spectroscopic data. Moreover, the decrease of a band at about 1460 cm^{-1} correlated with the appearance of the HMT at room temperature was previously observed by Muñoz Caro & Schutte (2003); unfortunately, because the infrared spectrum of

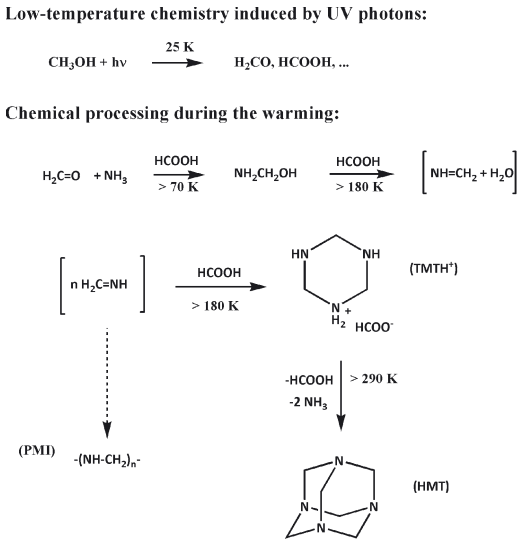

Fig. 9. Mechanism of HMT formation induced by UV photons and thermal activation from interstellar ice analogues.

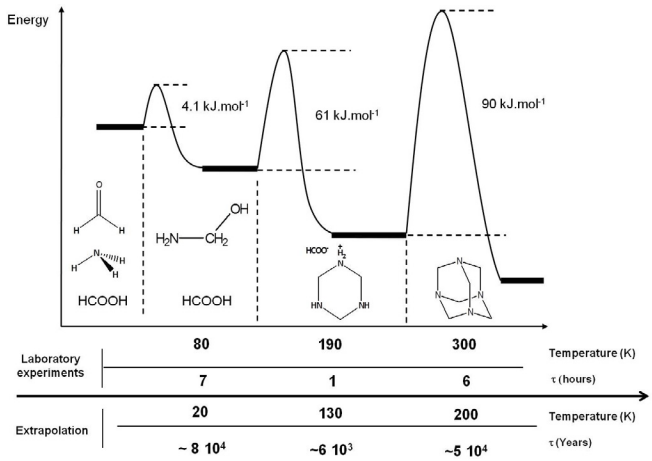

Fig. 10. Summary of HMT formation: representation of the activation barriers for the different intermediates (calculated with B3LYP/6-31G** and adapted from Vinogradoff et al. 2012b) with the corresponding temperature and time (τ) to form the intermediates in laboratory experiments. The extrapolation temperature and time were calculated by an Arrhenius law.

the $TMTH^+$ ion was not known at that time, they misattributed this band to the ammonium ion NH_4^+.

The mechanism of HMT formation is presented in Fig. 9 and has been split into two parts: the first part corresponds to the H_2CO and HCOOH production from CH_3OH and H_2O photolysis and occurs only at low temperature, while the second part is purely activated by the warming from 25 K to 300 K. Interestingly, the mechanism presented here is not so different from the one reported by Bernstein et al. (1995), based on the HMT formation in liquid phase.

The first difference comes from the presence of formic acid, which acts as a catalyst and stabilizer for two important steps. For $T > 180$ K, HCOOH allows the polymerisation of methylenimine, and then the formation of the salt $TMTH^+HCOO^-$, which maintain the molecule (TMT) needed at higher temperature to form HMT. The second main difference is the final cyclisation of TMT to form HMT. Bernstein et al. (1995) proposed, based on the mechanism in liquid phase, that additional reactions of TMT with formaldehyde and/or ammonia would lead to HMT just after the irradiation process at around 50 K. However, we showed that TMT is formed at around 180 K in laboratory conditions, a temperature at which both formaldehyde and ammonia have already sublimated. Instead, theoretical calculations show that the final cyclisation of HMT is the reaction between TMT and its decomposition products (precise mechanism can be found in Vinogradoff et al. 2012b) at only 290 K in laboratory conditions.

Moreover, Bernstein et al. (1995) mentioned that the reaction needs to be activated by UV photons because of the high activation barriers required to form HMT. But, the activation barriers are significantly reduced by the action of HCOOH, which acts as a catalyst that allows the reaction to proceed to the solid state (Fig. 10). Consequently, photons are only crucial to form formaldehyde and formic acid from methanol, and HMT is thermally formed from the right reactants, namely formaldehyde, ammonia, and formic acid, as shown by the EXP2.

In addition, we demonstrated that the residue also contains a polymer of methylenimine (PMI) that was previously postulated by Bernstein et al. (1995) but was never characterised experimentally due to the lack of spectroscopic data on this polymer at that time.

Hence, we showed the importance of studying only one energetic process at a time (photons or temperature) if we aim to fully understand the nature of the residue as well as the chemical processes that drive its formation. This study showed that HMT is no direct product of the photolysis but that its formation requires a warming at about 280 K (in laboratory conditions) because of the presence of a high activation barrier during the last step of the HMT synthesis (Fig. 10).

While HMT has already been detected in organic residue produced in laboratory for a long time, it has never been observed in astrophysical objects so far. We showed that HMT is synthesised only at a relatively high temperature: about 280 K in laboratory conditions in less than one day. In the interstellar medium, where reactions can occur on a much longer time scale, one might conclude that HMT could be formed at a lower temperature. Accordingly, we roughly extrapolated our results so that they match the ISM time scale (Fig. 10). We extrapolated our experimental laboratory conditions with an Arrhenius law, as shown in Fig. 10, by taking

$$k(T) = \frac{1}{\tau(T)} = A e^{\frac{-Ea}{RT}} \quad (1)$$

$$\frac{k(T1)}{k(T2)} = \frac{\tau(T2)}{\tau(T1)} = e^{\frac{-Ea}{R}\left(\frac{1}{T1}-\frac{1}{T2}\right)}, \quad (2)$$

with Ea the activation energy, R the universal gas constant, $T1$ the laboratory temperature, $T2$ the extrapolation temperature, and τ the time of formation. From the activation barriers for each intermediate, we are able to calculate an approximate formation time for each molecule as a function of temperature. The different temperatures were chosen to represent different interstellar objects, such as molecular clouds (around 20 K), proto-stellar environment (around 130 K), and proto-planetary disk or comets/asteroids in the inner solar-system environment for 200 K. In these conditions we estimate that HMT could be formed after 5×10^4 years at 200 K and that $TMTH^+$ could be found in colder (130 K) interstellar objects after 6×10^3 years. This extrapolation intends to give an idea about the formation kinetics in the ISM for HMT and its precursors if we exclude the presence of other molecules and/or other energetic processes and/or desorption processes in the grains. Nonetheless,

the Fig. 10 extrapolation shows that HMT could be detected in objects that have been submitted to thermal processing but not necessarily at temperatures as high as in our experiments.

Moreover, because HMT is transformed into amino acids through acid hydrolysis during an extraction process (Hulett et al. 1971), it could not be detected in meteoritic sample. Therefore, several reasons can be proposed to explain the present non-detection of HMT in astrophysical objects, first because of the specific conditions of its formation mechanism and second because of the aqueous and thermal alteration on the meteorite parent bodies that transform HMT into amino acids.

Furthermore, results from this study will be interesting for the analysis of the forthcoming Rosetta mission, which will perform in-situ analyses of the comet 67P/Churyumov-Gerasimenko. We showed that the HMT formation proceeds from several intermediates and that their domain of thermodynamical stability differs from one to the other. Thus, all these compounds, i.e. HMT, TMT, methylenimine, and aminomethanol, have to be searched for. At the nucleus surface, these compounds may be detected with the COSAC instrument (a gas chromatograph coupled with a time-of-flight mass spectrometer) onboard the Philae lander. In the cometary environment, HMT and its precursors can be searched for by mass spectrometry in solid as well as in gas phase with the COSIMA and ROSINA instruments, respectively. A detection of HMT or of one of its precursor in comet 67P/C-G could be used as a probe to estimate the maximal temperature range reached by cometary matter.

4. Conclusion

We showed that thermal processes play a key role in the HMT formation in photolysed ice analogues heated at 300 K. Using general and dedicated approaches, we showed the precise role of the UV photons and the thermal processing in the HMT formation. At low temperature UV photons are necessary for the formation of formaldehyde (H_2CO) and formic acid (HCOOH). Subsequent warming allows the reaction between formaldehyde and ammonia to produce aminomethanol (NH_2CH_2OH), which is the first intermediate towards the HMT synthesis. Then methylenimine (CH_2NH) is formed through the dehydration of aminomethanol catalysed by formic acid. Additional warming enables the conversion of methylenimine into TMT and then HMT. This chemical mechanism was revealed with a dedicated experiment in which the reactants were carefully chosen to clarify the different steps of this mechanism. It showed that HMT formation occurs after warming at about 280 K and not as a direct photolysis product. Thus, we predict that HMT may be present only in astrophysical media that have been thermally processed. We also identified for the first time a new product in the organic residue, the PMI (-(CH_2 - $NH)_n$-). Results from this study will be interesting for the analysis of the forthcoming Rosetta mission. We underline that HMT as well as its precursors have to be searched for by in-situ analyses in solid and gas phases in the cometary environment and nucleus. The detection of one or several of these compounds could give constraints on the maximum temperature as well as time heating reached by the organic matter that is to be analysed.

Acknowledgements. We acknowledge the CNES (Centre national des études spatiales), INSU (Institut national des Sciences de l'Univers) EPOV (Environnement planétaire et origines de la vie) and PCMI (Physique Chimie du Milieu Interstellaire) French programs for their financial support. This work has also been funded by the Provence Alpes Côtes d'Azur (PACA) region.

References

Agarwal, V., Schutte, W., Greenberg, J., et al. 1985, Origins of Life and Evolution of Biospheres, 16, 21
Allamandola, L., Sandford, S., & Valero, G. 1988, Icarus, 76, 225
Bernstein, M., Sandford, S., Allamandola, L., & Chang, S. 1994, J. Phys. Chem., 98, 12206
Bernstein, M., Allamandola, L., & Sandford, S. 1997, Adv. Space Res., 19, 991
Bernstein, M., Dworkin, J., Sandford, S., et al. 2002, Nature, 416, 401
Bernstein, M., Sandford, S., Allamandola, L., Chang, S., & Scharberg, M. 1995, ApJ, 454, 327
Bertin, M., Martin, I., Duvernay, F., et al. 2009, Phys. Chem. Chem. Phys., 11, 1838
Boogert, A., Pontoppidan, K., Knez, C., et al. 2008, ApJ, 678, 985
Bossa, J., Theulé, P., Duvernay, F., Borget, F., & Chiavassa, T. 2008, A&A, 492, 719
Bossa, J., Theule, P., Duvernay, F., & Chiavassa, T. 2009, ApJ, 707, 1524
Briggs, R., Ertem, G., Ferris, J., et al. 1992, Origins of Life and Evolution of Biospheres, 22, 287
Brucato, J., Baratta, G., & Strazzulla, G. 2006, A&A, 455, 395
Cottin, H., Szopa, C., & Moore, M. 2001, ApJ, 561, L139
Cottin, H., Moore, M., & Bénilan, Y. 2003, ApJ, 590, 874
Danger, G., Borget, F., Chomat, M., et al. 2011, A&A, 535, A47
Danger, G., Duvernay, F., Theulé, P., Borget, F., & Chiavassa, T. 2012a, ApJ, 756, 11
Danger, G., Orthous-Daunay, F.-R., de Marcellus, P., et al. 2012b, Geochim. Cosmochim. Acta, submitted
Fomenkova, M., Chang, S., & Mukhin, L. 1994, Geochim. Cosmochim. Acta, 58, 4503
Gálvez, O., Maté, B., Herrero, V., & Escribano, R. 2010, ApJ, 724, 539
Garrod, R., & Herbst, E. 2006, A&A, 457, 927
Gibb, E., Whittet, D., & Chiar, J. 2001, ApJ, 558, 702
Gibb, E., Whittet, D., Boogert, A., & Tielens, A. 2004, ApJS, 151, 35
Hudson, R., & Moore, M. 1999, Icarus, 140, 451
Hulett, H., Wolman, Y., Miller, S., et al. 1971, Science, 174, 1038
Ioppolo, S., Cuppen, H., van Dishoeck, E., & Linnartz, H. 2011, MNRAS, 410, 1089
Kaiser, R., & Roessler, K. 1998, ApJ, 503, 959
Kerkhof, O., Schutte, W., & Ehrenfreund, P. 1999, A&A, 346, 990
Kissel, J., & Krueger, F. 1987, Nature, 326, 755
Kissel, J., Krueger, F., Silén, J., & Clark, B. 2004, Science, 304, 1774
Knez, C., Boogert, A., Pontoppidan, K., et al. 2005, ApJ, 635, L145
Kobayashi, K., Kasamatsu, T., Kaneko, T., et al. 1995, Adv. Space Res., 16, 21
Le Roy, L., Briani, G., Briois, C., et al. 2012, Planet. Space Sci., 65, 83
Muñoz Caro, G., & Schutte, W. 2003, A&A, 412, 121
Muñoz Caro, G., Meierhenrich, U., Schutte, W., et al. 2002, Nature, 416, 403
Muñoz Caro, G., Meierhenrich, U., Schutte, W., Thiemann, W., & Greenberg, J. 2004, A&A, 413, 209
Öberg, K., Garrod, R., van Dishoeck, E., & Linnartz, H. 2009, A&A, 504, 891
Oró, J. 1961, Nature, 190, 389
Palumbo, M. 2005, J. Phys.: Conf. Ser., 6, 211
Pizzarello, S., Cooper, G., & Flynn, G. 2006, Meteorites and the early solar system II, 625
Schutte, W. 2002, Adv. Space Res., 30, 1409
Schutte, W., Allamandola, L., & Sandford, S. 1993, Icarus, 104, 118
Schutte, W., Boogert, A., Tielens, A., et al. 1999, A&A, 343, 966
Strazzulla, G., & Baratta, G. 1992, A&A, 266, 434
Tielens, A., & Hagen, W. 1982, A&A, 114, 245
Vinogradoff, V., Duvernay, F., Danger, G., Theulé, P., & Chiavassa, T. 2011, A&A, 530, A128
Vinogradoff, V., Duvernay, F., Farabet, M., et al. 2012a, J. Phys. Chem. A, 116, 2225
Vinogradoff, V., Rimola, A., Duvernay, F., et al. 2012b, Phys. Chem. Chem. Phys., 14, 12309
Vinogradoff, V., Duvernay, F., Danger, G., et al. 2013, A&A, 549

ARTICLE 11

Briani G., Fray N., Cottin H., Benilan Y., Gazeau M.-C. and Perrier S.

HMT production and sublimation during thermal process of cometary organic analogs. Implications for its detection with the ROSETTA instruments.

Icarus, submitted.

HMT production and sublimation during thermal process of cometary organic analogs. Implications for its detection with the ROSETTA instruments.

Giacomo Briani[a,1], Nicolas Fray[a], Hervé Cottin[a], Yves Benilan[a], Marie-Claire Gazeau[a], Sebastien Perrier[a]

[a]Laboratoire Interuniversitaire des Systèmes Atmosphériques (LISA)
UMR 7583 du CNRS
Université Paris Est – Créteil (UPEC)
Université Paris Diderot (UPD)
61 avenue du Général de Gaulle, 94010 Créteil, France

[1]present address: Centre de Spectrométrie Nucléaire et de Spectrométrie de Masse, UMR 8609, Université Paris Sud – CNRS, bâtiment 104, 91405 Orsay Campus, France

corresponding authors:
Nicolas Fray
Nicolas.Fray@lisa.u-pec.fr
Tel.: +33 01 45171543
&
Giacomo Briani
giacomo.briani@csnsm.in2p3.fr
Tel. : +33 01 69155297

Abstract

One important component of refractory organic residues synthesized from interstellar/cometary ice analogues is hexamethylenetetramine (HMT, $C_6H_{12}N_4$). However, HMT has never been observed in any astrophysical or planetary environment so far. We investigated thermal evolution of HMT above ambient temperature. The synthesis of the organic residue (ice deposition, photolysis and warming) as well as its heating to temperatures higher than 300 K are performed by means of the same experimental apparatus. The later also allows *in situ* continuous monitoring of both the solid organic residue (by FTIR spectrometry) and of the gas species (by mass spectrometry).

Two different ice mixtures, composed of H_2O:CH_3OH:NH_3=10:1:1 and H_2O:CH_3OH:NH_3:CO:CO_2=10:1:1:1:2, were deposited and simultaneously photolyzed at 29 K. Warming these photolyzed ices up to 300 K allows the production of refractory organic residues. At 300 K the organic residues clearly show the presence of HMT, but also some difference, in particular in their oxygenated components. Different evolutions of the organic residues are observed for temperatures > 300 K.

We characterized the organic residue thermal evolution for temperatures up to 500 K. We observed that HMT is still produced at temperatures higher than 300 K. Production of solid HMT and sublimation are simultaneous. HMT observed in the solid phase could be only a minor fraction of the total HMT production, the major fraction being sublimated. The kinetics of the HMT thermal evolution strongly depends on the organic residue composition at 300 K and seems to depend on the exact nature of the oxygenated fraction of the organic residue. The maximum temperature at which solid HMT is observed is 450 K. As HMT forms only for temperatures greater than 280 K in laboratory conditions, it implies that the detection of solid HMT in extraterrestrial samples will provide a strong indication of their thermal history. Consequently, the search for HMT in both solid cometary grains and gaseous phases in the coma of comet 67P/Churyumov-Gerasimenko will have to be performed by the Rosetta space mission, in particular with the COSIMA and ROSINA instruments.

Keywords

Comets, composition – Ices, IR spectroscopy – Organic chemistry – Hexamethylenetetramine

Highlights (max 85 characters per point, max 5 points)

- Synthesis of organic residues from ice photolysis and heating.
- High temperature evolution of hexamethylenetetramine (HMT, $C_6H_{12}N_4$) up to 500 K.
- Thermal production of HMT in the solid phase is still occuring at T > 300 K.
- Production and sublimation of HMT take place simultaneously.
- HMT detection by Rosetta would be an indicator of the thermal processing of cometary material.

1. Introduction

Comets are considered as the most primitive objects in the solar system. Indeed dark, low altered asteroids and comets exhibit a continuum of compositions and structures (Gounelle, 2011). However, comets were formed from planetesimals in the outer, cold regions of the solar system (beyond the "snow line", i.e. where temperature is low enough for water ice to condense) and experienced less thermal alteration than asteroids who formed in the inner, warmer regions (Brownlee, 2003). Hence, comets are expected to contain the most pristine information about the physico-chemical conditions which were prevailing in the solar nebula at the time of the planetesimal formation. Moreover, numerous comets fell into the primitive Earth and brought surface water and organic material which could have enabled the emergence of life (Chyba et al., 1990). The chemical characterization of cometary nuclei is of prime interest for the understanding of planets formation and emergence of life on Earth.

Cometary nuclei are composed of icy mixtures of volatile compounds, minerals and refractory organic matter. Even if only water ice has been directly detected thanks to its 1.5 and 2 µm absorption bands at the surface of comet 9P/Tempel nucleus (Sunshine et al., 2006), the nature and the abundances of the other volatile molecules (mostly organic) presents in cometary nuclei in the solid state are relatively well know from remote sensing observations of the gaseous phase of the coma at different wavelengths (Bockelée-Morvan et al., 2004). The nature of minerals can also be probed by thermal emission in the infrared (Hanner & Bradley, 2004). In particular, the presence of Mg-rich crystalline silicates has been clearly revealed in cometary grains of C/1995 O1 (Hale-Bopp)

(Crovisier et al., 1997; Crovisier et al., 2000). Moreover, the analysis of 81P/Wild (Wild 2) comet grains, returned by the Stardust mission in 2006, revealed numerous details concerning the mineralogy of the comets (Zolensky et al., 2006; Flynn, 2008). However, unlike volatile molecules and minerals, the physico-chemical nature of refractory organic matter remains very elusive.

The *in situ* measurements of cometary grains by mass spectrometers (PIA on board of Giotto (Kissel et al., 1986a), PUMA-1 and 2 on board of Vega 1 and 2, respectively (Kissel et al., 1986b) and CIDA on board of Stardust (Kissel et al., 2004), have shown that organic matter is also present in the form of a complex refractory component. As some of these grains seem to be mainly composed of solid organic matter made of carbon, hydrogen, oxygen and nitrogen atoms, they have been called “CHON grains” (Fomenkova, 1999). These *in situ* observations have also shown that “CHON” grains could be different one from each other, suggesting that cometary organic matter is heterogeneous at a very small scale in cometary nuclei (Fomenkova et al., 1994). Nevertheless, very few information were collected about the chemical nature of this refractory carbonaceous matter. Although the analysis of the grains returned by the Stardust probe has revealed the presence of various chemical functions by infrared spectroscopy and C-XANES (Sandford et al., 2006), the contamination of the aerogel (Sandford et al., 2010) makes the final interpretation of the data extremely difficult and only glycine has been firmly identified in 81P/Wild (Wild 2) grains so far (Elsila et al., 2009). Chondritic-porous interplanetary dust particles (CP-IDPs) and ultracarbonaceous Antarctic micrometeorites (UCAMMs) represent unaltered samples of mostly probable cometary origin (Bradley, 2003; Duprat et al., 2010). They show abundant organic matter which experienced a very low degree of metamorphism (Dobrică et al., 2011; Davidson et al., 2012), characterized by different textures and morphologies (Matrajt et al., 2012), containing aliphatic hydrocarbons (Flynn et al., 2000), polycyclic aromatic hydocarbons (Clemett et al., 1993; Dobrică et al., 2011) and showing elevated H and N isotopic anomalies (Floss et al., 2006; Duprat et al., 2010). In addition to observations and analysis of samples having extraterrestrial origin, experiments can be conducted in the laboratory to mimic the synthesis of cometary

refractory organic matter from ice mixtures submitted to energy deposition: UV, particles, thermal cycles (Bernstein et al., 1995; Cottin et al., 1999; Colangeli et al., 2004).

The temperatures experienced by the refractory organic content of comets have strong implications on its final molecular structure and composition. During the last decade, it has become more and more apparent that the thermal history of the cometary matter is extremely complex and that materials from various origins in the solar nebula are mixed. On the one hand, water ice has been detected at the surface of 9P/Tempel 1 (Sunshine et al., 2006) as well as in grains ejected in the cometary atmosphere (Lellouch et al., 1998). Furthermore, cometary nuclei contain very volatile compounds such as CO and CH_4 which have been detected in gas phase in the coma (Bockelée-Morvan et al., 2004). These observations show that part of the cometary nuclei has experienced only very low temperatures most of the time since its formation. On the other hand, some crystalline silicates have been detected in cometary grains (Crovisier et al., 1997; Hanner & Bradley, 2004; Keller et al., 2006). All the mechanisms proposed to explain the presence of Mg-rich crystalline silicates in comets require very high temperatures, of about 1000 K (Wooden et al., 2007). Consequently, silicate crystallization should have occurred in the solar nebula before their incorporation in cometary nuclei. Then, cometary refractory organic compounds are certainly a mixture of primitive and thermally evolved molecules. This could explain the heterogeneity of the chemical properties of the CHON grains measured in the environment of 1P/Halley (Fomenkova et al., 1994).

Once in the coma, the small cometary grains can reach temperatures higher than the blackbody temperature. For example, grains having a radius lower than 0.1 µm can reach 500 K at 1 UA (Kolokolova et al., 2004). Laboratory simulations showed that, at these temperatures, refractory organic compounds, such as polyoxymethylene, undergo thermal decomposition (Fray et al., 2004) leading to the production of gaseous molecules. This could be responsible for the observation of distributed sources in cometary environment (Cottin & Fray, 2008) as well as the decrease of the proportion of particles containing organic material with increasing nucleus distance (Fomenkova et al., 1994).

Studying the thermal evolution of organic residue from low (~ 10 K) to high (~ 600K) temperature is necessary to: i) constrain the thermal alteration that refractory organic matter could undergo in the solar nebula before their incorporation into cometary nuclei, and ii) explain the processes that take place in the coma. In this paper, we present a new experimental setup designed to study the thermal evolution up to 600 K of organic residues produced from the VUV photolysis of ice mixture at low temperature. So far, the thermal evolution of icy mixtures and organic residues, also called “yellow stuff”, have only been analyzed between 10 and 300 K (Greenberg, 1982; Bernstein et al., 1995; Muñoz Caro & Schutte, 2003; Bossa et al., 2009; Meinert et al., 2012). Hexamethylenetetramine ($C_6H_{12}N_4$, hereafter HMT) is one of the major components of refractory organic residues synthesized from interstellar/cometary ice analogues (Bernstein et al., 1995; Muñoz Caro & Schutte, 2003). However, HMT has never been observed in any astrophysical or planetary environment. In this paper, we report the thermal evolution of the organic residue during heating between 300 and 600 K, and we discuss in particular the formation and disappearance of HMT.

In section 2, we will present the experimental setup which has been specifically developed for the study of the thermal evolution of organic residues at high temperature ($T > 300$ K). Such organic residues are synthesized from ice mixture photolysis at low temperature ($T \sim 20$ K). We will present the experimental protocol in section 3, our results in section 4 and we will discuss their astrophysical significance in section 5.

2. Experimental setup

The OREGOC experimental setup (OREGOC stands for *ORigine et Evolution des Glaces et des composés Organiques Cométaires*, which means Origin and Evolution of Cometary Ices and Organics) is composed of a high vacuum chamber in which the temperature of a sample holder can be controlled between 20 and 800 K. Gas mixture is deposited on the sample holder at low temperature and simultaneously photolyzed using VUV lamp. The evolution of the solid sample is characterized by Fourier transform infrared spectrometry (FTIR) and the gas phase produced during sample heating is analyzed by mass spectrometry. This device has already been used to study the thermal degradation of polyoxymethylene (Le Roy et al., 2012) as well as the chemical mechanisms of HMT formation during the heating of photolyzed ice mixture (Vinogradoff et al., 2013).

2.1 Vacuum chamber

The high vacuum stainless steel chamber is kept to a pressure of ~10^{-8} mbar at room temperature by means of a turbo pump (Varian turbo-V 301) backed up by a primary pump (Varian SH110). The vacuum chamber has 8 external ports (see Fig. 1). The sample holder is located at the center of the high vacuum chamber. This sample holder is connected to a closed-cycle helium cryostat via a resistive heater and a thermal protection switch which allow controlling its temperature from 10 to 800K. The configuration (see Fig. 1) is such that the sample holder: 1) is at the level of the gas injection tubes; 2) is oriented at 45° with respect to the axial direction of the VUV photon flux; 3) crosses the beam of the IR spectrometer at an angle of 45°; 4) is in front of the mass spectrometer. Such a configuration allows performing i) the gas injection to form the initial ice film, ii) the photolysis of the ice by VUV photons, iii) the monitoring of the solid sample by FTIR spectrometry and iv) the analysis of the gases emitted from the solid sample by mass spectrometry simultaneously without moving the sample holder.

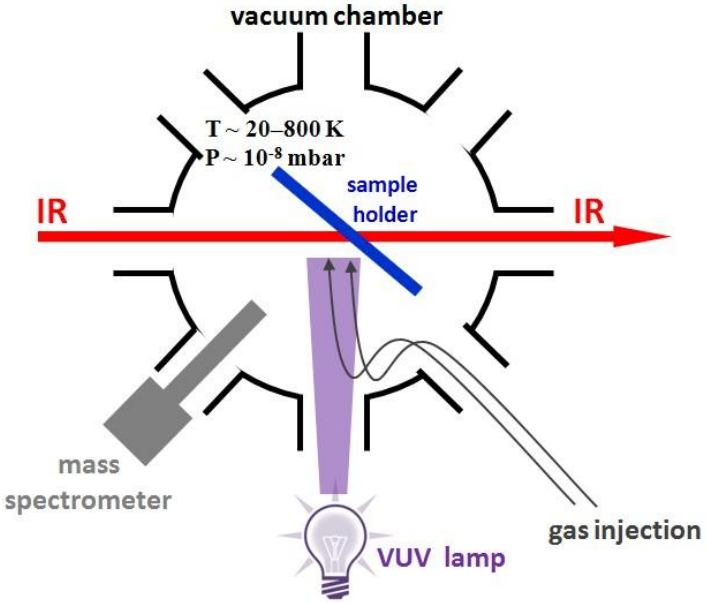

Figure 1: Schematic representation of a horizontal section of the OREGOC experimental setup.

2.2 Cryostat and sample holder

The closed-cycle helium cryostat (DE-204 AF T, Advanced Research Systems, Inc.) can cool the sample down to 20 K. The temperature of the second stage of the cryostat is measured thanks to a silicon diode. Two thermocouples (one type E and one Au Fe-Cr) and a Platinum resistance are fixed between the resistive heater and the sample holder. These four detectors, as well as the resistive heater, are connected to a temperature controller (LakeShore 340) which regulates the temperature by means of a proportional-integral-derivative (PID) feedback mechanism. The sample temperature can be controlled from 20 to 800 K. A thermal temperature switch made of sapphire is located between the cryostat and the electric resistance. The sapphire window is thermally conductive at low temperature and is thermally insulative at high temperature. This allows performing ice deposition at very low temperature (~ 20 K) and subsequently warming up the sample to 800 K, whereas the temperature of the cryostat second stage is kept lower than 300 K. The sample holder is a copper support covered by Ag in which an IR transparent CsI window is mounted using an indium seal to ensure good thermal conductivity. The diameter of the CsI windows is 10 mm.

2.3 Preparation of gas mixture

The gas mixtures prepared for our experiments contained in various proportion: H_2O (liquid, triply distilled); CH_3OH (liquid, Sigma-Aldrich 99.9%); CO (gas, Air Liquide 99.997 %); CO_2 (gas, Air Liquide 99.998 %) and NH_3 (gas, Air Liquid 99.999%). The gas mixtures are prepared thanks to a gas line composed of two separate parts to prevent reactions at room temperature: one for NH_3 and one for the other gases. The gas line can be evacuated down to a pressure of $\sim 10^{-7}$ mbar by a turbo molecular pump (Pfeiffer TMH 071) backed by a diaphragm pump (Pfeiffer vacuum MVP 015-2). The pressure in the gas line is monitored by two Baratron pressure gauges (MKS 627 B), one with a full scale range of 1.33 mbar and the second one with a full scale range of 1333 mbar. The gas mixture is prepared by filling the volume of a bulb with the different gases, except NH_3, to obtain the desired gas partial pressures. The flow toward the vacuum chamber of the H_2O:CH_3OH:CO_2:CO mixture is regulated using a micrometric valve, whereas the injection of NH_3 in the vacuum chamber is regulated by a mass flow controller (MFC 1179B, MKS), which assures a constant gas flow between 0.2 and 10 sccm (sccm = standard cubic centimeters per minute).

Several calibration experiments were carried out in order to determine the correct conditions that provide the desired ice growth rate and NH_3 molecular ratio in the ice mixtures. Different upstream pressures (always lower than 20 mbar to prevent condensation in the gas line) were tested in the injection line, as well as different apertures of the micrometric valve for the injection of the H_2O:CH_3OH:CO_2:CO mixture and different regulations of the MFC for the injection of NH_3. As the MFC requires an upstream pressure of about 1 bar, to achieve the desired NH_3 flow, NH_3 has been diluted in He, which is not incorporated in the ice given the temperature of the sample holder.

2.4 VUV lamp

The VUV photon flux used for the ice photolysis is produced by a microwave-powered plasma lamp in which an H_2-He mixture (98% He, 2% H_2) flows. This mixture allows maximizing the intensity of the H Lyman α (121.6 nm) emission (Davis & Braun, 1968)

whereas the VUV emission spectra show also a large band centered at about 160 nm. Previous works indicate that the photon flux emitted with this type of VUV lamp is about 10^{15} photons s^{-1} (Warneck, 1962; Davis & Braun, 1968). We calibrated the VUV lamp photon flux impinging our solid sample by performing actinometry experiment on a thick CO_2 ice film. Even if the ice film was thick, the combination band at 3600 cm^{-1} is not saturated and thanks to the infrared integrated cross sections measured by Gerakines et al., 1995), we can estimate a CO_2 column density of 5.5×10^{18} molecules cm^{-2}. Then, considering the CO_2 ice VUV cross section measured by Mason et al., 2006), we calculated that 98% of the H Lyman α (121.6 nm) photons are absorbed and that only 10% of the 160 nm photons are absorbed. During the photolysis, we followed the appearance of CO by infrared spectroscopy. Using the CO band strength published in Gerakines et al. (1995), we measured an appearance rate of 1.6×10^{13} molecules cm^{-2} s^{-1}. As all the photons are not absorbed by the CO_2 ice film and as the photolysis products, CO and O atoms, can recombine into CO_2, we consider that the VUV photon flux received by our samples is at least 1.6×10^{13} photons cm^{-2} s^{-1}.

2.5 FTIR and mass spectrometry

The evolution of the solid sample (from the initial ice to the final organic residue) is monitored by transmission infrared spectroscopy (Brüker – Vertex 70 FTIR spectrometer). We collected FTIR spectra in the wavenumber range 400 – 5000 cm^{-1} at a resolution of 1 cm^{-1}. Each spectrum corresponds to a mean of 256 scans giving time steps of ~390 s. The IR signal is collected by an external detector (MCT D316/B). The FTIR spectrometer and the external pathway to the detector are kept under dried atmosphere. Gaseous species emitted from the solid sample are characterized by means of a quadrupole mass spectrometer (QMG 220, Prisma Plus, Pfeiffer Vacuum). Mass spectra are continuously acquired in the m/z range 0 – 200, with a mass resolution Δ(m/z) ~1. Each mass spectrum corresponds to a time interval of ~125 s.

3. Experimental protocol

3.1 Ice deposition and photolysis

For each experiment a new CsI window is used for sample deposition in order to avoid contamination from previous experiments. First we inject all the gases at the desired flow rate when the sample holder has reached a constant temperature of 29 K. A visual inspection of the first four FTIR spectra allows verifying that the initial ice composition is correct (Fig. 2). Then, we switch on the VUV lamp. The ice deposition and photolysis are performed simultaneously at constant temperature during more than 15 hours (Fig. 3). The exact deposition and photolysis durations are indicated in Table 1.

The initial ice composition was chosen on the basis of the determination of molecular abundances in ices of dense molecular clouds (Gibb et al., 2004; Dartois, 2005) and comets (Bockelée-Morvan et al., 2004). It was close to the one used in some previous laboratory works dealing with organic residues synthesis from ice photolysis (Berstein et al., 1995; Munoz-Caro & Shutte 2003).

Table 1. Summary of the experiments

experiment	ice composition[a] $H_2O:CH_3OH:NH_3:CO:CO_2$	ice deposition temperature (K)	photolysis time	gas injection speed[b] (molecules.s^{-1})	dose [c] (photons / molecules)
Exp#1	10 : 1 : 1 : 0 : 0	29	15 h 40 min	$(1.1 \pm 0.2)\times10^{15}$	> 0.01
Exp#2	10 : 1 : 1 : 0 : 0	29	15 h 33 min	$(1.1 \pm 0.2)\times10^{15}$	> 0.01
Exp#3	10 : 1 : 1 : 0 : 0	29	15 h 42 min	$(1.1 \pm 0.2)\times10^{15}$	> 0.01
Exp#4	10 : 1 : 1 : 1 : 2	29	15 h 42 min	$(1.1 \pm 0.2)\times10^{15}$	> 0.01
Exp#5	10 : 1 : 1 : 0 : 0	29	0	$(1.1 \pm 0.2)\times10^{15}$	0
Exp#6 [d]	0 : 0 : 0 : 0 : 0	29	0	0	0

[a] Estimated on the basis of gas partial pressures in the gas injection column and ice growth rates in calibration experiments.
[b] Estimated on the basis of calibration experiments.
[c] Estimated using a photon flux on the sample equal to 10^{13} photons/s, as determined by CO_2 actinometry experiments (see text).
[d] Experiment #6 is a blank. We went through the complete protocol shown in Fig. 3 without ice deposition and without photolysis, acquiring FTIR and mass spectra to check for contaminations.

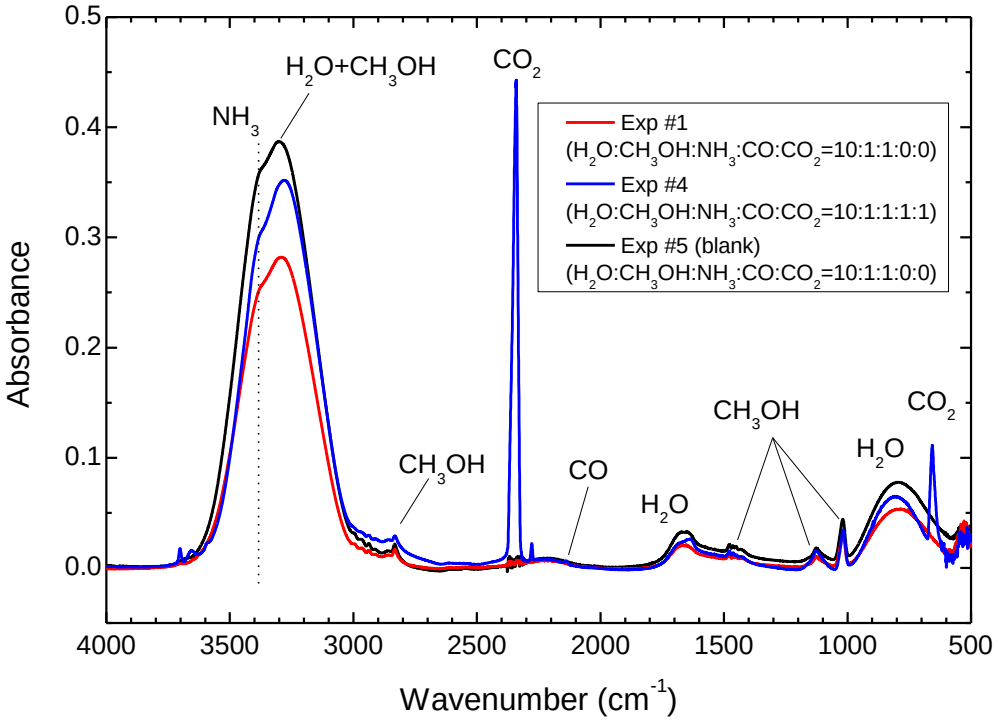

Figure 2: FTIR spectra of the deposited ice measured about 1000 s after the beginning of the gas injection and before the beginning of VUV photolysis. All the injected gases are present in the ice, as attested by their principal IR peaks. Details about the experiments can be found in Table 1.

The standard experiment with initial ice composition $H_2O:CH_3OH:NH_3:CO:CO_2$=10:1:1:0:0 was repeated three times to check the reproducibility of our results (Table 1: experiments #1 to #3, hereafter Exp#1, Exp#2 and Exp#3, respectively). For one experiment (experiment #4, hereafter Exp#4), we added CO and CO_2 to study the influence of both these molecules on the nature and thermal evolution of the final organic residue. Two blank experiments were performed (Table 1): one with the same ice

deposition than the standard experiment but without VUV photolysis (experiment #5) and one without any ice deposition (experiment #6).

3.2 Temperature evolution

In all experiments, we increased the sample temperature only after stopping ice deposition and VUV photolysis. The sample temperature was raised up to 300 K at a constant rate of 0.5 K/min (Fig. 3). Once the sample had reached 300 K, it was maintained at this constant temperature for ~16 hours. We did not observe significant variations of neither FTIR nor mass spectral features during this period. Then, we increased the temperature by successive steps of 50 K each (Fig. 3) to study the thermal evolution of the organic residue at T > 300 K. For all the experiments, the time interval spent by the sample at a given temperature is of the order of 80 minutes for 350 K < T < 500 K. The maximum difference among these time intervals in different experiments is 3 minutes.

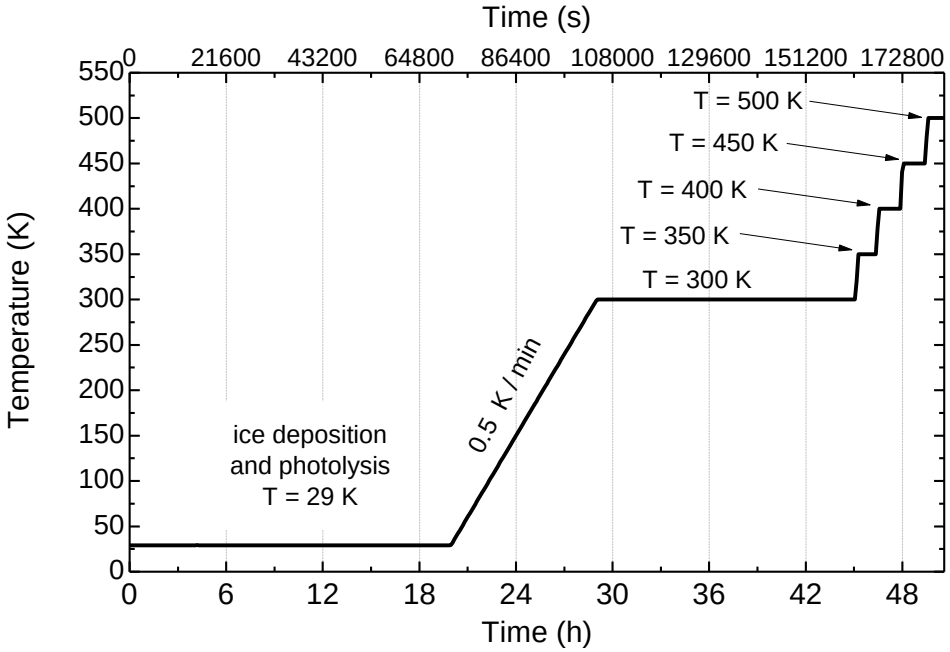

Figure 3. The temperature evolution in the OREGOC experiments reported in this work.

4. Results

4.1 Blank experiments

FTIR spectra of blank experiments (Exp#5 and Exp#6; see Table 1) do not show any significant feature between 400 and 5000 cm^{-1} at any temperature. The noise in absorbance is always lower than 3×10^{-3}. Therefore we consider that contaminations are negligible in all FTIR spectra.

Mass spectra collected during the blank experiments confirm that no significant contaminants are present since no peak due to organic molecules was observed. Nevertheless, as the total pressure is about 10^{-8} mbar, we observed, in these mass spectra, peaks due to residual atmospheric gases, such as N_2 and O_2. Blank experiments revealed, however, that the

50 K temperature steps cause a sudden and global increase in the intensity of mass spectra. In order to take into account this behavior when analyzing mass spectra of the gaseous phase emitted from the organic residue during the heating, we always compared mass spectra to those measured in the blank experiments.

4.2 The organic residue at 300 K

As we are interested in the high temperature (T > 300 K) evolution of HMT, we consider the organic residue at the end of the 300 K constant temperature step as the starting point for the analysis of our results. A detailed description of the chemical synthesis at T < 300 K of the organic residue is reported in Vinogradoff et al. (2013). In Fig. 4, we present the FTIR spectra of the organic residues synthesized in our experiments: Exp#1 and Exp#4. The FTIR peak assignments are reported in Table 2.

The organic residue FTIR spectrum of Exp#1 is dominated by HMT peaks (at 1461, 1366, 1235, 1045, 1005, 812 and 672 cm^{-1}; respectively labeled e, f, j, m, n, p and r in Fig. 4). Two other large peaks are present, at 1669 cm^{-1} (labeled b, probably due to C=O stretching in amides or in carboxylic acids, see the Discussion section) and a peak of formate ion ($HCOO^-$) at 1594 cm^{-1} (labeled c_2). Besides these, we observed broad peaks with low intensities which could be tentatively linked to the polymethanimine polymer (PMI) at 1355, 1209, 1091 and 970 cm^{-1} (respectively labeled g, k, l and o in Fig. 4) (Vinogradoff et al., 2012). In the corresponding mass spectra, at the end of the 300K temperature step, no peak, which could be due to gas molecules produced from the organic residue, is observed.

We obtained the same qualitative results in two other experiments (Exp#2 and Exp#3) performed with the same initial ice composition than Exp#1 to check reproducibility. The only observed variation is that the IR absorbance is weaker in Exp #2 and #3 than in Exp#1. For example, the HMT peak at 1005 cm^{-1} is ~4 times weaker. This is probably due variations in the VUV photon flux.

Some differences are instead observed in the FTIR spectra of the organic residue obtained in Exp#4 at 300 K, and for which CO and CO_2 were present in the initial ice composition. HMT peaks are still the dominant features, but: 1) the peak at 1669 cm^{-1} (label b), related to a C=O stretching, has a relative weaker absorbance than that in the FTIR spectrum of Exp#1, #2 or #3; 2) the $HCOO^-$ peak at 1594 cm^{-1} (labeled c_2 in Fig. 4) is replaced by a larger peak centered at 1601 cm^{-1} (labeled c_1 in Fig. 4), that we interpret as indicative of the presence of carboxylic acid salts ($R\text{-}COO^-$) different from the formate ion; 3) a small, broad peak is observed at 1743 cm^{-1} (labeled a in Fig. 4), which could be due to C=O stretching in esters; 4) an unidentified peak at 1302 cm^{-1} (labeled h in Fig. 4), present in FTIR spectrum of Exp#4 is absent in the spectra of Exp#1, #2 and #3.

The organic residue obtained at T = 300 K is indeed very complex, as shown by the abundance and complexity of peaks in the FTIR spectra (Fig. 4). Focusing on HMT thermal evolution, we did not investigate possible identification for all these peaks, but our results are very similar to those obtained in previous works (Bernstein et al., 1995; Muñoz Caro & Schutte, 2003), which make us confident about our experimental protocol. An exhaustive analysis of the spectra will be presented elsewhere. In the next sections, we will described separately the time evolution of the solid and gaseous phase in Exp#1 and then in Exp#4.

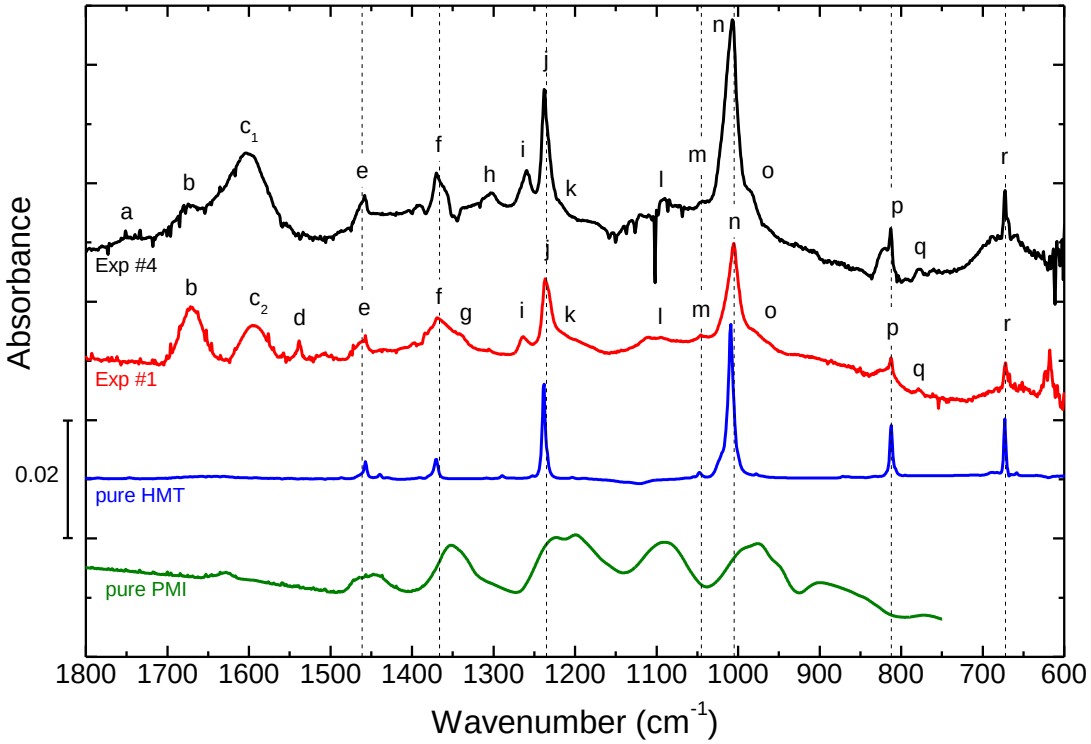

Figure 4: FTIR spectra of organic residues at 300 K for Exp#1 and Exp#4. Labels refer to peak assignments reported in Table 2. FTIR spectra of pure HMT and PMI are reported for comparison. Vertical dotted lines show the positions of the HMT peaks.

Table 2. Summary of organic residue peaks in FTIR spectra at 300 K.

Label	Position (cm^{-1})	Assignment	Species	References
a	1743	ν(C=O)	esters	1, 2
b	1669	ν(C=O) (??)	amides, RCOOH	1
c_1	1601	ν(COO^-)	R-COO^-	
c_2	1594	ν(COO^-)	$HCOO^-$	3
d	1538	–	unknown	
e	1461	δ(CH,NH)	HMT	1, 2
f	1366	δ(C-H)	HMT	1, 2
g	1355	δ(C-H)	PMI	4, 5
h	1302	–	unknown	
i	1261		unknown	
j	1235	ν(C-N)	HMT	1, 2
k	1209	ν(C-N)	PMI	4, 5
l	1091	ν(C-N)	PMI	4, 5
m	1045	Comb.	HMT	7
n	1005	ν(C-N)	HMT	1, 2
o	970	ν(C-N)	PMI	4, 5
p	812	ω(NH)	HMT	1, 2
q	769	δ(C–O)	$HCOO^-$	6
r	672	CNC def.	HMT	1, 2

Vibration mode: ν = stretching, δ = bending, ω = inversion, def.= deformation. Comb. = combination mode.

References. 1) Bernstein et al., 1995. 2) Muñoz-Caro & Shutte 2003. 3) Vinogradoff et al., 2011. 4) Danger et al., 2011. 5) Vinogradoff et al., 2012. 6) Schutte & Buijs, 1964. 7) Bertie & Solinas, 1974.

4.3 Thermal evolution of experiments #1, #2 and #3 (H_2O:CH_3OH:NH_3 =10:1:1)

As for the infrared spectrum at 300 K, we observe very similar thermal evolutions during Exp#1, #2 and #3. Therefore, we will only present the results of Exp#1 for which we obtained the largest production of organic material. The FTIR spectra collected at the end of each temperature step are shown in Fig. 5. Figures 6a show the temporal evolution of the HMT column density in the solid organic residue measured from FTIR spectra. To obtain the HMT column density from the 1005 and 1235 cm^{-1} peak (label n and j respectively in Fig. 4 and Table 2) we integrated their intensities over the regions reported in Bernstein et al., (1995): 1000 – 1020 cm^{-1} and 1228 – 1246 cm^{-1}, respectively, fitting the local baseline with a third order polynomial. Also, we used the integrated cross sections (A-values) reported in that same work: 5×10^{-18} cm $molecule^{-1}$ for the peak at 1005 cm^{-1} and 2.6×10^{-18} cm $molecule^{-1}$ for the peak at 1235 cm^{-1}.

The detection of gaseous HMT in mass spectra is proved by the presence of the molecular ion peak at m/z = 140, and by the fragment peaks at m/z = 42, 56, 69, 71, 83, 85, 96, 111 and 112 (Fig. 7). This is consistent with previous measurements by Bernstein et al., (1995). Fig. 6b shows the time evolution of the intensity of the HMT molecular ion peak at m/z = 140.

4.3.1 First temperature step: 300 – 350 K

Increasing the temperature of the sample up to 350 K, we observe an increase of the HMT peaks in FTIR spectra (Fig. 5). This increase is fast and it seems that HMT rapidly reaches a stationary state (Fig 6a). On the opposite, the 1594 cm^{-1} peak of formate ion and, to a lesser extent, that of C=O stretching in amides at 1669 cm^{-1}, decrease. For the gas phase, we observe that in mass spectra the HMT peak at m/z = 140 (Fig. 6b) rapidly increases and subsequently decreases. These results show that in the passage from T = 300 K to T = 350 K the amount of HMT increases in both the solid and the gas phase. When a constant temperature of 350 K is reached, the molecular ion peak at m/z = 140 does not decrease to the same intensity measured at the end of the 300 K step. Thus, it seems that a small amount of gaseous HMT is released from the solid residue while the column density of solid HMT seems to be in a stationary state.

4.3.2 Second temperature step: 350 – 400 K

Little decreases of the HMT and formate ion peaks in the FTIR spectra are observed when the temperature increases from 350 to 400 K (Fig. 5), indicating a slight decrease of the amount of these species in the solid phase. Mass spectra show again that the HMT peak at m/z = 140 clearly steps up when temperature is increased to 400 K (Fig. 6b). In particular, the HMT molecular ion peak shows an intensity one order of magnitude higher than the blank level. Its intensity rapidly decreases, but, as for the previous step, does not reach the level observed at the end of the 300 K step. Thus, production of gaseous HMT mainly happens in the time interval corresponding to the temperature change but seems to continue very slowly during the constant temperature time interval.

4.3.3 Third temperature step: 400 – 450 K

In the FTIR spectrum at 450 K the only HMT peak still visible is the one at 1005 cm^{-1} (Fig. 5) attesting of the quasi disappearance of HMT from the solid phase. Such a decrease is evident in Fig. 6a, and it appears to be very rapid: ~1 order of magnitude in ~10 minutes. Fig. 6a shows that 90% of the HMT is removed from the solid phase in the passage 400 – 450 K. When the temperature is increased to 450 K, in mass spectra the HMT peak at m/z = 140

reaches higher intensity than in the previous temperature steps (Fig. 6b) and then it rapidly decreases to a very low level corresponding to the absence of HMT in gas phase.

4.3.4 Fourth temperature step: 450-500 K

Increasing the temperature to 500 K completely erases HMT signatures from FTIR spectra (Fig. 5). No significant HMT peaks are observed in the mass spectra at 500 K.

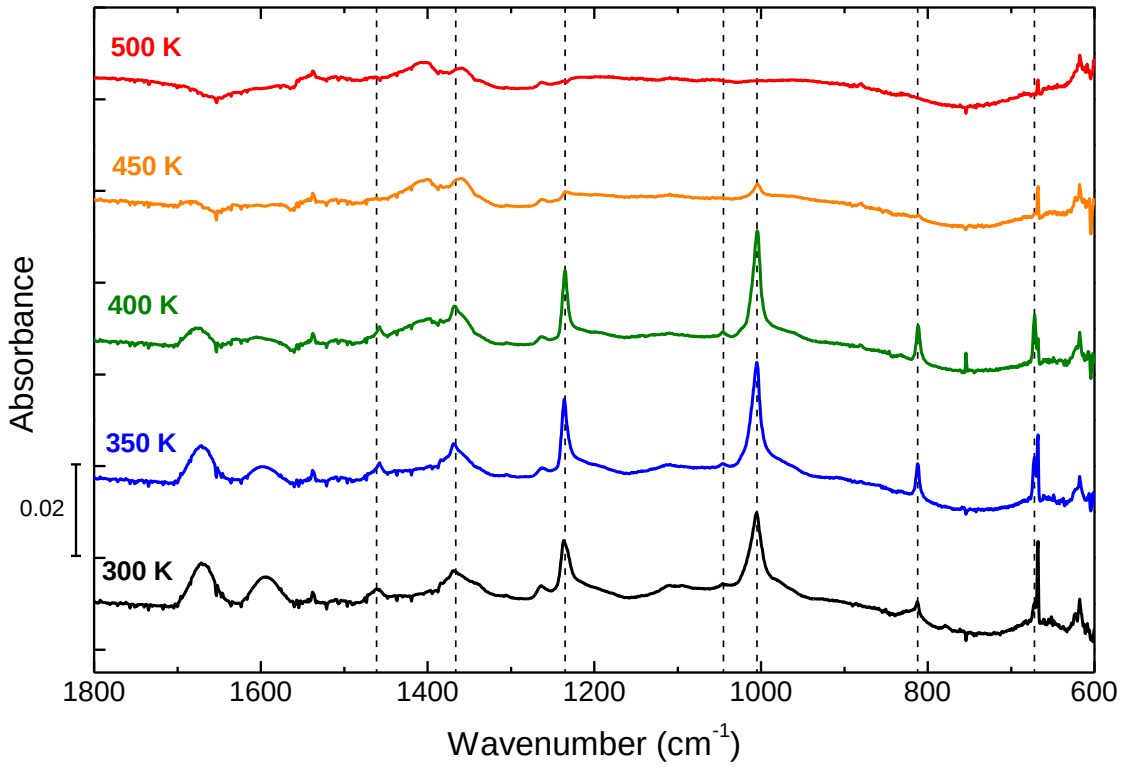

Figure 5: Evolution of the organic residue FTIR spectrum with increasing temperature for Exp#1. We report here the last FTIR spectrum acquired for each constant temperature time interval. Spectra are vertically shifted for clarity. Vertical dashed lines show the position of the HMT peaks.

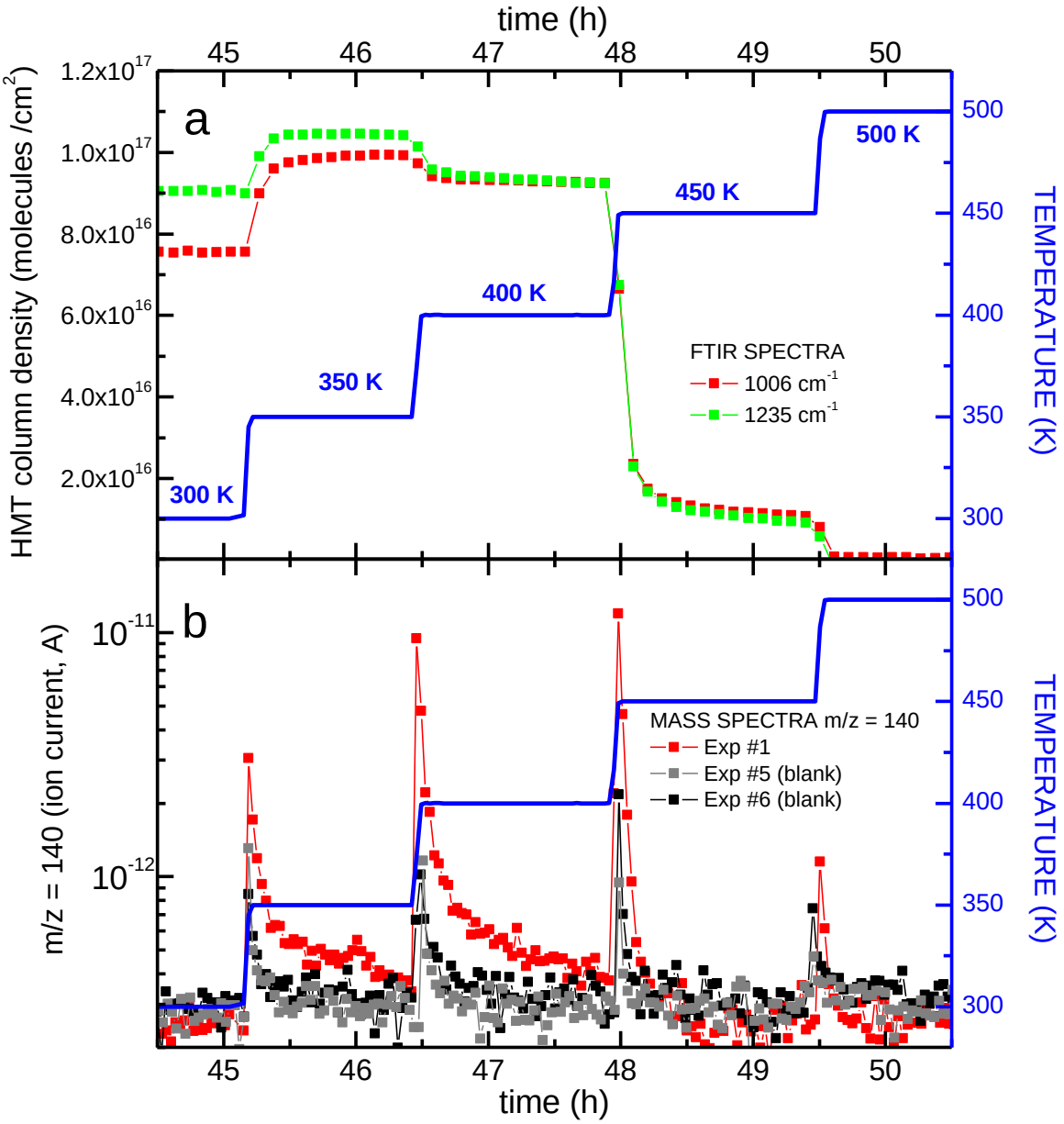

Figure 6: High temperature evolution of HMT in Exp#1. Panel (a) shows the time evolution of the column density of HMT in the solid organic residue from the FTIR peaks at 1005 cm^{-1} and 1235 cm^{-1}. Panels (b) shows the time evolution of the intensity of the mass spectrum peak at m/z = 140. The time scale is the same as in Fig. 3.

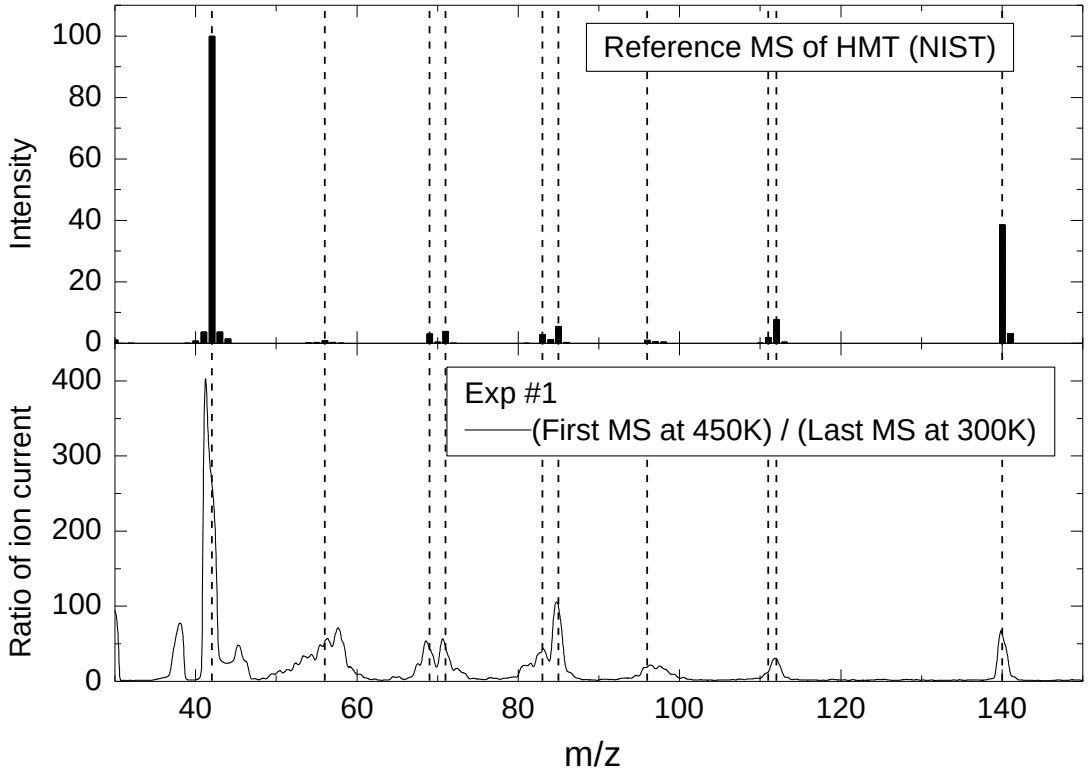

Figure 7: Ratio of the first mass spectrum at 450 K to the last mass spectrum at 300 K acquired during Exp#1 compared to the reference mass spectrum of HMT from the NIST Chemistry Database (http://webbook.nist.gov/chemistry/). Vertical dashed lines show the position of the HMT fragment peaks at m/z = 42, 56, 69, 71, 83, 85, 96, 111, 112 and 140.

4.4 Thermal evolution of Exp#4 (H_2O:CH_3OH:NH_3:CO:CO_2=10:1:1:1:2)

The FTIR spectra collected at the end of each temperature steps of Exp#4 are shown in Fig. 8. In Fig. 9, we present the time evolution of the HMT column density in the solid organic residue measured from FTIR spectra as well as the evolution of the intensity of the HMT molecular ion peak (m/z = 140) in mass spectra, which is related to the amount of gaseous HMT.

4.4.1 First temperature step: 300 – 350 K

HMT peaks in the 350 K FTIR spectrum are less intense than those in the 300 K spectrum (Fig. 8). However, Fig. 9a shows that the HMT amount in the solid phase first increases when the temperature changes from 300 K to 350 K. Such an increase is limited to a few minutes, and then the HMT amount in the solid phase slowly decreases during the whole duration of the temperature step. One can note that during this temperature step, the intensity of the carboxylic acid ion band at 1601 cm^{-1} decreases. In the mass spectra, the passage 300 – 350 K corresponds to a strong increase of the intensity of the peak at m/z = 140 (Fig. 9b). For the whole time interval at T = 350 K, the signal of this mass spectral peak slowly decreases but remains well above the blank level. This is drastically different from what was observed in Exp#1.

4.4.2 Second temperature step: 350 – 400 K

Increasing the temperature to 400 K causes a strong diminution of HMT peaks in the FTIR spectrum (Fig. 8). As shown in Fig. 9a this decrease is quite slow and lasts for the whole time interval. One can note that the band at 1601 cm^{-1} does not vanish. As for the previous temperature step, the HMT amount in the gas phase increases rapidly and then the HMT molecular ion peak decreases almost to the level observed at the end of the 300 K temperature step (Fig. 9b).

4.4.3 Third temperature step: 400 – 450 K

No HMT peak is present in the FTIR spectrum at 450 K (Fig. 8), and therefore all the HMT has been removed from the solid phase at the end of the time interval at 450 K, contrary to what is observed in Exp#1 (Fig. 5). The evolution of FTIR spectra (Fig. 9a) reveals that HMT is rapidly removed from the solid phase when the temperature is increased to 450 K. Simultaneously, we observe a spike in the mass spectra peak at m/z = 140 (Fig. 9b) indicating release of HMT in the gas phase. The absence of significant features in both FTIR and mass spectra corresponding to the temperature step 450 – 500 K confirms the complete removal of HMT from our organic residue at 450 K.

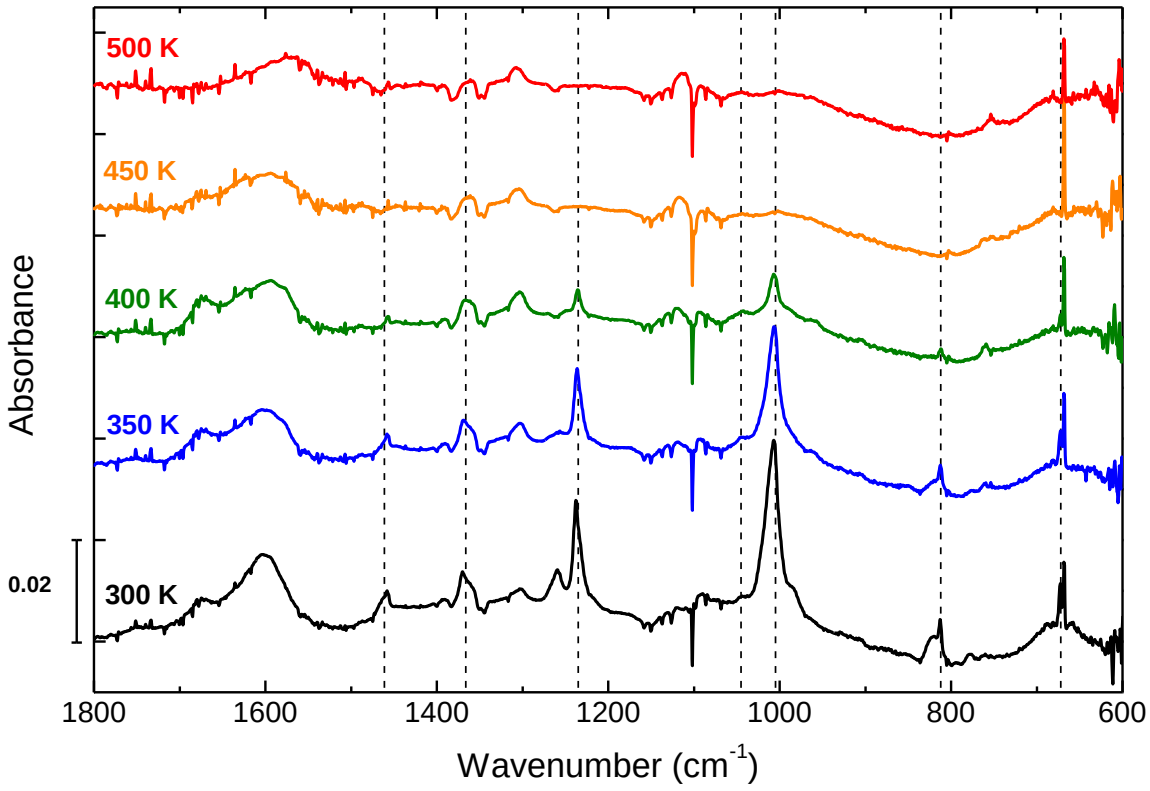

Figure 8: Evolution of the organic residue FTIR spectrum with increasing temperature for Exp#4. We report here the last FTIR spectrum acquired for each constant temperature time interval. Spectra are vertically shifted for clarity. Vertical dashed lines show the position of the HMT peaks. The positive peak at 668 cm^{-1} is due to instability of the gaseous CO_2 in the spectrometer and the negative peak at about 1100 cm^{-1} is due to vibration generated by the cryothermostat.

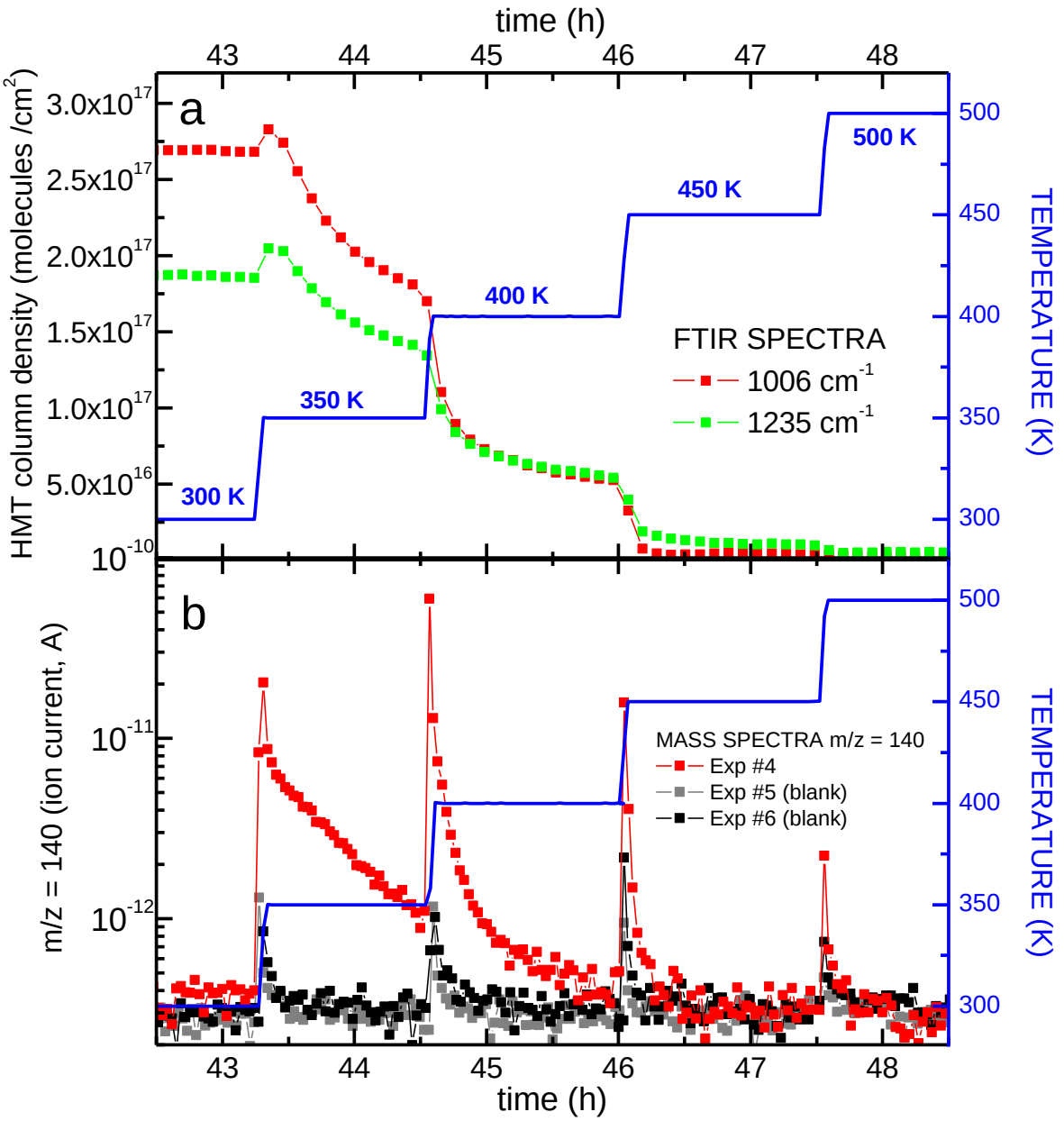

Figure 9: High temperature evolution of HMT in Exp#4. Panel (a) shows the time evolution of the HMT column density in the solid organic residue from the FTIR peaks at 1005 cm^{-1} and 1235 cm^{-1}. Panels (b) shows the time evolution of the intensity of the mass spectrum peak at m/z = 140. The time scale is the same as that reported in Fig. 3.

4.5. Discussion

In the organic residues synthesized by our experiments the presence of HMT at T = 300 K is firmly established by the observation of several characteristic peaks in the FTIR spectra (Fig. 4). Vinogradoff et al. (2013) described the chemical processes that take place at T < 300 K and explain the formation of HMT in our experiments. They reported that HMT forms at T > 280 K from the protonated ion of trimethylenetriamine ($TMTH^+$, $C_3H_{10}N_3^+$) and its decomposition products. A detailed chemical mechanism can be found in (Vinogradoff et al., 2012) but the last steps of HMT formation can be written:

$$2\ (TMTH^+;\ HCOO^-) \rightarrow HMT + 2\ HCOOH + 2\ NH_3 \qquad (1)$$

Fig. 10 shows the difference between the FTIR spectra of the organic residue for T = 350 K and T = 300 K. In this figure, upward peaks indicate an increase of the corresponding molecule, while downward peaks indicate a decrease. For Exp#1 (Fig. 10a) it is evident that at the end of the time interval at T = 350 K the amount of HMT in the solid phase is greater than that at T = 300 K, while the amount of $HCOO^-$ and $TMTH^+$ decreases. The decreases of $HCOO^-$ and $TMTH^+$ are identified following 4 downward peaks for $HCOO^-$ (Schutte et al., 1999) and one peak (1460 cm^{-1}) for $TMTH^+$ (Vinogradoff et al., 2012). This indicates that the synthesis of HMT from $TMTH^+$, identified by
(Vinogradoff et al., 2013) for T < 300 K, is still active until at least 350 K. For Exp#4, Fig. 10b shows that at the end of the time interval at T = 350 K the amount of HMT in the solid phase is lower than that at T = 300 K (as observed in Fig. 9a). Fig. 10 allows highlighting some differences between the organic residue of Exp#1 and Exp#4. In particular, the different position and shape of the peak around 1600 cm^{-1} (as observed in the FTIR spectrum at T = 300 K, Fig. 4) attest that the acid component of the organic residue is different in Exp#1 and Exp#4. Moreover, the comparison of panels a and b of Fig. 10 show that the behavior of HMT is drastically different in the two experiments. Nevertheless, we have to keep in mind that, for Exp#4, HMT production in the solid phase is active during the heating from 300 to 350 K (Fig. 9a) even if at the end of the 350 K step the column density of solid HMT is lower than at 300 K.

In Exp#1, the HMT absorption peaks in FTIR spectra vary significantly when the temperature increases by 50 K steps (Fig. 6a) but we observed little variations during the time intervals at constant temperature. This suggests that the chemistry inside the solid organic residue rapidly goes toward a quasi-stationary state after each temperature increment. In contrast, in Exp#4 we observe significant variations of the FTIR spectra during the time intervals at constant temperature (Fig. 9a): increasing the temperature from 300 K to 350 K induces an increase of HMT in the organic residue, but then, at T = 350 K, the amount of HMT clearly decreases and such a decrease continues during the whole time interval at T = 400 K. Thus, the kinetics of the thermal evolution is different between Exp#1 and Exp#4 (Fig. 10). We interpret these differences as being due to the different molecular composition of the organic residues at T = 300 K in the two experiments (Fig. 4), which results from the different initial ice composition (we added CO and CO_2 for Exp#4). This shows that the molecular composition of the initial ice mixture determine not only the composition of the organic residue at T = 300 K (Fig. 4), but also the kinetics of its thermal evolution above this temperature. The comparison of Fig. 6a and Fig. 9a, as well as Fig. 10, show that the evolution of a given molecule (HMT) strongly depends on the nature of the organic compound of which surround this molecule.

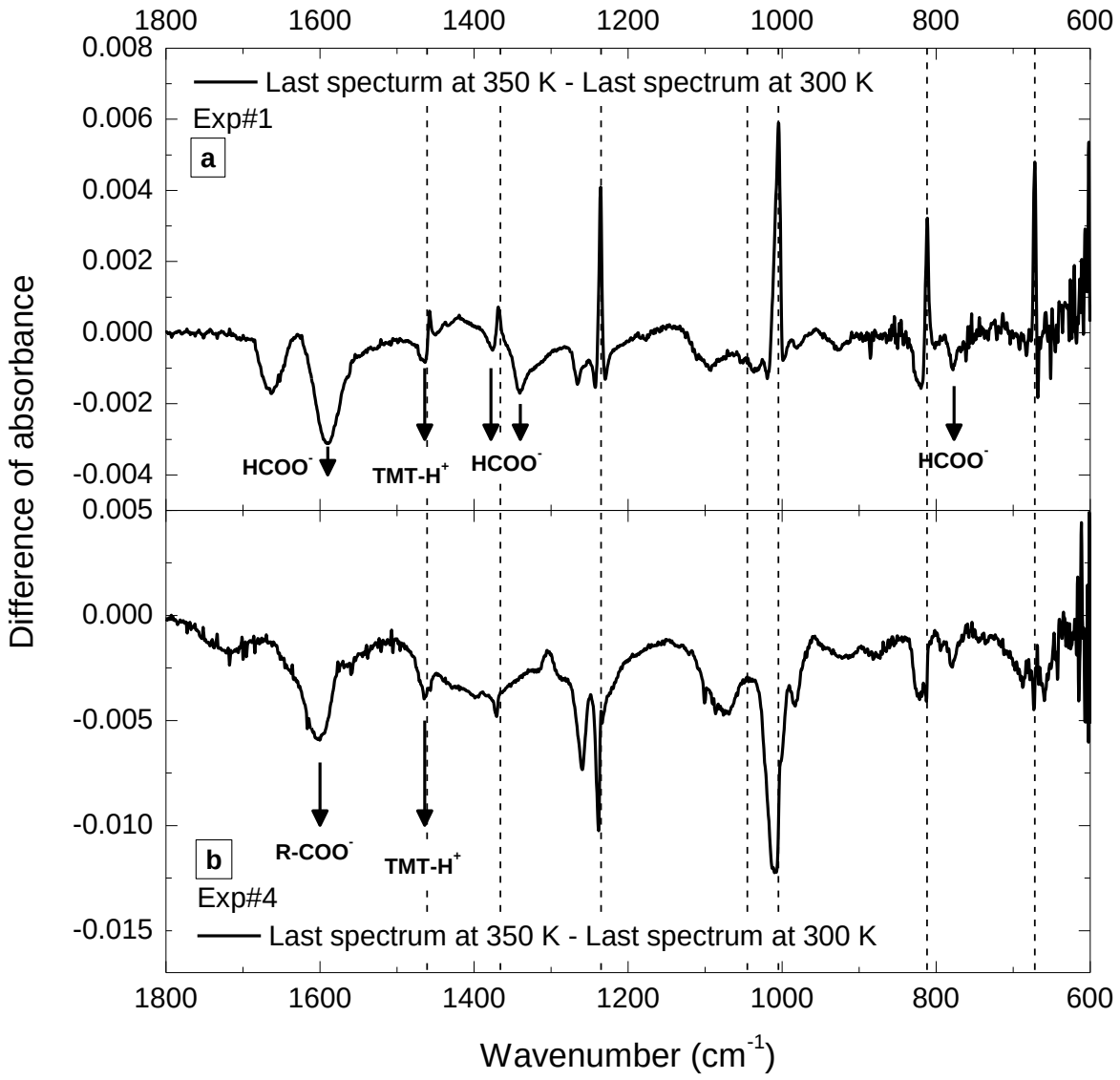

Figure 10: Difference between the organic residue FTIR spectra measured at T = 350 K and at T = 300 K during Exp#1 (a) and Exp#4 (b). Upward peaks indicate an increase of the corresponding molecule, while downward peaks indicate a decrease. Vertical dashed lines show the position of the HMT peaks. (a) In Exp#1 the amount of HMT increases, while those of $HCOO^-$ and $TMTH^+$ decrease, confirming reaction (1). The presence of other upward and downward peaks shows that this is not the only process caused by heating. (b) In Exp#4 the amount of HMT decreases.

Concerning the gas phase sampled by mass spectrometry, the effect of the 50 K temperature steps is a very rapid increase of the peak intensity. The observation of the molecular ion peak at m/z = 140 and of the fragment peaks (Fig. 7) attests that HMT is also present in gas phase. In particular, the intensity of the HMT peaks at m/z = 140 (molecular ion) is clearly above the blank level when the temperature is increased (Fig. 6b and Fig. 9b). Then, at constant temperature, we observe that HMT peaks gradually decrease with a kinetic that depends of the molecular composition of the organic residue in which the HMT is

embedded. In addition, the evolution of mass spectra with increasing temperature is correlated with that of HMT FTIR spectra: the temperature steps, for which the signal of gaseous HMT is the highest in both Exp#1 and Exp#4, are those for which the loss of solid HMT is the most important. This shows that gaseous HMT is produced by sublimation during the rapid temperature increments, and that the sublimation continues at constant temperature, gradually fading down.

The sublimation curve $P(T)$ for pure HMT can be calculated from the Clapeyron equation:

$$\frac{dP}{dT} = \frac{\Delta H_S(T)}{T\Delta V} \qquad (2)$$

where P = pressure (in Pa), T = temperature (in K), ΔH_S = enthalpy of sublimation (in J/mol), ΔV = variation of molar volume (in m^3/mol). In the case of HMT, the gas molar volume V_{gas} is larger than the solid molar volume V_{solid} by several orders of magnitude. As the HMT sublimation pressure is quite low (see below) we can use the perfect gas hypothesis. In such case, we have $\Delta V = V_{gas} - V_{solid} \approx V_{gas} = RT/P$ (R = 8.314 J/mol/K). Moreover, if we suppose $\Delta H_S(T) \approx$ constant, the relation for the sublimation curve $P(T)$ is:

$$\ln\left(\frac{P}{P_0}\right) \approx \frac{\Delta H_S}{R}\left(\frac{1}{T_0} - \frac{1}{T}\right). \qquad (3)$$

Using the thermodynamic data reported in De Wit et al., 1983) (ΔH_S = 78.8 kJ/mol and P_0(T_0=316 K) = 0.4 Pa), the sublimation pressure of pure HMT in the 280-450 K temperature range can be calculated (Fig. 11). We note that our extrapolation reproduces quite well the sublimation pressure of pure HMT independently measured at 367 K (Paorici et al., 2005).

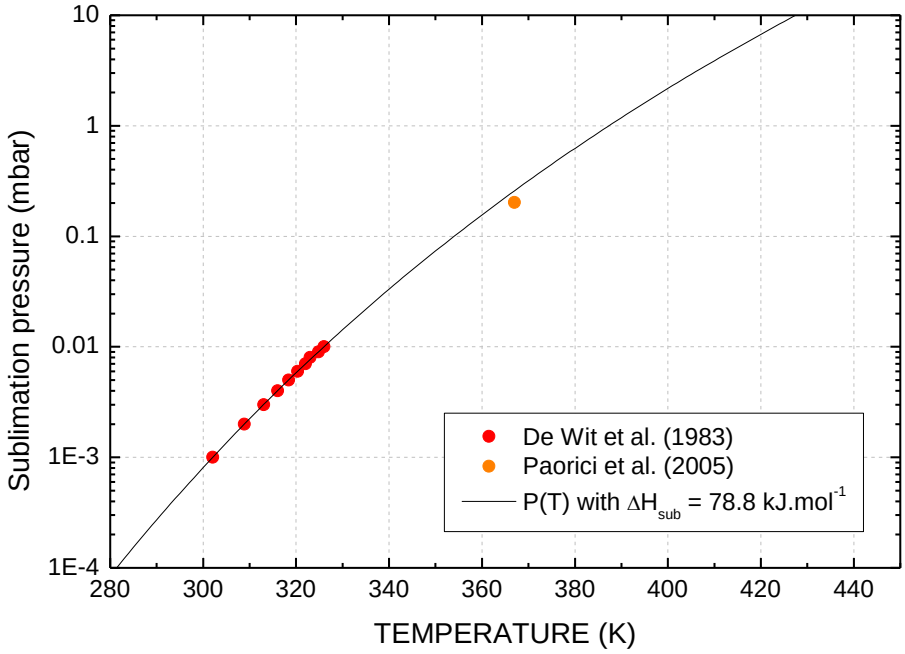

Figure 11: pure HMT sublimation curve (see text for details). Dots are the values measured by De Wit et al. (1983) and Paorici et al. (2005). The value of sublimation enthalpy (ΔH_S = 78.8 kJ/mol) comes from De Wit et al. (1983).

At 300 K, the vapor pressure of pure HMT is about 10^{-3} mbar. At the end of the 300 K time interval (16 hours), we observed no gaseous HMT (Fig. 6b and 9b). Solid HMT is present in the organic residue at 300 K whereas the pressure in the vacuum chamber is lower than the sublimation pressure of pure HMT by several orders of magnitude, as previously reported (Bernstein et al., 1995; Muñoz Caro et al., 2004). This shows: 1) that the kinetics of HMT sublimation is greatly changed by the fact that HMT is part of the organic residue matrix; and 2) that the interactions between HMT and others molecules of the organic residue, via hydrogen bonds or Van der Waals forces, are quite strong and prevent the HMT sublimation. The comparison between the behavior of HMT as pure compound and embedded in an organic matrix show that the sublimation or thermal desorption of HMT depends of its environment.

We observe that HMT production in the solid phase and HMT sublimation are simultaneous processes when the temperature increases above 300 K. The most obvious case is the 300-350 K temperature increment in Exp#1, during which we observe an increase of both solid and gaseous HMT (Fig 6a and 6b). In order to roughly estimate the intensity of both processes we can compare the integral of the mass peak at m/z = 140 over the time of each temperature step with the variation of the column density observed from infrared spectra. For Exp#1, the integral of the m/z = 140 mass peak is about 2.2×10^{-9} A s, 4.9×10^{-9} A s and 3.6×10^{-9} A s for the 350, 400, and 450 K time intervals, respectively. During the same time intervals, considering that the surface of the sample holder is about 1 cm^2, we observed that the variations of the number of HMT molecules are about $+2\times10^{16}$ molecules, -0.7×10^{16} molecules and -8.2×10^{16} molecules. Careful examination of the last infrared spectra measured at 400 K and 450 K show that there is no more HMT production during the 400-450 K temperature step, contrary to the previous ones. We can therefore estimate that for the m/z = 140 peak an integrated signal of 3.6×10^{-9} A s correspond to the sublimation of about 8.2×10^{16} molecules. Thus, we can estimate that during the 350 K and 400 K temperature time intervals, about 5×10^{16} and 11×10^{16} HMT molecules, respectively, sublimate. Thus, during the 350 K temperature step, we have a production of about 7×10^{16} molecules of HMT. About 30% of this production is remaining in the solid phase while 70% sublimates. Similarly, during the 400 K temperature step, the decrease of solid HMT is about 0.7×10^{16} molecules and sublimation represents 11×10^{16} molecules, thus the production of HMT should be at least of 10×10^{16} molecules. All these numbers have to be considered as orders of magnitude; nevertheless they show that the sublimation is a very efficient process and that most of the HMT produced in the solid phase sublimates immediately. This conclusion is coherent with the fact that the sublimation pressure of pure HMT is several orders of magnitude higher than the pressure in the experimental setup at these temperatures. Moreover the production during the 350 K and 400 K temperature steps is of the same order than the production which has taken place for temperature below 300 K. It means that the precursors of HMT could be more abundant in the residue at 300 K than the HMT itself. Similar conclusion could be drawn from Exp#4, whereas in this second case it is possible that the production of HMT is still occurring during the 400-450 K increment.

The quantitative description of the kinetics of the thermal evolution of HMT in organic residues is important as it could be used to extrapolated laboratory results to astrophysical environment. Unfortunately, the complete description of the kinetics seems to be very complex as different mechanism of formation and sublimation take place simultaneously and as HMT sublimation clearly depends of the molecular environment via different interactions with the organic matrix in which it is embedded.

The peak at 1669 cm^{-1} is a major feature in the organic residue FTIR spectra at 300 K (Fig. 4). We note that this peak appears at the same time than the HMT ones for temperatures comprised between 260 and 300 K (see Fig. 7 of Vinogradoff et al., 2013). Thus, it is linked

to a product of a chemical reaction promoted by the temperature increase and cannot be attributed to a product of the initial VUV photolysis. The molecular attribution of this peak is quite difficult, but it could be identified as a C=O stretching. Bernstein et al. (1995) observed a peak at 1665 cm^{-1} in the organic residue synthesized from VUV photolysis and warming of a H_2O:NH_3:CH_3OH:CO=100:10:50:10 ice mixture. The authors assigned it to C=O stretching in primary amides (H_2N-C(=O)–R). Muñoz-Caro & Schutte (2003) observed a peak at 1680 cm^{-1} in the organic residue synthesized in a similar way, and they also assigned it to C=O stretching in amides. The precise molecular attribution of such feature in FTIR spectra is beyond the scopes of this work. However we qualitatively observe that it decreases with increasing temperature. In Exp#1 (Fig. 5) and Exp#4 (Fig. 8) its decrease is particularly evident when the temperature increases from 400 K to 450 K, when at the same time HMT is totally removed from the solid phase.

5. Implications for the search of HMT in comets

Our laboratory simulations indicate that HMT can be trapped up to 450 K in the solid organic residue produced by VUV photolysis of an H_2O, CH_3OH, NH_3 ice mixture, and up to 400 K when CO and CO_2 are added to the initial ice composition. Vinogradoff et al. (2013), which studied the low temperature (T < 300 K) evolution of the same organic residue (same as Exp#1), reported that HMT is formed in the solid phase only when the temperature reaches > 280 K in laboratory conditions. Theoretical calculations have shown that the last step of the HMT formation has an action barrier of 90 kJ mol^{-1} (Vinogradoff et al., 2012). The formation of HMT could take place at lower temperature but on large time scales. Preliminary kinetic results showed that the HMT formation would require ~5×10^4 years at 200 K

(Vinogradoff et al., 2013). These observations have crucial implications on the possible astrophysical contexts in which HMT may be present in the solid phase. HMT could not have been formed in materials that have always experienced very low temperature, and in materials heated at high temperature (T > 450 K) HMT would not be present because it sublimates. Consequently, HMT can be present in materials only which have been slightly heated, between 280 K and 400 K. Temperatures suitable for HMT formation were certainly reached in the nascent solar system. Since comets accreted materials from both the outer, cold solar system regions and the inner, warm regions, then cometary nuclei could contain a small fraction of HMT.

In this context, the upcoming cometary mission Rosetta is of primary importance, as it will perform *in situ* analyses of the nucleus and the environment of comet 67P/Churyumov-Gerasimenko, starting in 2014. If HMT was detected by the Rosetta mission in solid organic material of comet 67P/Churyumov-Gerasimenko, it would be a very strong indicator of its thermal history. Temperatures suitable for HMT formation were determined at the surface of the nucleus of comet 1P/Halley (320 K as mean value, 400 K as maximum value, (Emerich et al., 1987), and the nucleus of comet 19P/Borrelly (300 – 340 K, (Soderblom et al., 2004). However, similar temperatures can be experienced by dust grains ejected from the nucleus

(Fray et al., 2006). Therefore HMT could form directly from refractory organics in the cometary coma. On board Rosetta, the most promising instrument for the detection of organic species in solid phase is COSIMA

(Kissel et al., 2007). COSIMA is a high mass resolution, time-of-flight secondary ion mass spectrometer (TOF-SIMS) designed for the collection and the analysis of cometary grains in the coma. Preliminary calibration experiments performed with the ground model of

COSIMA on organic residues similar to the ones presented in this paper show that the HMT signature is highly specific and then detectable by COSIMA.

As we showed that HMT sublimation is an important process, the Rosetta mission should also search for HMT in the gas phase. We have to keep in mind that HMT can not be detected at sub-millimetric wavelengths by remote sensing measurements, because it belongs to the Td symmetry group (Jensen, 2002) and thus has no permanent dipole and no allowed rotational transition. Some attempts could be performed in the infrared range. Among the Rosetta instruments, the VIRTIS infrared spectrometer will investigate the coma gaseous species in the 1 – 5 µm wavelength range (Coradini et al., 2007). Nevertheless, the most sensitive Rosetta instrument for searching for HMT in the gas phase will be ROSINA, which consists in two mass spectrometers, one for neutrals species and the other one for primary ions (Balsiger et al., 2007). Moreover, it has also already been shown that COSAC, which is a gas chromatograph coupled to a mass spectrometer on board of the Rosetta lander, has the capability to detect HMT directly at the surface of the nucleus (Cottin et al., 2001).

Therefore, the Rosetta space mission will have the ability to search for direct evidence of cometary HMT in both solid and gaseous phases, using the COSIMA and ROSINA spectrometers, respectively. This simultaneous search will be of crucial importance to have an unambiguous detection of HMT. Indeed, as cometary grains collected by the COSIMA time-of-flight spectrometer will experience temperatures between 253 K and 303 K during several days before analysis

(Kissel et al., 2007), HMT could form inside the instrument. Therefore, the ROSINA measurements will be essential to have confirmation of any possible detection of HMT in the cometary solid phase by COSIMA.

7. Conclusions

We experimentally simulated the thermal evolution of refractory organic residues synthesized by photolysis and subsequent warming of astrophysical ice analogues. We investigated for the first time the thermal evolution of the refractory organic material heated up to 550 K. We focused our attention on HMT, a molecule often produced in this kind of experimental simulations but never observed in the interstellar medium or in comets, so far.

In laboratory conditions, HMT is formed in the solid organic residue from the protonated ion of trimethylenetriamine ($TMTH^+$) and its decomposition products at $T > 280$ K (Vinogradoff et al., 2013). We were able to show that such a process is still active at temperatures as high as 350 K. For temperature higher than 300 K the HMT amount inside the solid organic residue is reduced by sublimation, rather than by decomposition to other molecules. Solid HMT production and sublimation take place simultaneously and the amount of HMT observed in the solid phase can be only a minor fraction of the total production of HMT, as a major fraction of HMT could disappear from the organic residue by sublimation. The quantitative measurements of the kinetics of each process seem to be very complex.

An important parameter that drives the HMT thermal evolution is the molecular composition of the organic residue in which it is embedded. Depending on the composition of the residue, HMT could be present in solid phase up to 400 or 450 K. Therefore, in an astrophysical environment, HMT can be present in the solid phase only in a very narrow temperature range ($280 \text{ K} < T < 400 \text{ K}$).

The upcoming space mission Rosetta, which will study comet 67P/Churyumov-Gerasimenko for several months during its approach to the Sun, will investigate if HMT is present in this comet. Solid cometary grains ejected from the nucleus will be analyzed by the COSIMA time-of-flight mass spectrometer. At the same time, the ROSINA spectrometer will

analyze the gas species in the coma. Thus, the Rosetta mission has the capacities to detect HMT in both the solid and gaseous phase. A detection of HMT will provide important indications on the thermal history of the cometary grains.

Acknowledgements

We would like to acknowledge UPEC (Université Paris-Est Créteil), INSU (Institut National des Sciences de l'Univers) and EPOV CNRS program (Environnements planétaires et origines de la vie) for funding in support of the OREGOC experiment. G.B. was supported by an UPEC position. This study was supported by the *Centre National d'Etudes Spatiales* (CNES), in the framework of the ROSETTA/COSIMA instrument project. We also thank V. Vinogradoff and F. Duvernay for providing us their infrared spectrum of PMI.

References

Balsiger, H., Altwegg, K., Bochsler, P., Eberhardt, P., Fischer, J., Graf, S., Jäckel, A., Kopp, E., Langer, U., Mildner, M., Müller, J., Riesen, T., Rubin, M., Scherer, S., Wurz, P., Wüthrich, S., Arijs, E., Delanoye, S., Keyser, J., Neefs, E., Nevejans, D., Rème, H., Aoustin, C., Mazelle, C., Médale, J.-L., Sauvaud, J., Berthelier, J.-J., Bertaux, J.-L., Duvet, L., Illiano, J.-M., Fuselier, S., Ghielmetti, A., Magoncelli, T., Shelley, E., Korth, A., Heerlein, K., Lauche, H., Livi, S., Loose, A., Mall, U., Wilken, B., Gliem, F., Fiethe, B., Gombosi, T., Block, B., Carignan, G., Fisk, L., Waite, J., Young, D. & Wollnik, H. (2007), 'Rosina – rosetta orbiter spectrometer for ion and neutral analysis', *Space Science Reviews* **128**, 745–801.

Bernstein, M. P., Sandford, S. A., Allamandola, L. J., Chang, S. & Scharberg, M. A. (1995), 'Organic Compounds Produced by Photolysis of Realistic Interstellar and Cometary Ice Analogs Containing Methanol', *Astrophysical Journal* **454**, 327–344.

Bertie, J. E. & Solinas, M. (1974), 'Infrared and raman spectra and the vibrational assignment of hexamethylenetetramine-h_{12} and -d_{12}', *Journal of Chemical Physics* **61**, 1666.

Bockelée-Morvan, D., Crovisier, J., Mumma, M. J. & Weaver, H. A. (2004), The composition of cometary volatiles, *in* M. C. Festou, H. U. Keller & H. A. Weaver, eds, 'Comets II', pp. 391–423.

Bossa, J. B., Duvernay, F., Theule, P., Borget, F., d'Hendecourt, L. & Chiavassa, T. (2009), 'Methylammonium methylcarbamate thermal formation in interstellar ice analogs: a glycine salt precursor in protostellar environments.', *Astronomy & Astrophysics* **506**, 601–608.

Bradley, J. P. (2003), Interplaneary Dust Particles, *in* A. M. Davis, H. D. Holland & K. K. Turekian, eds, 'Treatise on Geochemistry', Vol. 1, pp. 689–711.

Brownlee, D. E. (2003), Comets, *in* A. M. Davis, H. D. Holland & K. K. Turekian, eds, 'Treatise on Geochemistry', Vol. 1, pp. 663–688.

Chyba, C. F., Thomas, P. J., Brookshaw, L. & Sagan, C. (1990), 'Cometary delivery of organic molecules to the early earth', *Science* **249**, 366–373.

Clemett, S. J., Maechling, C. R., Zare, R. N., Swan, P. D. & Walker, R. M. (1993), 'Identification of Complex Aromatic Molecules in Individual Interplanetary Dust Particles', *Science* **262**, 721–725.

Colangeli, L., Brucato, J. R., Bar-Nun, A., Hudson, R. L. & Moore, M. H. (2004), Laboratory experiments on cometary materials, *in* M. C. Festou, H. U. Keller & H. A. Weaver, eds, 'Comets II', pp. 695–717.

Coradini, A., Capaccioni, F., Drossart, P., Arnold, G., Ammannito, E., Angrilli, F., Barucci, A., Bellucci, G., Benkhoff, J., Bianchini, G., Bibring, J. P., Blecka, M., Bockelee-Morvan, D., Capria, M. T., Carlson, R., Carsenty, U., Cerroni, P., Colangeli, L., Combes, M., Combi, M., Crovisier, J., De Sanctis, M. C., Encrenaz, E. T., Erard, S., Federico, C., Filacchione, G., Fink, U., Fonti, S., Formisano, V., Ip, W. H., Jaumann, R., Kuehrt, E., Langevin, Y., Magni, G., McCord, T., Mennella, V., Mottola, S., Neukum, G., Palumbo, P., Piccioni, G., Rauer, H., Saggin, B., Schmitt, B., Tiphene, D. & Tozzi, G. (2007), 'Virtis: An Imaging Spectrometer for the Rosetta Mission', *Space Science Review* **128**, 529–559.

Cottin, H. & Fray, N. (2008), 'Distributed Sources in Comets', *Space Science Reviews* **138**, 179–197.

Cottin, H., Gazeau, M. C. & Raulin, F. (1999), 'Cometary organic chemistry: a review from observations, numerical and experimental simulations', *Planetary and Space Science* **47**, 1141–1162.

Cottin, H., Szopa, C. & Moore, M. H. (2001), 'Production of Hexamethylenetetramine in Photolyzed and Irradiated Interstellar Cometary Ice Analogs', *The Astrophysical Journal* **561**, L139–L142.

Crovisier, J., Brooke, T. Y., Leech, K., Bockelée-Morvan, D., Lellouch, E., Hanner, M. S., Altieri, B., Keller, H. U., Lim, T., Encrenaz, S., Griffin, M., de Graauw, T., van Dishoeck, E. & Knacke, R. F. (2000), 'The Thermal Infrared Spectra of Comets Hale-Bopp and 103P/Hartley 2 Observed with the Infrared Space Observatory', *Thermal Emission Spectroscopy and Analysis of Dust, Disks, and Regoliths* **196**, 109–117.

Crovisier, J., Leech, K., Bockelee-Morvan, D., Brooke, T. Y., Hanner, M. S., Altieri, B., Keller, H. U. & Lellouch, E. (1997), 'The spectrum of Comet Hale-Bopp (C/1995 01) observed with the Infrared Space Observatory at 2.9 AU from the Sun', *Science* **275**, 1904–1907.

Dartois, E. (2005), 'The Ice Survey Opportunity of ISO', *Space Science Reviews* **119**, 293–310.

Davidson, J., Busemann, H. & Franchi, I. A. (2012), 'A NanoSIMS and Raman spectroscopic comparison of interplanetary dust particles from comet Grigg-Skjellerup and non-Grigg Skjellerup collections', *Meteoritics and Planetary Science* **47**, 1748–1771.

Davis, D. & Braun, W. (1968), 'Intense vacuum ultraviolet atomic line sources', *Applied Optics* **7**, 2071–2074.

De Wit, H. G. M., Van Miltenburg, J. C. & De Kruif, C. G. (1983), 'Thermodynamic properties of molecular organic crystals containing nitrogen, oxygen, and sulphur 1. vapour pressures and enthalpies of sublimation', *The Journal of Chemical Thermodynamics* **15**, 651 – 663.

Dobrică, E., Engrand, C., Quirico, E., Montagnac, G. & Duprat, J. (2011), 'Raman characterization of carbonaceous matter in CONCORDIA Antarctic micrometeorites', *Meteoritics and Planetary Science* **46**, 1363–1375.

Duprat, J., Dobrică, E., Engrand, C., Aléon, J., Marrocchi, Y., Mostefaoui, S., Meibom, A., Leroux, H., Rouzaud, J.-N., Gounelle, M. & Robert, F. (2010), 'Extreme deuterium excesses in ultracarbonaceous micrometeorites from central antarctic snow', *Science* **328**, 742–745.

Elsila, J. E., Glavin, D. P. & Dworkin, J. P. (2009), 'Cometary glycine detected in samples returned by Stardust', *Meteoritics and Planetary Science* **44**, 1323–1330.

Emerich, C., Lamarre, J. M., Moroz, V. I., Combes, M., Sanko, N. F., Nikolsky, Y. V., Rocard, F., Gispert, R., Coron, N., Bibring, J. P., Encrenaz, T. & Crovisier, J. (1987), 'Temperature and Size of the Nucleus of Comet p/ Halley Deduced from IKS Infrared VEGA-1 Measurements', *Astronomy & Astrophysics* **187**, 839.

Floss, C., Stadermann, F. J., Bradley, J. P., Dai, Z. R., Bajt, S., Graham, G. & Lea, A. S. (2006), 'Identification of isotopically primitive interplanetary dust particles: A NanoSIMS isotopic imaging study', *Geochimica et Cosmochimica Acta* **70**, 2371–2399.

Flynn, G. J. (2008), 'Physical, Chemical, and Mineralogical Properties of Comet 81P/Wild 2 Particles Collected by Stardust', *Earth Moon and Planets* **102**, 447–459.

Flynn, G., Keller, L. P., Jacobsen, C., Wirick, S. & Miller, M. A. (2000), Organic Carbon in Interplanetary Dust Particles, *in* G. Lemarchand & K. Meech, eds, 'Bioastronomy 99', Vol. 213 of *Astronomical Society of the Pacific Conference Series*, pp. 191–194.

Fomenkova, M. N. (1999), 'On the Organic Refractory Component of Cometary Dust', *Space Science Reviews* **90**, 109–114.

Fomenkova, M. N., Chang, S. & Mukhin, L. M. (1994), 'Carbonaceous components in the comet Halley dust', *Geochimica et Cosmochimica Acta* **58**, 4503–4512.

Fray, N., Bénilan, Y., Biver, N., Bockelée-Morvan, D., Cottin, H., Crovisier, J. & Gazeau, M.-C. (2006), 'Heliocentric evolution of the degradation of polyoxymethylene: Application to the origin of the formaldehyde (H_2CO) extended source in Comet C/1995 O1 (Hale Bopp)', *Icarus* **184**, 239–254.

Fray, N., Bénilan, Y., Cottin, H. & Gazeau, M.-C. (2004), 'New experimental results on the degradation of polyoxymethylene: Application to the origin of the formaldehyde extended source in comets', *Journal of Geophysical Research (Planets)* **109**, 7.

Gerakines, P. A., Schutte, W. A., Greenberg, J. M. & van Dishoeck, E. F. (1995), 'The infrared band strengths of H_2O, CO and CO_2 in laboratory simulations of astrophysical ice mixtures.', *Astronomy & Astrophysics* **296**, 810.

Gibb, E. L., Whittet, D. C. B., Boogert, A. C. A. & Tielens, A. G. G. M. (2004), 'Interstellar Ice: The Infrared Space Observatory Legacy', *The Astrophysical Journal Supplement Series* **151**, 35–73.

Gounelle, M. (2011), 'The asteroid-comet continuum: in search of lost primitivity', *Elements* **7**, 29–34.

Greenberg, J. M. (1982), *What are comets made of? A model based on interstellar dust*, University of Arizona Press, pp. 131–163.

Hanner, M. S. & Bradley, J. P. (2004), Composition and mineralogy of cometary dust, *in* M. C. Festou, H. U. Keller & H. A. Weaver, eds, 'Comets II', pp. 555–564.

Jensen, J. O. (2002), 'Vibrational frequencies and structural determinations of hexamethylenetetraamine', *Spectrochimica Acta Part A: Molecular and Biomolecular Spectroscopy* **58**, 1347–1364.

Keller, L. P., Bajt, S., Baratta, G. A., Borg, J., Bradley, J. P., Brownlee, D. E., Busemann, H., Brucato, J. R., Burchell, M., Colangeli, L., D'Hendecourt, L., Djouadi, Z., Ferrini, G., Flynn, G., Franchi, I. A., Fries, M., Grady, M. M., Graham, G. A., Grossemy, F., Kearsley, A., Matrajt, G., Nakamura-Messenger, K., Mennella, V., Nittler, L., Palumbo, M. E., Stadermann, F. J., Tsou, P., Rotundi, A., Sandford, S. A., Snead, C., Steele, A., Wooden, D. & Zolensky, M. (2006), 'Infrared Spectroscopy of Comet 81P/Wild 2 Samples Returned by Stardust', *Science* **314**, 1728–1731.

Kissel, J., Altwegg, K., Clark, B. C., Colangeli, L., Cottin, H., Czempiel, S., Eibl, J., Engrand, C., Fehringer, H. M., Feuerbacher, B., Fomenkova, M., Glasmachers, A., Greenberg, J. M., Grün, E., Haerendel, G., Henkel, H., Hilchenbach, M., von Hoerner, H., Höfner, H., Hornung, K., Jessberger, E. K., Koch, A., Krüger, H., Langevin, Y., Parigger, P., Raulin, F., Rüdenauer, F., Rynö, J., Schmid, E. R., Schulz, R., Silén, J., Steiger, W., Stephan, T., Thirkell, L., Thomas, R., Torkar, K., Utterback, N. G., Varmuza, K., Wanczek, K. P., Werther, W. & Zscheeg, H. (2007), 'Cosima High Resolution Time-of-Flight Secondary Ion Mass Spectrometer for the Analysis of Cometary Dust Particles onboard Rosetta', *Space Science Reviews* **128**, 823–867.

Kissel, J., Brownlee, D. E., Buchler, K., Clark, B. C., Fechtig, H., Grun, E., Hornung, K., Igenbergs, E. B., Jessberger, E. K., Krueger, F. R., Kuczera, H., McDonnell, J. A. M., Morfill, G. M., Rahe, J., Schwehm, G. H., Sekanina, Z., Utterback, N. G., Volk, H. J. & Zook, H. A. (1986a), 'Composition of comet Halley dust particles from Giotto observations', **321**, 336.

Kissel, J., Krueger, F. R., Silén, J. & Clark, B. C. (2004), 'The Cometary and Interstellar Dust Analyzer at Comet 81P/Wild 2', *Science* **304**, 1774–1776.

Kissel, J., Sagdeev, R. Z., Bertaux, J. L., Angarov, V. N., Audouze, J., Blamont, J. E., Buchler, K., Evlanov, E. N., Fechtig, H., Fomenkova, M. N., von Hoerner, H., Inogamov, N. A., Khromov, V. N., Knabe, W., Krueger, F. R., Langevin, Y., Leonasv, B., Levasseur-Regourd, A. C., Managadze, G. G., Podkolzin, S. N., Shapiro, V. D.,

Tabaldyev, S. R. & Zubkov, B. V. (1986b), 'Composition of comet Halley dust particles from VEGA observations', *Nature* **321**, 280–282.

Kolokolova, L., Hanner, M. S., Levasseur-Regourd, A.-C. & Gustafson, B. Å. S. (2004), Physical properties of cometary dust from light scattering and thermal emission, *in* M. C. Festou, H. U. Keller & H. A. Weaver, eds, 'Comets II', pp. 577–604.

Le Roy, L., Briani, G., Briois, C., Cottin, H., Fray, N., Thirkell, L., Poulet, G. & Hilchenbach, M. (2012), 'On the prospective detection of polyoxymethylene in comet 67P/Churyumov-Gerasimenko with the COSIMA instrument onboard Rosetta', *Planetary & Space Science* **65**, 83–92.

Lellouch, E., Crovisier, J., Lim, T., Bockelee-Morvan, D., Leech, K., Hanner, M. S., Altieri, B., Schmitt, B., Trotta, F. & Keller, H. U. (1998), 'Evidence for water ice and estimate of dust production rate in comet Hale-Bopp at 2.9 AU from the Sun', *Astronomy & Astrophysics* **339**, L9–L12.

Mason, N. J., Dawes, A., Holtom, P. D., Mukerji, R. J., Davis, M. P., Sivaraman, B., Kaiser, R. I., Hoffmann, S. V. & Shaw, D. A. (2006), 'VUV spectroscopy and photo-processing of astrochemical ices: an experimental study', *Faraday Discussions* **133**, 311.

Matrajt, G., Messenger, S., Brownlee, D. & Joswiak, D. (2012), 'Diverse forms of primordial organic matter identified in interplanetary dust particles', *Meteoritics and Planetary Science* **47**, 525–549.

Meinert, C., Filippi, J.-J., de Marcellus, P., Le Sergeant d'Hendecourt, L. & Meierhenrich, U. J. (2012), 'N-(2-aminoethyl)glycine and amino acids from interstellar ice analogues', *ChemPlusChem* **77**(3), 186–191.

Muñoz Caro, G. M., Meierhenrich, U., Schutte, W. A., Thiemann, W. H.-P. & Greenberg, J. M. (2004), 'UV-photoprocessing of interstellar ice analogs: Detection of hexamethylenetetramine-based species', *Astronomy & Astrophysics* **413**, 209–216.

Muñoz Caro, G. M. & Schutte, W. A. (2003), 'UV-photoprocessing of interstellar ice analogs: New infrared spectroscopic results', *Astronomy & Astrophysics* **412**, 121–132.

Paorici, C., Zha, M., Razzetti, C., Zanotti, L., Bassano, E. & Castagnolo, D. (2005), 'Progressive growth rate reduction due to impurity desorption in vapor grown hexamethylenetetramine crystals', *Crystal Research and Technology* **40**, 1076–1081.

Sandford, S. A., Aléon, J., Alexander, C. M. O. D., Araki, T., Bajt, S., Baratta, G. A., Borg, J., Bradley, J. P., Brownlee, D. E., Brucato, J. R., Burchell, M. J., Busemann, H., Butterworth, A., Clemett, S. J., Cody, G., Colangeli, L., Cooper, G., D'Hendecourt, L., Djouadi, Z., Dworkin, J. P., Ferrini, G., Fleckenstein, H., Flynn, G. J., Franchi, I. A., Fries, M., Gilles, M. K., Glavin, D. P., Gounelle, M., Grossemy, F., Jacobsen, C., Keller, L. P., Kilcoyne, A. L. D., Leitner, J., Matrajt, G., Meibom, A., Mennella, V., Mostefaoui, S., Nittler, L. R., Palumbo, M. E., Papanastassiou, D. A., Robert, F., Rotundi, A., Snead, C. J., Spencer, M. K., Stadermann, F. J., Steele, A., Stephan, T., Tsou, P., Tyliszczak, T., Westphal, A. J., Wirick, S., Wopenka, B., Yabuta, H., Zare, R. N. & Zolensky, M. E. (2006), 'Organics Captured from Comet 81P/Wild 2 by the Stardust Spacecraft', *Science* **314**, 1720–1724.

Sandford, S. A., Bajt, S., Clemett, S. J., Cody, G. D., Cooper, G., Degregorio, B. T., de Vera, V., Dworkin, J. P., Elsila, J. E., Flynn, G. J., Glavin, D. P., Lanzirotti, A., Limero, T., Martin, M. P., Snead, C. J., Spencer, M. K., Stephan, T., Westphal, A., Wirick, S., Zare, R. N. & Zolensky, M. E. (2010), 'Assessment and control of organic and other contaminants associated with the Stardust sample return from comet 81P/Wild 2', *Meteoritics and Planetary Science* **45**, 406–433.

Schutte, C. J. H. & Buijs, K. (1964), 'The infra-red spectrum of the formate ion', *Spectrochimica Acta* **20**, 187–195.

905 Schutte, W. A., Boogert, A. C. A., Tielens, A. G. G. M., Whittet, D. C. B., Gerakines, P. A.,
906 Chiar, J. E., Ehrenfreund, P., Greenberg, J. M., van Dishoeck, E. F. & de Graauw, T.
907 (1999), 'Weak ice absorption features at 7.24 and 7.41 MU M in the spectrum of the
908 obscured young stellar object W 33A', *Astronomy & Astrophysics* **343**, 966–976.
909 Soderblom, L. A., Britt, D. T., Brown, R. H., Buratti, B. J., Kirk, R. L., Owen, T. C. & Yelle,
910 R. V. (2004), 'Short-wavelength infrared (1.3-2.6 μm) observations of the nucleus of
911 Comet 19P/Borrelly', *Icarus* **167**, 100–112.
912 Sunshine, J. M., A'Hearn, M. F., Groussin, O., Li, J.-Y., Belton, M. J. S., Delamere, W. A.,
913 Kissel, J., Klaasen, K. P., McFadden, L. A., Meech, K. J., Melosh, H. J., Schultz,
914 P. H., Thomas, P. C., Veverka, J., Yeomans, D. K., Busko, I. C., Desnoyer, M.,
915 Farnham, T. L., Feaga, L. M., Hampton, D. L., Lindler, D. J., Lisse, C. M. & Wellnitz,
916 D. D. (2006), 'Exposed Water Ice Deposits on the Surface of Comet 9P/Tempel 1',
917 *Science* **311**, 1453–1455.
918 Vinogradoff, V., Duvernay, F., Danger, G., Theulé, P. & Chiavassa, T. (2011), 'New insight
919 into the formation of hexamethylenetetramine (HMT) in interstellar and cometary ice
920 analogs', *Astronomy & Astrophysics* **530**, A128.
921 Vinogradoff, V., Fray, N., Duvernay, F., Briani, G., Danger, G., Cottin, H., Theulé, P. &
922 Chiavassa, T. (2013), 'Importance of thermal reactivity for hexamethylenetetramine
923 formation from simulated interstellar ices', *Astronomy & Astrophysics* **551**, A128.
924 Vinogradoff, V., Rimola, A., Duvernay, F., Danger, G., Theulé, P. & Chiavassa, T. (2012),
925 'The mechanism of hexamethylenetetramine (HMT) formation in the solid state at low
926 temperature', *Physical Chemistry Chemical Physics (Incorporating Faraday*
927 *Transactions)* **14**, 12309.
928 Warneck, P. (1962), 'A microwave-powered hydrogen lamp for vacuum ultraviolet
929 photochemical research', *Applied Optics* **1**, 721–726.
930 Wooden, D., Desch, S., Harker, D., Gail, H.-P. & Keller, L. (2007), Comet Grains and
931 Implications for Heating and Radial Mixing in the Protoplanetary Disk, *in* B. Reipurth,
932 D. Jewitt & K. Keil, eds, 'Protostars and Planets V', pp. 815–833.
933 Zolensky, M. E., Zega, T. J., Yano, H., Wirick, S., Westphal, A. J., Weisberg, M. K., Weber,
934 I., Warren, J. L., Velbel, M. A., Tsuchiyama, A., Tsou, P., Toppani, A., Tomioka, N.,
935 Tomeoka, K., Teslich, N., Taheri, M., Susini, J., Stroud, R., Stephan, T., Stadermann,
936 F. J., Snead, C. J., Simon, S. B., Simionovici, A., See, T. H., Robert, F., Rietmeijer,
937 F. J. M., Rao, W., Perronnet, M. C., Papanastassiou, D. A., Okudaira, K., Ohsumi, K.,
938 Ohnishi, I., Nakamura-Messenger, K., Nakamura, T., Mostefaoui, S., Mikouchi, T.,
939 Meibom, A., Matrajt, G., Marcus, M. A., Leroux, H., Lemelle, L., Le, L., Lanzirotti,
940 A., Langenhorst, F., Krot, A. N., Keller, L. P., Kearsley, A. T., Joswiak, D., Jacob, D.,
941 Ishii, H., Harvey, R., Hagiya, K., Grossman, L., Grossman, J. N., Graham, G. A.,
942 Gounelle, M., Gillet, P., Genge, M. J., Flynn, G., Ferroir, T., Fallon, S., Ebel, D. S.,
943 Dai, Z. R., Cordier, P., Clark, B., Chi, M., Butterworth, A. L., Brownlee, D. E.,
944 Bridges, J. C., Brennan, S., Brearley, A., Bradley, J. P., Bleuet, P., Bland, P. A. &
945 Bastien, R. (2006), 'Mineralogy and Petrology of Comet 81P/Wild 2 Nucleus
946 Samples', *Science* **314**, 1735–1739.
947